
MAGNESIUM ALLOYS - CORROSION AND SURFACE TREATMENTS

Edited by **Frank Czerwinski**

INTECHWEB.ORG

Magnesium Alloys - Corrosion and Surface Treatments

Edited by Frank Czerwinski

Published by InTech

Janeza Trdine 9, 51000 Rijeka, Croatia

Copyright © 2011 InTech

All chapters are Open Access articles distributed under the Creative Commons Non Commercial Share Alike Attribution 3.0 license, which permits to copy, distribute, transmit, and adapt the work in any medium, so long as the original work is properly cited. After this work has been published by InTech, authors have the right to republish it, in whole or part, in any publication of which they are the author, and to make other personal use of the work. Any republication, referencing or personal use of the work must explicitly identify the original source.

Statements and opinions expressed in the chapters are these of the individual contributors and not necessarily those of the editors or publisher. No responsibility is accepted for the accuracy of information contained in the published articles. The publisher assumes no responsibility for any damage or injury to persons or property arising out of the use of any materials, instructions, methods or ideas contained in the book.

Publishing Process Manager Iva Lipovic

Technical Editor Teodora Smiljanic

Cover Designer Martina Sirotic

Image Copyright Leigh Prather, 2010. Used under license from Shutterstock.com

First published January, 2011

Printed in India

A free online edition of this book is available at www.intechopen.com

Additional hard copies can be obtained from orders@intechweb.org

Magnesium Alloys - Corrosion and Surface Treatments, Edited by Frank Czerwinski

p. cm.

ISBN 978-953-307-972-1

INTECH OPEN ACCESS
PUBLISHER

INTECH open

free online editions of InTech
Books and Journals can be found at
www.intechopen.com

Contents

Preface IX

- Chapter 1 **Thermally-Formed Oxide on Magnesium and Magnesium Alloys 1**
Teng-Shih, SHIH, Jyun-Bo LIU and Pai-Sheng WEI
- Chapter 2 **Oxidation Resistance of AM60, AM50, AE42 and AZ91 Magnesium Alloys 15**
Jožef Medved, Primož Mrvar and Maja Vončina
- Chapter 3 **In Situ Ellipsometric Study on Corrosion of Magnesium Alloys 29**
Lingjie LI, Jinglei LEI and Fusheng PAN
- Chapter 4 **Environmental Friendly Corrosion Inhibitors for Magnesium Alloys 47**
Jinglei LEI, Lingjie LI and Fusheng PAN
- Chapter 5 **Electrochemical Corrosion Behavior of Magnesium Alloys in Biological Solutions 65**
Amany Mohamed Fekry
- Chapter 6 **Magnesium Alloys as Promising Degradable Implant Materials in Orthopaedic Research 93**
Janin Reifenrath, Dirk Bormann and Andrea Meyer-Lindenberg
- Chapter 7 **Mg Alloys Development and Surface Modification for Biomedical Application 109**
Shaokang Guan, Junhua Hu, Liguang Wang, Shijie Zhu, Huanxin Wang, Jun Wang, Wen Li, Zhenwei Ren, Shuai Chen, Erchao Meng, Junheng Gao, Shusen Hou, Bin Wang and Binbn Chen
- Chapter 8 **Electroless and Electrochemical Deposition of Metallic Coatings on Magnesium Alloys Critical Literature Review 153**
Massimiliano Bestetti and Anna Da Forno

- Chapter 9 **Corrosion Protection of Magnesium Alloys by Cold Spray** 185
Julio Villafuerte and Wenyue Zheng
- Chapter 10 **Protective Coatings for Magnesium Alloys** 195
Stephen Abela
- Chapter 11 **Anodization of Magnesium Alloys Using Phosphate Solution** 221
Koji Murakami, Makoto Hino and Teruto Kanadani
- Chapter 12 **Improvement in Corrosion Fatigue Resistance of Mg Alloy due to Plating** 237
Sotomi Ishihara, Hisakimi Notoya and Tomonori Namito
- Chapter 13 **High Functionalization of Magnesium Alloy Surface by Superhydrophobic Treatment** 261
Takahiro Ishizaki, SunHyung Lee and Katsuya Teshima
- Chapter 14 **Application of Positron Annihilation Spectroscopy to Studies of Subsurface Zones Induced by Wear in Magnesium and its Alloy AZ31** 289
Jerzy Dryzek and Ewa Dryzek
- Chapter 15 **DLC Coating on Magnesium Alloy Sheet by Low-Temperature Plasma for Better Formability** 305
Yu IRIYAMA and Shoichiro YOSHIHARA
- Chapter 16 **Instrumental Chemical Analysis of Magnesium and Magnesium Alloys** 327
Michihisa Uemoto

Preface

The traditional application market of magnesium alloys is in automotive and aerospace industries where weight reduction is vital for economy of fuel consumption. It is believed that the transport industry needs magnesium to survive in sustainable world. Consumer electronics is an emerging market, exploring magnesium for housings of computers, cellular phones, cameras and other telecommunication hand-held devices. The small size and low weight of consumer electronics products is compensated by their high yearly demand reaching hundreds of millions of pieces, frequent upgrades requiring a model change and overall annual growth. Similar features fuel a use of magnesium in household and leisure products. Furthermore, magnesium application continues to increase in bio-materials sector. Magnesium alloys are biocompatible and research shows significant progress on bioabsorbable magnesium stents and orthopedic hardware. Resorbable magnesium alloy implants for osteosynthetic surgery would be advantageous to common implants of titanium or surgical steel thus eliminating a need of second surgery for implant removal.

A resistance to surface degradation at room and elevated temperatures is paramount for majority magnesium applications. High reactivity of magnesium and limited surface stability still represent major drawback in application expansion and create a serious challenge for scientists and engineers. As in the case of other metals, a basic distinction is made between high temperature oxidation and room temperature corrosion. Although typical service temperatures of magnesium parts are relatively low, the alloy processing and component manufacturing stages frequently require heat treatment may cause extensive oxidation. In general, room temperature corrosion of magnesium alloys is affected by the same factors important to other metals. However, the particular effect of corrosive environments of gases, sea water, engine coolant or human-body fluids is unique for magnesium alloys. A separate issue represents electrochemical corrosion where due to low electro-negativity of magnesium it is easily attacked in industrial joints. Hence, surface protection techniques for magnesium alloys are essential.

An emphasis of this book is on magnesium oxidation, corrosion and surface modifications, aimed at enhancement of alloy surface stability. First two chapters provide description of high temperature oxidation with details of oxide structures and oxidation characteristics of several commercial alloys. Following chapters cover elements of general corrosion, methods of its investigation and corrosion inhibitors. The subject of magnesium degradation in human-body fluids that controls medical applications for surgical implants, exploring bio-compatibility of magnesium alloys, is described

in subsequent three chapters. Several final chapters are devoted to methods of surface modification and coatings, designed to improve corrosion resistance, corrosion fatigue, wear and other properties. Each chapter contains a rich selection of references, useful for further reading.

A mixture of theory and technological details makes the book a valuable resource for professionals from both academia and industry, primarily dealing with light metals and magnesium alloys. I anticipate this book will also attract readers from outside the magnesium field and allow them to understand application opportunities created by this unique light metal.

December 2010

Frank Czerwinski
Bolton, Ontario,
Canada

FCzerwinski@sympatico.ca

Thermally-Formed Oxide on Magnesium and Magnesium Alloys

Teng-Shih, SHIH, Jyun-Bo LIU and Pai-Sheng WEI
National Central University (Department of Mechanical Engineering)
Taiwan (R.O.C)

1. Introduction

Magnesium alloys are commonly used in making automobile parts or by the communication industry due to their unique properties, such as low density, good damping capacity and ease of manufacturing. Magnesium alloys are very active and often cause fire hazards or surface degradation during the manufacturing processes, such as machining, melting or heat treatment. Understanding the combustion characteristics of different Mg alloys is necessary and of industrial interest.

Shih *et al.* (2002) studied the combustion of AZ61A alloys in different gases. They outlined possible reactions between Mg and O₂, CO₂ and CO based on their observations. Decreasing CO₂/Ar decreases the amount of heat derived from the oxidation reaction. Shih *et al.* also used a modified type of thermal analysis to study the combustion of magnesium alloyed with calcium or aluminum (Shih *et al.*, 2004). A Mg-5Ca alloy cake was ignition-proof up to 1000 K, while the solution-treated AZ91D alloy cake could also remain ignition-proof up to 1000 K during heating. The CaO oxide layer was dense so served to provide good thermal stability for the Mg-5Ca alloy. The oxide layer that formed on the surface of the solution-treated AZ91D was mainly composed of MgAl₂O₄ spinels, and it was this which improved the thermal stability of the solution-treated AZ91D.

Czerwinski (2002) studied the oxidation of AZ91D alloys via TGA test results. Samples were heated from 470 to 800 K. The oxidation process could be divided into three different periods: the protective layer, incubation and non-protective periods. The protective behavior was not discussed but the non-protective behavior was associated with the formation of oxide nodules and their coalescence into a loose fine-grained structure.

Zeng *et al.* (2001) studied the Auger depth profiles of AZB91 (Mg-9Al-0.5Zn-0.3Be) alloys heated at 923 and 1043 K for 10 s. For the AZ91 alloy with added Be, MgO should form prior to BeO at 923 K due to a high mole concentration ratio of Mg to Be. Beryllium possesses a lower density than magnesium (1.65 g/ml versus 1.74 g/ml) and tends to enrich its concentration beneath the top oxide layer (MgO). If the beryllium concentration is higher than 2.3 at%, BeO would form and become attached to the upper layer (or subsurface) decreasing the Be concentration in the nearby melt, where the Al concentration would gradually increase. Spinel possesses a lower free energy than BeO (-1878.75 kJ/mol versus -511.08 kJ/mol). This means that the inner layer is composed of complex oxides of MgO, BeO and spinel. The BeO possesses a low thermal expansion coefficient (17.8×10^{-6} at 298 K and $31.7 \times 10^{-6} \text{ K}^{-1}$ at 1000 K) compared with that of MgO ($44.3 \times 10^{-6} \text{ K}^{-1}$ from 993 to 1933

K) (Fei In *et al.*, 1995). Consequently, the duplex oxide of BeO and spinel existing in the inner layer enhances the thermal stability of the oxide film and thus reduce the possibility of microcracks formation. Houska showed that adding 0.001 wt.% of Beryllium could delay the combustion of Mg by about 200 K (Houska, 1988). Foerster (1998) found that adding 3–8 ppm Beryllium could greatly improve the oxidation resistance of the Mg alloy. Czerwinski (2004) used TGA to study the oxidation and evaporation behavior of AZ91D magnesium alloys with 5 and 10 ppm of beryllium at temperatures between 473 and 773 K. He found that the addition of beryllium delayed the transformation from protective to non-protective behavior. In addition, in an inert atmosphere, increasing the beryllium content reduced the magnesium evaporation rate.

In this study, we discuss the morphology of a thermally formed Mg oxide layer using TGA analysis and SEM observation. We then address the protective behavior of SF₆ during the heating and melting of pure Mg. The oxide films grew on AZ91 melt and heated AZ80 cake was compared and discussed.

2. Experimental procedure

Samples of pure Mg (99.9 wt.%) in size 5 mm × 5 mm × 10 mm were prepared. Each sample was polished by p400–2000 abrasive papers without lubricants to minimize the effect of amorphous oxide formation. The samples were then promptly removed to a muffle furnace and heated under different atmospheres at 700 K for two time spans of 1 and 25 h, respectively. For growing thermal oxides on the pure magnesium sample, air mixed with and without 2% SF₆ was used as the surrounding protective atmospheres. The heated pure Mg samples grew thermal oxides on their surfaces during heating. After being cooled to room temperature, the samples were sectioned and polished and to SEM and optical observations.

A Perkin-Elmer (TGA-7) apparatus was utilized to record the thermogravimetric analysis of the pure magnesium 5 mm × 5 mm × 5 mm specimens. The weight change when the sample was heated in an air atmosphere with a flow rate of 50 cm³/min was measured. The specimen was preheated up to 423 K at a heating rate of 10 K/min, then held for a period of 1800 s. It was then heated to the reaction temperature of 700 K at a heating rate of 10 K/min and held for 2.16×10^4 s.

Electron Spectroscopy for Chemical Analysis (ESCA, Thermo VG Scientific Sigma Probe) was used to analyze the composition of the surface oxides. The relationship of the composition-depth profiles was obtained by using a 3 keV argon ion beam at 0.1 cm⁻². The chemical composition of the thermally formed oxide layer was also checked by using an Electron Probe Micro Analyzer (EPMA, Joel JXA-8600SX). Experimental data for AZ91, from the work of (Zeng *et al.*, 2001), are also discussed.

3. Results and discussion

3.1 Thermogravimetric analysis at pure magnesium

The results of the thermogravimetric analysis of pure magnesium are recorded in Fig. 1. The data show a weight gain during the short time when the cubic sample was preheated at 423 K for 1800 s in an air atmosphere. When magnesium was heated in air, it became hydrated (>120 °C) to form brucite (Mg(OH)₂). However, brucite dehydration is reversible (brucite = periclase + water); this reaction can be shifted in either direction by increasing or decreasing

the water vapor pressure at the appropriate temperature (Sharma *et al.*, 2004) and (Schramke *et al.*, 1982). The weight change then decreased rapidly due to the dehydroxylation of brucite. The sample's weight stabilized when the temperature reached 700 K; see stage III in Fig. 1. After this stable period (or protective behavior), the weight again increased rapidly in stage IV, as shown in Fig. 1. When pure magnesium is placed in contact with oxygen, the following reactions occur: first, oxygen chemisorption on the surface of the magnesium, then the formation and coalescence of oxide islands, and finally oxide thickening. When there is water vapor, the reaction leads to the formation and growth of an oxide layer, but the reaction rate is much less than in an oxygen atmosphere, and the oxide layer will contain relatively large amounts of hydroxyl or hydroxide species (Splinter *et al.*, 1993) and (Fuggle *et al.*, 1975). The Gibbs free energy of brucite and periclase are -711.8 and -525.8 kJ/mol at 700 K, respectively (Robie *et al.*, 1978). When a pure magnesium sample is heated in an air atmosphere, brucite forms first, especially at low-temperatures. Brucite is then transformed to periclase by the dehydration or dehydroxylation associated with a large decrease in volume ($\sim 50\%$) during the reaction process (Sharma *et al.*, 2004).

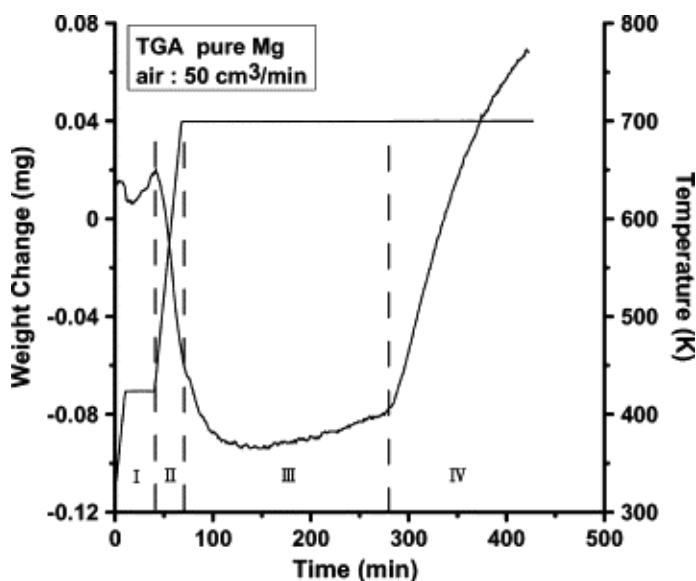


Fig. 1. Thermogravimetric analysis of pure magnesium (99.96 wt.%); heating rate $\partial T/\partial \tau = 10$ °C min⁻¹; air flowing rate = 50 cm³/min.

The protective behavior occurs during stage III (Fig. 1) due to a lack of easy paths for fast Mg transport (Shih *et al.*, 2006). Fig. 2a and b shows the sectional morphologies of a sample heated at 700 K for 3.6×10^3 s. The protective behavior for this holding time is shown by the thermogravimetric analysis; Fig. 1. Microchannels and microcracks are visible, but these channels or cracks do not penetrate through the oxide film; meaning, there are no easy path for magnesium transport. Brucite dehydrated and formed lamella MgO during heating. Concurrently, dehydroxylation also brought water vapor to the surface of the brucite film. Crystalline MgO can be rehydroxylated by increasing the water vapor pressure (Schramke *et al.*, 1982). During heating, dehydroxylation is energetically favorable for transforming

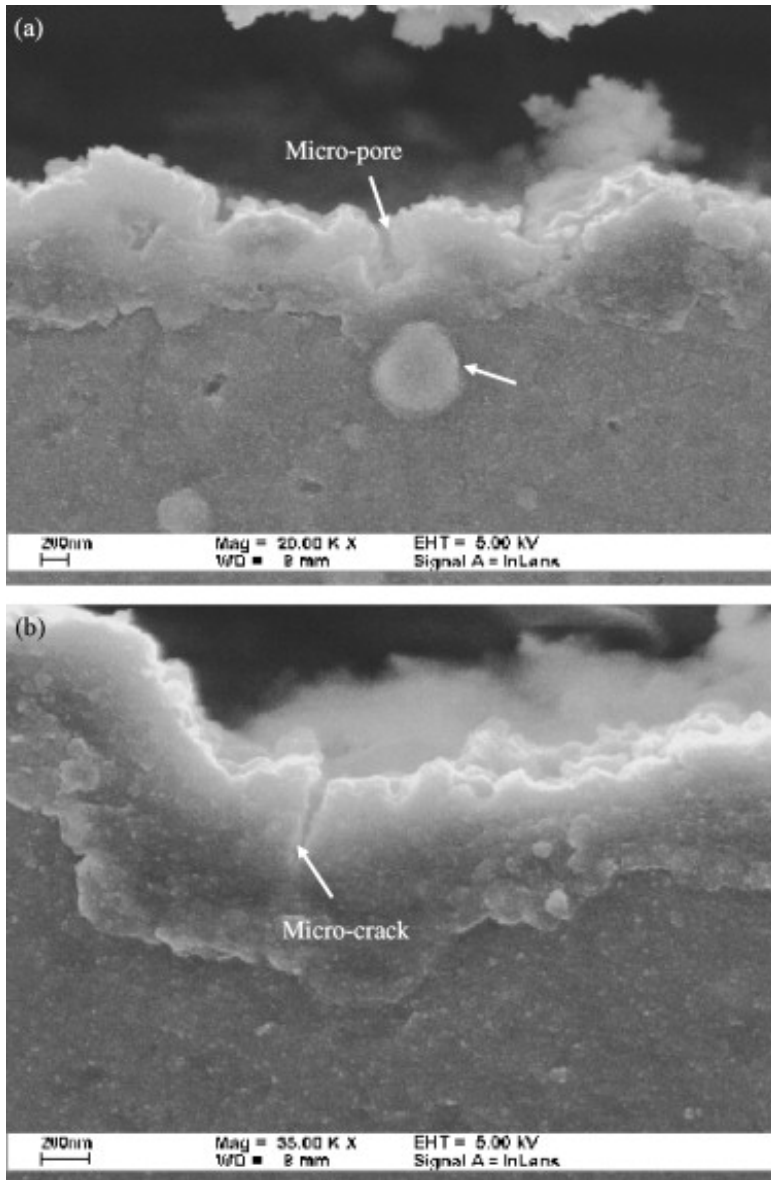


Fig. 2. SEM photos showing the sectional view including oxide film and substrate; sample (99.956 wt.% Mg) heated at 700 K for 1 h after being polished by abrasive paper; (a) magnification 20,000 \times and (b) magnification 35,000 \times .

brucite into MgO. Rehydroxylation may also occur locally at points which a high vapor pressure exists. Nanoscale cracking and fragmentation occur during dehydroxylation (Sharma *et al.*, 2004). Then, magnesium containing species could fill the cracks due to high mobility during heating. They react with the steam vapor to form brucite, which heals the microcracks. In our experiments, the fresh brucite on the microcrack walls and valley is transformed into periclase due to dehydroxylation at 700 K. The above reactions proceeded periodically during heating causing a protective behavior in stage III; see Fig. 1. When most of the brucite was transformed to MgO, the water vapor was almost completely depleted. The great difference in thermal expansion coefficient between magnesium and MgO caused the oxide film to crack. These cracks acted as channels for transporting magnesium vapor outward to react with the oxygen, result in the formation of ridges and/or nodules associated with a rapid weight gain (a non-protective behavior) in stage IV of Fig. 1.

Fig. 2a shows an inclusion particle located underneath the oxide film and a microchannel that is pointing to but not open to the particle. The thickness of the oxide layer varied from 0.6 to 1 μm and the microcracks were open for about half the thickness of the layer. This microcrack formation may have been triggered by the particles so that dehydroxylation and rehydroxylation could persist for a longer period of time.

Non-protective behavior occurs when the rehydroxylation process terminates and all the oxide has become periclase. Open microcracks allow the transportation of Mg to react with

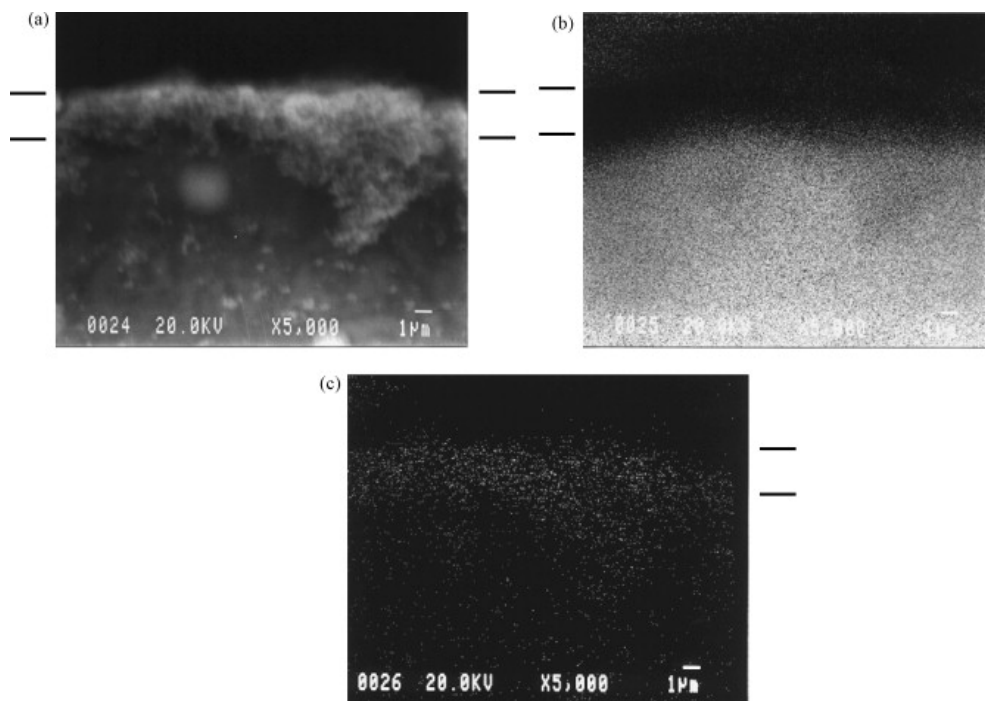


Fig. 3. EPMA photos showing the sectional view including oxide film and substrate; sample (99.956 wt.% Mg) heated in air at 700 K for 25 h, sample polished by abrasive papers; (a) magnification 5000 \times ; (b) Mg mapping and (c) O mapping.

the oxygen to form periclase. Fig. 3 shows the oxide penetration into the pure Mg substrate. Ridges formed after the sample was heated in air at 700 K for 9×10^4 s. Extending the heating time or raising the temperature causes the reaction to become much more rigorous, forming more nodules on the oxide film, leading to a loose structure, as illustrated by Czerwinski (2004).

3.2 The effect of SF₆ on the oxide film on pure magnesium

During the melting of magnesium alloys, CO₂, SO₂ and SF₆ gases are often used as the protective atmospheres. Using SF₆ can efficiently prevent magnesium ignition, but it also has a significant negative impact due to the greenhouse effect. A better understanding of the reaction of Mg with SF₆ is thus of industrial interest.

Samples of pure Mg were heated at 700 K for 9×10^4 s in an atmosphere of air mixed with 2% SF₆. The samples were sectioned, polished, and then observed by SEM and analyzed by an Electron Probe Micro Analyzer. Fig. 4b–d shows the Al, F and S mapping, respectively. The tested fluorine resided at the interface between the substrate and the thermally formed oxide layer. Sulfur was incorporated with the fluorine near the oxide layer, but its intensity was far less than that of the fluorine. Aluminum showed locally at the substrate and oxide layer interface indicating the possibility of the existence of spinels.

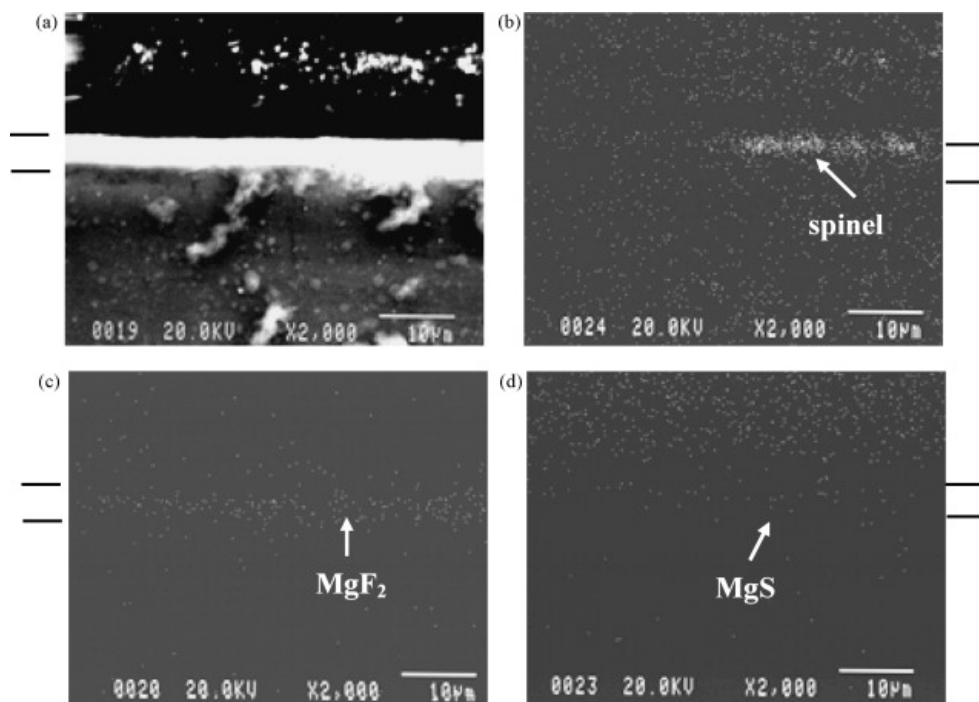


Fig. 4. EPMA photos showing the sectional view including oxide film and substrate; sample (99.956 wt.% Mg) heated in a protective atmosphere (0.2% SF₆) at 700 K for 25 h; sample polished by abrasive papers; (a) magnification 2000 \times ; (b) Al mapping; (c) F mapping and (d) S mapping.

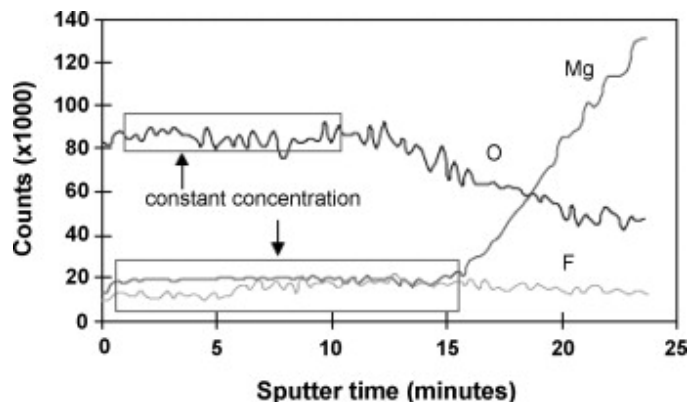


Fig. 5. The square of the film thickness versus film exposure time, for film samples produced under a cover gas of air containing 0.3% at 973 K

As explained previously, brucite formed during heating. It turned out to become periclase when dehydroxylation occurred. At a high-temperature (700 K), magnesium containing species diffused out from the substrate via the microcracks to react with oxygen to form periclase and also released latent heat ($\Delta H = 600.5$ kJ/mol). The protective atmosphere contained a small fraction of SF_6 (about 2%) which is heavier than CO_2 and air (6.4 kg dm^{-3} for SF_6 , 1.9×10^{-3} kg dm^{-3} for CO_2 , and 1.2×10^{-3} kg dm^{-3} for air). The SF_6 might fill up the microcracks in the thermally formed oxide layer and was heated by the reacting periclase. SF_6 can be decomposed if sufficient heat is available: $\Delta H = -1221.6$ kJ/mol. In other words, a reaction of two moles of MgO can offer enough latent heat to decompose one mole of SF_6 . The SF_6 was heated and reacted with Mg to form MgF_2 (formation enthalpy -1120.1 kJ/mol; formation energy -1001.2 kJ/mol (Barin, 1995)). The above reactions occurred persistently; forming periclase, decomposing SF_6 , and then producing MgF_2 . The MgF_2 was incubated in the microcracks and gradually filled the interface between the magnesium substrate and the oxide layer.

In this study, we used an atmosphere of air mixed with 2% SF_6 . It is reasonable to postulate that MgF_2 and MgS coexisted at the interfacial layer between the oxide and the substrate, as indicated by the F and S mapping. Aluminum is soluble in magnesium and would thus diffuse out to form spinel during heating since the formation energy is -2005.6 kJ/mol at 700 K, which is more favorable than MgF_2 (-1001.2 kJ/mol) or MgO (-525.8 kJ/mol). When the Mg sample was heated and held at 700 K in an atmosphere of air mixed with 2% SF_6 , spinel could form at the interfacial layer between the oxide and the substrate, where MgF_2 formed on the surface of the substrate. MgF_2 possesses a cubic structure similar to TiO_2 and has a low thermal expansion coefficient of 18×10^{-6} K^{-1} (a_a) and 13.7×10^{-6} K^{-1} (a_c), compared with MgO which is 44.3×10^{-6} K^{-1} (Fei In et al., 1995) and (Krishna Rao *et al.*, 1962). The MgF_2 film can therefore provide protection to the magnesium during heating.

Cashion *et al* (2002). prepared a film sample by melting Mg in a covering gas of air containing 0.3% SF_6 at 973 K. The film was about 0.25 μm in thickness after an exposure time of 1 h. In this study, the thermally formed oxide layer was about 6 – 8 μm , as indicated in Fig. 4, after magnesium was heated at 700 K in air containing 2% SF_6 . The thickness of the thermally formed oxide film was far greater than that of the film deposited on the melt, although the former was heated at 700 K and the latter was treated at 973 K.

The Auger electron spectroscopy tests show the relation of the film composition versus sputtering time; see Fig. 5 (Cashion *et al.*, 2002a). Fluorine can be detected. The MgF_2 product showed from the interfacial layer between the oxide film and the substrate was about one-half the thickness of the film. In this study, the MgF_2 occupies less than one half of the territory of the thermally formed oxide film (which was formed at 700 K for 1 h under a covering gas containing 2% SF_6); see Fig. 4. Two important observations can be made after comparing Fig. 4 and Fig. 5. First, MgF_2 was apparently preferentially located at the interfacial layer between the oxide film and the Mg substrate. Second, increasing the heating temperature increased the MgF_2 in the oxide film was evident experimentally.

During the heating thermally formed oxides first formed brucite which was then transformed to periclase at a high-temperature. Microcracks formed and the magnesium containing species diffused outward to react with the oxygen. The MgO would cover the surface of the heated Mg whether in the solid or in the melt. The reacting MgO product released heat, decomposing SF_6 , resulting in the formation of MgF_2 . Magnesium diffused out from the substrate via microcracks. Therefore, the MgF_2 product was preferentially located in the microcrack valleys. Increasing the heating temperature increased the reaction rate for forming MgO , offering a higher driving force for decomposing SF_6 and forming MgF_2 at the microcrack valleys. Therefore, MgF_2 was deposited underneath the MgO , and grew from the interfacial layer. The thickness of the MgF_2 layer increased following an increase in temperature and/or heating time. It therefore occupied a greater fraction of the oxide film and provided protection for the Mg melt as is the case in Fig. 5 (film on the melt) and in Fig. 4 (thermally formed film).

Spinel (MgAl_2O_4) is more energetically favorable at 700 K (-2005.6 kJ/mol) than either AlF_3 (-1326.2 kJ/mol) or MgF_2 (-1001.2 kJ/mol). It preferentially forms at areas where aluminum has diffused out from the Mg matrix and reacted with oxygen. The reacting spinel releases latent heat (-2297.8 kJ/mol) which generates a great driving force for decomposing SF_6 . Fluorine mapping thus shows the obvious intensity nearby the colony, corresponding to the Al mapping in Fig. 4.

3.3 Oxidation of AZ80 heated in air

The solution-treated AZ80 alloy sample was heated in air at 700K up to 1h. The surface of the heated sample changed in color from a bright metallic to a matt gray, reflecting the existence of the oxide film. Optical observation indicated that there were some small nodules distributed over the surface. Fig. 6a and b shows sectional views of the sample observed by SEM. Microcracks resided within the thermally formed oxide film. The crack sizes were less than those found within the thermally formed oxide film from the pure Mg sample; Fig. 2a and b. These microcracks can act as an easy path allowing the diffusion of Mg, to react with the oxygen, which produced the nodular structure.

The ESCA analysis shows the concentration-depth profile of the solution-treated AZ80 sample; see Fig. 7. The outer layer is mainly MgO . The concentration profiles of magnesium, oxygen and aluminum show a plateau on the intermediate region. This region is mostly composed of MgO and some spinel (MgAl_2O_4). The latter phase increased with the depth of oxide film in conjunction with the increase in the aluminum content. The spinel fraction increased up to a point where the oxygen content became level after dropping. The atomic percentage of oxygen and magnesium in the spinel was about 57.1 and 14.3%, respectively. Spinel formation would consume a large amount of oxygen. The oxygen diffused inward from the surrounding atmosphere. Increasing the oxide film thickness increased the difficulty for oxygen diffusion, limiting the spinel reaction to some extent, as shown in Fig. 7.

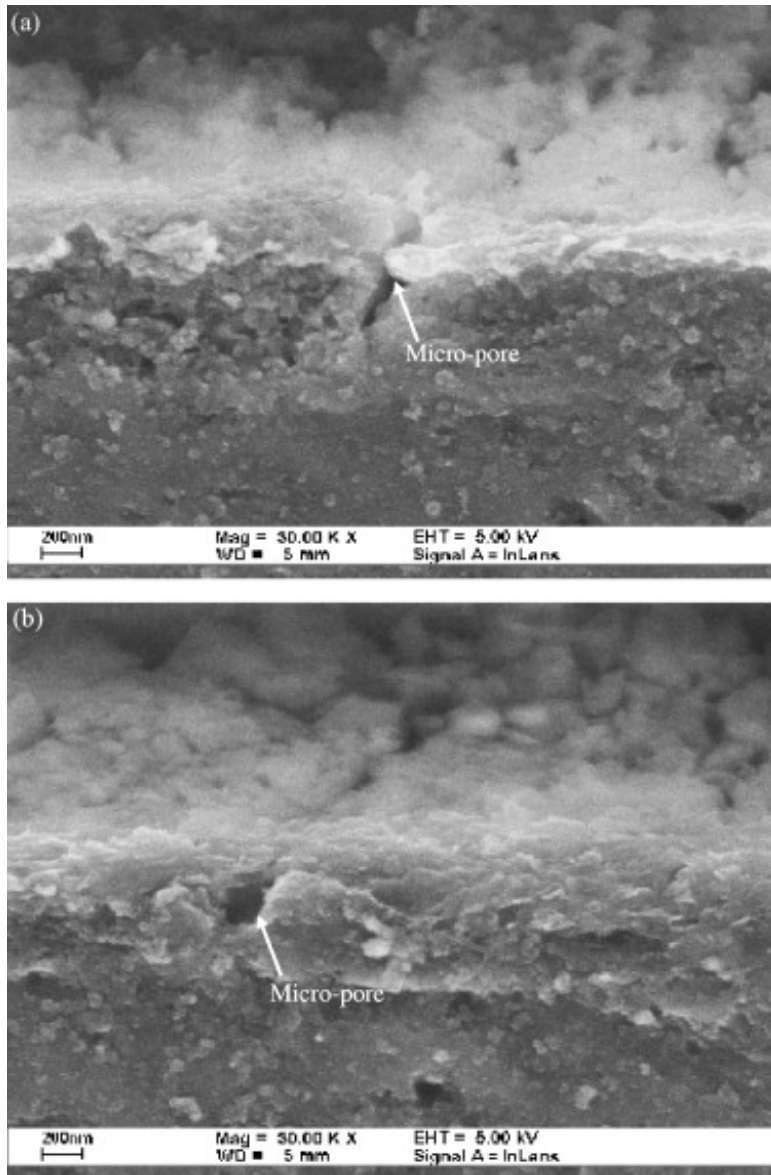


Fig. 6. SEM photo shows the sectional view of solution-treated AZ80 sample after polish by abrasive papers and heated in air at 700 K for 1 h; (a) and (b) magnification 30,000 \times showing the existence of micropore.

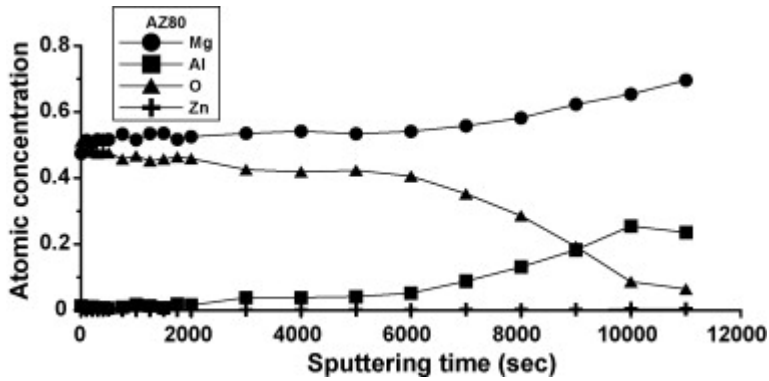


Fig. 7. ESCA analyses showing the measured atomic concentrations of Mg, O, Al and Zn versus sputtering time on solution-treated AZ80 after polished by abrasive papers and heated at 700 K for 1 h; the total sputtering time 11000 s.

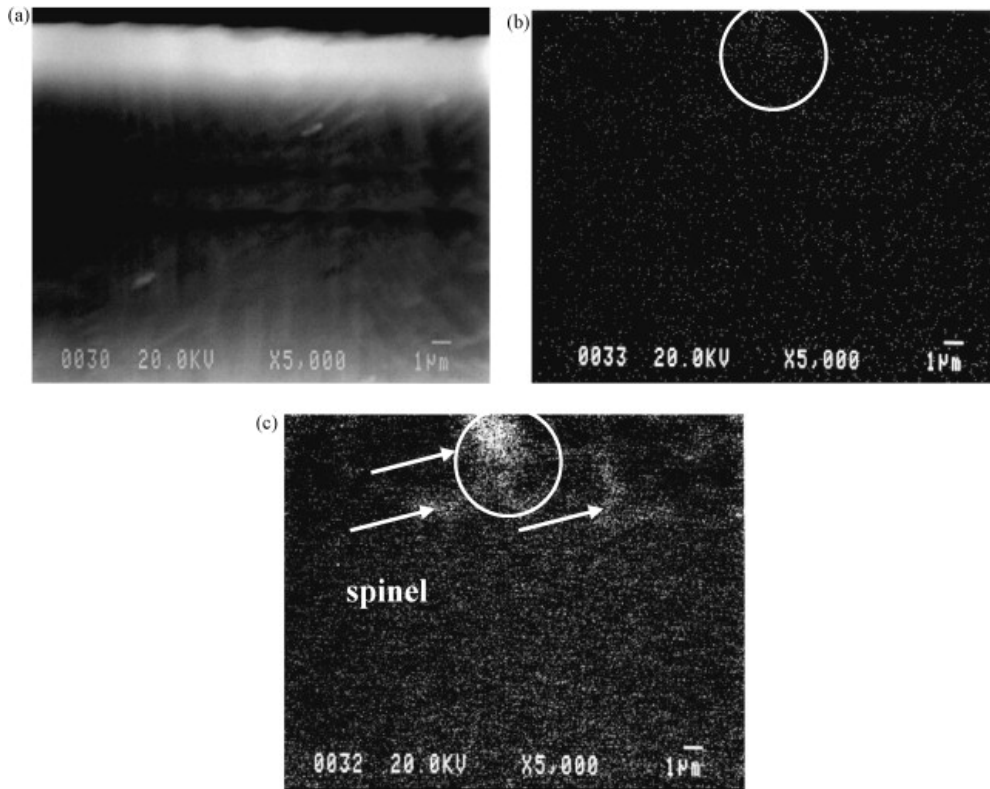


Fig. 8. EPMA photos showing the sectional view including oxide film and substrate; solution-treated AZ80 heated in air at 700 K for 1 h; sample polished by abrasive papers; (a) magnification 5000 \times ; (b) O mapping and (c) Al mapping.

Fig. 8 shows the EPMA analyses of oxygen and aluminum. From the coexistence of Al, O and Mg, it can be reasonably postulated that this area is composed of spinel. This is distributed near the interfacial layer, but is more like a network in the oxide film. The formation energies of spinel and periclase are -1878.75 and -493.09 kJ/mol (at 1000 K), respectively. After being heated, MgO will form on the sample surface first after which aluminum concentration in the substrate increases. This is energetically favorable for formation spinel. The thermal expansion coefficient of spinels, 29.4×10^{-6} K $^{-1}$, is far less than that of MgO, 44.3×10^{-6} K $^{-1}$, at a heating temperature of 1000 K (Fei In *et al.*, 1995). Spinel is much more thermally stable than MgO. This means that the solution-treated AZ80A could resist ignition up to 823 K (Shih *et al.*, 2004).

3.4 Oxidation films on the AZ91 melt and AZ80 heated cake

In the reference work of Zeng *et al.*, an AZ91 (Mg-9Al-0.5Zn) alloy was prepared using commercially pure Mg, Al, and Zn. The alloy was melted in an electric resistance furnace. When the melt temperature reached 973 K, the oxide film was removed from the melt. The melt was then poured into a permanent mold to obtain cakes with a diameter of 80 and 70 mm in thickness. The cakes were remelted in a crucible at 923 K for 10 s to prepare the surface oxide samples.

ESCA analyses were done to show the concentration-depth profiles of the elements on the oxide film; see Fig. 9a. The surface layer is rich in magnesium; the ratio of magnesium to oxygen is greater than 1. The oxygen content remains constant for a short distance then gradually decreases with depth. Periclase is the main constituent phase in this layer with some magnesium trapped in the MgO making the magnesium to oxygen ratio greater than 1. The magnesium concentration drops when there is a significant increase in the aluminum concentration indicating the existence of spinel in this region, Fig. 9b.

Comparing Fig. 7 and Fig. 9, we can make the following conclusions: (1) the thickness of the oxide film developed from the AZ91 melt is about 0.5–0.6 μm and the thermally formed oxide film deposited on the solution-treated AZ80 is about 4–6 μm . The former sample was melted at 923 K for 10 s and the latter was heated at 700 K for 3600 s. In other words, the reaction time is the influential factor in determining the thickness of the oxide film; (2) the concentrations of Mg, Al and O versus depth profiles of both the AZ 91 and AZ80 samples show a similar pattern and (3) the oxide film developed from the AZ91 melt possesses a higher magnesium concentration in the top layer than that obtained from the heated AZ80. The former oxide film contains more than 50% magnesium and the latter about 50% Mg. This difference was caused by the heating temperature (Fig. 10).

Fig. 9b schematically illustrates the prospective phases contained in the oxide film on the AZ91 sample. The top layer (zone I) is rich in MgO, with some Mg trapped in the microcracks. The intermediate layer (zone II) is composed of spinel, MgO and trapped Mg. In this layer, the spinel comprises a high fraction in the region close to the inner layer (zone III) but MgO is dense in the region close to the outer layer (zone I). The MgO and spinel have decreased fractions in the inner layer, but Mg greatly increases in concentration approaching the substrate.

During heating, brucite is transformed to periclase by the incorporation of voids and microcracks. Magnesium diffuses from the microcracks to react with oxygen, increasing the thickness of the periclase in conjunction with the magnesium trapped in the oxide layer. When periclase increases in thickness to some extent, the microcracks will again open, and

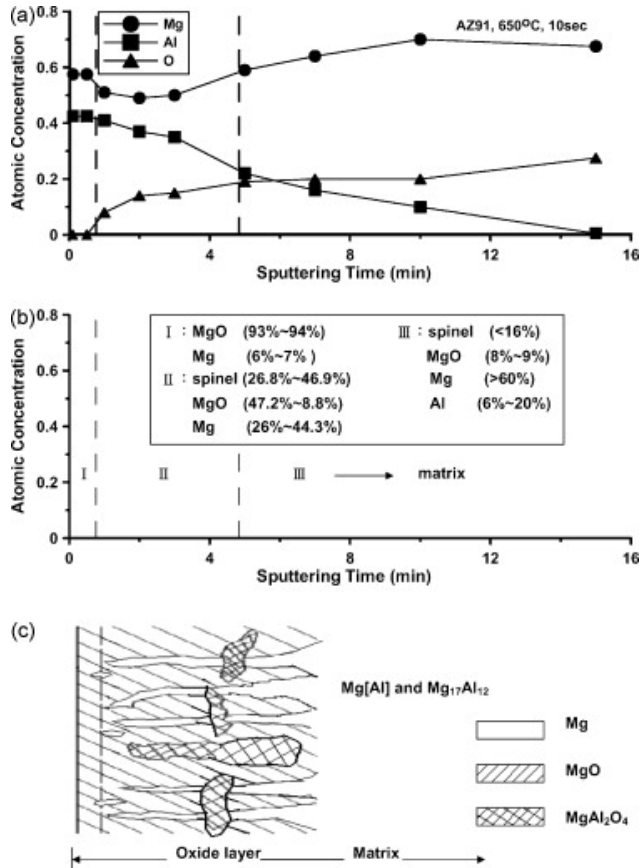


Fig. 9. (a) Relationship of Al, O and Mg concentrations versus sputtering time for sample of AZ91 alloy melted at 923 K for 10 s (Zeng *et al.*, 2001); (b) the prospective phases along with the estimated fractions of each oxide resided at different zones in the oxide film and (c) schematically illustrated the different oxide and trapped Mg in the oxide film.

newly formed periclase erupts into the melt forming a new layer of oxides. This process persists, increasing the thickness of the oxide film and also allowing for chance to form spinels. There are two possible paths for spinel formation: (1) metastable MgO can react with the Al-Mg melt to form spinel by $4\text{MgO} + 2\text{Al} \Rightarrow \text{MgAl}_2\text{O}_4 + 3\text{Mg}$ (Salas *et al.*, 1991) and (2) the oxide film fractures generating a chance for the reaction of oxygen with the Mg-Al melt. Aluminum has a higher density than Mg (2.7 g/cm^3 versus 1.74 g/cm^3) so after the top surface layer of the MgO increases in thickness, the Al content in the subsurface of the melt tends to increase. Spinel formed via this reaction (path (1)) is likely to be located at the oxide film and substrate interface but that formed via the microcrack, path (2), would more likely be located within the oxide film; see Fig. 8b. Once the spinel fraction in the oxide film increased the thermal stability of the oxide film improved blocking the microchannels transporting metal from the melt (Cashion *et al.*, 2002b). Fig. 9c schematically illustrates the distribution of MgO, spinel and Mg trapped in the oxide film.

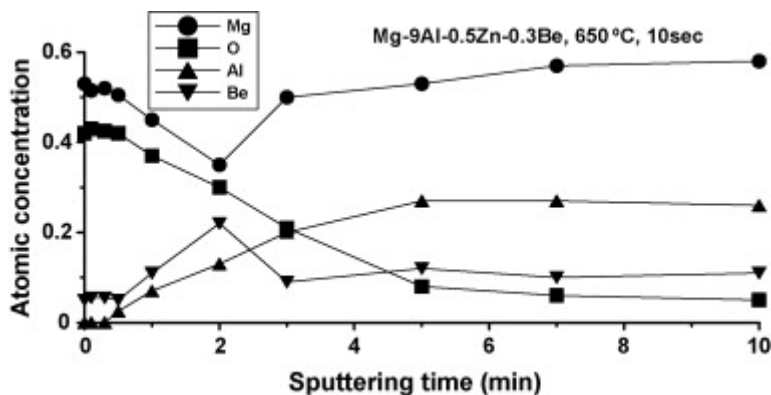


Fig. 10. Relation of Al, O, Mg and Be concentrations versus sputtering time for sample of AZB91 alloy melted at 923 K for 10 s

4. Conclusion

The ignition-proofing of a magnesium alloy can be obtained by using an inert gas atmosphere and/or by an alloying procedure. Magnesium alloys can usually be protected by CO_2 , SO_2 or SF_6 using an inert gas atmosphere. There are many elements of the alloying procedure that have already been studied, including calcium, aluminum and so on. Based on the present studies, the following conclusions can be made:

- (1) Brucite forms on magnesium and is transformed into periclase by the dehydration process. Microcracks caused by the large volume change of dehydration provide an easy path for evaporating Mg. Each path can produce a nodule on the surface of the oxide film. For an oxide film with a high population of nodules, the reacting MgO will ignite the melt or the heated alloy.
- (2) When inert gas SF_6 was used, MgF_2 or MgS, can form on the surface of pure magnesium at the interfacial layer between the oxide and the substrate where the reacting MgF_2 could block the diffusion of Mg from the substrate.
- (3) As a result of adding element Al, a trace of spinel was observed in the magnesium oxide layer. The reacting spinel tended to form at the interfacial layer which affected Mg diffusion from the substrate, improving the ignition-proofing of heated sample.

(Paper had originally published in Materials Chemistry and Physics 104 (2007))

5. Reference

- Shih, T. S., Chung, C. B. and Chong, K. Z. (2002). *Mater. Chem. Phys.* 74, 66.
- Shih, T. S., Wang, J.H., and Chong, K. Z. (2004). *Mater. Chem. Phys.* 85, 302.
- Czerwinski, F. (2002). *Acta Mater.* 50 2639.
- Zeng, X. Q., Wang, Q. D., Lu, Y. Z., Ding, W. J., Zhu, Y. P., Zhai, C. Q., Lu, C. and Xu, X. P. (2001). *Mater. Sci. Eng. A Struct. Mater.: Prop. Microstruct. Process.* 301, 154.
- Fei In, Y. (1995), "Mineral Physics and Crystallography: a Handbook of Physical Constants", Ahrens, T. J., ISBN-0875908527, American Geophysical Union, Washington, D.C.

- Houska, C. (1988). *Met. Mater.* 4, 100.
- Foerster, G. (1998). *Adv. Mater. Process.* 154, 79.
- Czerwinski, F. (2004). *Corros. Sci.* 46, 377.
- Sharma, R. McKelvy, M. J., Bearat, H. Chizmeshya, A. V. G. and Carpenter, R. W. (2004). *Philos. Mag. A Phys. Condens. Matter Defects Mech. Prop.* 84, 2711.
- Schramke, J. A., Kerrick, D. M. and Blencoe, J. G. (1982). *Am. Miner.* 67, 269.
- Splinter, S. J., McIntyre, N. S., Lennard, W. N., Griffiths, K. and Palumbo, G. (1993). *Surf. Sci.* 293, 130.
- Fuggle, J. C., Watson L. M. and Fabian, D. J. (1975). *Surf. Sci.* 49, 61.
- Robie, R. A., Hemingway, B. S. and Fisher J. R. (1978). "*Thermodynamic Properties of Minerals and Related Substances at 298.15 K and 1 Bar Pressure and at High Temperature*", ISBN-1-933762-07-1, U.S. Geological Survey Bulletin. 1452.
- Shih, T. S. and Liu, Z. B. (2006). *Mater. Trans. JIM* 47, 1347.
- Barin, I. (1995), "*Thermochemical Data of Pure Substances (third ed.)*", VCH Publishers, ISBN-3527287450, New York.
- Krishna Rao, K. V., Nagender Naidu, S. V. and Setty, P. L. N. (1962). *Acta Crystallogr.* 15, 528.
- Cashion, S. P., Ricketts, N. J. and Hayes, P. C. (2002a). *J. Light Met.* 2, 37.
- Salas, O., Ni, H., Jayaram, V., Vlach, K. C., Levi, C. G. and Mehrabian, R. (1991) *J. Mater. Res.* 6, 1964.
- Cashion, S. P., Ricketts, N. J. and Hayes, P. C. (2002b) *J. Light Met.* 2, 43.

Oxidation Resistance of AM60, AM50, AE42 and AZ91 Magnesium Alloys

Jožef Medved, Primož Mrvar and Maja Vončina
*University of Ljubljana, Faculty of Natural Sciences and Engineering, Department of
Materials and Metallurgy, Aškerčeva 12, 1000 Ljubljana
Slovenia*

1. Introduction

Because of the rapid development in automotive, aircraft, and electro industry the use of light alloys and their development is extensively increased. This increase is especially evident in the use of light magnesium alloys. The advantage of the Mg-alloys is in the mass/strength ratio, i.e. small mass of final products and their good mechanical properties; these alloys also have a good corrosion resistance (Kainer & Von Buch, 2003).

Magnesium alloys are usually used at room temperatures but they can also stay at higher temperatures and oxidizing atmospheres in different stages of processing, such as: overheating of the charge, melting, casting, heat treatment and mechanical processing, recycling etc. But those conditions result undesirable effects that change chemical properties and deteriorate structural properties of the surface layers. Therefore the knowledge of oxidation of Mg-alloys at different temperatures is important for development of new Mg-based materials and the optimization of their technological processes.

Various Mg alloys: AE42, AZ91, AM50, and AM60 were exposed to oxidation at different temperatures in order to determinate high-temperature oxidation resistance.

1.1 Oxidation of magnesium

1.1.1 Low temperature oxidation

Corrosion of all grades of magnesium and Mg-alloys is of the electrochemical nature [Vehovar, 1991]. High corrosion potential is needed due to the high negative standard electrode potential of Mg. In pure or alkaline water $Mg(OH)_2$ passive films of crystalline nature are formed on the surface of magnesium (Kurze & Ahc, 2003). In the water solution having $pH < 10$ this passive layer is unstable because of high compressive stresses inside the layer (geometric incompatibility with the Mg-lattice), causing the separation of layer and the commencement of corrosion. Hydrogen liberated in corrosion causes further separation of this passive layer. In pure alkaline water solution with $pH > 10.5$ the layer is very stable. In water solutions containing chloride, sulphide, or carbonate ions (fluoride ions are exception), the passive $Mg(OH)_2$ layer is destroyed and dissolved. Such corrosion occurs if magnesium is exposed to exhaust gases, acid rain and salts.

In the same way corrosion attacks the whole passive layer. The corrosion of Mg has two magnitudes. Higher values of corrosion are obtained in the solutions containing chloride or sulphide ions than in pure distilled water. Formation of hydrogen is the main cathode

reaction in this corrosion mechanism. The source of porous corrosion layer is in the inhomogeneous crystal structures, e.g., when $Mg_{17}Al_{12}$ phase is precipitated on grain boundaries. These structures have higher standard potential and they cause electrolytic process within the surrounding matrix. This electrochemical corrosion creates traces of porous corrosion product (Kainer & Von Buch, 2003, Ghali et al., 2004). In the Mg alloys, the pressure corrosion cracking appears when the internal or external tensile stresses are combined with the effect of corrosion media (chloride, sulphide and chlorate solutions). This leads to brittleness at the crack points because hydrogen, formed during the corrosion process, is absorbed (Kainer & Von Buch, 2003).

Electrochemical corrosion appears because of formation of galvanic cells. It frequently occurs in the Mg alloys that contain more electrochemically stable metals (alloy components or impurities), e.g., heavy metals, especially iron, copper, and nickel that are in electric contact with the matrix. Electrochemical corrosion is intensified in the high-purity Mg-alloys and in dry atmosphere (when no electrolyte is present).

Corrosion resistance of Mg-alloys (Kurze & Ahc, 2003) is increased with higher purity of alloys, with addition of special alloying elements (Y, Nd, La, Zr and Ce), and with surface treatment procedures (cleaning of surface, colouring, anodic treatment...).

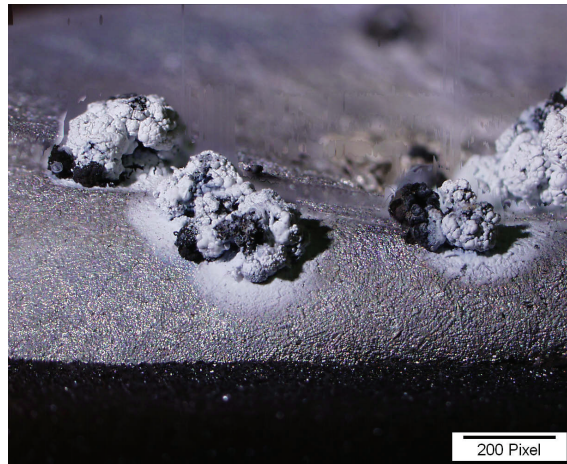
1.1.2 High-temperature oxidation

The course of high-temperature oxidation of magnesium is linear. At higher temperatures, particularly around 437 °C (eutectic temperature) (Massalski & Okamoto, 1990), a different behaviour was noticed at Mg-Al alloys. The obvious difference at higher temperatures resulted from the fact that chemical properties and relative volumes of phases in Mg-Al alloys were changed because of the diffusion process. The alloys at lower temperatures form transformed eutectic; but at temperatures above 437 °C the eutectic spheroidizes and progressively decays, while the magnesium region is homogenized throughout the matrix. Aluminium, that is the main alloying element, has a very different oxidizing and volatilization properties from Mg. Though aluminium itself forms a very resistant film of Al_2O_3 , the addition of over 1 mass % Al increases the oxidation of magnesium (Czerwinski, 2004).

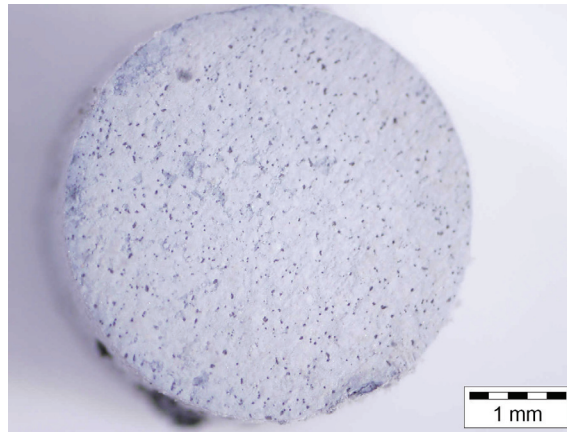
It is known that in the atmosphere containing oxygen, the growth of oxide film is diffusion controlled in the solid state, forming a compact oxide surface. In Mg-alloys at higher temperatures the lattice diffusion is reduced due to a noticeable lack of simple ways for quick transport of Mg vapours to the surface. Therefore the oxide film stays stable and protective for a longer time. Diffusivity of Mg in MgO lattice is known, and it is (Lea & Molinari, 1984): $D = 1.0 \cdot 10 \exp(-150/RT) \text{ m}^2/\text{s}$.

Observations show that the thin oxide layer that is formed presents a good protection (Czerwinski, 2004). At lower temperatures transformed eutectic is formed in the alloy. It spheroidizes and progressively decays at temperatures above 437 °C, while, as already mentioned, the magnesium region is homogenized throughout the matrix. Protective oxide film is destroyed by formation of the so-called oxide spongy spots (Fig. 1) (Medved & Mrvar, 2006). The morphology of the oxide spongy spots that are randomly distributed on the surface of the alloy does not show any evident uniform growth of those spots. Such type of structures shows the formation of "fresh" oxide on oxide/metal contacts and on the surfaces. It is believed that these spongy spots are formed in the presence of the oxygen penetrating through the cracks. This creates the condition for the reaction between oxygen and metal on crack walls and a spongy oxide layer is formed. The intensity of this reaction depends on the size of cracks and the rate of their healing, respectively, filling the cracks

with fresh oxygen. The growth of thick MgO layers is controlled by the first-order reaction. Generally, it is desirable that such a type of uncontrolled oxidation does not depend on the thickness of layer. It is also confirmed that oxygen can easily penetrate through the surface of the metal.



(a) The growth of oxide sponges



(b) Protective oxide layer

Fig. 1. Morphology of protective oxidation and growth of the oxide sponges (Medved & Mrvar, 2006)

The correlation between the thermo-gravimetric kinetics and the microstructure demonstrates that there is a relation between the increasing oxidation and the growth of oxide sponges. The growth of these sponges is activated in the stage of in-homogeneity, especially during the formation of the metal liquid phase with high vapour pressure of magnesium. At high temperatures magnesium can sublime by the diffusion through the oxide film after the incubation period. Of greater importance is the elimination of Mg

vapours from the metal surface. They cause that compact oxide film decays into a porous layer. Above 437 °C the degree of Mg volatility is so high that vapour does not only fill up all the pores in nodules but also fills the surface where the oxide films are formed. The opened oxide sponges continue to grow by the transfer of magnesium vapours through the pores and simultaneous reaction with the oxygen forming a product that has morphology of "a cauliflower". It was noticed that the simultaneous oxidation of magnesium led to formation of an alloy, where oxide fills up the places of the "consumed" metal. It seems that oxidation is intensified with time and at temperatures higher than 472 °C and it is also related to the enlargement of spots and pores. (Zerwinski, 2004, Zerwinski, 2002) These spots and pores are suitable for vapour condensing inside the layer, and this increases the surface of metal that is exposed to oxygen. Further growth of the oxide film depends on the selection of oxidizing components of the alloy that stimulate the reaction on the surface between the oxide and metal, and this increases the surface available for evaporation. The progress of oxidation was experimentally determined with the TG curves for the Mg-Al alloys. A physical model was calculated on the basis of this time relationship. A model of the Mg-Al alloy oxidation (Medved & Mrvar, 2006) was calculated from the TG curves, as (see Equation 1 and 2):

$$\Delta m = 5 \cdot 10^{-0.5} t^3 - 0.0022 t^2 - 0.0315 t + 100.01 [\%] \quad \text{protective oxidation} \quad (1)$$

$$\Delta m = 0.159 t^4 - 2.0942 t^3 + 103.72 t^2 - 2277.8 t + 118597 [\%] \quad \text{progressive oxidation} \quad (2)$$

2. Experimental work

Cylindrical samples with 4.0 mm diameter and 2.0 mm height were prepared and placed on platinum carrier (Fig.2). The samples were examined thermogravimetrically (TG) with the 449c Jupiter Instrument (NETZSCH) for simultaneous thermal analysis (STA). They were heated in protective atmosphere (nitrogen) to various oxidation temperatures (200, 400, 450 and 500 °C), with the heating rate of 10 K/min. The samples were then held in oxygen atmosphere for 12 h and afterwards cooled at 10 K/min to the room temperature. After the DSC analysis the macrographs of specimens were made with the Olympus SZ61 stereomicroscope.

Chemical composition of the examined alloys is presented in Table 1.

DSC analyses were made with all the alloy samples. Atomic force microscopy (AFM) was used to determine the shape of oxides in the specimen from AM60 oxidized at 400 °C. Auger electron spectroscopy (AES) was used to determine the depth of diffused oxygen and the thickness if the oxide layer.

Alloy	Mg (mass %)	Al (mass %)	Si (mass %)	Mn (mass %)	Zn (mass %)	RE (mass %)
AE42	Rest	4.2	0.03	0.29	0.15	1.5
AM50	94.7	4.7	-	0.40	0.12	-
AM60	93.7	5.84	0.028	0.33	0.05	-
AZ91	Rest	8.5-9.5	-	0.17-0.4	0.45-0.9	-

Table 1. The chemical composition of examined alloys



(a) Before the experiment



(b) After the experiment

Fig. 2. Sample on the TG carrier made of platinum

3. Results and discussion

In Figures 3 to 6 the TG curves of oxidation and the macrographs of examined alloys are presented. At low oxidation temperature (200 °C) a thin oxide layer was formed on the sample surface. At oxidation of AM50, AM60, and AE42 alloys a small increase of mass in the range of 0.1 - 0.5 mass % was found; in the AZ91 alloy the mass was reduced for approximately 0.1 mass %.

At 400 °C the oxidation of the AE42 alloy was quite scarce and a change of mass of approximately 0.1 mass % was determined; in the AZ91 alloy the change of mass was higher, 0.85 mass %. At the temperature of 450 °C, an excessive oxidation of the AZ91 alloy took place as also reported by (CZERWINSKI, 2004, CZERWINSKI, 2002). At the oxidation of the AM50, AM60, and AE42 alloys the change of mass was higher and it varied between 0.2 and 3.8 mass %. At the highest oxidation temperature (500 °C), the change of mass in the AE42 alloy was 0.7 mass %. At the oxidation temperature of 500 °C the highest mass change was found for the AM60 alloy, it exceeded 30 mass %.

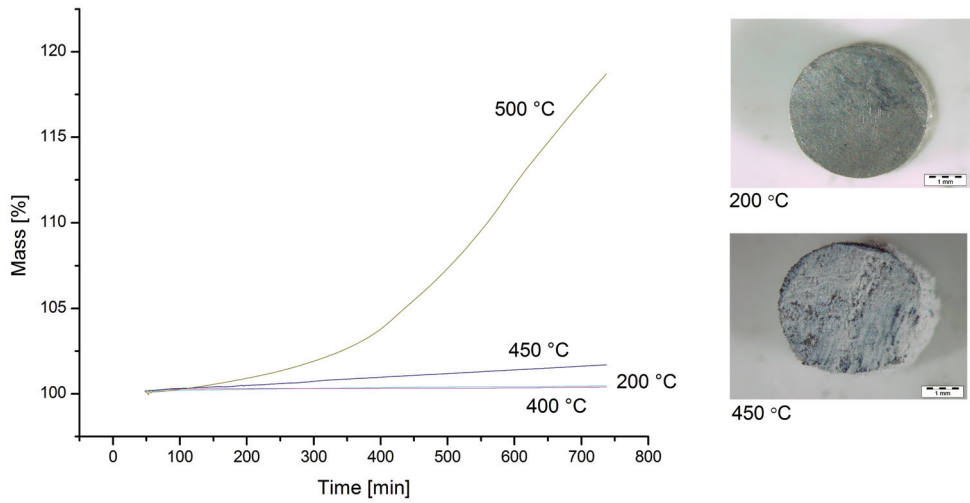


Fig. 3. TG curves and macrographs of examined specimen of the AE42 alloy

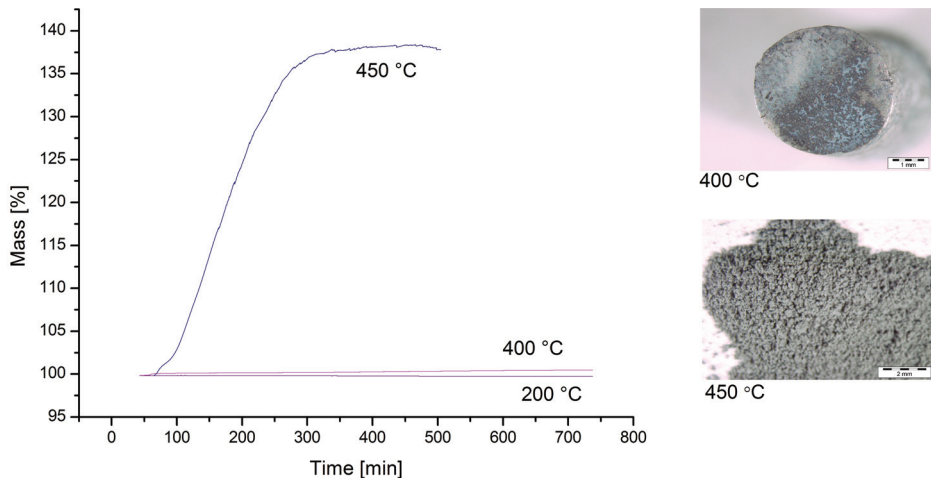


Fig. 4. TG curves and macrographs of examined specimen of the AZ91 alloy

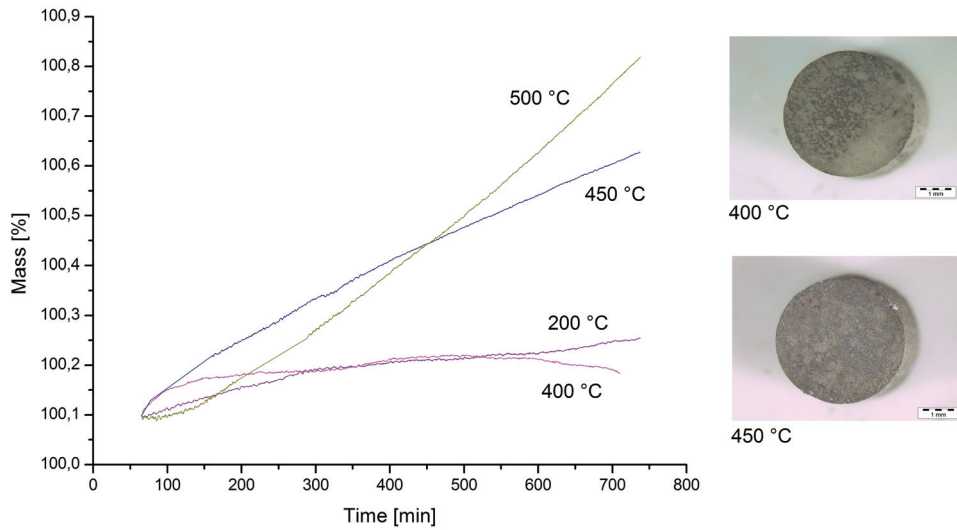


Fig. 5. TG curves and macrographs of examined specimen of the AM50 alloy

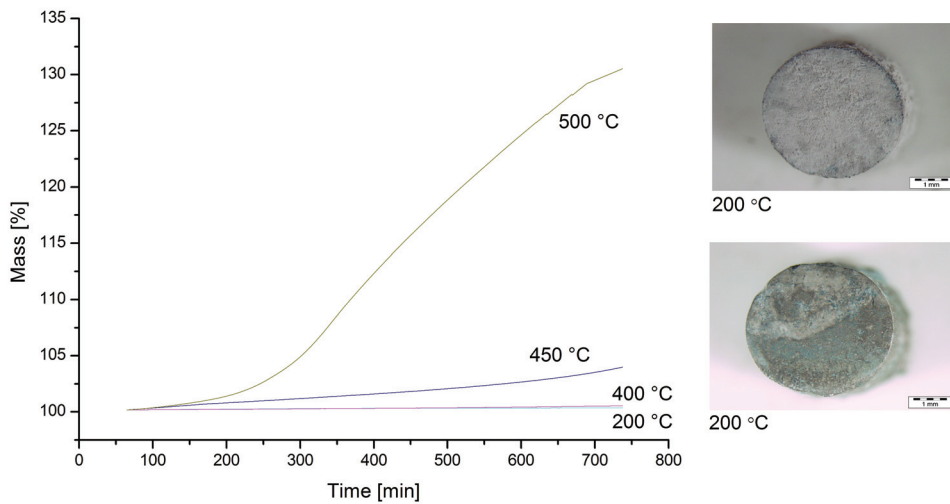


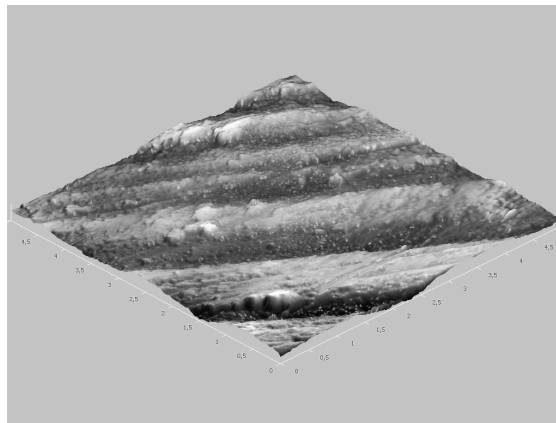
Fig. 6. TG curves and macrographs of examined specimen of the AM60 alloy

The specimen taken from the AM60 alloy before and after the 12-hour oxidation at the temperature of 400 °C was analysed by the AFM analysis (Fig.7) and AES analysis (Fig.8).

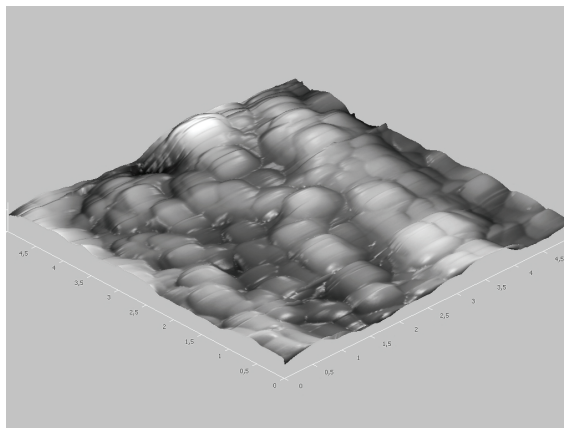
Figure 7.a gives evidence only of abrasion on the specimen surface. Here the oxidation did not take place. Figure 7.b presents the surface of the specimen after the oxidation at 400 °C for 12 hours. On the surface oxide sponges that were formed in the oxidation atmosphere were evident.

The comparison of different alloys at the same temperature (Fig.8 and 9) showed that at low temperatures (Fig. 8) all alloys had good corrosion resistances. At higher temperature (Fig. 9) AZ91 alloy was unstable; the most stable alloy was AE42. The corrosion stability becomes lower with a larger Al addition.

The profile analysis was made on specimens before the oxidation and after the oxidation at 200 °C and 400 °C for 12 hours. From Figure 10.a it is evident that the oxygen decreases continuously with the etching time so the oxide layer is very thin. The concentration of the



(a) Before oxidation



(b) After oxidation

Fig. 7. AFM picture of the specimen from the AM60 alloy at 400 °C

oxygen decreases slower at the oxidized specimen at 200 °C/12h, the oxide layer is a bit thicker (Fig.10.b). When the specimen was under the oxidation atmosphere at 400 °C the profile analysis with AES showed that the oxygen diffused deep to the specimen and the concentration did not decrease while etching the specimen.

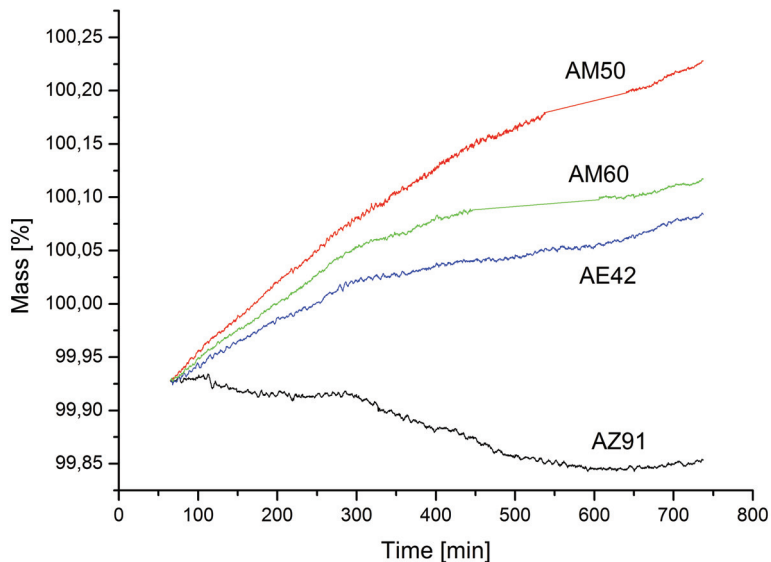


Fig. 8. Mass changes as a function of time for all samples at 200 °C

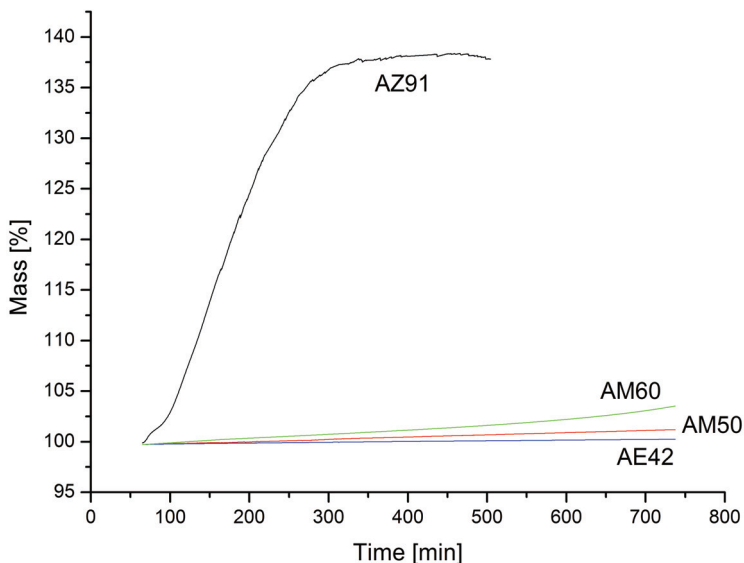
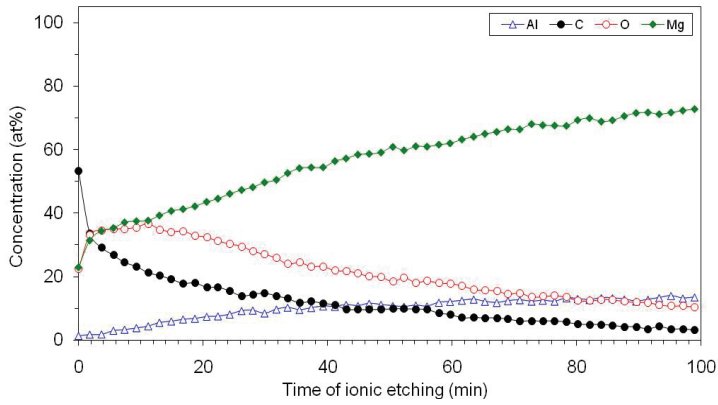
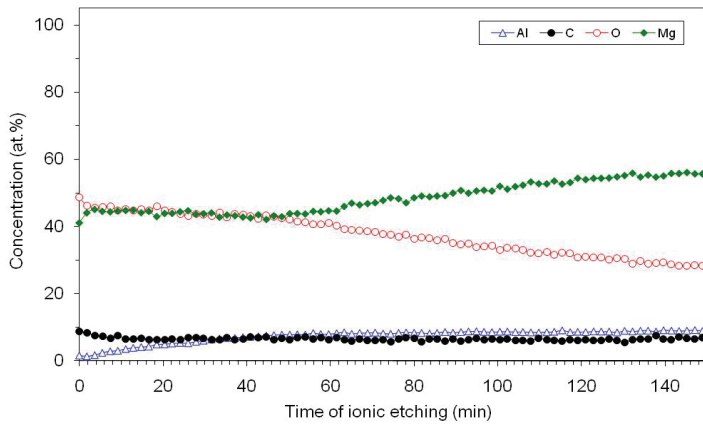


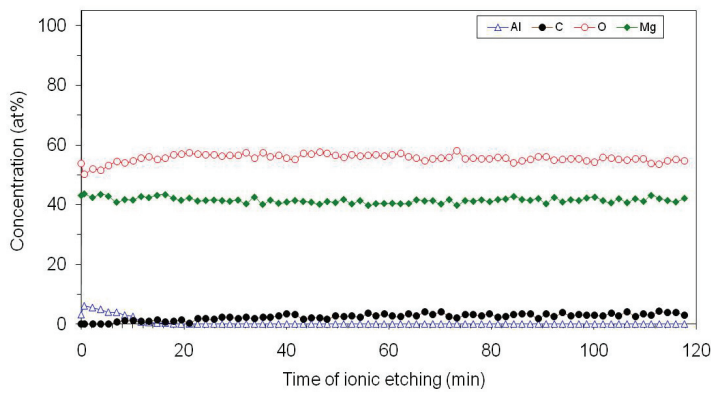
Fig. 9. Mass changes as function of time for all samples at 450 °C



(a) Before the oxidation



(b) After oxidation at 200 °C



(c) After oxidation at 400 °C

Fig. 10. Profile analysis of AM60 alloy

The kinetic models of examined alloys were made out of TG measurements and are described by the following equations (time t is in minutes):

At 200 °C:

$$\begin{aligned}\Delta m_{AM50} &= 99.87651 + 8.17415 \cdot 10^{-4} \cdot t - 4.80721 \cdot 10^{-7} \cdot t^2 \\ \Delta m_{AZ91} &= 99.98293 - 0.00112 \cdot t + 7.52251 \cdot 10^{-6} \cdot t^2 - 2.32339 \cdot 10^{-8} \cdot t^3 + \\ &\quad + 3.04034 \cdot 10^{-11} \cdot t^4 - 1.40687 \cdot 10^{-14} \cdot t^5 \\ \Delta m_{AE42} &= 99.87012 + 8.42615 \cdot 10^{-4} \cdot t - 1.47838 \cdot 10^{-6} \cdot t^2 + 9.88355 \cdot 10^{-10} \cdot t^3 \\ \Delta m_{AM60} &= 99.8961 + 4.16135 \cdot 10^{-4} \cdot t + 1.31073 \cdot 10^{-6} \cdot t^2 - 4.2518 \cdot 10^{-9} \cdot t^3 + 3.07167 \cdot 10^{-12} \cdot t^4\end{aligned}$$

At 400 °C:

$$\begin{aligned}\Delta m_{AM50} &= 99.97025 + 0.00259 \cdot t - 1.32636 \cdot 10^{-5} \cdot t^2 + 3.33877 \cdot 10^{-8} \cdot t^3 - \\ &\quad - 4.0335 \cdot 10^{-11} \cdot t^4 + 1.89828 \cdot 10^{-14} \cdot t^5 \\ \Delta m_{AZ91} &= 99.9179 + 0.0037 \cdot t - 2.13318 \cdot 10^{-5} \cdot t^2 + 6.00119 \cdot 10^{-8} \cdot t^3 - \\ &\quad - 7.32255 \cdot 10^{-11} \cdot t^4 + 3.22439 \cdot 10^{-14} \cdot t^5 \\ \Delta m_{AE42} &= 99.94066 + 0.00321 \cdot t - 1.87755 \cdot 10^{-5} \cdot t^2 + 5.2823 \cdot 10^{-8} \cdot t^3 \\ &\quad - 6.87294 \cdot 10^{-11} \cdot t^4 + 3.30968 \cdot 10^{-14} \cdot t^5 \\ \Delta m_{AM60} &= 100.04052 + 4.90799 \cdot 10^{-4} \cdot t - 3.92013 \cdot 10^{-7} \cdot t^2 + 6.32061 \cdot 10^{-10} \cdot t^3\end{aligned}$$

At 450 °C:

$$\begin{aligned}\Delta m_{AM50} &= 99.55591 + 0.00222 \cdot t \\ \Delta m_{AE42} &= 99.70671 + 7.42442 \cdot 10^{-4} \cdot t \\ \Delta m_{AM60} &= 99.26979 + 0.00712 \cdot t - 1.12601 \cdot 10^{-5} \cdot t^2 + 1.26182 \cdot 10^{-8} \cdot t^3 \\ \Delta m_{AZ91} &= 121.55408 - 0.74693 \cdot t + 0.0083 \cdot t^2 - 3.16601 \cdot 10^{-5} \cdot t^3 + \\ &\quad + 5.24557 \cdot 10^{-8} \cdot t^4 - 3.22361 \cdot 10^{-11} \cdot t^5\end{aligned}$$

At 475 °C:

$$\begin{aligned}\Delta m_{AM50} &= 98.43285 + 0.03175 \cdot t - 1.65827 \cdot 10^{-4} \cdot t^2 + 4.01739 \cdot 10^{-7} \cdot t^3 - 2.50182 \cdot 10^{-10} \cdot t^4 \\ \Delta m_{AE42} &= 100.01846 + 0.00112 \cdot t \\ \Delta m_{AM60} &= 99.75402 + 0.02563 \cdot t - 3.45083 \cdot 10^{-4} \cdot t^2 + 1.78234 \cdot 10^{-6} \cdot t^3 - 2.80083 \cdot 10^{-9} \cdot t^4 + \\ &\quad + 1.43864 \cdot 10^{-12} \cdot t^5\end{aligned}$$

Figures 11 and 12 present the comparison of DSC curves of the examined Mg-alloys. During the heating of Mg-Al alloys, two regions of melting were detected, except with the AE42 alloy. The first peaks on the curves in the lower temperature interval (419-431 °C) could be attributed to the melting of eutectic ($\alpha_{Mg} + Al_{17}Mg_{12}$). Because of different fractions of the eutectic, the areas under the curves, that represented the consumed heat and thus the quantity of eutectic too, differed. The second peaks on the curves indicated the melting of the α_{Mg} primary phase in all the alloys. They had different courses because of different

amounts of Al in the alloys, and melting commenced the first with the alloys having higher amounts of aluminium. This meant that aluminium decreased the alloy melting point and it influenced the amount of the ($\alpha_{Mg} + Al_{17}Mg_{12}$) eutectic in the microstructure too. Considering the phase diagram (Fig.13), all the alloys are in the range where eutectic should not be formed. This means that eutectic is a non-equilibrium phase.

The experiments have shown that the oxidation took place in heating and it progressed when holding specimens at constant elevated temperature. This oxide layer had a "protective" nature and grew unisotropically across the microstructure; it was stable under certain defined conditions and its thickness partly depended on the temperature and the time of oxidation.

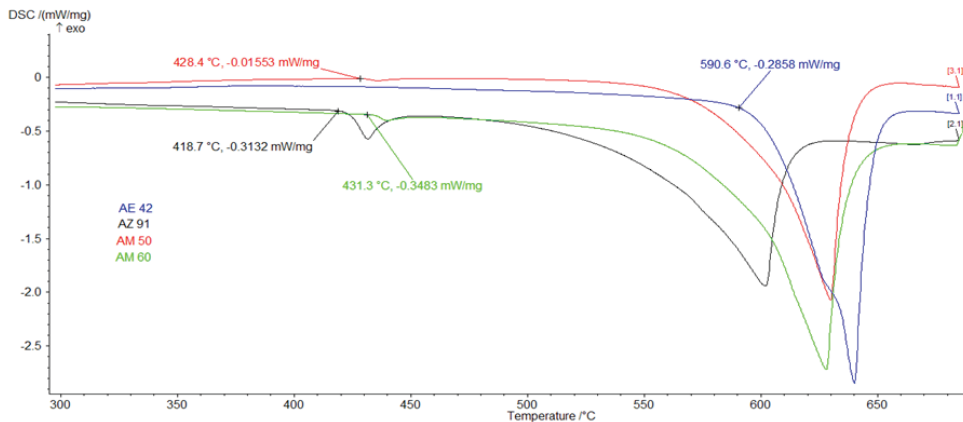


Fig. 11. DSC analyses of the melting process of Mg- alloys

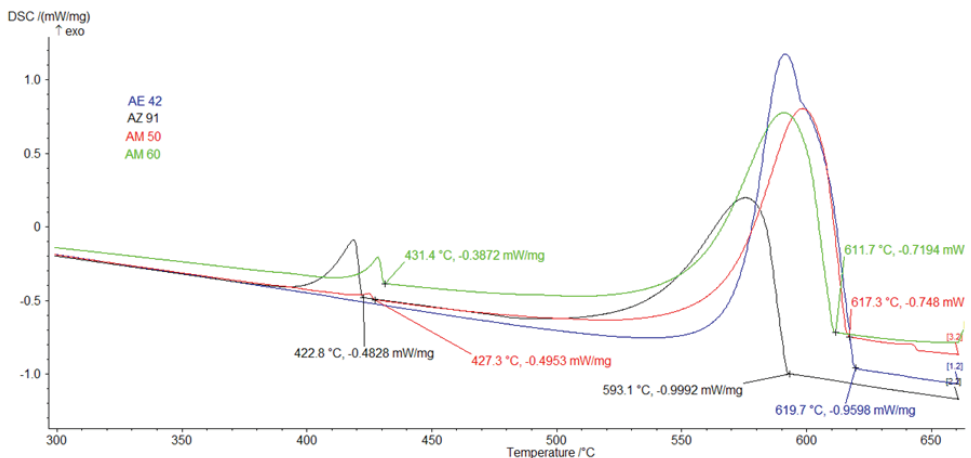


Fig. 12. DSC analyses of solidification of Mg- alloys

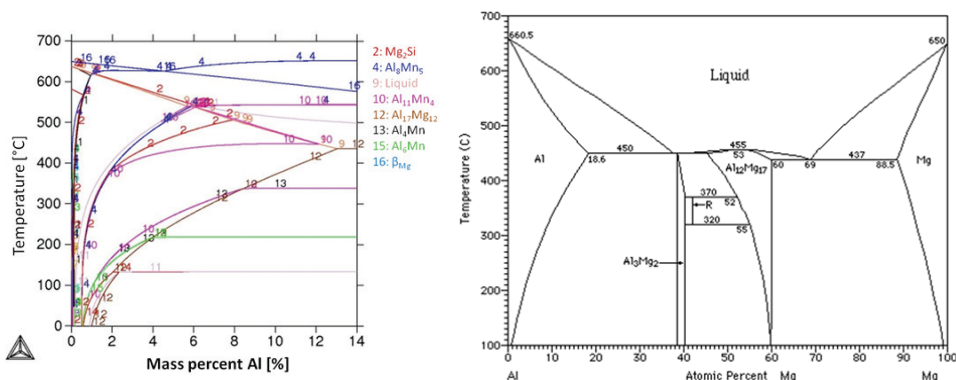


Fig. 13. Calculated phase diagram of the examined AM60 alloy containing 0.028 % Si, 0.33 % Mn, and 0.05 Zn (a) and the Al-Mg binary phase diagram (b) (Massalski & Okamoto, 1990)

Equilibrium melting point of the eutectic is 437 °C (Fig. 13.b). The DSC determined the temperature of eutectic melting at 431 °C (Fig. 12). At this temperature the first liquid phase (Medved & Mrvar, 2006) appeared. The morphology of uniform oxide distribution was changed into oxide “sponges” that were formed due to the evaporation of magnesium. Oxidation became more intense with time because of long exposure to higher temperatures. Under such conditions the diffusion of the magnesium to the surface is intense and the oxide grows in the form of the so called “sponges”, until the complete material is “disintegrated”.

4. Conclusions

The purpose of the examination was to determine the course of oxidation of the Mg alloys in the oxygen atmosphere at different temperatures in 12 hours. The results showed that the oxide layer could protect material against the progressive oxidation until some critical temperature has been reached. The nature of the oxide layer depended on several external conditions, such as atmosphere, temperature of the oxidation process, and also on the type of alloy. Regarding the obtained results the following conclusions can be made.

The heating and cooling DSC curves indicated the course of melting and of solidification of Mg-Al alloys. The additions of Al decreased the liquidus temperatures. DSC curves showed that the second peak appeared on the solidification curves when alloys contained 4 or more mass % of Al. Optical microscopy revealed that this was due to non-equilibrium eutectic crystallization during the cooling process.

TG curves indicated the course of oxidation. It has been proved that in all the examined alloys during the heating to the oxidation temperature, a thin oxide layer with a protective nature was formed. This layer was independent of the alloy composition and it was stable till the alloy melted down. The alloys that contained eutectic phase in their microstructure were protected by the oxide layer up to the first incipient fusion (equilibrium up to 437 °C). In the alloys without the eutectic phase the protective oxide layer existed to higher temperatures (at least up to 450 °C). In the alloys with eutectic phase the protective oxide layer was destroyed above the eutectic temperature and under these conditions the so-called

spongy growth of oxide became evident. Oxidation of this kind is destructive and usually leads to complete degradation of the material.

It is evident that the most stable alloy at high temperatures was the AE42 alloy and the most unstable one was the AZ91 alloy. Alloys with higher Al additions had lower corrosion stability.

After the 12-hour oxidation of the AM60 alloy it was found that the concentration of the oxygen was increasing to some depth and it remained constant afterwards. The fractions of magnesium and oxygen did not change. The concentrations of aluminium and carbon were reduced to only few at. %.

The kinetic model of high-temperature oxidation of examined cast magnesium alloys was made regarding the time and temperature.

5. References

- Czerwinski F. (2002). The oxidation behaviour of an AZ91D magnesium alloy at high temperatures, *Acta Materialia* 50, pp. 2639-2654.
- Czerwinski, F. (May 2004). Factors Affecting the Oxidation of Magnesium Alloy. *JOM (A Publication of the Minerals, Metals & Materials Society)*, Volume 56, Number 5, p. 29.
- Czerwinski, F. (2004). The early stage oxidation and evaporation of Mg-9%Al.1%Zn alloy, *Corrosion Science* 46, pp. 377-386.
- Ghali, E., Dietzel, W. & Kainer, K. U. (February 2004). General and Localized Corrosion of Magnesium Alloys: A Critical Review, *Journal of Material Engineering and Performance*, Volume 13(1), pp. 7-23.
- Kainer, K.U. & Von Buch, F. (2003). The Current State of Technology and Potential for further Development of Magnesium Applications. V. Kainer: *Magnesium- Alloys and Technologies*. Institut für Werkstofforschung, Translation by Frank Kaiser; Wiley-VCH Verlag GmbH & Co, pp. 1-23.
- Kurze, P.AHC (2003). Oberflächentechnik GmbH & Co. OHG, Kerpen. *Corrosion and Corrosion Protection of Magnesium*. V.Kainer: *Magnesium-Alloys and Technologies*, Institut für Werkstofforschung, Translation by Frank Kaiser; Wiley-VCH Verlag GmbH & Co, pp. 218-225.
- Lea, C., Molinari, J., *Journal of Material Science*, 19, 1984, p. 2336
- Massalski, T.B. & Okamoto, H. (1990). *Binary Alloys Phase Diagrams*, 2nd Edition, Sufbramanian, L., Kaprzak eds., ASM, Metal Park, Ohio,
- Medved J. & Mrvar, P. (2006). High-temperature oxidation of Mg alloys, *Livarski vestnik*, 3, pp. 98-111.
- Medved J. & Mrvar, P. (2006). Thermal analysis of the Mg-Al alloys. *Mater.Sci.Forum*, Vol. 508, 2, pp. 603-608.
- Vehovar, L. (1991). *Korozija kovin in korozijsko preskušanje*, Ljubljana, pp. 1-48.

In Situ Ellipsometric Study on Corrosion of Magnesium Alloys

Lingjie LI¹, Jinglei LEI¹ and Fusheng PAN²

¹*Coll. Chem. & Chem. Eng., Chongqing University*

²*Coll. Mat. Sci. & Eng., Chongqing University*

P. R. China

1. Introduction

Magnesium is the 8th most abundant element on the earth. Moreover, it is the lightest structural metal. Magnesium and alloys have numerous advantageous properties such as high specific strength, high thermal conductivity, high dimensional stability, high damping capacity, good machinability, good electromagnetic shielding characteristics and easily-recycling characteristics. These excellent properties make them an ideal choice for a number of applications including automobile parts, computer and mobile components, sporting goods, aerospace equipment, household equipment, and implanted materials (Zhang & Zhang, 2004).

However, magnesium and alloys are chemically active (the standard potential of Mg^{2+}/Mg is $-2.356V$ vs. N.H.E. at $25^{\circ}C$ (Bard & Faulkner, 2001)). Hence, they are extremely susceptible to corrosion whether in wet atmosphere or acid, neutral and weak alkaline solutions. The poor corrosion resistance seriously hinders their widespread use in many applications. Hence, a lot of researches have been performed on the corrosion of magnesium and alloys (Song & Atrens, 2003; Song, 2005; Song, 2006; Wei et al, 2007; Li et al, 2008a-c).

In the investigations on the corrosion of magnesium alloys, the hydrogen evolution and weight loss measurements, the electrochemical techniques such as polarization curves and electrochemical impedance spectroscopy (EIS), the corrosion morphology characterization techniques such as optical microscopy and scanning electron microscopy (SEM), the corrosion products identification methods such as X-ray diffraction (XRD), X-ray photoelectron spectroscopy (XPS) and energy dispersive spectroscopy (EDS), etc., are often used. These conventional methods can provide the information of corrosion rate, corrosion resistance, corrosion morphology, corrosion products composition (Song, 2006). However, they fail to provide the micro-dynamic information of the "magnesium alloy - corrosive medium" interfaces, which is critical for understanding the corrosion mechanism and hence developing anti-corrosive magnesium alloys. Moreover, these conventional investigations are always carried out in such a way producing much perturbation of the "magnesium alloy - corrosive medium" interfaces. Therefore, employing appropriate methods to clarify the micro-dynamic details of the "magnesium alloy - corrosive medium" interfaces with minimal electrochemical and physical perturbation is very necessary.

The use of in situ ellipsometry to investigate the metal-solution interfaces in the corrosive medium in real-time and without perturbation is well established. Our group simultaneously used ellipsometry and electrochemical measurements (cyclic voltammetry and EIS) to investigate the corrosion behaviors of copper electrode in borax solution and in weak-alkaline medium with the aggressive ion Cl^- (Lei et al, 2001 a-b). M.V. Vinnichenko et al. employed in situ ellipsometry to investigate stainless steel corrosion behavior in buffered solutions with amino acids (Vinnichenko et al, 2003). R. Bogdanowicz et al. used in situ ellipsometry and cyclic voltammetry measurements for the investigation of oxide growth on copper in 0.1 M NaOH solution (Bogdanowicz et al, 2009). In these studies, the optical properties and thickness of the metal-solution interfaces or the surface films on the metals were obtained by deconvoluting the ellipsometric data based on certain models. Thus the micro-dynamic details of the corrosion interfaces were clarified.

In this chapter, we briefly introduce the ellipsometric theory and present some original experimental and interpretive studies on the corrosion behaviors of magnesium alloys in some typical corrosive mediums, such as the simulated sea water, the simulated acid rain and the simulated industrial cooling water, with the principal means of in situ spectroscopic ellipsometry. In addition, the inhibition of sodium molybdate (an environmental-friendly inhibitor) on the corrosion of magnesium alloy in the simulated industrial cooling water is identified and explained. It has to be pointed out that in this work the "magnesium alloy - corrosive medium" interfaces are considered as homogeneous and hence are regarded as a single layer with the aim to simplify the heavy deconvolution task. By deconvoluting the dynamic spectroscopic ellipsometric data, the refractive indexes and thickness of the "magnesium alloy - corrosive medium" interfaces during the different corrosion processes are obtained. The corrosion mechanism of magnesium alloys in these different corrosive mediums is proposed. The influence factors on the corrosivity of the mediums are discussed. The use of the in situ spectroscopic ellipsometry technique enables detailed characterization of the evolution of the thickness and optical properties of the "magnesium alloy - corrosive medium" interfaces during the corrosion processes. These studies are extremely important for clarifying the corrosion mechanism and reconstructing the corrosive interface structure of magnesium alloys.

2. Experimental and ellipsometry theoretical

2.1 Experimental

Materials. — Among the various magnesium alloys, the Mg-Al-Zn system, which includes alloys containing 2-10% Al, combined with minor additions of zinc and manganese, is the earliest commercially used and the most widely used (Zhang & Zhang, 2004). Hence, in this work, a Mg-Al-Zn magnesium alloy, namely AZ40, is chosen to be investigated. The AZ40 magnesium alloy rod was manufactured by Chongqing Magnesium, Ltd, P. R. China. Table1 lists the chemical composition of the alloy.

Elements	Al	Zn	Mn	Si	Cu	Ni	Fe	Mg
Content (mass %)	4.07	0.31	0.12	0.01	0.02	0.003	0.01	Bal.

Table 1. Chemical composition of the AZ40 magnesium alloy.

The AZ40 magnesium alloy electrode was cut from the rod of the alloy with cross-section area of 1.0 cm² and embedded in epoxy resin holders. Before each experiment, the electrode surface was mechanically polished with 300, 600, 1000, 1800# grit emery papers to get a plane mirror finish, then degreased ultrasonically in acetone for 3 min, rinsed with distilled water and dried in air.

Corrosive mediums. — The corrosion resistance of one magnesium alloy is dependent on the medium to which it is exposed (Papavinasam, 2000). In this work, three typical corrosive mediums, including the simulated sea water, the simulated acid rain and the simulated industrial cooling water, are chosen to be investigated.

The simulated sea water is actually 3.5% NaCl solution (pH=5.30), which is the most typical corrosive medium and represents the strong aggressive Cl⁻ environment.

The acid rain is a serious pollution all over the world, which has attracted a lot of attention from environmentalists and researchers. Chongqing, as an important city of the southwest China with rapid developing of the magnesium industries, was one of the most serious acid rain areas in the world several years ago. In this work, the simulated acid rain is chosen as a typical corrosive medium for investigation. The simulated acid rain was prepared according to the research results on Chongqing rain water (Tang & Bai, 2000). The composition of the Chongqing rain water is listed in Table 2. The pH value of the simulated acid rain was adjusted to 4.67 (very close to the pH value of the rain water) by dilute sulphuric acid.

Ions	SO ₄ ²⁻	Cl ⁻	NO ₃ ⁻	Ca ²⁺	Mg ²⁺	K ⁺	Na ⁺	NH ₄ ⁺	F ⁻
Content (mg/L)	46.3	2.46	4.04	15.29	0.92	0.84	0.76	3.86	0.64

Table 2. Composition of the Chongqing rain water (Tang & Bai, 2000).

The industrial cooling water is an important medium in industrial production, which is corrosive to the metal equipments. The concentration of Cl⁻ in the industrial cooling water is about 200 mg/L, which is much lower than that in the sea water. In this work, the simulated industrial cooling water is regarded as a typical corrosive medium for study. Since our purpose focuses on the corrosion of AZ40 magnesium alloy caused by the aggressive ion Cl⁻ in the simulated cooling water, the simulated cooling water is actually 200 mg/L NaCl solution (pH=5.23). Moreover, the inhibition of sodium molybdate, an environmental-friendly inhibitor, on the corrosion of magnesium alloy in the simulated cooling water is studied. According to our previous work (Li et al, 2008 b), the concentration of sodium molybdate is chosen as 1000 mg/L.

The corrosive mediums mentioned above were prepared from analytical grade chemicals and distilled water. All chemicals were offered by the Sinopharm Chemical Reagent Company of China.

Measurements. — Open circuit potential (OCP) and in situ spectroscopic ellipsometry measurements were conducted simultaneously at the room temperature.

OCP measurements were carried out on a CHI660B electrochemical workstation supplied by the Shanghai Chenhua Instruments Company of China. The electrochemical cell consisted of a conventional three-electrode configuration with a platinum sheet as the counter electrode and a saturated calomel electrode as the reference electrode. The working electrode was the cleaned AZ40 magnesium alloy electrode.

In situ spectroscopic ellipsometry measurements were performed using a Woollam ellipsometer M-2000U which was made in USA. Two ellipsometric parameters, Δ and ψ ,

were acquired. The measured wavelength range was from 245 nm to 1000 nm and the incident angle was fixed at 70°. The light beam reflected from the sample surface became weak due to the increasing roughness of the corrosion interfaces, which led to some spectral noise at 245-390 nm and 780-1000 nm during the measurements. Hence, only the experimental spectra within 390-780 nm were deconvoluted and reported in this work. A Woollam program (based on a Marquardt-Levenberg algorithm), WVASE32, was used for numerical analysis of the experimental ellipsometric data.

The refractive indexes of the corrosive mediums (the simulated sea water, the simulated acid rain, and the simulated industrial cooling water without and with sodium molybdate) were respectively 1.3391, 1.3323, 1.3324 and 1.3328, which were measured using an Abbé refractometer at the room temperature.

2.2 Ellipsometry theoretical

The following theoretical background for ellipsometry was described elsewhere (Bogdanowicz et al, 2009), which is excerpted here to help comprehending the ellipsometry technique.

The ellipsometry is an optical method for thin layer analysis. It is based on polarization state measurement of the light beam reflected from the sample. Such a procedure is used for thickness monitoring of dielectric and semiconductor layers synthesized during physical vapor deposition or chemical vapor deposition processes.

Following assumptions describing the analyzed optical model should be made. A model of a single layer for thin oxide film is considered (Stein et al, 1998). Linearly polarized light beam is incident on the sample at $\phi_0=70^\circ$ angle, where layer thickness is d_1 . N_0 is a refractive index of medium, where substrate is located. Thin oxide films cover the strongly absorbing metal substrate characterized by refractive index N_2 . The complex refractive indexes of investigated layers are denoted as N_1 . For ellipsometric purposes, the complex-amplitude parameter ρ is defined as a ratio of total reflection coefficients:

$$\rho = \frac{r^p}{r^s} = \tan \Psi e^{j\Delta} \quad (1)$$

The ellipsometric angles Δ and Ψ represent the amplitude and phase ratio difference between p - and s -polarization of light beam (Fujiwara, 2007). The amplitude reflectance coefficients in both polarization modes are expressed as follow:

$$\frac{r^p}{r^s} = \left[\frac{r_{01}^p + r_{12}^p \exp(-j2\beta_1)}{1 + r_{01}^p r_{12}^p \exp(-j2\beta_1)} \right] \Bigg/ \left[\frac{r_{01}^s + r_{12}^s \exp(-j2\beta_1)}{1 + r_{01}^s r_{12}^s \exp(-j2\beta_1)} \right] \quad (2)$$

where r_{01} , r_{12} are the Fresnel reflection coefficient defined at boundaries of various i -medium, which depends on $N_i = n_i - ik_i$ complex refractive index (Fujiwara, 2007). The phase shift due to light beam refraction of angle ϕ_1 is expressed by:

$$\beta_i = 4\pi \left(\frac{d_i}{\lambda} \right) N_i \cos \phi_i \quad (3)$$

All refractive indices N_0 , N_1 , and N_2 are complex functions of the λ wavelength of incident light beam. The substitution of Fresnel reflection coefficients and Eqs. 2 and 3 in Eq. 1 gives

complex ratio ρ as a function of medium refractive indexes, light wavelength, and layer thickness.

3. Results and discussion

3.1 AZ40 magnesium alloy in the air

First, the experimental ellipsometric spectra of the AZ40 magnesium alloy in the air was collected and deconvoluted with the aim to determine the optical constants of the AZ40 magnesium alloy.

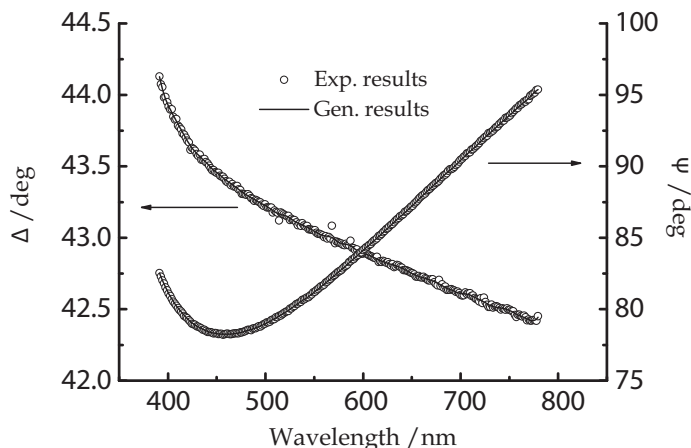


Fig. 1. Ellipsometric spectra of the AZ40 magnesium alloy in the air.

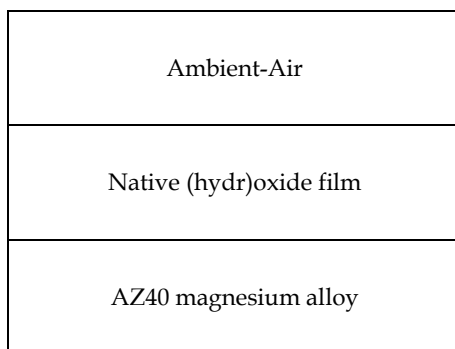


Fig. 2. Optical model for deconvoluting the ellipsometric spectra of the AZ40 magnesium alloy in the air.

Fig.1 shows the experimental ellipsometric spectra (as dots) of the AZ40 magnesium alloy in the air. Considering that a native (hydr)oxide film always exists on the alloy surface, a one-layer optical model (AZ40 magnesium alloy - native (hydr)oxide film - air) shown in Fig.2 is used to deconvolute the ellipsometric data. The generated ellipsometric spectra are shown as the solid lines in Fig.1, which are in good agreements with the experimental spectra. By

deconvolution, the thickness of the native (hydr)oxide film is determined to be approximately 40.0 nm. Moreover, the optical constants (n , k) at different wavelengths for the AZ40 magnesium alloy are obtained, which are illustrated in Fig.3. For comparison, the optical constants (n , k) (within 550-850 nm wavelength) of the AZ31 magnesium alloy obtained in our previous work (Li et al, 2008 a) are also shown in Fig.3. The n and k values of the AZ40 magnesium alloy are larger than those of the AZ31 magnesium alloy at the same wavelength, which is attributed to the different surface status that caused by different alloy composition and pretreatments. However, the variation tendency of the n and k values with the wavelength is similar for the two magnesium alloys. These optical constants for different magnesium alloys can certainly enrich the current database for the optical constants of materials.

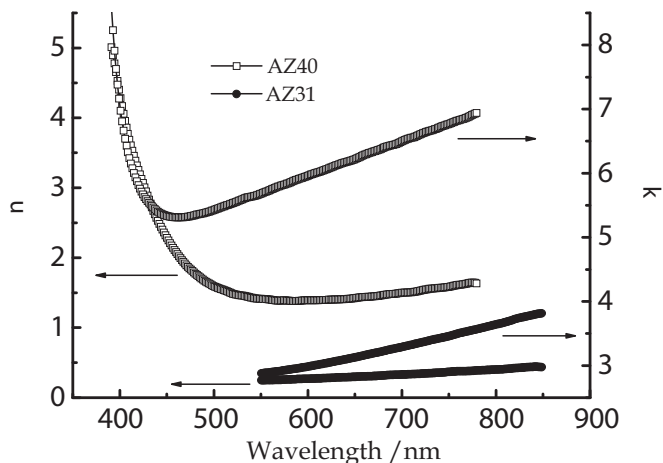


Fig. 3. Optical constants of the AZ40 and AZ31 magnesium alloys.

3.2 AZ40 magnesium alloy in the simulated sea water

The aggressive ion Cl^- in the simulated sea water is strongly corrosive to most metals and alloys. Fig.4(a) illustrates the evolution of OCP of the AZ40 magnesium alloy upon immersion in the simulated sea water.

During the initial 4.8 min, the OCP shifts positively from the beginning -1.624V to -1.558V, which indicates that some corrosion products are unsolvable and stack on the sample surface to provide slight protection to the alloy. After that, the OCP drops suddenly to -1.571V at 4.9min and then gradually stabilizes at about -1.588V from 8.4min till the immersion end. The sudden drop of the OCP is likely due to the falling off of the corrosion products from the alloy surface. The stable OCP reflects that the corrosion achieves dynamic-equilibrium and the corrosion rate varies little.

Fig.4(b) shows the corresponding variation of the ellipsometric parameters Δ and Ψ (at the wavelength $\lambda = 670.0$ nm) with the immersion time. The two parameters both increase slightly upon immersion.

To get the quantitative information on the thickness and optical properties of the corrosion interface during immersion, an optical model should be built and the dynamic spectroscopic ellipsometric data will be further deconvoluted.

Generally, the corrosion interface is composition-complex and heterogeneous, which is very difficult to simulate. In the present work, to simplify the deconvolution, the corrosion interface is equivalent to a homogeneous layer. Hence, a one-layer model (AZ40 magnesium alloy - corrosion interface - corrosive medium) shown in Fig.5 is used to deconvolute the dynamic spectroscopic ellipsometric data during immersion. Some ellipsometric spectra generated by the deconvolution are shown as the solid lines in Fig.6, which are in good agreements with the experimental spectra shown as the dots in Fig.6.

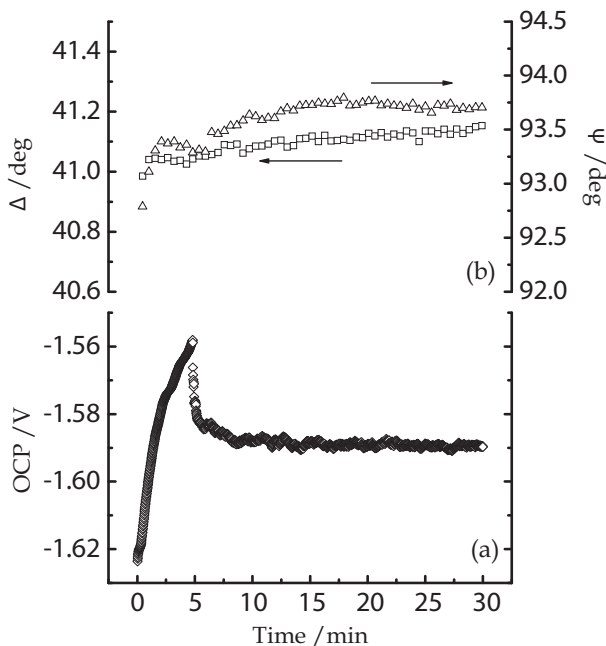


Fig. 4. Evolution of (a) OCP, (b) Δ and Ψ (at $\lambda = 670.0$ nm) upon immersion of the AZ40 magnesium alloy in the simulated sea water.

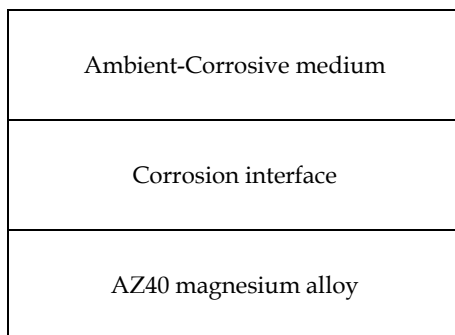


Fig. 5. Optical model for deconvoluting the ellipsometric spectra of the AZ40 magnesium alloy in the corrosive medium.

Fig.7(a) and (b) respectively show the changes of the thickness d and the refractive index n (at $\lambda = 670.0$ nm) of the corrosion interface layer with the immersion time. The variation of the thickness d and the refractive index n of the layer generally are correlated with the layer properties (Ord & Huang, 1985). The decrease of the thickness d usually corresponds to the dissolution of the surface film while the increase of the thickness d often reflects the formation of the adsorption/precipitation film. The linear increase of the layer thickness d with time indicates the poor protection performance of the layer. The changes of the layer thickness d upon immersion follow a logarithmic function, which reflects that the layer can provide good protection. In addition, the larger refractive index n often means the higher density and better protection of the layer. These rules are useful for the subsequent analyzing of the corrosion interface properties.

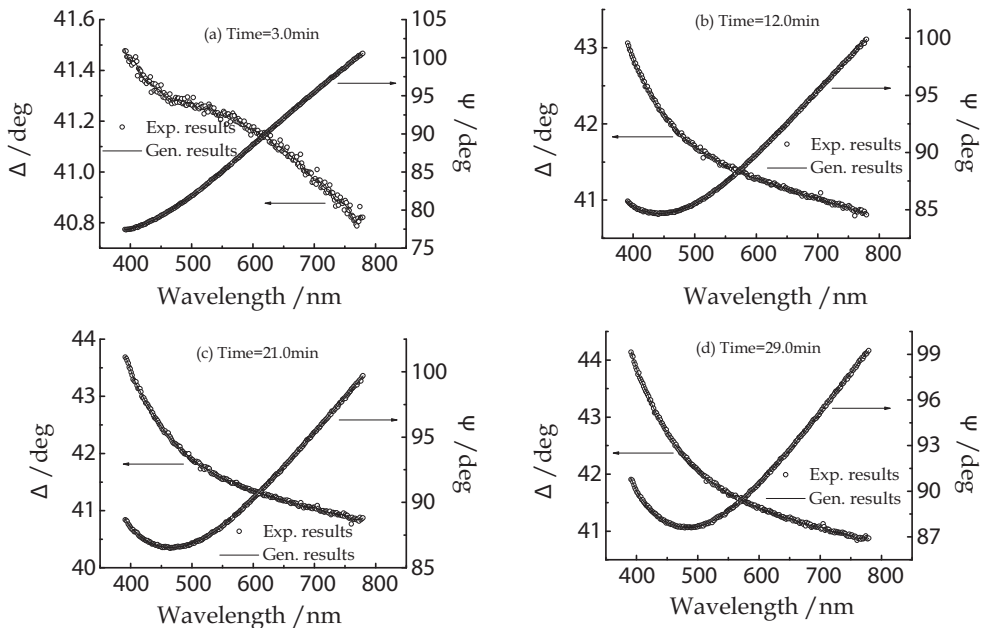


Fig. 6. Experimental and generated ellipsometric spectra during immersion of the AZ40 magnesium alloy in the simulated sea water for different time.

According to the evolution of the thickness d and refractive index n of the corrosion interface layer between the AZ40 magnesium alloy and the simulated sea water shown in Fig.7, and the evolution of OCP shown in Fig.4(a) as well as the SEM and EDS analysis in our previous work (Li et al, 2008 c), the corrosion details of the AZ40 magnesium alloy in the simulated sea water can be speculated as follows.

The corrosion process can be divided into I, II and III three stages, as shown in Fig.7.

Stage I: It may include the dissolution of both the native (hydr)oxide film and the AZ40 magnesium alloy as well as the deposition of some unsolvable corrosion products on the AZ40 magnesium alloy surface, which can be inferred from the huge changes of the thickness d and refractive index n of the surface layer in the air and the first measured value (about 0.9min) after the alloy contacts with the simulated sea water. The thickness d of the

surface layer changes from 40.0 nm in the air to 165.0 nm at 0.9min after the alloy contacts with the corrosive medium. The refractive index n of the surface layer changes from 1.7325 to 1.5535. Due to the strong corrosive nature of the simulated sea water, the reactions in the stage take place very quickly.

Stage II: The stage lasts within 0.9-8.0min immersion, during which the thickness d of the corrosion interface layer decreases slightly and the refractive index n increases little. This stage mainly includes the dissolution of the AZ40 magnesium alloy and the falling off and re-filing in of the corrosion products on the alloy surface. The falling and re-filing of the corrosion products makes the slightly decreasing heterogeneity of the corrosion interface. The decrease of the thickness d of the corrosion interface layer in this stage follows a linear relationship:

$$d / \text{nm} = -0.8596 \times t / \text{min} + 165.45 \quad (R^2 = 0.9964) \quad (4)$$

Stage III: This stage starts at 8min till 30min immersion end. In this stage, the thickness d and refractive index n of the corrosion interface layer are almost constant, which reflects that the corrosion of the AZ40 magnesium alloy in the simulated sea water has achieved the dynamic-equilibrium and the corrosion rate varies little.

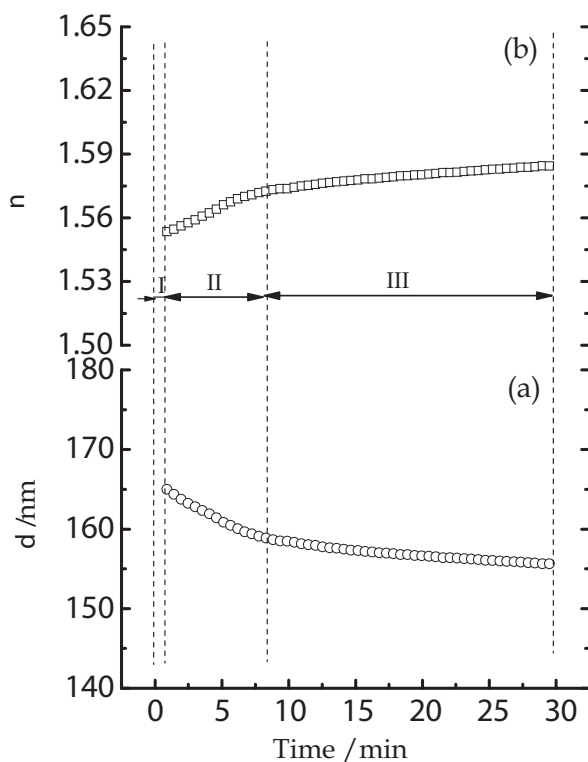


Fig. 7. Evolution of (a) the thickness d , (b) the refractive index n (at $\lambda=670.0$ nm) of the corrosion interface between the AZ40 magnesium alloy and the simulated sea water during immersion.

3.3 AZ40 magnesium alloy in the simulated acid rain

Fig.8(a) illustrates the evolution of OCP of the AZ40 magnesium alloy upon immersion in the simulated acid rain. The OCP shifts about +100mV during the initial 4.8min immersion and then keeps increasing slightly. Fig.8(b) shows the corresponding changes of the ellipsometric parameters Δ and Ψ at the wavelength $\lambda = 670.0$ nm during immersion. The parameter Δ first increases slightly with immersion time, and then increases more obviously. The parameter Ψ shows the trend of decreasing and then minor increasing. The quantitative information on the thickness and optical properties of the corrosion interface during immersion of the AZ40 magnesium alloy in the simulated acid rain is acquired by deconvoluting the dynamic spectroscopic ellipsometric data according to the one-layer model (AZ40 magnesium alloy - corrosion interface - corrosive medium) shown in Fig.5. Fig.9 illustrates some experimental (as dots) and generated ellipsometric spectra (as solid lines) during immersion, which are in good agreements.

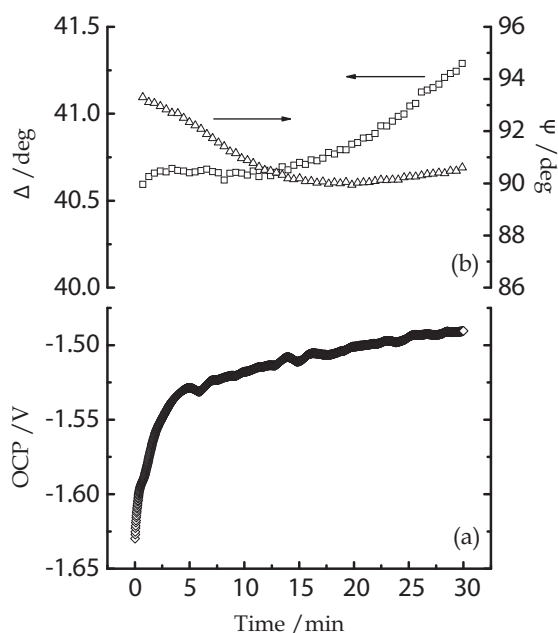


Fig. 8. Evolution of (a) OCP, (b) Δ and Ψ (at $\lambda = 670.0$ nm) upon immersion of the AZ40 magnesium alloy in the simulated acid rain.

Fig.10(a) and (b) respectively show the evolution of the thickness d and the refractive index n (at $\lambda = 670.0$ nm) of the corrosion interface layer upon immersion. Combining with the evolution of OCP shown in Fig.8(a) as well as the other electrochemical results in our previous study, the corrosion details of the AZ40 magnesium alloy in the simulated acid rain can be conferred.

Similarly, the corrosion evolution undergoes I, II and III three stages, which are illustrated in Fig.10.

Stage I: Due to the lower pH value of the simulated acid rain, the natural (hydr)oxide film on the AZ40 magnesium alloy surface dissolves very quickly after the alloy contacts with

the simulated acid rain and then the alloy dissolves. From the large increase of the thickness d (40.0 nm in the air and 148.4 nm at 0.8min after the alloy contacts with the simulated acid rain) as well as the decrease of the refractive index n (changing from 1.7325 to 1.6153) of the surface layer, it can be inferred that the anions such as SO_4^{2-} and NO_3^- in the simulated acid rain easily adsorb on the alloy surface and the unsolvable corrosion products likely precipitate on the surface to form the surface layer. The above dissolution, adsorption and precipitation occur very rapidly.

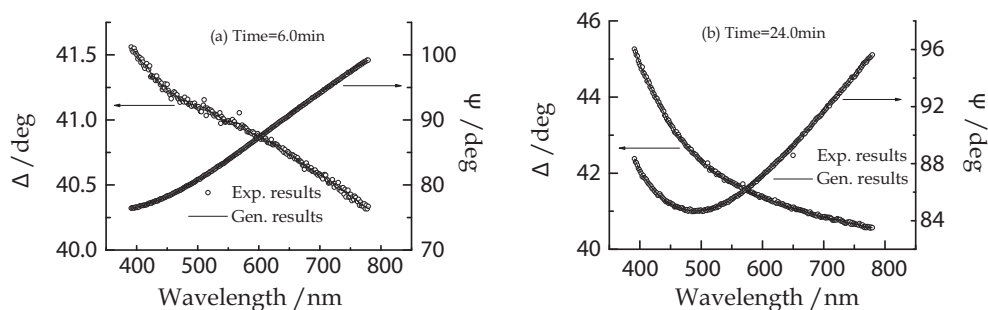


Fig. 9. Experimental and generated ellipsometric spectra during immersion of the AZ40 magnesium alloy in the simulated acid rain for different time.

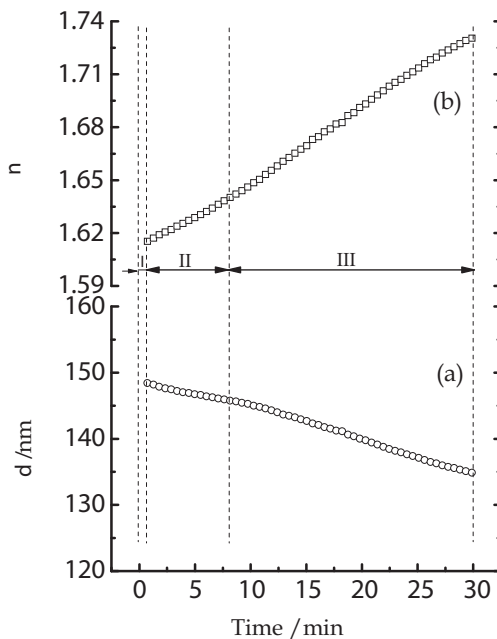


Fig. 10. Evolution of (a) the thickness d , (b) the refractive index n (at $\lambda=670.0$ nm) of the corrosion interface between the AZ40 magnesium alloy and the simulated acid rain during immersion.

Stage II: The stage lasts within 0.8-8.2min immersion of the AZ40 magnesium alloy in the simulated acid rain. At about 8.2min immersion, there is a turning point on the d (thickness)- t (time) curve and n (refractive index)- t curve, after which the thickness d decreases and the refractive index n increases at a different rate. Hence, this stage is inferred to mainly include the dissolution of the AZ40 magnesium alloy, the desorption and re-adsorption of the anions as well as the falling off and re-filing in of the corrosion products on the alloy surface, which make the decreasing heterogeneity of the corrosion interface. The thickness d of the corrosion interface layer decreases linearly as the following relationship:

$$d / \text{nm} = -0.3448 \times t / \text{min} + 148.50 \quad (R^2 = 0.9946) \quad (5)$$

Stage III: This stage starts at 8.2min till 30min immersion end. The processes occur in this stage are similar to those in stage II. But the rates of the dissolution of the AZ40 magnesium alloy, of the desorption and re-adsorption of the anions as well as of the falling off and re-filing in of the corrosion products on the alloy surface in these two stages are slightly different, which makes the different decrease rate of the thickness d and the different increase rate of the refractive index n of the corrosion interface layer in these two stages. The decrease of the thickness d of the corrosion interface layer in this stage follows a linear relationship:

$$d / \text{nm} = -0.5314 \times t / \text{min} + 150.54 \quad (R^2 = 0.9994) \quad (6)$$

3.4 AZ40 magnesium alloy in the simulated cooling water

Fig.11(a) shows the evolution of OCP of the AZ40 magnesium alloy upon immersion in the simulated cooling water without and with sodium molybdate (the inhibitor). The OCP in these two cases both shifts about +120mV once the magnesium alloy contacts with the mediums, and then keeps constant. The OCP in simulated cooling water with the inhibitor is always more positive than that without the inhibitor. Fig.11(b) and (c) respectively show the corresponding changes of the ellipsometric parameters Δ and Ψ (at $\lambda = 670.0 \text{ nm}$) during immersion. The parameter Δ in the two cases both increases with time, which is more obvious in the simulated cooling water with the inhibitor. The parameter Ψ shows the trend of increasing, decreasing, and then increasing with time in the simulated cooling water without the inhibitor, which is opposite to the trend in the presence of the inhibitor. By deconvoluting the dynamic spectroscopic ellipsometric data according to the one-layer model (AZ40 magnesium alloy - corrosion interface - corrosive medium) shown in Fig.5, the quantitative information on the thickness and optical properties of the corrosion interface during immersion can be obtained. Fig.12 and Fig.13 respectively show some experimental (as dots) and corresponding generated ellipsometric spectra (as solid lines) during immersion of the AZ40 magnesium alloy in the simulated cooling water without and with the inhibitor. The experimental spectra agree well with the generated ones.

Fig.14(a) and (a') respectively illustrate the thickness d evolution of the corrosion interface layer upon immersion of the AZ40 magnesium alloy in the simulated cooling water without and with the inhibitor. Fig.14(b) and (b') respectively show the corresponding changes of the refractive index n (at $\lambda = 670.0 \text{ nm}$) of the corrosion interface layer. Combining with the evolution of OCP shown in Fig.11(a) as well as the EIS, SEM and EDS analysis in our previous research (Li et al, 2008 b), the corrosion details of the AZ40 magnesium alloy in the simulated cooling water without and with the inhibitor are presumed.

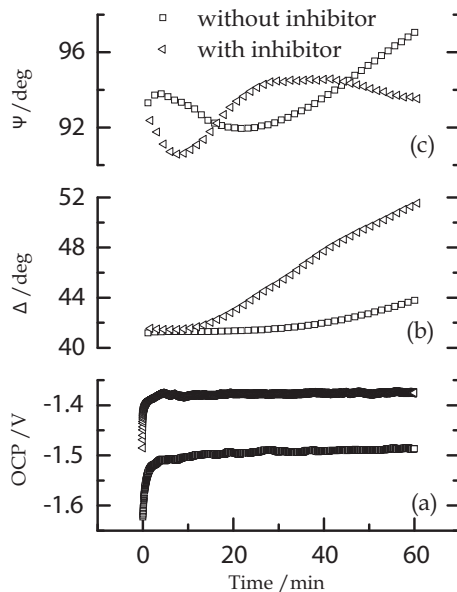


Fig. 11. Evolution of (a) OCP, (b) Δ and (c) Ψ (at $\lambda = 670.0$ nm) upon immersion of the AZ40 magnesium alloy in the simulated cooling water without and with the inhibitor.

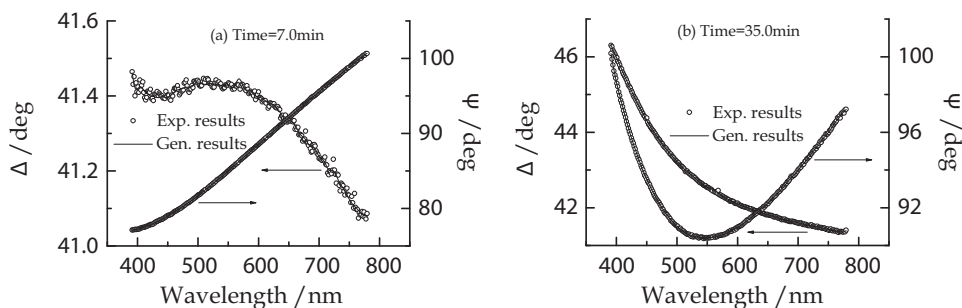


Fig. 12. Experimental and generated ellipsometric spectra during immersion of the AZ40 magnesium alloy in the simulated cooling water without the inhibitor.

As shown in Fig.14, the corrosion processes of the AZ40 magnesium alloy in the simulated cooling water without the inhibitor include I, II and III three stages.

Stage I: The stage lasts 4.0min after the alloy contacts with the medium. The thickness d and refractive index n of the corrosion interface layer change very little during this stage, which indicates that the stage mainly corresponds to the dissolution of the native (hydr)oxide film on the alloy surface.

Stage II: The stage lasts within 4.0-19.0min immersion. The thickness d and refractive index n of the corrosion interface layer both increase slightly. This stage is speculated to mainly include the minor dissolution of the alloy and the adsorption of OH^- that produced during the dissolution process to form the adsorption film on the alloy surface.

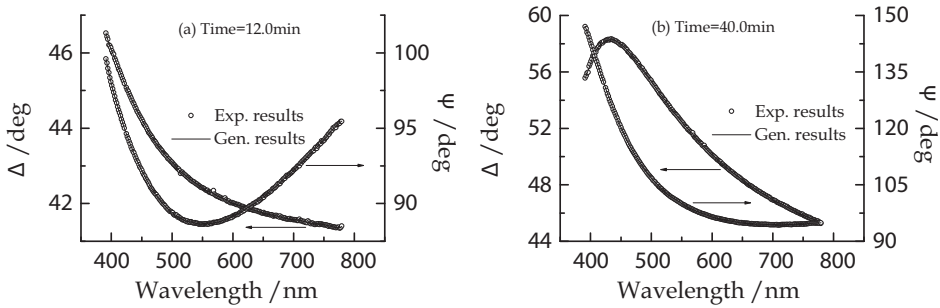


Fig. 13. Experimental and generated ellipsometric spectra during immersion of the AZ40 magnesium alloy in the simulated cooling water with the inhibitor.

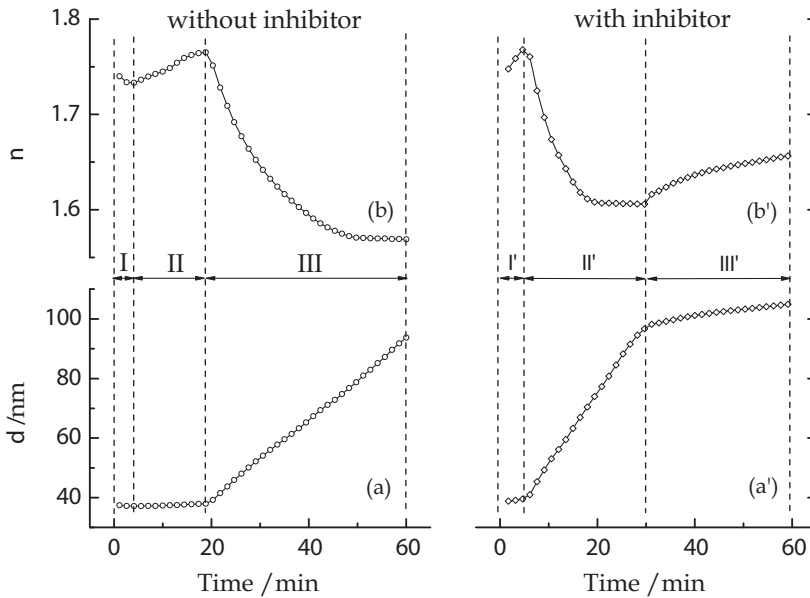


Fig. 14. Evolution of (a) and (a') the thickness d , (b) and (b') the refractive index n (at $\lambda=670.0$ nm) of the corrosion interfaces between the AZ40 magnesium alloy and the simulated cooling water without and with the inhibitor.

Stage III: This stage starts at 19.0min till 60.0min immersion end. The refractive index n of the corrosion interface layer decreases. The layer thickness increases linearly with the immersion time, which can be described as the following relationship:

$$d / \text{nm} = 1.3386 \times t / \text{min} + 12.631 \quad (R^2 = 0.9997) \quad (7)$$

This stage is inferred to mainly correspond to the minor dissolution of the alloy and the deposition of the unsolvable corrosion products such as $\text{Mg}(\text{OH})_2$ on the alloy surface.

Similarly, the corrosion processes of the AZ40 magnesium alloy in the simulated cooling water with the inhibitor can be divided into I', II' and III' three stages, as shown in Fig.14.

Stage I': The stage lasts 5.0min after the alloy contacts with the medium. The thickness d of the corrosion interface layer has little change while the refractive index n increases slightly, which indicates that the stage mainly includes the slight dissolution of the native (hydr)oxide film, and the adsorption of the poly-molybdenum anions (such as $[\text{Mo}_7\text{O}_{24}]^{6-}$ and $[\text{Mo}_8\text{O}_{26}]^{4-}$) that generated by the polymerization of the inhibitor ions (Mu et al, 2006) as well as OH^- that produced during the dissolution process to form the adsorption film on the alloy surface.

Stage II': The stage lasts within 5.0-30.0min immersion. The refractive index n of the interface layer decreases and gradually tends to be constant. The layer thickness d increases linearly with the immersion time. The linear relationship can be described as:

$$d/\text{nm} = 2.3786 \times t/\text{min} + 27.559 \quad (R^2 = 0.9998) \quad (8)$$

This stage is speculated to mainly include the slight dissolution of the alloy, the precipitation of magnesium poly-molybdate and the deposition of the unsolvable corrosion products such as $\text{Mg}(\text{OH})_2$ on the alloy surface.

Stage III': This stage starts at 30.0min till 60.0min immersion end. The refractive index n of the interface layer keeps stable increasing. The layer thickness increases logarithmic with the following relationship:

$$d/\text{nm} = 81.605 + 6.1962 \times \ln(t/\text{min} - 16.802) \quad (R^2 = 0.9995) \quad (9)$$

This stage is presumed to mainly correspond to the increasing homogeneity and compactness of the interface layer, which makes the layer more protective to the alloy.

3.5 Discussion of the influence of the corrosive medium

As well known, Mg^{2+} is the sole stable magnesium species in aqueous solutions with pH value lower than 8.50. Therefore, the native (hydr)oxide film on the AZ40 magnesium alloy surface will dissolve after the alloy contacts with the acidic corrosive medium especially the medium with low pH value such like the simulated acid rain in this work. After the dissolution of the (hydr)oxide film, the primary anodic reaction (the dissolution of magnesium) occurs:



Spontaneously, the cathodic reaction (the reduction of protons) occurs:



The OH^- producing in reaction (11) leads to the pH increase at the corrosion interface. Once the interfacial pH is high enough, Mg^{2+} will precipitate as solid hydroxide $\text{Mg}(\text{OH})_2$ (The solubility product constant $\text{p}K_{\text{sp}}$ of $\text{Mg}(\text{OH})_2$ is 11.25 (Dean, 1999).) and then deposit on the alloy surface.

If some special ions exist in the corrosive medium, the unsolvable precipitates, such as magnesium poly-molybdate in the simulated cooling water with sodium molybdate, will deposit on the alloy surface, too.

From the analysis in sections 3.2-3.4, it is obvious that in the present work the simulated sea water is the most corrosive medium to the AZ40 magnesium alloy, and the simulated acid rain is secondly corrosive while the simulated cooling water is the least corrosive. The dissolution of the native (hydr)oxide film as well as the AZ40 magnesium alloy in the

simulated sea water takes place very rapidly. The thickness of the corrosion interface layer between the AZ40 magnesium alloy and the simulated sea water changes linearly and the layer has smaller refractive index values, which indicates the poor protection of the layer to the alloy. In the simulated acid rain, the native (hydr) oxide film and the AZ40 magnesium alloy also dissolve very quickly due to the more acidic nature of the medium. The thickness of the corrosion interface layer changes linearly while the refractive indexes of the layer are not small, which indicates that the layer can provide some protection to the alloy and the corrosion of the alloy in the simulated acid rain is not very serious. In case of the simulated cooling water, the dissolution rate of the native (hydr)oxide film on the alloy surface is slow and the AZ40 magnesium alloy dissolves slightly. The thickness of the interface layer increases linearly and the layer has large refractive indexes, which indicates that the layer can provide good protection to the alloy and the corrosion of the alloy in the simulated cooling water is slight. With the addition of the inhibitor (sodium molybdate) in the simulated cooling water, the dissolution rate of the native (hydr)oxide film on the alloy surface is much slower. The thickness of the interface layer increases logarithmic and the layer has larger refractive indexes, which reflects that the layer can provide much stronger protection to the alloy.

Hence, the pH value of the corrosive medium and the concentration of the aggression ion Cl⁻ in the medium greatly determine the corrosive nature of the medium. The lower pH value and the more Cl⁻ ions, the more corrosive of the medium, and thus the more poor protection of the corrosion interface layer and the more serious corrosion of the alloy. The molybdate inhibits the corrosion of the AZ40 magnesium alloy in the simulated cooling water by improving the homogeneity and compactness of the interface between the alloy and the corrosive medium.

4. Summary and outlook

In this work, the feasibility of using in situ spectroscopic ellipsometry as a powerful tool for obtaining a better understanding of the corrosion details and mechanism of the AZ40 magnesium alloy in three typical corrosive mediums (the simulated sea water, the simulated acid rain, and the simulated industrial cooling water without or with sodium molybdate) was explored. The refractive indexes and thickness of the "magnesium alloy - corrosive medium" interfaces upon different corrosion evolution are obtained by deconvoluting the dynamic spectroscopic ellipsometric data according to a one-layer model. The corrosion details and mechanism of the AZ40 magnesium alloy in different corrosive mediums are analyzed by correlating the variation of the refractive indexes and thickness of the corrosion interfaces with the layer protective properties. The inhibition mechanism of sodium molybdate on the corrosion of the AZ40 magnesium alloy in the simulated cooling water is elucidated. The corrosion dynamics during different stages is explicit. The corrosivity of the three corrosive mediums in the present work is compared and the influence factors on the corrosivity of the medium are discussed.

The corrosion details and mechanism described in the present work are very useful to reconstruct the corrosive interface structure of magnesium alloys in the corrosive mediums and will absolutely supplement the current investigations on the corrosion of magnesium alloys by the conventional methods. Moreover, the optical constants of the AZ40 magnesium alloy especially the abundant optical constants of the "AZ40 magnesium alloy - corrosive medium" interfaces upon different corrosion evolution obtained in the present

work can greatly enrich current database for optical constants of materials. Thus, the application of in situ spectroscopic ellipsometry to the study of the corrosion processes for magnesium alloys shows considerable promise.

However, some work remains to be done to refine the interpretive approach. For example, adopting a multi-components EMA (Efficient medium approximation) model instead of a one-layer model to represent the corrosion interface during deconvoluting the dynamic spectroscopic ellipsometric data, the results are expected to better reflect the composition-complex and heterogeneous natures of the corrosion interface.

5. Acknowledgments

The authors thank the Natural Science Foundation of Chongqing government (CSTC 2009BA4023), the National Natural Science Foundation of China (NSFC 20803097, 20603049), the National Outstanding Youth Science Foundation of China (NSFC 50725413) and the Fundamental Research Funds for the Central Universities (CDJRC10220002) for financially supporting the research.

6. References

- Bard, A. & Faulkner, L. (2001). *Electrochemical methods, fundamentals and applications*, John Wiley & Sons, Inc., ISBN 0-471-04372-9, New York.
- Bogdanowicz, R.; Ryl, J.; Darowicki, K.; et al. (2009). Ellipsometric study of oxide formation on Cu electrode in 0.1 M NaOH. *Journal of Solid State Electrochemistry*, 13, 1639-1644, ISSN 1432-8488.
- Dean, J. (1999). *Lange's handbook of chemistry* (15th Ed.), McGraw-Hill, Inc., ISBN 0-07-016384-7, New York.
- Fujiwara, H. (2007). *Spectroscopic ellipsometry, principles and applications*, John Wiley & Sons Ltd., ISBN 978-0-470-01608-4, West Sussex.
- Lei, J.; Li, L.; Zhang, S.; et al. (2001 a). Studies on corrosion behavior of copper electrode in weak alkaline solution. *Acta Chimica Sinica*, 59, 1216-1221, ISSN 0567-7351.
- Lei, J.; Li, L.; Cai, S.; et al. (2001 b). Effect of Cl⁻ on the corrosion behavior of copper electrode in weak-alkaline medium. *Acta Physico-Chimica Sinica*, 17, 1107-1111, ISSN 1000-6818.
- Li, L.; Lei, J.; Yu, S.; et al. (2008 a). In situ ellipsometric studies of formation kinetics of rare earth metal conversion coating on magnesium alloys. *Physica Status Solidi (c)*, 5: 1308-1311, ISSN 1610-1642.
- Li, L.; Lei, J.; Yu, S.; et al. (2008 b). Inhibition of corrosion of magnesium alloy by molybdate in simulated cooling water. *Journal of Chemical Industry and Engineering (China)*, 59: 1223-1227, ISSN 0438-1157.
- Li, L.; Yu, S.; Lei, J.; et al. (2008 c). Corrosion behavior and mechanism of AZ40 magnesium alloy in simulated sea water. *Journal of Chongqing University*, 31, 702-706, ISSN 1005-2909.
- Ord, J. & Huang, Z. (1985). An optical study of the deposition, discharge, and recharge of manganese dioxide films. *Journal of The Electrochemical Society*, 132, 1183-1186, ISSN 0013-4651.
- Papavinasam, S. (2000). Corrosion inhibitors, In: *Uhlig's corrosion handbook* (2nd Ed.), Ravie, R. (Ed.), 1089-1105, John Wiley & Sons, Inc., ISBN 0-471-15777-5, New York.

- Song, G. & Atrens, A. (2003). Understanding magnesium corrosion. *Advanced Engineering Materials*, 5, 837-858, ISSN 1616-301X.
- Song, G. (2005). Recent progress in corrosion and protection of magnesium alloys. *Advanced Engineering Materials*, 7, 563-586, ISSN 1616-301X.
- Song, G. (2006). *The corrosion and protection of magnesium alloys*, Chemical Industry Press of China, ISBN 7-5025-8565-6, Beijing.
- Stein, N.; Johann, L.; Rapin, C.; et al. (1998). In situ ellipsometric study of copper passivation by copper heptanoate through electrochemical oxidation. *Electrochimica Acta*, 43, 3227-3234, ISSN 0013-4686.
- Tang, G. & Bai, N. (2000). An analysis of precipitation chemistry data in China with genetic neural network. *Acta Scientiae Circumstance*, 20, 542-, ISSN 0253-2468.
- Vinnichenko, M.; Pham, M. & Chevolleau, T.; et al. (2003). In situ ellipsometric investigation of stainless steel corrosion behavior in buffered solutions with amino acids. *Applied Surface Science*, 207, 176-182, ISSN 0169-4332.
- Wei, Y. & Xu, B. (2007). *Theory and practice of corrosion and protection for magnesium alloys*. Metallurgy Industry Press of China, ISBN 978-7-5024-4232-3, Beijing.
- Zhang, J. & Zhang, Z. (2004). *Magnesium alloys and their applications*, Chemical Industry Press of China, ISBN 7-5025-5709-9, Beijing.

Environmental Friendly Corrosion Inhibitors for Magnesium Alloys

Jinglei LEI¹, Lingjie LI¹ and Fusheng PAN²

¹*Coll. Chem. & Chem. Eng., Chongqing University*

²*Coll. Mat. Sci. & Eng., Chongqing University*

P. R. China

1. Introduction

Magnesium is an important engineering material because of its light weight and excellent properties. Its density is 1.74 g·cm⁻³, only 2/3 that of aluminum and 1/4 that of iron. Moreover, it also has many advantageous properties such as good castability, hot formability, excellent machinability, good electromagnetic shielding characteristics, good biocompatibility, and recyclability (Cao et al, 2006; Staiger et al, 2006). Therefore, magnesium and its alloys have the potential to replace steel and aluminum in many applications. They have already been used in aerospace, aircraft, automotive, mobile electronics, biomaterials and other fields (Zhang & Zhang, 2004).

However, there are some challenges for applications of magnesium and its alloys in a larger scale. The most important one is improving their poor corrosion resistance. Magnesium is a very active metal, and the standard potential of Mg²⁺/Mg is -2.356V (vs. N.H.E. at 25°C) (Bard & Faulkner, 2001). Therefore, magnesium and its alloys are extremely susceptible to corrosion, which can cause the decreased mechanical stability and unattractive appearance (Gray & Luan, 2002). To protect magnesium and its alloys from being corroded, the following techniques are frequently used (Zhang & Zhang, 2004):

- Conversion surface treatments, as chromating, phosphating, etc.,
- Anodizing,
- Electroplating and electroless plating,
- Adding corrosion inhibitors.

A great number of scientific studies have been devoted to the subjects of the first 3 techniques above (Song, 2005). But the last one, adding corrosion inhibitors has been seldom involved. Inhibitors are chemicals that react with a metallic surface, or the environment this surface is exposed to, giving the surface a certain level of protection (Roberge, 2000). For the metals widely employed in the industry such as iron, copper, zinc and aluminum, adding corrosion inhibitors is an effective and convenient method to decrease the corrosion rate. For magnesium and its alloys, there are very few publications on their corrosion inhibitors and only few inhibitors such as the salts of F⁻ (Song, 2005), Cr₂O₇²⁻ (Song, 2006), 8-hydroxyquinoline (Galio et al, 2010), and so on, are involved. Since F⁻ and Cr₂O₇²⁻ pollute the environment seriously, it is quite necessary to pay more attention to develop the environmental friendly corrosion inhibitors for magnesium and its alloys.

In this chapter, we briefly show our recent research progress in the environmental friendly corrosion inhibitors, sodium benzoate (SB) and sodium dodecylbenzenesulphonate (SDBS), for AZ31 magnesium alloy, an important and widely used magnesium alloy, in an aggressive medium, 3.5% NaCl solution. In comparison with the traditional inhibitors of the salts of F^- and $Cr_2O_7^{2-}$, these green inhibitors, SB and SDBS, are promising widely used for magnesium alloys because of their advantages of high inhibition efficiency and harmless to the environment. Our research provides a basis for understanding their anti-corrosion mechanism and indicates the potential approaches for improving the corrosion inhibition efficiency.

2. Corrosion of AZ31 magnesium alloy in 3.5% NaCl solution

2.1 Electrochemical impedance spectra (EIS) measurements

In general, the corrosion resistance of magnesium alloys is less than that of aluminum alloys because the oxide layer on the magnesium alloys is not compact (Zhang & Zhang, 2004; Song, 2006). When a magnesium alloy contacts some aggressive media such as the solution contains Cl^- , the aggressive media will penetrate the oxide layer, reach the surface of the alloy and react with the metal substrate, which leads to the occurrence of corrosion. Usually, the rates of the penetration and chemical reactions increase upon the temperature rising. As the results, the corrosion at higher temperature is more serious than that at low temperature. To obtain some information about the corrosion and the influence of the temperature on the corrosion, the electrochemical impedance spectra (EIS) of AZ31 magnesium alloy samples in 3.5% NaCl solution at different temperatures were recorded and showed in Fig.1. The EIS were acquired at open circuit potential (OCP) after the samples exposed to the NaCl solution for 1 h.

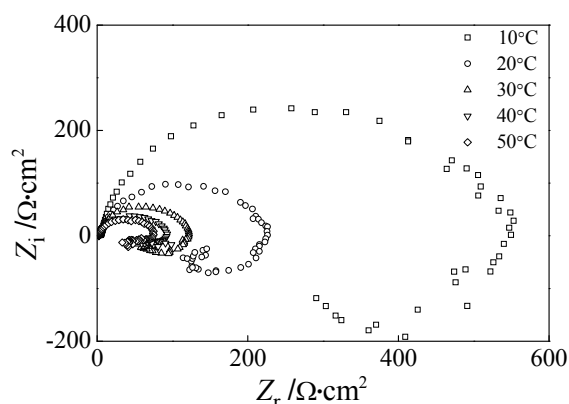


Fig. 1. EIS of AZ31 magnesium alloy in 3.5%NaCl solution without inhibitors at different temperatures.

From Fig.1, it could be observed that EIS at every experimental temperature comprised a capacitive resistance loop at high and medium frequency and an inductance loop at low frequency. Generally, the capacitive loop in the high and medium frequency region reflects the information of resistance capacitance relaxation process that related to the charge transfer resistance R_t and the electric double layer capacity C_{dl} ; the inductance loop in the low frequency region may be attributed to the instability of the electrode surface when the

aggressive ions such as Cl^- were adsorbed (Cao & Zhang, 2002). It also could be found, from Fig.1, that the shape of all EIS at different temperatures was almost the same and the diameters of the capacitive resistance loops at high frequency region decreased with the temperature rising. This meant that the temperature only had a little influence on the mechanism of AZ31 magnesium alloy and the serious corrosion occurred under the high temperature condition.

To determine quantitatively the impedance parameters of AZ31 magnesium alloy in the 3.5% NaCl solution, the capacitive loop in the high and medium frequency range of the measured EIS data were fitted with the equivalent circuit showed in Fig. 2. In the circuit, the dispersion effect was considered and a constant phase element (CPE) was used to substitute for the capacitive element C_{dl} (Cao & Zhang, 2002). Two electrochemical parameters, charge transfer resistance R_t and the double layer capacitance CPE_{dl} were calculated simultaneously and were listed in Table 1. The calculated R_t decreased rapidly from 545.6 to 73.34 $\Omega\cdot\text{cm}^2$ when the temperature was raised from 10 to 50°C. Generally, R_t is related to the charge transfer reaction and reflects the corrosion resistance of the sample. According to the change of R_t , it could be inferred that the corrosion reactions of AZ31 magnesium alloy occurred at high temperature much easier than that at low temperature, which meant that, the magnesium alloy corroded more easily at elevated temperature.

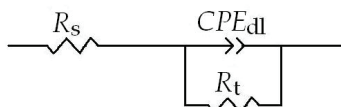


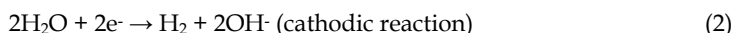
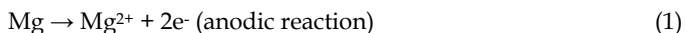
Fig. 2. Equivalent circuit for fitting EIS of AZ31 magnesium alloy in 3.5%NaCl solution.

$T/^\circ\text{C}$	$R_t/\Omega\cdot\text{cm}^2$	$CPE_{dl} -T/\mu\text{F}\cdot\text{cm}^2$	$CPE_{dl} -P$
10	545.6	15.49	0.9074
20	230.0	29.48	0.8653
30	121.7	29.90	0.9123
40	90.00	39.18	0.9070
50	73.34	25.97	0.9225

Table 1. Electrochemical parameters obtained by fitting EIS data.

2.2 Polarization curve measurements

In Fig.3, the polarization curves of AZ31 magnesium alloy samples in the solution with 3.5% NaCl at 10 and 30°C were illustrated. The slopes of the anodic branches were very large, which meant that a small increase in the overpotential would lead to a large increase in the anodic current. This phenomenon could be attributed to the poor protection of the surface layer of AZ31 magnesium alloy. When the corrosion reactions take place for magnesium alloys, the reactions can be expressed simply as following (Song, 2006):



The unsolvable corrosion product $\text{Mg}(\text{OH})_2$ precipitates on the surface of magnesium alloy and form a surface layer. The layer could protect the magnesium alloy from being corroded slightly. However, this protection effect is very poor because that the $\text{Mg}(\text{OH})_2$ layer is not compact (Song, 2006). When a corrosive medium containing Cl^- contacts with AZ31 magnesium alloy, Cl^- , a kind of aggressive ion with small radius, can penetrate this loose $\text{Mg}(\text{OH})_2$ layer easily, reach the surface of the magnesium alloy and accelerate the reaction (1). Therefore, the surface layer which composed with the corrosion products $\text{Mg}(\text{OH})_2$ only has a little protective function for the magnesium alloys in the solution with Cl^- , which led to that the current increased sharply upon the anodic overpotential increasing as if the $\text{Mg}(\text{OH})_2$ layer did not exist.

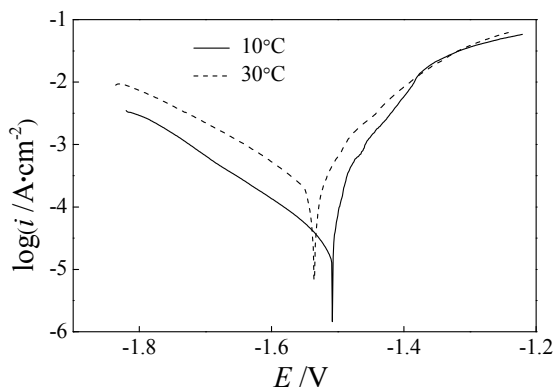


Fig. 3. Polarization curves of AZ31 magnesium alloy samples in the 3.5% NaCl solution at 10 and 30°C.

Compared with the two polarization curves obtained at different temperature in Fig.3, it could be found that the corrosion potential shifted about 30 mV in the negative direction and the corrosion current increased about 10 times when the temperature was raised from 10 to 30°C. The increased current indicated that the corrosion was more serious at elevated temperature than that at lower temperature, which was in agreement with the results of EIS measurements above.

3. Inhibition effect of sodium benzoate (SB) for AZ31 magnesium alloy

Sodium benzoate (SB) is the sodium salt of benzoic acid. Its structure was showed in Fig. 4.

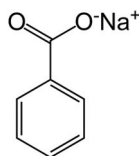


Fig. 4. The skeletal chemical structure of SB.

SB has been recognized as safe as a direct food additive for a long time, and also been used as a corrosion inhibitor for steel, zinc, copper, copper alloys, aluminum and aluminum

alloys (Papavinasam, 2000). Therefore, SB is a kind of environmental friendly corrosion inhibitor. In a corrosion system with the presence of SB, the benzoic acid anion $C_6H_5COO^-$ is adsorbed onto the metal surface via carboxyl groups, which reduces the free energy of the system and impedes the passage of ion-atom of the metal from the lattice into the solution. Sequentially, the corrosion reaction (1) has been inhibited (Afshari & Dehghanian, 2010). There are many reports which involve the inhibition effect of SB on various metals. However, the inhibition effect of SB on magnesium alloys has rarely been reported.

3.1 EIS measurements

Fig.5 showed the EIS results of AZ31 magnesium alloy samples after being exposed to the 3.5% NaCl solutions with different concentrations of SB at 20°C. When the SB concentration was low (less than $0.3 \text{ mol}\cdot\text{L}^{-1}$), the main characteristic of EIS was the same as that of the EIS without SB. They were still composed of a capacitive resistance loop at high and medium frequency and an inductance loop at low frequency. The capacitive resistance loop at high and medium frequency enlarged upon the SB concentration increasing, which indicated the increase in the corrosion resistance. When the SB concentration increased to a relative high level (greater than $0.4 \text{ mol}\cdot\text{L}^{-1}$), the capacitive resistance loop at high and medium frequency kept in enlarging. However, the inductance loop at low frequency was substituted by a capacitive resistance loop. This capacitive resistance loop at low frequency generally was considered to be related to the adsorption-desorption processes of corrosion inhibitor molecules on the surface of magnesium alloy electrodes (Cao & Zhang, 2002).

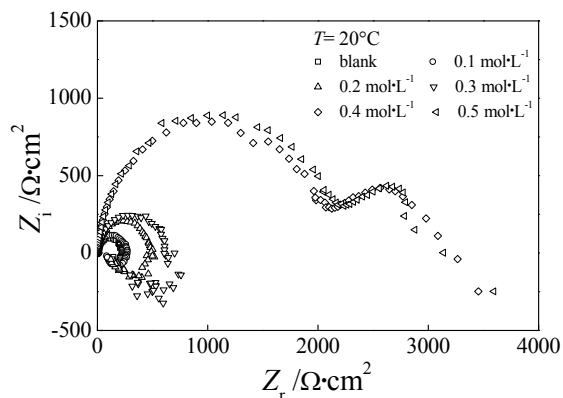


Fig. 5. EIS of AZ31 magnesium alloy in 3.5%NaCl solutions with different concentrations of corrosion inhibitor SB at 20°C.

By analyzing the capacitive resistance loop in the high and medium frequency range with the equivalent circuit showed in Fig.2, both the charge transfer resistance R_t and the interfacial capacitance CPE_{dl} were calculated and listed in Table 2.

In Table 2, the corrosion inhibition efficiency η was also listed. The values of η were calculated according to the following formula:

$$\eta = \frac{R_t - R_t^0}{R_t} \times 100\% \quad (4)$$

where R_t^0 and R_t represent the charge transfer resistance of the system without and with the corrosion inhibitor SB, respectively. The inhibition efficiency η reached 88% till the concentration of SB was $0.4 \text{ mol}\cdot\text{L}^{-1}$, and η increased very little when the SB concentration was higher. Therefore, the concentration $0.4 \text{ mol}\cdot\text{L}^{-1}$ could be treated as the “most economic concentration” for SB. Moreover, it should be noted that all η in Table 2 were less than 90%, which indicated that SB was not a desirable inhibitor for the magnesium alloys.

$c_{\text{SB}} / \text{mol}\cdot\text{L}^{-1}$	$R_t / \Omega\cdot\text{cm}^2$	$CPE_{dl-T} / \mu\text{F}\cdot\text{cm}^{-2}$	CPE_{dl-P}	$\eta / \%$
0	230.0	29.49	0.8653	—
0.1	288.4	36.16	0.8246	20.25
0.2	515.6	28.77	0.8411	55.39
0.3	644.1	29.50	0.8392	64.29
0.4	2005	12.54	0.9222	88.53
0.5	2121	13.44	0.9215	89.16

Table 2. Electrochemical parameters obtained by fitting EIS data and the calculated corrosion inhibition efficiency of SB at $20 \text{ }^\circ\text{C}$.

3.2 Adsorption isotherm for SB on magnesium alloy

Assuming that the adsorption process of SB onto the AZ31 magnesium alloy sample surface was governed by Temkin adsorption isotherm, the relationship among the corrosion inhibitor concentration c , the adsorption equilibrium constant K and the surface coverage θ would be (Mu et al, 2005; Sahin & Bilgic, 1999):

$$\exp(-2\alpha\theta) = Kc \quad (5)$$

where α is the molecular interaction parameter, which represents the interaction among the different substances in the adsorptive layer. When $\alpha = 0$, there is no interaction between the adsorptive substances; when $\alpha > 0$ or $\alpha < 0$, there exists attractive or repulsive force among the adsorptive substances, respectively. Formula (5) could be converted into formula (6) as following:

$$\ln c = -2\alpha\theta - \ln K \quad (6)$$

To simply the calculation, the coverage θ could be substituted approximatively by the corrosion inhibition efficiency η (Cao & Zhang, 2002). Thus, the relationship between c and η was fitted as a linear function and the results were showed in Fig. 6. The linear correlation coefficient of the fitting was 0.981, very close to 1, which indicated that our assumption about the adsorption process was correct, which meant that, the adsorption of SB on AZ31 magnesium alloy obeyed Temkin adsorption isotherm.

The adsorption equilibrium constant K was $15.61 \text{ L}\cdot\text{mol}^{-1}$, which was calculated from the intercept of the fitted straight line in Fig.6. The value of α , calculated from the slope of the fitted line, was -1.104 . The negative sign of α suggested that the intermolecular repulsion existed among the adsorbed SB molecules on the surface of AZ31 magnesium alloy sample. The repulsion is a possible reason for the large dosage of SB and the undesirable corrosion inhibition efficiency.

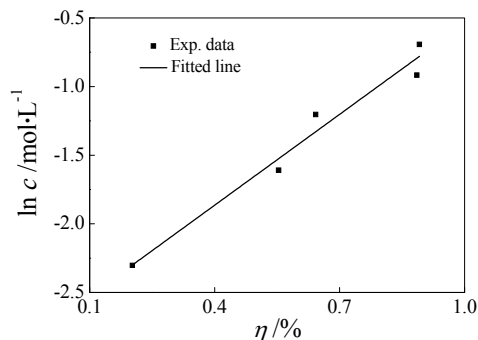


Fig. 6. The relationship between $\ln c$ - η for the adsorption of SB at 20°C.

3.3 Influence of the temperature on the inhibition effect of SB

To investigate the influence of the temperature on the inhibition effect of SB for AZ31 magnesium alloys, the temperature of the medium was cooled to 10°C. The EIS were illustrated in Fig. 7. Since the main characteristic of EIS in Fig. 7 was the same as that in Fig.5, the same equivalent circuit, showed in Fig.2, could be used to fit the EIS. The charge transfer resistance R_t and the interfacial capacitance CPE_{dl} were calculated and listed in Table 3, then the corrosion inhibition efficiency η was obtained with the formula (4), too.

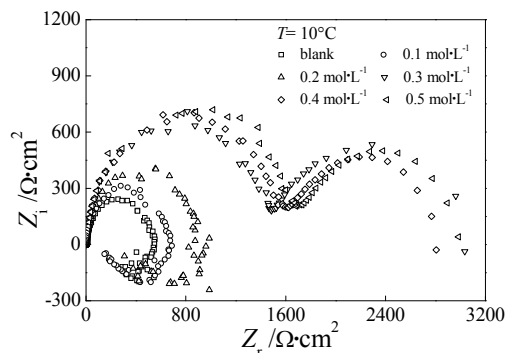


Fig. 7. EIS of AZ31 magnesium alloy in 3.5%NaCl solutions with different concentrations of corrosion inhibitor SB at 10°C.

$c_{SB} / \text{mol}\cdot\text{L}^{-1}$	$R_t / \Omega\cdot\text{cm}^2$	$CPE_{dl} - T / \mu\text{F}\cdot\text{cm}^{-2}$	$CPE_{dl} - P$	$\eta / \%$
0	545.6	15.49	0.9074	—
0.1	674.3	13.54	0.9051	19.09
0.2	910.1	10.86	0.9316	40.06
0.3	1467	12.55	0.9227	62.81
0.4	1593	12.08	0.9268	65.75
0.5	1695	10.82	0.9423	67.81

Table 3. Electrochemical parameters obtained by fitting EIS data and the calculated corrosion inhibition efficiency of SB at 10 °C.

The values of the corrosion inhibition efficiency η in Table 3 were greater those that in Table 2, which indicated that the elevated temperature was helpful to inhibit the corrosion of magnesium alloys.

By using the same procedure as that to deal with the data at 20°C, the linear relationship between $\ln c - \eta$ at 10°C was drawn in Fig. 8 (the correlation coefficient of the fitting was 0.970), and the parameters of Temkin adsorption isotherm (molecular interaction parameter $\alpha = -1.474$, adsorption equilibrium constant $K = 17.31 \text{ L}\cdot\text{mol}^{-1}$) were obtained.

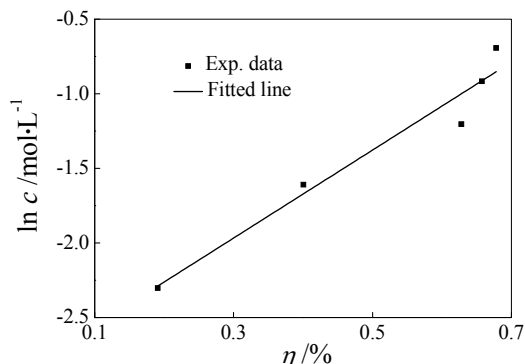


Fig. 8. The relationship between $\ln c - \eta$ for the adsorption of SB at 10°C.

3.4 Thermodynamic parameters for adsorption of SB on magnesium alloy

Thermodynamic model is very helpful to understand the adsorption phenomenon of inhibitor molecules. By using the obtained adsorption equilibrium constant above, the adsorption free energy, adsorption heat and adsorption entropy can be calculated based on the Van't Hoff equation of physical chemistry (Atkins & Paula, 2006):

$$\ln K = \frac{-\Delta H}{RT} + \text{Constant} \quad (7)$$

where ΔH is the adsorption heat. Obviously, the relationship between $\ln K$ and $1/T$ could be described as a linear function, hence ΔH could be obtained from the slope of the straight line. Fig. 9 showed the linear relationship between $\ln K$ and $1/T$, and the adsorption heat was calculated as $-4.296 \text{ kJ}\cdot\text{mol}^{-1}$. Under the experimental conditions, the adsorption heat can be approximately regarded as the standard adsorption heat ΔH^0 (Mu et al, 2005).

To obtain the standard adsorption free energy ΔG^0 , the following equation was employed (Mu et al, 2005):

$$K = \frac{1}{55.5} \exp\left(\frac{-\Delta G^0}{RT}\right) \quad (8)$$

where the value of 55.5 is the concentration of water in solution expressed in $\text{mol}\cdot\text{L}^{-1}$.

Then the standard adsorption entropy ΔS^0 could be calculated based on the thermodynamic basic equation (9):

$$\Delta G^0 = \Delta H^0 - T\Delta S^0 \quad (9)$$

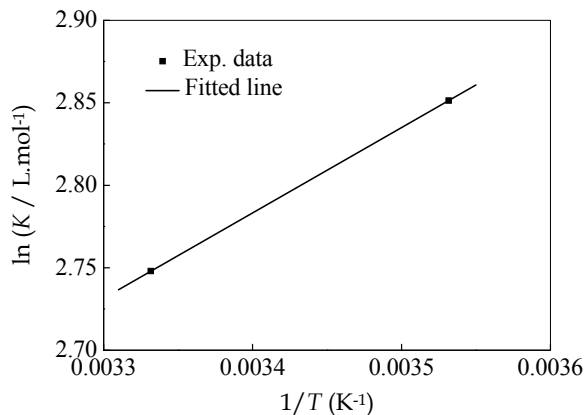


Fig. 9. The relationship between $\ln K$ and $1/T$ for the adsorption of SB.

All the calculated thermodynamic parameters were listed in Table 4.

$T / ^\circ\text{C}$	$\Delta H^0 / \text{kJ}\cdot\text{mol}^{-1}$	$\Delta G^0 / \text{kJ}\cdot\text{mol}^{-1}$	$\Delta S^0 / \text{J}\cdot\text{mol}^{-1}\cdot\text{K}^{-1}$
10	-4.296	-16.17	41.92
20	-4.296	-16.48	41.58

Table 4. Calculated thermodynamic parameters for the adsorption of SB on AZ31 magnesium alloy surface at 10 and 20°C.

The negative value of ΔH^0 indicates that the adsorption of SB is an exothermic process. And according to the magnitude of ΔH^0 , it seems reasonable to assume that physical adsorption takes place for SB on AZ31 magnesium alloy surface. The negative value of ΔG^0 means that the adsorption of SB on AZ31 magnesium alloy surface is a spontaneous process. The positive values of ΔS^0 suggest that the adsorption is a process accompanied by an increase in entropy. The increased entropy might be related to that the repulsive force exists among the adsorptive molecules of corrosion inhibitor SB, which leads to the disordered arrangement of SB molecules on AZ31 magnesium alloy surface.

3.5 Polarization curve measurements

Polarization curve experiments can provide an insight into the mechanism of the SB corrosion inhibition effect. Since the temperature has a little influence on the EIS results, here we only show the potentiodynamic polarization curves of AZ31 magnesium alloy in 3.5% NaCl solutions with and without additions of 0.5 mol·L⁻¹ SB at 10°C in Fig. 10.

The corrosion potential E_{corr} and pitting potential E_{pit} were marked in Fig. 10. In 3.5% NaCl solution without SB, E_{pit} of AZ31 magnesium alloy was more negative than E_{corr} , which was similar to the result reported in the literature (Song & Atrens, 2003). This indicated that pitting occurred spontaneously when AZ31 magnesium alloy contacted with the aggressive medium, which meant that AZ31 magnesium alloy was unstable in the NaCl solution. When the solution contained SB, E_{corr} was more negative than E_{pit} . It also could be observed that E_{corr} shifted in the positive direction about 20 mV after SB was added into the solution. Moreover, compared with the situation without SB in the solution, the current density of anodic branch decreased obviously while the cathodic branch current density only changed little.

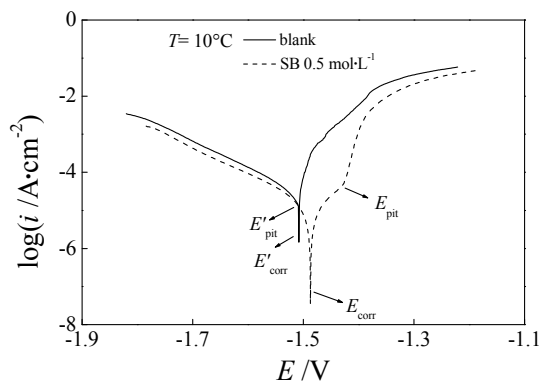


Fig. 10. Polarization curves of AZ31 magnesium alloy samples in 3.5% NaCl solutions with and without SB at 10°C.

Therefore, it could be inferred that SB was a kind of anodic corrosion inhibitor for AZ31 magnesium alloy.

3.6 Scanning electron microscope (SEM) characterization

To observe the inhibition effect of SB directly, the surface morphology of AZ31 magnesium alloy samples was acquired with Scanning Electron Microscope (SEM) and showed in Fig. 11. Before the SEM observations, the magnesium alloy samples had been immersed in the 3.5% NaCl solution contained SB 0.4 mol·L⁻¹ at OCP at 30°C for 1h. As the comparison, the SEM image of surface morphology of the sample exposed to the solution without SB at OCP for 1h was also acquired and showed in Fig. 11 (a). The image of Fig. 11 (a) indicated that the serious corrosion occurred, the corrosion products covered the sample surface and there were many cracks in the surface layer of the products. In Fig. 11 (b), the sample surface after immersion test in SB solution was still very smooth, which meant that SB inhibited the corrosion of AZ31 magnesium alloy effectively.

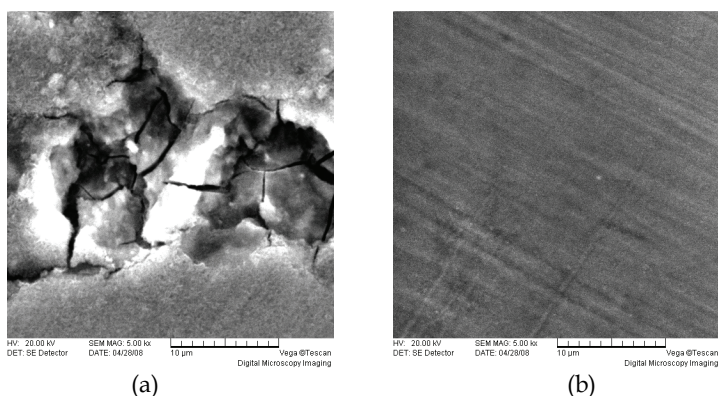


Fig. 11. SEM images of AZ31 magnesium alloy samples after 1h immersion at 30°C in the solutions contained (a) no inhibitors; (b) 0.4 mol·L⁻¹ SB.

4. Inhibition effect of sodium dodecylbenzenesulfonate (SDBS) for AZ31 magnesium alloy

The structure of sodium dodecylbenzenesulfonate (SDBS) was showed in Fig. 12. SDBS is an anionic surfactant with good biological degradability and usually used to produce industrial and daily detergents. It has also been recognized as a kind of environmental friendly corrosion inhibitor for some metals and alloys. However, besides our work (Li et al, 2009), there are few reports on its inhibition effect for magnesium alloys.

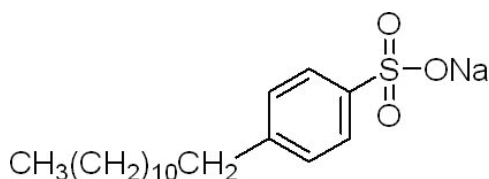


Fig. 12. The skeletal chemical structure of SDBS.

4.1 EIS measurements

Fig. 13 and Fig. 14 showed the EIS of AZ31 magnesium alloy samples, which were acquired in the 3.5% NaCl solutions with different concentration of SDSB at 30 and 50°C respectively.

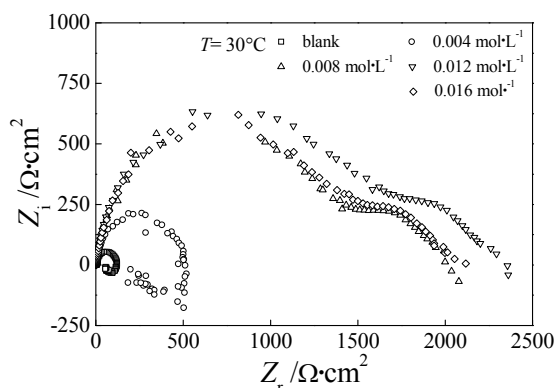


Fig. 13. EIS of AZ31 magnesium alloy in 3.5%NaCl solutions with different concentrations of corrosion inhibitor SDBS at 30°C.

The main characteristic of EIS, including a capacitive resistance loop at high and medium frequency and an inductance loop at low frequency, was the same as that of the EIS with SB, which were illustrated in Fig. 5. Therefore, the equivalent circuit in Fig.2, which was used to analyze the EIS with SB, could also be used to fit the EIS data here. Both the charge transfer resistance R_t and the interfacial capacitance CPE_{dl} were calculated and listed in Table 5 and Table 6, respectively. Moreover, the corrosion inhibition efficiency η was obtained with the formula (4) and listed in the tables, too. Obviously, the “most economic concentration” of SDBS was 0.008 mol·L⁻¹. Compared with SB, whose “most economic concentration” was 0.4 mol·L⁻¹ and the highest inhibition efficiency was less than 90%, SDBS was a better inhibitor for AZ31 magnesium alloy because of the lower dosage and higher inhibition efficiency.

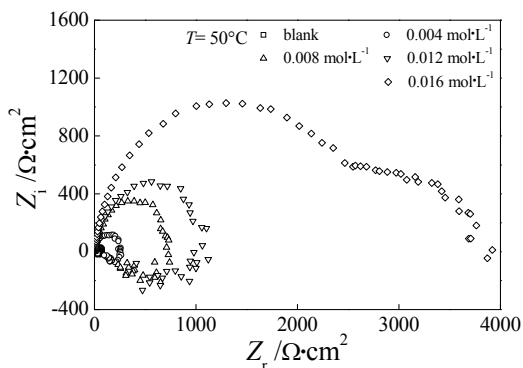


Fig. 14. EIS of AZ31 magnesium alloy in 3.5%NaCl solutions with different concentrations of corrosion inhibitor SDBS at 50°C.

$c_{\text{SDBS}} / \text{mol}\cdot\text{L}^{-1}$	$R_t / \Omega\cdot\text{cm}^2$	$CPE_{\text{dl}} - T / \mu\text{F}\cdot\text{cm}^{-2}$	$CPE_{\text{dl}} - P$	$\eta / \%$
0	121.7	29.91	0.9123	—
0.004	510.1	16.24	0.8867	76.14
0.008	1442	13.83	0.8871	91.56
0.012	1597	13.22	0.8889	92.38
0.016	1512	15.80	0.8715	91.95

Table 5. Electrochemical parameters obtained by fitting EIS data and the calculated corrosion inhibition efficiency of SDBS at 30 °C.

$c_{\text{SDBS}} / \text{mol}\cdot\text{L}^{-1}$	$R_t / \Omega\cdot\text{cm}^2$	$CPE_{\text{dl}} - T / \mu\text{F}\cdot\text{cm}^{-2}$	$CPE_{\text{dl}} - P$	$\eta / \%$
0	73.34	25.97	0.9225	—
0.004	278.4	20.29	0.8777	73.66
0.008	767.1	9.807	0.9243	90.44
0.012	1115	11.39	0.8932	93.42
0.016	2557	11.00	0.8967	97.13

Table 6. Electrochemical parameters obtained by fitting EIS data and the calculated corrosion inhibition efficiency of SDBS at 50 °C.

It should be noted that the temperature only had little influence on the corrosion inhibition efficiency of SDBS based on the calculated values in Table 5 and Table 6.

4.2 Adsorption isotherm and adsorption thermodynamic parameters for SDBS on magnesium alloy

By testing graphically, it was found that Langmuir adsorption isotherm described the relationship between the surface coverage value θ and the concentration of the corrosion inhibitor SDBS perfectly:

$$\frac{c}{\theta} = \frac{1}{K} + c \quad (10)$$

where K denoted the adsorption equilibrium constant. Here the coverage θ also was substituted by the corrosion inhibition efficiency η approximately to simply the calculation. According to the equation (10), linear regressions between c/θ and c at 30 and 50°C were carried out and the results were illustrated in Fig. 15 and Fig. 16, respectively. The slopes of the straight lines, the linear correlation coefficients and the equilibrium constants K were listed in Table 7.

In Table 7, the slopes of the straight lines, the linear correlation coefficients were very close to 1, which confirmed that the adsorption of inhibitor SDBS onto AZ31 magnesium alloy surface was governed by the Langmuir adsorption isotherm.

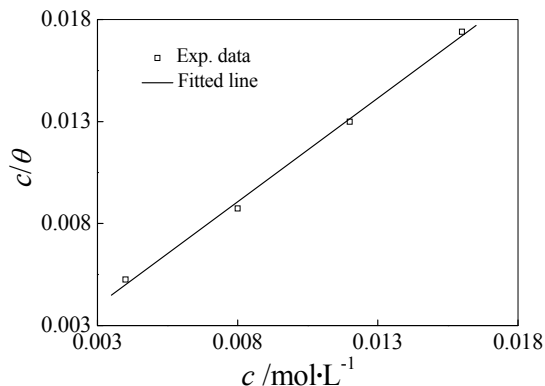


Fig. 15. The relationship between $c/\theta - c$ for the adsorption of SDBS at 30°C.

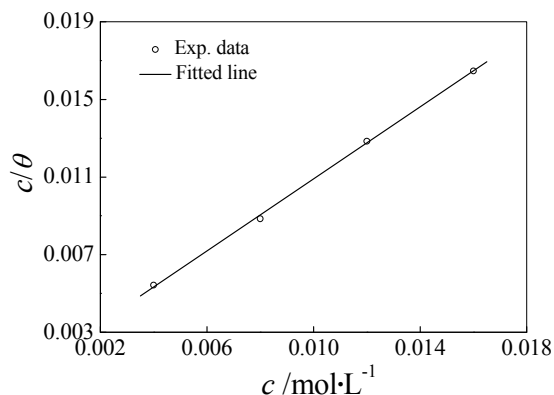


Fig. 16. The relationship between $c/\theta - c$ for the adsorption of SDBS at 50°C.

$T / ^\circ\text{C}$	$K / \text{L}\cdot\text{mol}^{-1}$	Slope	r
30	1085	1.017	0.996
50	617.3	0.9282	0.999

Table 7. Linear regression parameters of $c/\theta - c$ for the adsorption of SDBS.

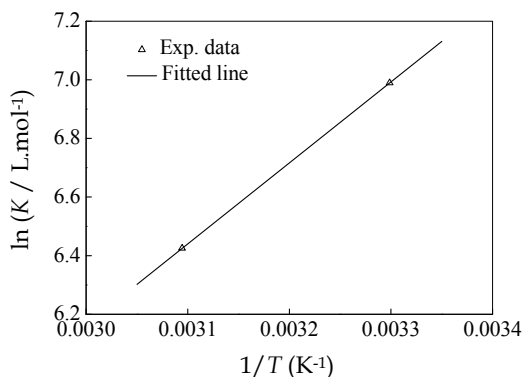


Fig. 17. The relationship between $\ln K$ and $1/T$ for the adsorption of SDBS.

Using the values of K in Table 7, a linear relationship between $\ln K$ and $1/T$, which were used to calculate standard adsorption heat ΔH^0 based on the formula (7), were obtained and illustrated in Fig. 17. Then, the standard adsorption free energy ΔG^0 and standard adsorption entropy ΔS^0 were calculated with the formulas (8) - (9) and given in Table 8.

$T / ^\circ\text{C}$	$\Delta H^0 / \text{kJ}\cdot\text{mol}^{-1}$	$\Delta G^0 / \text{kJ}\cdot\text{mol}^{-1}$	$\Delta S^0 / \text{J}\cdot\text{mol}^{-1}\cdot\text{K}^{-1}$
30	-22.96	-35.43	41.14
50	-22.96	-37.77	45.82

Table 8. Calculated thermodynamic parameters for the adsorption of SDBS on AZ31 magnesium alloy surface at 30 and 50°C.

According to the value of ΔH^0 , it could be inferred that the adsorption of SDBS on AZ31 magnesium alloy surface is an exothermic process and belongs to the physical adsorption. The negative value of ΔG^0 indicates that the adsorption of SDBS onto AZ31 magnesium alloy surface is a spontaneous process. The positive values of ΔS^0 suggest that the adsorption is a process accompanied by an increase in entropy.

4.3 Polarization curve measurements

The polarization behaviors of AZ31 magnesium alloy samples in 3.5% NaCl solutions without and with 0.012 mol·L⁻¹ SDBS at 30°C were showed in Fig. 18. The presence of SDBS in the solution led to that corrosion potential E_{corr} shifted in the positive direction about 15 mV and E_{corr} was more negative than the pitting potential E_{pit} . Moreover, the current densities of both the anodic and cathodic branch decreased, it could be inferred that SDBS is a kind of mixed corrosion inhibitor for AZ31 magnesium alloy.

4.4 SEM characterization

SEM technique was used to characterize the surface morphology of AZ31 magnesium alloy samples. After being exposed to the 3.5% NaCl solution with 0.012 mol·L⁻¹ SDBS for 1h, the sample still had a smooth surface, which was given in Fig. 19. Compared with the rough surface of the sample immersed in the solution without any corrosion inhibitors, (illustrated in Fig. 11 (a)), it could be concluded that SDBS was an effective corrosion inhibitor for AZ31 magnesium alloy.

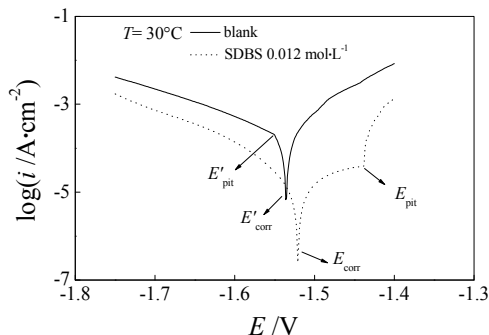


Fig. 18. Polarization curves of AZ31 magnesium alloy samples in 3.5% NaCl solutions without and with $0.012 \text{ mol}\cdot\text{L}^{-1}$ SDBS at 30°C .

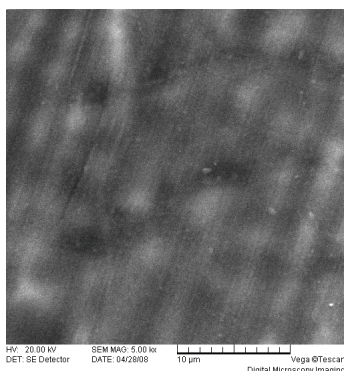


Fig. 19. SEM image of AZ31 magnesium alloy sample after 1h immersion at 30°C in the solution contained $0.012 \text{ mol}\cdot\text{L}^{-1}$ SDBS.

5. Comparison of the effect of inhibitors for AZ31 magnesium alloy

To evaluate the corrosion inhibition effect of SB and SDBS, their inhibition efficiency was compared with that of the salts of F^- and $\text{Cr}_2\text{O}_7^{2-}$. The salts chosen here were KF and $\text{K}_2\text{Cr}_2\text{O}_7$, the widely used corrosion inhibitors for magnesium alloys at present (Song, 2005; Song, 2006).

First, polarization curve measurements were carried out. Fig. 20 illustrated the polarization curves for AZ31 magnesium alloy samples in the 3.5% NaCl solutions contained one of the inhibitors of SB, SDBS, KF and $\text{K}_2\text{Cr}_2\text{O}_7$ at 30°C , respectively.

Since the negative difference effect (NDE) exists for magnesium alloys (Song & Atrens, 2003), the corrosion current density calculated from the polarization curve is not reliable. Here we only analyzed the polarization curves qualitatively. In Fig. 20, it could be observed that the current decreased with the presence of the inhibitors, which suggested that every inhibitors studied here could inhibit the corrosion of magnesium alloy effectively. According to the shifts of the corrosion potential, it could be inferred that SDBS, KF and $\text{K}_2\text{Cr}_2\text{O}_7$ were mixed inhibitors while SB was an anodic inhibitor for magnesium alloys.

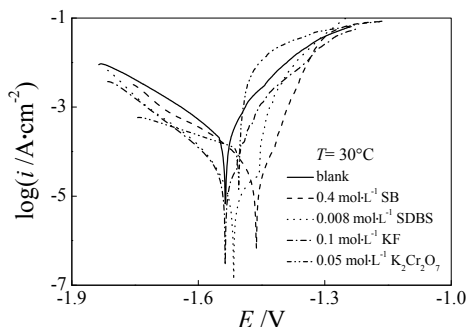


Fig. 20. Polarization curves of AZ31 magnesium alloy samples in 3.5%NaCl solutions with different inhibitors at 30°C.

EIS technique was also employed to evaluate the inhibition effect. Fig. 21 showed the EIS of AZ31 magnesium alloy in 3.5% NaCl solutions without and with the different corrosion inhibitors at 30°C. The capacitive resistance loop at high and medium frequency enlarged obviously upon the presence of the inhibitors, which indicated that all inhibitors reduce the corrosion of AZ31 magnesium alloy effectively. The results of EIS and polarization curve measurements were in good agreement qualitatively. Moreover, by fitting the EIS data in the high and medium frequency range with the equivalent circuit showed in Fig.2, the values showed in charge transfer resistance R_t and other electrochemical parameters could be calculated quantitatively. Table 9 listed the electrochemical parameters obtained by fitting EIS data and the corrosion inhibition efficiency η calculated with the formula (4).

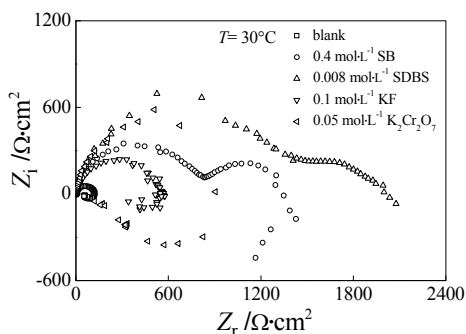


Fig. 21. EIS of AZ31 magnesium alloy samples in 3.5%NaCl solutions with different inhibitors at 30°C.

$c_{\text{inhibitor}} / \text{mol} \cdot \text{L}^{-1}$	$R_t / \Omega \cdot \text{cm}^2$	$CPE_{\text{dl}} - T / \mu\text{F} \cdot \text{cm}^{-2}$	$CPE_{\text{dl}} - P$	$\eta / \%$
0	121.70	29.91	0.9123	—
0.4 mol·L ⁻¹ SB	818.40	15.73	0.9114	85.13
0.008 mol·L ⁻¹ SDBS	1442.0	13.83	0.8870	91.56
0.1 mol·L ⁻¹ KF	557.10	10.26	0.8677	78.15
0.05 mol·L ⁻¹ K ₂ Cr ₂ O ₇	1054.0	73.38	0.9636	88.45

Table 9. Electrochemical parameters obtained by fitting EIS data and the calculated corrosion and inhibition efficiency of different inhibitors at 30 °C.

Based on the polarization curves in Fig. 20 and the corrosion inhibition efficiency η in Table 9, the sort order of the corrosion inhibition efficiency for the different inhibitors should be:

$$\eta_{\text{SDBS}} > \eta_{\text{Cr}_2\text{O}_7^{2-}} > \eta_{\text{SB}} > \eta_{\text{F}^-} \quad (11)$$

Considering the toxicity of F^- and $\text{Cr}_2\text{O}_7^{2-}$, SDBS and SB are promising widely used for magnesium alloys because of their advantages of high inhibitive efficiency and environmental friendly property.

6. Conclusions

In this chapter, EIS, potentiodynamic polarization and SEM measurements were conducted to study the effect of environmental friendly corrosion inhibitors of SB and SDBS on the AZ31 magnesium alloy in 3.5% NaCl solutions. Our investigations show that both SB and SDBS are the effective inhibitors for magnesium alloys, which provides a basis for understanding their anti-corrosion performance and indicates the potential approaches for improving the corrosion inhibition efficiency.

SB is as an anodic inhibitor for magnesium alloys. The inhibition efficiency increases with the increased concentration and the elevated temperature. The adsorption process of SB onto magnesium alloys is a spontaneous exothermic process and follows the Temkin adsorption isotherm with negative molecular interaction parameter, which suggests the existence of repulsive forces in the adsorbed layer.

SDBS inhibits both the anodic and cathodic processes simultaneously and acts as a mixed inhibitor for magnesium alloys. The inhibition efficiency increases with the increased concentration and the temperature has little influence on the inhibition efficiency. The adsorption process of SDBS onto magnesium alloys is a spontaneous exothermic process and obeys a Langmuir adsorption isotherm. As a corrosion inhibitor, SDBS is better than SB because of the lower dosage and higher inhibition efficiency.

Compared with the traditional corrosion inhibitors for magnesium alloys such as $\text{Cr}_2\text{O}_7^{2-}$ and F^- , these inhibitors, SDBS and SB, are promising widely used for magnesium alloys because of their advantages of high inhibitive efficiency and environmental friendly property.

It should be pointed that there is much scope for developing the environmental friendly inhibitors for magnesium alloys. One topic of the future investigations is the effect of other green inhibitors, such as the salts of MoO_4^{2-} , for magnesium alloys. Another topic is the study on the synergistic effect of the complex corrosion inhibitors. For example, it is helpful to improve the inhibition effect by employing other suitable environmental friendly inhibitors which could be adsorbed onto the magnesium surface, weaken or remove the repulsive forces in the adsorbed layer of SB and make the protective layer more compact. The development of high efficiency environmental friendly inhibitors for magnesium alloys will fasten the engineering applications of magnesium alloys in a larger scale.

7. Acknowledgments

This work was sponsored by the Natural Science Foundation Project of CQ (CSTC2009BA4023), the National Natural Science Foundation of China (NSFC20803097), the National Science Fund for Distinguished Young Scholars of China (50725413) and the Fundamental Research Funds for the Central Universities (CDJRC 10220002).

8. References

- Afshari, V. & Dehghanian, C. (2010). Inhibitor effect of sodium benzoate on the corrosion behavior of nanocrystalline pure iron metal in near-neutral aqueous solutions. *Journal of Solid State Electrochemistry*, 14, 1855-1861, ISSN 1432-8488.
- Atkins, P. & Paula, J. (2006). *Physical chemistry* (8th Ed.), Oxford University Press, ISBN 9780198700722, Oxford.
- Bard, A. & Faulkner, L. (2001). *Electrochemical methods, fundamentals and applications*, John Wiley & Sons, Inc., ISBN 0-471-04372-9, New York.
- Cao, C. & Zhang, J. (2002). *Introduction of electrochemical impedance spectroscopy*, Science Press of China, ISBN 7-03-009854-4, Beijing.
- Cao, X.; Jahazi, M.; Immarigeon, J.; et al. (2006). A review of laser techniques for magnesium alloys. *Journal of Materials Processing Technology*, 171, 188-204, ISSN 0924-0136.
- Galio, A.; Lamaka, S.; Zheludkevich, M.; et al. (2010). Inhibitor-doped sol-gel coatings for corrosion protection of magnesium alloy AZ31. *Surface & Coatings Technology*, 204, 1479-1486, ISSN 0257-8972.
- Gary, J. & Luan, B. (2002). Protective coating on magnesium and its alloys - a critical review. *Journal of Alloys and Compounds*, 336, 88-113, ISSN 0925-8388.
- Li, L; Yao, Z.; Lei, J.; et al. (2009). Adsorption and corrosion inhibition behavior of sodium dodecylbenzenesulfonate on AZ31magnesium alloy. *Acta Physico-Chimica Sinica*, 25, 1332-1336, ISSN 1000-6818.
- Mu, G.; Li, X.; Liu, G. (2005). Synergistic inhibition between tween 60 and NaCl on the corrosion of cold rolled steel in 0.5M sulfuric acid. *Corrosion Science*, 47, 1932-1952, ISSN 0010-938X.
- Papavinasam, S. (2000). Corrosion inhibitors, In: *Uhlig's corrosion handbook* (2nd Ed.), Ravie, R. (Ed.), 1089-1105, John Wiley & Sons, Inc., ISBN 0-471-15777-5, New York.
- Roberge, P. (2000). *Handbook of corrosion engineering*, McGraw-Hill Com. Inc., ISBN 0-07-076516-2, New York.
- Sahin, M. & Bilgic, S. (1999). The effect of crotyl alcohol on the corrosion of austenitic chromium-nickel steel. *Applied Surface Science*, 147, 27-32, ISSN 0169-4332.
- Song, G. & Atrens, A. (2003). Understanding magnesium corrosion. *Advanced Engineering Materials*, 5, 837-858, ISSN 1616-301X.
- Song, G. (2005). Recent progress in corrosion and protection of magnesium alloys. *Advanced Engineering Materials*, 7, 563-586, ISSN 1616-301X.
- Song, G. (2006). *The corrosion and protection of magnesium alloys*, Chemical Industry Press of China, ISBN 7-5025-8565-6, Beijing.
- Staiger, M.; Pietak, A.; Huadmai, J.; et al. (2006). Magnesium and its alloys as orthopedic biomaterials: a review. *Biomaterials*, 27, 1728-1734, ISSN 0142-9612.
- Zhang, J. & Zhang, Z. (2004). *Magnesium alloys and their applications*, Chemical Industry Press of China, ISBN 7-5025-5709-9, Beijing.

Electrochemical Corrosion Behavior of Magnesium Alloys in Biological Solutions

Amany Mohamed Fekry
Cairo University (Faculty of Science)
Egypt

1. Introduction

Magnesium (Mg) is the fourth most abundant cation in the human body [Fekry & El-Sherief, 2009]. It is very abundant in the Earth being considered the fourth highest, following iron, oxygen and silicon. The raw ores of Mg are dolomite ($\text{MgCO}_3 \cdot \text{CaCO}_3$) and magnesite (MgCO_3), and Mg is the second most abundant metal in seawater following sodium. It is therefore a comparatively low cost material. Magnesium is the lightest of all metals in practical use, and has a density (1.74 g cm^{-3}) of about two thirds of aluminum and only one quarter that of iron. Pure magnesium metal has useful properties such as shielding against electromagnetic waves, vibration damping, dent resistance, machinability and low toxicity in humans, in addition to its recyclability as it has a lower specific heat and a lower melting point than other metals. On the other hand, magnesium has shortcomings such as insufficient strength, elongation and heat resistance as well as being subject to corrosion. To put Mg to practical use, it is necessary to deal with its shortcomings and improve its performance through alloying with various elements. Alloying magnesium improves its strength, heat resistance and creep resistance (creep is defined as deformation at a high temperature and under load). However, the addition of alloying elements modifies the corrosion behavior of magnesium in such a way that it can be beneficial or deleterious.

Some advantages of magnesium alloys are their high stiffness-to-weight ratio, great ease of machinability, good casting qualities suitable for high pressure die-casting, high damping capacity and good weldability under controlled atmosphere. Magnesium can form intermetallic phases with most alloying elements, the stability of this phase increases with the electronegativity of the other element [Kainer, 2003]. Aluminum (Al) had already become the most important alloying element for significantly increasing the tensile strength, specifically by forming the intermetallic phase $\text{Mg}_{17}\text{Al}_{12}$. Similar effects can be achieved with zinc (Zn) and manganese (Mn), while the addition of silver (Ag) leads to improve high-temperature strength. The identification of magnesium alloys is standardized worldwide in the ASTM norm; each alloy is marked with letters indicating the main alloy elements, followed by the rounded figures of each (usually two) weight in percentage terms. The last letter in each identification number indicates the stage of development of the alloy.

However, according to the elemental composition two major magnesium alloy systems are available to the designer. The first includes alloys containing 2 - 10 wt% Al, combined with minor additions of zinc and manganese. These alloys are widely available at moderate cost,

Abbreviation letter	Alloying element	Abbreviation letter	Alloying element
A	Aluminum	N	Nickel
B	Bismuth	P	Lead
C	Copper	Q	Silver
D	Cadmium	R	Chromium
E	Rare earths	S	Silicon
F	Iron	T	Tin
H	Thorium	W	Yttrium
K	Zirconium	Y	Antimony
L	Lithium	Z	Zinc
M	Manganese		

Table 1. ASTM codes for magnesium's alloying elements

and maintain their room-temperature mechanical properties up to 95° to 120° C. Beyond this, increase in temperature adversely affects mechanical properties and the corrosion properties deteriorate rapidly. The most important alloys of this group are AZ-, AM- and AS - Mg based systems. The second group consists of magnesium alloyed with various elements (rare earths, zinc, thorium, and silver) except aluminum, all containing a small but effective zirconium content that imparts a fine grain structure and thus improved mechanical properties. These alloys generally possess much better elevated-temperature properties, but they are more costly. The most important alloys of this group are ZE, HK and ZK [Kainer, 2003].

Magnesium alloys as potential biodegradable material provides both biocompatibility and suitable mechanical properties [Song, 2007]. Mg^{2+} is an essential element and present in large amounts in the human body. It is the fourth most abundant cation in the human body, with an estimated 1 mol of magnesium stored in the body of a normal 70 kg adult, with approximately half of the total physiological magnesium stored in bone tissue [Song & song, 2007]. The presence of magnesium in the bone system is beneficial to bone strength and growth. Magnesium alloys have specific density (1.74-2 g/cm³) and Young's modulus (41-45 GPa) most close to those (1.8-2.1 g/cm³, 3-20 GPa) of human body's bone. Therefore, in orthopedic and bone repairing or replacement applications magnesium alloys are particularly superior to any other metallic or polymer implants in terms of physical and mechanical properties, as the dissimilarity in Young's modulus between an implant and natural bone can result in stress shielding effects, leading to concentration of stress at the interface between the bone and implant reducing stimulation of new bone growth and decreasing implant stability [Song, 2007].

On the other side, magnesium is 1.6 and 4.5 times less dense than aluminum and steel, respectively. Moreover, magnesium is essential to human metabolism and is naturally found in bone tissue [Fekry & El-Sherief, 2009]. Biodegradable implant materials in the human body can be gradually dissolved, absorbed, consumed or excreted, so there is no need for the secondary surgery to remove implants after the surgery regions have healed. Metallic materials continue to play an essential role as biomaterials to assist with the repair or replacement of bone tissue that has become diseased or damaged. Thus, it is projected

that magnesium and its alloys be applied as lightweight, degradable, load bearing orthopedic implants, which would remain present in the body and maintain mechanical integrity over a time scale of 12–18 weeks while the bone tissue heals, eventually being replaced by natural tissue [Staiger et al., 2006]. Also, magnesium has a high negative standard electrode potential (-2.37 V at 25 °C) and thus is corroded relatively faster than other metallic materials, especially in Cl^- containing aqueous environment, indicating that magnesium can degrade/or be corroded in a human body environment. Thus interface problems such as interface loosening and inflammation can be resolved and the second removal surgical operation for the case of bone screws and plates can be avoided. Thus, Mg alloy can gradually be dissolved and adsorbed after implanting [Revell et al., 2004; Zreiqat et al., 2002; Yamasaki, 2002 & 2003]. A suitable degradation rate is critical to a biodegradable Mg implant before the tissue has been sufficiently recovered or healed [Witte, 2005]. After the recovery or healing, the implant should be gradually dissolved, consumed or absorbed by the human body. In fact, with recent developments and understandings of corrosion and prevention of Mg alloy, controlling the corrosion performance of Mg alloy should be possible now [Yamasaki, 2003; Song & Atrens, 2003]. Extruded Mg alloys as AZ91E and AZ31E are getting more and more widely used because of their considerably high plasticity in comparison with the die-cast Mg alloys [Zenner & Renner, 2002]. Several studies [Song, 2007; Witte et al. 2008; Song et al., 1999] have shown that the corrosion behavior of Mg alloys is significantly dependent on the alloying elements and the microstructure.

Glucosamine ($\text{C}_6\text{H}_{13}\text{NO}_5$) is an amino sugar. All of the glucosamine forms originated from shellfish. Some carrier molecules are needed (such as sulphate or HCl) because raw glucosamine is unstable by itself - it needs to be bound to the sulfate or HCl carrier in order to be stored for any period of time. Glucosamine sulfate is a naturally occurring chemical compound found in the human body. It is used by the body to produce a variety of other chemicals that are involved in building tendons, ligaments, cartilage, and the thick fluid that surrounds joints. Glucosamine sulfate used in dietary supplements does not always come from natural sources. It can also be made in a laboratory. Glucosamine sulfate is commonly used for arthritis. Scientists have studied it extensively for this use [Giordano et al., 2009].

Osteoarthritis (OA) is the most common form of arthritis that can affect the hands, hips, shoulders and knees. In OA, the cartilage that protects the ends of the bones breaks down and becomes thin. This results in more joint friction, pain, and stiffness. Researchers think that taking glucosamine supplements may either increase the cartilage and fluid surrounding joints or help to prevent breakdown of these substances, or may be both. Supplemental glucosamine may help to prevent cartilage degeneration and treat arthritis.

This chapter reviews the biological performance of magnesium based alloys (biodegradable materials for temporary implant) as AZ91D alloy in simulated body fluid (SBF), AZ31E alloy in Ringer's and AZ31E, AZ91E in Hank's solution at 37 °C that have been used as orthopedic biomaterials. Their corrosion behavior was studied by the analysis of corrosion resistance variation with immersion time, using electrochemical impedance spectroscopy (EIS) tests and corrosion current density using potentiodynamic polarization technique. The results were confirmed by scanning electron micrographs. The aim is to explore possible routes to improve limiting factors such as the corrosion resistance and improve integration of the implant with tissue, and ultimately highlights the need for further research. It is aimed to find the best magnesium alloy with low cost and low corrosion rate as implant in human body. Furthermore, the feasibility to slow down the biodegradation (i.e. corrosion)

of magnesium alloys to solve the rapidly corroding magnesium implant problems was demonstrated by studying the effect of adding glucosamine sulphate to Hank's solution on the corrosion behavior of AZ31 alloy. This line of research was still under consideration.

2. The main problem and how to solve?

Recently, a number of studies had been carried out to investigate the corrosion behavior of magnesium alloy in artificial physiological fluids. However, most of them were considering an Al containing Mg alloy [Witte et al. 2006]. Most alloying elements will dissolve into the human body during the magnesium alloy degradation. Magnesium alloys did not perform well due to inappropriately high corrosion rates [Song & Song, 2007]. The screws and plates made of these magnesium alloys corroded too quickly due to high impurities of the alloys and as a consequence, subcutaneous gas cavities appeared in treated patients [Song & Song, 2007]. However, slower corrosion rates are needed for magnesium alloys to be suitable as a potential biomaterial [Witte et al. 2005]. Mn and Zn were selected to develop a Mg-Zn-Mn magnesium alloy for biomedical application due to the good biocompatibility of Zn and Mn elements [Zhang et al. 2009]. The development of biodegradable implants is one of the most important research areas in medical science [Song & Song, 2007; Mani et al., 2007]. Compared with traditional permanent implants, biodegradable materials will not cause permanent physical irritation or chronic inflammatory discomfort. Mg or its alloys are non-toxic to the human body.

Thus in this study, it was observed that corrosion resistance for AZ91D in Simulated body fluid increase with increasing time of immersion until 35 h. Also, it found to increase for AZ31E in Ringer's solution increases with increasing immersion time till 100 h of immersion. Also, the corrosion resistance of AZ91E and AZ31E alloys increase with immersion time in Hank's solution for 100 h. However, the corrosion resistance of AZ31E alloy is much better than AZ91E alloy at all times of immersion. All results are confirmed by scanning electron micrographs. Also, by addition of Glucosamine as inhibitor for corrosion of AZ31E in Hank's solution, it was evaluated that total resistance R_T or relative thickness $1/C_T$ of the film formed are higher compared to the values in absence of glucosamine. However, the best corrosion inhibition is observed by addition of 0.01 mM Glucosamine and this was confirmed by SEM images.

3. Experimental

A die cast magnesium aluminum alloy (AZ91D) with composition (wt%): 9.0 Al, 0.67 Zn, 0.33 Mn, 0.03 Cu, 0.01 Si, 0.005 Fe, 0.002 Ni, 0.0008 Be and balance Mg, an extruded magnesium aluminum alloys with chemical composition (wt%): 2.8 Al, 0.96 Zn, 0.28 Mn, 0.0017 Cu, 0.0111 Fe, 0.0007 Ni, 0.0001 Be and balance Mg for AZ31E and 9.0 Al, 0.7 Zn, 0.13 Mn, 0.03 Cu, 0.01 Si, 0.006 Fe, 0.004 Ni, 0.0007 Be and balance Mg for AZ91E. All donated from Department of mining, Metallurgy and Materials Engineering, Laval University, Canada. The sample was divided into small coupons. Each coupon was welded to an electrical wire and fixed with Araldite epoxy resin in a glass tube leaving cross-sectional area of the specimen 0.2 cm² for AZ91D alloy and 0.196 cm² for both AZ91E and AZ31E alloys. The solutions used were simulated biological fluid (SBF), recommended by Cigada, which contains (g/l): NaCl 8.74, NaHCO₃ 0.35, Na₂HPO₄ 0.06, NaH₂PO₄ 0.06 [Fekry & El-

Sherief, 2009], Ringer's solution (RS) (g/l): NaCl 8.6, CaCl₂ 0.33, KCl 0.3, Hank's balanced salt solution with composition (g/l): NaCl 8.00, NaHCO₃ 0.35, Na₂HPO₄ 0.0477, KH₂PO₄ 0.06, KCl 0.40, D-Glucose 1.0 [Ghoneim et al., 2010]. The pH of the solution was 7.4. Glucosamine sulphate (C₆ H₁₄ NO₅)₂SO₄.2KCl and all solutions are prepared using triply distilled water. The surface of the test electrode was mechanically polished by emery papers with 400 up to 1000 grit to ensure the same surface roughness, degreasing in acetone, rinsing with ethanol and drying in air. The cell used was a typical three-electrode one fitted with a large platinum sheet of size 15×20×2mm as a counter electrode (CE), saturated calomel (SCE) as a reference electrode (RE) and the alloy as the working electrode (WE). The impedance diagrams were recorded at the free immersion potential (OCP) by applying a 10 mV sinusoidal potential through a frequency domain from 100 kHz down to 100 mHz. The EIS was recorded after reading a steady state open-circuit potential. The polarization scans were carried out at a rate of 1 mV/s over the potential range from -2.5 to 0 mV vs. saturated calomel electrode (SCE). Prior to the potential sweep, the electrode was left under open-circuit in the respective solution until a steady free corrosion potential was recorded. Corrosion current, i_{corr} , which is equivalent to the corrosion rate is given by the intersection of the Tafel lines extrapolation. In the weight loss measurements, the treated samples were weighed before and after the immersion in Hank's solution in absence and in presence of different concentrations of glucosamine sulphate. The instrument used is the electrochemical workstation IM6e Zahner-elektrik, GmbH, (Kronach, Germany). The electrochemical and weight loss experiments were always carried inside an air thermostat which was kept at 37°C, unless otherwise stated. The SEM micrographs were collected using a JEOL JXA-840A electron probe microanalyzer.

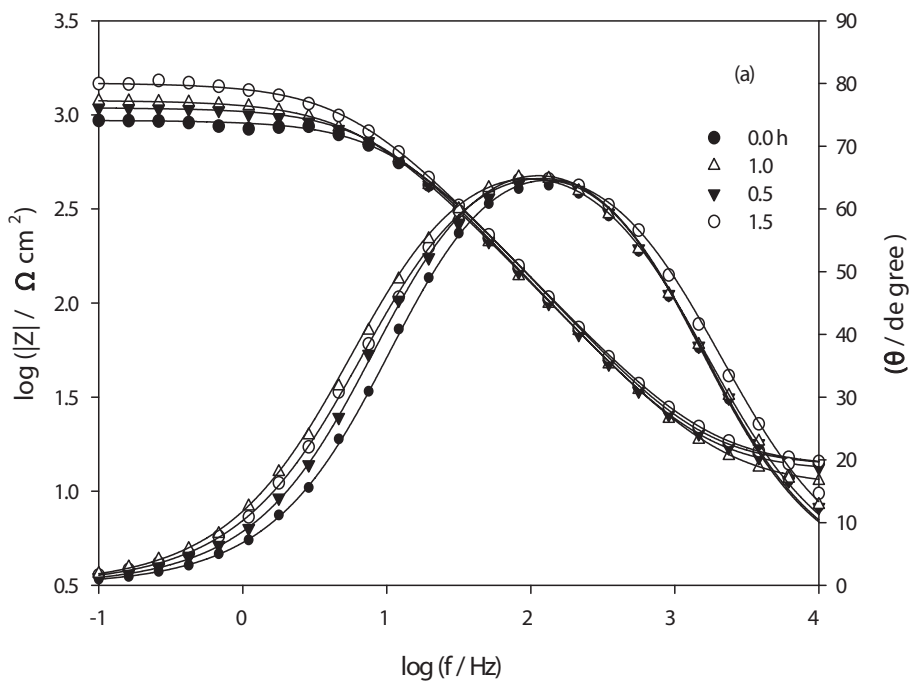
4. Results and discussion

4.1 Electrochemical impedance measurements

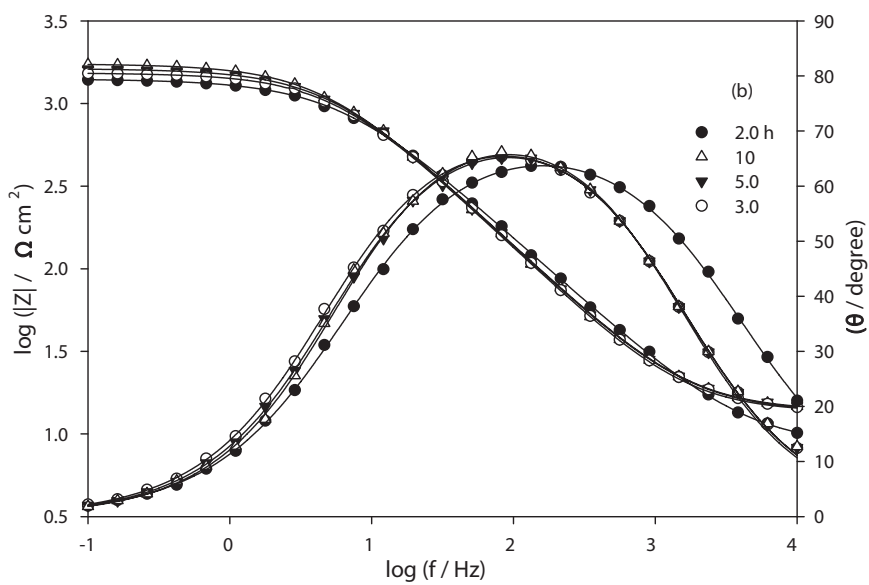
4.1.1 AZ91D alloy in simulated body fluid (SBF)

The EIS scans as Bode plots in Fig. 1a-c. for AZ91D alloy in dependence on the immersion time were recorded in the test solution for 35 h. The diagrams show resistive regions at high and low frequencies and capacitive contribution at intermediate frequencies. The impedance ($|Z|$) as well as the phase shift (θ) of AZ91D alloy is clearly found to depend on immersion time. It is of interest to observe that an increase in time of immersion, from 0 to 1.5 h (Fig. 1a), continuously increases the $|Z|$ value whilst θ_{max} is nearly constant.

However, at 2.0 to 10 h (Fig. 1b), the impedance value increases but not sharply. At higher immersion time 15-35 h (Fig. 1c), an increase in the immersion time increases the $|Z|$ value whilst θ_{max} gradually decreases with a concomitant shift to lower frequencies. This trend is most likely a result of a decrease in the surface film capacitance commensurate with a decrease in the adsorbed amount of anions forming SBF as Cl⁻, HCO₃⁻, H₂PO₄⁻ or HPO₄²⁻ on the electrode surface [Fekry & El-Sherief, 2010]. The results in general reveal two clear trends concerning the number of peaks observed in the patterns of the phase shift. The first one is for the behavior of AZ91D alloy at time of immersion from 0 to 5 h, where the Bode plots display only one maximum phase lag (Fig. 1a, b). The second trend is for the alloy at immersion time from 10 to 35 h where another peak of phase lag appears at the low frequency region (Fig. 1c).



(a)



(b)

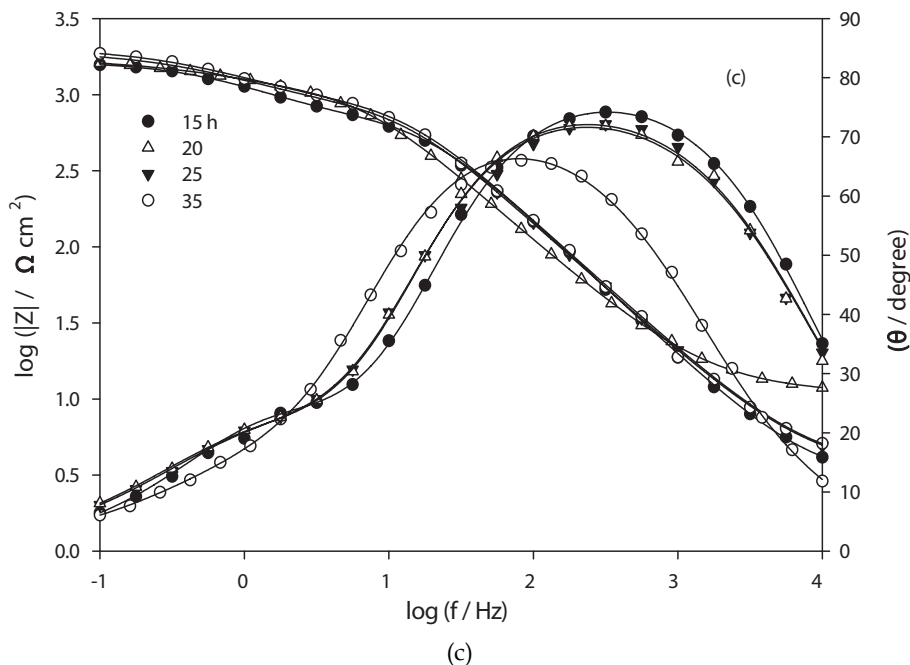


Fig. 1. a-c. Bode plots of AZ91D alloy as a function of immersion time in SBF at 37 °C.

The impedance data were thus simulated to the appropriate equivalent circuit for the cases with one time constant (Fig. 2a) and the others exhibiting two time constants (Fig. 2b), respectively. This is the simulation that gave a reasonable fit using the minimum amount of circuit components. Generally, the impedance response of an actively corroding metal in an aqueous solution is well simulated by the classic parallel resistor capacitor (R_1C_1) combination in series with the solution resistance (R_s) between the specimen and the RE. In this model a charge transfer resistance (R_1) is in parallel with the double layer capacitance (C_1), as depicted in Fig. 2a. In this case, the electrode surface is covered with a passive film R_1 and C_1 , the film resistance and capacitance, respectively. On the other hand, for the impedance diagrams with two time constants the appropriate equivalent model consists of two circuits in series from R_1C_1 and R_2C_2 parallel combination and the two are in series with R_s . In this way C_1 is related to contribution from the capacitance of the outer layer and the faradaic reaction therein and C_2 pertains to the inner layer, while R_1 and R_2 are the respective resistances of the outer and inner layers constituting the surface film, respectively [Wu et al., 2008]. Analysis of the experimental spectra were made by best fitting to the corresponding equivalent circuit using Thales software provided with the workstation where the dispersion formula suitable to each model was used [Fekry, 2009]. In this complex formula an empirical exponent (α) varying between 0 and 1, is introduced to account for the deviation from the ideal capacitive behavior due to surface inhomogeneties, roughness factors and adsorption effects [Fekry, 2009]. In all cases, good conformity between theoretical and experimental was obtained for the whole frequency range.

The experimental values are correlated to the theoretical impedance parameters of the equivalent model shown in Fig. 3. It was found that film healing and thickening (R_T) becomes effective by increasing time of immersion in SBF solution leading to a quasi-steady state thickness at longer times ($1/C_T$). This is caused by the formation of adherent corrosion products on the sample surface as $Mg(OH)_2$ which is precipitated from the solution during the corrosion of magnesium alloys due to saturation and localized alkalization [Gu et al., 2009]. Metal ions released from corrodible alloys to the surrounding tissues, may cause

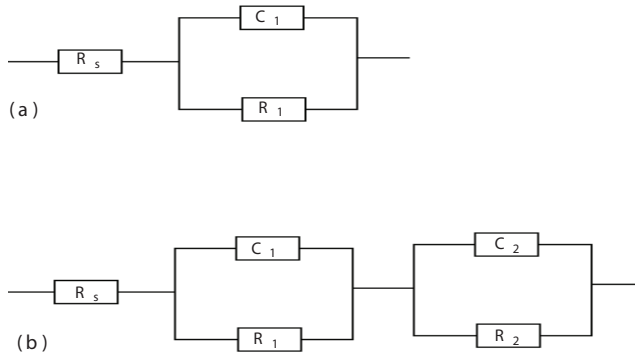


Fig. 2. Equivalent circuit model representing (a) one, and (b) two time constants for an electrode/electrolyte solution interface.

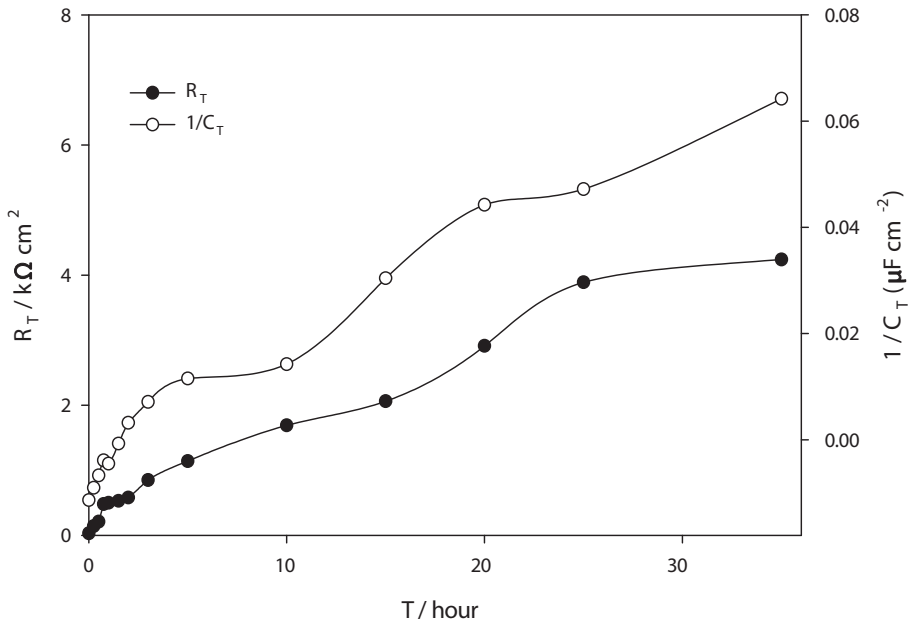


Fig. 3. The total resistance (R_T) and relative thickness ($1/C_T$) for AZ91D alloy as a function of immersion time in SBF at 37 °C.

biological responses in short term or prolonged periods. The toxicity of a metallic material is governed not only by its composition and toxicity of the component elements but also by its corrosion and wear resistance [Gu et al., 2009]. In a saline environment, magnesium-based alloys would be degraded to magnesium chloride, oxide, sulphate or phosphate [Fekry & El-Sherief., 2009] and the same occur in SBF. Also, magnesium carbonate precipitated on the surface of magnesium alloy improved the corrosion resistance of magnesium alloy in the case of atmospheric corrosion [Jönsson et al., 2007]. For chloride ions, in poorly buffered chloride solutions, they reveal low corrosion rates due to the formation of a partially protective $Mg(OH)_2$ layer. Also, phosphates inhibit dissolution of the oxide film and raise the corrosion potentials with increasing immersion time [Narayanan & Seshadri, 2007]. Phosphate is formed on the oxide surface and prevents dissolution. Generally, SBF improves slightly the corrosion resistance of AZ91D alloy with time.

It should be also emphasized that formation of a complete surface layer of oxidation products looks to be very difficult. This can be confirmed by SEM examination of AZ91D alloy surface after 35 h immersion in the respective SBF (pH 7.4) as shown in Fig. 4 compared to that of the polished sample (blank) at magnifications of 1000x. As can be seen, the micrograph for blank consists from uniform distribution, however, after immersion; it shows microcracks [Heakal et al., 2009 & 2009] which determine the existence of film vulnerable region. The relatively fine β -phase ($Mg_{17}Al_{12}$) precipitated at the outer portions of the platelets has light appearance with a shiny white color. However, flower-like $MnAl_2$ intermetallic inclusions [Pardo et al., 2008] are also found deposited on some few areas from the surface.

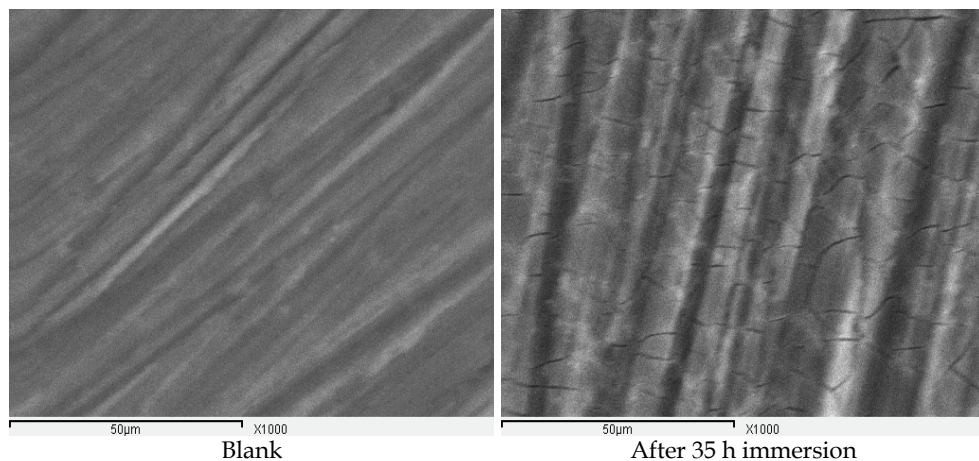
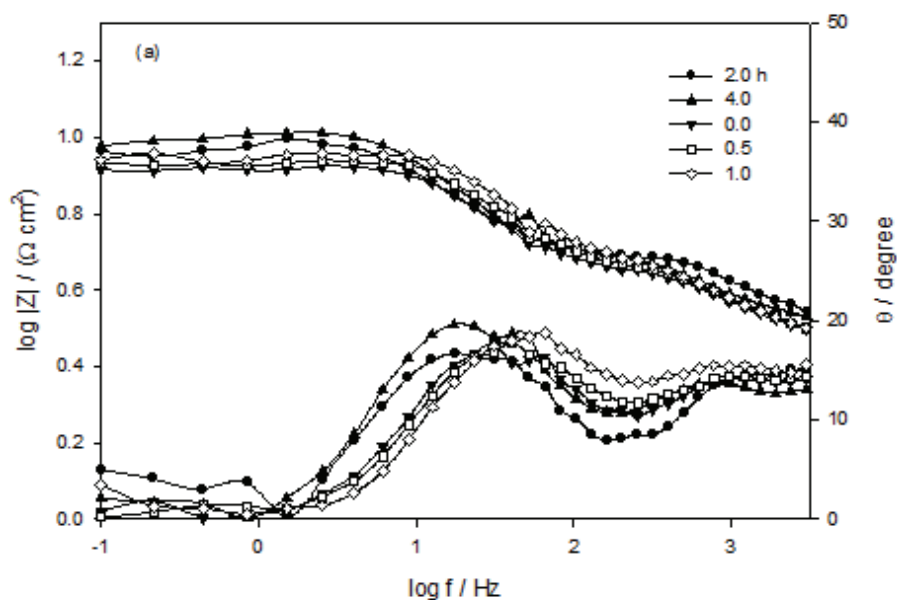


Fig. 4. SEM images of AZ91D alloy in air after polishing (blank) and in SBF at 37 °C after 35 h of immersion.

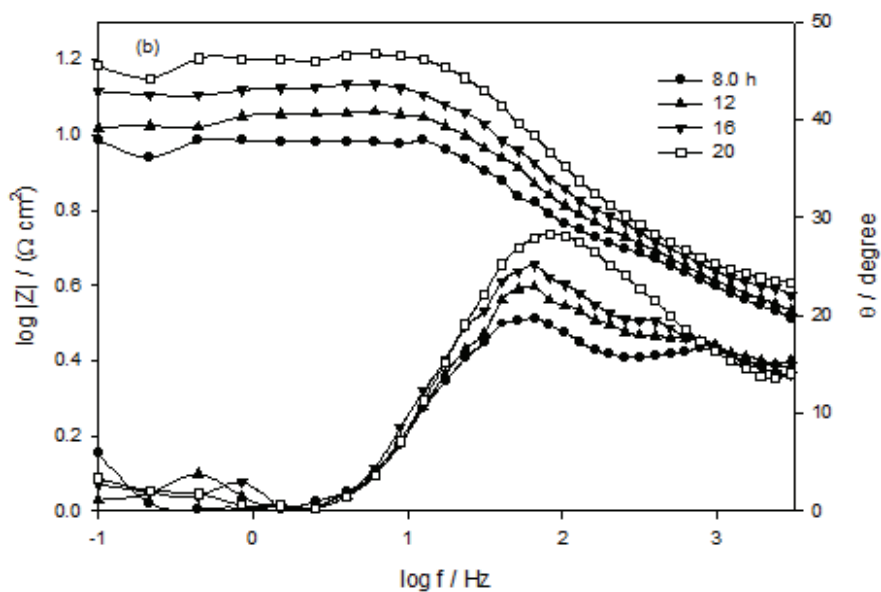
4.1.2 AZ31E alloy in Ringer's Solution (RS)

The EIS scans as Bode plots, in Fig. 5a-c, for AZ31E alloy, as function of the immersion time, were recorded in the test solution for 100 h. The diagrams show resistive regions at high frequencies. The impedance ($|Z|$) as well as the phase shift (θ) of AZ31E alloy is clearly dependent on immersion time. It is of interest to observe that an increase in the time of

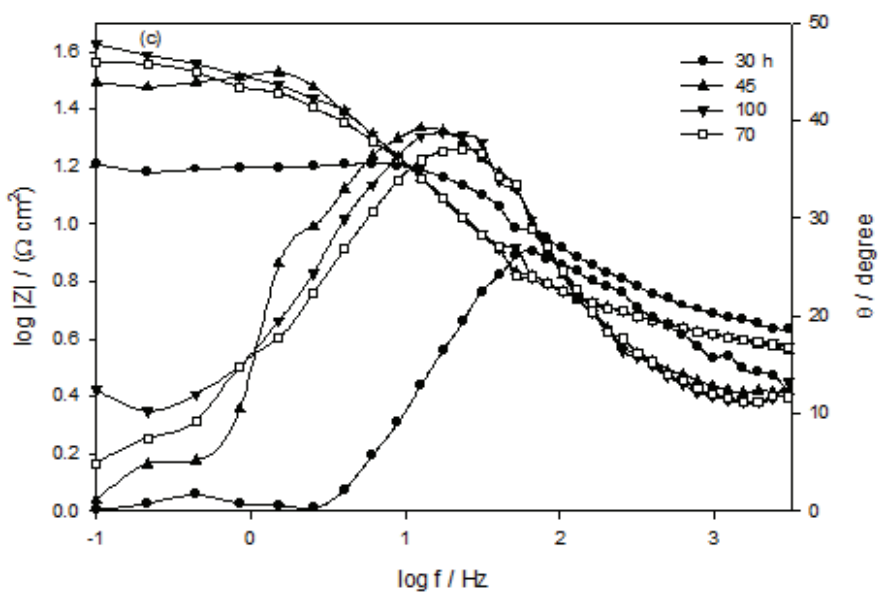
immersion, from 0 to 4.0 h (Fig. 5a), gradually increases the $|Z|$ value, whereas θ_{\max} is nearly constant. From 8.0 to 20 h (Fig. 5b), the impedance and θ_{\max} values increase gradually. For larger immersion time from 30-70 h (Fig. 5c), both $|Z|$ value and θ_{\max} increase sharply. The results in general show that Bode plots display two maximum phase lags. Fig. 6, as an example for 1h immersion of AZ31E alloy, manifested two depressed capacitive semicircles, typical of Randles element, at higher and lower frequencies regions, separated by an inductive loop at intermediate frequencies. Inductive loops can be explained by the occurrence of an adsorbed intermediate on the surface. The experimental data were consistent with the involvement of the intermediate species Mg^+ in magnesium dissolution at film imperfections or on a film-free surface. At such sites, magnesium is first oxidised electrochemically to the intermediate species Mg^+ , and then the intermediate species react chemically with water to produce hydrogen and Mg^{2+} . The presence of Cl^- ions increases the film free area, and accelerates the electrochemical reaction rate from magnesium metal to Mg^+ [Song et al., 1997]. The capacitive semicircle at higher frequencies is attributed to the redox $Mg-Mg^+$ reaction since it was assumed to be the rate determining step in the charge transfer process. Therefore, the resistance value obtained from intercepts of the first capacitive semicircle with real axis corresponds to the charge transfer resistance. On the other hand, the second capacitive semicircle could be attributed to the fast complementary corrosion reaction. The curve manifested that addition of chloride ions leads to increase in the size of the capacitive semicircles with immersion time, an indication of increasing the resistances and decreasing the corrosion rate. The increase in resistivity arises from the change in chemical composition of the surface film due to incorporation of Cl^- ions into the film especially through defect sites with low ionic resistance.



(a)



(b)



(c)

Fig. 5. a-c. Bode plots of AZ31E alloy as a function of immersion time in RS at 37 °C.

The impedance data were thus simulated to the appropriate equivalent circuit for the case with two time constants (Fig. 7). The model includes the solution resistance R_s , a series combination of resistance, R , and inductance, L , in parallel with charge transfer resistance (R_{ct1}), and the constant phase element (CPE_1). In the high frequency limit, the inductive contribution to the overall impedance is insignificant. Therefore, the Nyquist plot of the impedance is a semicircle characteristic of the parallel arrangement of the double layer capacitance and charge transfer resistance corresponding to the corrosion reaction. Contribution to the total impedance at intermediate frequencies comes mainly from the charge transfer resistance and inductive component in parallel. The inductor arising from adsorption effects could be defined as ($L = R\tau$), where τ is the relaxation time for adsorption on the electrode surface. The low frequency locus displays the characteristics of parallel RC circuit. This circuit includes another constant phase element (CPE_2) which is placed in parallel to charge transfer resistance element (R_{ct1}). The (R_{ct1}) value is a measure of charge transfer resistance corresponding to the $Mg^+ - Mg^{2+}$ reaction. The CPE is used in this model to compensate for non-homogeneity in the system and is defined by two values, Q and a .

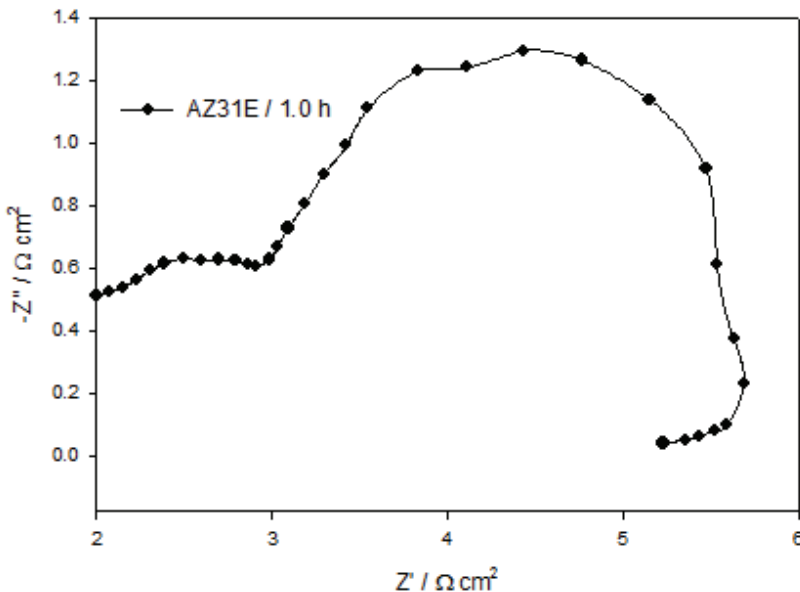


Fig. 6. Nyquist plot after 1 h of immersion in RS at 37 °C.

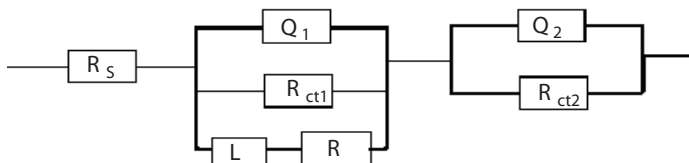


Fig. 7. Equivalent circuit model representing two series time constants for an electrode/electrolyte solution interface.

The impedance of CPE is represented by $Z_{CPE} = Q^{-1}(i\omega)^{-a}$, where $i = (-1)^{1/2}$, ω is frequency in rad s^{-1} , $\omega = 2\pi f$ and f is the frequency in Hz. If a equals one, the impedance of CPE is identical to that of a capacitor, $Z_C = (i\omega C)^{-1}$ and in this case Q gives a pure capacitance (C). For non-homogeneous systems, a values range from 0.9-1. Computer fitting of the spectrum allows evolution of the elements of the circuit analogue. The aim of the fitting procedure is to find those values of the parameters which best describe the data. The experimental and computer fit results are given in Table 2. It was found that the fit results were consistent with the experimental data within 5% error.

As shown in Table 2, film healing and thickening becomes effective by increasing the time of immersion in Ringer's solution, leading to a quasi-steady state thickness at longer times. This is caused by the formation of adherent corrosion products on the sample surface as $Mg(OH)_2$ which is precipitated from the solution during the corrosion of magnesium alloys due to saturation and localized alkalization [Fekry & El-Sherief, 2009]. This is confirmed by measuring the pH of Ringer's solution after completing the experiment, which becomes 11.0. Calcium could improve both the corrosion resistance in NaCl solution and the mechanical properties of magnesium alloy. Moreover, Ca is a major component in human bone and can accelerate the bone growth [Azza et al., 2010]. It was thought that the presence of Ca ion benefits the bone healing. However, for chloride ions, low corrosion rates were obtained due to the formation of a partially protective $Mg(OH)_2$ layer. The growth of the polarization resistance with the immersion time is consistent with the continual decrease of the bio-corrosion rate.

SEM examination of AZ31E alloy surface after 100 h immersion in the same RS is shown in Fig. 8, as compared to that of the uniform distribution for polished sample (blank). After immersion; it shows microcracks [Fekry & El-Sherief, 2009], which indicate the existence of a vulnerable film. There are plenty of visible corrosion products on the surface of AZ31 after 100 h immersion.

Time Hour	$R_s /$ $\Omega \text{ cm}^2$	$(R_{ct})_1 /$ $\Omega \text{ cm}^2$	$Q_1 /$ $\mu\text{F cm}^{-2}$	α_1	$R /$ $\Omega \text{ cm}^2$	L	$(R_{ct})_2 /$ $\Omega \text{ cm}^2$	$Q_2 /$ $\mu\text{F cm}^{-2}$	α_2
0.00	0.18	5.29	416.9	0.98	53.45	0.032	5.40	154.3	0.94
0.50	0.18	5.31	311.2	0.98	54.90	0.035	5.67	90.05	0.94
1.00	0.18	5.32	299.3	0.96	56.27	0.040	5.89	89.13	0.95
2.00	0.18	5.32	172.1	0.97	60.49	0.044	6.01	86.79	0.97
4.00	0.18	5.33	161.9	0.97	67.35	0.051	6.29	81.07	0.96
8.00	0.19	5.35	157.7	0.99	73.36	0.055	7.34	72.45	0.93
12.00	0.19	5.37	147.6	0.99	86.83	0.059	8.37	69.95	0.95
16.00	0.19	5.38	146.9	0.98	105.2	0.061	9.01	55.87	0.94
20.00	0.19	5.38	143.8	0.99	106.2	0.061	9.06	45.21	0.98
30.00	0.22	6.37	139.8	0.99	248.3	0.145	24.9	41.14	0.97
45.00	0.39	6.40	135.5	0.98	258.7	0.147	25.1	30.30	0.97
70.00	0.58	6.45	132.8	0.99	307.5	0.151	30.6	17.15	0.97
100.00	0.59	6.53	116.3	0.99	405.1	0.154	36.8	14.23	0.98

Table 2. Impedance parameters of AZ31E alloy in RS at 37 °C.

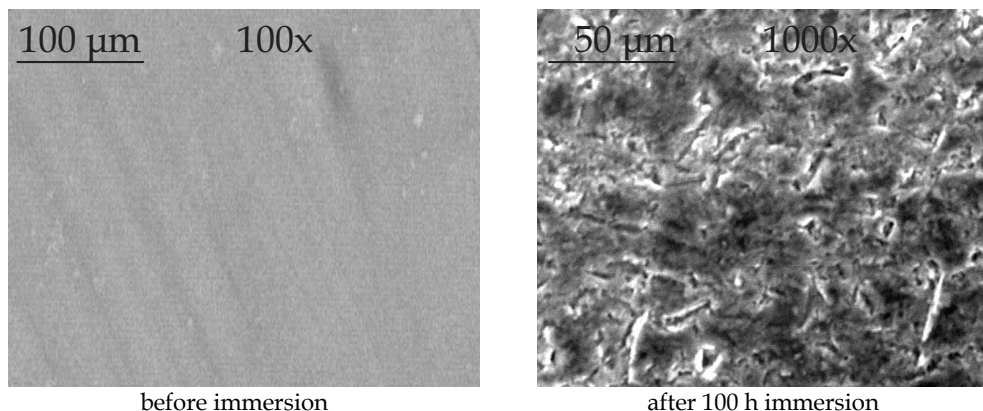


Fig. 8. SEM images of (a) Ti-6Al-4V alloy and (b) AZ31E in air after polishing (blank) and in RS at 37 °C after 100 h of immersion.

4.1.3 AZ31E and AZ91E alloy in Hank's Solution (HS)

Electrochemical impedance (EIS) is a technique with small perturbative signal and the surface damage of the sample is very little. In these experiments, the immersion of the two magnesium alloys was carried out continuously in Hank's solution which is used to simulate the biochemical reaction of the magnesium alloys in human physiological conditions. The specimens were suspended in Hank's solution up to 100 hour. The EIS scans as Bode plots at different immersion times are given in Fig. 9 (a,b) & 10 (a,b) for AZ31 and AZ91 respectively. It can be seen that these diagrams for both alloys show resistive regions at high and low frequencies and capacitive contribution at intermediate frequencies. It is of interest to observe that an increase in time of immersion, from 0 to 10 h (Fig. 9a) for AZ31E and (Fig. 10a, b) for AZ91E, continuously increases the $|Z|$ and θ values. That is, as shown in (Fig. 9), θ_{\max} increases with time from 26° at 0 h to 65° at 10 h of immersion for AZ31E alloy. However, at higher immersion time from 20 to 100 h (Fig. 9b) for AZ31E, the impedance value increases and θ_{\max} value gradually decreases but not sharply (from ~ 65° to 58°) with a concomitant shift to lower frequencies. For AZ91E alloy (Fig. 10), θ_{\max} increases with time from 22° at 0 h to 28° at 100 h of immersion that is nearly constant. However, at any immersion time the values of $|Z|$ or θ_{\max} is always higher for AZ31E alloy as compared to AZ91E alloy, suggesting that AZ31E alloy is much more passive than AZ91E alloy in the test solution. Also $|Z|$ values increase with increasing immersion time for both tested alloys as shown in Fig. 9 and 10. This trend is due to a decrease in the surface film capacitance which is directly proportional to the decrease in the adsorbed amount of aggressive anions as Cl^- [Heakal et al., 2009].

The Bode format of Fig. 9&10 confirms the presence of two time constants as there are two maximum phase lags appears at medium frequencies (MF), and low frequencies (LF). On the other hand, for the impedance diagrams with two time constants the appropriate equivalent model, shown in Fig. 2b, is the most appropriate one. Analysis of the experimental spectra was made by best fitting to the corresponding equivalent circuit using Thales software provided with the workstation where the dispersion formula suitable to each model was used [Fekry & El-Sherief, 2009].

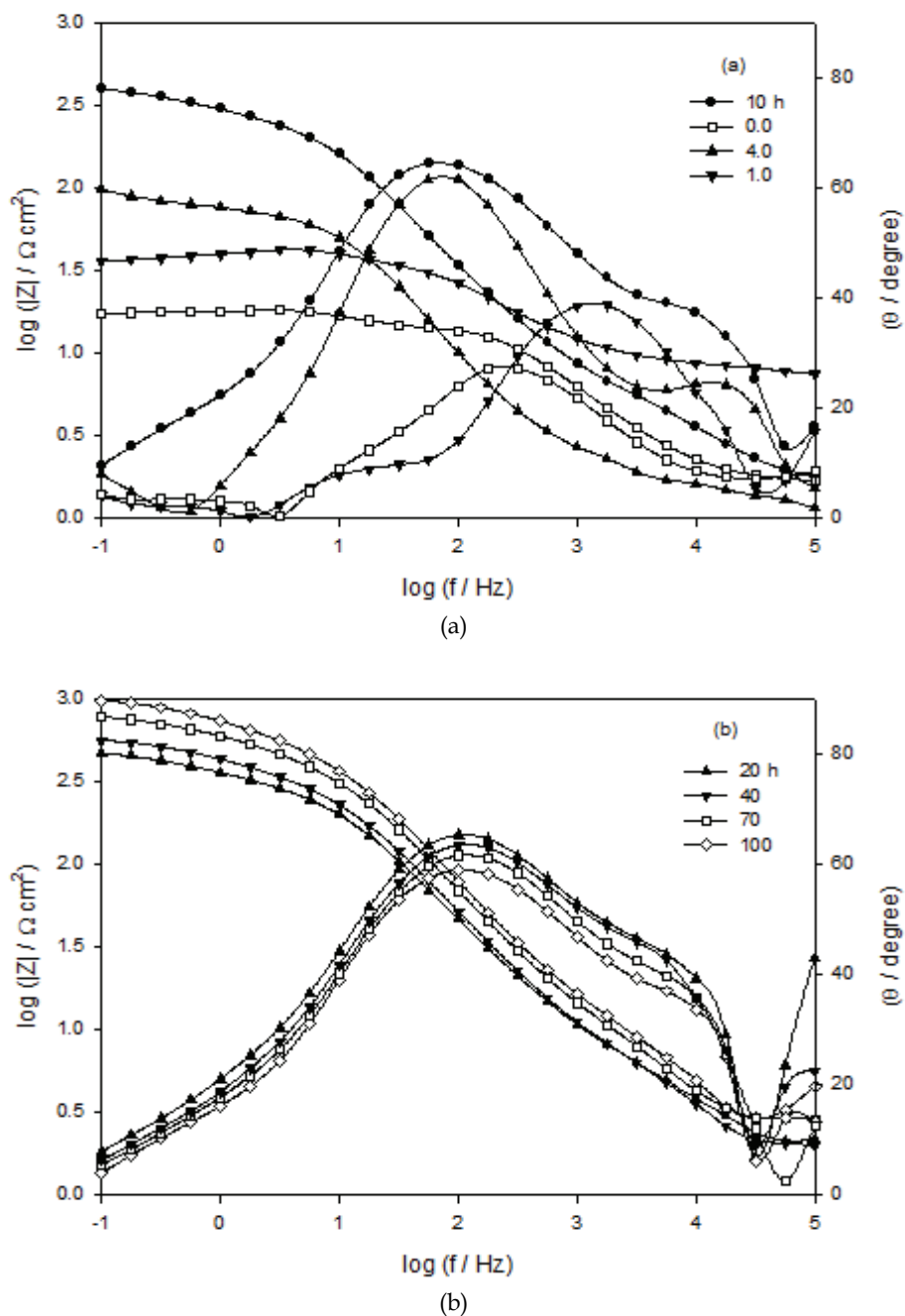


Fig. 9. a,b. Bode plots of AZ31E alloy as a function of immersion time in Hank's solution at 37 °C.

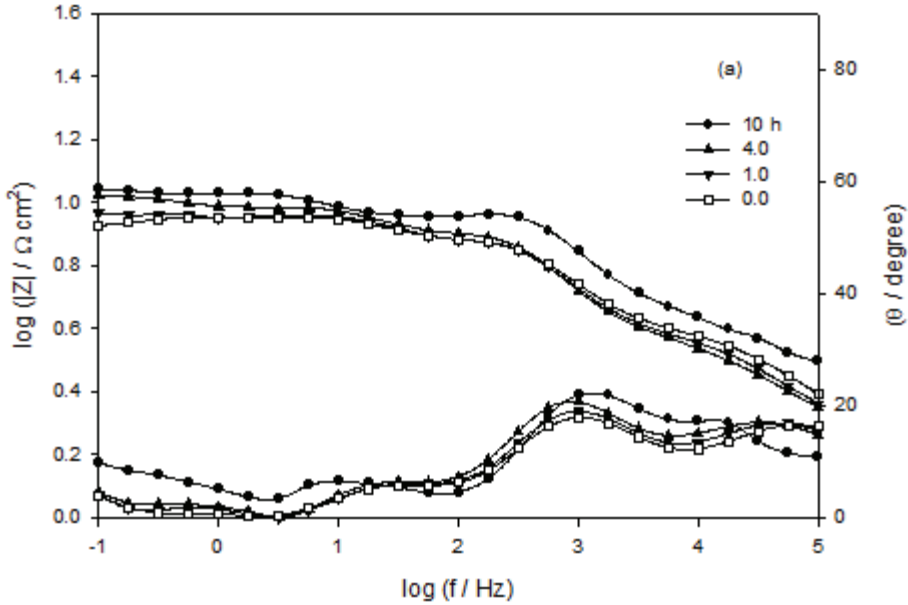


Fig. 10. a,b. Bode plots of AZ91E alloy as a function of immersion time in Hank's solution at 37 °C.

For this model the electrode impedance is represented by the following transfer function [Ameer et al., 2009]:

$$Z(\omega) = R_o + \frac{R_1}{1 + R_1 C_1 (j\omega)^{\alpha_1}} + \frac{R_2}{1 + R_2 C_2 (j\omega)^{\alpha_2}} \quad (1)$$

The above formula takes into account the deviation from the ideal RC behavior and considers, for a more realistic approach that each oxide layer as non-homogeneous. Thereby, the impedance associated with the capacitance of each layer is described by a constant phase element (CPE).

In all cases, good conformity between theoretical and experimental was obtained for the whole frequency range with an average error of 3%. The experimental values are correlated to the theoretical impedance parameters of the equivalent model, the data were presented in Tables 3&4 for AZ31E and AZ91E alloys, respectively. As given in Tables 3&4, R_s is nearly the same for both alloys. It was also seen that R_1 , R_2 values increases and C_1 , C_2 values decreases for both tested alloys with immersion time, that is film healing and thickening becomes effective by increasing time of immersion in Hank's solution leading to a quasi-steady state thickness at longer times. This is caused by the formation of adherent corrosion products on the sample surface including, magnesium hydroxide, as well as phosphates and carbonates [Wang et al., 2008]. They are precipitated from the solution during the corrosion of magnesium alloys due to saturation and localized alkalization [Gu et al., 2009]. Metal ions released from corrodible alloys to the surrounding tissues may cause biological responses in short term or prolonged periods. The toxicity of a metallic material is governed not only by its composition and toxicity of the component elements but also by its corrosion and wear

resistance [Gu et al., 2009]. In a saline environment, magnesium-based alloys would be degraded to magnesium chloride, oxide, sulphate or phosphate [Fekry & El-Sherief, 2009] and the same occur in Hank's solution. Also, magnesium carbonate precipitated on the surface of magnesium alloy improved the corrosion resistance of magnesium alloy in the case of atmospheric corrosion. For chloride ions, in poorly buffered chloride solutions, they reveal low corrosion rates due to the formation of a partially protective $Mg(OH)_2$ layer. Also, phosphates formed on the oxide surface inhibit dissolution of the oxide film with increasing immersion time [Narayanan & Seshadri, 2007]. For the values of the empirical exponent (α) given in Tables 3 & 4, it is seen that it is higher for AZ31E (~ 0.88 - 0.93) than that of AZ91E (~ 0.71 - 0.79) alloy. It is near to the ideal value ($\alpha = 1$) for AZ31E alloy. Also, as given in Tables 3 & 4, R_1 or R_2 values at any given time is higher for AZ31E alloy than that for AZ91E alloy. This confirms that AZ31E is more resistant than AZ91E alloy in Hank's solution. Generally, Hank's solution improves slightly the corrosion resistance of AZ91E and AZ31E alloys with time.

Time hour	$R_s /$ $\Omega \text{ cm}^2$	$R_1 /$ $\Omega \text{ cm}^2$	$C_1 /$ $\mu\text{F cm}^{-2}$	α_1	$R_2 /$ $\Omega \text{ cm}^2$	$C_2 /$ $\mu\text{F cm}^{-2}$	α_2
0.00	2.21	2.10	90.3	0.88	17.9	24.7	0.88
0.25	2.20	2.14	87.5	0.89	22.5	23.5	0.89
0.50	1.97	2.32	81.3	0.89	25.2	22.2	0.88
1.00	2.10	2.38	78.5	0.87	40.3	21.8	0.90
4.00	2.15	9.66	71.4	0.87	105.4	19.2	0.90
10.00	2.65	37.77	67.1	0.91	482.3	18.7	0.89
20.00	2.85	65.18	65.8	0.89	584.9	17.8	0.92
40.00	2.42	82.11	63.9	0.91	667.9	17.1	0.92
70.00	2.61	126.23	61.7	0.91	867.7	16.7	0.92
100.00	3.00	197.35	59.0	0.90	985.0	16.4	0.93

Table 3. Impedance Parameters of AZ31E alloy in Hank's solution at 37°C.

Time hour	$R_s /$ $\Omega \text{ cm}^2$	$R_1 /$ $\Omega \text{ cm}^2$	$C_1 /$ $\mu\text{F cm}^{-2}$	α_1	$R_2 /$ $\Omega \text{ cm}^2$	$C_2 /$ $\mu\text{F cm}^{-2}$	α_2
0.00	2.60	1.04	150.8	0.75	8.5	50.3	0.71
0.25	2.03	1.16	143.1	0.78	8.7	47.8	0.74
0.50	1.91	1.25	135.6	0.76	8.8	43.2	0.75
1.00	1.82	1.47	122.0	0.78	11.0	35.5	0.72
4.00	1.27	1.64	117.1	0.75	11.8	32.1	0.72
10.00	2.65	1.79	111.0	0.77	13.8	29.9	0.75
20.00	2.67	1.99	105.5	0.76	15.7	27.5	0.75
40.00	2.71	2.13	101.3	0.77	18.2	25.1	0.74
70.00	2.69	2.18	97.1	0.76	32.6	21.4	0.72
100.00	2.03	2.55	85.7	0.79	43.1	21.0	0.74

Table 4. Impedance Parameters of AZ91E alloy in Hank's solution at 37°C.

It should be noted that the alloying elements Al and Zn tend to have a stabilizing effect on the protective film formed on Mg alloy. Indeed, without these alloying elements, pure magnesium experiences a much faster biodegradation under similar testing conditions

[Song & Song, 2007]. The previous electrochemical results show that the corrosion resistance of AZ31 is much higher than that of AZ91 alloy. The results may be caused by the different distribution of alloying elements in microscopic scale and the microstructure of alloys, which are the fundamental reasons for the metal corrosion morphology and corrosion resistance.

In the literature [Ballerini et al., 2005], it was found that the heterogeneous microstructure of AZ91 stimulates a localized corrosion morphology that is dictated by the distribution of microgalvanic coupling with the $Mg_{17}Al_{12}$ intermetallic particles in the matrix. The content of Al in the second-phase particles [Azza et al., 2010] might be the β phase ($Mg_{17}Al_{12}$), the electrode potential of the β phase is higher than the matrix; therefore, it will form microcells with the adjacent matrix and accelerate the corrosion process. Because the Al content in AZ91 is higher than that of AZ31, the content of β phase of AZ91 will be higher than that of AZ31 and the number of corrosion microcells of AZ91 is also larger than that of AZ31, as a result, the corrosion resistance of AZ91 is lower than that of AZ31.

The corrosion behavior of the Mg alloys is determined by the important aspects include composition, porosity, grain size, and amount and distribution of β phase. Fig. 11 represents the surface morphologies of AZ91 and AZ31 magnesium alloys, the microstructure of AZ31 magnesium alloy shows a nearly continuous network of grain boundary phase ($Mg_{17}Al_{12}$). However, AZ91 contains a few amounts of β -phase. The phase was more stable in NaCl and was more inert to corrosion. The phase corrodes due to the tendency for the corrosion rate of the β -phase to be accelerated by microgalvanic coupling between the α -phase and the β -phase. The phase mainly served as a galvanic cathode and accelerated the corrosion process of the matrix if the volume fraction of β -phase was small; however, for a high volume fraction, the phase might act as an anodic barrier to inhibit the overall corrosion of the alloy. Song et al [Song & Atrens, 1999, 2003 & 2007] showed that the β phase plays a dual role, it can act either as a barrier or as a galvanic anode depending on its content, size and distribution. When the mass fraction of ($Mg_{17}Al_{12}$) β phase is high, the grain size of magnesium alloy is small, and the β phase distributes continuously on the matrix α phase, so it may play the role of a barrier layer to deter corrosion as shown in the Figure for AZ31. On the contrary, if the grain size is larger and the distance between β phases is enlarged, galvanic corrosion may occur and cause the decline of the corrosion resistance (for AZ91).

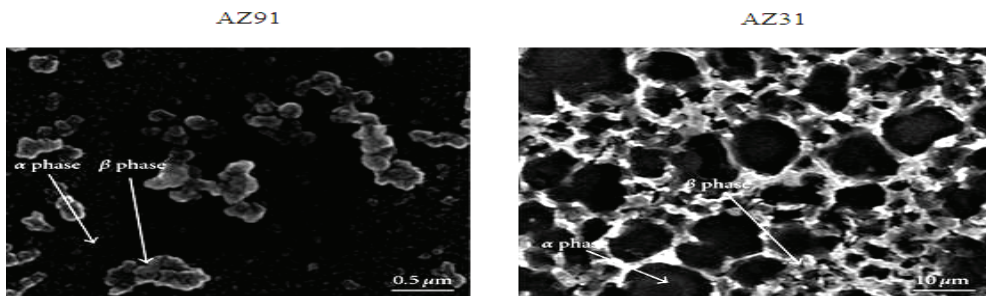


Fig. 11. Surface morphologies of AZ91 and AZ31 magnesium alloys.

Glucosamine is an amino-monosaccharide produced in the body. Glucosamine sulphate acts mainly as a substrate for biosynthesis of mucopolysaccharides and biopolymers of joints and bones and, thus, contributes to restoration of damaged cartilage. About 90% of

glucosamine administered orally as a glucosamine salt gets absorbed from the small intestine and from there it is transported to the liver. Healthy men have serum glucosamine concentration of 0.04 mmol/L when they are not consuming supplemental glucosamine [Ghoneim et al., 2010]. Ingestion of recommended oral doses of glucosamine in humans achieves serum levels of approximately 0.06 mmol/L [Anderson et al., 2005], its oral administration at very large doses (5000–15,000 mg/kg body weight) is well tolerated without documented toxicity. It is not presently known how much of an ingested dose is taken up in the joints in humans. Most relevant clinical trials have used glucosamine sulphate in 1500mg, once a day for 12 weeks [Giordano et al., 2009], this is a prescription drug in most European and non-European countries.

Thus, it is intended in this part to study the effect of adding glucosamine sulphate to Hank's solution on the electrochemical behavior of the biodegradable AZ31 alloy, which is much better than AZ91 alloy against corrosion. Fig. 12 Shows EIS results probed after 4h immersion in Hank's solution in presence of various concentrations of glucosamine sulphate in the range from 0.01 to 10 mM, and presented as Bode and Nyquist plots, the spectra are dominated by the capacitance of the HF time constant. The general features of the plots are not substantially different from those obtained in absence of glucosamine. This suggests that the presence of glucosamine in the solution do not alter the reaction responsible for corrosion. The Nyquist format in Fig. 12 confirms the presence of two well defined depressed semicircles at high and medium frequency regions. In all solutions the impedance, $|Z|$ value decrease with increasing added glucosamine concentration, however the 10 mM shows a critical concentration which has higher resistance compared to that of 1.0 and 0.1 mM glucosamine solution. However, 0.01 mM Glucosamine concentration is much better than 10 mM concentration.

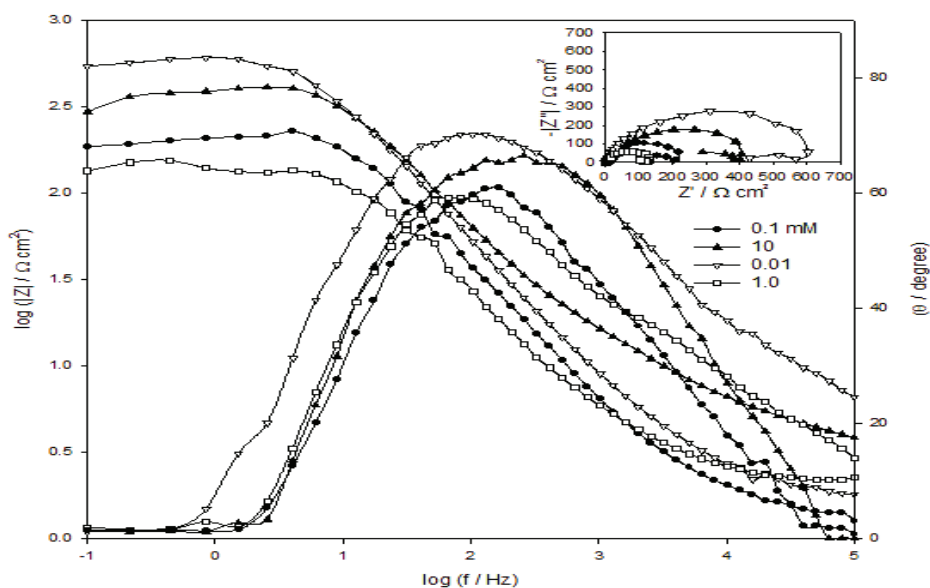


Fig. 12. Bode and Nyquist plots of AZ31E alloy as a function of concentration for Glucosamine in Hank's solution at 37 °C.

The total resistance (R_T) and the relative thickness ($1/C_T$) for AZ31 alloy in Hank's solution in presence of 10 and 0.01 mM glucosamine solutions as a function of the immersion time are presented in Fig. 13. The impedance data were simulated to the equivalent circuit represented in Fig. 2b. Both values increase with immersion time. Also, the total resistance R_T and the relative thickness $1/C_T$ of the film formed on the alloy show always higher values compared to the values in absence of glucosamine as illustrated in Fig. 13.

This was confirmed by Scanning electron microscope (SEM) images shown in Fig. 14a-c. Fig. 14c shows a smoother film adsorbed on the alloy surface for 0.01 mM than that formed on 10 mM concentration Fig. 14b. Also the two are much better than the blank shown in Fig. 14a.

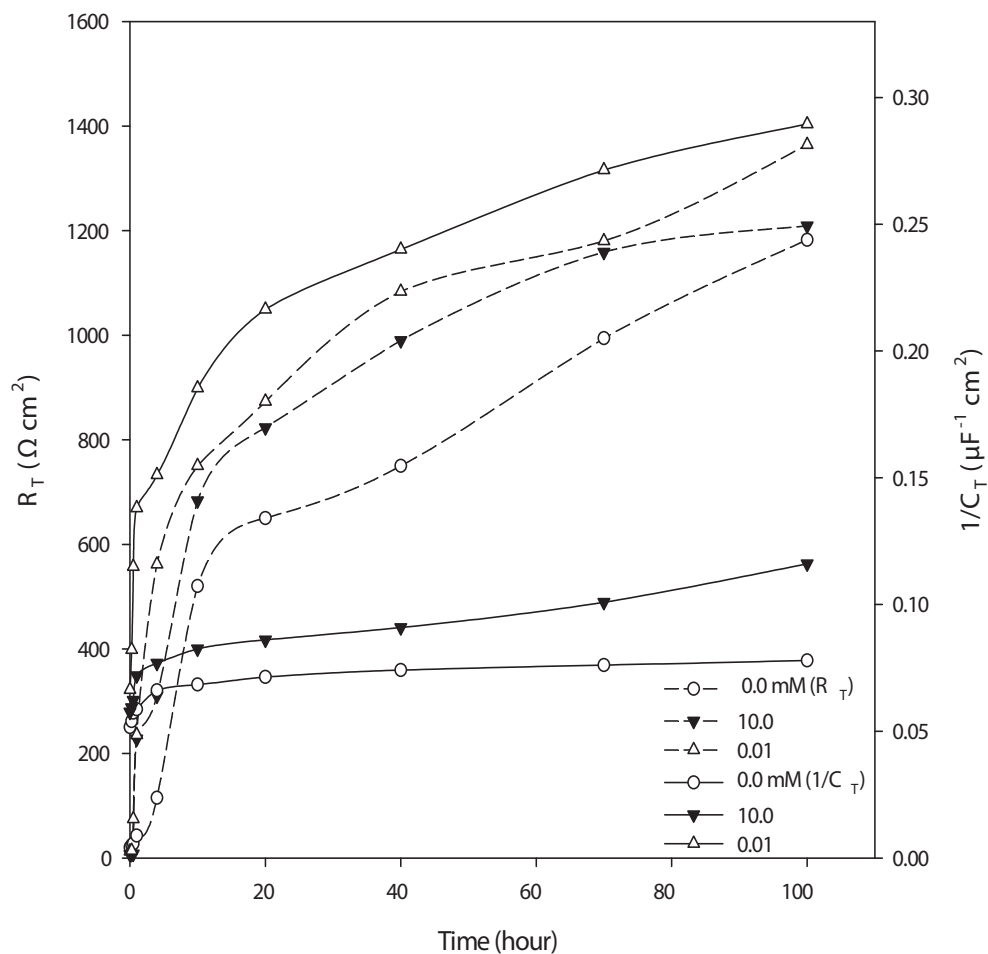
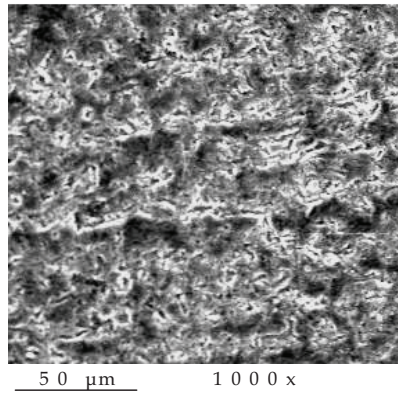
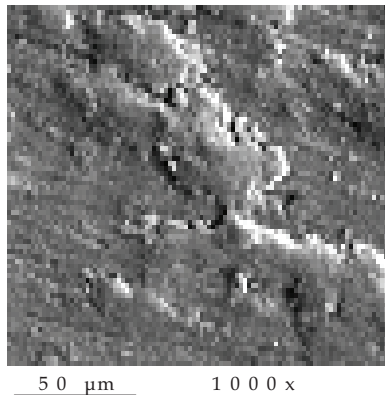


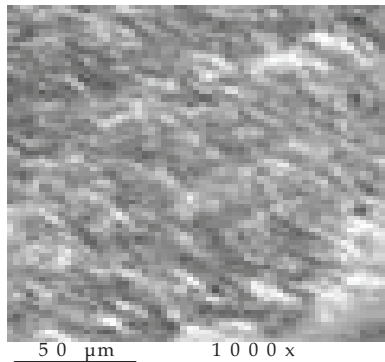
Fig. 13. The total resistance (R_T) and relative thickness ($1/C_T$) for AZ31E alloy with and without Glucoseamine as a function of immersion time in Hank's solution at 37 °C.



(a) after 100 h immersion in Hank's solution



(b) after 100 h immersion in 10 mM Glucosamine containing Hank's solution



(c) after 100 h immersion in 0.01 mM Glucosamine containing Hank's solution

Fig. 14. SEM micrographs for AZ31E alloy after 100 h of immersion in Hank's solution (a) without Glucosamine (b) with 10 mM Glucosamine and (c) with 0.01 mM Glucosamine.

4.2 Potentiodynamic measurements

Anodic dissolution and passivation behavior of AZ91 and AZ31 alloys were studied in Hank's solution using potentiodynamic polarization measurements (Fig. 14) at a scan rate of 1.0 m V s^{-1} . Prior to the potential scan the electrode was left under open circuit conditions in the respective solution for 100 h until a steady free corrosion potential value was recorded. Basically, the two alloys exhibit the same curve shape, no active-passive transition peak can discerned in the anodic trace, but a passivation plateau extending to a large domain of potential is observed. The corrosion potential (E_{corr}) and corrosion current density (i_{corr}) were calculated from the intersection of the anodic and cathodic Tafel lines extrapolation. The values of i_{corr} were 0.01 and 0.58 mA cm^{-2} for AZ31 and AZ91 respectively. It can be acquired from these experiments that the corrosion resistance of AZ31 alloy is much higher than AZ91. This means that AZ31 has a superior anticorrosion performance in Hank's solution.

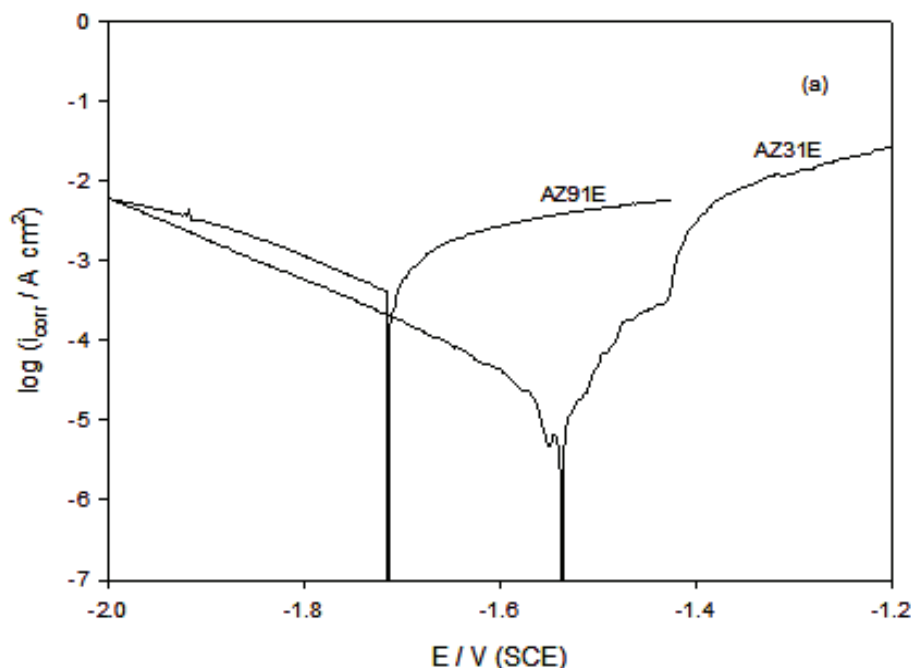


Fig. 15. Potentiodynamic polarization curves for AZ91E and AZ31E alloys in Hank's solution, at 37°C .

Figure 16 shows the anodic and cathodic scans of AZ31 alloy immersed for 100 h in Hank's solution in absence and in presence of various concentrations of glucosamine sulphate in the range from 0.01 to 10 mM. The polarization curves reveal clearly that the solution concentration affects both the cathodic and anodic overpotentials, where there is a remarkable shift in the position of the Tafel plots mainly towards more positive values with

decreasing glucosamine concentration. However, 10 mM glucosamine is considered as a critical concentration. The calculated values of i_{corr} were 0.005, 0.003, 0.001 mA/cm² for 0.1 mM, 10 mM, 0.01mM glucosamine solution, respectively. These results indicate that addition of glucosamine had a pronounced inhibition effect on the corrosion current, it acts by merely blocking the reaction sites of the metal surface without changing the anodic and cathodic reaction mechanisms. This inhibition is attributed to strong adsorption of molecular species through the active centers as NH₃⁺ and OH⁻ or oxygen heteroatom [Fekry & Mohamed, 2010]. It has been observed that adsorption mainly depends on the presence of π -electrons in C=C, electron pairs on heteroatoms as oxygen or nitrogen, which induce greater adsorption of glucosamine onto the surface of the alloy.

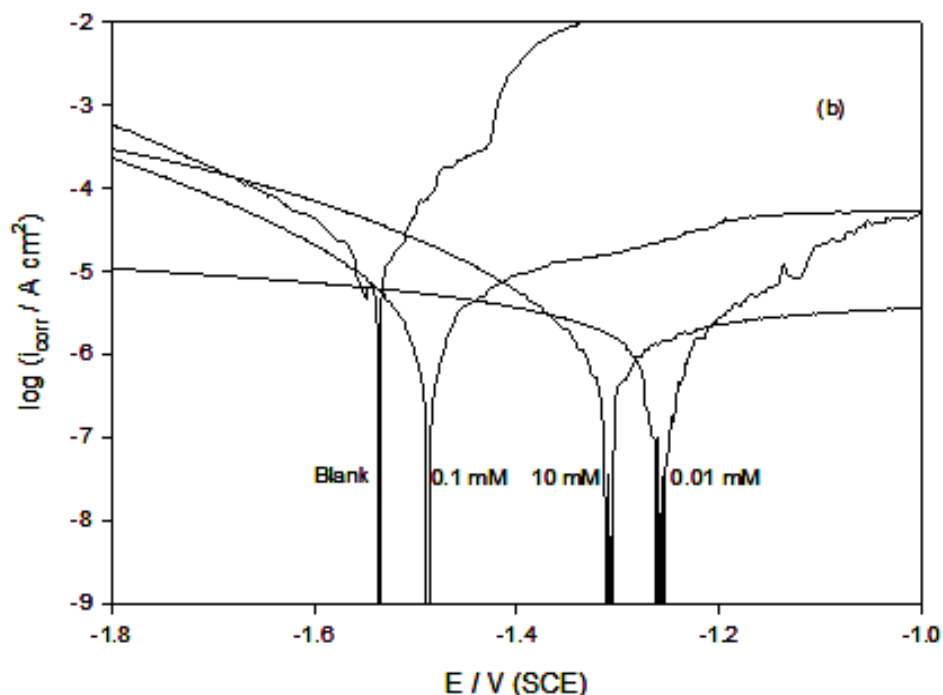


Fig. 16. Potentiodynamic polarization curves for AZ31E alloy as a function of concentration of glucosamine in Hank's Solution at 37 °C .

Generally, the polarization results are in agreement with those obtained from EIS, and suggest that the quality of the spontaneously formed film, as a protective layer against corrosion, improves greatly at lower glucosamine concentration. Finally, for magnesium alloys to be used as biodegradable implant materials, their degradation rates should not exceed the rate of healing of the affected tissue, and also the degradation products should not be more than the body's acceptable absorption level. The present study has shown that the

biodegradation rate of alloy AZ31 in Hank's solution can be significantly reduced by adding glucosamine sulphate to the solution on the basis of the observed corrosion retardation.

5. Conclusions

This work reviews the biological performance of magnesium based alloys (biodegradable materials for temporary implant) as AZ91D alloy in simulated body fluid (SBF), AZ31E alloy in Ringer's and AZ31E, AZ91E in Hank's solution at 37 °C that have been used as orthopedic biomaterials. Their corrosion behavior was studied by the analysis of corrosion resistance variation with immersion time, using electrochemical impedance spectroscopy (EIS) tests and corrosion current density using potentiodynamic polarization technique. The results were confirmed by scanning electron micrographs.

The aim is to explore possible routes to improve limiting factors such as the corrosion resistance and improve integration of the implant with tissue, and ultimately highlights the need for further research. It is aimed to find the best magnesium alloy with low cost and low corrosion rate as implant in human body. Furthermore, the feasibility to slow down the biodegradation (i.e. corrosion) of magnesium alloys to solve the rapidly corroding magnesium implant problems was demonstrated by studying the effect of adding glucosamine sulphate to Hank's solution on the corrosion behavior of AZ31 alloy.

It was observed that:

1. The corrosion resistance for AZ91D in Simulated body fluid increase with increasing time of immersion until 35 h. It was found to be better than the blank (AZ91D alloy before immersion). It was found that film healing and thickening (increasing R_T value) becomes effective by increasing time of immersion in SBF solution leading to a quasi-steady state thickness at longer times. Generally, SBF improves slightly the corrosion resistance of AZ91D alloy with time.
2. Corrosion resistance found to increase for AZ31E in Ringer's solution with increasing immersion time till 100 h. This is caused by the formation of adherent corrosion products on the sample surface as $Mg(OH)_2$ which is precipitated from the solution during the corrosion of magnesium alloys due to saturation and localized alkalization. This is confirmed by measuring the pH of Ringer's solution after completing the experiment, which becomes 11.0. Also, Ca could improve both the corrosion resistance in NaCl solution and the mechanical properties of magnesium alloy, it is a major component in human bone and can accelerate the bone growth. The growth of the polarization resistance with the immersion time is consistent with the continual decrease of the bio-corrosion rate.
3. The corrosion resistance of AZ91E and AZ31E alloys increase with immersion time in Hank's solution for 100 h. However, the corrosion resistance of AZ31E alloy is much better than AZ91E alloy at all times of immersion.
4. All results are confirmed by scanning electron micrographs and potentiodynamic polarization tests. Thus, AZ31E was found to be the best alloy.
5. By addition of Glucosamine as inhibitor for corrosion of AZ31E in Hank's solution, it was evaluated that total resistance R_T or relative thickness $1/C_T$ of the film formed are higher compared to the values in absence of glucosamine. However, the best corrosion inhibition is observed by addition of 0.01 mM Glucosamine and this was confirmed by SEM images.

6. Thus, AZ31E alloy can be used as temporary implant in human body. It is low in its cost and will dissolve after a time that is the bone become healed. It doesn't need to do another surgery to remove it from human body; it is non-toxic to human body. Thus, Mg alloy can gradually be dissolved and adsorbed after implanting.
7. The previous electrochemical results show that the corrosion resistance of AZ31 is much higher than that of AZ91 alloy. The results may be caused by the different distribution of alloying elements in microscopic scale and the microstructure of alloys, which are the fundamental reasons for the metal corrosion morphology and corrosion resistance.

6. References

- Anderson, J.; Nicolosi, R. & Borzelleca, J. (2005). Glucosamine effects in humans: a review of effects on glucose metabolism, side effects, safety considerations and efficacy. *Food and Chemical Toxicology*, Vol. 43, No. 2, (February 2005), Pages (187-201), ISSN: 0278-6915.
- Ballerini, G.; Bardi, U.; Bignucolo, R. & Ceraolo, G. (2005). About some corrosion mechanisms of AZ91D magnesium alloy. *Corrosion Science*, Vol. 47, No. 9, (September 2005), Pages (2173-2184), ISSN: 0010-938X.
- a. Fekry, A. (2009). The influence of chloride and sulphate ions on the corrosion behavior of Ti and Ti-6Al-4V alloy in oxalic acid. *Electrochimica Acta*, Vol. 54, No. 12, (30 April 2009), Pages (3480-3489), ISSN: 0013-4686.
 - b. Fekry, A. & El-Sherief, R. (2009). Electrochemical corrosion behavior of magnesium and titanium alloys in simulated body fluid. *Electrochimica Acta*, Vol. 54, No. 28, (1 December 2009), Pages (7280-7285), ISSN: 0013-4686 .
 - c. Fekry, A & Mohamed, R. (2010). Acetyl thiourea chitosan as an eco-friendly inhibitor for mild steel in sulphuric acid medium. *Electrochimica Acta*, Vol. 55, No. 6, (15 February 2010), Pages (1933-1939), ISSN: 0013-4686.
- Ghoneim, A.; Fekry, A. & Ameer, A. Electrochemical behavior of magnesium alloys as biodegradable materials in Hank's solution. *Electrochimica Acta*, Vol. 55, No. 20, (1 August 2010), Pages (6028-6035), ISSN: 0013-4686.
- Giordano, N.; Fioravanti, A.; Papakostas, P.; Montella, A.; Giorgi, G. & Nuti, R. (2009). The efficacy and tolerability of glucosamine sulfate in the treatment of knee osteoarthritis: A randomized, double-blind, placebo-controlled trial. *Current Therapeutic Research*, Vol. 70, No. 3. (June 2009), pages (185-196), ISSN: 0011-393X.
- Gu, X.; Zheng, Y.; Cheng, Y.; Zhong, S. & Xi, T. (2009). In vitro corrosion and biocompatibility of binary magnesium alloys. *Biomaterials*, Vol. 30, No. 4, (February 2009), Pages (484-498). ISSN: 0142-9612.
- a. Heikal, F.; Fekry, A. & Fatayerji, M. (2009). Electrochemical behavior of AZ91D magnesium alloy in phosphate medium—part I. Effect of pH. *Journal of Applied Electrochemistry*, Vol. 39, No. 5 (May 2009), pages (583-591), ISSN: 0021-891X.
 - b. Heikal, F.; Fekry, A. & Fatayerji, M. (2009). Electrochemical behavior of AZ91D magnesium alloy in phosphate medium: Part II. Induced passivation. *Journal of*

- Applied Electrochemistry, Vol. 39, No. 9, (September 2009), pages (1633-1642), ISSN: 0021-891X.
- c. Heakal, F.; Fekry, A. & Fatayerji, M. (2009). Influence of halides on the dissolution and passivation behavior of AZ91D magnesium alloy in aqueous solutions. *Electrochimica Acta*, Vol. 54, No. 5, (February 2009), Pages (1545-1557), ISSN: 0013-4686.
- Jönsson, M.; Persson, D. & Thierry, D. (2007). Corrosion product formation during NaCl induced atmospheric corrosion of magnesium alloy AZ91D. *Corrosion Science*, Vol. 49, No. 3, (March 2007), Pages (1540-1558), ISSN: 0010-938X.
- Kainer, K.; Buch, F. (2003). Chapter 1: The Current State of Technology and Potential for Further Development of Magnesium Applications, In: *Magnesium-Alloys and Technology*. Kainer, k. (June 2003), pages (1-22), Wiley-VCH Verlag GmbH & Co. KG aA, Weinheim (2003). ISBN: 9783527305704, Germany.
- Mani, G.; Feldman, M.; Patel, D. & Agrawal, M. (2007). Coronary stents: A materials perspective. *Biomaterials*, Vol. 28, No. 9, (March 2007), Pages (1689-1710), ISSN: 0142-9612.
- Narayanan, R. & Seshadri, S. Phosphoric acid anodization of Ti-6Al-4V-Structural and corrosion aspects *Corrosion Science*, Vol. 49, No. 2, (February 2007), Pages (542-558), ISSN: 0010-938X.
- Pardo, A.; Merino, M.; Coy, A.; Arrabal, R.; Viejo, F. & Matykina, A. (2008). Corrosion behaviour of magnesium/aluminium alloys in 3.5 wt.% NaCl. *Corrosion Science*, Vol. 50, No. 3, (March 2008), Pages (823-834), ISSN: 0010-938X.
- Revell, P.; Damien, E.; Zhang, X.; Evans, P. & Howlett, C. (2004). The effect of magnesium ions on bone bonding to hydroxyapatite coating on titanium alloy implants, *Key Eng. Mater.* 254 (2004) 447-450.
- Staiger, M.; Pietak, A.; Huadmai, J. & Dias, G. (2006). Magnesium and its alloys as orthopedic biomaterials: A review *Biomaterials*, Vol. 27, No. 9, (March 2006), Pages (1728-1734), ISSN: 0142-9612.
- a. Song, G.; Atrens, A; St John, D.; Wu, X. & Nairn, J. (1997). The anodic dissolution of magnesium in chloride and sulphate solutions. *Corrosion Science*, Vol. 39, No. 10-11, (October-November 1997), Pages (1981-2004), ISSN: 0010-938X.
- b. Song, G.; Atrens, A & Dargusch, M. (1998). Influence of microstructure on the corrosion of diecast AZ91D *Corrosion Science*, Vol. 41, No. 2, (February 1998), Pages (249-273), ISSN: 0010-938X.
- c. Song, G. & Atrens, A. (2003). Understanding magnesium corrosion. A framework for improved alloy performance. *Advanced Engineering Materials*, Vol. 5, No. 12, (December 2003), Pages (837-858), ISSN: 1438-1656.
- d. Song, G. (2005). Recent progress in corrosion and protection of magnesium alloys. *Advanced Engineering Materials*, Vol. 7, No. 7, (July 2005), Pages (563-586), ISSN: 1438-1656.

- e. Song, G. & Atrens, A. (2007). Recent Insights into the Mechanism of Magnesium Corrosion and Research Suggestions. *Advanced Engineering Materials*, Vol. 9, No. 3, (March 2007), Pages (177-183), ISSN: 1438-1656.
- f. Song, G. (2007). Control of biodegradation of biocompatible magnesium alloys. *Corrosion Science*, Vol. 49, No. 4, (April 2007), Pages (1696-1701), ISSN: 0010-938X.
- g. Song, G. & Song, S. (2007). A Possible Biodegradable Magnesium Implant Material. *Advanced Engineering Materials*, Vol. 9, No. 4, (April 2007), Pages (298-302), ISSN: 1438-1656.
- Wang, H.; Estrin, Y. & Zúberová, Z. (2008). Bio-corrosion of a magnesium alloy with different processing histories. *Materials Letters*, Vol. 62, No. 16, 15, (June 2008), Pages (2476-2479), ISSN: 0167-577X.
- a. Witte, F.; Kaese, V.; Switzer, H.; Meyer-Lindenberg, A.; Wirth, C. & Windhagen, H. (2005). In vivo corrosion of four magnesium alloys and the associated bone response. *Biomaterials*, Vol. 26, No. 17, (June 2005), Pages (3557-3563), ISSN: 0142-9612.
- b. Witte, F.; Fisher, J.; Nellesen, J.; Crostack, H.; Kaese, V.; Pisch, A.; Beckmann, F. & Windhagen, H. (2006). In vitro and in vivo corrosion measurements of magnesium alloys. *Biomaterials*, Vol. 27, No. 7, (March 2006), Pages (1013-1018), ISSN: 0142-9612.
- c. Witte, F.; Hort, N.; Vogt, C.; Cohen, S.; Kainer, K.; Willumeit, R. & Feyerabend, F. (2008). Degradable biomaterials based on magnesium corrosion. *Current Opinion in Solid State and Materials Science*, Vol. 12, No. 5-6, (October-December 2008), Pages (63-72), ISSN: 1359-0286.
- Wu, G.; Fan, Y.; Atrens, A.; Zhai, C. & Ding, W. (2008). Electrochemical behavior of magnesium alloys AZ91D, AZCe2, and AZLa1 in chloride and sulfate solutions. *Journal of Applied Electrochemistry*, Vol. 38, No. 2, (February 2008), pages (251-257), ISSN: 0021-891X.
- Yamasaki, Y.; Yoshida, Y.; Okazaki, M.; Shimazu, A.; Uchida, T. & Kubo, T. (2002). Synthesis of functionally graded MgCO₃ apatite accelerating osteoblast adhesion. *Journal of Biomedical Materials Research*, Vol. 62, No. 1, (October 2002), pages (99-105), ISSN: 1549-3296.
- Yamasaki, Y.; Yoshida, Y.; Okazaki, M.; Shimazu, A.; Kubo, T. & Akagawa, Y. (2003). Action of FGMgCO₃Ap-collagen composite in promoting bone formation. *Biomaterials*, Vol. 24, No. 27, (December 2003), Pages (4913-4920), ISSN: 0142-9612.
- Zenner, H. & Renner, F. (2002). Cyclic material behavior of magnesium die castings and extrusions. *International journal of Fatigue*, Vol. 24, No. 12, (December 2002), pages (1255-1260), ISSN: 0142-1123.
- Zhang, E.; Yin, D.; Xu, L.; Yang, L. & Yang, K. (2009). Microstructure, mechanical and corrosion properties and biocompatibility of Mg-Zn-Mn alloys for biomedical application. *Materials Science and Engineering: C*, Vol. 29, No. 3, (30 April 2009), Pages (987-993), ISSN: 0928-4931.

Zreiqat, H.; Howlett, C.; Zannettino, A. & Evans, P. (2002). Mechanisms of magnesium stimulated adhesion of osteoblastic cells to commonly used orthopaedic implants. *Journal of Biomedical Materials Research*, Vol. 62, No. 2, (November 2002), Pages (175-184), ISSN: 1549-3296.

Magnesium Alloys as Promising Degradable Implant Materials in Orthopaedic Research

Janin Reifenrath¹, Dirk Bormann² and Andrea Meyer-Lindenberg¹

¹*Small Animal Clinic, University of Veterinary Medicine Hannover*

²*Institute for Material Science, University of Hannover
Germany*

1. Introduction

Magnesium alloys as degradable implant materials in orthopaedic research received a lot of interest in recent years (Witte et al., 2007a; Xu et al., 2008; Zhang et al., 2010). The application of resorbable implant material avoids an implant removal surgery and therewith helps to diminish the costs and the burden for the patient. In comparison to other degradable implant materials like polymers, magnesium alloys excel in higher tensile and compressive strength and the young's modulus is near to cortical bone (Hofmann, 1995; Staiger et al., 2006; Kaese, 2002). Another advantage that leads to the choice of magnesium alloys as implant material is the fact, that magnesium is a natural component of the body and furthermore has many important functions within the body (Hartwig, 2001). Magnesium is tested as non-allergenic (Witte et al., 2007a) and due to several studies it is assumed, that it stimulates new bone formation in vitro and in vivo (Revell et al., 2004; Zreiqat et al., 2002; Witte et al., 2007b).

For the application as orthopedic implant material in weight bearing bones, only magnesium alloys with a slow corrosion rate are useful. A high corrosion rate results in gas formation, a too fast loss of mechanical stability and a considerably higher bone remodelling activity (Thomann et al., 2009; Krause et al., 2010). Beside to different coating facilities (Witte et al., 2009; Zhang et al., 2010) and surface treatments (von der Höh et al., 2006; Hänni et al., 2008), in particular the alloying of aluminium, lithium, rare earth metals or calcium decrease the corrosion rate in vitro and in vivo (Kaese, 2002; Staiger, 2006; Hänni et al., 2008; Krause et al., 2010; Thomann et al., 2009). However, in vivo and in vitro corrosion rates can be quite different (Witte et al., 2006; Zhang et al., 2010), which makes it more difficult to develop and adapt magnesium alloys for biomedical use.

In order to investigate if the chosen magnesium-alloys are suitable for the use in orthopedic applications, in vivo-studies in rabbit tibiae were conducted. Therefore the selected and in vitro examined magnesium alloys LAE442, WE43, MgCa0.8, AX30, ZEK100 were implanted into the rabbit tibia and examined with regard to the mechanical stability, the in vivo corrosion rate and the biocompatibility.

For the in vivo investigation of the implant materials, the rabbit was used as established animal model for orthopaedic applications (Pearce, 2007). All animal experiments were conducted under an ethic committee approved protocol in accordance with German federal welfare legislation. Five rabbits were used for each group. Extruded pins with 2.5 mm in

diameter and 25 mm length were implanted into both tibiae (Fig.1a). Four tibiae remained without implant and served as control.

The used alloys contained adjacent to magnesium the elements lithium, aluminium and a rare earth composition metal (LAE442), yttrium and a rare earth composition metal (WE43), calcium (MgCa0.8), aluminium and calcium (AX30) or zinc, a rare earth composition metal and zirconium (ZEK100). The numbers describe the percentage of the alloying elements adjacent to magnesium, in accordance with the ASTM-standard. At the time of surgery, all rabbits were older than six months and hence adult. In general anaesthesia, a hole was drilled into the tibial plateau and the implant was inserted. The detailed operation procedure is described elsewhere (Thomann et al., 2009). Radiographs of two planes were taken immediately after surgery (Fig. 1b).



Fig. 1. Implant material and implant location: extruded magnesium pin (a) and radiographical picture of the implant location in the rabbit tibia (b)

Postoperative observation periods with daily clinical and weekly radiographical examinations of three, six and in some material groups (LAE442 and MgCa0.8) twelve months were studied. During the observation period, intravital fluorescent labelling was performed (Tab. 1) and evaluated in the LAE442 group, as rare-earth containing alloy, and in the MgCa0.8 group, as calcium containing alloy, as well as in the controls. The fluorochromes calcein green (Calcein, Fa. Sigma Aldrich, Germany), calcein blue (Methylumbiliferone, Fa. Sigma Aldrich, Germany), tetracycline (Ursocyclin, Serumwerk Bernburg, Germany) and Xylenolorange (Fa. Sigma Aldrich, Germany) were used (Rahn et al., 1980).

Time period	first staining (days)	fluorochrome	second staining (days)	fluorochrome
1	3 and 5	calcein green	30 and 33	xylenolorange
2	30 and 33	xylenolorange	60 and 63	calceinblue
3	60 and 63	calceinblue	90 and 93	tetracycline
4	90 and 93	tetracycline	120 and 123	calceinblue
5	120 and 123	calceinblue	150 and 153	xylenolorange
6	150 and 153	xylenolorange	180 and 183	calceingreen

Table 1. Time points and fluorochromes of intravital fluorescent labelling for the measurement of the bone remodelling and the calculation of the MAR.

At the end of the observation period, the rabbits were euthanized and the tibiae removed. In the left tibiae, the implants were taken out for measurement of weight reduction, scanning electron microscopy (SEM) and evaluation of the mechanical stability with three point bending test. To determine the decrease of weight, the adhering organic material was

removed into a dipping bath of 40% hydrofluoric acid for five minutes, cleaned in distilled water and ethyl alcohol for 10 sec and air dried. SEM allowed an examination of the surface of the implant and was done at a LEO1455VP (Fa. Zeiss, Germany) with a Rutherford Back-Scattered Detector and a 30-fold magnification. Three point bending was performed using a 10-kN load cell to measure the maximal applied force (Krause et al., 2010). Additionally to all explanted pins, three pins of each alloy were tested in their initial state. The right tibiae were left as the bone-implant-compound for μ -computed tomographical and histological examinations. Four tibiae without implant material served as control for the μ -computed tomographical and the histological analysis.

In μ -computed tomography, samples were analysed with a slice sickness of $36\mu\text{m}$ and a scanning time of 1s. An evaluation of endosteal and periosteal bone remodeling as well as bone adhesion on the implant material was done with a semi quantitative scoring system (Krause et al., 2010; Thomann et al., 2009) (Fig. 2).

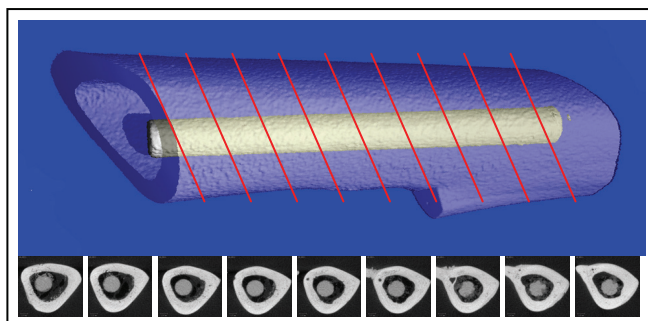


Fig. 2. Evaluation of the implant degradation and the bone morphology with μ -computed tomography (schematic picture): nine cross sectional slices of each tibia were evaluated

For histological analysis, the samples were dehydrated and embedded in Glycolmethacrylat (Technovit 7200, Kulzer, Germany). Histological slices were prepared according to the cutting and grinding technique (Donath & Breuner, 1982). With this technique, there was no need to decalcify the bone material, which could lead to a loss of the degradable magnesium alloy and fluorochromes prior to evaluation. Measurement of the bone remodelling and calculation of the MAR (MgCa0.8 and LAE442) was done. Therefore the distance between the different fluochrome labels, which were administered at different time points, were measured at twelve defined points within each section (Fig. 3). A calculation of the mineral apposition rate (MAR) was possible with the following equation (Parfitt et al., 1987):

$$\text{MAR } (\mu\text{m}/\text{d}) = \text{distance fluorescent bands } (\mu\text{m}) / \text{time period between labelling (d)} \quad (1)$$

Evaluation of the bone structure, the bone remodelling and the bone implant interface was done with toluidine blue as standard staining method for bone material. Bone morphology and cells were assessed with a semi quantitative scoring system (Tab. 2).

Additional to the standard staining method, TRAP-staining was used for osteoclast detection (Schäfer et al., unpublished data). As calcium-containing alloy, MgCa0.8 was examined, as examples for rare earth containing alloys, WE43 and LAE442 were stained and evaluated. For statistical analysis ANOVA and t-test were performed.

Parameter	Score	Interpretation
overall impression of bone structure (BS)	0	smooth
	1	irregular
bone cavities (BC)	0	≤ 3 osteonlike cavities
	1	4 to 6 osteonlike cavities or ≤10 smaller
	2	7 to 10 osteonlike cavities or 11 to 20 smaller
	3	≥11 osteonlike cavities or 21 smaller or ≥3 doubleosteonlike cavities
periosteal remodelling (pR)	0	no
	1	≥ ¼ periosteal bone, 1 osteon thick
	2	≥ ¼ periosteal, 2 osteon thick
	3	≥ ¼ periosteal bone, 3 osteon thick
endosteal remodelling (eR)	0	no
	1	≥ ¼ endosteal bone, 1 osteon thick
	2	≥ ¼ endosteal bone, 2 osteon thick
	3	≥ ¼ endosteal bone, 3 osteon thick
periosteal apposition (pA)	0	no
	1	yes
periimplant bone formation (PIF)	0	no
	1	yes
periimplant fibrosis	0	no
	1	≤ 25% implantsurface
	2	26-50% implantsurface
	3	≥ 51% implantsurface
lymphoplasmacellular reaction (Lym)	0	< 30 cells per section
	1	30-50 cells per section
	2	51-100 per section
	3	> 100 cells per section
Macrophages (Mph)	0	< 3 cells per section
	1	3- 20 cells per section
	2	> 20 cells per section
giant cells (GC)	1	no
	2	1-5 cells per section
	3	> 10 cells per section
gas bubbles	0	no
	1	yes

Table 2. Scoring system for the evaluation of histological sections, staining toluidine blue

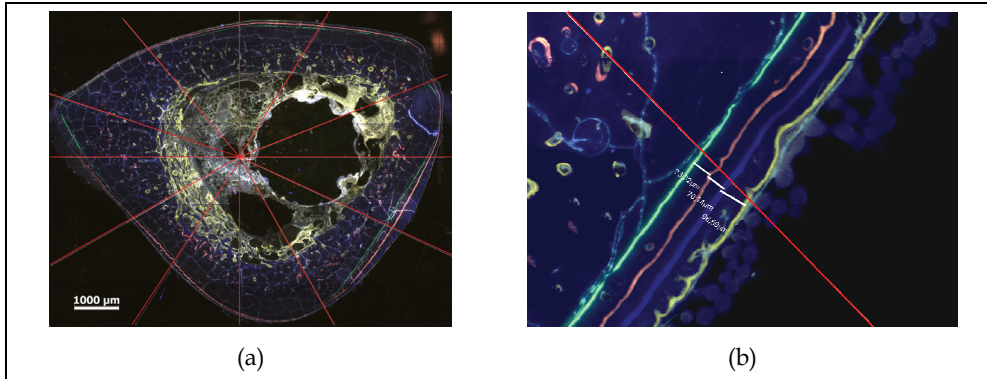


Fig. 3. Evaluation of the fluorescent labelling with measurement of the distances between the different flourochrome bands (observation time three months); 12 measurement lines per section (a) and measurement of the distance between fluorescent bands (b).

2. Results

Clinically, all tested materials were tolerated well and gas formation could not be detected. For all implants weight loss, according with the degree of degradation (Xu et al., 2008) and a decrease of mechanical stability could be found during in vivo observation periods of three, six (all implant groups) and twelve months (LAE442 and MgCa0.8). MgCa0.8 and WE43 showed highest weight losses with a mean value (MV) of 61.4% (MgCa0.8) and 66.4% (WE43) of their initial weights after six months in comparison to LAE442 (MV 75.3%), ZEK100 (MV 76.1) and AX30 (79.8) which showed less weight reduction (Fig. 4a). After 12 months MgCa0.8 was highly degraded and the residual implant material showed only 33.0% of the initial weight. LAE442 corroded slower, ending up with a weight of 52.9%. In the three point bending tests, the maximal applied force (F_{max} [N]), which indicates the residual implant strength, decreased faster in the calcium containing than in the rare-earth containing alloys. After six months, the maximal force of MgCa0.8 was measured with 29.6% of the initial value (178.7 ± 84.6 N) and AX30 showed similar results with 29.7% of the

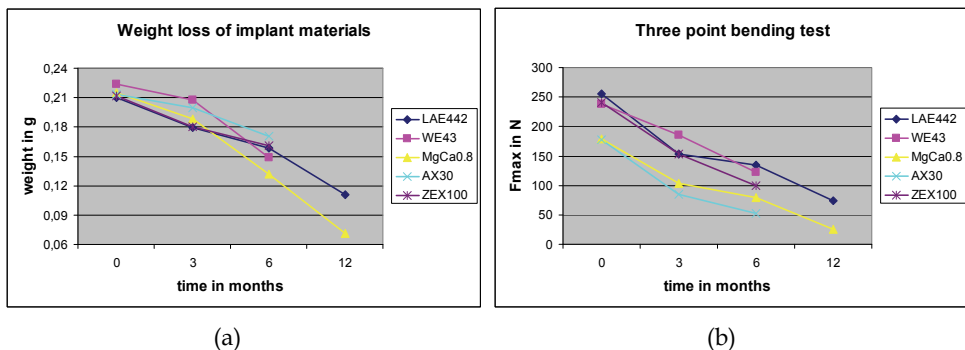


Fig. 4. Weight loss (a) and mechanical stability (b) of the different implant materials after three and six (all materials) and twelve months (LAE442 and MgCa0.8).

initial value (177.4 ± 16.4 N). The rare earth containing alloys retained 41.3% (ZEK100, initial value 240.8 ± 2.4 N), 51.3% (WE43, initial value 238.1 ± 21.68 N), and 52.7% (LAE442, initial value 255.7 ± 5.7 N) of their initial strength.

LAE442 decreased to a level of 28.7% even after an observation period of 12 months. It could be shown, that weight reduction as sign of degradation and loss of mechanical stability in vivo do not necessarily correspond in the examined degradable magnesium alloys. The corrosion morphology of the different alloys appeared quite different. After three months all implant materials preserved their cylindrical shape with corrosion layers of different extend on the implant surface. After six months implantation time the corrosion process at the implant surfaces proceeded. With the exception of ZEK100, all implant materials still showed their cylindrical shape. ZEK100 showed cleft surfaces and losses of implant material in greater extend than in the other groups. The surfaces of MgCa0.8 (Fig 5a), AX30 and ZEK100 were characterized by pitting corrosion. WE43 showed soil-like ablations on the surface (Fig 5b) and LAE442 homogeneous fissured corrosion (Fig. 5c). After an implantation period of twelve months (LAE442 and MgCa0.8), MgCa0.8 was highly degraded. Only one implanted pin could be removed completely. It showed deep pits of corrosion. The other implants could be taken out in sections. In contrast, in the LAE442 group, all implants remained cylindrical to a large extend after an implantation period of six and even after an implantation period of twelve months. Uniform fissure corrosion could be observed.

Bone reactions as sign of biocompatibility were less in the groups with the slower and more uniform degrading implant materials, particularly in the LAE442 group (Fig. 6).

In μ -computed tomography, WE43 showed inhomogeneous implant degradation and a gradual loss of the bone structure. Trabecular new bone formation could be found in the majority of μ -computed tomography slices of the bones around the implant. In the MgCa0.8 groups, after six months, bone adhesion at the implant material could be detected only sporadically. After twelve months 55% of the evaluated slices showed bone-implant contact of different degree. Some slices showed trabecular bone formation other partly or full ring bone contact around the implant material.

In the LAE442 group after six months 35% of the evaluated slices showed trabecular bone-implant contact, after twelve months 89% of the evaluated slices showed endosteal new bone formation and 53% trabecular bone-implant contact.

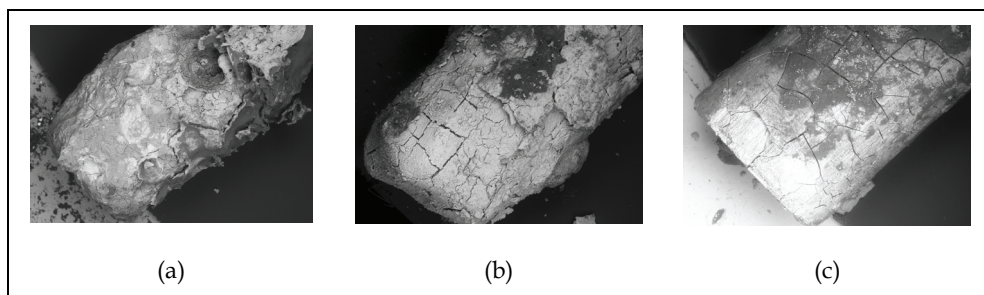


Fig. 5. Comparison of the surface morphology of the magnesium alloys MgCa0.8 (a), WE43 (b) and LAE442 (c) after 6 months postoperative observation period (REM, magnification 30x).

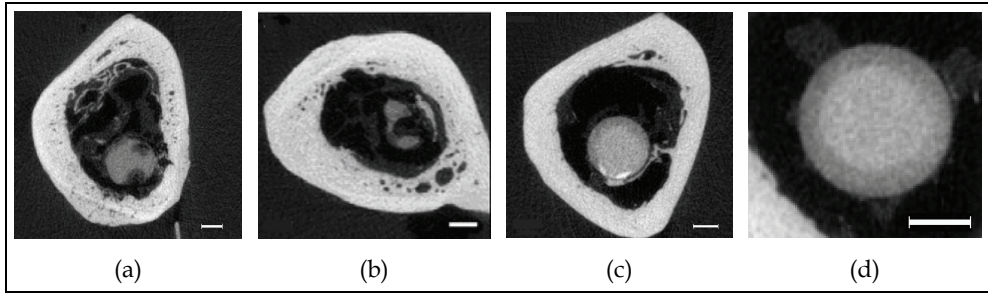


Fig. 6. μ -computed tomographical picture of the fast degrading alloys AX30 (a), 6 months postoperatively and MgCa0,8 (b), 12 months postoperatively with bone reactions and a slow degrading alloy LAE442 (c), 12 months postoperatively with endosteal new bone formation and trabecular bone-implant contact, loss of implant density as sign for implant corrosion (d), white bar = 1 cm

In the histological examination polychrome sequence labelling was evaluated. In comparison to the control tibiae, the examined groups with magnesium implants showed an increased bone remodeling with a higher MAR. Especially in the first month the MAR was with $4.29\mu\text{m}/\text{d}$ in the MgCa0.8 group and with $3.36\mu\text{m}/\text{d}$ in the LAE442 group higher than in the control group without implant material (MAR $0.87\mu\text{m}/\text{d}$). During the observation period, a decrease of MAR in the magnesium groups could be observed (Fig. 7).

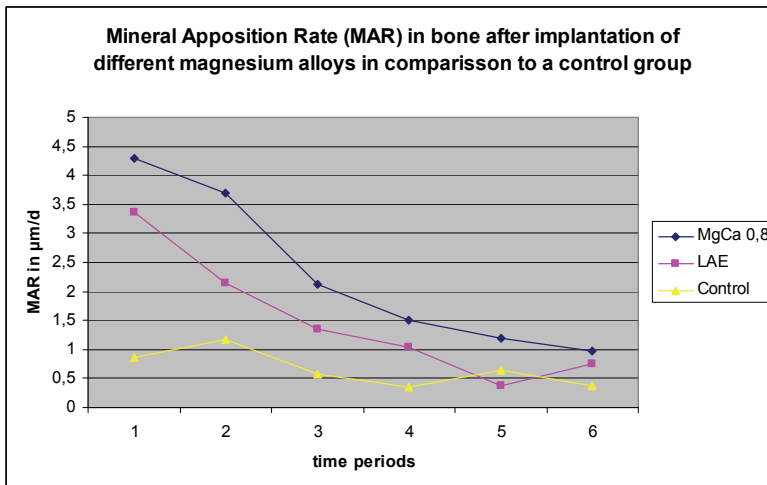


Fig. 7. MAR in the bone during the observation period of 6 months after the implantation of different magnesium alloys in comparisson to control tibiae without implants.

Additionally to fluorescent labelling, the conventional histological toluidine blue staining was evaluated (Fig. 8 a-c) and after six months an irregular bone structure (Score value 1) could be observed in all examined material groups which, in the two longer observed groups, decreased with the increasing observation time. In the LAE442 group, the score value was reduced from 0.80 after six months to 0.00 after twelve months and in the

MgCa0.8 group in the same period from a score value of 1.00 to 0.47 (SD 0.52). Different degrees of periosteal and endosteal remodelling were detected in all examined material groups (Tab. 3). Fibrous tissue covered less than 25% of the implant surface in all examined groups. For macrophages a score value of 1 could be observed after six months in all material groups as well as giant cells. In the MgCa0.8 group the macrophages and giant cells decreased by trend to a score of 0.8 (SD 0.41) and 0.87 (SD 0.64) after twelve months, in the LAE442 group a slight increase was found for macrophages (MV 1.17, SD 0.39) and giant cells (MV 1.08, SD 0.51). Histologically visible gas bubbles were found in all material groups after all observation periods (Tab. 3).

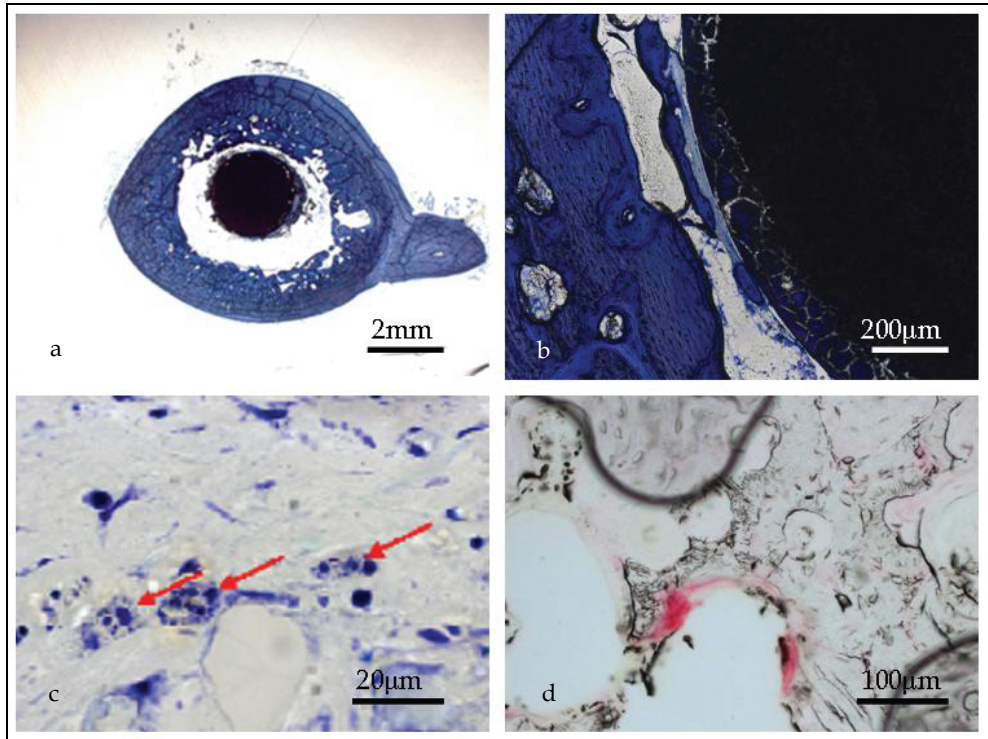


Fig. 8. WE 6 months (a) with an irregular bone structure with remaining implant material in the bone cavity; MgCa0.8 12 months (b, c), trabecular bone structures at the implant surface (b) and macrophages (red arrows) in the bone cavity (c), staining toluidine blue (a-c); TRAP-staining for osteoclast detection (osteoclasts = red areas)

TRAP-staining was used additionally in the MgCa0.8, the WE43 and the LAE442 groups after three and six, and in the MgCa0.8 and in the LAE442 groups after twelve months to evaluate quantitative data measurement for bone remodeling activity (Fig. 9)

In the calcium-containing alloy MgCa0.8 more osteoclasts could be found in all time groups, but the differences between the time and material groups after three and six months were not significant. After twelve months implantation duration the total and cortical osteoclast number was significant lower ($p \leq 0.001$) in the LAE442 group than in the MgCa0.8 group.

		BS	BC	pR	eR	pA	PIF	Fibrosis	Lym	Mph	GC	bubbles
WE43	MV	1,00	2,90	1,50	3,00	0,00	0,60	0,70	0,00	1,00	1,00	1,00
6 months	SD	0,00	0,32	1,35	0,00	0,00	0,52	0,82	0,00	0,00	0,00	0,00
MgCa0.8	MV	1,00	2,30	2,40	2,80	0,00	0,80	0,90	0,00	1,00	1,00	1,00
6 months	SD	0,00	0,82	0,70	0,42	0,00	0,42	0,99	0,00	0,00	0,00	0,00
LAE442	MV	0,80	2,10	1,00	2,30	0,10	1,00	0,20	0,20	1,00	1,00	1,00
6 months	SD	0,42	0,74	1,15	0,82	0,32	0,00	0,42	0,42	0,00	0,00	0,00
MgCa0.8	MV	0,47	0,73	1,93	1,13	0,00	0,60	0,00	0,00	0,80	0,87	1,00
12 months	SD	0,52	1,03	1,10	0,35	0,00	0,51	0,00	0,00	0,41	0,64	0,00
LAE442	MV	0,00	0,00	1,83	0,50	0,00	0,17	0,25	0,08	1,17	1,08	1,00
12 months	SD	0,00	0,00	0,72	0,90	0,00	0,39	0,45	0,29	0,39	0,51	0,00

Table 3. Score values of histological sections in the different material groups after 6 and 12 months implantation time, staining toluidine blue, Abbreviations are described in table 2

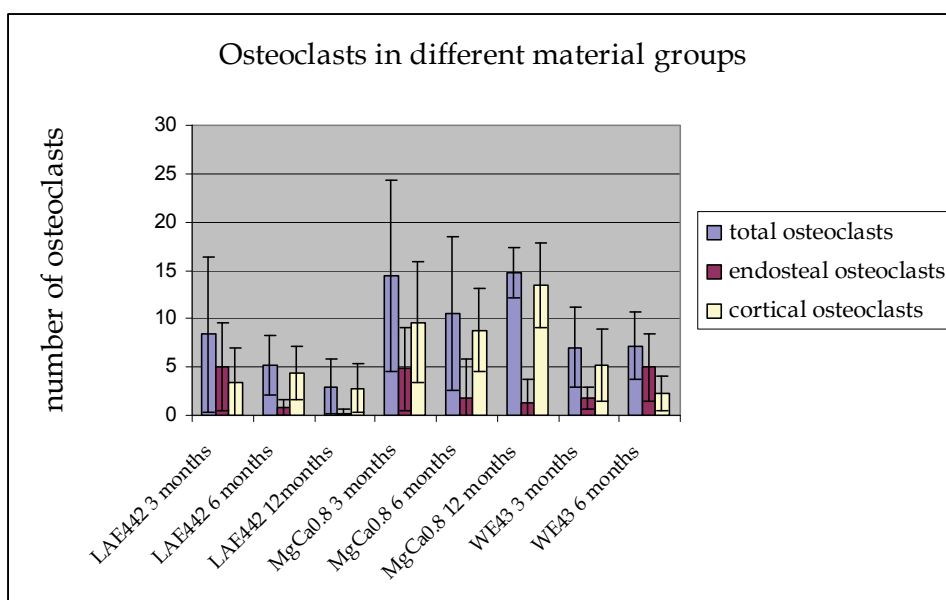


Fig. 9. Osteoclasts in different material groups after 3, 6 and in MgCa0.8 and LAE442 12 months of implantation duration.

3. Discussion

The purpose of all described studies was to investigate the applicability of different magnesium alloys as biodegradable materials in osteosynthesis. Beside an adequate primary mechanical stability and the ability to degrade without side effects, a good biocompatibility is required.

Magnesium itself is described as relatively safe and assessed as non-toxic (Staiger et al., 2006). It is an essential element for the human body and fulfils many functions in the

organism. More than 300 enzymatic reactions are triggered with magnesium as part of enzymes or coenzymes and it is essential for the neuromuscular transmittance of stimuli (Topf & Murray, 2003). About 50% of the human body-magnesium is stored in the bone. Other reservoirs for magnesium are the muscle and inner organs, especially the liver. Only about 1% is in the blood plasma. The body-magnesium is regulated by renal excretion.

Since pure magnesium corrodes much too fast in vitro (Pardo et al., 2008) and in vivo (Huang et al., 2007) alloying of elements is necessary to slow down the degradation process. A lot of studies describe in vitro corrosion properties and characteristics of magnesium alloys in synthetic medium as NaCl, Hank's solution or SBF (Müller et al., 2007; Pardo et al., 2008; Xu et al., 2008; Hänni et al., 2009; Gu & Zheng, 2010) and biocompatibility in cell culture (Xu et al., 2009). Unfortunately, until now, there is no in vitro method, which can predict the in vivo corrosion characteristics and in vitro and in vivo results can differ gravely (Witte et al., 2006; Gu & Zheng, 2010; Zhang et al. 2010). Therefore in vivo studies are essential to investigate in vivo corrosion and biocompatibility. Only few different magnesium alloys have been examined in vivo yet (Tab. 4). In our studies additionally to earlier described magnesium alloys WE43, LAE442 and MgCa0.8, the magnesium alloys ZEK100 and AX30 were investigated, which consisted of different alloying elements to optimize the characteristics of magnesium itself. Aluminium, as alloying element in AX30 and LAE442 is known to diminish the corrosion rate by stabilizing hydroxides in chloride environment. It is reported, that the corrosion rate decreases rapidly with increasing aluminium up to 4%, further additions up to 9% give only a modest further improvement (Song & Atrens, 1999). AZ31 and AZ91 are other aluminium containing alloys which are often used materials in in vitro (Müller et al., 2007; Witte et al., 2006) and in vivo studies (Witte et al., 2005; Huang et al., 2005), but the in vivo corrosion process is too fast, with a clinically observable gas production (Witte et al., 2005; Witte et al., 2007b) and the mechanical stability is not satisfactory for the use as weight bearing material (Gu et al., 2010). Although Witte et al. did not find any negative influence of corroding material on the surrounding bone (Witte et al., 2007b), toxic effects of high amounts of corroding aluminium especially in osteosynthesis systems, like intramedullary nailing or plates and screws, with high amounts of metallic material, can not be excluded (Yuen et al., 2010).

Lithium, as alloying element in LAE442, is known to alkalize the corrosion layer and therefore stabilize it (Wang, 1997). This element is used therapeutically in manic-depressive psychosis with a daily clinical uptake of lithium-carbonate up to 1300 mg (Grandjean & Aubry, 2009a). In these therapeutic cases, negative effects like gastrointestinal pain or discomfort, renal involvement with reduced urinary concentration capacity, expressed as polyuria, as well as negative effects on memory, vigilance and reaction time are observed (Grandjean & Aubry, 2009b). Another study with rats could even find a potential of lithium to reduce aluminium-induced cytotoxic effects in the brain (Bhalla et al., 2010). The dissolving elements from LAE442 can reach only a fraction of therapeutically used dosages. Witte et al. (2009) calculated a corrosion rate of 0.58 mm/y in the first two postoperative weeks, which decreased during longer observation periods. Therefore a general toxic effect of lithium is very unlikely. Whether marginal lithium concentrations can have direct effects on the surrounding bone is not described yet.

Calcium, as alloying element in MgCa0.8 and AX30, increases the corrosion resistance already in low concentrations (Li et al., 2008). It is an essential element in the human body and naturally belongs to the bone (Kannan & Ramann, 2008).

Zinc, as alloying element in ZEK100, can increase the tolerance limits in the magnesium alloys and reduce the effect of impurities on corrosion processes once the tolerance limit has been exceeded. Zinc overdoses can reduce the erythrocyte superoxide dismutase level, but the tolerable exposure level is with $0.83 \text{ mg kg bw}^{-1} \text{ day}^{-1}$ (Yuen & Ip, 2010) and with 1 wt% in the ZEK100 alloy unlikely to reach.

Zirconium in magnesium alloys is used to form complexes with zinc and certain elements which are impurities (Avedesian & Baker, 1999) to improve the corrosion resistance. The daily human uptake has been known to be as high as 125 mg, toxic effects induced by very high concentrations are non-specific in nature (Ghosh et al., 1992). Negative effects on the circumjacent bone are not described (Lit). In magnesium alloys, an exposure limit for zirconium is not known yet (Yuen & Ip, 2010).

Rare Earth metals as alloying elements in LAE442, WE43 and ZEK100 reduce the corrosion resistance by forming solid solutions or intermetallic compounds, a rare earth enrichment in the oxide film and possibly a formation of an additional magnesium hydride layer. Therefore they have beneficial effects on the castability, improve the tensile and creep properties as well as the corrosion resistance (Nakatsugawa et al., 1998). In the human body, chelated rare earths are rapidly excreted via urine, while unchelated ionic rare earths easily form colloid in blood and the colloid material is taken up by phagocytic cells of the liver and spleen. An other target organ of the rare earths is the bone, but it is not clear, what cells of the bone take up the most rare earths. The clearance of the bone is known to be very slow, but the general potential toxicity is described to be low (Hirano & Suzuki, 1996).

Beneath to different alloying elements, the surface treatment can have an effect on in vivo corrosion properties as well. Von der Höh et al. (Von der Höh et al., 2006) showed, that MgCa0.8 alloys with sand-blasted surface machining treatment had a higher corrosion rate in vivo than implants with a smooth surface. Witte et al. used a fluoride coating to reduce the in vivo corrosion rate of LAE442 (Witte et al., 2009). These results are in contrast to the results of Thomann et al., who could not find a reduction of the corrosion rate in MgCa0.8-implants with fluoride coating although the fluoride layer could be detected at the end of the implantation period of six months (Thomann et al., 2010).

Based on slow degradation rates of the used alloys, toxic effects were not expected in the present studies. All implant materials used showed no clinically and radiographically observable gas generation. Even the degradation celerity in the faster degrading alloys was apparently slow enough for the body to remove the emerging gas during the corrosion process. After six months implantation duration the cylinders of all groups still existed, even all implant materials showed obvious signs of corrosion, which were different between the alloys. MgCa0.8 and WE43 degraded to a greater extent than the other materials Ax30, ZEK100 and LAE442. Especially LAE442 showed a very uniform and slow degradation process even after an observation period of 12 months. This slow degradation process of LAE442 was confirmed in other studies (Witte et al., 2009). The reactions of the bone could be used to evaluate the biocompatibility (Sumner-Smith & Fackelmann, 2002). After observation periods of six and twelve months, the majority of the μ -computed tomography slices of all alloys showed new endosteally based bone formation which increased in the two groups with longer observation periods (MgCa0.8 and LAE442). After 12 months the bone-implant contact with mostly trabecular bone formation was clearly stronger in the MgCa 0.8 group, although the degradation had progressed further. On the one hand a possible explanation for this divergence could be the 9% higher magnesium amount of the MgCa0.8 implants. On the other hand the calcium content could enhance the formation of precipitates

of calcium and phosphorous in the implant periphery which is discussed as a possible mineralization source (Lu & Leng, 2005).

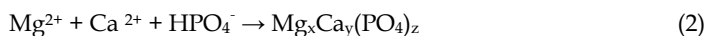
With the intravital fluorescence labelling, increased bone remodelling activity of the magnesium alloys MgCa0.8 and LAE442 during an observation period of six months in comparison to the control group could be observed, which confirmed the observations in

in-vivo studies of magnesium alloys for orthopedic research

Mg-alloy	coating	animal model	implant location	observation time	gas formation	author	year
LAE442							
LAE442	no	rabbit	tibia	3 and 6 months	no	Krause et al.	2010
LAE442	no	rabbit	tibia	9 and 12 months	no	Thomann et al.	2010
LAE442	no/ fluoride	rabbit	femora	2, 4, 6 and 12 weeks	no	Witte et al.	2010
LAE442	no	guinea pig	femora	18 weeks	yes	Witte et al.	2005
MgCa							
MgCa0.8	no	rabbit	tibia	3 and 6 months	no	Krause et al.	2010
MgCa0.8	no	rabbit	tibia	9 and 12 months	no	Thomann et al.	2010a
MgCa0.8	fluoride	rabbit	tibia	3 and 6 months	no	Thomann et al.	2010b
MgCa0.2-2.0	no	rabbit	femora		some	Von der Höh et al.	2008
MgCa1.0	no	rabbit	femora	1, 2 and 3 months	yes	Li et al.	2008
AZ							
AZ91/AZ31	no	guinea pig	femora	18 weeks	yes	Witte et al.	2005
AZ91	no	rabbit	femora	3 and 6 months	yes	Witte et al.	2007a/b
AZ31	no	rabbit	femora	1 and 9 weeks		Huang et al. / Ren et al.	2007
WE							
WE43	no	rabbit	tibia		no	Krause et al.	2010
WE43	no	guinea pig	femora	18 weeks		Witte et al.	2005
MgZnMn							
MgZn1Mn1.2	no	rat	femora	9 and 18 weeks		Xu et al.	2007
MgMn1Zn0.8	no	rat	femora	6, 10 and 26 weeks		Zhang et al.	2008
MgMn1.2Zn1.0	no/ Ca-P	rabbit	femora	1, 2, 3 and 4 weeks		Xu et al.	2009
MgZn							
MgZn6	no	rabbit	femora	6 and 18 weeks	yes	Zhang et al.	2008
MgZnCa							
MgZn20/23/29/35Ca5	no	pig	abdominal cavity/-wall	27 and 91 days	some	Zberg et al.	2009
ZEK							
ZEK100	no	rabbit	tibia	3 and six months	no	present results	
AX							
AX30	no	rabbit	tibia	3 and six months	no	present results	

Table 4. In vivo-studies of different magnesium alloys in different animal models and with different time periods

the μ -computed tomography. In both examined groups, the mineral apposition rate as sign for bone remodelling activity (Parfitt et al., 1987) was highest in the first time period (between the third and the 33th postoperative day), and even higher in the MgCa0.8 group in comparison to the LAE442-group, which was seen in the μ -computed tomography as well. A decreased MAR around magnesium scaffolds was also found in other studies (Witte et al., 2007b). In both groups of our studies the MAR showed a decrease during postoperative time and from three to six months only marginal differences in comparison to the control, although the MAR in the MgCa0.8 group remained little higher than in the control group and the LAE442 group. The number of osteoclasts, as a sign for bone remodelling activity, which was counted in the TRAP-stained sections, confirmed these results but showed increased bone remodelling activity in the group with MgCa0.8 alloys even after twelve months implantation duration. The number of osteoclasts in the LAE442 group decreased over time albeit no significances could be found. The increased bone remodelling could be indicative of magnesium alloy induced osteoinductive properties. These osteoinductive properties are supposed by other authors as well (Li et al., 2008; Xu et al., 2007; Witte et al., 2007b). As possible reason for the observed osteoinductive effects, Xu et al. summarized the degradation process of magnesium alloy implants as following: just after implantation, the surface of magnesium implants will react in the body fluids and the magnesium alloy will start to dissolve. With the increasing concentration of magnesium ions, a magnesium-containing calcium phosphate will precipitate from the body fluid on the surface of the magnesium implant, per following reaction:



The high Ca^{2+} and Mg^{2+} contents in this degradation layer in turn accelerate the deposition of biological calcium phosphate on the surface and thereby induce the formation of new bone (Xu et al., 2007). A further explanation for the enhanced bone remodeling activity is the regenerating effect of magnesium ions on alkaline phosphatase activity (Bonucci et al., 1992), which is directly related to the mineralization of the osteoid matrix (Roach, 1999). A higher bone volume per tissue volume around degrading magnesium implants and a more mature bone structure in comparison to a control group was described in other studies as well (Witte et al., 2007b; Xu et al., 2009).

Besides the biocompatibility, the tensile strength is regarded to be the critical mechanical characteristic of an implant that is supposed to be used as implant material in weight bearing bones and to stabilize bone fragments (McKibbin, 1978), while its ductility is of less importance (Hort et al., 2009; Krause et al. 2010). As it is known and even found in the described studies, magnesium alloys have a tendency for pitting corrosion (Song et al., 2005). These pits reduce the mechanical stability of the implant because they locally decrease the cross sectional diameter. As the calcium containing alloys have lower mechanical stabilities as shown in the described studies, for the use as implant material in weight bearing bones, the rare earth containing alloys should be preferred for these indications. All rare earth containing alloys had similar initial tensile strengths, LAE442 with 255.67 N even the highest. After 6 months, ZEK showed 41%, LAE442 and WE43 still more than 50% of their initial tensile strength. Therefor the mechanical characteristics appear suitable for the application as materials for biodegradable implants in weight bearing bones. After six months, LAE442 therefor showed a very good biocompatibility even during observation periods of 12 months, with a smooth overall impression of the bone structure, which was seen in no other material group.

It can be concluded, that magnesium alloys are very promising implant materials for orthopaedic research. Especially the rare-earth containing alloys have favourable mechanical characteristics and in particular LAE442 shows a very slow a homogeneous in vivo degradation with favourable biocompatibility even after observation periods of 12 months.

4. References

- [1] Avedesian, M. M. & Baker, H. (1999), Magnesium and magnesium alloys, Metallographic and Fractographic Techniques and Microstructures, ASM International. Handbook Committee, 26-35
- [2] Bhalla, P.; Singla, N. & Dhawan, D.K. (2010), Potential of lithium to reduce aluminium-induced cytotoxic effects in rat brain, *Biomaterials*, 23, 2, 197-206
- [3] Bonucci, E.; Silvestrini, G. & Bianco, P. (1992), Extracellular alkaline phosphatase activity in mineralizing matrices of cartilage and bone: Ultrastructural localization using cerium-based method, *Histochemistry*, 97, 323-327
- [4] Donert, K. & Breuner, G. (1982), A method for the study of undecalcified bones and teeth with attached soft tissues. The Säge-Schliff (sawing and grinding) technique, *J. Oral Pathol.*, 11, 318-326
- [5] Ghosh, S.; Sharma, A. & Talukder, G. (1992), Zirconium. An abnormal trace element in biology, *Biol. Trace Elem. Res.*, 35, 3, 247-271
- [6] Grandjean, E. M. & Aubry, J.M (2009a), Lithium: updated human knowledge using an evidence-based approach. Part II: Clinical pharmacology and therapeutic monitoring, *CNS Drugs*, 23, 4, 331-349
- [7] Grandjean, E. M. & Aubry, J.M. (2009b), Lithium: updated human knowledge using an evidence-based approach. Part III: clinical safety, *CNS Drugs*, 23, 5, 397-418
- [8] Gu, X.; Zheng, Y.; Cheng, Y.; Zhong, S. & Xi, T. (2009), In vitro corrosion and biocompatibility of binary magnesium alloys, *Biomaterials*, 30, 4, 484-498
- [9] Gu, X. & Zheng, F. (2010), A review on magnesium alloys as biodegradable materials, *Front. Mater. Sci. China*, 4, 2, 111-115
- [10] Gu, X.; Zhou, W. R.; Zheng, Y. F.; Cheng, Y.; Wei, S. C.; Zhong, S. P.; Xi, T. F. & Chen, L. J. (2010), Corrosion fatigue behaviour of two biomedical Mg alloys - AZ91D and WE43 - In simulated body fluid, *Acta Biomater.*, doi:10.1016/j.actabio.2010.07.026
- [11] Hänzi, A. C.; Gunde, P.; Schinhammer, M. & Ugguwitzer, P. J. (2008), On the biodegradation performance of an Mg-Y-RE alloy with various surface conditions in simulated body fluid, *Acta Biomater.*, 5, 162-171
- [12] Hartwig, A. (2001), Role of magnesium in genomic stability, *Mutation research*, 475, 113-121
- [13] Hirano, S. & Suzuki, K. T. (1996), Exposure, Metabolism, and Toxicity of Rare Earths and Related compounds, *Environ Health Perspect.*, 104, Suppl. 1, 85-95
- [14] Hofmann G. (1995), Biodegradable implants in traumatology: a review on the state-of-the-art, *Arch. Orthop. Trauma Surg.*, 114, 123-132
- [15] Hort, N.; Huang, Y.; Fechner, D.; Störmer, M.; Blawert, C.; Witte, F.; Vogt, C.; Drücker, H.; Willumeit, R.; Kainer, K. U. & Feyerabend, F. (2009), Magnesium alloys as implant materials - Principles of property design for Mg-RE alloys, *Acta Biomater.*, 5, 1, 1-13

- [16] Huang J.; Ren, Y.; Jiang, Y.; Zhang, B. & Yang, K. (2007), In vivo study of degradable magnesium and magnesium alloy as bone implant, *Front. Mater. Sci. China*, 1, 4, 405-409
- [17] Kaese, V. (2002), Beitrag zum korrosionsschützenden Legieren von Magnesiumwerkstoffen, *Fortschrittberichte VDI*, 5, Nr. 666
- [18] Li, Z.; Gu, X.; Lou, S. & Zhang, Y. (2008), The development of binary Mg-Ca alloys for use as biodegradable materials within bone, *Biomaterials*, 29, 1329-1344
- [19] McKibbin, B. (1978), The Biology of Fracture Healing in Long Bones, *J. Bone Joint Surg.*, 60, 2, 150-162
- [20] Müller, W.D.; Nascimento, M. L.; Zeddies, M.; Corsico, M.; Gassa, L. M. & Lorenzo de Mele, M. A. F. (2007), Magnesium and its alloys as degradable biomaterials. Corrosion studies using potentiodynamic and EIS electrochemical techniques, *Mater. Res.*, 10, 1, 5-10
- [21] Pardo, A.; Merino, M. C.; Coy, A. E.; Arrabal, R.; Viejo, F. & Matykina, E. (2007), Corrosion behaviour of magnesium/ aluminium alloys in 3.5 wt.% NaCl, *Corr. Sci.*, 50, 3, 823-834
- [22] Parfitt, A. M.; Drezner, M. K.; Glorieux, F. H.; Kanis, J. A.; Malluche, H.; Meunier, P. J.; Ott, S. M. & Recker, R. R. (1987), Bone Histomorphometry: Standardization of Nomenclature, Symbols and Units, *J. Bone Miner. Res.*, 2, 6, 595-610
- [23] Pearce, A.; Richards, R. G.; Milz, S.; Schneider, E. & Pearce, S. G. (2007), Animal models for implant biomaterial research in bone: a review, *European Cells and Materials*, 13, 1-10
- [24] Rahn, B. A.; Bacellar, F. C.; Tarapp, L. & Perren, S. M. (1980), *Aktuelle Traumatologie*, 10, 2, 109-115
- [25] Revell, P. A. (2004), The effect of magnesium ions on bone bonding to hydroxyapatite. *Key. Eng. Mater.*, 254-256, 447-450
- [26] Roach, H. I. (1999), Association of matrix acid and alkaline phosphatases with mineralization of cartilage and ancondral bone, *Histochem. J.*, 31, 53-61
- [27] Sumner-Smith, G. & Fackelmann, G. E. (2002), *Bone in clinical orthopedics*, 2nd ed., Thieme, ISBN 9783131257215 Stuttgart
- [28] Staiger, M. P.; Pietak, A. M.; Huadmai, J. & Dias, G. (2006), Magnesium and its alloys as orthopedic biomaterials: a review. *Biomaterials*, 27, 1728-1734
- [29] Thomann, M.; Krause, C.; Bormann, D.; Von der Höh, N.; Windhagen, H. & Meyer-Lindenberg, A. (2009), Comparison of the resorbable magnesium alloy LAE442 an MgCa0,8 concerning their mechanical properties, gradient degradation and bone implant-contact after 12 month implantation in rabbit model, *Materialwissenschaft und Werkstofftechnik*, 40, 1-2, 82-88
- [30] Thomann, M.; Krause, C.; Angrisani, N.; Bormann, D.; Hassel, T.; Windhagen, H. & Meyer-Lindenberg, A. (2010), Influence of a magnesium-fluoride coating of magnesium-based implants (MgCa0.8) on degradation in a rabbit model, *J. Biomed. Mat. Res. A*, 93, 4, 1609-1619
- [31] Topf, J. & Murray, P. (2003), Hypomagnesemia and Hypermagnesemia, *Rev. Endocr. Metab. Disord.*, 4, 195-206
- [32] Von der Höh, N.; Krause, A.; Hackenbroich, C.; Bormann, D.; Lukas, A. & Meyer-Lindenberg, A. (2006), Influence of different surface machining treatments of resorbable implants made from different magnesium-calcium alloys on their

- degradation- a pilot study in a rabbit models, *Dtsch. tierärztl. Wochenschr.*, 113, 439-446
- [33] Wang Y. (1997), Beitrag zur Verbesserung korrosiver Eigenschaften von superleichten Magnesium-Lithium-Basislegierungen, *VDI-Verlag*, Düsseldorf,
- [34] Witte F.; Kaese, V.; Haferkamp, H.; Switzer, E.; Meyer-Lindenberg, A.; Wirth, C. J.; Windhagen, H. (2005), In vivo corrosion of four magnesium alloys and the associated bone response, *Biomaterials*, 26, 3557-3563
- [35] Witte F.; Fischer, J.; Nellesen, J.; Crostack, H. A.; Kaese, V.; Pisch, A.; Beckmann, F.; Windhagen, H. (2006) In vitro and in vivo corrosion measurements of magnesium alloys, *Biomaterials* 27, 7, 1013-1018
- [36] Witte, F.; Abeln, I.; Switzer, E.; Kaese, V.; Meyer-Lindenberg, A.; Windhagen, H. (2007a), Evaluation of the skin sensitizing potential of biodegradable magnesium alloys, *J. Biomed. Mater. Res. A*, 86, 4, 1041-1047
- [37] Witte, F.; Ulrich, H.; Palm, C.; Willbold, E. (2007b), Biodegradable magnesium scaffolds: Part II: Peri-implant bone remodeling, *J. Biomed. Mater. Res. A*, 81, 3, 757-765
- [38] Xu, L.; Zhang, E.; Yin, D.; Zeng, S.; Yang, K. (2008), In vitro corrosion behaviour of Mg alloys in a phosphate buffered solution for bone implant application. *J. Mater. Sci. Mater. Med.*, 19, 3, 1017-1025
- [39] Xu, L.; Pan, F.; Yu, G.; Yang, L.; Zhang, E.; Yang, K. (2009), In vitro and in vivo evaluation of the surface bioactivity of calcium phosphate coated magnesium alloy, *Biomaterials*, 30, 1512-1532
- [40] Yuen, C. K.; Ip, W. Y. (2010), Theoretical risk assessment of magnesium alloys as degradable biomedical implants, *Acta Biomat.*, doi:10.1016/j.actbio.2009.11.036
- [41] Zhang, S.; Zhang, X.; Zhao, C.; Li, J.; Song, Y.; Xie, C.; Tao, H.; Zhang, Y.; He, Y.; Jiang, Y. & Bian, Y. (2010), Research on a Mg-Zn alloy as a degradable biomaterial, *Acta Biomater.*, 6, 262-640
- [42] Zreiqat, H.; Howlett, C. R.; Zannettino, A.; Evans, P.; Schulze-Tanzil, G.; Knabe, C.; Shakibaei, M. (2002), Mechanisms of magnesium-stimulated adhesion of osteoblastic cells to commonly used orthopaedic implants, *J. Biomed. Mater. Res.*, 62, 175-184

Mg Alloys Development and Surface Modification for Biomedical Application

Shaokang Guan, Junhua Hu, Ligu Wang, Shijie Zhu, Huanxin Wang,
Jun Wang, Wen Li, Zhenwei Ren, Shuai Chen, Erchao Meng,
Junheng Gao, Shusen Hou, Bin Wang and Binbn Chen
*Materials Research Centre, Zhengzhou University
China*

1. Introduction

The development of biodegradable implants has grown into one of the important areas in medical science (Mani et al., 2007), since they can be gradually dissolved, absorbed, consumed or excreted in human body environment, and then disappear spontaneously after the bone tissues heal. The biodegradable materials available in the current market are mainly made of polymeric or ceramic materials, while these implants have an unsatisfactory mechanical strength when used for load-bearing parts (Staiger et al., 2006). Compared with the currently approved biomaterials, Mg alloys have a lot of advantages (Song et al., 2007; Witte et al., 2007; Witte et al., 2005; Song et al., 2007). First, with high strength/weight ratio, Mg alloy exhibits an appropriate mechanical integrity and is more suitable for load-bearing implantation. Its fracture toughness is higher than ceramic biomaterials (e.g. HA), and the elastic modulus and compressive yield strength of magnesium are closer to those of natural bone than other metallic implants (Table 1.1). Thus it will help to reduce or avoid “stress shielding effects” that can lead to reducing stimulation of new bone growth and remodeling. Moreover, magnesium has little toxicity to human body. Magnesium is essential to human metabolism and is naturally found in bone tissue. It is the fourth most abundant cation in the human body, with an estimated 1 mol of magnesium stored in the body of a normal 70 kg adult. Approximately, half of the total physiological Mg is stored in bone tissue. Thirdly,

Material	Density (g/cm ³)	E (Gpa)	Compressive yield strength (Mpa)	Fracture toughness (MPa.m ^{1/2})
Natural bone	1.8-2.1	3-20	130-180	3-6
Mg	1.74-2.0	41-45	65-100	15-40
Ti alloy	4.4-4.5	110-117	758-1117	55-115
Co-Cr alloy	8.3-9.2	230	450-1000	/
Stainless steel	7.9-8.1	189-205	170-310	50-200
Synthetic HA	3.1	73-117	600	0.7
PLA	1.25-1.29	2.2-3.3	/	/

Table 1.1. Properties of various implant materials (Staiger et al., 2006; Gupta et al., 2007).

magnesium is biodegradable in human body. Because it has very low standard electrode potential (-2.37 V), magnesium can be gradually dissolved and adsorbed after implanting in human body. The produced Mg^{2+} ions are absorbed by surrounding tissues or excreted out by human body fluids. Compared with the permanent implants, the second surgery for the removal of implant might be avoided, which decreases costs of the health care system and further morbidity to the patients. Lastly, magnesium is naturally abundant in the earth's crust and sea water, and its price is low, approximately equal to one third of titanium. In this chapter, the corrosion resistance and biocompatibility of Mg based implants produced by several approaches will be investigated in vitro and in vivo.

2. Materials and experiments

2.1 Alloy development

To develop a new alloy, we took the toxicity and strengthening effect of alloy elements into consideration comprehensively. The effect of alloying elements on Mg alloys and their toxicological characteristics have been summarized (F.Witter 2008). For new Mg-Zn-Ca alloys, the content of zinc should be moderate (G.Song, 2007). High content of zinc would deteriorate the corrosion resistance of alloys, and low content would not improve the mechanical properties (Li et al., 2008; GU et al., 2009). The Mg-Zn-Y-Nd alloys were developed basing on the following considerations. When the atomic Zn/Y \approx 6:1 in Mg-Zn-Y alloys with low Zn content under certain solidification rate, I-phase (icosahedral quasicrystal phase $Mg_{30}Zn_{60}Y_{10}$) would appear which possesses many interesting properties, such as high corrosion resistance, high hardness and low interface energy; Nd was chosen to improve the plasticity. Mg-Zn-Y-Nd alloy was prepared by melting high purity Mg, high purity Zn, Mg-Y and Mg-Nd master alloys in an electronic resistance furnace and casting into a mild steel crucible at approximately 740°C under CO_2/SF_6 atmosphere. For Mg-Zn-Ca alloy casting, pure magnesium was melt at approximately 730°C, and pure zinc and other alloy elements were added subsequently. To add silicon, the temperature should be raised. Ca was added after other alloys were completely melted and the temperature was decreased slightly to avoid the burning loss of it. Then, the liquid was stirred and stewed. At the temperature of 680°C, the molten metal was poured into a steel model.

2.2 Alloy processing technique

(1)The Mg-Zn-Y-Nd alloys were extruded at 340°C, with the extrusion ratio of 17.4 and extruded diameter of 12 mm. (2) The sub-rapidly solidified bars were prepared by copper mould splat cooling method at 700°C under Ar atmosphere. The cooling rate of prepared Φ 2mm bars was about 200K/s, which was within the cooling rate range of sub-rapid solidification.

2.3 Surface modification

Before electrochemical deposition, the samples were polished by silicon carbide papers of 100~1000 grits, then cleaned ultrasonically in acetone for 10min to remove residual grease. The clean substrates were activated with 40% HF for 10 min; then the treated specimens were dried for deposition. **(1) Constant current electrochemical deposition (CED).** An electrochemical workstation (RST5200) was used to deposit HA coating. Deposition was

carried out at an optimized current density of 0.4 mA/cm² at 85 °C for 60 min. The electrolyte was a solution with 0.042 mol/l Ca(NO₃)₂, 0.025 mol/l NH₄H₂PO₄ and 0.1 mol/l NaNO₃. During the electrochemical deposition, a graphite plate was used as an anode, while the Mg alloy specimen was cathode. After coated, alloys were removed from the electrolyte and rinsed in distilled water. Additionally, alkali-heat treatment was conducted by immersion as-deposited samples in 0.25 mol/l NaOH solution at 80 °C for 4h. **(2) Pulsed electrochemical deposition (PED)**. The pulse reverse current (PRC) parameters were used (H.X.Wang,et.al 2010). Note that the positive pulse was wider than negative one in order to develop a Ca-P coating of certain thickness. The deposition process lasted for 30 min at about 85 °C, after which the sample was removed from the electrolyte, rinsed with distilled water and dried for about 4 h in air. **(3) Micro-arc oxidation (MAO)/ electrochemical deposition (ED)**. The MAO process was conducted with a 10-kW power supply. The Mg-Zn-Ca alloy samples were used as the anode, while the stainless steel plate as the cathode. The electrolyte for the MAO was prepared as a solution of sodium phosphate and sodium hydroxide with concentrations of 0.5mol/l and 0.05mol/l, respectively. Samples were treated in the electrolyte with the cell potential increased step by step till 225V for 30 min. During the experiment process, the electrolyte was stirred at 40°C. The Mg-Zn-Ca alloy samples treated by MAO were used as the cathode. The deposition process was the same as described in CED section (2.3.1). **(4) Liquid phase deposition (LPD)**. TiO₂ layer was prepared by hydrolysis of modified ammonium hexafluorotitanate [NH₄]₂TiF₆ with concentration of 0.2mol/l. After pre-treatment, the AZ31 samples were immersed into the mother solution and suspended therein vertically for 20h. After deposition, the annealing process was carried out in the vacuum furnace (2×10⁻⁴Pa). The annealing temperature was from 250 ~ 380°C and the annealing time was 1~3h. **(5) Magnetic sputting**. A direct current magnetic sputtering machine was used to deposit Ti-O film. The base pressure in the chamber was 5×10⁻⁵Pa, and the working pressure was 0.5Pa. The target was titanium dioxide (99.999%) with a dimension of 150mm×40mm×5mm. The working gas was argon (99.999%) with a constant flow of 40sccm. The working voltage was about 390V, and current was 0.45A. The deposition rate was about 2nm/min. The HA coating was deposited under a constant current model as described in section CED(2.3.1).

2.4 In vitro performance

(1) Potentiodynamic polarization. A three-electrode cell was used for electrochemical measurements. The counter electrode was made of platinum and the reference electrode was saturated calomel electrode (SCE). The scanning rate was 5mV/s. The test solution was simulated body fluid (SBF), and the temperature was 37°C. The potentiodynamic polarization was also measured in a dynamic SBF (flow 2ml/100mlmin⁻¹)(J.wang, et.al. 2010). **(2) Electrochemical impedance spectroscopy**. The electrochemical impedance spectroscopy (EIS) test and the polarization curve experiment were both conducted with an electrochemical workstation (RST5000). The signal amplitude of EIS test was 10mV and the frequency ranged from 100 kHz to 0.001Hz. The sweep rate of the polarization curve measurement was 0.5mV/s. **(3) Slow strain rate tensile (SSRT) testing**. The mechanical properties of the alloys were studied using slow strain rate tensile (SSRT) testing in SBF at 36.5±0.5 °C. Cylindrical tensile specimens with gauge dimensions of 10×φ4mm were used in SSRT test. These samples were pulled at a strain rate of 2.16×10⁻⁵mm/s until fracture. **(4)**

Immersion test. The immersion test was carried out in SBF. The pH of SBF was adjusted with HCl and $(\text{CH}_2\text{OH})_3\text{CNH}_2$, and the temperature was kept at 37°C using water bath. The immersion solution was refreshed every 24h. The sample weight was measured before and after the immersion test. The corrosion rate was calculated by following equation (2.1), Where, W_0 : original weight; W_1 : weight after immersion; S : original surface area exposed to the test solution; t : immersion time. **(5)Hydrogen evolution test.** The hydrogen evolution test was carried out in SBF at a temperature of $(36.5\pm 0.5)^\circ\text{C}$. The volume of evolved hydrogen was measured everyday. The pH value of the solution was also recorded during the hydrogen evolution tests.

$$\text{CR}=(W_0-W_1)/(St) \quad (2.1)$$

2.5 Materials characterization

The microstructures of the alloys were observed by optical microscopy (OM). The crystal structure of coated/uncoated alloy was investigated by X-ray diffraction (XRD) instrument (Philips PW-1700X; Bruker D8 Advance) with $\text{Cu K}\alpha$ ($\lambda=0.15406\text{nm}$). The surface and cross-section morphology were observed with scanning electron microscopy (FE-SEM JEOL-6700F; SEM Philips Quanta-200). Energy dispersive spectroscopy (EDS) was employed to determine the elements composition of the layers. Transmission electron microscope (TEM, Fischione model 1010) was used to characterize samples in detail.

2.6 Mechanical properties measurement

The hardness of the alloys was measured on microhardness instrument (HX-100M). The tension and compression strength were measured on a universal material testing machine (Instron). According to ASTM F 1044-05, the shear strength of the coating and substrate was evaluated with a universal tensile machine (Hitachi AG-IS 10KN) according to (Wei & Ruys, 1999). The adhesion strength data were reported as the average values of three samples.

2.7 In vivo experiment

All animal experiments were conducted according to the ISO 10993-2:1992 animal welfare requirements. The rod samples were implanted into the left femoral shaft of rabbits. Intravital staining was performed monthly using subcutaneous injections of achemycin ($0.3\text{mg}/\text{kg}$) to observe the newly formed bone. **(1)Ion concentration tests.** Blood and urine samples were taken from the rabbits at 8, 12 and 18 weeks after surgery. The ion concentrations of Mg^{2+} in the blood and urine were examined. **(2) Radiographic and pathological evaluation.** Radiographs were used to observe the change around the implants. Heart, kidney, spleen and liver tissues from the rabbits were inspected to verify whether degradation of the magnesium alloy harmed these visceral organs. Bone samples including implants after 8 and 12 weeks implantation were taken out to observe os integration and assess the bioactivity of samples. The micro-computed tomographic were used to evaluate the residual volume of the implants. The volume of implants was measured at 8, 12 and 18 weeks post-implantation. **(3) In vivo mechanical integrity.** The rod samples were taken out of the bone at 8, 12 and 18 weeks for mechanical measurement. The compression tests were carried out with INSTRON universal tensile testing machine to observe the influence of weight loss on mechanical integrity.

3. Novel Mg alloys development for implants

3.1 Mg-Zn-Ca alloy

The content of zinc in Mg-Zn alloy was fixed in 2 wt. %. Calcium was added to improve the mechanical properties. The microstructure of the as-cast alloy was shown in Fig.3.1 (a). Second phase ($\text{Ca}_2\text{Mg}_6\text{Zn}_3$) distributed inconspicuously. But when the calcium content reached to 0.46%, the second phases distributed along grain boundaries continuously. With the increase of calcium content, the amount of second phase increased, while the grain size of matrix decreased. The formation of $\text{Ca}_2\text{Mg}_6\text{Zn}_3$ restricted the grain growth, which was beneficial to the improvement of mechanical properties. It was reported that the addition of calcium in Mg-Zn alloys should be controlled within 0.3%. Above the level, the formation of second phases might generate embrittlement. Moreover, in Fig.3.1, the second phases distributing in the alloy uniformly will contribute to the grain refinement of matrix. So the content of calcium must be moderate. As shown in Tab.3.1, there was a slight improvement in yield strength among the alloys with different calcium content. The yield strength was about 83MPa, while the tensile strength varied between 140~170MPa. However, there was a significant difference in elongation among the alloys. The alloy with 0.22 wt% Ca exhibited the highest elongation and best tensile strength. When the content of calcium was below 0.22%, the amount of second phase increased with the increase of calcium, which contributed to the higher tensile strength and elongation for their pinning effect. But when calcium was above 0.22%, the increase in calcium content resulted in the decreased elongation, which may be because excessive brittle intermetallic phase deteriorated the mechanical properties. Fig.3.2 showed the bending and compression strength of the alloys with different calcium content, respectively. The bending and compression strength of the alloys were optimized when the calcium content reached to 0.22%. The increasing of calcium content above 0.22% reduced the bending strength, but didn't deteriorate the compression strength.

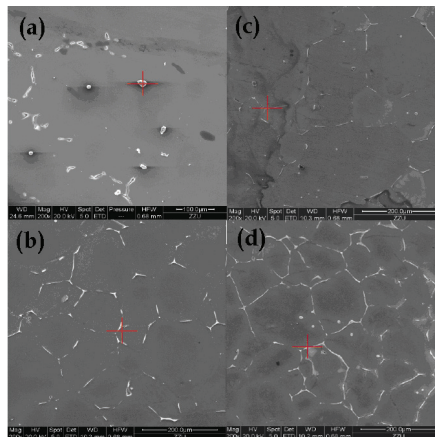


Fig. 3.1 SEM images of as-cast alloys with different Ca contents: (a) 0.024%Ca; (b) 0.22%Ca; (c) 0.29%Ca; (d) 0.46%Ca.

The polarization curves in SBF (Kokubo, 2006) (Fig.3.3) showed that the alloy with 0.22%Ca held the highest corrosion potential of about -1.7V; while the alloy with 0.46%Ca possessed

the lowest potential of about -1.8V. The change in calcium content in alloys didn't give a significant effect on the corrosion resistance. In Tab.3.2 the corrosion current of each alloy was summarized. The corrosion rate in human body could be evaluated according to the mass loss in SBF approximately. In Fig.3.4, among the alloys, the alloy with 0.22%Ca possessed the lowest degradation rate. At the beginning of the tests, the weight of the samples increased for the sake of absorption of water and deposits from solution. The corrosion behaviors of the alloys were also assessed by the pH evolution tests. The sample with 0.22%Ca held the lowest increase rate.

Alloy	Yield strength /MPa	Tensile strength /MPa	Elongation / %
0.024% Ca	80	141	8
0.220 %Ca	84	172	11
0.290% Ca	83	156	7
0.460 %Ca	85	154	5

Table 3.1. The tensile test of as-cast alloys

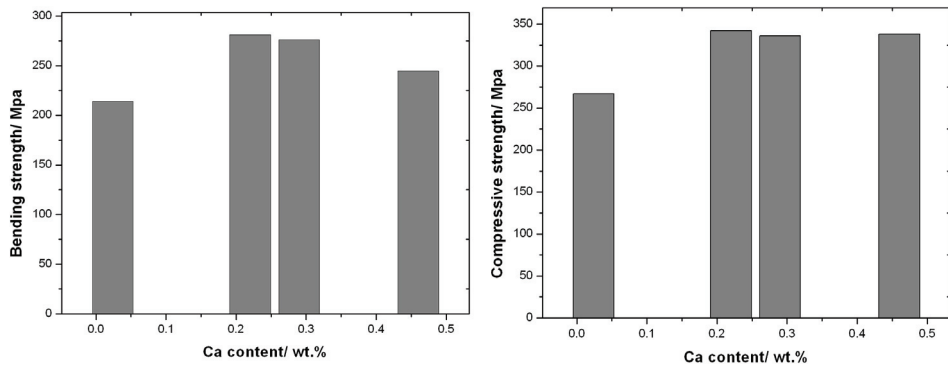


Fig. 3.2. Bending and compression strength of the as-cast alloys with different calcium contents

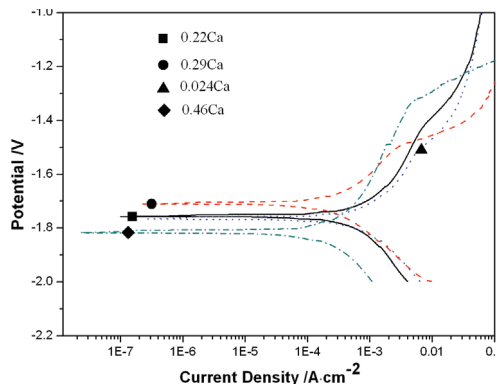


Fig. 3.3. The polarization curves of different alloys in SBF at 37°C

With the increase of calcium, the amount of $\text{Ca}_2\text{Mg}_6\text{Zn}_3$ increased. In SBF, primary cell units formed between $\text{Ca}_2\text{Mg}_6\text{Zn}_3$ as cathodes and $\alpha\text{-Mg}$ as anodes. The cell units helped the generation of $\text{Mg}(\text{OH})_2$ on $\alpha\text{-Mg}$ and the corrosion product could protect matrix from further corrosion. But the increasing amount of $\text{Ca}_2\text{Mg}_6\text{Zn}_3$ deteriorated the $\alpha\text{-Mg}$ corrosion resistance because the increasing interface between $\text{Ca}_2\text{Mg}_6\text{Zn}_3$ and $\alpha\text{-Mg}$ prevented the formation of $\text{Mg}(\text{OH})_2$.

Alloy	Corrosion potential (E_{corr} , V)	corrosion current (I_{corr} , A/cm ²)
0.024Ca	-1.77	5.6×10^{-4}
0.220Ca	-1.71	1.3×10^{-4}
0.290Ca	-1.76	5.1×10^{-4}
0.460Ca	-1.82	4×10^{-4}

Table 3.2. The corrosion potential and current of the alloys

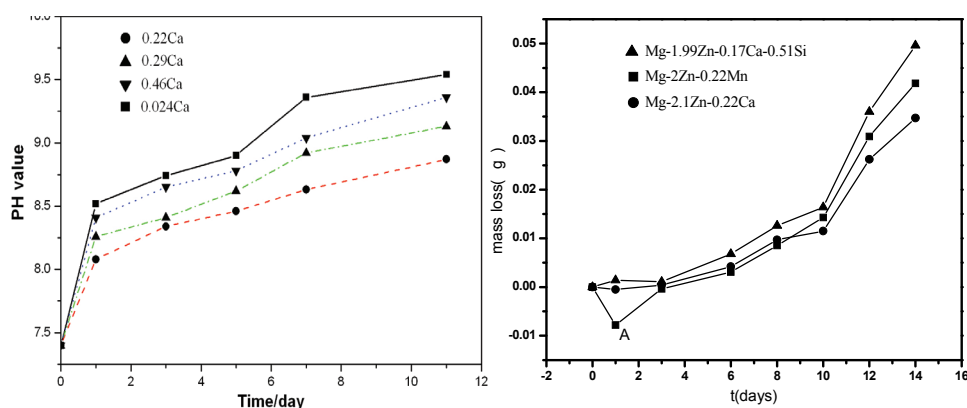


Fig. 3.4. The pH evolution (left) and mass loss (right) of alloys in the corrosion test

3.2 Mg-Zn-Y-Nd for stent implant

3.2.1 As-cast Mg-Zn-Y-Nd with varied Zn and Y contents and fixed Zn/Y ratio

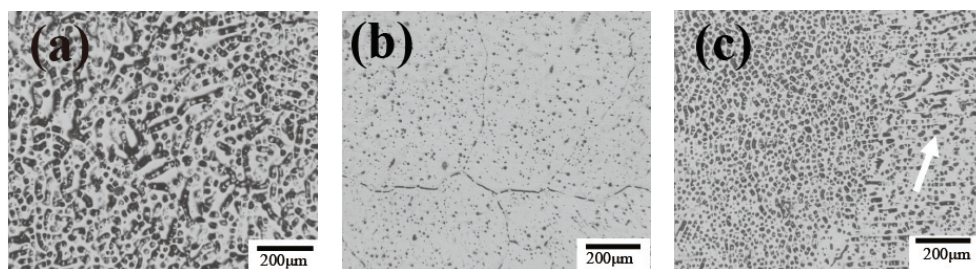


Fig. 3.5. Microstructures of as-cast alloys with different Zn, Y contents: (a) 1#: Zn/Y=1/0.23 ; (b) 2#: Zn/Y=2/0.46 ; (c) 3#: Zn/Y=3/0.69.

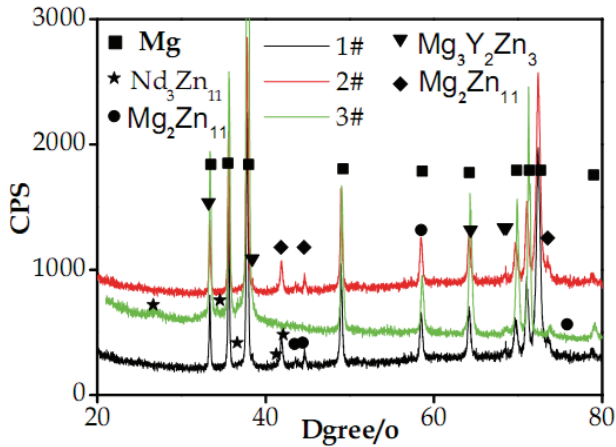


Fig. 3.6 XRD patterns of as-cast alloys (a) 1#alloy (b) 2#alloy (c) 3#alloy

In Mg-Zn-Y-Nd alloy, the Nd content was fixed at 0.5wt.%. And the Zn/Y weight ratio was 6:1. In Fig.3.5, the content of Zn/Y had evident effects on the microstructure of alloys. In Fig.3.5 (b), 2# alloy was with the smallest dendrite size and the lowest second phase volume percentage among the three alloys. The distribution of the second phase changed from continuous in Fig.3.5 (a) into diffusive in Fig.3.5 (b) and semi-continuous in Fig.3.5(c). With the combination of Zn, Y, Nd addition into Mg, these elements interacted with each other, resulting in the decreased solid solubility in α -Mg. Meanwhile, the metal molds used here had high cooling rate. The factors mentioned together resulted in gross dendritic crystals. Fig. 3.6 showed the XRD spectra of 1#~3#alloys. With the increasing content of Zn and Y, the phase compositions were α -Mg, Mg_2Zn_{11} , Nd_3Zn_{11} ; α -Mg, Nd_3Zn_{11} ; α -Mg, Mg_2Zn_{11} , $Mg_3Y_2Zn_3$, Nd_3Zn_{11} , respectively. This result together with microstructures (Fig.3.5), indicated that when Y content was low in α -Mg, no phase containing Y was discovered due to its solid solubility up to 12.4%; as Zn content increased, the amount of Mg_2Zn_{11} and Nd_3Zn_{11} phases in 3# alloy increased apparently. Due to the simultaneous increase of Zn and Y content, $Mg_3Y_2Zn_3$ phase appeared in 3# alloy.

Corrosion polarization curves and immersion experiments were conducted in SBF (Kokubo et al, 2006). From Fig.3.7, it can be seen that with the addition of 2wt% Zn, the corrosion potential was improved to a certain extent. The E_{corr} of 2# alloy was higher than that of 1# and 3#; meanwhile, I_{corr} of 2# was lower than that of 1# and 3#, indicating 2# alloy possessed the best corrosion resistance. The electrochemical parameters were summarized from the polarization curves of as-cast alloys and shown in Table 3.3

Alloys	E_{corr1} (V)	E_{corr2} (V)	I_{corr} (A.cm ⁻²)
1#	-1.81	-1.80	4.36×10^{-4}
2#	-1.80	-1.76	5.30×10^{-5}
3#	-1.82	-1.79	3.13×10^{-4}

Table 3.3. Electrochemical parameters summarized from polarization curves of as-cast alloys.

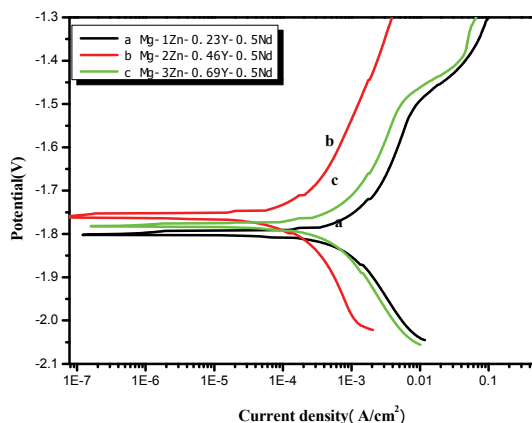


Fig. 3.7. Corrosion polarization curves of (a) 1# alloy (b) 2# alloy (c) 3# alloy

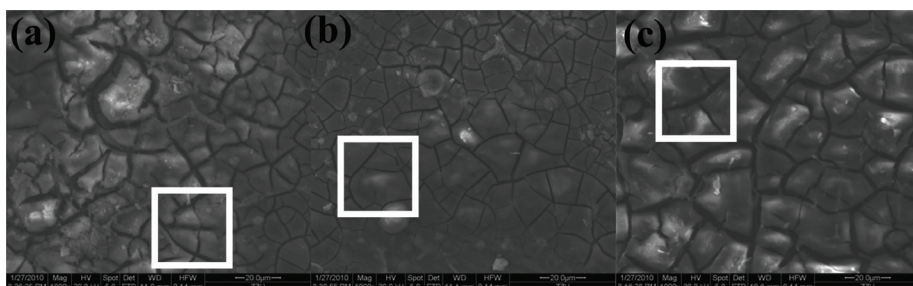


Fig. 3.8. SEM morphology of (a) 1# alloy (b) 2# alloy (c) 3# alloy after immersion for 12 h.

Moreover, Fig.3.8 revealed that after immersion in SBF for 12h, deposits containing O, C, P, Ca and Na etc formed on the surface. Among these three alloys, 2# alloy, with thin and homogenous film of corrosion products and second phases, indicated the best corrosion resistance, which was consistent with corrosion polarization results. 2# alloy possessed the favorable microstructure and corrosion resistance and would be optimized further concerning Nd content in the section 3.2.2.

3.2.2 As-cast Mg-Zn-Y-Nd alloys with varied Nd content

In Fig.3.9, with the increasing content of Nd, the amount of the second phases increased, and the distribution of the second phase changed from continuous in Fig.3.9a into diffusive in Fig.3.9b and semi-continuous distribution in Fig.3.9c. Meanwhile, with Nd addition, the interdendritic distance was reduced. This might be mainly because the added Nd accumulated in the front of solid-liquid interface, and increased the constitutional undercooling in the diffusion layer, leading to decreased grain size. In Fig.3.10, with the increase of Nd content, the phase compositions were α -Mg, $Y_2Zn_3 \rightarrow \alpha$ -Mg, $Nd_3Zn_{11} \rightarrow \alpha$ -Mg, $Mg_{41}Nd_5$ and NdZn. The electronegativity difference between Zn and Y(0.43) is much higher than that between Mg and Y (0.09), and electronegativity difference between Zn and Nd is the highest (0.51). So Zn and Nd have the priority to form Nd_3Zn_{11} phase.

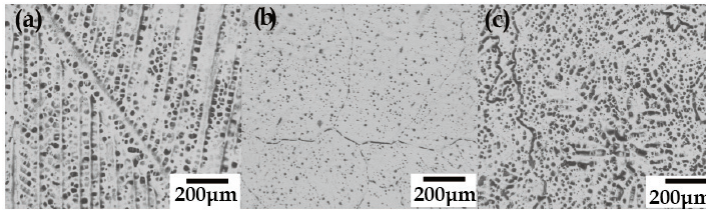


Fig. 3.9. Microstructures of as-cast alloys: (a) 4#0.0Nd (b) 5#0.5Nd (c) 6#1.0Nd.

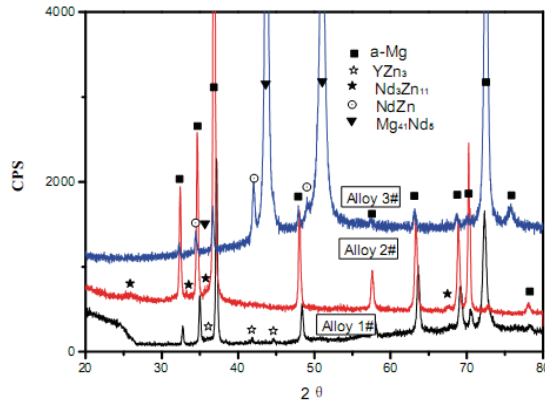


Fig. 3.10. XRD patterns of (a) 4#0.0Nd (b) 5#0.5Nd (c) 6#1.0Nd.

3.2.3 Extruded Mg-Zn-Y-Nd alloys with varied Nd contents

Extrusion can effectively improve the mechanical properties of Mg alloys through optimizing microstructure, such as refining grains, eliminating casting defects, homogenizing both α -Mg and second phases. The alloys prepared in section 3.2.2 were extruded at 340°C with extrusion ratio of 17.4. We re-marked the extruded ones as 7#, 8# and 9#, respectively. After extrusion, the microstructures were shown in Fig.3.11. Clearly, inhomogeneous grains could be found in Fig.3.11 (a) when no Nd was added in the Mg-Zn-Y alloys. With the addition of Nd(0.5% and 1.0%), a *narrow grain size distribution* and equiaxed grains could be observed from Fig.3.11 (b) and (c) evidently. Second phases with billet-shape morphology on grain boundaries (Fig.3.11b) changed gradually to line-shape (Fig.3.11c) and the amount of granules in matrix increased. All the alloys had equiaxed grains

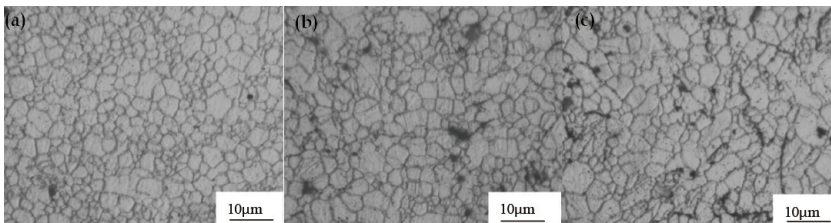


Fig. 3.11. Microstructures of the extruded alloys (a) 7#0.0Nd (b) 8#0.5Nd (c) 9#1.0Nd.

with an average size of 3 ~ 4 μ m, among which the optimized structure appeared in 8# alloys. In terms of the microstructure, a modest amount of Nd was preferred. As shown in Fig.3.12 (a) and (b), the addition of Nd led to the increase in amount of second phases. Phases like Mg₂Y, Mg₄₁Nd₅, and NdZn₂ were detected when the content of Nd reached 1.0w% in Fig.3.12 (b). EDS analysis confirmed the existence of Nd-rich phase in grain boundaries (Fig.3.12 c~f). Nd, Zn and Y formed new second phases and the amount of these phases rose with the increase of Nd addition.

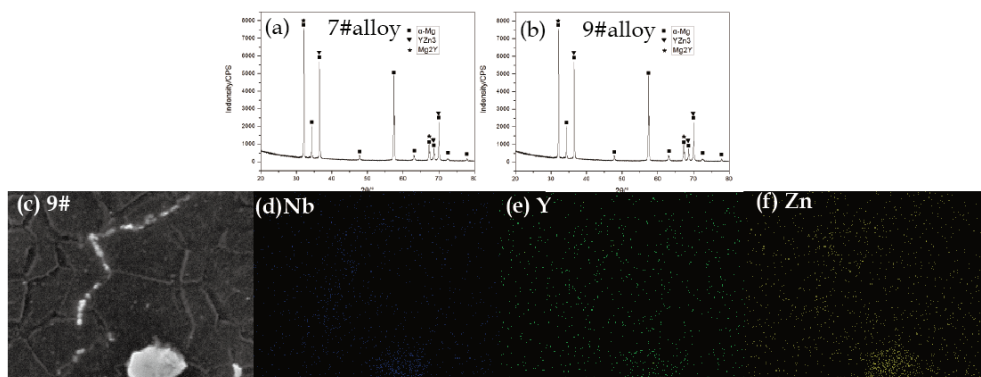


Fig. 3.12. XRD patterns of extruded alloys (a) 7# alloy (b) 9# alloy; EDS mapping of 9# alloy

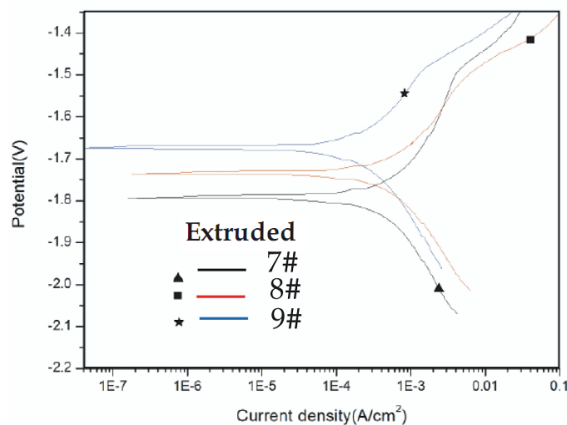


Fig. 3.13. Corrosion polarization curves of the alloys with different Nd content

Alloys	E_{corr}/V	$I_{corr}/A.cm^{-2}$
7#	-1.792	6.361×10^{-4}
8#	-1.735	5.275×10^{-4}
9#	-1.673	9.56×10^{-5}

Table 3.4. Electrochemical parameters summarized from Fig. 3.13

With the increase of Nd, corrosion potential shifted positively as showed in Fig.3.13. Electrochemical parameters summarized from Fig.3.13 were listed in Tab.3.4. These results proved that with the increasing amount of Nd addition, corrosion potential was improved and corrosion current density was decreased, demonstrating Nd's effective enhancement in corrosion resistance of extruded Mg-Zn-Y-Nd alloys.

Furthermore, possible reasons for the improvements in anticorrosion properties of alloys by Nd addition were listed below. (1) The addition of Nd could raise the electrode potential of matrix so as to improve corrosion resistance, which was exhibited from the variation of the slope of anodic polarization curves. (2) The second phases, with favorable passivity, morphology and distribution, formed after the addition of Nd and protected matrix in which they could block corrosion process. (3) The homogenization of the extruded microstructure, especially the grain size, as a consequence of addition of Nd, together with the small granule phase might effectively enhance the corrosion resistance. (4) Nd, as a kind of rare earth element, can purify melt and eliminate as-cast defects and impurities. (5) Nd might improve the compactness of oxidation film to prevent further corrosion.

Alloys	7#	8#	9#
Micro-hardness (HV)	60.00	62.00	64.00
Tensile strength (MPa)	270.56	268.96	281.47
Elongation (%)	20.00	24.00	16.00

Table 3.5. Strength and elongation of extruded alloys with different Nd content

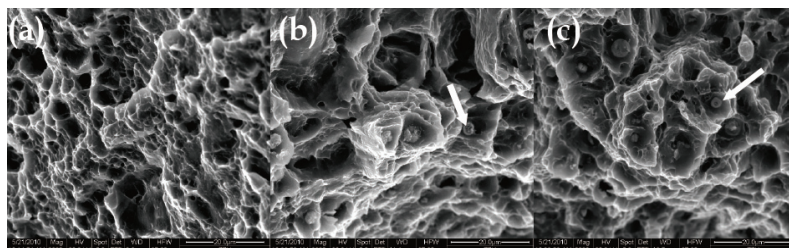


Fig. 3.14. Fracture morphology of the alloys (a) 7# alloy, (b) 8# alloy, (c) 9# alloy.

The effects of Nd addition on the final mechanical properties of extruded Mg alloys were investigated and summarized in Table 3.5. The micro-hardness increased slightly with the addition of Nd, which could be ascribed to dispersion strengthening caused by second phases and solid solution strengthening of Nd. Addition of 0.5wt% Nd improved the ductility (20% to 24%), with a slight decrease in tensile strength (270.56MPa to 268.96MPa). When the content of Nd was up to 1.0%, strength increased from 268.96MPa to 281.47MPa at the expense of decrease of ductility, which remarkably reduced from 24% to 16%. Mechanical properties of alloys are mainly determined by their composition and microstructure; and here, the content of Nd in the extruded alloy decided the microstructure features, such as the grain size, amount and distribution of second phases. The increasing addition of Nd had slight influence on grain size and thus the evolution of second phases played a significant role on properties. A small amount of Nd addition resulted in the formation of granules in matrix and consequently the elongation of the alloy was improved.

However, with further addition of Nd, when the second phase transformed to line-shape and continuous distribution along grain boundaries, tensile strength increased due to dispersion strengthening of second phase and solution strengthening of Nd; whereas, the ductility decreased significantly because of the morphology and nature of second phase. In Tab3.4, 8# alloys showed the best mechanical properties. This phenomenon was also confirmed by the fracture morphology in Fig.3.14. Compared with 7# and 9# alloys, the ductile dimples in 8# fracture were more homogenous and deeper. Additionally, many second phases were found resided in the center of the dimples, especially in 9# alloy. The mechanical properties of extruded alloy can meet the requirement of vascular stent.

3.2.4 Sub-rapid solidified Mg-Zn-Y-Nd alloy and Mg-Y-Gd-Nd alloy (WE43)

Mg-Zn-Y-Nd and Mg-4Y-1Gd-2Nd (supplied by National Engineering Research Center of Light Alloys Net Forming, Shanghai Jiao Tong University) alloys were used as mater alloys. From Fig.3.15, as cast Mg-Y-Gd-Nd alloy was mainly composed of equiaxed grains and partially divorced interdendritic eutectics (by A), with average grain size about 70 μm . In Fig.3.16a, the main intermetallic compound in as cast Mg-Y-Gd-Nd alloy was MgGd₃ phase. After sub-rapid solidification at 700°C, Mg₂Y and Mg₄₁Nd₅ appeared. However, the microstructure of the as-cast Mg-Zn-Y-Nd alloy consisted of two kinds of phases: a-Mg and some small particles (Nd₃Zn₁₁), shown in Fig.3.15 (c) and Fig.3.16(c). The corresponding sub-rapid solidified Mg-Zn-Y-d alloy had new phases: I-phase (Mg₃YZn₆) and Mg₄₁Nd₅, identified in Fig. 3.16(d). Furthermore, the average grain size of as sub-rapid solidified both Mg-Y-Gd-Nd and Mg-Zn-Y-Nd alloy was reduced significantly to about 15 μm compared with as cast ones. The increase in cooling rate resulted in solute closure, notable decrease of grain size, more second phases and uniform distribution of elements.

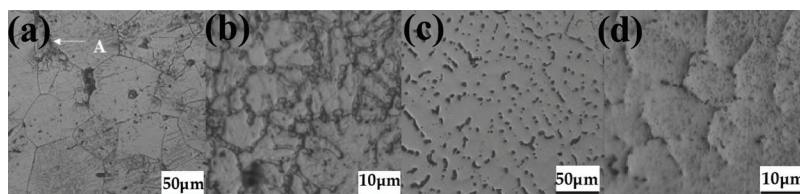


Fig. 3.15. Optical images of alloys: (a) as cast Mg-Y-Gd-Nd; (b) sub-rapid solidified Mg-Y-Gd-Nd; (c) as cast Mg-Zn-Y-Nd; (d) sub-rapid solidified Mg-Zn-Y-Nd

A small amount of I-phase (Mg₃YZn₆) was detected in XRD pattern (Fig.3.16d). SEM microstructure in Fig.3.17(a) revealed that its morphology was spherical. Mg₃Zn₆Y (I-phase) in Mg-Zn-Y alloys was primarily reported by (Luo et al, 1994). But Mg₃Zn₆Y (I-phase) in Mg-Zn-Y-Nd alloys with low Zn and low Y content (Zn/Y atom ratio 6) was firstly discovered in this study. The average grain size of quasicrystal was about 500 nm. For both Mg-Y-Gd-Nd and Mg-Zn-Y-Nd alloys, sub-rapid solidification resulted in the formation of new phases: Mg₂Y and Mg₄₁Nd₅ in Mg-Y-Gd-Nd while I-phase and Mg₄₁Nd₅ in Mg-Zn-Y-Nd alloy.

The solidification rate should be beyond certain threshold to avoid the transformation of I-phase to crystallite; meanwhile, I-phase formed by nucleation and growing, which were controlled by diffusion process. Since the sub-rapid solidification has certain restrictions on atom diffusion, it is favorable to the formation of I-phase. However, the growing mechanism of quasicrystal still remains an unsolved and debating problem. Because of the special

quasicrystal nature, including both crystal and non-crystal character, the alloys with I-phase will exhibit excellent corrosion-resistance.

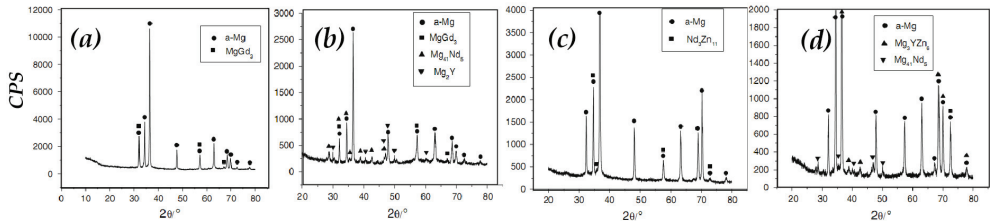


Fig. 3.16. XRD patterns of corresponding alloys shown in Fig.3.15.

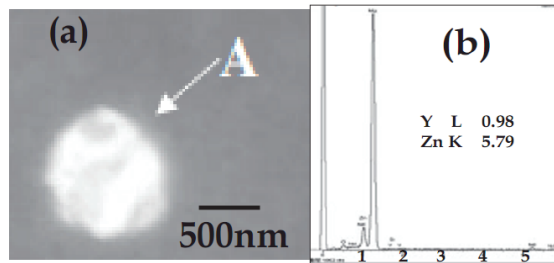


Fig. 3.17. (a) SEM morphology of spherical I-phase; (b) EDS of I phase.

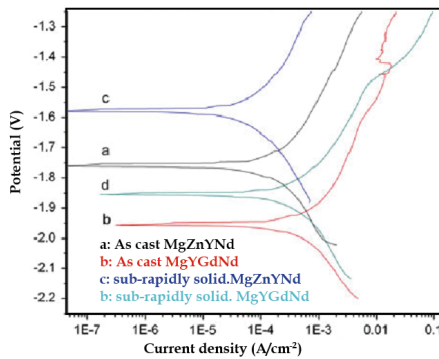


Fig. 3.18. Polarization curves of alloys under different process conditions in dynamic SBF

Alloys	State	E _{corr} /V	I _{corr} (A/cm ²)
Mg-Y-Gd-Nd	As cast	-1.95	1.86×10 ⁻⁴
	Sub-rapid solidification	-1.83	1.45×10 ⁻⁴
Mg-Zn-Y-Nd	As cast	-1.76	5.3×10 ⁻⁵
	Sub-rapid solidification	-1.57	2.62×10 ⁻⁵

Table 3.6. Corrosion potential and corrosion current

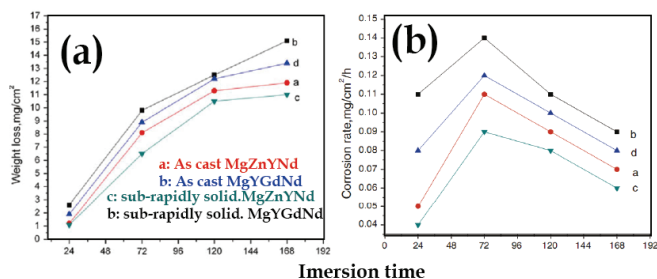


Fig. 3.19. Weight loss (a) and corrosion rate (b) of alloys shown in Fig.3.18

From results of the polarization curves in Fig.3.18 and immersion results in Figs.3.19, the sub-rapidly solidified Mg-Zn-Y-Nd alloy showed the highest corrosion resistance than others. The sub-rapid solidification not only refined grains, but also expanded the scope of the alloying and made the composition and microstructure more uniform. After sub-rapid solidification, the grain size became more uniform and the stability of grain boundary increased, which can reduce the amount of local pitting, thus, significantly improve corrosion resistance. For as cast alloys, the corrosion potential (-1.95 V for Mg-Y-Gd-Nd and -1.76 V for Mg-Zn-Y-Nd) was lower than that of as sub-rapidly solidified ones (-1.83 V for Mg-Y-Gd-Nd and -1.57 V for Mg-Zn-Y-Nd) (Table 3.6). Meanwhile, the current density of as cast or as sub-rapidly solidified Mg-Zn-Y-Nd alloy was much lower than that of Mg-Y-Gd-Nd alloy, demonstrating the corrosion properties of Mg-Zn-Y-Nd alloys, as sub-rapid solidification or as cast, were better than that of the Mg-Y-Gd-Nd alloys. The main reasons were as follows: Firstly, I-phase, which had low interfacial energy making it possess stable interface, appeared in as sub-rapidly solidified Mg-Zn-Y-Nd alloys; Secondly, I-phase owned excellent corrosion resistance itself; Thirdly, it has been widely accepted that Zn can reduce the detrimental effects of Fe, Ni on corrosion resistance and then improve the anticorrosion properties of Mg alloys (C.J. Boehlert, 2006). In Fig. 3.19, the corrosion rate of every alloy increased with the time increasing before 72 h, achieving the maximum at 72 h. After 72 h, the corrosion rate of every alloy declined with the time increasing. In the initial corrosion stage, the entire surface was exposed to the corrosive medium and the attack of medium was intensive. With the immersion time increasing, the corrosion products accumulated on the surface, which deposited and covered part of the surface, blocking the direct contact between the medium and the surface of samples and exhibiting certain protective effects. Thus, the corrosion rate of every alloy declined.

In Fig.3.20, for the same alloy, the corrosion potential improved by about 80 mV in dynamic SBF (D-SBF) compared with that in static SBF. Firstly, in the SBF, the concentration of Cl^- had a great influence on corrosion resistance. The Cl^- converts $\text{Mg}(\text{OH})_2$, which was protective to alloy surface, into dissoluble MgCl_2 . Secondly, Cl^- , with small radius, could penetrate the surface film easily. Then Cl^- took the place of O^{2-} and OH^- which were absorbed onto the surface of alloys to form the soluble complex. The continuously cycling of dynamic SBF resulted in the stable and lesser Cl^- concentration in the sample chamber, which made the corrosion morphology of alloys more uniform and then the corrosion rate slower. While in static SBF, as anodic reaction occurred, more and more Mg^{2+} dissolved into the solution; HCO_3^- and HPO_4^{2-} were consumed, making the concentration of Cl^- increase relatively and then the corrosion potential reduced and corrosion resistance decreased.

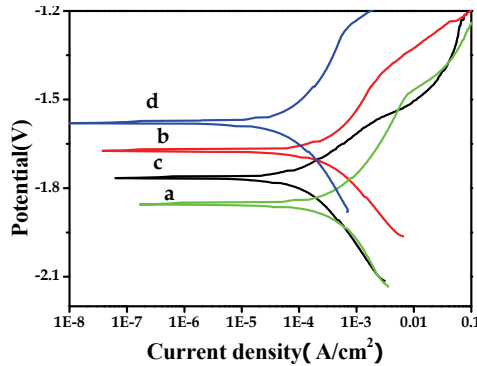


Fig. 3.20. Polarization curves of as sub-rapid solidification alloys: Mg-Y-Gd-Nd alloy in static (a) and dynamic (c) SBF; Mg-Zn-Y-Nd alloy in static (b) and dynamic (d) SBF.

4. Surface modification of Mg alloy

Although magnesium alloys are usually alloyed with elements, such as aluminum, manganese and zinc to improve corrosion resistance, further surface treatment is also required to physically prevent contact with the environment. The coating technologies, including the electrochemical deposition (ED), micro arc oxidation (MAO), liquid phase deposition (LPD) were used to achieve the corrosion resistance

4.1 TiO₂/AZ31 prepared by LPD

Fig.4.1 showed the XRD patterns of TiO₂/AZ31 prepared at different conditions. As comparison, a standard powder diffraction file (PDF) of anatase TiO₂ was shown in Fig. 4.1(d). In Fig.4.1, diffraction peaks corresponding to anatase TiO₂ were observed, and the

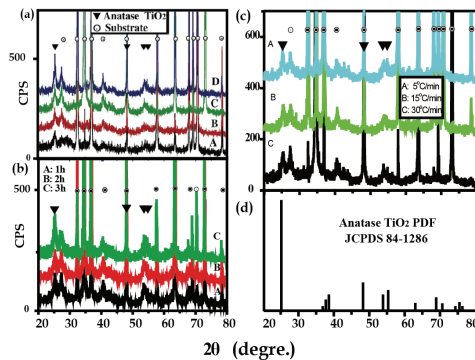


Fig. 4.1. (a) XRD patterns of TiO₂/AZ31 prepared at the annealing temperature of (A)250 °C, (B)300 °C, (C)350 °C and (D)380 °C for 1.5 h. The diffraction peaks of anatase TiO₂ and AZ31 were shown by the mark of triangle and circle, respectively. (b) XRD patterns of TiO₂/AZ31 prepared at the annealing temperature of 250 °C for 1h (A), 2h (B) and 3h (C). (c) XRD patterns of TiO₂/AZ31 prepared at the annealing temperature of 380 °C for 2h with heating rate of 5°C/min (a), 15°C/min (b) and 30 °C/min (c). (d) Standard PDF for Anatase TiO₂ (JCPDS 84-1286).

spectra agreed with that of PDF file. The peak intensity of anatase TiO_2 increased with the increase in annealing temperature or time, which proved that crystallinity of anatase can be improved by the increase in annealing temperature or time. The (101) peak intensity of anatase was almost independent of heating rate. The crystallinity of anatase was not influenced by heating rate at the fixed temperature.

From Fig.4.2(a), which showed the image of an as-deposited TiO_2 layer, the loosely deposited particles on the substrate can be found. As shown by the XRD results in Fig. 1(a), after annealing, the crystallization of anatase was improved, which can also be proved by the morphology evolution revealed in Fig.2(b) and (c). In Fig. 2(b), pinholes can be found on the surface of TiO_2 layer annealed at 250 °C. And they got eliminated by the annealing at 350 °C as shown in Fig.4.2(c). In Fig.4.2(c), the surface of the layer, consisting of fine particles, was finished, uniform and compact. Fig.4. 2(d) shows the enlarged image of one

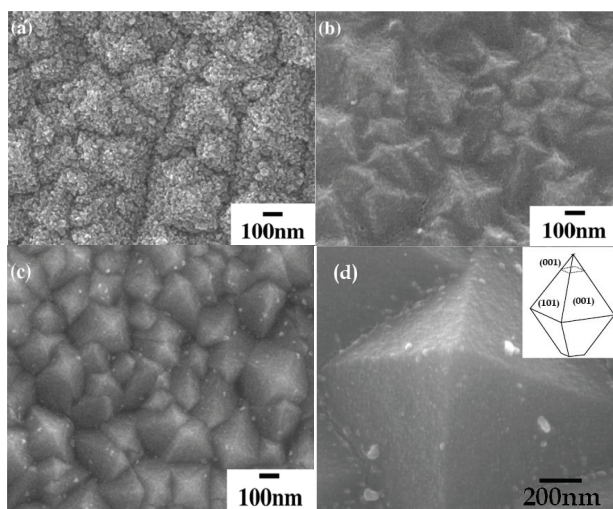


Fig. 4.2. FE-SEM images of surface morphology of TiO_2 layer. (a) as-deposited TiO_2 layer; annealed at 250 °C(b),at 350 °C(c); (d) enlarged image of the particles (c).

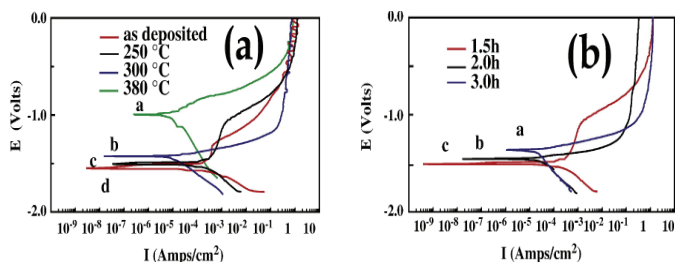


Fig. 4.3. (a) Tafel polarization curves of samples prepared at different annealing temperature of 380 °C (a), 300 °C (b) and 250 °C (c) for 1.5h. The polarization curve of an as-deposited specimen was presented as (d). Fig.4.3 (b).Tafel polarization curves of samples prepared at the annealing time of 3h (a), 2h (b) and 1.5h(c) at the annealing temperature of 250 °C.

particle on the surface of Fig.4.2(c). The particles on the surface, with the size of several hundreds nanometers, have the characteristically octahedral shape of anatase TiO₂. According to Wuff. construction and surface energy calculation of anatase (Ulrike Diebold et al.,2003), the surfaces of the octahedral particle were limited by (101) natural surface (H. Berger et al.,1993).

Sample	E_{corr}	I_{corr}	R_p
	V	A.cm ⁻²	Ω.cm ²
380 °C	-1.111	6.19568×10 ⁻⁶	28448.29±451
300 °C	-1.448	1.31383×10 ⁻⁵	20876.3±650
250 °C	-1.468	1.38381×10 ⁻⁴	1914.28±116
As-deposited	-1.518	2.73441×10 ⁻⁴	1220.33±142
Blank AZ31	-1.524	2.91413×10 ⁻⁴	/
3.0h	-1.377	1.83167×10 ⁻⁵	13780.24±742
2.0h	-1.450	2.33769×10 ⁻⁵	11101.36±580
1.5h	-1.468	1.38381×10 ⁻⁴	1914.28±116

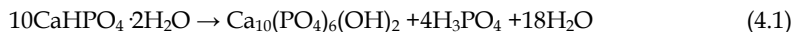
Table 4.1. Electrochemical parameters obtained from Tafel polarization curves

Fig.4.3 (a) showed the Tafel polarization curves of samples prepared at different annealing temperatures. The samples were deposited in the same condition for 20 h and then annealed at the temperature of 250 °C, 300 °C and 380 °C, respectively, for 1.5 h. The polarization curve of a specimen without annealing was also presented as Fig.4.3(d). It is visible when the potential reached a certain stage, curve of the as-deposited specimen became zigzag. The electrochemical parameters were shown in the Table 4.1. With the increase of annealing temperature from 250 °C to 380 °C, it was shown that the I_{corr} decreased by several tens of times of magnitude and the R_p increases by almost the same order of magnitudes. The E_{corr} is shifted positively by 0.357 V. The corrosion protection of the as-deposited specimen was not improved much compared with that of the bare AZ31 alloy. Fig.4.3 (b) showed the influence of annealing time on the polarization curves at the annealing temperature of 250 °C, which showed similar tendency with that of annealing temperature. The analyzed results were listed in the bottom row of Table 4.1. It can be found the corrosion resistance increased with the prolongation of annealing time. When the annealing time increased from 1.5 h to 3 h, the corrosion potential increased by 0.091 V; I_{corr} decreased by several times and R_p increased by almost same times. It also can be found that increase of annealing time had a mild influence compared with that of annealing temperature. By the TiO₂ layer and annealing treatment, the corrosion protection of AZ31 alloy was improved evidently. It can be found the as-deposited layers were not compact and cannot prevent contact with the corrosive environment (Fig.4. 2a). In Fig.4. 4, it also can be found that corrosion potential of as-deposited samples was only -1.518 V, which was just a little above that of bare AZ31 substrate. During the procedure of thermal treatment, improvement of crystallization of anatase TiO₂ occurred, accompanied by the elimination of some structure defects in the layer, e.g. pinholes, pores, and the compactness of TiO₂ layer was therefore increased. As a result, the corrosion resistance would be enhanced by annealing treatment. However, the annealing parameters were limited by the thermal stability of the substrate. Compared with the influence of deposition condition, namely deposition time and hydrolysis temperature (J.h.Hu. et al., 2006), the annealing temperature and time played mild roles in corrosion protection. The possible explanation is that, in the deposition process, the deposition

condition controlled the deposition rate, particle size and increase of thickness. Usually, formation of structure defects and increase of thickness, which played decisive roles in the protection of substrate, correlated with the deposition process.

4.2 HA coating prepared by CED

The XRD patterns of as-deposited and alkali-heat-treated samples were shown in Fig.4.4, which indicated that the as-deposited coating was the mixture of HA and $\text{CaHPO}_4 \cdot 2\text{H}_2\text{O}$ (DCPD). However, the mixture transformed into HA single phase completely after post-treated with NaOH solution. The following reaction showed the transforming process:



The (002) peak is dominant in XRD patterns. According to Scherrer's formula, the (002) peak was chosen to calculate the average crystallite size of the HA. The calculated particle size of the as-deposited HA and DCPD was about 40 nm. And after post-treated with NaOH solution, the crystallite size of HA was about 35 nm.

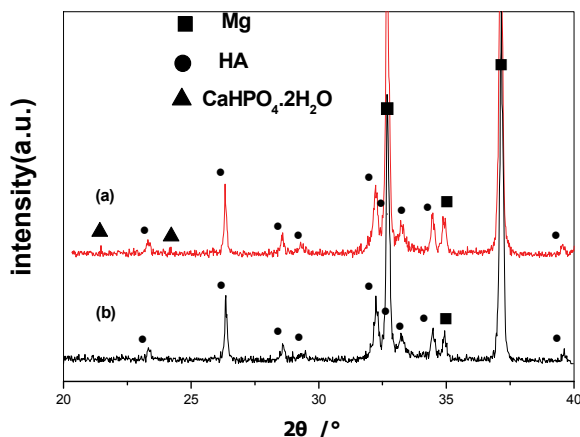


Fig. 4.4. XRD patterns of (a) as deposited coating, (b) post-treated coating on AZ31.

The surface morphologies of the as-deposited and post-treated coatings were shown in Fig.4.5 (a) and (c), respectively. Both the as-deposited and post-treated coatings exhibited morphologies like chrysanthemum flowers aggregating on the surface of the substrate. The as-deposited coating was mainly composed of radial plates-like structure, while nearly needle-like phase was presented on the post-treated coatings. A small amount of DCPD contained in the as-deposits was the possible reason for the morphology difference. The EDS in Fig.4.5 (b and d) showed that the coating was consisted of Ca, P, O, Na, Mg and C elements. The Mg^{2+} and Na^{+} ions might substitute the Ca^{2+} , which was similar with the composition of biological apatite from natural bone mineral. It was found that Ca/P atom ratio was always improved to a certain extent after post-treatment by NaOH, due to transmission of DCPD to HA. The average Ca/P atom ratios of as-deposited and post-treated was calculated about 1.40 and 1.50, respectively. Both were Ca-deficient HA (CDHA) coatings.

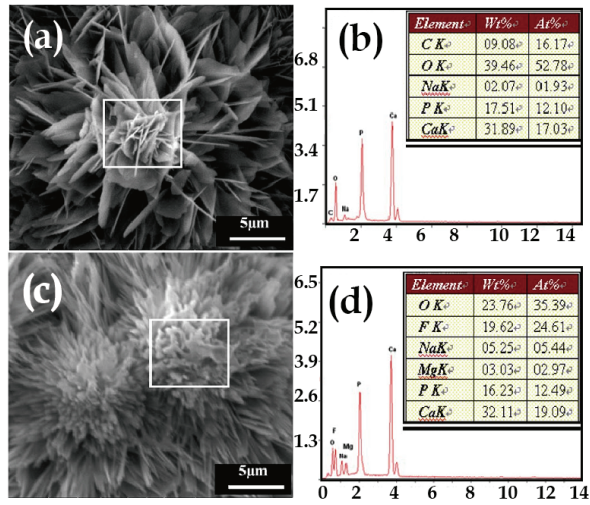


Fig. 4.5. Morphology and EDS of coatings: (a, b) as-deposited; (c, d) post-treated by NaOH.

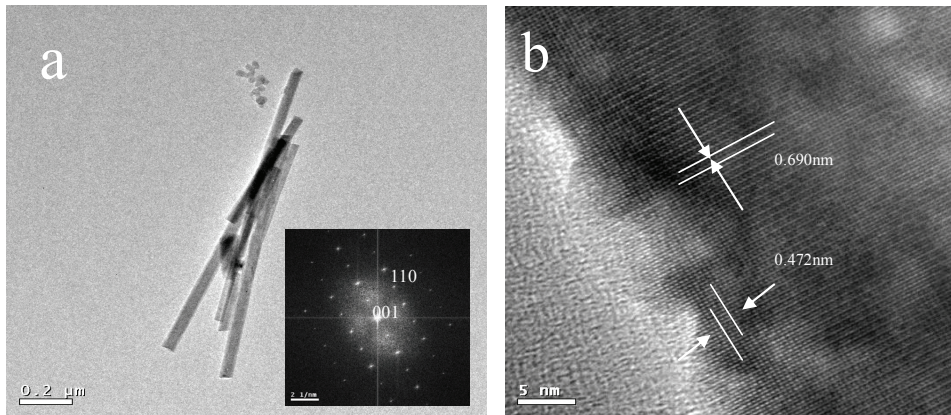


Fig. 4.6. TEM images of particles of post-treated coating: (a) TEM; (b) HRTEM.

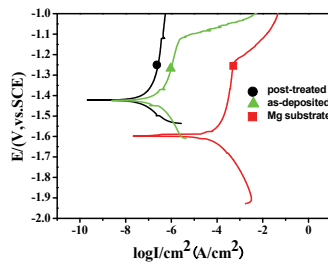


Fig. 4.7. Polarization curves in SBF (Hank's solution) of specimen.

TEM was employed to study the microstructure of post-treated coating. Needle-like particles of 1000 nm in length and 35 nm in diameter (Fig.4.6a) had a slenderness ratio about 28.6. A typical crystallographic structure was shown by HRTEM (Fig.4.6b). The distances between the lattice lines are 0.690 and 0.472nm, respectively, which was comparable with the standard (001) and (110) planes distances of 0.688 and 0.472nm of HA. The FFT inset in Fig.4.6 (a) showed the incident direction of electron beam and growth direction of nano needle, which agreed with that analyzed from Fig.4.6 (b). The average grain size of HA crystal face (002) was about 35nm from Fig.4.6 (a), which was similar with the calculated value by using XRD pattern.

Compared with blank magnesium alloy substrate, the E_{corr} increased from -1.6 to -1.42 V significantly after surface was modified by HA. According to the polarization curves, it was observed that I_{corr} of substrate reduced from 2.51×10^{-5} to 2.51×10^{-8} A/cm². It was clear that HA coating could improve effectively corrosion resistance of the substrate in SBF. It could also be seen that the E_{corr} hardly had any change after alkali treatment. However, there was an evident I_{corr} change from 3.98×10^{-8} to 2.51×10^{-8} A. It could be concluded that the alkali treatment could help to decrease the degradation rate.

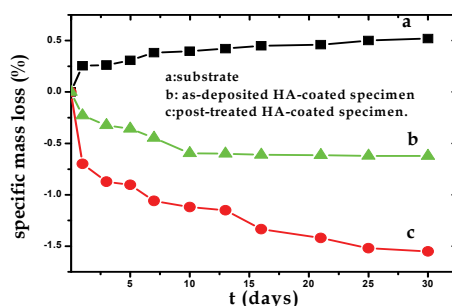


Fig. 4.8. The specific mass loss of specimens immersed in SBF

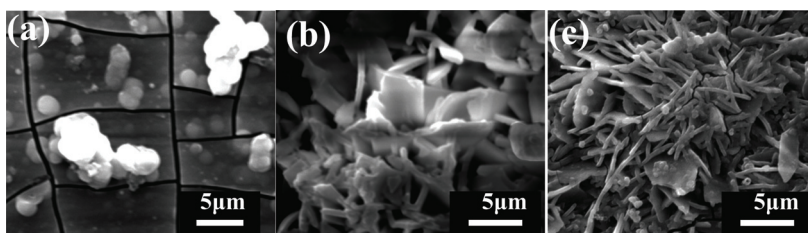


Fig. 4.9. SEM images of corresponding specimens in Fig.4.8 immersed for 7 days.

In vitro test was performed by immersion in SBF for 30 days. There was a sharp mass loss of bare magnesium alloy in the first 2 days (Fig.4.8a), because there was high Cl⁻ concentration in SBF. After 7 days' immersing, the mass loss rate was not as fast as before, for the possible reason of the Ca-P-Mg deposits on substrate would inhibit the further corrosion. SEM image in Fig.4.9 (a) testified the deposition of Ca-P-Mg apatite. There was also corrosion pits observed on specimen surface of Mg alloy substrate after 7 days' immersing. The deposits were mainly made up of Ca, P, O, C, Na and Mg elements from the EDS analysis. Fig.4.8 (b) and (c) were the as-deposited and post-treated coatings, respectively. There was obvious

specific mass gain on both specimens for initial 10 immersing days. In the initial corrosion stage, the release of Mg^{2+} would increase its concentration on the interface. The Mg^{2+} rich interface would help the deposition of Ca-P-Mg apatite. The Ca-P-Mg apatite would increase the thickness of the coating and protect the substrate from further corroding. There was much more mass gain on post-treated coating than as-deposited coating. The mass loss of as-deposited specimens kept stable, while the mass gain of post-treated specimens increased slightly in the following 20 days. Compared with the as-deposited specimen in SBF, post-treated coating containing single HA phase was much more stable. The needle-like morphology would offer a much larger surface to contact with SBF solution and induce more apatite to deposit. The morphology of as-deposited and post-treated coating immersed in SBF for 7 days were showed in Fig.8 (b) and (c). There was apatite with Ca/P \approx 1.60 deposited on post-treated coating. But the deposition of apatite on as-deposited coating was not evident.

4.3 Pulsed electrochemical deposition

In a traditional cathodic ED process, when a static potential is applied, loose, porous and low adhesive coatings can be easily developed. The main reasons are: first, a polarization in concentrations is formed, since the speed of ion diffusion from the main body of the solution to the surface of the metallic substrate is too low; secondly, H_2 is produced in the cathode due to the reduction of H_2O . To solve this problem, it is suggested that pulsed power be used for depositing the adherent coating. Fig.4.10 showed the XRD patterns of HA coated magnesium and bare substrate. Clearly, peaks of the coating can be ascribed to the hexagonal HA (PDF No. 09-432). The lattice constants of the as-deposited HA were $a = 9.397 \text{ \AA}$ and $c = 6.838 \text{ \AA}$, which did not match stoichiometric HA ($a = 9.418 \text{ \AA}$ and $c = 6.884 \text{ \AA}$). The reason for this might be trace doping of Mg^{2+} , Na^+ . According to Scherrer's formula, the (0 0 2) peak was chosen to calculate the average grain size of the as-deposited HA (Li et al., 2008). The crystallite size of HA was about 40 nm.

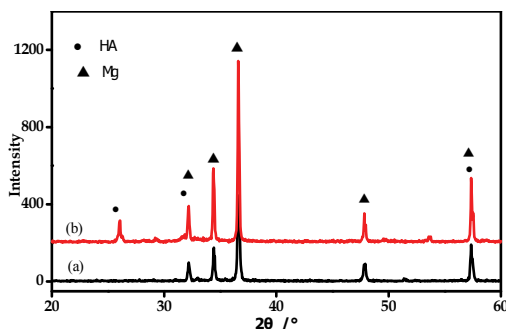


Fig. 4.10. XRD patterns of Mg-Zn-Ca alloy (a) without and (b) with the as-deposited coating.

Fig.4.11 presented SEM micrographs of the Ca-P coating. Two different morphologies of the coating were observed (Fig.4.11a): a tabular region consist of irregular flake-like structure of approximately 100nm in thickness (Fig.4.11b), and a fluffy region composed of fine floc structure with less than 100 nm in diameter (Fig.4.11c) which partly covered plate-like coating. The acicular structure was regarded as the new nuclei of crystal and grew into the platelet ones gradually, as can be seen from the structures of the coatings deposited at 30

and 60 s (Fig.4.12a, b). Moreover, it can be seen from the images that these flakes develop almost perpendicularly to the substrate. It may be beneficial to have a flake-like structure for bone growth, since the inorganic apatite in bone has a plate-shaped morphology 2~3 nm in thickness and tens of nanometers in length and width. Moreover, it can be seen from Fig.4.12, that there were no cracks in the deposited coating though the stress introduced by the thermal cycling. The EDS results of the as-deposited coating showed that the Ca/P atomic ratio was approximately 1.34 evidently lower than 1.67. The reason might be trace doping of Mg^{2+} , Na^+ . These Mg^{2+} and Na^+ ions might substitute the Ca^{2+} , which was similar with the composition of biological apatite from natural bone mineral. The as-deposited coating was proved to be composed of Ca-def. HA. This just meets the requirements for biodegradable implants, because many studies have indicated that the dissolution of HA in the human body after implantation is too slow to achieve optimal results, while Ca-def HA seems to be more soluble and may induce precipitation of a new bonelike apatite after implantation (Guan et al., 2008).

The bonding strength between the coating and Mg alloy measured by a shear strength test was 41.8 ± 2.7 MPa. This value was higher than the measured shear strength of natural cortical bone (35 MPa), was also greater than that of HA coatings prepared by traditional electrodeposition methods (14 MPa), and close to that of Ca-P coatings deposited on titanium by pulse electrodeposition (35-52 MPa). So HA coating prepared in pulse electrochemical deposition is of acceptable mechanical properties for using in high load-bearing conditions as an implant biomaterial.

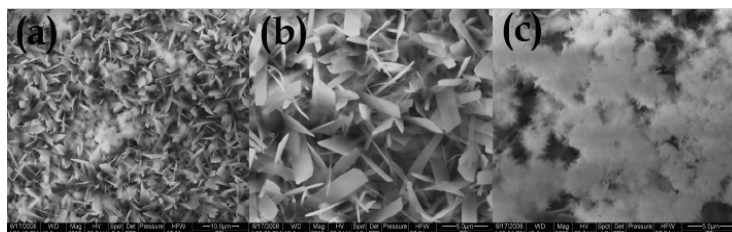


Fig. 4.11. SEM images of the as-deposited coating: (a) low magnification (b) high magnification of the tabular region and (c) high magnification of the fluffy region

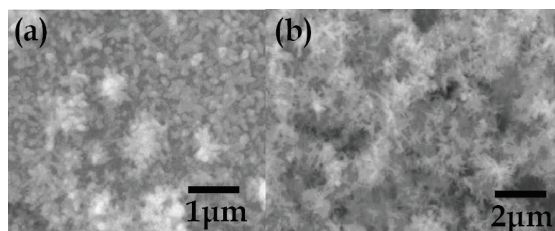
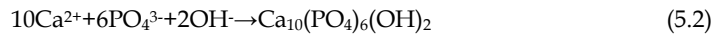


Fig. 4.12. HA coatings deposited at the initial stage. (a)30 s and (b)60 s.

Small amount of Mg element was also detected on the coating surface, which was probably caused by the diffusion of Mg cations. Mg^{2+} ions, which were produced from Mg substrate when the high anode current density (-20 mA/cm²) was applied, played an important role in increasing the adhesion strength as it was incorporated in the coatings. The inter-

diffusion of Mg and O indicated the formation of metallurgic bonding on the HA/Mg alloy interface due to ready formation of O-Mg band. Generally speaking, surface modified implants are expected to have a well adhered interface, namely metallurgic bonding interface, which will improve their stress resistance and avoid the peeling-off of the coating during service. Those loose HA particles may be resolved, thus only adherent HA particles can continue to grow. Based on the above results, it is clear that the adherent Ca-def HA coating can be directly formed by the proper pulse electrode position process without any post-treatment. Similar to Ti alloy (Yamasaki et al., 2002), the principle of the pulse electrodeposition of Ca-P phases on the Mg alloy was analyzed. In this process, when a high cathode current density (10 mA/cm²) was applied, the cathodic polarization of the Mg alloy led to an increase in pH at the interface between the alloy and the electrolyte due to the formation of OH⁻ ions. This sudden increase in pH triggered crystal nucleation and initiated crystal growth of the desired Ca-P phase directly on the substrate surface. There are four kinds of calcium phosphates, which are, in order of increasing solubility: Ca₁₀(PO₄)₆(OH)₂(HA), Ca₂(PO₄)₃.nH₂O (TCP), Ca₈H₂(PO₄)₆.5H₂O (OCP) and Ca(H₂PO₄).5H₂O (DCPD). Under local strongly basic conditions, HA is the most stable calcium phosphate and is hence deposited on the Mg substrate according to the following reaction.



Representative electrochemical polarization curves for different samples in SBF (Kokubo, 2006) were given in Fig.4.13. The cathodic parts of the curves in Fig.4.13 indicated that the cathodic polarization current of the hydrogen evolution reaction on the Ca-def HA-coated Mg alloy was much higher than that on the uncoated Mg substrate. The overpotential of the cathodic hydrogen evolution reaction was lower on the Ca-def HA-coated Mg alloy than that on the uncoated Mg substrate. This also revealed that the cathodic reaction was easier kinetically on the Ca-def HA-coated specimen than on the bare one, which may be due to the existence of the Ca-def HA coating. For the uncoated Mg alloy, the anodic polarization curve showed a passivation-like region, which indicated the existence of some protective film on its surface. Kannan and Raman (Denissen et al., 1980) reported that phosphate, sulphate and calcium ions in modified SBF could precipitate on the surface of Mg alloy, causing the same effect. For the Ca-def. HA-coated Mg alloy, however, there was no such phenomenon in the range of ~250 mV. Values of the corrosion potential E_{corr} and the corrosion current density I_{corr} were extracted from these curves and were shown in Table 5.2. Due to the presence of the Ca-def HA coating, the E_{corr} values were increased by about 230 mV, while the corrosion current density I_{corr} was about one order of magnitude lower than that of the uncoated magnesium. This result further indicated that the corrosion resistance of magnesium had been improved by the Ca-def HA coating. This was because the phosphorus in HA formed a gel-like layer and covered the surface completely, thereby protecting the underlying coating from environmental attack. The increase in resistance would greatly reduce the initial corrosion rate of implants and was important for maintaining the implant's mechanical strength in the initial bone reunion period. In terms of the design of degradable implants, this means that a thinner or less bulky bone plate could be used compared with untreated Mg implants having the same service life.

Basing on the hydrogen evolution rate (which is proportional to the metal dissolution or corrosion rate), Song (Dumelie et al., 2008) has suggested that a potential magnesium-based implant should possess a six times lower hydrogen evolution rate than AZ91 alloy. When

comparing the present electrochemical experimental results of the Ca-def. HA-coated Mg alloy with those of AZ91 alloy, the improvement in the corrosion resistance achieved was very encouraging, i.e. the I_{corr} value of the Ca-def HA-coated Mg alloy was about one-third as high as that of AZ91 alloy. Note that the data for AZ91 were taken from the literature reported by Kannan and Raman (Denissen et al., 1980). Thus Mg-Zn-Ca alloy coated with Ca-def HA is a promising candidate for biodegradable orthopaedic implants.

The slow strain rate tensile (SSRT) results of uncoated and Ca-def HA-coated Mg alloy in air and in SBF were given in Table 5.3. The mechanical properties of bare Mg alloy decreased by only 11.1% (for UTS) and 11.3% (for TOF) when tested in SBF, in comparison with those in air. This illustrated that Mg-Zn-Ca alloy was not highly susceptible to stress corrosion. Because of the protection of Ca-def. HA coating, the mechanical properties of the coated alloy increased by 5.6% (for UTS) and 16.6% (for TOF) when tested in SBF, which were closer to those of the uncoated alloy in air. If only considering the alloy's strength, the mechanical properties of bare and Ca-def HA-coated Mg alloy in SBF were both great enough to use as an implant material, because the maximum stress in bones during running or jumping was considered to be of the order of 100 MPa (Manso et al., 2000). However, the Ca-def HA coating delayed the decrease in strength of the Mg alloy, which would be helpful in supporting the fractured bone for a longer time. Moreover, the mechanical properties of the coated Mg alloy were similar to those of the substrate when tested in air (Kuo & Yen, 2002).

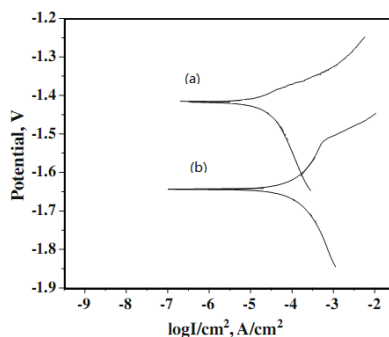


Fig. 4.13. Polarization curves in SBF of (a) uncoated and coated (b) Mg-Zn-Ca alloy.

Sample	Corrosion potential, E_{corr} (mV)	Corrosion current density, I_{corr} ($\mu\text{A}/\text{cm}^2$)
Bare Mg alloy	-1645	110
Ca-def. HA/Mg alloy	-1414	25

Table 4.2. Electrochemical parameters obtained from the polarization curves.

Sample	In SBF		In air	
	TOF(h)	UTS(MPa)	TOF(h)	UTS(MPa)
Bare Mg alloy	38.6 \pm 1.4	144 \pm 3	43.5 \pm 0.8	162 \pm 2
Ca-def. HA/Mg alloy	45.0 \pm 1.0	152 \pm 5	44.3 \pm 0.5	175 \pm 3

Table 4.3. SSRT results of Mg alloy with and without Ca-def HA coating. UTS:ultimate tensile strength; TOF: time of fracture.

4.4 Micro-arc oxidation (MAO)/ electrochemical deposition (ED) composite coatings

Micro-arc oxidation (MAO) had been well developed as a room-temperature electrochemical process suitable for the formation of native ceramic films with porous structure on the surface of Ti, Al, Mg alloys. It was found that the MAO coating offered porous surface and good adhesion strength with the substrate. When the MAO coating was introduced as a transition layer, it is expected that the pores on MAO coating can provide pinning sites for the ED coating. Fig.4.14 showed the surface morphology of the single MAO (a) coating and the composite coating of HA/MAO (b). The pores with different size were randomly distributed on the single MAO coating (Fig.4.14a), which resulted from the molten oxide and gas bubbles thrown out of micro-arc discharge channels. No micro-cracks existed on the surface of the MAO coating though the rapid solidification of the molten oxide in the cooling electrolyte always caused stress. The porous surface of the MAO coating provided a template for the ED process. It can be clearly seen that the composite coatings were composed of irregular needle-like structure (Fig.4.14b), which uniformly distributed on the sample surface. Compared with the HA grown on the Mg alloy substrate directly in section 4.2, the HA/MAO coating had quite low dimensions. The pores which formed during MAO treatment (Fig.4.14a) were the conductive channel in the ED process. Under the electric field, ions in the electrolyte moved into the pores and deposited on the wall of the pores. The nucleation and growth of HA were limited physically by these pores structure. For the ED process in the low deposition temperature which reduced the thermal stress, there were no micro-cracks appeared on the composite coatings. The surface of the composite coatings composed of the nanoneedle-like structure still retained the porous characteristic of the single MAO coating. As a bone implant material, porous surface is beneficial to cell attachment, propagation, bone tissue growth and anchoring of implant to bone.

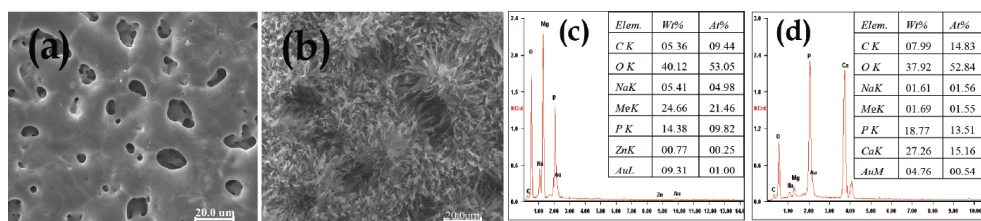


Fig. 4.14. Morphology of (a) single MAO coating and (b) composite coatings and corresponding EDS spectra.

EDS analysis of the surface of the MAO coating and the composite coatings were showed in Fig.4.14(c) and (d), respectively. The element of the single MAO coating consisted of Mg, O, P, C, Na and Zn elements (Fig.4.14c). The element Mg and trace Zn were derived from the Mg-Zn-Ca alloy transferring through micro-pores, and other elements were from electrolyte. Compared with the elemental composition of single MAO coating, the element Ca was deposited on the composite coatings (Fig.4.14b). In addition, the amount of element Mg was decreased sharply. It was possible that the Mg element was sealed in the substrate and MAO coating by the HA coating.

The cross-section morphology and corresponding elemental distribution across the composite coatings were analyzed with SEM and EDS line analysis and shown in Fig.4.15 (a) and (b), respectively. From the cross-section morphology (Fig.4.15a), the thickness of the composite coatings was about 15 μm and no apparent defects were observed. Moreover,

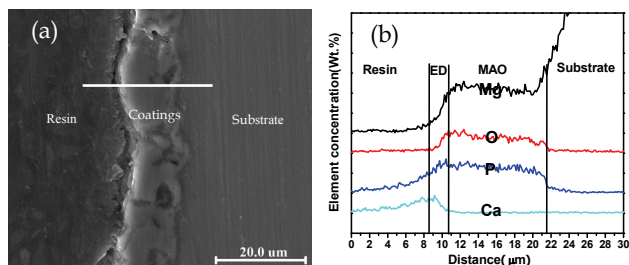


Fig. 4.15. Element distribution of the composite coatings in the depth direction (a) the cross-section micrograph. The white line showed the scanning direction. (b) the element distribution pattern.

there was no distinct discontinuity along the interfaces of HA/MAO/ substrate, which revealed that the HA coating tightly adhered with the MAO coating on substrate. Between the MAO coating and the ED coating, no clear boundary was observed, a metallurgic combination was concluded. At the same time, the phase contrast of HA/MAO coating is not sensitive to electron beam. The elemental distribution across the composite coatings (Fig.4.15b) showed that the amount of Mg, coming from the substrate, kept constant in the MAO coating and then decreased in the ED coating, which proved that corrosion of substrate was effectively inhibited. The dissolving of Mg was suppressed greatly. Both Ca and P were deposited from the electrolyte. The amount of P kept constant and no Ca was detected in the MAO coating, and Ca aggregated in the ED coating. From the elemental distribution, the thickness of the ED coating was about 2 μm .

The XRD patterns of the single MAO coating and the composite coatings were showed in Fig.4.16. Three phases of Mg, MgO and $\text{Mg}_3(\text{PO}_4)_2$ were observed on the spectrum of single MAO coating (Fig.4.16a). The peak of Mg probably was because of the porous MAO coating and X ray can penetrate it. MgO and $\text{Mg}_3(\text{PO}_4)_2$ are typical for the MAO coating. Hydroxyapatite (HA) and octacalcium phosphate (OCP) phases were deposited on the surface of the MAO coating (Fig.4.16b). Due to the chemical and structural similarities to bone and tooth minerals (H. W. Denissen et.al. 1980), HA had excellent biocompatibility and bioactivity and was used to improve the surface biocompatibility of Ti, Mg and stainless steel alloys (Wang, et al, 2010; Kuo, et al, 2002). OCP, as a calcium phosphate, had been suggested to be a precursor of biological apatite in bone (Brown, et al, 1962; Crane, et al, 2006). Therefore, the HA and OCP phases in the composite coatings will be helpful to improve the biocompatibility of the Mg-Zn-Ca alloy when the samples are implanted into the body.

Adhesion of the composite coatings with the magnesium substrate was one of the most important properties for the implant in physiological conditions. In the lap shear adhesion test, it was found that the composite coatings on all samples were not stripped from interface of the MAO/ED coating or the MAO/substrate. All delamination occurred inside the epoxy resin layer. It revealed that the adhesion strength of the composite coatings exceeded the tensile strength of the epoxy resin and was higher than 40MPa. In other words, the adhesion strength of the composite coatings was much higher than that of HA deposited directly on magnesium alloy, with the strength of 14MPa (Han, et al, 2001). Therefore, the composite coatings prepared in this work fully meet the requirement for implant biomaterial ($\geq 35\text{MPa}$) (Wei, et al, 1999).

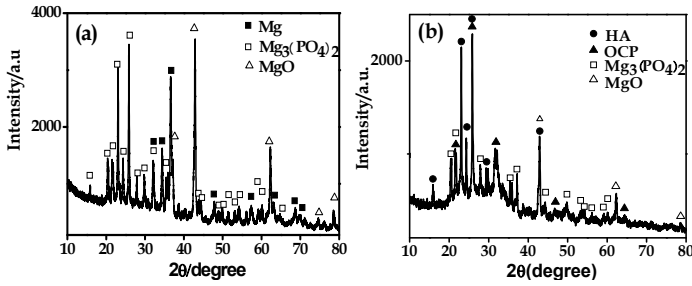


Fig. 4.16. XRD patterns of (a) the single MAO coating and (b) the composite coatings on Mg-Zn-Ca alloy

The corrosion resistances of the substrate, MAO/substrate and HA/MAO/substrate samples were evaluated through potentiodynamic polarization tests in SBF solution at 37°C (Kokubo, 2006). Fig.4.17 showed the polarization curves for different samples. In Fig.4.17, the anodic polarization curve of the substrate and the MAO coating modified samples showed a passivation-like region, which indicated the deposition of some protective films on their surface. Kannan and Raman (Kannan, et al, 2008) reported that phosphate, sulphate and calcium ions in modified SBF could precipitate on the surface of Mg alloy. But the composite coatings modified samples did not have such phenomenon. The corrosion potential (E_{corr}) and corrosion current density (I_{corr}) were extracted from the polarization curves and summarized in Table 5.4. As can be seen in Tab.5.4, the corrosion potential E_{corr} of the single MAO coating and the composite coatings modified samples were -1.614V and -1.495V, respectively. Both of them showed more positive than the substrate with -1.705V, while the corrosion current density I_{corr} of two coatings were about two orders and three orders of magnitude lower than that of the substrate, respectively. These results indicated that the corrosion resistance of magnesium alloy had been evidently improved by the single MAO coating and the composite coatings, and these also showed that the corrosion resistance of the sample with the composite coatings was better than the single MAO coating. The improvement of corrosion resistance will effectively reduce the initial corrosion rate of implants and greatly maintain the mechanical strength of the implants in the pre-bone healing.

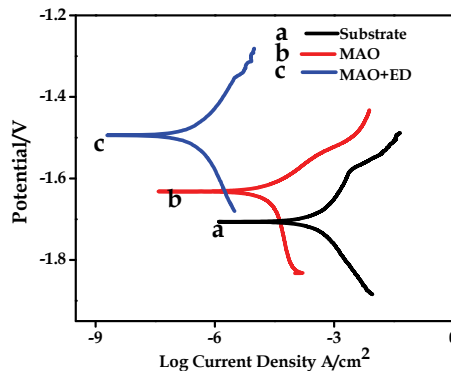


Fig. 4.17. Polarization curves of different samples in SBF solution at 37°C

Sample	Corrosion potential (E_{corr} , V)	Current density (I_{corr} , A/cm ²)
Bare Mg alloy	-1.705	3.84×10^{-4}
MAO /Substrate	-1.614	6.51×10^{-6}
MAO/ED/Substrate	-1.495	9.13×10^{-7}

Table 4.4. Electrochemical parameters of the samples obtained from the polarization curves

The protection capacity of the single MAO coating and the composite coatings to the Mg-Zn-Ca alloy was also evaluated by the hydrogen evolution test. Hydrogen volume was shown in Fig.4.18 as a function of immersion period. There was sharp hydrogen evolution of Mg-Zn-Ca substrate in the first 3 days (Fig.4.18a), because there was high Cl⁻ concentration in SBF which caused the substrate to corrode fast. As the time increased, the corrosion rate of the magnesium alloy decreased. The possible reason was that Ca-P compounds deposited on the specimens surface, forming a new protective layer, and reducing the corrosion rate. Fig.4.19 (a) showed the surface morphology of the substrate immersed for 7 days. The particles and the cracks were observed on the surface of the Mg-Zn-Ca alloy, and the element of the particles mainly consisted of Ca, P, C, O, Na, Mg and Zn from the EDS analysis, which was in agreement with the literature (Kannan, et al, 2008).

Fig.4.18 (b) showed the amount of hydrogen evolution of the MAO/substrate sample, which was much less than the substrate, and the increase rate decreased as the immersion time. As can be seen in Fig.4.19(b), the surface of MAO/substrate sample was modified slightly after soaking for 7 days in SBF, and deposits particles were observed on the surface and in the pores. The ions in the SBF penetrated through the micro-pores and deposited in the pores and surface. Therefore, the corrosion rate of the single MAO/substrate sample was reduced as the immersion time because the pores were sealed little by little during immersion period.

The corrosion rate of ED/ MAO/substrate sample was slower than the single MAO/substrate samples. The hydrogen evolution rate was about 0.04 ml/cm²/day after immersion for 3 days. It was about two-third of that of hydrogen evolution rate of AZ91D (Song, 2007). The reported value was little higher than the tolerated level, which was used to screen out biodegradable candidates for human body implants. The entire surface of the

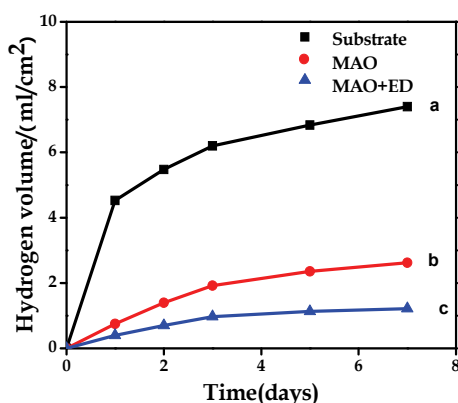


Fig. 4.18. The amount of hydrogen evolution of specimens immersed in SBF: (a) substrate, (b) the MAO/substrate sample and (c) the ED/ MAO/substrate sample.

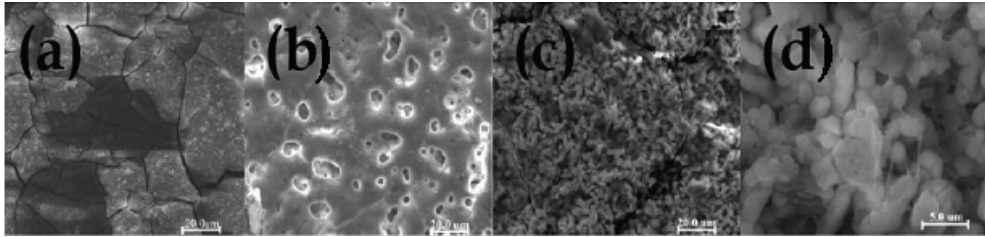


Fig. 4.19. SEM images of corresponding specimens in Fig.4.18 immersed in SBF for 7days

ED/ MAO/substrate sample after immersion for 7 days was covered by deposits (Fig.4.19c). The new deposits layer was shown in detail in Fig.4.19 (d), which showed the new layer was composed by many rod-like precipitates. The main elements of the new layer were Ca, P and O, which revealed that the composite coatings could induce the Ca/P salt deposition and had fine biomimetic mineralization ability. The new layer improved the thickness of the composite coatings and further enhanced the protection effect to the substrate. Additionally, the surface morphology evolution of the ED/ MAO/substrate sample after immersion for 7 days proved that the composite coating had better Ca-P salt induction property than that of pure HA coating (Wen, et al, 2009).

Fig.4.20 showed the compressive load of the substrate and the ED/ MAO/substrate immersed in SBF for different time. The results of the compressive load and compressive strength of the samples were shown in Tab.5.5 (The corrosion area changed of the cross-section was neglected to calculate the compressive strength). In Fig.4.20, the compressive load and strength of the ED/ MAO/substrate were higher than those of the substrate after 2 and 6 weeks immersion. The results indicated that the composite coatings delayed the strength loss of the Mg-Zn-Ca alloy. As shown in Tab.5.5, the compressive loads of the substrate were decreased to 19.5 KN and 13.9 KN after 2 and 6 weeks immersion, and the compressive strength were 248.2 MPa and 177.2 MPa respectively. Because of the protection of the composite coatings, the compressive load and strength of the ED/ MAO/substrate were 21.7 KN and 276.1 MPa after 2 weeks immersion, and 18.2 KN and 231.1 MPa for 6 weeks immersion. Generally, the compressive strengths of human bones were 100~230 MPa in cortical bone and 2~12 MPa in cancellous bone (A. Rakngarma, 2009). Therefore, the composite coatings effectively delayed the decrease in mechanical properties of the Mg-Zn-Ca alloy, and provided adequate support for the pre-healing of fracture bone.

Sample	Before immersion	ED/ MAO/substrate		MAO/ substrate	
		2 weeks	6 weeks	2 weeks	6 weeks
Compressive load(KN)	26.1	21.7	18.2	19.5	13.9
Compressive strength(MPa)	332.9	276.1	231.1	248.2	177.2

Table 4.5. Compression test results after immersion for a period.

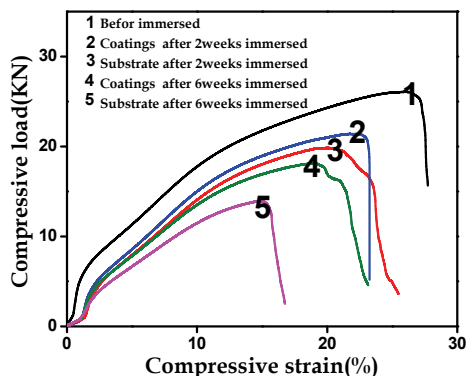


Fig. 4.20. The compression curve of the immersed samples

4.5 HA / Ti-O film / Mg alloy

In the research of NiTi stents, it was found that titanium oxide film formed because of oxidization, and the film improved the biocompatibility (Christine et al., 1997). N.Huang fabricated titanium oxide film on permanent stent, and demonstrated the improved biocompatibility and good bonding strength with substrates (Huang et al., 2003). In this section, titanium oxide was deposited on magnesium alloy substrate and served as intermediate layers to protect from rapid corrosion. Hydroxyapatite, as outer layer, was deposited on titanium oxide film.

Fig.4.21 showed the XRD patterns of the samples. It could be seen that the sample with titanium oxide film exhibited only magnesium peaks. No peaks of titanium dioxide were found. It has been proved that without heat treatment, it is hard to form rutile and anatase. So the titanium oxide on the sample should be amorphous. It was reported that the amorphous Ti-O film had evident biocompatibility, though less than crystalline Ti-O films. The XRD pattern of hydroxyapatite was also shown in Fig.4.21, the diffraction peaks of HA could be observed. The diffraction at 25.6° is seen as the typical peak of hydroxyapatite. So it could be sure that the hydroxyapatite was deposited on the titanium oxide.

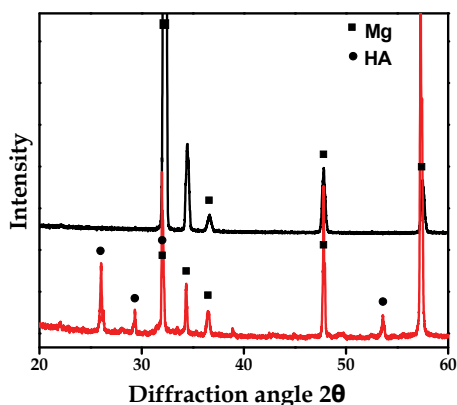


Fig. 4.21. The XRD patterns of the sample with Ti-O film and composite coating

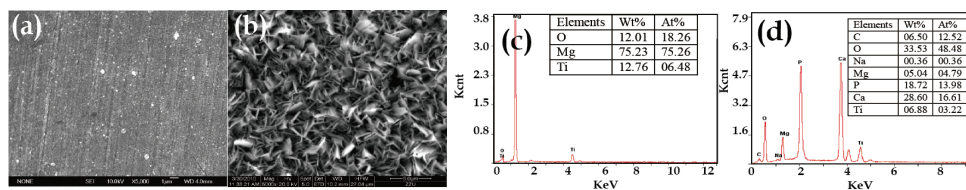


Fig. 4.22. The morphology of Ti-O film and hydroxyapatite

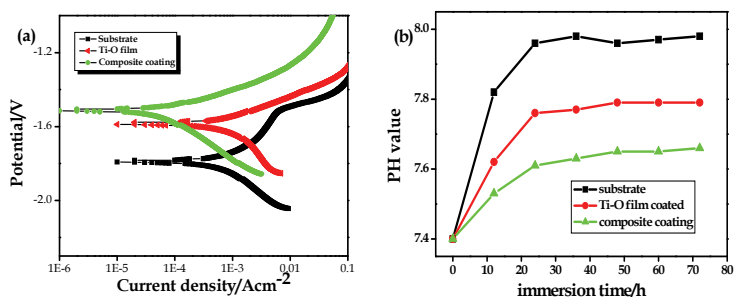


Fig. 4.23. (a) The polarization curves of the sample in SBF, (b) pH value change of SBF.

It could be observed from the FESEM images that the titanium oxide film was uniform, no crack was found in Fig.4.22 (a). According to the calculation by the deposition rate, the titanium oxide was with a thickness of about 200nm, after deposition for 2 hours. The outer layer was composed of flake-like HA, which was typical morphology for HA. The EDS results showed that only three elements were detected in the Ti-O/substrate sample. Because the thickness of the film was about 200nm the substrate was detected by X-ray, so it couldn't be concluded that there was magnesium atoms in the titanium oxide film while in the EDS results of HA/Ti-O coating, calcium, magnesium, oxygen, phosphorus, sodium were observed. Calcium, oxygen, and phosphorus were all components in HA. During the formation of HA, the magnesium and sodium would take the place of calcium in crystal structure, thus the Ca/P atomic rate was reduced. The tests in section 4.3 have showed that calcium-deficient HA coatings were more susceptible to degradation.

In Fig.4.23(a), it could be observed that the potential of magnesium substrate in SBF(Kokubo et al., 2006) was about -1.8V. And the corrosion potential was improved by 200mV and 300mV by Ti-O film and Ti-O/HA composite coating, respectively. The titanium oxide film prevented the interaction of substrate with the fluid, and the deposition of HA coatings improved the corrosion resistance further. The improvement in corrosion resistance by Ti-O film and composite coating was also demonstrated by pH value test. With the protection of Ti-O film and composite coating, the corresponding pH value increased with a low rate and reached to 7.75 and 7.63, respectively. The bare substrate reacted with the solution quickly, and caused a sudden increase of PH value even in the first immersion day. In the first day, the pH value increased up to 7.95.

5. In vivo biodegradation

A wide consideration has been given to improve the biocompatibility and corrosion resistance of Mg alloy. Almost all the evaluations have been done in the SBF environment.

The *in vivo* performance of implants requires further experiment due to the difference between the simulated physiological environment and real condition even in the dynamic SBF system.

5.1 HA/AZ31

Fig.5.1.(a-d) showed the surface SEM images of the uncoated and HA-coated AZ31 implants after 6 weeks implantation. As seen in Fig.5.1(a, c), uncoated sample surface was coarse and the surface presented a crackled appearance maybe due to fast degradation. For the HA-coated sample, the surface coverage was uniform and no localized corrosion was observed (Fig.5.1b). The coated implant surface was covered by a new mineralized layer (Fig.5.1d). The original HA surface was also found somewhere where the typical needle-like HA coating was exposed (typically area A, inset in Fig.5.1d). The EDS results showed that the presence of carbon, oxygen, phosphorus, calcium, magnesium and aluminum on the surface of the uncoated implant, and the calcium and phosphorus atomic ratio of deposition was 0.87. In contrast, the HA-coated sample was only rich in carbon, oxygen, phosphorus, and calcium, no magnesium and aluminum were detected. The calcium and phosphorus atomic ratio was 1.82, higher than the theoretical value 1.67 of HA.

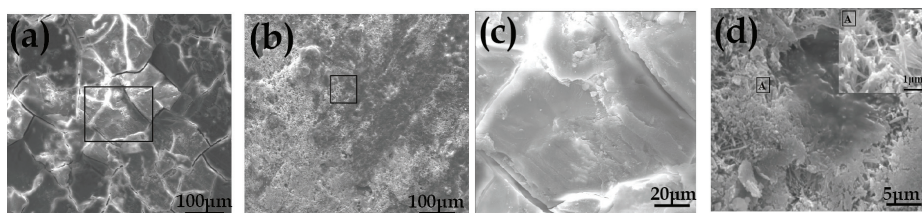


Fig. 5.1. SEM micrographs of (a) uncoated (b) HA-coated implant after 6 weeks implantation, (c) and (b) high magnification images of selected area in (a) and (b), respectively.

After 12 weeks implantation (Fig.5.2), the uncoated sample was covered with corrosion products. The surface integrity was destroyed due to severe selective corrosion. As shown in Fig.5.2 (a), besides the formation of serious crack, sample surface was undermined and some deep pits were left on the surface (by white arrow in Fig.5.2a). The surface of HA-coated sample was covered by the Ca-P deposits partly. The EDS analysis results showed that the surface contained a little zinc and Mn. Both of them were not detected after 6 weeks implantation. The EDS spectrum difference proved the continuous corrosion of alloy. In the case of HA-coated sample, the flower needle-like HA coating dissolved (Fig.5.2b). Some positions of the coating exhibited the peeled-off feature (Fig.5.2b).

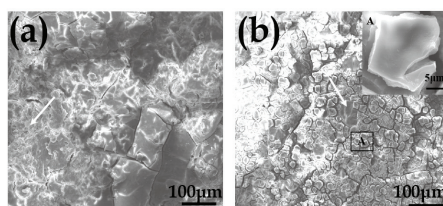


Fig. 5.2. SEM images of (a) uncoated, (b) HA-coated implants after 12 weeks implantation.

Fig.5.3a-c illustrated the surface of the HA-coated AZ31 after 18, 24, 30 weeks, respectively. Selective corrosion pits were not observed on the surface with increasing implantation time. The surface of implants was attached by more and more porous network structure gradually from 18 weeks to 30 weeks. The pore structure was conducive to the growth of bone cells and tissue recovery. EDS results (Fig.5.3d) showed that composition of selected area B in Fig.5.3a was mainly composed of calcium and phosphorus and a small amount of Mg, Al, Zn. A. L. Boskey pointed out that Mg^{2+} concentration has a great effect on mineralization process, if magnesium and calcium atomic ratio is more than 0.2, it will hamper mineralization transformation from precursor amorphous HA (ACP) to the HA (Boskey & Posner, 1974). In contrast, the area A in Fig.5.3a was highly rich in carbon and oxygen and little amount of calcium and phosphorus. It could be also seen that carbon content increased significantly with the increasing implantation time. It was concluded the deposition of protein from physiological environment and growth of new body tissue occurred from 18 weeks. It might be hypothesized that precipitations of calcium phosphates and corrosion products such as magnesium oxides and magnesium hydroxides formed a complex corrosion layer on the implants in vivo that may slow down the corrosion process and played a further protection role (Witte et al., 2005).

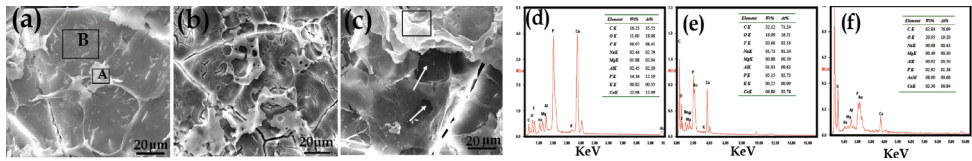


Fig. 5.3. SEM micrographs of coated implants at (a) 18 weeks, (b) 24 weeks, (c) 30 weeks, (d) EDS spectrum of area A in (a), (e) EDS spectrum of area B in (a), and (f) EDS spectrum of (c).

Fig.5.4 showed the weight change of the HA/AZ31 rods after 6, 12, 18, 24, 30 weeks implantation. There was obvious mass gain for initial 12 weeks implantation. Then the mass decreased throughout the following implantation period, indicating a continuous biodegradation process inside the rabbit femora. The average biodegradation rate of HA-coated AZ31 alloy rods was calculated to be about 0.21 mg/cm²/day. But for the uncoated sample, (35±0.22)% mass loss happened after 12 weeks implantation, the average biodegradation rate was calculated to be about 0.54 mg/cm²/day. Intake of a certain amount of magnesium (300-400 mg/day) is normally required for the human body's metabolic activities. According to the measured weight loss rate of HA-coated samples (0.21 mg/cm²/day), as long as the total surface area is less than 1429 cm², for uncoated samples (0.54 mg/cm²/day) as long as the total surface area is less than 556 cm², the dissolved magnesium would be easily absorbed or consumed by the human body.

Fig.5.5 showed the radiographs of rabbit femora with implantation of uncoated AZ31 rods at 6, 12 weeks and HA/AZ31 rods at 6, 12, 18, 24 and 30 weeks. In contrast to uncoated samples at 6, 12 weeks (Fig.5.5a~d), the profiles of HA-coated samples were clearer at the corresponding time (Fig.5.5e~h). Fig.5.5 indicated degradation process of uncoated and HA-coated AZ31 rods during the whole experiment period, which was evaluated by the reducing diameter of rods. From Fig.5.5a~d, it was proved that uncoated samples degraded fast because rod profiles presented an irregular shape and were fuzzier than that of 6 weeks. What is more, gas shadows (arrow in Fig.5.5b) were observed in soft tissues and bone marrow cavity around the uncoated samples at 6 weeks. After 12 weeks implantation, the

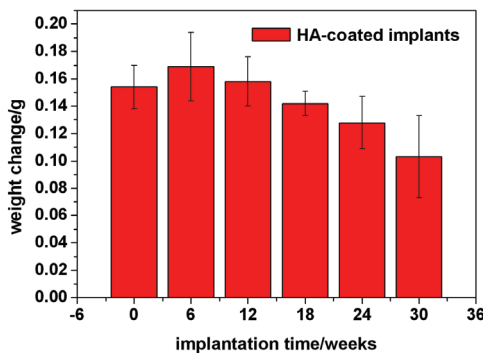


Fig. 5.4. Weight change of the HA/AZ31 rods during implantation period.

gas shadows vanished (Fig.5.6d) without a special treatment. Compared to uncoated samples, gas shadows were not detected during the whole experiment period. HA-coated samples maintained original column shape during the first 18 weeks (Fig.5.5e-j). After 18 weeks, the profiles of HA-coated samples were not distinct, indicating the evident degradation of sample. Moreover, the periosteal reaction was observed around the HA-coated samples which indicated the formation of new bone. (Fig.5.5k~n).

Fig.5.6 showed histological analysis of the bone tissue response to the uncoated samples at 6, 12 weeks and HA-coated samples at 6, 12, 18, 24 and 30 weeks. It could be clearly seen that the newly formed bone lamellar trabecula was formed in the bone tissue around both uncoated and coated samples (Fig.5.6a~f). There is growing evidence that if the releasing of magnesium is acceptable by human body, it will help to stimulate the healing of bone tissue. There were some inflammation response and congestion phenomena in uncoated sample group at 6, 12weeks (rectangles marked in Fig.5.6a, c), without any multinucleated giant cells. In contrast, not any inflammation response and congestion phenomena were observed in HA-coated sample group. The newly formed bone was clearly seen in HA-coated sample group, which was evident by a large number of osteoblasts (ellipses in Fig.5.6b, d~g). Osteoblasts and osteocytes increased and became more orderly with the time increasing from 6 weeks to 18 weeks (Fig.5.6b, d~c), then they stabilized at the following stage (Fig.5.6f). Periosteum ossification phenomenon was found after 30 weeks implantation (Fig.5.6g). The presence of HA coating improved the bone-biomaterial interface absorptiveness, which showed the histological attachment of bone to the implant surface. This result indicated that HA/AZ31 actually has good osteoconductivity and stimulatory effect on the growth of new bone tissue due to its functional roles and presence in the bone. It was reported that the presence of magnesium on orthopedic implants could enhance the adhesion of osteoblastic cells and promote optimal osteogenesis (Zreiqat et al., 2002).

Table 6.1 listed the the serum magnesium and calcium concentration levels of rabbits before and after implantation at different periods. No significant difference was found in each item before implantation and after 6, 12, 18, 24, 30 weeks implantation. It is important that the alloy was degraded in an appropriate rate that the rabbit can absorb the released Mg^{2+} until the new bone grew. The physiological equilibrium of magnesium in the body could keep the serum level constant. Mg element maybe absorbed into the muscle and the bone as storage areas, while the excess magnesium in the serum would be metabolized via the kidneys.

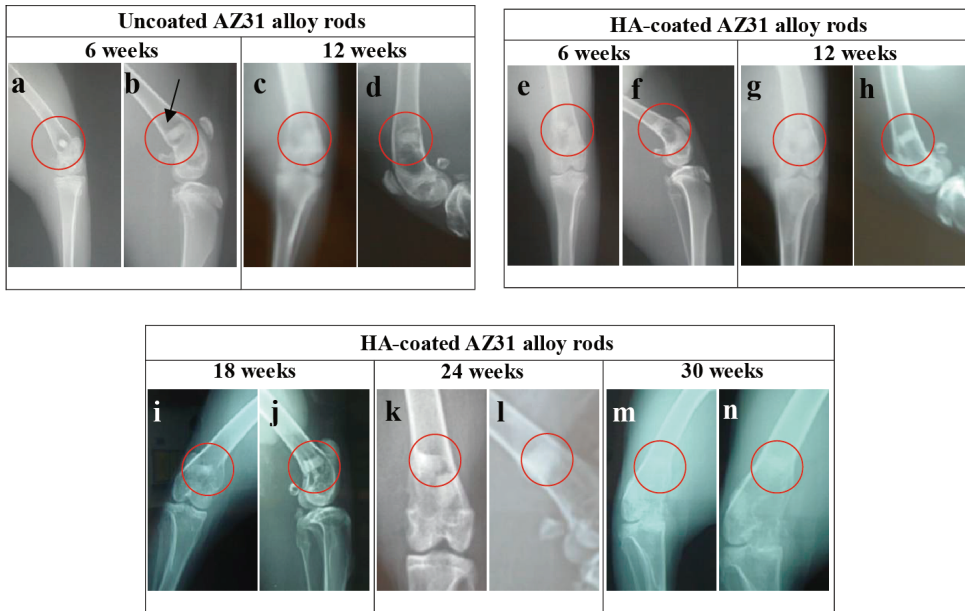


Fig. 5.5. Femora radiographs of rabbits with implants at different periods. Uncoated AZ31 alloy rods at (a& b) 6 weeks, (c & d) 12 weeks implantation, and HA-coated AZ31 alloy rods at (e& f) 6 weeks, (g & h) 12 weeks, (i & j) 18 weeks, (k & l) 24 weeks, (m & n) 30 weeks implantation. The parallel images are from different directions.

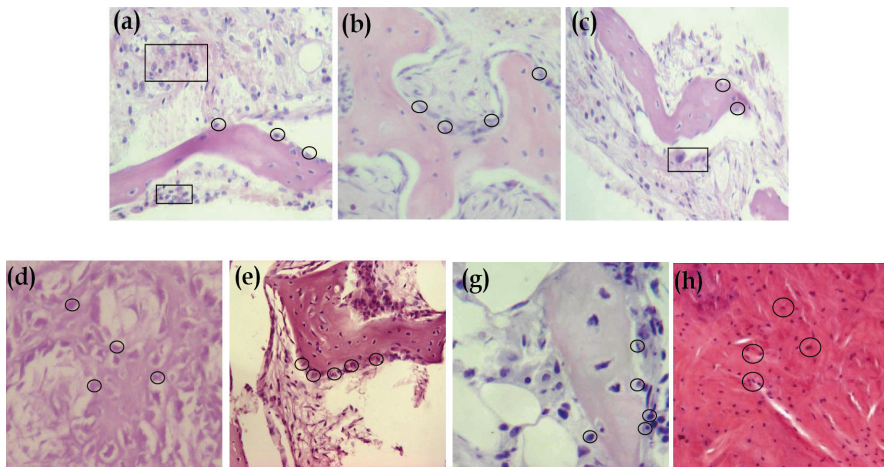


Fig. 5.6. Histological photographs of the bone tissues around uncoated implants at (a) 6 weeks, (b) 12 weeks, and HA-coated implants at (c) 6 weeks, (d) 12 weeks, (e) 18 weeks, (f) 24 weeks, and (g) 30 weeks. Ellipses indicate osteoblast; rectangles indicate inflammation response and congestion phenomena. Magnification: 20 \times .

Item	Magnesium (mmol/l)	Calcium (mmol/l)
Before implantation	0.845±0.16	1.196±0.13
Uncoated implants (6 weeks)	0.881±0.25	1.197±0.18
Uncoated implants (12 weeks)	0.926±0.18	1.369±0.10
HA-coated implants (6 weeks)	0.878±0.09	1.411±0.08
HA-coated implants (12 weeks)	0.869±0.13	1.409±0.06
HA-coated implants (18 weeks)	0.852±0.10	1.210±0.13
HA-coated implants (24 weeks)	0.807±0.17	1.155±0.05
HA-coated implants (30 weeks)	0.815±0.12	1.181±0.07

Table 5.1. Serum magnesium and calcium concentration of rabbits.

5.2 HA/MAO/ Mg-Zn-Ca alloy

The degradation of the naked and HA/MAO coated Mg-Zn-Ca alloy in the rabbit femoral shaft after 8, 12 and 18 weeks implantation were in suit observed non-destructively by micro-CT with 3D reconstruction (Fig.5.7). The implants were in the os integumental and marrow cavity. It could be clearly observed, within the 12weeks, that the substrate samples degraded (volume loss) much more rapidly than the HA-coated samples, and serious pitting occurred on the substrate samples. In Fig.5.7(d), within the 12th week, the HA-coated sample could still keep the integrity and can absorb load apparently. So it could be concluded that the composite coatings delayed the rapid corrosion of substrate, which was also demonstrated in the following research. Fig.5.8(a) showed the compressive strength of the samples after implantation for different time. It was observed that the loss of mechanical integrity was much greater than the following period, which was attributed to the local corrosion in the early period. After implantation for 8 weeks, the compressive integrity of substrate was about 116.2 MPa. It was reported that the compression strength of natural bone was about 100~230 MPa. So it was demonstrated that after 8 weeks implantation, the substrate samples could absorb the load effectively. While the compressive strength of samples with composite coatings after implantation for 8 and 18 weeks were 218.6 and 119 MPa, respectively, which were much higher than that of substrate samples, and could fully meet the requirement of bone implants. The compressive integrity of samples in vivo test showed that the samples after modification with composite coatings could compromise mechanical integrity and degradation rate perfectly during the healing period, which provided clinical application with valuable data.

Fig.5.8 (b) showed the calcium and zinc ion concentration in the blood and urine of rabbits after implantation for different time. It was seen that before implantation the magnesium ions in urine of the two groups was about 1.8mmol/l, higher than that in the blood, which could be ascribed to the metabolism of magnesium ions by kidney. The concentration of magnesium ions in the blood of two groups in 8th, 12th, 24th week fluctuated between 0.7 and 0.8mmol/l, which was quite low. Extremely higher concentration of magnesium ions than the standard (Brown W.,1962) didn't appear in the test, it was indicated that the excess

magnesium ions could be absorbed and exported by rabbits properly. The magnesium ions concentrations in the urine in the two groups were similar and acceptable. After implantation for 8, 12, 18, 24 weeks, the concentration of zinc ions in urine of the two groups was close to that before implantation (Fig5.8c). No superfluous zinc ions were found in the blood and urines in both group, which illustrated the good biocompatibility of the substrate and HA-coated samples.

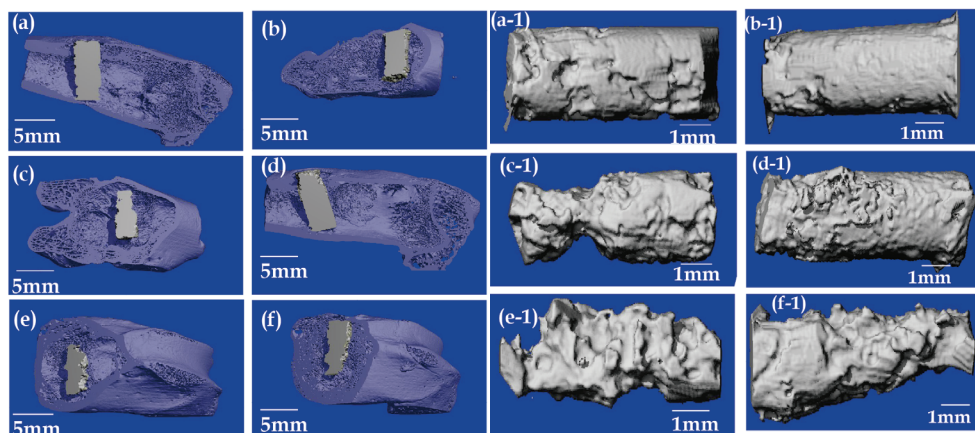


Fig. 5.7. (a),(c) and (e) show the cross-section images of the bone with residual implants at 8 week, 12 week and 18 weeks; (b),(d) and (f) show the cross-section images of the bone with coated implants at the corresponding weeks. All the three-dimensional reconstruction images of residual implants was shown in Fig.5.7 (a-1) ~ (f-1), respectively.

The pathological analysis proved that the typical tissues in heart, liver, kidney, spleen was normal and healthy with regular structure. Slight congestion presented in spleen tissue with normal splenic corpuscles and cords, it might be caused during the sacrifice but did not indicate diseases. The corrosion products including metallic ions didn't deteriorate the function of the important tissues, such as circulation, immunity and urination.

Fig.5.9 showed the radiographs of rabbits leg bones implanted by alloy and coated alloy after 1, 8 and 18 weeks implantation. No gas bubbles were observed around the implants, which showed that the gas bubbles disappeared through physiological action, and without side effects. In Fig.5.9 (a), (c) the profile of substrate and coated samples was the same as that before implantation. No evident degradation was observed. There was gap between samples and bone tissues. It was reported that after implantation of AZ31D samples for 1 week, gas bubbles were observed, and gradually disappeared during 2~3 weeks. It indicated that the gas could be absorbed and exported by animals, but the hydrogen evolution rate was higher than the rate of being absorbed. In this study, after implantation for 1 week, no gas bubbles was observed, which demonstrated the better biocompatibility of AZ31 than AZ91D alloy. After implantation of substrate samples for 8 weeks, evident degradation was observed, and the gap between samples and bone tissue was wider than that at 1 week. It could be attributed to the rapid corrosion, and the newly formed bone could not occupy the space after corrosion. While the HA-coated samples degraded more slowly, it could be seen from the dim interface between samples and bone tissues. The

newly formed bone tissues grow closely along surface of the implants. After implantation for 12 weeks, although there was still gap between coated samples and bone tissue and the degradation continued, the newly formed bone was more than that in 8th week. The bone density was close to that of mature bone, but due to the weaker inducing, the healing rate of bone was slower than that contact with coated samples. It must be noticed that gap appeared in the 12th week, it might be caused by rapid corrosion after the dissolution of composite coatings.

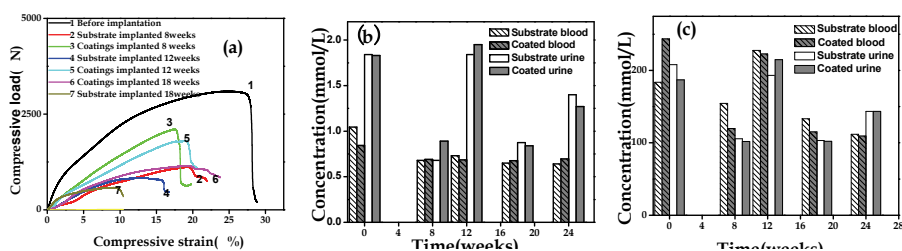


Fig. 5.8. (a) Compression curve of residual implants after implantation for different period; Calcium and zinc ions concentration in the blood and urine of rabbits after implantation for 8, 12, 18, 24 weeks: (b) substrate; (c) with composite coating.



Fig. 5.9. The radiograph of rabbit bone after implantation for different time: (a) substrate, 1 week; (b) substrate, 8 weeks; (c) coated, 1 week; (d) coated, 8 weeks; (e) coated, 12 weeks.

In Fig.5.10(a), the sample was surrounded by spongy bone and the red circle showed the initial outline of substrate sample. On the surface of substrate, serious pitting was observed. The EDS showed us the distribution of element Ca, P, Mg. The element Ca, P could approximately indicate the existence of bone adhered to the substrate, while the Mg could explain the dissolution and degradation of magnesium. The concentration of calcium and phosphate in the spongy bone was close to that of mature bone, but the concentration of magnesium in pitting sites (pointed by red arrows) was higher than that in bone tissue and lower than that in implant. It was seen that magnesium ions were released from the sample and aggregated around the sample, and excess magnesium ions caused inflammation observed in 8th week. In Fig.5.10(b) the sample didn't degrade rapidly, which was accordant to the previous analysis. The distribution of magnesium was uniform, and no aggregation of magnesium ions was observed in local areas. It indicated that the composite coating improved the corrosion resistance of the sample, and the release rate of magnesium ions was lower than absorbing and exporting rate. The EDS result showed the similar

concentration of calcium and magnesium, which indicated the formation of new bone, and good compatibility and bone-inducing ability of composite coatings (Crane N.,2006)

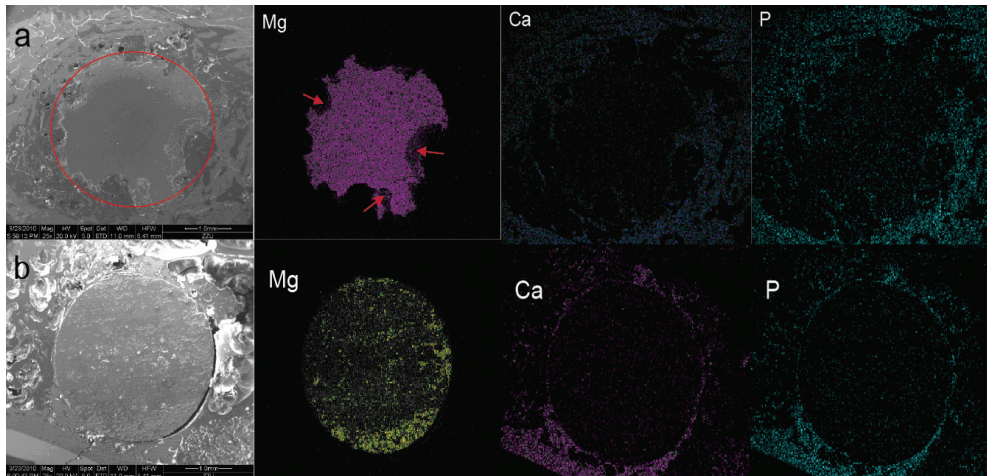


Fig. 5.10. The SEM and EDS results of samples: (a) substrate; (b) coated alloy.

6. Conclusion

A wide range of techniques were taken into account to develop novel Mg alloys based materials for implants. The degradation of Mg-based materials, including existing off-the-shelf alloy, newly developed alloy and surface treated alloy, in SBF and physiological environment have been investigated systemically. The corrosion resistant variations and non-toxicity of related Mg-based materials have been thoroughly evaluated. The alloy with different microstructures and surface coatings with various morphologies determines the electrochemical performance in terms of corrosion potential and corrosion current density. Fig.6.1 summarized the historical progress of the corrosion performance of alloys involved in the chapter. It is clear that the substrate alloys play important roles in the corrosion performance of the samples. Although the newly developed alloys possessed low corrosion potential, a comparable E_{corr} value can be obtained by the composite coating techniques. In the Fig.6.1, the improvement in the corrosion potential of Mg-Zn-Ca and Mg-Zn-Y-Nd by composite coating was in a wider range than that by single coating and alloy processing techniques. By composite coating, I_{corr} decreased to the magnitude of 10^{-5} or 10^{-6} . At the same time, the implanted alloy can keep acceptable mechanical integrity in the healing (or virtual) period. All these results indicate a promising prospect of Mg-based materials for implant application.

To develop a novel alloy for clinical application, a more systematic approach is needed. The developed alloys based on the physiological toxicity consideration had more negative corrosion potential and higher corrosion current density than the existing alloys (Fig.6.1). And the traditional approaches by adding rare earth elements and aluminum etc were not recommended (F.Witter 2008). At the moment, the list of potential medical applications for biodegradable Mg alloys seems still limited.

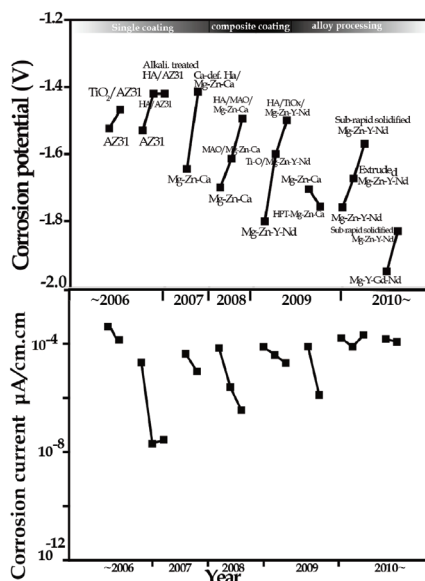


Fig. 6.1. Progress in involved Mg-based materials for implants application.

The evident improvement in corrosion resistance has been obtained by HA coating in different systems although the HA exhibited a typical porous surface. Further study about the conjunction structures in detail is required to control their degradation behaviors intentionally. The inherent micron/nano porous surface of HA coating makes it can be endowed with the local drug delivery functions, which will enlarge the application fields of biodegradable Mg-based materials. At the same time, it is suggested that other surface modification techniques could be applied to improve the corrosion resistance of Mg alloys, such as surface alloying, ion implantation and surface silidification.

There are numerous studies about Mg alloy corrosion. Corrosion behaviors of different alloys in different environments were compared. Researchers also proposed some practical designs to avoid serious corrosion, and summarized various effects of environmental and metallurgical factors on the corrosion of magnesium alloys. All these results provide us empirical information to design degradable materials for implants. However, there have been very few mechanism studies and some fundamental questions are still not clear. If the role of phases, microstructures and the coating with different morphology in the corrosion process are well understood, we can design more elaborated corrosion resistance material system and control the degradation rate in different environments.

It is likely that further research will improve the corrosion resistance of Mg-based implants, and that low-priced, high performance magnesium alloys will be commercially available. The long-term joint efforts from multidisciplinary researchers will be needed to make significant advances for the benefit of patients.

7. Acknowledgment

We are grateful for the financial support of the National Basic Research Program of China (Grant No. 2008CB617509) and the National Natural Science Foundation of China (No.

30870634). The authors would like to thank Prof. Yisheng. Wang at Medical College of Zhengzhou University for his operation on animals. The authors also would like to thank Dr. S.H. Wang and Mr. J.L. Xue at the Laboratory Animal Center of Henan Province for the assistance in the animal experiments.

8. Reference

- Berger, H.; H., Tang and F., Levy. (1993). Growth and Raman spectroscopic characterization of TiO₂ anatase single crystals, *J. Cryst. Growth* 130, 1-2, 108-112, ISSN 0022-0248.
- Boehlert, C.J; K.; Knittel; K., Venkatesan. (2006). The microstructure, tensile properties and creep behavior of Mg-Zn alloys containing 0~4.4% Zn, *Mater. Sci. Eng. A*, 417: 315-321, ISSN 0921-5093.
- Boskey, A., L.; A., S., Posner (1974). Magnesium stabilization of amorphous calcium phosphate: A kinetic study. *Mater Res Bulletin*, 9, 7, 907-16, ISSN 0025-5408.
- Brown, W; et.al. (1962). Crystallographic and chemical relations between octacalcium phosphate and hydroxyapatite. *Nature*, 196, 15, 1050-1055, ISSN 0028-2836.
- Christine, Trépanier; Maryam, Tabrizian; et.al. (1999). Effect of modification of oxide layer on NiTi stent corrosion resistance. *Journal of Biomedical Materials Research Part B: Applied Biomaterials*. 48,1, 433-40, ISSN 1552-4981.
- Crane, N; Popescu, V; Morris, M; Steenhuis, P; Igelzi, MJ,. (2006). Raman spectroscopic evidence for octacalcium phosphate and other transient mineral species deposited during intramembranous mineralization, *Bone*, 39,3, 434-442,ISSN 8756-3282.
- Denissen, H.W.; K., de Groot; et.al.(2004). Tissue response to dense apatite implants in rats, *J. Biomed. Mater. Res.* 14,6,713-721,ISSN 1549-3296.
- Dumelie, N.; H., Benhayoune; D., Richard; et al.. (2008).In vitro precipitation of electrodeposited calcium deficient hydroxyapatite coatings on Ti6Al4V substrate. *Mater. Charact.* 59,2, 129-133,ISSN 1044-5803.
- Gupta, A.P.; Vimal, Kumar. (2007). New emerging trends in synthetic biodegradable polymers polylactide: a critique, *Eur. Polym. J.*, 43, 10, 4053-4074. ISSN: 0014-3057.
- Gu, Xuenan; Zheng, Yufeng; et al. (2009). In vitro corrosion and biocompatibility of binary magnesium alloy, *Biomaterials*, 30,4 484-498 ISSN 0142-9612..
- Han, Y; Fu, T; Lu, J. (2001). Characterization and stability of hydroxyapatite coatings prepared by electrodeposition and alkaline-treatment process, *Journal of Biomedical Materials Research*. 54,1, 96-101, ISSN: 1552-4965.
- Huang, N; Yang, P;et al. (2003). Hemocompatibility of titanium oxide films, *Biomaterials*. 24,13,2177-87, ISSN 0142-9612.
- Hu ,J.h.; S.k. ,Guan; et.al. (2006). Corrosion protection of AZ31 magnesium alloy by a TiO₂ coating, *Corr. Sci. Protec. Tech.*, 2003, 13,2017-2020, ISSN1002-6495.
- Kannan, M., Bobby; R.K., Singh, Raman. (2008). In vitro degradation and mechanical integrity of calcium-containing magnesium alloys in modified-simulated body fluid, *Biomaterials*. 29: 2306-2314, ISSN 0142-9612.

- Kokubo, T; Takadama, H. (2006). How useful is SBF in predicting in vivo bone bioactivity? *Biomaterials*. 27: 2907-15, ISSN 0142-9612.
- Kuo, M.C.; S.K., Yen. (2002). The process of electrochemical deposited hydroxyapatite coatings on biomedical titanium at room temperature, *Materials Science and Engineering C*. 21,1-2,153-160, ISSN: 0928-4931.
- Li, Zijian; Gu, Xunan; et al. (2008). The development of binary Mg-Ca alloys for use as biodegradable materials within bone, *Biomaterials*, 29, 10, 1329-44, ISSN 0142-9612.
- Luo, Z. P.; S. Q., Zhang; Y. L., Tang; et al. (1994). On the stable quasicrystals in slowly cooled Mg-Zn-Y alloys, *Scripta Mater* 32, 9, 1411-1416, ISSN: 1359-6462.
- Manso, M.; C., Jimenez; C. Moranta.(2000).Electrodeposition of hydroxyapatite coatings in basic conditions,*Biomaterials* 21,17, 1755-1761,ISSN 0142-9612
- Rakngarma, A.; Y., Mutoh. (2009). Characterization and fatigue damage of plasma sprayed HAp top coat with Ti and HAp/Ti bond coat layers on commercially pure titanium substrate. *J. Mech. Behav. Biomed. Mater.*, 2,5, 444-453, ISSN 1751-6161.
- Song, Guangling; Shizhe, Song. (2007). A Possible biodegradable magnesium implant material, *Adv. Eng. Mater.*,9, 4, 298-302,ISSN 1527-2648.
- Staiger., M.P; Pietak., A.M, Huadmai; Dias., J, G. (2006). Magnesium and its alloys as orthopedic biomaterials. *Biomaterials*, 27,8,17-28, ISSN 0142-9612
- Ulrike Diebold. (2003) . The surface science of titanium dioxide. *Surf. Sci. Rep.* 48, 5-8., 53-229, ISSN 0167-5729.
- Wang, H.X.; S.K., Guan; X., Wang; et al. (2010). In vitro degradation and mechanical integrity of Mg-Zn-Ca alloy coated with Ca-deficient hydroxyapatite by the pulse electrodeposition process. *Acta Biomaterialia*. 6, 5,1743-1748, ISSN 1742-7061
- Wei, M.; A.J., Ruys; Swain, M.V.; Kim, S.H.;Mithorpe, B.K.; Sorrell, C.C. (1999). Interfacial Bond Strength of Electrophoretically Deposited Hydroxyapatite Coatings on Metals. *Journal of Materials Science: Materials in Medicine*. 10, 7,401-409,ISSN 0957-4530.
- Wen, C.L; S.K., Guan; L.,Peng; C.X., Ren; et al. (2009). Characterization and degradation behavior of AZ31 alloy surface modified by bone-like hydroxyapatite for implant applications. *Applied Surface Science*. 255, 13-14, 6433-6438, ISSN 0169-4332.
- Witte, F.; H, Ulrich; et al.(2007). Biodegradable magnesium scaffolds: Part I: appropriate inflammatory response. *J. Biomed. Mater. Res. A*, 81, 4, 748-756, ISSN 1549-3296.
- Witte, F.; V., Kaese; H., Haferkamp; et al.(2005). In vivo corrosion of four magnesium alloys and the associated bone response, *Biomater.*, 26,17, 3557-3563, ISSN 0142-9612.
- Witte, Frank; et. al. (2008). Degradable biomaterials based on magnesium corrosion. *Current Opinion in Solid State and Materials Science*, 12,5-6, 63-72, ISSN: 1359-0286.

Yamasaki, Y; Yoshida, Y; Okazaki, M; Shimazum, A; Uchida, T; Kubom T; et al. (2002).
Synthesis of functionally graded MgCO₃ apatite accelerating osteoblast adhesion. *J Biomed Mater Res*, 62, 1,99-105, ISSN 0021-9304.

Electroless and Electrochemical Deposition of Metallic Coatings on Magnesium Alloys

Critical Literature Review

Massimiliano Bestetti and Anna Da Forno

Politecnico di Milano

Dipartimento di Chimica, Materiali e Ingegneria Chimica "G.Natta"

Via Mancinelli 7, Milano 20131

Italy

1. Introduction

A critical review pertaining to surface treatments on magnesium alloys was published in 2002 (Gray & Luan, 2002). Two years later, another review paper on the same subject was published (Natarajan et al., 2004). According to the authors of both reviews, only complex and multilayer coatings are able to produce optimum results in term of corrosion and wear protection of magnesium alloys, and a great deal of research has to be done furthermore to develop technically and economically viable coating systems.

One of the main challenges in the plating treatments of magnesium alloys is their susceptibility to corrosion. A way to prevent corrosion is by providing a barrier between the metal substrate and the environment. A coating has to be uniform, adherent, pore and crack free, and self-healing in the applications where damage of the coating can occur. The high reactivity of magnesium alloys causes the formation of a natural oxide when the metal is in contact with air and water. A treatment process for cleaning and removal of these oxides, that are unfavourable for coatings adhesion, is necessary before any electroplating and electroless plating treatment.

The electrochemical and electroless depositions of coatings on magnesium alloys demand significant technical requirements. In fact, magnesium is subjected to corrosion in acidic aqueous environments and is only partly protected by an hydroxide layer that forms at pH higher than 9-10. Moreover, the most widely used commercial alloys, i.e. AZ91D and AM60B, contain alloying elements which form intermetallic phases (Fig. 1a). From an electrochemical point of view those phases have different behavior when the alloy is immersed into a solution for plating or chemical treatment. This means that the surface must be made equipotential by modifying the metallurgical structure before the coating process or by a specific surface pretreatment. Lunder reported that the corrosion potential of β -Mg₁₇Al₁₂ phase in 5% NaCl saturated with Mg(OH)₂ is approximately -1.2 V vs. SCE, whereas the values for pure Mg and AZ91 are -1.66 V and -1.62 V vs SCE, respectively (Lunder et al., 1989). The heterogeneous structure of the alloys affects their corrosion resistance behavior and has a strong influence on the behavior of the alloy in the aqueous treatments processes, such as electroless and electrochemical depositions, and chemical conversions. A successful electroless or

electrochemical deposition process depends greatly on metallurgical process of fabrication. Casting defects, such as porosity, incomplete mold filling and flash, can make magnesium alloys difficult to plate (Bellemare, 2010).

2. Electroless plating

2.1 Introduction

Electroless plating consists in the deposition of a coating from a solution of metallic salts and reducing agents and, as consequence of the chemical and autocatalytic nature of the process, uniform layers are deposited onto the substrates irrespective of their shape. Most important electroless coatings are nickel based coatings (EN), which are used as protective layers against wear and corrosion of the substrate. Electroless Ni-P coatings on magnesium are usually preferred to the electrodeposited ones because of the corrosion resistance and the uniformity of the coatings on complex shapes. The corrosion potential E_{corr} of Ni-P alloys becomes more noble with increasing phosphorus content. Recently, the treatment has been performed successfully on wrought magnesium alloys such as AZ31B, AE42 and ZRE1 previously coated by a zinc layer. An improvement in corrosion resistance of the magnesium alloys is achieved especially after heat treatment, typically at 400°C for 1 hour.

Xiang published a paper on the state of the surface after the pretreatment stages (alkaline cleaning + chromate acid etch + fluoride activation) and a second paper on the initial mechanism of EN plating on AZ91D alloy from carbonate bath (Xiang et al., 2001 and 2001b). Electroless nickel deposition nucleates preferentially on β -phase and according to the authors the initial stage of deposition is due to a galvanic coupling between β -phase and eutectic structure and primary α -phase. The electrons produced by the anodic dissolution of magnesium from the α -phase are consumed by the cathodic deposition of nickel on β -phase. The absence of phosphorus in the region of nucleation supports the galvanic displacement mechanism, i.e. the initial deposition is not a process involving hypophosphite. They showed also that different F/O ratios due to different pretreatments followed by direct EN deposition result in different deposition rates, higher in the case of a lower F/O ratio. Similar results on initial mechanism of EN nucleation on AZ91D alloy were reported by Ambat using similar plating procedure (Fig. 1) (Ambat and Zhou, 2004).

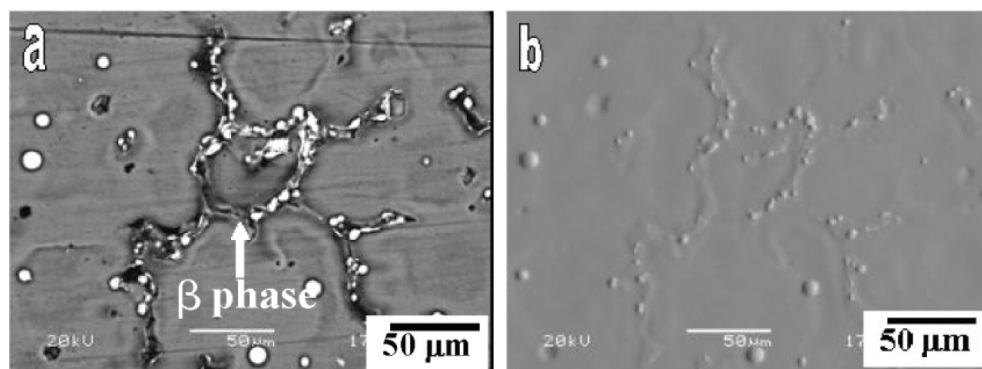


Fig. 1. Initial stages of nickel growth on AZ91 alloy (after 1 min): a) secondary and (b) topographic mode (Ambat & Zhou., 2004).

2.2 Surface preparation

After surface cleaning in alkaline solutions followed by surface etching in solutions of chromates and fluorides, or phosphates and fluorides, the magnesium alloys are generally plated with a zinc layer, referred also as zinc transition layer, obtained by immersion in alkaline zincate solutions. However, zinc transition layers obtained by immersion are too thin, therefore a double-zincate treatment is performed (Kushner, 2009) or a compact film can be produced by electroplating a second zinc layer on the single-zincate layer. With a double-zincate process zinc layer has a better coverage of the magnesium surface as the crystal grains are finer and adhesion is improved. Chen recently proposed a new galvanizing process that eliminates the need to deposit a layer of copper, and it is based on the deposition of a zinc film by immersion followed by the deposition of a layer of electroplated zinc (Chen et al., 2006). The addition of FeCl_3 salts to the zincate bath helped to change the zinc crystal structure and then the coverage and adhesion of the zinc layer (Fig. 2).

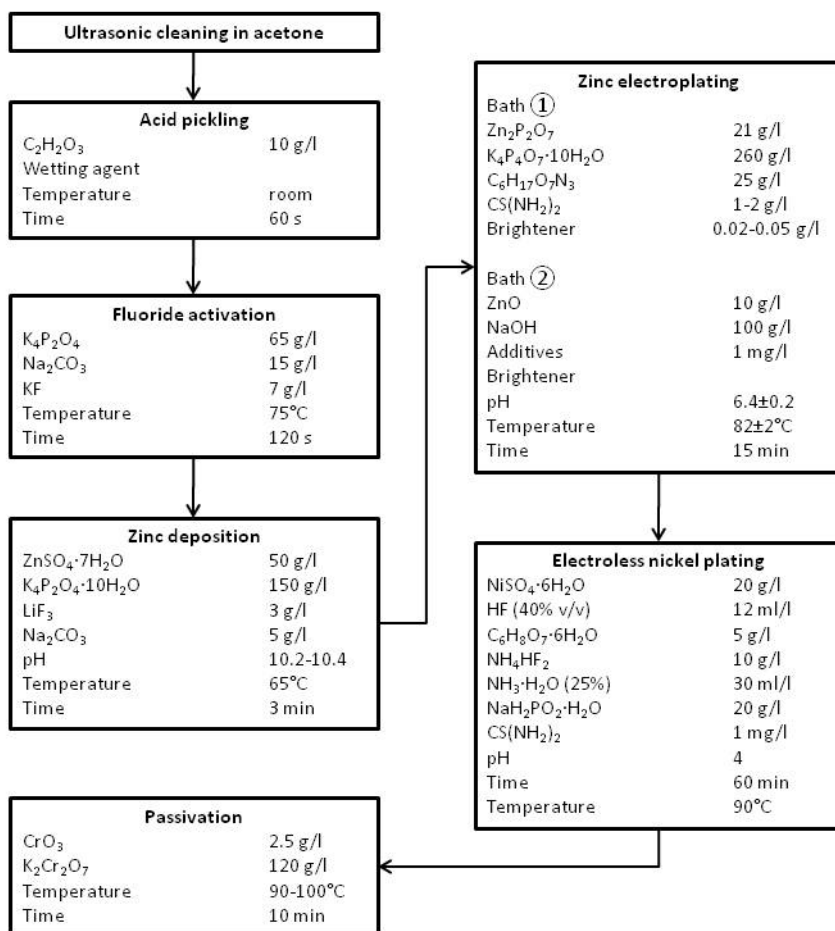


Fig. 2. Flowchart of the overall procedure for coating on the AZ91D magnesium alloy (Chen et al., 2006).

Before the electroless plating or the electrodeposition on magnesium alloys, a copper strike layer, usually cyanide bath, is electrodeposited on zinc layer in order to provide a uniform coverage. Yu studied the deposition (displacement + electrodeposition) of copper from a pyrophosphate solution over a zinc transition layer deposited from pyrophosphate solution (Yu et al., 2005).

In another study, a protective copper film on AZ31 magnesium alloy, without zinc pretreatment, was proposed. The aqueous solution containing 0.4M $\text{Na}_4\text{P}_2\text{O}_7$ + 0.08M $\text{Cu}_2\text{P}_2\text{O}_7$ + 0.24M CuSO_4 + 0.05M NaF was used. A galvanic displacement reaction occurs between copper and magnesium, then copper film is formed on magnesium substrate. After that, electroplating is carried out applying direct current and pulse current using the same copper solution.

Yang proposed a procedure in which a copper layer is deposited onto AZ91D, by immersion plating, before EN plating. The solution was optimized in term of temperature, pH and fluoride content by searching the maximum coverage (Yang et al., 2005, 2005b, and 2006). Ultrasonication was found effective in improving the copper immersion coating process, particularly during extended deposition times, beyond the initial stages (Yang et al., 2005c). Higher coverage of magnesium alloy surface (> 80%) by copper immersion coating were also achieved by using an alkaline bath. The procedure proposed by Yang is schematically represented in Fig. 3 (Yang et al., 2006).

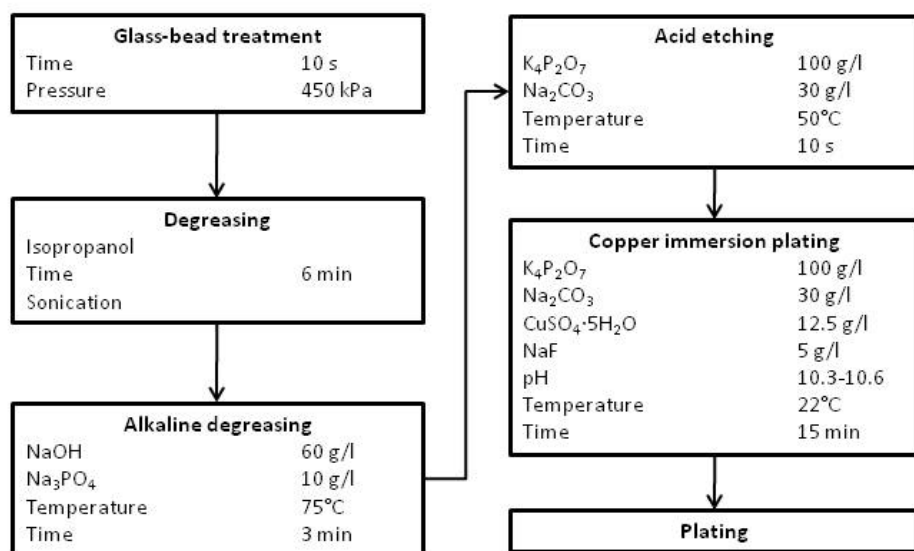


Fig. 3. Flowchart of the procedure for copper immersion coating on the AZ91D magnesium alloy (Yang et al., 2006).

2.2 Substrate morphology

The effect of the magnesium alloy AZ91 microstructure and roughness on the nucleation, deposition rate, coating microstructure, and mechanical properties of the EN coatings was recently investigated (Liu & Gao, 2006). Experimental results show that surface sandblasting pre-treatment ($R_a = 0.05 \mu\text{m}$) enhances the nucleation and coalescence of nickel crystallites.

Authors concluded that the sandblasting reduces the negative effect of microstructural heterogeneity of AZ91 alloy on EN plating, even though it increases the EN coating surface roughness. Moreover, while coating adhesion increases with roughness, wear tests show that the nickel coatings on roughened substrate have higher friction coefficients than those of polished surfaces ($R_a = 0.05 \mu\text{m}$).

2.3 Porosity

The nickel/magnesium system is a typical example of a “cathodic coating on an anodic substrate”. Therefore, the nickel layer provides only a physical barrier against the corrosion attack of magnesium substrate and, for this reason, it must be uniform, adherent and pore free. The assessment of the porosity in a coating deposited onto a magnesium alloy is a major issue in determining the quality of a protective layer. A study on the porosity in EN on AZ91D alloy was recently published (Li et al., 2006). The coated samples are dipped in corrodokote solution (5 ml HCl and 6 g NaCl in 100 ml H₂O) for 5 min, then they are immersed into an indicator solution for 3 min. The conclusion of the study is that eriochrome black T indicator offers more readable color point on filter paper than using magneson and sodium alizarin sulfonate indicators. The optimized solution composition for EN deposition, in relation to porosity assessment, contains sodium hypophosphite and nickel carbonate with a mass ratio equal to 1.75, 25 g/l of fluorides, 1.5 mg/l of thiourea, and 20 g/l of buffering chemicals (sodium acetate or sodium carbonate).

Zou described a way to seal the micropores of EN on magnesium by means of a post-treatment with fluoropolymers. The hardness of the coating reached 600 HV, the coefficient of friction of the coating was less than 0.15 suitable for dry lubrication. The corrosion resistance was also excellent to endure 5% neutral salt spray test for 500 hours (Zou et al., 2005).

2.4 Alternatives to chromate and fluorides pre-treatment

The most difficult part of plating magnesium is the development of an appropriate pre-treatment. There are currently two alternatives to treat magnesium alloys before plating: zinc immersion and a treatment based on chromates etching and conversion with fluorides. Organic coatings are a popular, simple and cost effective mode for protection for metallic objects and structures. The use of an organo-silicon coating as primer has been studied by Zhao et al. as alternative to chromates and fluorides in the pre-treatment of the surface. They proposed a method for protecting AZ31 magnesium alloy using an organic layer as primer and an electroless silver layer (Zhao et al., 2007). In another investigation an electroless copper film was deposited on AZ31 magnesium alloy using organic coatings as interlayer (Fig.5) (Zhao et al., 2008b). The surface of the organic interlayer must be sensitized and activated before electroless deposition. Fig.5 shows the surface and cross-section morphology of the coating. The organic interlayer is uniform and compact and with thickness of about 60 μm . The thickness of the metallic layer is about 7 μm and contains copper (99.5 wt%) and phosphorus (0.5 wt%). Electrochemical measurements in 3.5% NaCl showed that the corrosion potentials (E_{corr} vs SCE) of the AZ31 alloy and copper coated samples are -1569 mV and -1368 mV, respectively.

Electroless nickel-phosphorus layers were also deposited on AZ31 alloy coated with an organic interlayer of about 50 μm (Zhao et al., 2007b, 2008, and 2010). In a study the activation of the organic layer was carried out by means of palladium salts. The Ni-P coating (4 μm after 60 min of deposition) was found to contain 12.3% phosphorus.

Electrochemical measurements in 3.5% NaCl showed that the corrosion potentials (E_{corr} vs SCE) of the AZ31 alloy and copper coated samples are -1569 mV and -1316 mV, respectively (Zhao et al., 2007b).

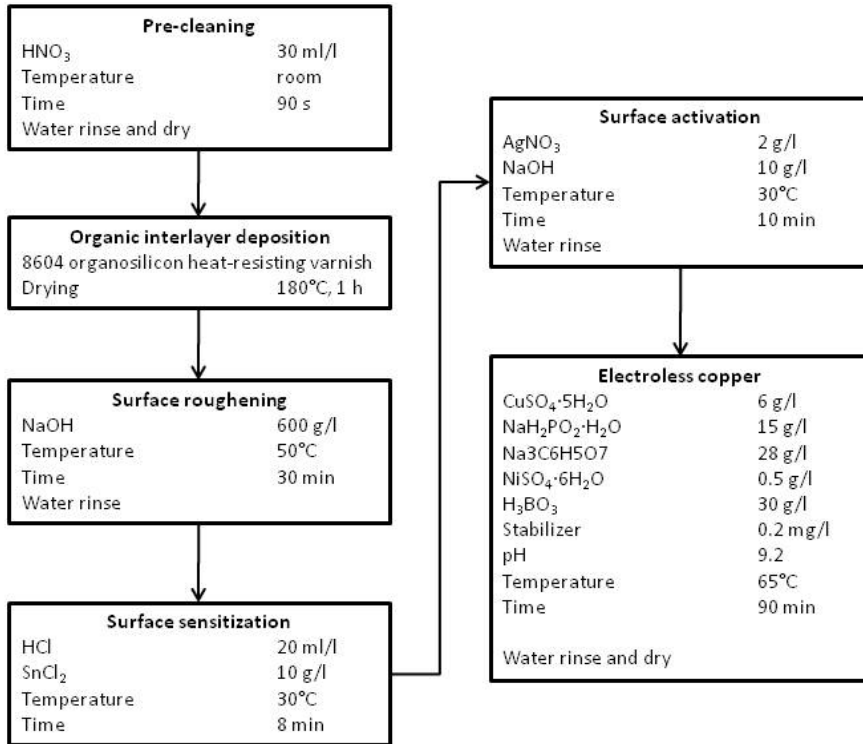


Fig. 4. Flowchart of the organic coating and electroless Cu deposition on the AZ31 magnesium alloy (Zhao et al., 2008). In Zhao et al., 2008b AgNO₃ was reported 12 g/l.

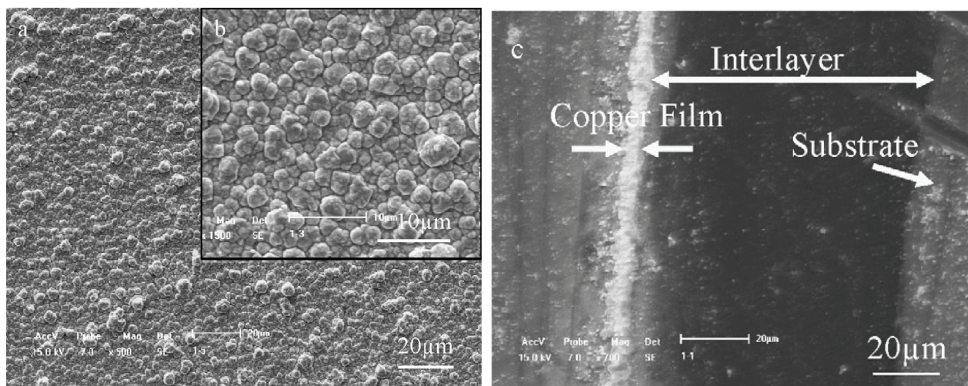


Fig. 5. Surface (a,b) and cross-section morphology (c) of electroless copper (90 min) deposited on AZ31D alloy with an organic interlayer (Zhao et al. 2008).

Electroless Ni-P plating	
$\text{NiSO}_4 \cdot 6\text{H}_2\text{O}$	16 g/l
$\text{Na}_2\text{H}_2\text{PO}_2 \cdot \text{H}_2\text{O}$	16 g/l
$\text{Na}_4\text{P}_2\text{O}_7 \cdot 10\text{H}_2\text{O}$	60 g/l
$\text{NH}_3 \cdot \text{H}_2\text{O}$ (38%)	8 ml/l
Surfactant	20 mg/l
Stabilizer	1 mg/l
pH	9.5
Temperature	50°C

Fig. 6. Electroless Ni-P bath composition and operating conditions (Zhao et al., 2007).

Yang presented the results of a research on EN deposition (8 μm, 4.74% phosphorous) and molybdate conversion film pre-treatment on Mg-8Li alloy (Yang et al., 2009). (Fig.7)

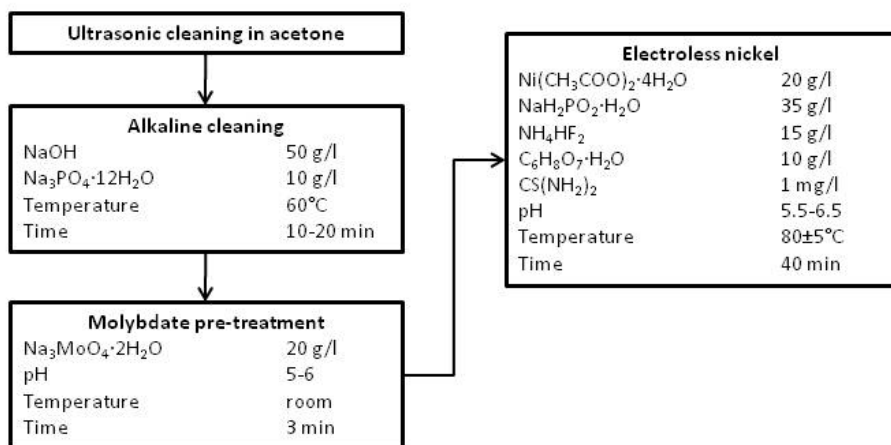


Fig. 7. Flowchart of the molybdate coating and electroless Ni deposition on the Mg-8Li magnesium alloy (Yang et al., 2009).

	E_{corr} (mV vs SCE)	i_{corr} (A cm ⁻²)
Mg-8Li substrate	-1594	1.046×10^{-3}
Molybdate pre-treatment	-1466	1.213×10^{-4}
Ni-P (8 μm)	-1083	2.247×10^{-5}

Table 1. Electrochemical parameters of magnesium substrate, with molybdate pre-treatment and Ni-P coating (in 3.5% NaCl) (Yang et al., 2009).

A phosphate-manganese conversion film was proposed as pre-treatment layer on AZ91D magnesium alloy before EN plating from sulphate bath (Zhang et al., 2007)(Fig. 8). After the pre-treatment, α phase on the substrate was eroded and β phase (Mg₁₇Al₁₂) was exposed on the surface.

According to the authors, both the precipitation of phosphate and manganese and the increase of the volume fraction of β phase may improve the corrosion resistance of the substrate (Table 2).

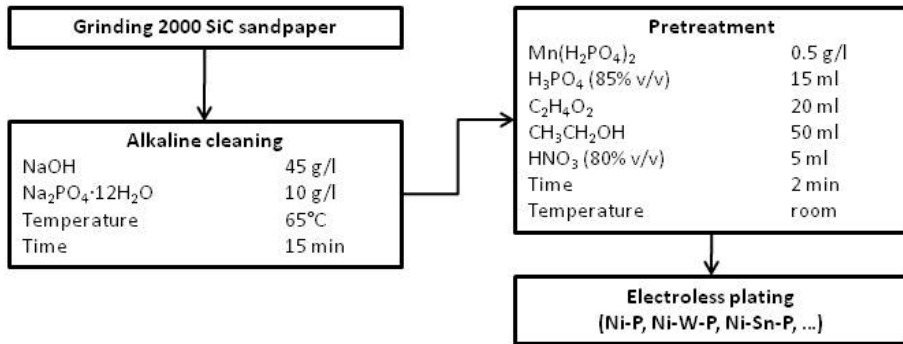


Fig. 8. Flowchart of the manganese-phosphate pretreatment and electroless plating on magnesium alloys (Zhang et al., 2007).

	E_{corr} (mV vs Ag/AgCl)	i_{corr} ($\mu\text{A cm}^{-2}$)
AZ91D	-1502	411.8
Phosphate - manganese pre-treatment	-1442	48.91
Ni-P (~20 μm , 5.6% P)	-599	15.98

Table 2. Electrochemical parameters of magnesium substrate, with phosphate-manganese pre-treatment and Ni-P coating (in 3% NaCl) (Zhang et al., 2007).

A zinc phosphating treatment before EN was proposed by some researchers (Lian et al., 2006). The composition of the phosphating solution is reported in Fig.9. The results show that metal zinc in the conversion coating acts as catalyst for nickel deposition. The addition of Na_2MoO_4 in the phosphating bath resulted in the increase of zinc content in the coating. Denser Ni-P coating were obtained on AZ91D alloy pretreated with a phosphating bath containing 2.0-2.5 g/l Na_2MoO_4 . Salt spray tests showed that the Ni-P coating can withstand for 150 h without corrosion (Lian et al., 2006).

Phosphating solution	
Phosphoric acid	17.5 g/l
Zinc oxide	3.2 g/l
Sodium fluoride	1.7 g/l
Nitroguanidine	0.2 g/l
Tartaric acid	2.2 g/l
Sodium nitrate	2.5 g/l
Sodium molybdate	0-2.5 g/l
pH	2.1-3.3
Temperature	45°C
Time	2-3 min

Fig. 9. Composition and operating conditions of the phosphate solution for AZ91D pretreatment before electroless Ni-P deposition (Lian et al., 2006).

Some authors proposed a double layer coating on magnesium alloys composed by a bottom layer obtained by anodic oxidation and an electroless metallic layer. Liu showed that the

presence of an anodic oxide on the AZ91 substrate provides high density of nucleation sites for nickel plating, resulting in the reduction of porosity of the metallic layer and providing better adhesion strength (Liu & Gao, 2006).

Zeng proposed the plasma electrolytic oxidation in silicate bath followed by electroless Ni-P deposition. The porous inner layer, mainly consisting of MgO and MgSiO₄, was activated in a solution of palladium salt. The electrochemical tests showed that the breakdown potential E_{bd} increased by 1.395 V, i.e. the pitting corrosion resistance was improved greatly in comparison with bare AZ91D alloy (Zeng et al., 2010)(Fig. 10).

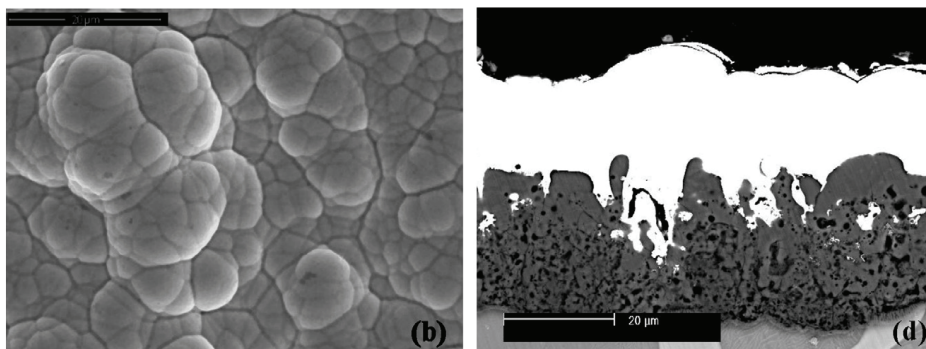


Fig. 10. Surface (left) and cross section (right) morphologies of a double layer coating PEO + EN (Zeng et al., 2008).

An EN plating process was established on the anodized (Dow process) AZ91D alloy that uses TiB₂ powders as catalyst instead of palladium (Sun et al., 2008). The catalytic powder of TiB₂ was mixed with the epoxy resin and curing agent to form a dilute solution with solvent addition. The weight ratio of TiB₂ with organic adhesive was 1.5:1. The anodized specimens were dipped in the solution for a certain time and then lift out to form a thin film on the surface. The specimens were finally cured at 70°C for 30 min. The thickness of catalytic layer film was about 10–15 μm. The deposition rate (10 μm/h) of the new process was close to that of the traditional process but somewhat lower than that of Pd-activation process on PEO film (Fig. 11).

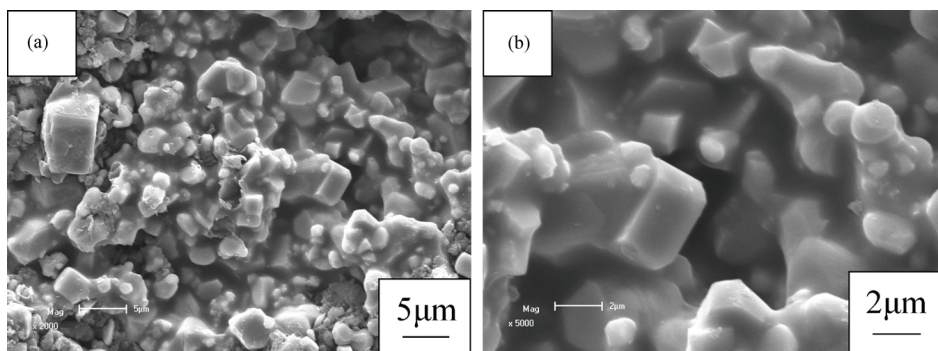


Fig. 11. Surface morphology of the catalytic TiB₂ layer before EN plating at two magnifications (Sun et al., 2008).

Jiang fabricated a composite coating on AZ91 by combining a PEO treatment and electroless copper plating passivated with benzotriazole (Jiang et al., 2010). In the paper the operating conditions are not specified, and it is shown that the composite coating has a positive corrosion potential shift in 5% NaCl solution of 300 mV, and no corrosion pits are visible after 168h of neutral salt spray test. The electroless copper layer adheres to the PEO oxide by mechanical interlocking of the metal in the oxide pores.

2.5 Ternary electroless coatings

The traditional nickel-plating baths are acidic with sulphate being the main salt. However, magnesium is readily corroded in acid solutions. For this reason Zhang investigated an alkaline bath for the deposition of Ni-W-P coatings. (Zhang et al., 2007b).

After grinding with 2000 SiC paper, the magnesium substrate was cleaned in 10% sodium hydroxide solution for 15 min to remove soils or greases on the surface and thoroughly rinsed with water to remove alkaline compounds. Then, the magnesium alloy sample was treated for 2 min in a bath where H_3PO_4 and $Mn(H_2PO_4)_2$ are the main ingredients to obtain a conversion film. The bath composition and operation parameters for the electroless Ni-W-P deposition are listed in Fig. 12.

Electroless Ni-W-P plating	
$NiSO_4 \cdot 6H_2O$	15 g/l
Na_4WO_4	10 g/l
$Na_2H_2PO_2 \cdot H_2O$	20 g/l
Na_4CO_3	20 g/l
$Na_3C_6H_5O_7 \cdot 2H_2O$	40 g/l
NH_4HF_2	8 g/l
$CS(NH_2)_2$	1 mg/l
pH	9
Temperature	$80 \pm 2^\circ C$

Fig. 12. Electroless Ni-W-P bath composition and operating conditions (Zhang et al., 2007b).

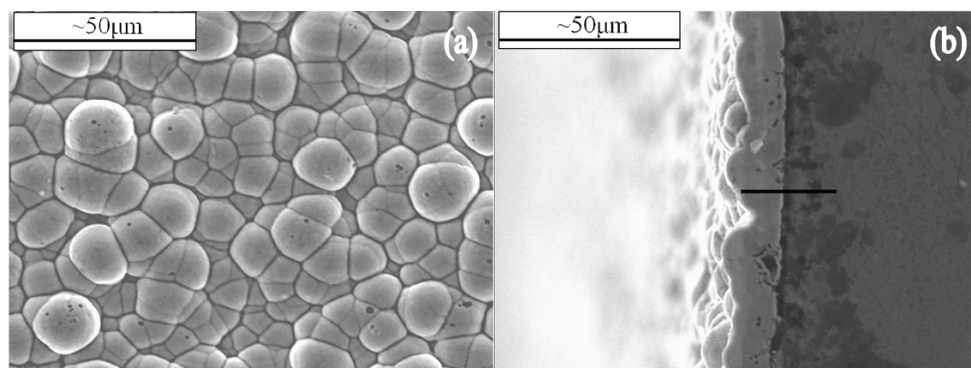


Fig. 13. Surface (a) and cross-section morphology (b) of the electroless Ni-W-P coating (Zhang et al., 2007).

Codeposition of the tungsten resulted in ternary Ni-W-P coating with phosphorus content of 4.9 wt.% and tungsten content of 4.5 wt.%. The hardness of the as-deposited Ni-W-P coating is about 660 VHN, which is higher than that of the as-deposited Ni-P coating with similar phosphorus (5.6 wt.%) content on magnesium alloy (approximately 580 HV) and far higher than that of the AZ91D magnesium alloy substrate (about 100 HV).

The porosity test, acid immersion test and electrochemical measurements (Table 3) reveal that the presence of tungsten and the dense and pore-free microstructure make the coating suitable for corrosion resistance applications. The same researchers published a paper on electroless ternary Ni-Sn-P (Zhang et al., 2008).

Electroless Ni-Sn-P plating	
NiSO ₄ ·6H ₂ O	15 g/l
Na ₂ SnO ₃ ·3H ₂ O	4 g/l
Na ₂ H ₂ PO ₄ ·H ₂ O	20 g/l
Na ₃ C ₆ H ₅ O ₇ ·2H ₂ O	80 g/l
NH ₄ HF ₂	15 g/l
CS(NH ₂) ₂	1 mg/l
pH	9±0.2
Temperature	90±2°C

Fig. 14. Electroless Ni-Sn-P bath composition and operating conditions (Zhang et al., 2008).

The ternary Ni-Sn-P coating grow at a rate of 6 μm/h, with phosphorus content of 8.51 wt.% and tin content of 2.48 wt.%. The hardness of the as-deposited Ni-Sn-P coating is about 670 HV. Due to the presence of tin in Ni-P, the porosity is low and the coating is compact.

	E _{corr} (mV vs Ag/AgCl)	i _{corr} (μA cm ⁻²)
AZ91D substrate	-1502	411.8
Ni-W-P (24 μm, 4.5% W, 4.9% P)	-701	7.809
Ni-Sn-P (25 μm, 2.48% Sn, 8.51% P)	-645	5.29
Ni-P (28 μm, 4.9% P)	-781	17.79

Table 3. Electrochemical parameters of magnesium substrate, with Ni-W-P, Ni-Sn-P and Ni-P coating (in 3% NaCl) (Zhang et al., 2007 and 2008).

2.6 Composites

Codeposition of ceramic, polymer, metal or other particles dispersed within a metal matrix can provide an increase of the properties such as wear and corrosion resistance, hardness, and self-lubricating behaviour.

Song investigated the corrosion properties of an electroless coating Ni-P-ZrO₂. The corrosion resistance of this coating has been demonstrated higher than that of Ni-P because of the effect of zirconia (diameter 20 nm). The greater corrosion resistance is due to a moderate anodic dissolution of Ni-P-ZrO₂ owing to the reduction of the active surface due to the presence of the inert ZrO₂ nanoparticles (Song et al., 2007). According to the authors Ni-P-ZrO₂ coatings are better in term of corrosion resistance in respect to Ni-P coatings, but in strong corrosive environment, the single Ni-P-ZrO₂ coatings cannot provide enough protection to the magnesium alloys substrate, therefore multilayer coatings have been proposed.

Electroless deposition of Ni-P-B₄C composite coating has been performed onto AZ91 alloy, and the micro hardness was higher than that of Ni-P of the same thickness (50 μm), but the presence of B₄C particles (diameter 1.5 μm) reduced the corrosion resistance. The cause is attributed to the presence of micro-cracks in the composite coatings. The pin-on-disc test showed that Ni-P-B₄C coating had better wear resistance than Ni-P coating (Araghi and Paydar, 2010)(Fig. 15).

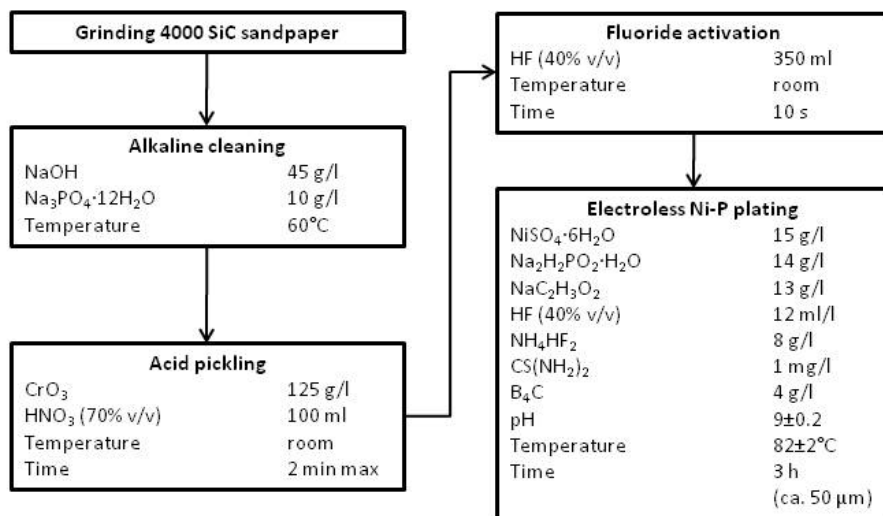


Fig. 15. Composition and operating conditions of the electroless Ni-P-B₄C composite coating on AZ91D magnesium alloy (Araghi and Paydar, 2010).

	E_{corr} (mV vs Ag/AgCl)	i_{corr} ($\mu\text{A cm}^{-2}$)	HV _{50g,15s} (MPa)
AZ91D substrate	-1636	350	100
Ni-P (50 μm)	-808	7	700
Ni-P-B ₄ C (50 μm)	-1031	84	1200

Table 4. Electrochemical parameters of magnesium substrate, with Ni-P coating or Ni-P-B₄C coating (in 3% NaCl). Last column lists the microhardness values in MPa (Araghi and Paydar, 2010).

Fig. 16 shows the weight loss as a function of distance for both substrate alloy AZ91D and 50 μm-thickness Ni-P-B₄C composite coating obtained from a pin-on-disc test (load 10 N, disk rotation speed 0.06 m s⁻¹, distance 500 m).

A recent paper is about a composite coating on AZ91D alloy with electroless nickel coating as bottom layer and electrodeposited Ni-TiO₂ as top layer. The mean nominal diameter of TiO₂ particles was 10 nm and the TiO₂ content in the composite coatings amounted to 2.2±0.2 wt.% (Zhang et al., 2010)(Fig. 17).

The double layer structure improves corrosion resistance and mechanical protection of the AZ91D alloy compared with single electroless nickel coating (Table 5).

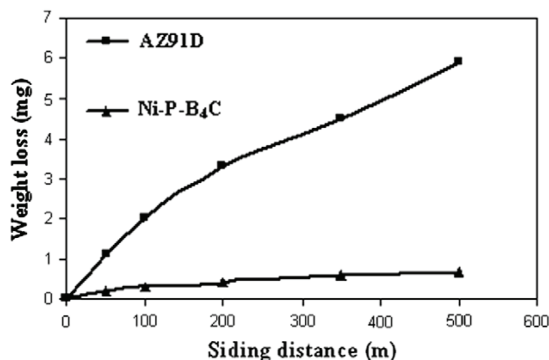


Fig. 16. Weight loss as a function of distance for both substrate and 50 μm thickness Ni-P-B₄C composite coating obtained from pin-on-disc test (Araghi and Paydar, 2010).

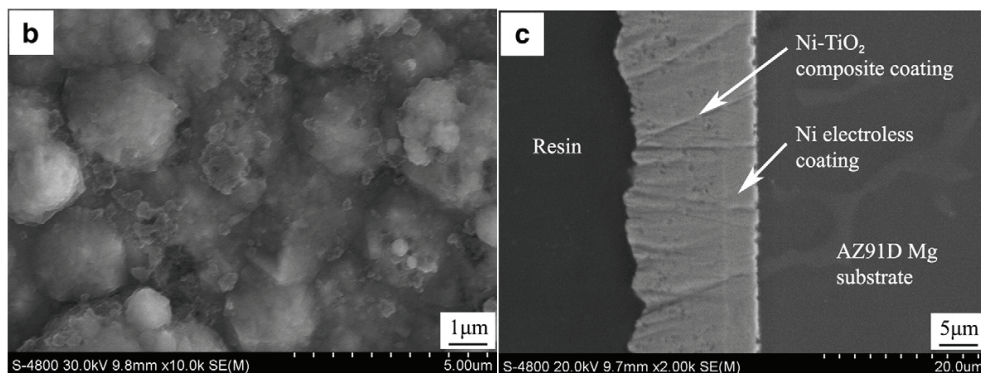


Fig. 17. Surface and cross section morphology of EN and electrodeposited Ni-TiO₂ coatings (Zhang et al., 2010).

	OCP (mV vs SCE)	E _{corr} (mV vs SCE)	i _{corr} (μA cm ⁻²)	Corrosion rate (mm y ⁻¹)	HV _{100g,15s}
AZ91D substrate	-1585	-1491	10.80	0.11	78
Electroless nickel coating	-514	-464	0.96	0.01	145
Ni-TiO ₂ composite coating	-251	-325	0.44	5.18e-3	445

Table 5. Electrochemical parameters of magnesium substrate, with EN coating and double layer EN + EDP Ni-TiO₂ coating (in 3.5% NaCl). Last column lists the microhardness values.

Electroless nickel deposited onto magnesium alloys increases the corrosion resistance and also the wear resistance. In addition, micro and nanoparticles can be codeposited into the electroless nickel matrix in order to improve hardness and friction coefficient. Table 6 shows the wear rate (Taber Wear Index, TWI) of some substrates and coatings.

Ishihara evaluated the corrosion fatigue resistance of AZ31 alloy plated with EN (24 μm, 8% P), polished and glass bead-blasted (Ishihara et al., 2008). In laboratory air, the effect of surface treatments on the fatigue lives of specimens was found to be minimal. However, in 3% NaCl solution, the EN-plated specimens were found to have shorter fatigue lives than

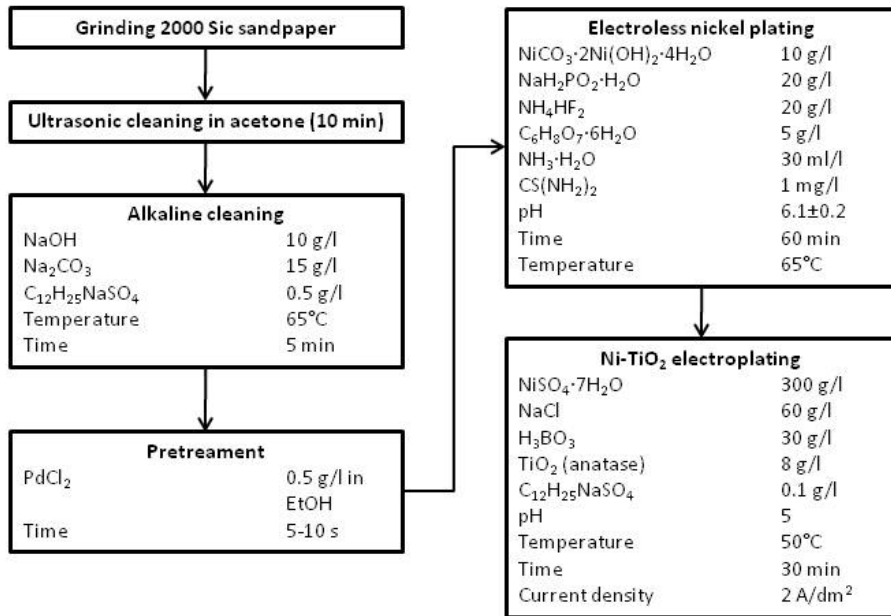


Fig. 18. Composition and operating conditions of the electroless Ni coating and Ni-TiO₂ composite coating on AZ91D magnesium alloy (Zhang et al., 2010).

	TWI (mg/1000 cycles)
AZ91D	49.98
Al 356	13.77
Electroless nickel	13.95
Hard chrome	0.9

Table 6. Wear data of some substrates and coatings (Shahin, 2001).

those of the polished and blasted specimens. Their electroless Ni-P coatings were characterized by compressive stresses, but the experimental data indicate that those are not sufficient to increase the fatigue life of EN. According to the authors, aggressive components infiltrate from the deposition solution through the pores of the Ni-P coating arriving to the interface between substrate and coating, and leading to pits formation. A crack initiates at the bottom of the pit and leads to the failure of the sample (Fig. 19).

A similar study was recently carried out by Ishihara on corrosion fatigue resistance of AZ31 alloy electroplated with a 20 µm thick multilayer coating of copper, semi gloss nickel, gloss nickel and chromium top layer. The crack initiation and the propagation behavior of both coated and uncoated specimens were also investigated to estimate the effect of the multilayer coating.

Experimental observations lead to conclude that two kinds of crack initiation mechanism occur. The cracks initiated from depressions on the surface or from depressions at the interface between the substrate and copper layer. The authors conclude that the fatigue life

of Ni plated specimens could be improved by eliminating surface and interface depressions produced during the electrodeposition, which are sites of stresses concentration and therefore responsible for cracks formation (Fig. 20).

EP Ni-P coatings are hardened by thermal treatment at high temperature to transform the crystal structure from amorphous to crystalline. As a consequence of the treatment, cracks form in the coating thus exposing the magnesium alloy substrate to corrosion.

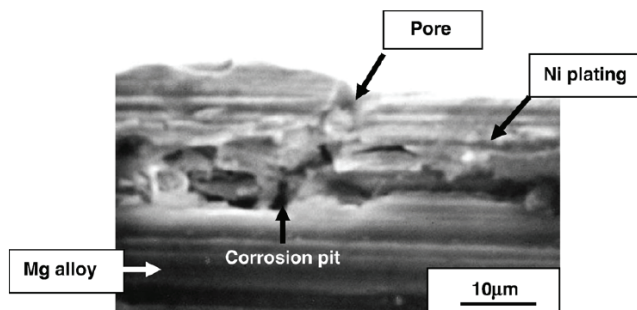


Fig. 19. Cross section of the electroless Ni plated specimen, tested and interrupted during fatigue in sodium chloride solution (Ishihara et al., 2008).

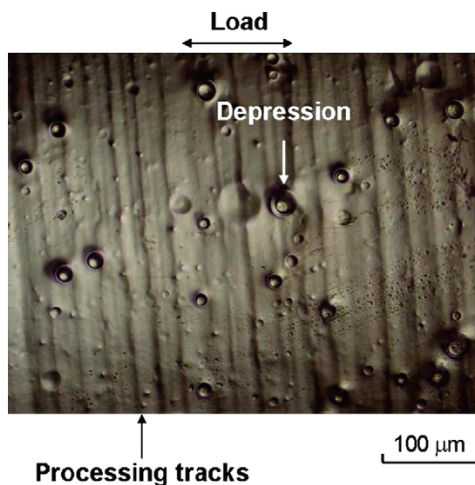


Fig. 20. Optical micrograph of the plated surface (Cu, Ni semi-gloss, Ni gloss, Cr; 20 μm). (Ishihara et al., 2010).

3. Electroplating

3.1 Introduction

Among surface treatments of magnesium, metal electrodeposition is considered as one of the most effective ways to produce corrosion and wear resistant coatings. Magnesium is a very reactive metal and electroplated metal coatings, such as copper, nickel, zinc and chromium act as physical barrier to prevent corrosion attack of the substrate. Magnesium is

classified as a difficult to plate metal due to the extreme corrosion attack on magnesium substrates by aqueous electrolyte, high reactivity that quickly forms poor immersion layers on the surface by galvanic displacement. Because of these layers, the subsequent electrochemical deposition is inhibited and it's equally hindered by the rapid formation of magnesium oxide/hydroxide films.

Process	Solution compositions	Operating conditions
(1) Alkaline cleaning		
NaOH	50 g/l	60±5°C
Na ₃ PO ₄ ·12H ₂ O	10 g/l	10-15 min
OP emulgator	3 ml/l	
(2) Acid pickling A		
CrO ₃	125 g/l	T room
HNO ₃ (68%)	110 ml/l	30 s - 1 min
(2) Acid pickling B		
H ₃ PO ₄ (85%)	605 ml/l	T room
HNO ₃ (68%)	30 ml/l	40 s
(2) Pickling activation C		
Na ₃ PO ₄ ·12H ₂ O	100 g/l	T room
H ₃ PO ₄	30 g/l	1-9 min
KMnO ₄	20 g/l	pH 4-5
Additives		
(3) Activation A		
HF (40% v/v)	385 ml/l	20°C 10 min
(3) Activation B		
K ₄ P ₄ O ₇ ·3H ₂ O	76 g/l	75°C
Na ₂ CO ₃	15 g/l	2 min
KF·2H ₂ O	7 g/l	
(4) Zinc immersion		
ZnSO ₄ ·7H ₂ O	50 g/l	65°C
K ₄ P ₄ O ₇ ·3H ₂ O	175 g/l	70 s for AZ91D
Na ₂ CO ₃	5 g/l	150 s for AM60B
KF·2H ₂ O	10 g/l	

Fig. 21. Pretreatment solutions and operating conditions (Lei et al., 2010).

Electroplated coatings are generally comprised of a sequence of layers. There is no a single galvanic layer that protects the magnesium alloy but a sequence of layers. Cibis (Cibis et al., 2010) observed in pilot plant tests that corrosion resistance in the salt spray chamber of AZ91D and AM Lite alloys improves significantly by making a vibro finish pre-treatment before the deposition of a nickel layer from sulphamate bath in place of the deposition of copper (cyanide and then acid). This is important if pores and cracks are present in the magnesium alloys and become exposed or enhanced as a consequence of the chemical surface preparation. The operation of vibratory finishing allows to "close" the cracks and defects, thereby facilitating the adhesion of galvanic coatings.

The authors of a recent paper consider electrodeposition on magnesium alloys more advantageous compared with electroless nickel plating, in term of lower production cost, higher coatings thickness, lower porosity, better corrosion resistance and higher production efficiency (Lei et al., 2010). Pretreatment and pre-plating stages are critical for a protective coating system and in their paper they describe three pre-plating processes, i.e. Ni-P alloy, Ni and Cu as interlayers on industrial components (AZ91D engine shell and AM60B wheel hub) of magnesium alloys using different pretreatments before electrodeposition of Cu/Ni/Cr coatings from cyanide free solutions.

Before any pre-plating stage, the following process sequence was used: alkaline cleaning, pickling, activation and zinc immersion. Fig. 21 shows the solutions composition and the operating conditions for the above mentioned pretreatment processes.

Process	Solution compositions	Operating conditions
(1) Electroless nickel-phosphorus		
NiSO ₄ ·6H ₂ O	20 g/l	70°C
HF (40%)	12 ml/l	pH 5.5. – 7.0
NH ₄ HF ₂	10 g/l	
Na ₂ H ₂ PO ₂ ·H ₂ O	20 g/l	
NH ₃ ·H ₂ O (25%)	30 ml/l	
CS(NH ₂) ₂	1 mg/l	
Ligands (3)		
(2) Nickel plating		
NiSO ₄ ·6H ₂ O	110-130 g/l	45-55°C,
F ⁻	1.0-1.5 mol/l	2.0-3.5 A/dm ² (pref. 3.0)
Buffer agent		Time 15-20 min (pref. 20)
		pH 4.8-5.4
(3) Copper plating		
Cu ₂ P ₂ O ₇	60 g/l	45°C
K ₄ P ₄ O ₇ ·3H ₂ O	300 g/l	0.8-2 A/dm ² (pref. 1.5)
(NH ₄) ₃ C ₆ H ₅ O ₇	25 g/l	Time 20 min

Fig. 22. Compositions and operating conditions of electroless nickel-phosphorus, nickel electroplating and copper electroplating solutions (Lei et al., 2010).

Among the different possibilities to pretreat the magnesium alloys before electroless Ni-P deposition, the authors suggest the following sequence: alkaline cleaning, acid pickling A, activation A, electroless nickel plating (Fig. 22). Electrodeposited nickel can be used as intermediate layer instead of EN. The pretreatment before Ni electrodeposition consists of: alkaline cleaning, acid pickling B, activation B, zinc immersion, Ni electrodeposition (Fig. 22). A third preplating procedure was proposed by the authors: alkaline cleaning, acid pickling activation C, zinc immersion, Cu electrodeposition from pyrophosphate solution (Fig. 22).

Because of the good adhesion and enhanced corrosion resistance, these coatings play a role of improved protection for these substrates.

Electroless Ni-P for both even and complex shapes, electrodeposited nickel and electrodeposited copper are suitable interlayers between the magnesium substrate and Cu/Ni/Cr composite multilayers, as they provide good adhesion and corrosion resistance (see Table 7 for corrosion potentials in 3.5% NaCl solution).

	E_{corr} (mV vs SCE)
AZ91D	-1510
AM60B	-1530
Electroless Ni-P	-682
Electroplated Ni	-832
Electroplated Cu	+63.2

Table 7. Electrochemical parameters of magnesium substrates, with different pre-plating layers in 3.5% NaCl (Lei et al., 2010).

3.2 Dual coatings

Gu (Gu et al., 2005 and 2006) proposed a combination of a nickel electroless intermediate layer plus an electrodeposited layer of nanocrystalline nickel to obtain high corrosion resistance with good wear resistance on magnesium AZ91D (Fig.23).

To date only zinc and nickel have been directly plated onto magnesium and have been used as intermediate layer before the subsequent metal deposition. Cu-Ni-Cr plating is useful for many applications in indoor and in mild outdoor. The pretreatments currently used for magnesium alloys are zinc immersion and electroless nickel plating from a fluoride containing bath. A zinc layer by galvanic displacement is usually deposited onto magnesium alloys before a strike of copper from cyanide bath and multilayer electrodeposited coatings, typically Cu-Ni-Cr. In the papers and patents about this process, it is stressed that magnesium alloys with an aluminium content greater than 6-7% are difficult to treat and the deposit is not satisfactory. Nickel electroless plating has been proposed instead of zinc immersion treatment for AZ91 alloy. It was found that electroless nickel coating shows a good adherence on AZ91D magnesium alloy after pre-treatment and excellent properties including corrosion resistance and conductivity, therefore it's an excellent interlayer for electrodeposition (Jia et al., 2007).

Recently, a galvanostatic etching followed by copper electrodeposition from the same alkaline bath has been proposed as a pretreatment of AZ31 alloy surface (Huang et al., 2008). After a mechanical grinding of the surface, the alloy is anodically etched at 25 mA cm⁻² for 500 s in the bath used for copper electrodeposition, i.e. an alkaline solution of copper sulfate. The layer of copper was deposited at constant plating charge of 24 C cm⁻². As shown in Fig. 24 the copper layer is quite uniform and the coverage of the alloy is complete. The interface between the copper layer and the magnesium alloy is dense and pore-free, and free of any oxide or hydroxide-rich interlayer.

Such pre-treatment was used as basis for depositing multilayer coatings on magnesium alloys such as those shown in Fig. 25 (Huang et al., 2008, 2008b and 2010).

Zhu proposed a protective multilayer coating process on AZ91D alloy schematized in the flowsheet in Fig. 26 (Zhu et al., 2006). In this process a final thermal treatment in air is performed in order to improve the adhesion of the coating to the substrate. After thermal treatment, tin diffused through the zinc layer and reached the magnesium alloy, where it formed the compound Mg₂Sn.

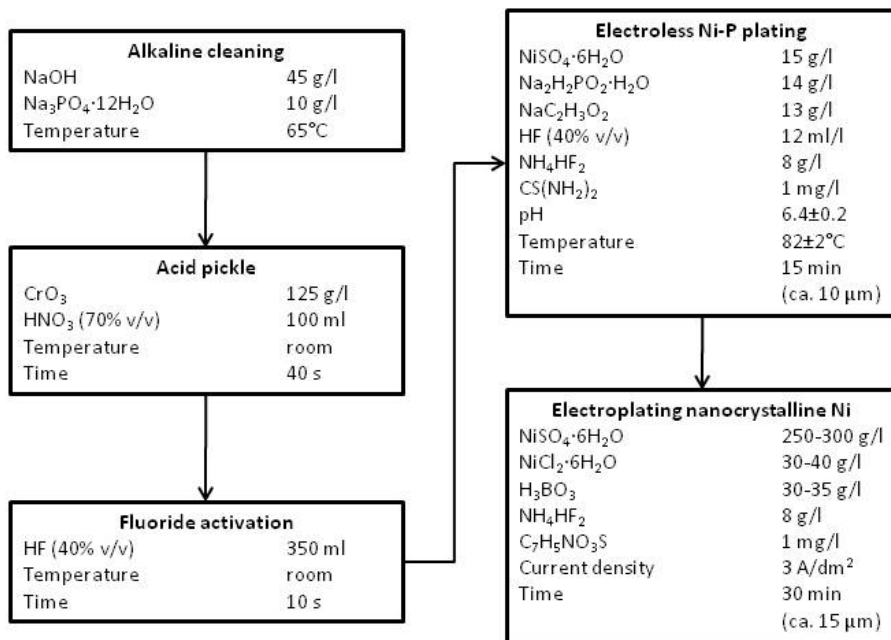


Fig. 23. Flowchart of the electroless Ni and electroplated nanocrystalline Ni on the AZ91D magnesium alloy (Gu et al., 2005 and 2006).

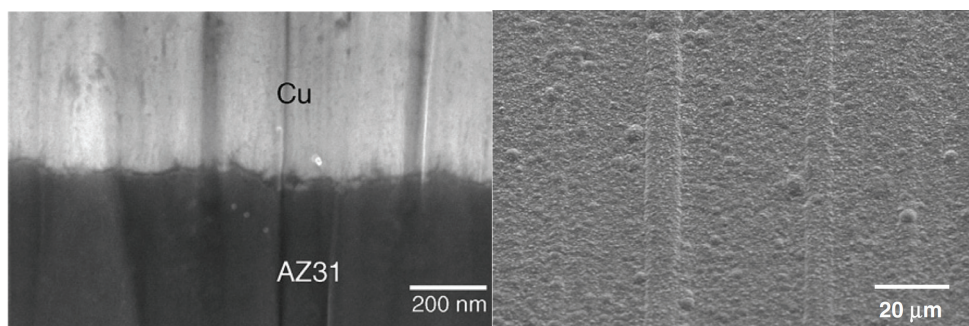


Fig. 24. SEM surface morphology of copper plated AZ31 alloy (left). Interface between the AZ31 alloy and electrodeposited copper layer (right). (Huang et al., 2008).

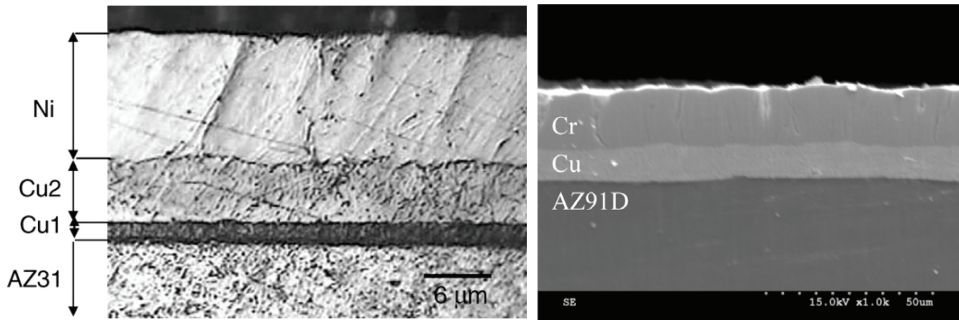


Fig. 25. Cross section morphologies of multilayer coatings on magnesium alloys. Left: Cu1 / Cu2 / Ni on AZ31 (Huang et al., 2008). Right: Cu / Cr in AZ91D (Huang et al., 2010).

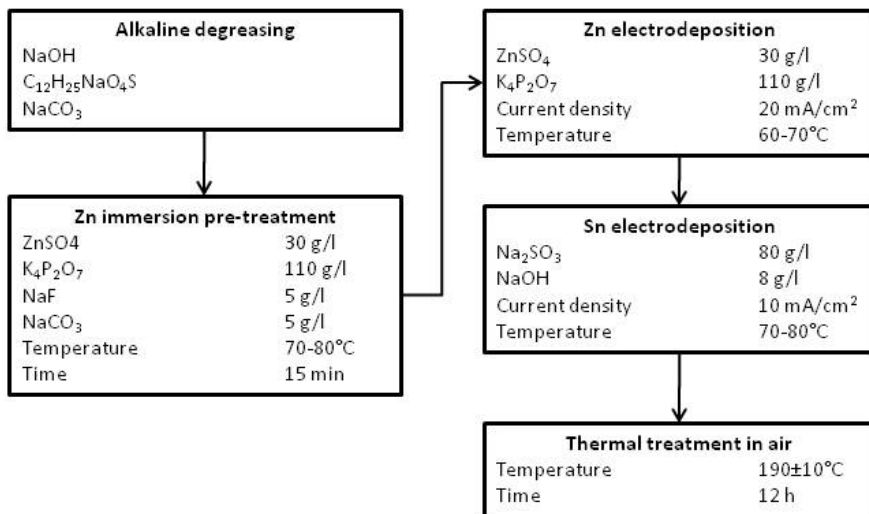


Fig. 26. Flowchart of the zinc and tin electroplating process on the AZ91D magnesium alloy (Zhu et al., 2006).

The coating has a three layers structure, shown in Fig. 27. A bottom layer, compact and pore free Sn and Mg₂Sn layer, formed by reaction of Mg and Sn; a middle layer, Zn and ZnO, formed by electroplating; an upper, loose and porous Sn layer formed by electroplating. The authors demonstrated that such three-layer structure provides better corrosion protection for the AZ91D alloy in comparison to the as plated Zn-Sn alloy without thermal treatment.

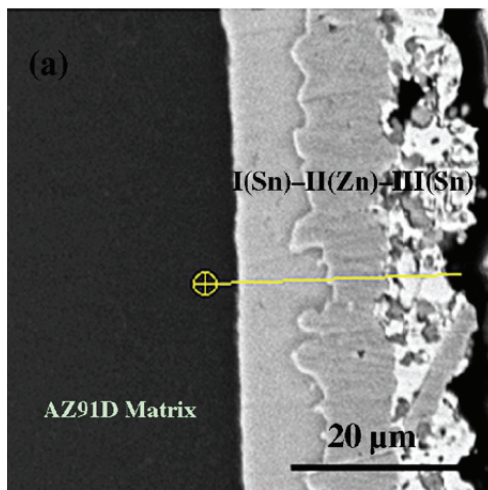


Fig. 27. Cross-section image of the Zn-Sn plated coating on AZ91D alloy after thermal treatment at 190°C for 12 h (Zhu et al., 2006).

3.3 Alloys electrodeposition from aqueous solutions

The pulse plating of Zn-Ni coatings on AZ91 alloy was investigated by Jiang (Jiang et al., 2003, 2005 and 2005b) for protecting the alloy from corrosion. The process is schematized in Fig. 28. Zinc-nickel coatings have anticorrosion properties when the content of Ni is 12-14% due to the presence of the intermetallic phase $Zn_{12}Ni_5$. The pulse electrodeposition induces a high rate of nucleation and the coating structure has a grain refined structure. The thickness of Zn-Ni layers increases almost linearly along with the increase of both deposition time and electric current density while there is no obvious relationship between the thickness of Zn-Ni layers and the value of t_{on} / t_{off} . The Ni content in Zn-Ni coating generally increases with both electric frequency and electric current density and increases with t_{on} / t_{off} firstly and then decreases. The maximum value of Ni content is about 18% when t_{on} / t_{off} is about 30%. The microhardness of Zn-Ni coatings also increases with the increase of processing time, electric current density, electric frequency and mostly with the increase of t_{on} / t_{off} (140 - 240 HV).

Fig. 29 shows a typical cross section and surface morphology of a coating composed by a zinc layer of about 4 μm , a Zn-Cu layer of about 8 μm and a Zn-Ni layer of about 20 μm . Some microvoids can be observed at the interface between Zn-Cu and Zn-Ni layers.

More recently, a paper on Zn-Ni electroplating on AZ91D was published (Abdel Aal, 2008). Prior the deposition of the Zn-Ni coating, AZ91D substrate was treated in Zn(II) containing solution and then in a phosphate-permanganate solution to facilitate the adhesion of the Zn-Ni external layer (Fig. 30).

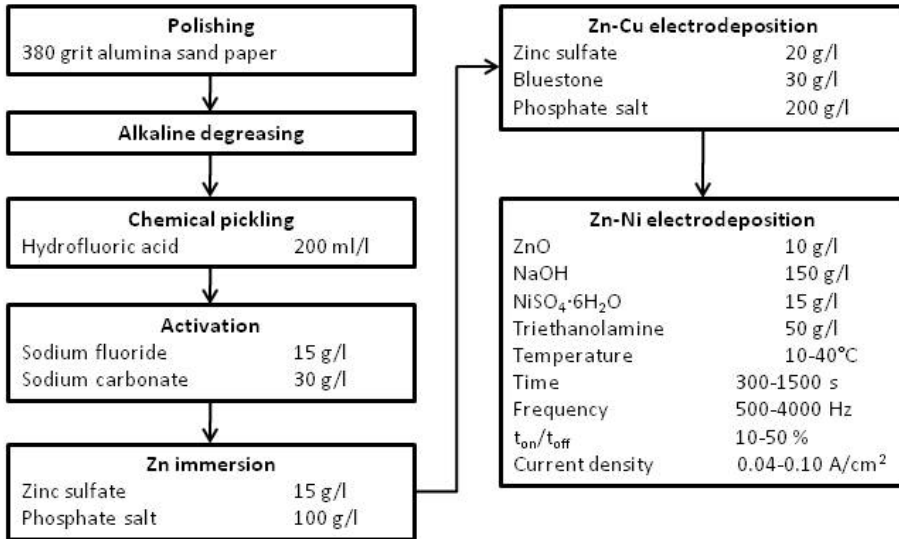


Fig. 28. Flowchart of the Zn-Ni electroplating process on the AZ91D magnesium alloy (Jiang et al., 2005b).

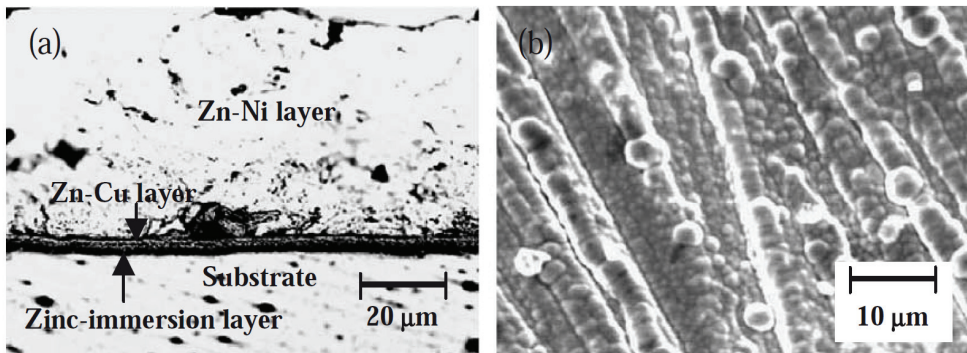


Fig. 29. Optical cross section (left) and SEM surface morphology (right) of a Zn / Zn-Cu / Zn-Ni coating (Zn-Ni: 600 s, 1 kHz, t_{on}/t_{off} 10%, 0.04 A/cm²). (Jiang et al., 2005b).

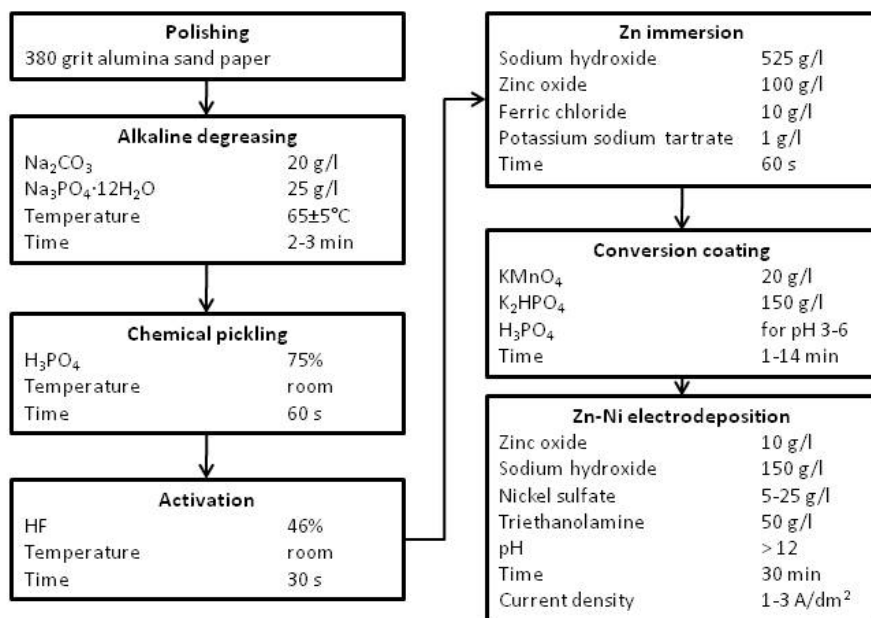


Fig. 30. Flowchart of the Zn-Ni electroplating process on the AZ91D magnesium alloy (Abdel Aal, 2008).

Fig. 31 displays the surface morphology of the coating obtained at a current density of 3 A/dm². When the Zn-Ni coating is exposed to corrosive environments, zinc dissolves preferentially leaving an external layer enriched with nickel, that acts as a barrier to further attack. The higher corrosion resistance is obtained for the alloy containing 13 wt.% Ni, and this could be explained by the lower porosity of the coating and its single γ -phase structure and hence the absence of local microgalvanic cells between different phases.

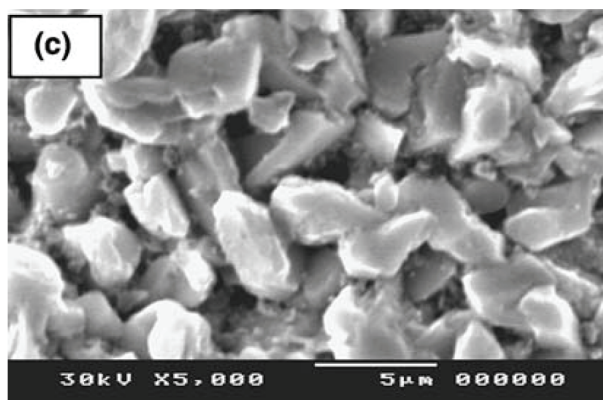


Fig. 31. SEM images of AZ91D Mg alloy coated with Zn-Ni at current density 3 A/dm². (Abdel Aal, 2008).

	E_{corr} (mV vs Ag/AgCl)	i_{corr} (A cm ⁻²)
Substrate AZ91D	-1685	5.6×10^{-4}
Phosphate - permanganate	-1635	5.1×10^{-5}
Zn - 13% Ni	-1515	5.8×10^{-5}

Table 8. Electrochemical parameters of magnesium substrate, with phosphate-permanganate and Zn-Ni coating (in 3.5% NaCl) (Abdel Aal, 2008).

3.4 Non-aqueous electroplating

Magnesium alloys are sensitive to aqueous environment and thus non-aqueous processes have been proposed for metal plating on magnesium alloys. The electrodeposition of zinc onto magnesium alloys from two types of ionic liquid, stable in air and in the presence of water, was recently proposed (Bakkar and Neubert, 2007). One type of ionic liquid is obtained by mixing (ratio 1:2) choline chloride (ChCl), as amine salt ($\text{HOC}_2\text{H}_4\text{N}(\text{CH}_3)_3^+\text{Cl}^-$), with a hydrogen bond donor such as urea (NH_2CONH_2), ethylene glycol ($\text{HOCH}_2\text{CH}_2\text{OH}$), malonic acid ($\text{HOOCCH}_2\text{COOH}$), or glycerol ($\text{HOCH}_2\text{CH}(\text{OH})\text{CH}_2\text{OH}$). The other type is formed by mixing ChCl with a metal halide. The water content in the ionic liquid was in the range 3.5-7.2%. The electrodeposition solutions were prepared by dissolving 0.5 M of ZnCl_2 in the ionic liquid at 90°C. The magnesium substrates used for electrodeposition were: cp Mg, AZ31, AZ61, AZ91, AS41, AE42, WE43-T6, QE22, MgGd5Sc1 and MgY4Sc1.

The electrochemical tests showed that magnesium has the best corrosion resistance behavior in ChCl/urea 1:2 and therefore ionic liquids were suggested to test the possibility of electroplating magnesium alloys. Successful electrodeposition of metallic zinc layers onto Mg-RE alloys free of Al was obtained while the other ionic liquids produced either powdery deposits or corrosion of the substrate. Pulsed current produced uniform, shiny and dense deposits free of defects (Fig. 32). Potentiodynamic polarisation tests in 0.1M NaCl showed that the zinc deposited by pulsed current densities exhibits a corrosion behaviour similar to that of pure zinc (Table 9).

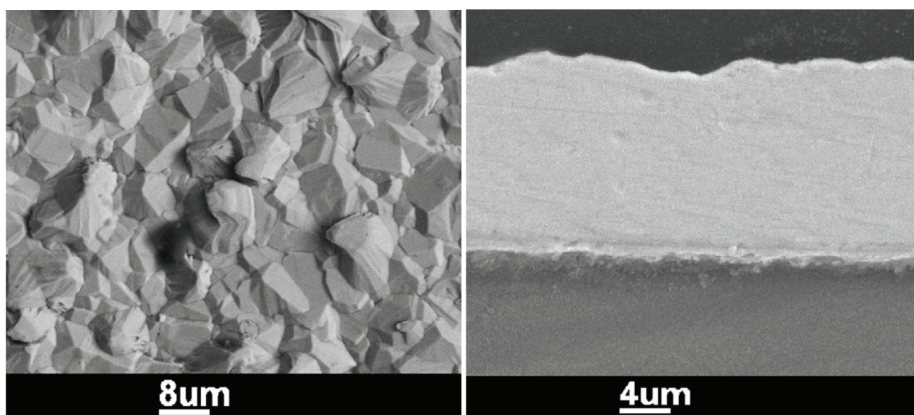


Fig. 32. SEM surface (left) and cross section (right) micrographs of electrodeposited Zn onto WE43 Mg alloy from ChCl/urea + 0.5M ZnCl_2 at $\text{CD} = 5 \text{ mA/cm}^2$, $T = 60^\circ\text{C}$. Pulsed current (2 s on-time, 1 s off-time).

	E_{corr} (mV vs SCE)	i_{corr} ($\mu\text{A cm}^{-2}$)
WE43 substrate	-1705	14.67
Zinc coating on WE43 (pulsed)	-1129	1.38
Zinc sheet	-1006	1.89

Table 9. Electrochemical parameters of zinc sheet, WE43 alloy and Zn coating on the magnesium alloy (0.1 M NaCl) (Bakkar and Neubert, 2007).

Several papers on Al (Chang et al., 2007, 2008 and 2008b) and Al-Zn (Pan et al., 2010) electrodeposition from EMIC (1-ethyl-methylimidazolium chloride) has been recently published. In the electrodeposition of aluminium on AZ91D, a solution of AlCl_3 -EMIC (1.5:1) was prepared and handled in a glove box under nitrogen atmosphere, in which the moisture and oxygen content were maintained below 1 ppm. Before electrodeposition, each sample was ground with SiC paper to 1000 grit. Electrodeposition tests were carried out both at constant potential (-0.2 V and -0.4 V vs Al wire) (Chang et al., 2007) and at constant current density (Chang et al., 2008). The surface and cross-section morphologies of the sample produced at -0.2 V are shown in Fig. 33. On the contrary, samples deposited at -0.4 V were less compact, with nodular microstructure and cracks.

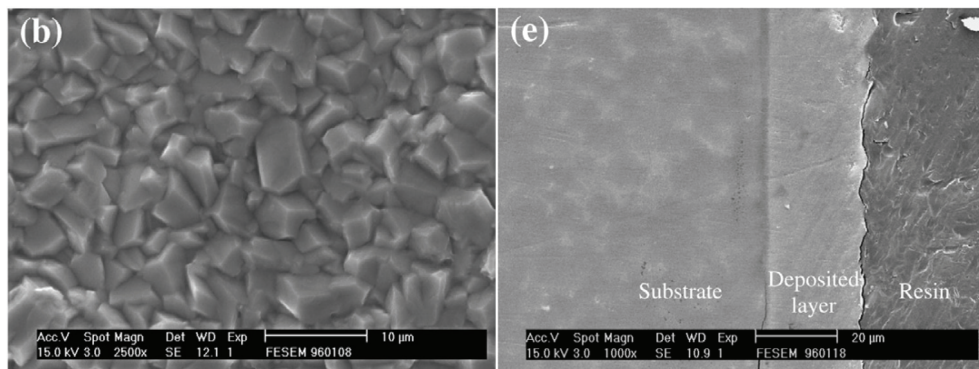


Fig. 33. SEM surface (left) and cross section (right) micrographs of electrodeposited Al onto AZ91D alloy from AlCl_3 -EMIC at -0.2 V vs Al wire for 2550 s (5 C) at 25°C (Chang et al., 2007).

Experimental results show that aluminium coatings give satisfactory protection for the AZ91D alloy against corrosion (Fig. 34). The deposition current density is the factor that controls the coating properties and the corrosion resistance of the Al layer deposited. In fact, a lower deposition rate results in a more uniform and compact coating layer and also thicker and, consequently, give rise to a better performance for corrosion protection.

Pan demonstrated the possibility of plating thick coatings of Al-Zn alloys on AZ91D substrate from AlCl_3 -EMIC (60:40 molar ratio) ionic liquid containing 1wt.% ZnCl_2 (Pan et al., 2010). The zinc content in the coating can be controlled in the range 20-100% by varying the potential of deposition. Uniformity in the coating composition was obtained when the deposition was performed at -0.2 V vs Al.

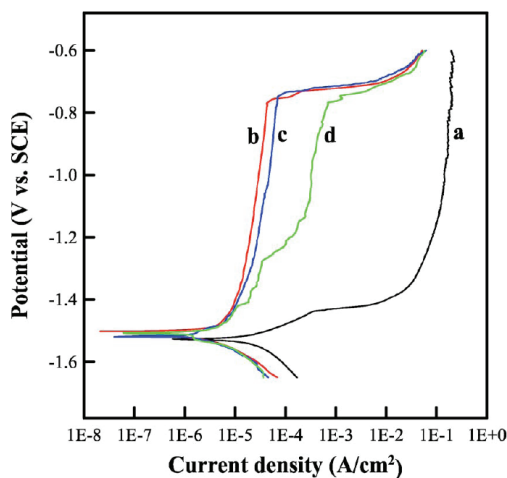


Fig. 34. Polarization curves of AZ91D alloy (a) and Al-deposited Mg electrodes (b -15, c -20, and d -40 mA/cm²) in 3.5% NaCl at 25°C (Chang et al., 2008).

The effects of different acid pickling processes on the adhesion between the AZ91D magnesium alloy substrate and aluminum coatings electrodeposited from the acid AlCl₃-EMIC room temperature molten salts were studied by Qian (Qian et al., 2009). The results show that the aluminum coating is not dense and the adhesion between the coatings and substrate is not good after mechanical pretreatment on AZ91D substrate. Dense and uniform coatings can be electrodeposited on the AZ91D substrate after hydrofluoric acid pickling. The density of coatings and the adhesion can be improved simultaneously by using diluted phosphoric acid as pickling solution, and thus, the coating provides good protection to the substrate.

The electrodeposition of Al-Mn coatings on AZ31B magnesium alloy was investigated by Zhang (Zhang et al., 2009). Experiments were carried out by using molten AlCl₃-NaCl-KCl-MnCl₂ at 170°C. The substrate was pre-plated with a zinc layer (5 μm) as interlayer to prevent corrosion during Al-Mn deposition in molten salts. The addition of MnCl₂ to the molten bath results in compact coatings. The coating of Fig. 35 (right) has a content of Mn of about 22.5 %. By increasing the Mn content in the coating, the structure change from partly crystalline (Fig. 35 left) to amorphous (Fig. 35 right). Table 10 lists the electrochemical parameter obtained from corrosion tests (Al-Mn coating thickness of about 16 μm).

Corrosion resistance of magnesium alloys can be improved by addition of rare earth elements. Recently the electrodeposition of Mg-Yb alloy film on magnesium from molten LiCl-KCl-YbCl₃ (2wt.%) at 500°C under argon atmosphere was investigated by Chen (Chen et al., 2010). A thin film of about 200 nm of Mg₂Yb was formed at -1.85 V (vs Ag/AgCl) for 12 h, and a film of about 450 nm was obtained at -2.5 V for 2.5 h.

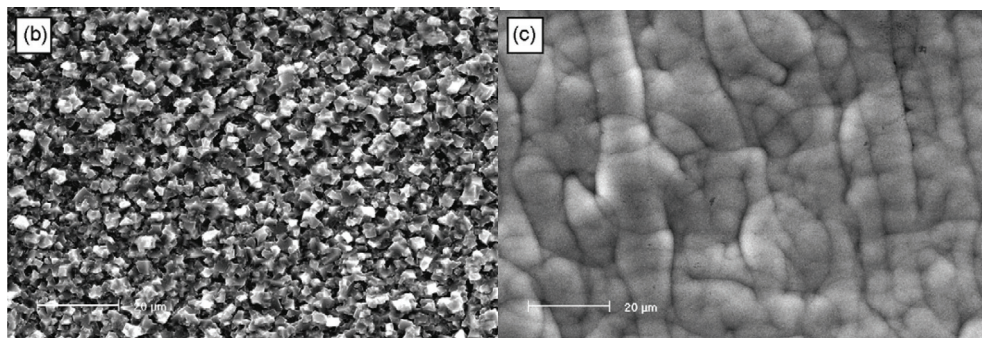


Fig. 35. SEM surface morphologies of Al-Mn coatings from molten salts with various MnCl₂ content (left 0.5%, right 1%) (Zhang et al., 2009).

	E_{corr} (mV vs SCE)	i_{corr} (A cm ⁻²)
AZ31B	-1523	1.60×10^{-5}
Zn layer	-1463	2.02×10^{-4}
9.2 Mn	-1276	5.15×10^{-5}
22.7 Mn	-1271	2.89×10^{-7}
25.4 Mn	-1162	2.59×10^{-8}
29.3 Mn	-713	3.71×10^{-9}

Table 10. Electrochemical parameters of different specimens in 3.5% NaCl) (Zhang et al., 2009).

4. Conclusions

The review on the scientific literature on coatings deposited by electroless and electroplating processes shows that magnesium alloys are difficult to plate substrates. However, processes based on metal deposition by electroless and electrodeposition are used and a great deal of research is done in order to develop environmentally friendly processes. The problem of electroless and electroplating magnesium alloys can be solved by using complex schemes, that combine surface preparation procedures with multilayer coating systems.

5. References

- Abdel Aal, A. (2008). Protective coating for magnesium alloy. *Journal of Materials Science*, Vol.43, No.8, pp.2947-2954, ISSN: 0022-2461.
- Ambat, R. & Zhou, W. (2004). Electroless nickel-plating on AZ91D magnesium alloy: Effect of substrate microstructure and plating parameters. *Surface and Coatings Technology*, Vol.179, No.2-3, pp.124-134, ISSN: 0257-8972.
- Araghi, A. & Paydar, M.H. (2010). Electroless deposition of Ni-P-B₄C composite coating on AZ91D magnesium alloy and investigation on its wear and corrosion resistance. *Materials and Design*, Vol.31, No.6, pp.3095-3099, ISSN: 0261-3069.

- Bakkar, A. & Neubert, V. (2007). Electrodeposition onto magnesium in air and water stable ionic liquids: from corrosion to successful plating. *Electrochemistry Communications*, Vol.9, No.9, pp.2428-2435, ISSN: 13882481.
- Bellemare, R. (2009). Magnesium applications abound. Direct EN plating makes it possible. *Products Finishing*, Vol.73, No.5, pp.12-16, ISSN:0032-9940.
- Blawert, C.; Heitmann, V.; Dietzel, W.; Nykyforchyn, H.M. & Klapkiv, M.D. (2005). Influence of process parameters on the corrosion properties of electrolytic conversion plasma coated magnesium alloys. *Surface & Coatings Technology*, Vol.200, No.1-4, pp.68-72. ISSN: 0257-8972.
- Chang, J.K.; Chen, S.Y.; Tsai, W.T.; Deng, M.J.; Sun, I.W. (2007). Electrodeposition of aluminum on magnesium alloy in aluminum chloride ($AlCl_3$)-1-ethyl-3-methylimidazolium chloride (EMIC) ionic liquid and its corrosion behaviour. *Electrochemistry Communications*, Vol.9, No.7, pp.1602-1606, ISSN: 1388-2481.
- Chang, J.K.; Chen, S.Y.; Tsai, W.T.; Deng, M.J.; Sun, I.W. (2008). Improved corrosion resistance of magnesium alloy with a surface aluminum coating electrodeposited in ionic liquid. *Journal of the Electrochemical Society*, Vol.155, No.3, pp.C112-C116, ISSN: 0013-4651.
- Chang, J.K.; Sun, I.W.; Pan, S.J.; Chuang, M.H.; Deng, M.J. & Tsai, W.T. (2008b). Electrodeposition of Al coating on Mg alloy from Al chloride / 1-ethyl-3-methylimidazolium chloride ionic liquids with different Lewis acidity. *Transactions of the Institute of Metal Finishing*, Vol.86, No.4, pp.227-233, ISSN: 0020-2967.
- Chen, J.; Yu, G.; Hu, B.; Liu, Z.; Ye, L. & Wang, Z. (2006). A zinc transition layer in electroless nickel plating. *Surface and Coatings Technology*, Vol.201, No.3-4, pp.686-690, ISSN: 0257-8972.
- Chen, Y.; Ye, K. & Zhang, M. (2010). Preparation of Mg-Yb alloy film by electrolysis in the molten $LiCl-KCl-YbCl_3$ system at low temperature. *Journal of Rare Earths*, Vol. 28, No.1, pp.128-133, ISSN: 1002-0721.
- Cibis, R.; Kielbus, A. & Moskal, G. (2010). Galvanic technology of coating deposition on magnesium alloys, *Proceedings of the 8th International conference on magnesium alloys and their applications*, pp.974-979, ISBN: 978-3-527-32732-4, Weimar (Germany), October 2009, Wiley-VCH, Weinheim.
- Gray, J.E. & Luan B. (2002). Protective coatings on magnesium and its alloys – a critical review. *Journal of Alloys and Compounds*, Vol.336, No.1-2, pp.88-113, ISSN: 0925-8388.
- Gu, C.; Lian, J.; He, J.; Jiang, Z. & Jiang, Q. (2006). High corrosion-resistance nanocrystalline Ni coating on AZ91D magnesium alloy. *Surface & Coatings Technology*, Vol.200, No.18-19, pp.5413-5418, ISSN: 0257-8972.
- Gu, C.; Lian, J.; Li, G.; Niu, L. & Jiang, Z. (2005). Electroless Ni-P plating on AZ91D magnesium alloy from a sulfate solution. *Journal of Alloys and Compounds*, Vol.391, No.1-2, pp.104-109, ISSN: 0925-8388.
- Huang, C.A.; Wang, T.H.; Weirich, T. & Neubert, V. (2008). Electrodeposition of a protective copper/nickel deposit on the magnesium alloy (AZ31). *Corrosion Science*, Vol.50, No.5, pp.1385-1390, ISSN: 0010-938X.

- Huang, C.A.; Wang, T.H.; Weirich, T. & Neubert, V. (2008b). A pretreatment with galvanostatic etching for copper electrodeposition on pure magnesium and magnesium alloys in an alkaline copper-sulfate bath. *Electrochimica Acta*, Vol.53, No.24, pp.7235-7241, ISSN: 0013-4686.
- Huang, C.A.; Lin, C.K. & Yeh, Y.H. (2010). Increasing the wear and corrosion resistance of magnesium alloy (AZ91D) with electrodeposition from eco-friendly copper- and trivalent chromium-plating baths. *Surface and Coatings Technology*, Vol.205, No.1, pp.139-145, ISSN: 0257-8972.
- Ishihara, S.; Notoya, H.; Okada, A.; Nan, Z.Y. & Goshima, T. (2008). Effect of electroless-Ni-plating on corrosion fatigue behavior of magnesium alloy. *Surface and Coatings Technology*, Vol.202, No.10, pp.2085-2092, ISSN: 0257-8972.
- Ishihara, S.; Namito, T.; Notoya, H. & Okada, A. (2010). The corrosion fatigue resistance of an electrolytically-plated magnesium alloy. *International Journal of Fatigue*, Vol.32, No.8, pp.1299-1305, ISSN: 0142-1123.
- Jiang, Y.F.; Guo, X.W.; Zhai, C.Q.; Zhu, Y.P. & Ding, W.J. (2003). The influence of pulse parameters on Zn-Ni alloy coatings plated on AZ91 magnesium alloy. *Transactions of the Institute of Metal Finishing*, Vol.81, No.6, pp.182-185, ISSN: 0020-2967.
- Jiang, Y.F.; Zhai, C.Q.; Liu, L.F.; Zhu, Y.P. & Ding, W.J. (2005). Zn-Ni alloy coatings pulse-plated on magnesium alloy. *Surface and Coatings Technology*, Vol.191, No.2-3, pp.393-399, ISSN: 0257-8972.
- Jiang, Y.F.; Liu, L.F.; Zhai, C.Q.; Zhu, Y.P. & Ding, W.J. (2005b). Corrosion behavior of pulse-plated Zn-Ni alloy coatings on AZ91 magnesium alloy in alkaline solutions. *Thin Solid Films*, Vol.484, No.1-2, pp.232-237, ISSN: 0040-6090.
- Jiang, Y.F.; Bao, Y.F. & Zhang, G.W. (2010). Corrosion protection of composite coating combining ceramic layer, copper layer and benzotriazole layer on magnesium alloy. *Transactions of Nonferrous Metals Society of China (English Edition)*, Vol.20, No.SUPPL. 2, pp.s693-s696, ISSN: 1003-6326.
- Jia, S.Q.; Jia, S.S. & Yao, J. (2007). Electroless nickel-plating on die cast magnesium alloy AZ91D. *Transactions of Nonferrous Metals Society of China*, Vol.17, No.4, pp.866-870, ISSN: 1003-6326.
- Lei, X.P.; Yu, G.; Zhu, Y.P.; Zhang, Z.P.; He, X.M.; Hu, B.N. & Chen, Y. (2010). Successful cyanide free plating protocols on magnesium alloys. *Transactions of the Institute of Metal Finishing*, Vol.88, No.2, pp.75-80, ISSN: 0020-2967.
- Li, J.; Tian, Y.; Huang, Z.; Zhang, X. (2006). Studies of the porosity in electroless nickel deposits on magnesium alloy. *Applied Surface Science*, Vol.252, No.8, pp.2839-2846, ISSN: 0169-4332.
- Li, J.Z.; Huang, J.G.; Tian, Y.W. & Liu, C.S. (2009). Corrosion action and passivation mechanism of magnesium alloy in fluoride solution. *Transactions of Nonferrous Metals Society of China (English Edition)*, Vol.19, No.1, pp.50-54, ISSN: 1003-6326.
- Lian, J.S.; Li, G.Y.; Niu, L.Y.; Gu, C.D.; Jiang, Z.H. & Jiang, Q. (2006). Electroless Ni-P deposition plus zinc phosphate coating on AZ91D magnesium alloy. *Surface and Coatings Technology*, Vol.200, No.20-21, pp.5956-5962, ISSN: 0257-8972.
- Liu, Z. & Gao, W. (2006). Electroless nickel plating on AZ91 Mg alloy substrate. *Surface & Coatings Technology*, Vol. 200, No.16-17, pp. 5087-5093, ISSN: 0257-8972.

- Liu, Z. & Gao, W. (2006b). A novel process of electroless Ni-P plating with plasma electrolytic oxidation pretreatment. *Applied Surface Science*, Vol. 253, No.5, pp. 2988-2991, ISSN: 0169-4332.
- Lunder, O.; Lein, J.E.; Aune, T.K. & Nisancioglu, K. (1989). Role of Mg₁₇Al₁₂ phase in the corrosion of AZ91, *Corrosion*, Vol.45, No.9, pp. 741-748, ISSN: 0010-9312.
- Natarajan S.; Sivan, V.; Tennyson, P.G. & Kiran, V.R. (2004). Protective coatings on magnesium and its alloys - a critical review. *Journal of Corrosion prevention & Control*, Vol.51, No.4, pp.142-163, ISSN: 0010-9371.
- Pan, S.J.; Tsai, W.T.; Chang, J.K. & Sun, I.W. (2010). Co-deposition of Al-Zn on AZ91D magnesium alloy in AlCl₃-1-ethyl-3-methylimidazolium chloride ionic liquid. *Electrochimica Acta*, Vol.55, No.6, pp.2158-2162, ISSN: 0013-4686.
- Qian, H.M.; Li, Y. & Ling, G.P. (2009). Influence of acid pickling on electrodeposition of aluminum on magnesium alloy in room temperature molten salts. *Zhongguo Youse Jinshu Xuebao/Chinese Journal of Nonferrous Metals*, Vol.19, No.5, pp.854-860, ISSN: 1004-0609.
- Song, Y.W.; Shan, D.Y. & Han, E.H. (2007). Comparative study on corrosion protection properties of electroless Ni-P-ZrO₂ and Ni-P coatings on AZ91D magnesium alloy. *Materials and Corrosion*, Vol.58, No.7, pp.506-510, ISSN: 1521-4176.
- Sun, S. Liu, J.; Yan, C. & Wang, F. (2008). A novel process for electroless nickel plating on anodized magnesium alloy. *Applied Surface Science*, Vol.254, No.16, pp.5016-5022, ISSN: 0169-4332.
- Yang, L.; Luan, B. (2005). Copper immersion deposition on magnesium alloy: The effect of fluoride and temperature. *Journal of the Electrochemical Society*, Vol.152, No.7, pp.C474-C481, ISSN: 0013-4651.
- Yang, L.; Luan, B.; Cheong, W.J. & Jiang, J. (2005b). Optimization and performance analysis of copper immersion coating on AZ91 magnesium alloy. *Journal of Coatings Technology Research*, Vol.2, No.6, pp. 493-498, ISSN: 1547-0091.
- Yang, L.; Luan, B.; Cheong, W.J. & Jiang, J. (2005c). Sono-immersion deposition on magnesium alloy. *Journal of the Electrochemical Society*, Vol.152, No.3, pp. C131-C136, ISSN: 0013-4651.
- Yang, L.; Luan, B. & Nagata, J. (2006). Novel copper immersion coating on magnesium alloy AZ91D in an alkaline bath. *Journal of Coatings Technology Research*, Vol.3, No.3, pp.241-246, ISSN: 1547-0091.
- Yang, L.; Li, J.; Zheng, Y.; Jiang, W.; Zhang, M. (2009). Electroless Ni-P plating with molybdate pretreatment on Mg-8Li alloy. *Journal of Alloys and Compounds*, Vol.467, No.1-2, pp.562-566, ISSN: 0925-8388.
- Yang, L.; Li, J.; Zheng, Y.; Jiang, W. & Zhang, M. (2009b). Electroless Ni-P plating with molybdate pretreatment on Mg-8Li alloy. *Journal of Alloys and Compounds*, Vol.467, No.1-2, pp.562-566, ISSN: 0925-8388.
- Yu, G.; Liu, Y.E.; Hu, B.N.; Liu, Z. & Ye, L.Y. (2005). Investigation of electroplating copper in pyrophosphate on magnesium alloy. *Hunan Daxue Xuebao/Journal of Hunan University Natural Sciences*, Vol.32, No.4, pp.77-81, ISSN: 1000-2472.

- Xiang, Y.; Hu, W.; Liu, X.; Zhao, C. & Ding, W. (2001). Initial deposition mechanism of electroless nickel plating on magnesium alloys. *Transactions of the Institute of Metal Finishing*, Vol.79, No.1, pp.27-29, ISSN: 0020-2967.
- Xiang, Y.; Hu, W.; Liu, X.; Zhao, C. & Ding, W. (2001b). Initial deposition mechanism of electroless nickel plating on magnesium alloys. *Transactions of the Institute of Metal Finishing*, Vol.79, No.1, pp.30-32, ISSN: 0020-2967.
- Zeng, L.; Yang, S.; Zhang, W.; Guo, Y. & Yan, C. (2010). Preparation and characterization of a double-layer coating on magnesium alloy AZ91D. *Electrochimica Acta*, Vol.55, No.9, pp.3376-3383, ISSN: 0013-4686.
- Zhang, W.X.; He, J.G.; Jiang, Z.H.; Jiang, Q. & Lian, J.S. (2007). Electroless Ni-P layer with chromium-free pretreatment on AZ91D magnesium alloy. *Surface & Coatings Technology*, Vol.201, No.8, pp.4594-4600, ISSN: 0257-8972.
- Zhang, W.X.; Huang, N.; He, J.G.; Jiang, Z.H.; Jiang, Q. & Lian, J.S. (2007b). Electroless deposition of Ni-W-P coating on AZ91D magnesium alloy. *Applied Surface Science*, Vol.253, No.11, pp.5116-5121, ISSN: 0169-4332.
- Zhang, W.X.; Jiang, Z.H.; Li, G.Y.; Jiang, Q. & Lian, J.S. (2008). Electroless Ni-Sn-P coating on AZ91D magnesium alloy and its corrosion resistance. *Surface & Coatings Technology*, Vol.202, No.12, pp.2570-2576, ISSN: 0257-8972.
- Zhang, J.; Yan, C. & Wang, F. (2009). Electrodeposition of Al-Mn alloy on AZ31B magnesium alloy in molten salts. *Applied Surface Science*, Vol.255, No.9, pp.4926-4932, ISSN: 0169-4332.
- Zhang, S.; Li, Q.; Yang, X.; Zhong, X.; Dai, Y. & Luo, F. (2010). Corrosion resistance of AZ91D magnesium alloy with electroless plating pretreatment and Ni-TiO₂ composite coating. *Materials Characterization*, Vol.61, No.3, pp.269-276, ISSN: 1044-5803.
- Zhao, H. & Cui, J. (2007). Electroless plating of silver on AZ31 magnesium alloy substrate. *Surface & Coatings Technology*, Vol.201, No.8, pp.4512-4517. ISSN: 0257-8972.
- Zhao, H.; Huang, Z. & Cui, J. (2007b). A new method for electroless Ni-P plating on AZ31 magnesium alloy. *Surface & Coatings Technology*, Vol.202, No.1, pp.133-139. ISSN: 0257-8972.
- Zhao, H.; Huang, Z. & Cui, J. (2008). A novel method of electroless plating on AZ31 magnesium alloy sheet. *Journal of Materials Processing Technology*, Vol.203, No.1-3, pp.310-314, ISSN: 0924-0136.
- Zhao, H.; Huang, Z. & Cui, J. (2008b). Electroless plating of copper on AZ31 magnesium alloy substrates. *Microelectronic Engineering*, Vol.85, No.2, pp.253-258, ISSN: 01679317.
- Zhao, H.; Huang, Z.; Li, P. & Cui, J. (2010). A novel method for the preparation of electroless coating on magnesium alloy. *Magnesium Technology*, pp.141-144, 2010, *Magnesium Technology 2010 - TMS 2010 Annual Meeting and Exhibition*, February 14, 2010 - February 18, 2010, Seattle (USA). ISSN: 15454150.
- Zhu, L.; Li, W. & Shan, D. (2006). Effects of low temperature thermal treatment on zinc and/or tin plated coatings of AZ91D magnesium alloy. *Surface and Coatings Technology*, Vol.201, No.6, pp.2768-2775, ISSN: 0257-8972.

Zou, H.Q.; Lu, J.C.; Zhang, J.; Wu, H.C. & Fang, M. (2005). Synergistic fluoropolymer coating on magnesium alloys. *Materials Science Forum*, Vol.488-489, pp.673-676, Magnesium - Science, Technology and Applications, Mg - Proceedings of the International Conference on Magnesium - Science, Technology and Applications, ISSN: 0255-5476.

Corrosion Protection of Magnesium Alloys by Cold Spray

Julio Villafuerte¹ and Wenyue Zheng²

¹*CenterLine (Windsor) Ltd., Windsor, Ontario*

²*CANMET-MTL, Hamilton, Ontario
Canada*

1. Introduction

Magnesium is the lightest of all structural metals, being 35% lighter than aluminum and 78% lighter than steel. As a constituent of many minerals, it represents about 2% of mineral deposits and 0.13% of seawater. The lightweight characteristics, high strength-to-weight ratio and wide availability make magnesium alloys ideal for production of weight-sensitive components such as those in aircraft, cars, light trucks, and other transportation modes.

Ever since the extraction of magnesium from its ores was made possible in commercial quantities by 1920, magnesium alloys have been employed to manufacture components in racing cars. In the 1930's the popular Volkswagen Beetle started using magnesium castings. Later in the 60's, there was a surge in the use of magnesium castings in military aircraft [1], particularly rotorcraft in order to further reduce weight while improving performance. By 1971, over 18 kilograms of the metal had been installed in the Beetle's powertrain.

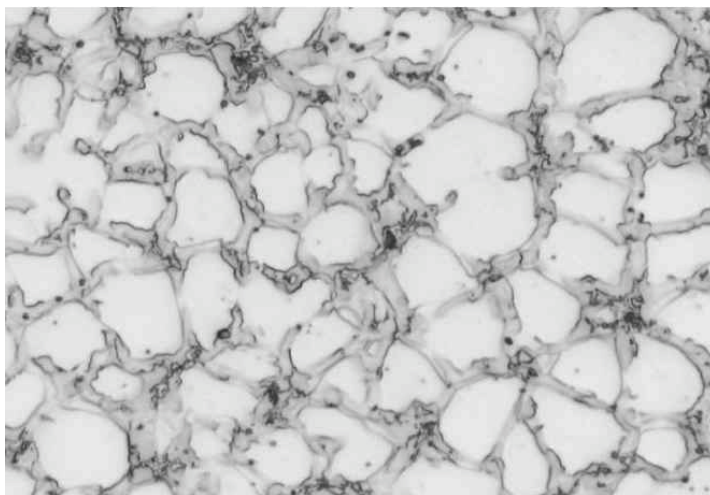


Fig. 1. Corrosion damage in magnesium AM60 alloys showing the preferential attack on the primary (alpha) phase leaving a network of Al-rich beta-phase on the corroded surface.

However, when all vehicles are considered, the percentage of magnesium alloys used in mass-produced vehicles is relatively low, with an average of less than 5 Kg in a typical vehicle. The main reasons for the reluctance to use magnesium in mass-produced vehicles are related to its limitations in corrosion resistance and high temperature (creep) performance. Pure magnesium readily reacts in the presence of oxygen and water producing magnesium hydroxide. Unlike other similar metals, such as aluminum, the passivation film on magnesium could become very unstable in many environments, including neutral or acid ranges of pH. Additionally, magnesium is anodic to most engineering metals, making it very prone to severe galvanic corrosion when coupled with dissimilar metals, such as steel.

Over the years, there have been significant advances in alloy development and as a result, new improved magnesium alloys have become commercially available. This has been possible due to additions of aluminum, zinc, manganese, for better corrosion resistance as well as additions of zirconium, rare earths, thorium, and silver for better elevated temperature mechanical properties all, in combination with the reduction of harmful impurities such as iron, nickel, copper during the alloy making process.

In recent years, the demand for lighter, more fuel-efficient vehicles, has spurred increased interest by automakers to consider the use of magnesium in more critical components such as engine blocks, engine cradles and transmission housings (See Figure 2). This has led to the formation of special interests industrial consortiums to develop solutions to the technical and economical challenges facing wide applications of magnesium and its alloys [2,3]. It has also been reported [4] that costly magnesium components in aircraft often experience significant corrosion issues which often require premature removal from service affecting the readiness, safety and cost of maintenance of aircraft (see Figure 3).

General corrosion rates of modern high-grade magnesium alloys, especially when adequately coated, are acceptable in most applications. Galvanic corrosion, however, remains a challenge in many situations. Therefore, design considerations need to be made in order to avoid galvanic contact with other dissimilar metals. This is particularly important

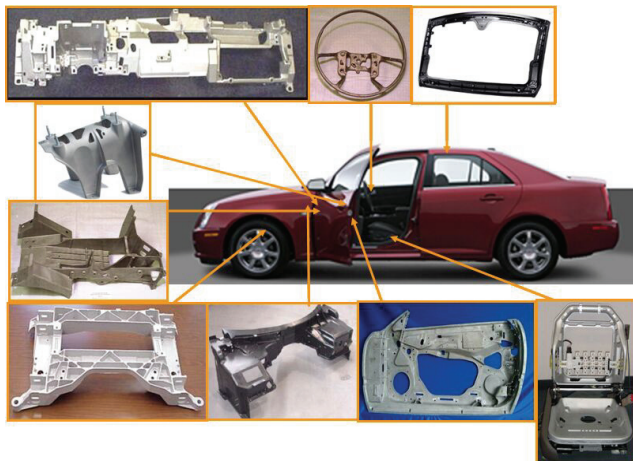


Fig. 2. Automotive applications for Magnesium alloys (Picture courtesy of Dr. Alan A. Luo, General Motors, "Magnesium Front End Development - USAMP Activities", paper presented at the SAE World Congress, Detroit, MI, April 18, 2007).

in components exposed to exterior environments such as road salts and slurries which can easily damage conventional organic coatings, creating sites for rapid electrochemical dissolution of magnesium. This is the case of many dissimilar joints, where salts and debris accumulate around bolts and crevices causing localized galvanic corrosion (See Figure 4).



Fig. 3. Corrosion damage in magnesium alloy castings used in rotorcraft.



Fig. 4. Magnesium alloy casting fastened to a steel bracket using a coated steel bolt. The interface between the steel bracket and the magnesium casting surface is prone to galvanic corrosion.

2. Current methods of protection for galvanic and general corrosion

Besides the development of more corrosion resistant magnesium alloys, current methods for general corrosion protection of magnesium include conversion and organic coatings. By conversion coatings, the surface of a magnesium component is forced to chemically react in a special chemical bath to produce a uniform and continuous film that protects the material underneath from further corroding. Conversion coatings can be achieved by electrochemical reactions, chemical immersion, or by heat treatments. One of these methods is anodizing, where the formation of complex magnesium oxide films is induced under controlled high-voltage anodic polarization conditions. There are a number of proprietary commercial anodizing techniques including Tagnite, Keronite, Magoxide, and Anomag.

Chromate coatings are excellent for general corrosion protection, however, with the recent restrictions on the use of hexavalent chromium during processing, most of these solutions have been banned, and alternative chromate-free chemistries have evolved [5]. Other low-cost conversion coatings include Alodine and Magpass, which produce a type of protective

chemistries on the magnesium surface in a way very similar to phosphates and chromates; these are done by immersion in specially formulated chemical solutions. Any of these techniques can also be combined with a finishing sealer and then a polymeric coat. For less demanding service, organic coatings are often preferred including epoxy, poly-amide, polyester, acrylic, Latex, poly-urethane, and paraffin based products, which can be applied as powders or as water-based paintable solutions.

Both conversion and organic coatings often require stringent surface preparations (water rinsing, alkaline treatment, acid pickling), and post-treatments (neutralization, water rinsing, drying); in most cases, these treatments carry environmental and health risks [6]. Organic coatings are also prone to localized failure due to poor workmanship or chipping damage, which may result in localized, severe corrosion.

These factors drive the continuous evolution of new corrosion protection strategies [5]. Although any of these techniques can be acceptable to prevent general corrosion of magnesium, they lack the ability to locally protect magnesium in the area of galvanic attack [2]. Galvanic corrosion typically occurs within 5 mm of fasteners or dissimilar interfaces. Therefore, one of the methods to combat galvanic attack is to use isolation materials to prevent direct electrical contact between bare magnesium and the dissimilar metal, increasing the electrolytic resistance of the corrosion cell. Where a high torque load is required, such isolation materials must be made of special metals or inorganic substances that take the loading without failure. In fact, the use of aluminum washers in dissimilar joints, despite the associated costs, has been a standard practice with automakers in an attempt to stop galvanic corrosion of magnesium. The effectiveness of such method depends on the chemical composition of the washer (See Figure 5).

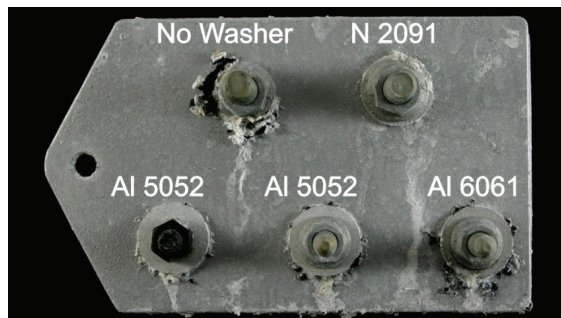


Fig. 5. Conversion-treated and powder-coated magnesium AM60 alloy plate after 40 days testing following the GM9540P standard. This sample shows different levels of corrosion when utilizing aluminum washers of various compositions coupled with different nuts. Note that, even in powder-coated magnesium, severe galvanic corrosion may still occur if no aluminum washer is utilized [7].

3. Cold spray technology

In conventional thermal spray processes the elevated process temperatures expose both the coating and substrate materials to rapid oxidation, metallurgical transformations and adverse residual stresses. Unlike thermal spray, cold spray is capable of producing dense and thick coatings exhibiting extremely low porosity (< 0.5%), while avoiding oxidation,

phase transformations and adverse residual stresses for a wide selection of metals, cermets, and other material mixtures.

Cold spray is a solid-state spraying process in which the coating materials are not melted in the spray gun (such as in conventional thermal spray); instead, the kinetic energy of fast-travelling solid particles is converted into interfacial deformation and localized heat upon impact with the substrate [8], producing a combination of mechanical interlock and metallurgical bonding. The bonding mechanisms for cold spray can be quite complex. It is generally accepted that spray-able materials require a critical amount of energy (related to the velocity of the particles and impact temperature) for effective bonding to occur [9]. Around the particle-substrate collision interface, high strain rate deformation occurs producing microscopic protrusion of material and localized heating which may lead to metallurgical bonding [8].

The original concept for cold spray was published early in the 1900's [10]. However, it was not until the 80's that a new generation of researchers at the Institute of Theoretical and Applied Mechanics in Novosibirsk, Russia, rediscover the "cold spray" phenomenon and designed a device for accelerating powder particles to produce thick dense coatings [11,12,13]. Later on, early in the 90's, researchers at the Obninsk Center for Powder Spraying (OCPS), Obninsk, Russia, introduced new developments [14], which enabled the fabrication of low-cost portable cold spray equipment suitable for a wide number of repair and restoration applications. The latter was the foundation of one of the lead manufacturers of cold spray equipment in Russia. Widespread commercial development of the cold spray technology outside Russia started only in the early 2000s. Ever since, there has been increased interest in the cold spray technology as demonstrated by the exponential growth of publications and patent applications [10]. Today, all of the cold spray methods may be categorized within three main families of processes, namely high pressure cold spray, low pressure cold spray, and shockwave-induced spraying.

In low pressure cold spray (CGSP-L), pressurized air, nitrogen, or helium (5 - 17 bar) is heated (up to 550°C) and forced through a converging-diverging nozzle (*DeLaval* nozzle) where the gas accelerates to about 600 m/s . The feedstock is introduced downstream into

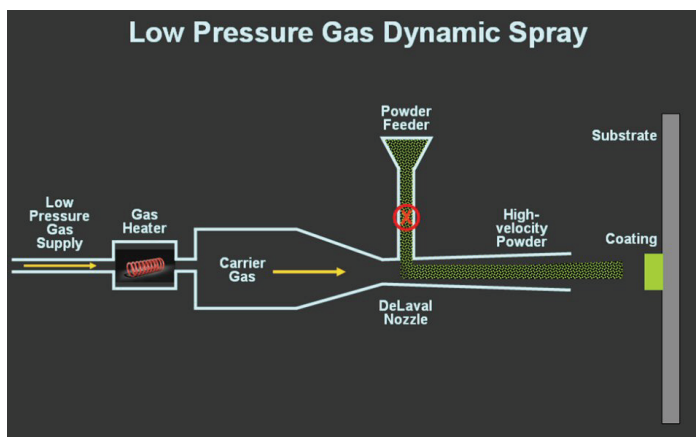


Fig. 6. Principles of low-pressure cold spray



Fig. 7. Commercial low-pressure cold spray equipment (Picture courtesy of OCPS, Obninsk, Russia).



Fig. 8. Commercial low-pressure cold spray equipment (Picture courtesy of SST, a Division of CenterLine (Windsor) Ltd.).

the divergent section of the nozzle at low pressures [5,8] (see Figure 6). Subsequently, CGSP-L systems can be simple, portable, and relatively inexpensive to operate. Low pressure systems are best suited for spraying ductile metals such as aluminum, copper, zinc, tin, nickel, or even titanium onto a variety of metallic and ceramic substrates, including magnesium. Pure metals can be mixed with aluminum oxide or other ceramic constituents to further enhance spray-ability, producing a coating of high density and bond strength. Today, there are a number of commercially available low pressure cold spray systems in the market (See figures 7 and 8).

High pressure cold spray (CGSP-H) can use helium or nitrogen as carrier gases at higher pressures (up to 55 bar). The gases can be accelerated to supersonic speeds (up to 1200 m/s) by heating them up to 1000°C and forcing them through a *DeLaval* nozzle. In this case, the

feedstock powder is introduced in the high pressure side of, prior to the nozzle throat [11,12] (See Figure 9). The levels of energy that can be attained are sufficient to spray higher temperature less ductile materials including 316L s steels, Nickel alloys, Tantalum, Titanium, and Molybdenum. However, these high energy levels can only be achieved at the expense of more equipment complexity, higher operational costs, and lower portability. In shockwave Induced Spraying [1,9,15] (SISP), fast opening/closing of a control valve downstream of a high pressure gas source generates trains of shockwaves that compress the gas in front of them as they travel through a straight nozzle. This creates pulses (10-30Hz) of heated supersonic wave fronts, where each front can be matched with a determined amount of powder in the nozzle. As the gas pulse passes through the powder dispensing zone, the powder is picked up, heated (below its melting point) and accelerated down the nozzle (See Figures 10 and 11). In contrast to traditional cold spray, a converging-diverging *DeLaval* nozzle is not required and therefore, materials can be accelerated and heated at the same time. This allows the effective deposition of other materials such as stainless steels (300 and 400 series), aluminum alloys, nickel alloys, titanium, WC-Co / WC-Cr, copper alloys, and brazing alloys.

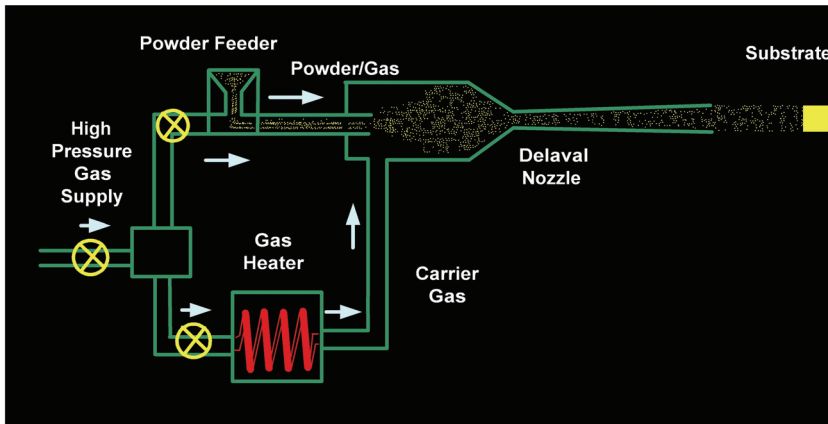


Fig. 9. Principles of high-pressure cold spray

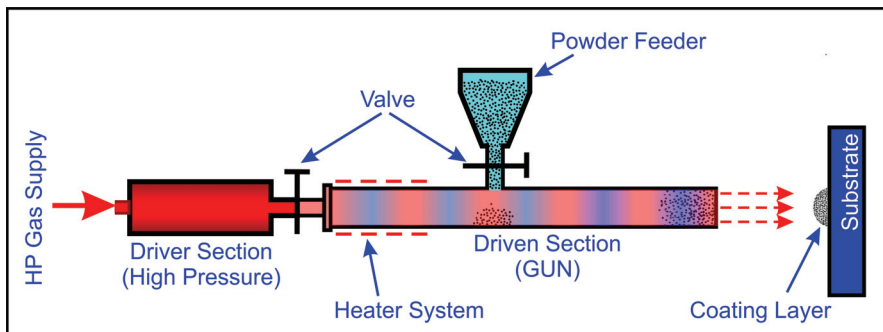


Fig. 10. Working principle for shockwave induced spraying



Fig. 11. Shockwave Induced Spraying (SISP) equipment or “Waverider”. (Picture courtesy of CenterLine (Windsor) Ltd.).

4. Corrosion protection by cold spray

While there are numerous applications for cold spray [15], metallic coatings for localized corrosion protection come up as the most attractive application for this technology, given the economical, technical and environmental challenges posed by traditional coating methods. Because of its passivation behavior, Aluminum has superior general corrosion resistance compared to other metals. Cold spray represents a cost-effective technique to deposit thick metallic aluminum coatings on magnesium alloy surfaces with minimum surface preparation and without mechanically or thermally compromising the substrate properties (see Figure 12). The presence of aluminum on the surface of magnesium has been shown to reduce the general and galvanic corrosion tendency of magnesium components (see Figure 13a). In galvanic corrosion, only small areas surrounding the dissimilar interface require protection, for which cold spray represents an innovative alternative to the use of washers and insulating bushings (see Figure 13b).

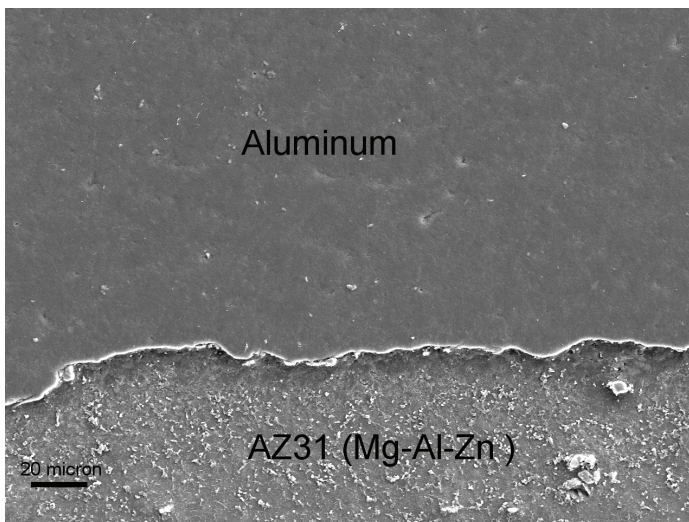


Fig. 12. Scanning electron micrograph illustrating a high-density aluminum cold spray deposit on magnesium alloy AZ31.



Fig. 13. (a) Magnesium casting alloy AE44 plate on which the central area was selectively cold sprayed with aluminum, after 100 hours of salt-spray exposure, as per ASTM B117. Note that the cold-sprayed area (between the three washers) is free of corrosion attack. (Courtesy of CANMET-MTL, Natural Resources Canada) (b) Magnesium alloy AM60 plate, where the area surrounding the fastener hole was selectively cold sprayed with aluminum, after 1000 hours corrosion test, as per ASTM B117. (Courtesy of NRC *Integrated Manufacturing Technologies Institute*, London, Ontario, Canada)

5. Conclusion

Corrosion protection by cold spray is a revolutionary method whereby protective metals can be directly and locally applied to magnesium alloys to reduce or eliminate general or galvanic corrosion in specific areas. Cold spray represents a viable alternative to traditional methods for localized galvanic corrosion protection of magnesium and its alloys. The use of Al alloy powder as the coating materials means a good galvanic compatibility between the coating and the underlying substrate. The relatively soft nature of Al powder also leads to high-degree of deformation in the powder particle during the deposition process producing a dense coating layer with low permeability to corrosion agents such as salts.

6. References

- [1] Levy M. et al "Assessment of Some Corrosion Protection Schemes for Magnesium Alloy ZE41A-75", Tri-service corrosion Conference, Atlantic City, 1989
- [2] Zheng, W., Osborne, R., Derushie, C., and Lo, J. (2005), "Corrosion Protection of Structural Magnesium Alloys", paper 2005-01-0732 read to the SAE World Congress
- [3] Powell, B.R. (2003), "The USAMP Magnesium Powertain Cast Components Project", *Proceedings of the 60th Annual World Magnesium Conference*, International Magnesium Association, May 11-12, 2003, pp. 44-51.

- [4] Champagne v., editor, "The Cold Spray Materials Deposition Process", Woodhead Publishing ISBN978-1-84569-181-3, CRC Press ISBN 978-1-4200-6670-8, Cambridge, 2007, pp 327-352
- [5] U.S. AUTOMOTIVE MATERIALS PARTNERSHIP (USAMP), DOE / USAMP Cooperative Research and Development Agreement (2006), *Structural Cast Magnesium Development*, Contract No.: FC26-02OR22910, August 2006.
- [6] Avedesian, M. (Editor), and Baker, H. (Editor), (1998), *ASM Specialty Handbook: Magnesium and Magnesium Alloys*, ASM International.
- [7] Zheng, W., Derushie, C., Lo, J., and Essadigi, E. (2006), "Corrosion Protection of Joining Areas in Magnesium Die Cast and Sheet Products", *Materials Science Forum*, 546-549, pp.523-528.
- [8] Assadi, H., Gartner, F., Stoltenhoff, T., and Kreye, H. (2003) "Bonding Mechanism in Cold Gas Spraying", *Acta Materialia*, (51)15, September 3, 2003, pp.4379-4397.
- [9] Van Steenkiste, T.H., Smith, J.R., and Teets, R.E. (2002), "Aluminum Coatings Via Kinetic Spray With Relatively Large Particles", *Surface & Coatings Technologies*, Elsevier, (154)2, May 15, 2002, pp. 237-252.
- [10] Eric Irissou, Jean-Gabriel Legoux, Anatoly N. Ryabinin, Bertrand Jodoin, and Christian Moreau, "Review on Cold Spray Process and Technology: Part I—Intellectual Property" *Journal of Thermal Spray Technology*, Volume 17(4) December 2008, pp 495-516
- [11] Alkhimov, A.P., Kosarev, V.F., and Papyrin, A.N. (1990), "A Method of Cold Gas Dynamic Deposition", *Dokl Akad Nauk (USSR)*, 315, pp. 1062-1065.
- [12] Alkhimov, A.P., Papyrin, A.N., Kosarev, V.F., Nesterovich N.I., and Shushpanov M.M. (1994), "Gas-Dynamic Spraying Method for Applying a Coating", US Patent 5,302,414, April 12, 1994.
- [13] Papyrin A., Kosarev V., Klinkov KV, Alkimov A., and Fomin V, "Cold Spray Technology", Elsevier, Oxford, ISBN-13: 978-0-08-045155-8, 2007
- [14] Kashirin, A.I., Klyuev, O.F., and Buzdygar, T.V. (2002), "Apparatus for Gas-Dynamic Coating", US Patent 6,402,050, June 11, 2002.
- [15] Villafuerte, J. (2005), "Cold Spray: A New Technology", *Welding Journal*, 84(5), pp 25-29.

Protective Coatings for Magnesium Alloys

Dr. Ing. Stephen Abela

*University of Malta, Department of Metallurgy and Materials Engineering
Malta*

1. Introduction

In the past two decades considerable effort was dedicated to the development of a series of low temperature Physical Vapour Deposition (PVD) techniques suitable for the protection of magnesium alloys. Only a handful of the developed technologies have produced promising results. Some variants of the Ion beam sputter deposition (IBSD), ion beam assisted deposition (IBAD), and reactive ion beam assisted deposition (RIBAD) are among the most promising, as these allow the deposition of hard and dense protective coatings even at room temperature. In the first part of this chapter, the wear and corrosion properties of the selected coating systems will be presented together with a critical analysis of the work published by the author and selected researchers. This will be followed by a more in depth description of the IBAD and RIBAD process. The effect of the various processing parameters on the coating endurance as well as the surface integrity of the substrate materials will be discussed. The relative wear resistance to the pin on disc wear test will be presented and discussed in the light of various experimental evidence collected by the author over the years. This will be followed by a description of a series of test conducted to establish the effectiveness of various coatings in protecting the substrate from electrochemical corrosion in acidified NaCl solutions. The chapter will be concluded with an overview of the current state of PVD technologies with particular emphasis on the strengths and limitations of the existent technology as far as the treatment of light alloys is concerned. Based on the acquired knowledge, the author will endeavour in a discussion of the future trends in PVD and plasma surface modification technologies. A handful of innovative processes and some preliminary results will be included.

2. Background

At the December 1997 Kyoto Conference on climate change, more than 159 countries undertook to reduce their emissions of a group of greenhouse gases, by 8% during the period 2008 to 2012 relative to 1990 levels. In response to this commitment, the European Parliament approved Council Directive 1999/94/EC of the 13th December 1999, related to the availability of consumer information on fuel economy and CO₂ emissions, in respect of the marketing of new passenger cars. In 2007 EU leaders endorsed an integrated approach to climate and energy policy and committed to transforming Europe into a highly energy-efficient, low carbon economy. They made a unilateral commitment that Europe would cut

its emissions by at least 20% of 1990 levels by 2020. This commitment is being implemented through a package of binding legislations. In addition to these already stringent measures, the EU has offered to increase its emissions reduction to 30% by 2020, on the condition that other major emitting countries in the developed and developing worlds commit to do their fair share under a future global climate agreement. This agreement should take effect at the start of 2013 when the Kyoto Protocol's first commitment period will have expired. Across the Atlantic, Senator John Kerry (D-MA) pushed legislation to raise the current Corporate Average Fuel Economy (CAFE) standards to 37 miles per gallon, up from the current 27.5 mpg for passenger cars, and 20.7 mpg for light trucks.

In order to abide to the new regulations and be competitive, automobile manufacturers must find ways and means to reduce the fuel consumption of the vehicles they produce. Apart from automobile, the attainment of these energy consumption targets would invariably involve weight reduction in a myriad of other mobile equipment and products. To mention just a few: aeroplanes, space vehicles, cargo containers, various tools and fixtures which has to be transported from site to site, sports and accessibility equipment, ships, suit cases, and the list goes on. There are various ways in which this weight reduction can be accomplished. Often these modifications almost always involve the use of stronger and / or lighter materials.

Magnesium offers a set of highly attractive properties for the manufacturing industry. The most obvious of which is magnesium's low density, but there are many more. Magnesium has a low specific heat capacity namely 1025 J/KgK and a relatively low latent heat of fusion 368 KJ/Kg; both properties desirable for all sort of casting processes resulting in a significant reduction in energy consumption in its processing. Moreover, this element has a low affinity to steel. Due to this property, steel moulding tools used for the casting of magnesium alloys, last three to four times longer than those used to cast aluminium. Other attractive properties are excellent castability, high dimensional stability, easily predictable shrinkage, high strength-to-weight ratio, low melting temperature, shock and dent resistance, excellent damping properties [1], practically transparent to high energy neutron radiation, and good electromagnetic shielding [2]. Magnesium is abundant. It is the eighth most common element; seawater, the main source of supply, contains 0.13% Mg, which represents a virtually unlimited supply. Magnesium is also recyclable, and instituting a recycling system would extend supplies and save energy.

In the past the use of these versatile materials has been hindered by their prominent tendency to staining and corrosion in wet and salt-laden atmospheres [3]. On top of this, their poor wear resistance considerably limits the applicable contact loads. These two significant limitations were the culprits for the initial setback for the use of magnesium alloys.

For many years, RZ5 alloy has been the preferred material for helicopter transmission casings due to the combination of low density and good mechanical properties. More recently, however, the requirement for longer intervals between overhauls and hence improved corrosion properties has caused manufacturers to reconsider material choice. In an effort to mitigate this problem WE43 was introduced instead of RZ5 for various components including the main rotor gearbox castings.

In automobile applications the penetration of magnesium was not so successful following the significant setback of the late 60's. Magnesium alloys are currently used in relatively small quantities for auto parts, generally limited to die casting. Studies conducted at the

Argonne National Laboratory, Transportation Technology R&D Centre investigated the use of magnesium sheet in non-structural and semi-structural body applications and the use of extrusions for structural applications as spaceframes, L. Gaines et. al. [4]. This study identifies high cost as the major barrier to greatly increased magnesium use in automobile.

In Europe, the increase in using magnesium as a structural lightweight material is being led by the Volkswagen Group of companies, with the material also being used by other leading manufacturers including DaimlerChrysler (Mercedes Benz), BMW, Ford and Jaguar. Presently, around 14kgs of magnesium are used in the VW Passat, Audi A4 & A6. All those vehicles use magnesium transmission casings cast in AZ91D, offering a 20%-25% weight saving over aluminium. Other applications include instrument panels, seat frames, intake manifolds, cylinder head covers, inner boot lid sections, steering wheels, and steering components which utilise the more ductile AM50A & AM60B alloys. In North America, the use of magnesium for auto applications is more advanced. The GM full sized Savana & Express vans use up to 26kg of magnesium alloy. Several Technical barriers remain inhibiting the high-volume uptake of Mg in the automobile industry, galvanic corrosion being second only to the economical issues.

The application of durable anodic or conversion coatings typically provides moderate protection. Anodic coatings such as Keronite™, Magnellan™, and Thixomat™ are tougher and offer better protection from wear and corrosion than conversion coatings, but their cost is too high for the mass production of common goods. Chromate-based conversion coatings are cheaper, but the hexavalent chromium ion involved in this process is both carcinogenic and a hazardous air pollutant. Directive 2000/53/EC on end-of-life vehicles makes explicit reference to the reduction or elimination of its use in cars. Other European regulations are also in place, to control the disposal of process waste and to protect staff in the workplace which could potentially limit the use of such treatments.

The relatively low intrinsic hardness of magnesium and its alloys makes them prone to mechanical damage (wear). In practice, magnesium alloys are protected either by the use of bushings and various metallic inserts. This, however, often leads to galvanic corrosion problems, and require complex and expensive assemblies in order to minimize contact corrosion. It can therefore be safely concluded that the main technological disadvantages of magnesium with respect to other competing materials (mainly plastic, wood, and aluminium alloys) are the poor corrosion and tribological properties.

One of the most important goals for the automotive industry of the future is to extend the use of Mg alloys to other bulky components of the car including external parts such as frames and panels [4], [5]. For active components applications, such as pistons, cylinder blocks, and turbine components, both erosion and corrosion resistance are mandatory if magnesium alloys are to be successfully used. Wear and corrosion protective coating system for magnesium alloys are required in order to unlock the full potential of this virtually inexhaustible recourse. Ideally such coatings would allow the design of magnesium components without bearing inserts and the need of complex fixtures intended to electrically isolate the components from other materials. Reducing the risk of galvanic corrosion by means of a suitable protective coating would therefore result in an overall reduction in production costs and increased reliability. These protective systems have to be compatible with modern magnesium alloys as well as the environment. This can only be achieved if the effect of the required processing parameters on the substrate material is well understood. Also the process itself and the applied coating systems have to be

environmentally friendly, both in terms of energy consumption as well as emissions in the environment during the entire product lifecycle.

3. Surface engineering of magnesium alloys

Associated with the ever-increasing need for efficiency and better performing engineering components, there is a corresponding increase in the demands placed on engineering materials. Materials need to be strong, hard, light, ductile, wear resistant, corrosion resistant and aesthetically attractive. Indeed, for some applications, even specific magnetic and optical properties are also required; this is particularly true for the electrical and electronic industry. It is therefore, becoming increasingly difficult for any material, to satisfy all the requirements for a particular application.

Surface engineering enables the modification of the material's surface without drastically affecting the properties of its bulk. This emerging branch of engineering was defined by the late Professor Tom Bell [6] as... "*Surface engineering is the application of traditional and innovative surface technology to engineer components and material, in order to produce a composite material with properties unattainable in either the base or the surface material*". With these new techniques, it is possible to select a material for its bulk properties, and afterwards engineer its surface to achieve the required set of properties [7]. Surface modification techniques can be tailored to satisfy the requirements of specific class of materials. In the case of magnesium alloys this involves the development of low temperature processing techniques which can modify the surface without degrading the properties of the bulk material.

Surface treatments are primarily applied to magnesium parts to improve their appearance and corrosion resistance [1 pg.143-161]. The selected surface treatments are dependent on the service conditions, aesthetics, alloy composition, size, and the shape of the component to be treated. In the past couple of decades, a large number of surface treatments were developed for magnesium and its alloys, but only few processes have actually achieved commercial importance. The coatings and surface treatments used in industry to protect magnesium alloys are:

- Oils and waxes: *used for temporary protection.*
- Chemical-conversion coatings: *temporary protection or paint base.*
- Anodized coatings: *wear resistance as well as a superior paint base.*
- Paints and powder coatings: *corrosion protection and appearance.*
- Metallic plating: *appearance, surface conductivity, solderability and limited corrosion protection.*

The available surface treatments and coatings offer a wide range of performance and processing cost. Chemical conversion coatings, for instance, can provide limited stand-alone protection for interior environment applications. Anodised coatings are inherently porous, and unless they are properly sealed with paint or resin, are not suitable for exposure to corrosive environments. Metallic coatings are restricted to special applications, because of the high processing costs involved in deposition. Table 1 includes a list of magnesium alloys components, their exposure conditions and the applied surface treatment [1 pg.139].

3.1 Chemical conversion treatments

Chemical conversion treatments are, by far, the most common and diverse surface treatments for magnesium alloys. These treatments are sometimes used on their own, but

Part	Form	Requirement	Pre-treatment	Finish
<i>Automotive parts</i>				
Under hood parts (valve covers, fuel induction housing)	Die cast	Appearance, durability, resistance to salt splash, oils	Wet abrasion or alkaline clean plus chrome-pickle or ion phosphate	Epoxy or epoxy-polyester powder coat
Power-train components (clutch housings, transfer cases)	Die cast	Resistance to salt splash	None	None
Engine brackets and	Die cast	Resistance to heat, salt splash, oils	Wet abrasion of none	None
Wheels	Die cast	Appearance, resistance to UV exposure, , brake dust, stone chipping, humidity	Chrome pickle or ion phosphate	E-coat, TGIC(a) polyester powder and acrylic powder clear coat
Interior parts (hidden items)	Die cast	Humidity	Cut wire aluminium blast, wire brush or none	None
Exterior parts (visible items)	Die cast	Appearance, resistance to weather, resistance to stone chipping, salt splash, UV, break dust	Chrome-pickle or ion phosphate	E-coat, liquid acrylic coat and acrylic powder clear coat
<i>Electronics / computer</i>				
housings	Die cast	Mild interior, sales appeal, durability, adhesion	Chrome pickle or ion phosphate	Sprayed acrylic, polyester or urethane, exterior coating textured epoxy powder coat.
Disc drive activator arm	Die cast / Extruded	Mild interior, limited temperature and humidity variations. No particle release allowed	Dichromate No. 7 or chrome-pickle final dichromate or none on machined surfaces	E-coat on die-cast surfaces, none on extruded surfaces
<i>Aerospace parts</i>				
Aircraft auxiliary components and helicopter gear-box housing	Sand cast	Exterior severe marine and tropical	Sand blast and acid pickle, Dichromate No 7	Backed epoxy primer, polyurethane exterior finish coat or silicate anodize and epoxy coat
<i>Other Parts</i>				
Portable tool housing (chain saws, drillers)	Die cast	Moderate exterior, sales appeal, low cost, adhesion, durability, weather, UV	Wet abrasion and alkaline clean plus chrome pickle or ion phosphate	Modified alkyd or backed alkyd liquid, or electrostatic powder coat with polyester or polyester urethane

Part	Form	Requirement	Pre-treatment	Finish
Compound-archery bow handles	Die cast	Exterior, sales appeal, low cost, adhesion, durability, weather, UV	Chrome pickle or ion phosphate	Electrostatic powder coat with polyester or polyester urethane
Luggage frames	Extruded	Interior plus mild exterior	Chrome pickle or ion phosphate	Clear acrylic
Luggage frames	Die cast	Interior plus mild exterior	Ferric nitrate pickle No 21	Polyester powder coat
Lawnmower decks	Die cast	Moderate exterior	Alkaline clean plus ion phosphate	Polyester powder coat
Photographic plates	Rolled plate	Interior, resistance to wear and corrosion by water based inks on long run painting on can stock	Zincate plus copper strike	Hard chromium electroplate

Table 1. Industrial protection coating techniques for magnesium alloys

most often as surface preparation for subsequent coating. Magnesium metal surface is inherently alkaline and thus its surface must be pre-treated to render it more compatible with paints and other organic coatings in order to enhance adhesion. The protection offered by stand-alone conversion coatings is however limited. This is only sufficient for safeguarding this material during transport and storage. Conversion coatings are also satisfactory for the protection of components intended to operate in relatively mild conditions, such as housing for electronic components and parts for components which are intended for indoor use.

The essential active ingredient in the vast majority of the chemical-conversion treatments of magnesium and its alloys is the hexavalent chromium ion, Cr^{6+} . Epidemiological studies have shown that workers employed in chromate production facilities have increased incidences of lung cancer, nasal irritation, atrophy, and nasal septum perforation as well as upper and lower respiratory effects. Chromium-exposed workers are exposed to both the chromium (III) and (VI) compound, but only chromium (VI) has been found to be carcinogenic. Much effort has been dedicated in finding effective substitutes for chromate treatments. Several commercial phosphate treatments, and simple phosphate formulations, emerged in the past decade as paint bases for high purity die-cast alloys, such as the AZ91D, AM50A, AM60B, and AS41B. However, as stand-alone coatings, the original chromate treatment still offer superior corrosion protection, and continues to be the first step in the finishing of many magnesium parts. This is particularly true for components used in severely corrosive environments and sand castings, intended for used in aerospace and military application [3]. The most common conversion coatings used in industry are: the chrome-pickle, Dichromate, Chrome manganese, Ferric nitride pickle, and the phosphate treatments.

3.2 Anodic treatments

Anodic treatments are conducted by applying an electric current to the component being treated, while it is immersed in a specifically formulated anodizing solution. During the process, the component's surface is forced to react rapidly with the solution, resulting in the

formation of a complex coating, in a number of steps. First the surface of the magnesium alloys forms a thick parent metal oxide. Then, as soon as the dielectric strength of this film reaches the level of the applied impressed voltage, arcing takes place at the metal solution interface. The heat generated by arcing, decomposes chemical precursors in the solution, and results in the concurrent deposition of oxides of other elements. The outcome is a thick and hard coating which significantly modifies the surface properties and favours the adhesion of post-treatment coatings, for example painting [8]. Anodizing treatments require a higher capital investment and have higher running costs, than most chemical conversion coatings. These are also generally environmentally cleaner than chemical conversion processes, despite most formulations in use include fluoride salts [9]. However, the result is a tougher and better supporting paint base, with superior wear resistance. In addition, the porous anodized surface can be infiltrated with organic sealants to give enhanced corrosion resistance in aggressive environments.

Anodised surfaces can be infused with a variety of polymeric substances to produce coatings, having special surface properties, such as lubricity and enhanced paint adhesion. Proprietary coatings of this type are commercially available. One such protection system is an anodic protection film, produced by Thixomat, (Chemical treatment No9 - galvanic anodizing). This treatment is a low voltage dc process, producing a thick black conversion coating, used mainly as a paint base. For rigorous service conditions, such as aerospace applications, thicker coatings can be achieved by using chemical treatment No17 or HAE. These processes can produce coating thicknesses in the range 5-30 μm . Thick coatings provide an excellent base for heavy-duty paints and offer significant resistance to abrasion.

3.3 Other coatings used for magnesium alloys

Magnesium alloys can be electroplated by many commercial plating systems provided proper pre-plating operations are conducted. However, the only metals which can be plated directly on magnesium are zinc and nickel. Zinc and nickel under-coatings serve as surface preparation for cadmium, copper, brass, nickel, chromium, gold, silver, and rhodium coatings. With the exception of gold plating, metal coatings have found little commercial applications. This is because they offer limited protection against wear and corrosion, and also because of the high processing costs. Gold plating is still used in space applications, because of its extreme stability in all operating environments, resistance to tarnish and radiation, high superficial electrical conductivity, low infrared emissivity, and resistance to cold welding in high vacuum. Metal plated wrought alloys give better and more reproducible corrosion resistance than cast alloys. This has been attributed to the surface porosity found in cast alloys [3].

Organic coatings are used on magnesium alloys to provide corrosion protection and for decoration. Organic finish paints range from single coats applied, on a pre-treated surface, to complex multicoat™ systems involving anodizing, epoxy surface sealing, priming, and one or more topcoats. Surface sealing with epoxy resin was developed, as a first step in the finish of casting for the aerospace and military applications. This sealing is an important step to increase the corrosion performance of the complex finishing systems required in aggressive environments and to seal the inherent surface porosity of cast alloys [3].

3.4 Low temperature physical vapour deposition (IBAD)

Plasma processing of materials has matured at an incredible rate. Since the first international conference, on plasma surface engineering, held on the 19-23 September 1988, in Garmisch-

Partenkirchen, the state of technology has made unprecedented strides. As early as 1989, low temperature ion assisted film growth processes, were already predominantly forcing their way for the fabrication of microelectronic devices. Plasma Assisted Physical Vapour Deposition provided a useful way to make the condensable particles move around on the substrate surface by colliding energetic particles from the plasma with those being adsorbed on the surface. This is accomplished by applying a negative potential to the substrate during deposition. In this way the deposition temperature required to achieve relatively dense and hard coatings was steadily reduced lowering energy consumption and reducing the heat input to the substrate during deposition. Heightened environmental concerns, in recent years has made plasma processes increasingly important in the surface engineering of materials.

Ion beam assisted deposition (IBAD), also referred to by some scientist as ion beam enhanced deposition (IBED), is a combination of two surface treatment processes, namely, physical vapour deposition (PVD) and ion implantation [10]. In this case the source of condensable particles and energetic particles are distinct and can be controlled independently. The deposition process is usually accountable for the material build-up, while the ion flux imparts the kinetic energy required to achieve adhesion and the required coating properties [11]. The kinetic energy imparted by the ion beam activates a number of processes on the surface of the growing film. Surface atoms are displaced, enhancing migration of atoms along the surface and thereby increasing the coating density even at very low deposition temperature. The ion beam, also provides the required stitching (ion beam mixing) of the coating to the substrate at a low temperature [12]. This process is therefore applicable to a wider range of materials [13, 14, 15]. Furthermore, accurate tuning of the ion to condensable flux ratio, enables the control of coating stoichiometry, structure, and residual stresses [16].

The main difference between the IBAD deposition technique and other ion assisted deposition processes is that, in the former, the energetic ion source and the condensable material flux source are separated into two distinct devices. Thus in IBAD, these two parameters can be controlled independently. In comparison, other plasma based deposition techniques such as DC and RF magnetron sputtering, as with all other PEPVD techniques, the condensable material and ion fluxes are extracted from the same plasma source. This feature gives the IBAD process more control over the deposition parameters, as compared to other deposition processes [17]. Another important difference is the operating pressure. Plasma assisted coatings usually operate between 0.1×10^{-2} – 13 mbar, which is the pressure required to sustain a plasma. In contrast, IBAD techniques usually operate at high vacuum, between 2×10^{-6} and 2×10^{-10} mbar. This is mainly due to physical limitations of the hardware and mean free path restrictions, R. Emmerich et al. [18]. IBAD techniques operate in the collision free pressure regime, thus the evaporant and the ion beam flux travel in straight lines to the substrate. This is a serious limitation of IBAD process, which restricts the complexity of the parts that can be treated which would otherwise cast shadows on the surface to be coated. This limitation is known as line-of-sight.

Conventional plasma assisted deposition techniques allow for the deposition of coatings with thickness ranging in the tens of microns. However, the interface between the coating and the substrate is often very thin, especially, when the process is conducted at low temperatures. Frequently, this results in poor coating adhesion, particularly for coatings hicker than three microns. Ion beam mixing can potentially solve this problem. In this process, the substrate is coated up to a thickness which is shallower than the penetration

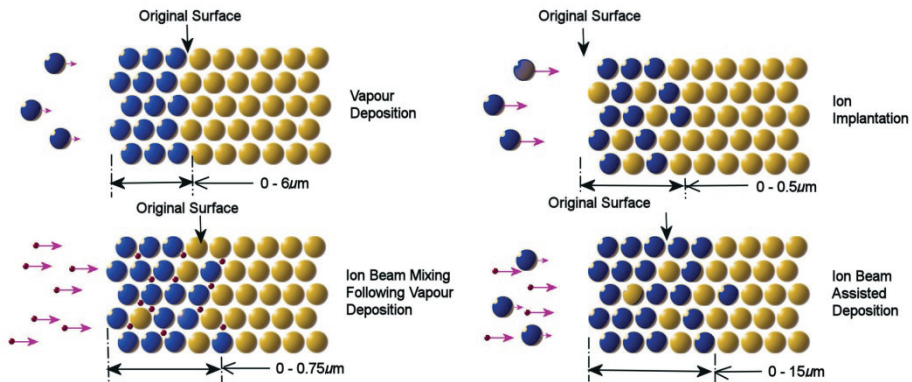


Fig. n.1. Physical vapour deposition processes [19]

depth or the ions. This thickness is dependent on the maximum available ion energy. The newly formed surface is subsequently ion implanted such that, the original interface is broadened by the ballistic effect of the ion beam as shown in figure n.1 [20, 21]. The resulting coating is very shallow, in the range of $0.2 - 0.5\mu\text{m}$, but the physical properties are vastly superior to those produced by traditional methods. This shallow coating provides an excellent foundation for additional coatings. By combining ion irradiation and deposition, the IBAD process allows for the deposition of relatively thick coatings sometimes with a thickness of more than $30\mu\text{m}$ and excellent adhesion to the substrate. In addition, it provides a means to control the residual stresses, as well as, the texture of the coating produced.

There are two principal ways to carry out IBAD process. The coating can be deposited under simultaneous or alternating ion bombardment. In the first case, low energy ion sources with no mass separation are used, such as the broad-beam Kaufman type. In the second case, higher beam energy is required, depending on the thickness deposited between each irradiation intervals, figure n.3. The increment in thickness on each successive pass is, usually, a few tenths of nanometres. In both cases, the typical energy range used for IBAD / RIBAD is $100\text{eV} - 300\text{eV}$, $30\text{KeV} - 100\text{KeV}$. When energies higher than a few hundred eV are used, decomposition of the deposited compounds occurs and the coating structure is damaged. This is particularly the case in the RIBAD process [22]. Figure n.2 illustrates a grid array of nano hardness measurement taken from an AM50 magnesium substrate coated with IBAD alumina. For the preparation of these alumina layers the growing alumina film was irradiated with a low intensity flux of 80KeV Ar^+ ions. The hardness values shown in this figure suggest the presence of hard crystalline sapphire crystals in a soft amorphous matrix. The presence of these structures in coatings deposited with different ion beam to condensable flux ration was verified using polarised light, figure n.3.

An alternative method for material deposition commonly in use is the sputtering of condensable material from a solid target, which is situated in front of the substrate. This can be accomplished either by immersing the target in dense plasma and applying a substrate bias or by irradiating the target with a high intensity ion beam with energies in the range $100\text{eV} - 600\text{eV}$. The former process is known as magnetron sputtering while the latter process is known as ion beam sputter deposition (IBSD). Magnetron sputtering allows for very high deposition rates but in order to obtain dense coatings higher temperature are

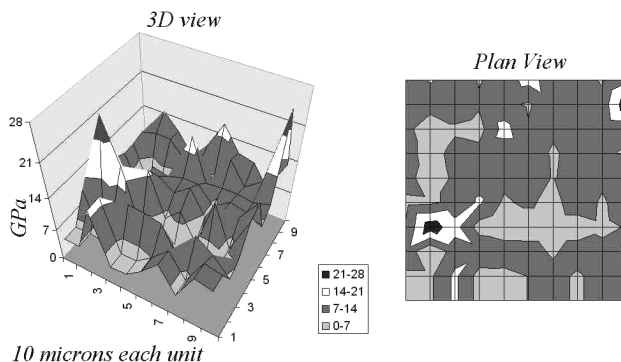


Fig. n.2. Nano hardness measurements on IBAD Al_2O_3 coating with I/C ratio of 0.3 to determine the hardness of the phases present.

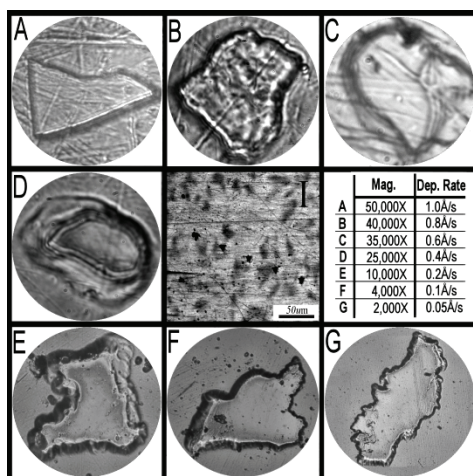


Fig. n.3. Selected areas from a series of IBAD Al_2O_3 coatings (plate A - D) prepared with different I/C ratios. Plate I at the centre illustrates the distribution of the hard island on the surface along with a series of nano indentations

required. In IBSD, the condensable material sputtered from the target attains very high energies 60eV - 100eV and through self bombardment can yield very dense coatings even at cryogenic temperatures. In the bottom of Figure n.4, a single ion source IBSD setup is illustrated, while the top part of the same figure shows the two ion sources configuration. IBSD sputtering usually result in very low deposition rates and require ultra high vacuum, to limit coating contamination from the residual gas and avoid scattering of the condensable particles by the residual gas particles which would result in inferior mechanical properties. The high kinetic energies of the condensable particles impart excellent adhesion and coating densification resulting in superior wear and corrosion protection, B. Valvoda [23]. It is because of this high kinetic energy, that IBSD can be conducted at lower temperatures than any other physical deposition process [24].

Clearly, the two ion source configuration offers greater flexibility and control over coating structure and stoichiometry [25]. Then again, multiple evaporation and ion sources may be required for the synthesis of compound coatings. A configuration of two separately controlled ion sources has achieved a relative degree of success in the United States. One institution using this system in the early 1980's, was the U.S. Naval research laboratory, which developed a series of processes suitable for high temperature aerospace applications [15].

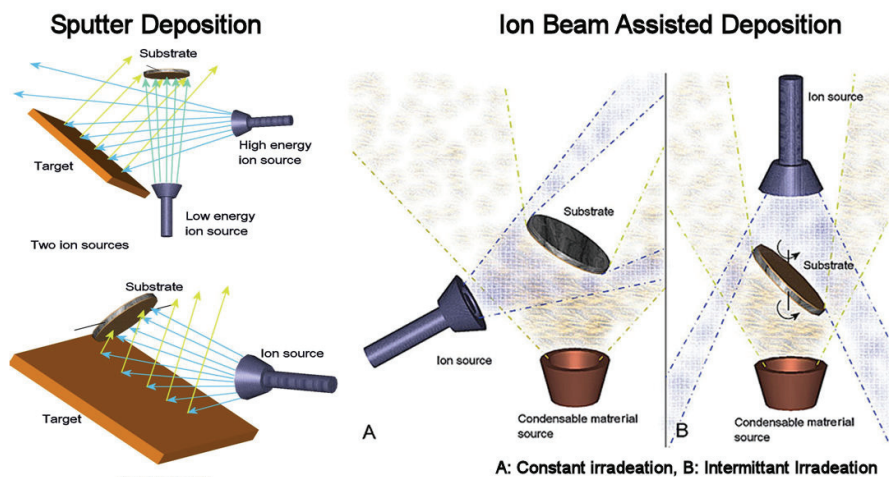


Fig. n.4. Deposition Configuration

3.5 Mechanical properties of low temperature PVD coatings for magnesium alloys

The physical properties of the resulting PVD films are extremely sensitive to a broad range deposition parameters used for their preparation. The substrate surface conditions (roughness, hardness, crystal orientation, and density of point defects) and to a larger extent contaminants present on its surface also have a huge impact of such properties. The limited ad-atom mobility at low temperature tends to make films deposit under such condition more sensitive to the presence of contaminants on the substrate surface and relatively high concentration of residual gas molecules in the processing chamber. The effect of the latter is usually more pronounced when the deposition rate is very low (less than $2\text{\AA}\cdot\text{s}^{-1}$).

As part of an extensive investigation intended to develop protective coatings which could be applied to magnesium alloys in existent industrial deposition facilities, a number of deposition techniques were evaluated. The coatings produced in this investigation were subsequently compared using pin on disk tribo test configuration and various electrochemical tests. The base pressure of the equipment available in this case was 2×10^{-6} mbar and the deposition temperature for all coatings was maintained below 80°C . A selection of the physical properties of the coatings obtained from this investigation is included in tables 1 and 2.

Under the investigated conditions, ion beam sputtered aluminium oxide, titanium oxide and carbon, coatings have very high wear rates compared to those of sputtered W and ion beam assisted deposition coatings. The best performing coating is RIBAD TiN, resulting in a wear rate of $2.51 \times 10^{-12} \text{mm}^3(\text{Nm})^{-1}$. This is followed by IBAD alumina (I/C 0.3) which resulted in a

wear rate of $8 \times 10^{-6} \text{ mm}^3(\text{Nm})^{-1}$. The far right pyramid, in this chart, represents the wear rate of $1 \mu\text{m}$ sputtered carbon on top of a $5 \mu\text{m}$ IBAD alumina ($I/C = 0.3$) coating. This composite coating wears at a rate of $2.8 \times 10^{-7} \text{ mm}^3(\text{Nm})^{-1}$, and shows, therefore, an improvement over the monolithic IBAD alumina coating.

The poor performance of the IBSD coatings in this investigation is attributable to the high residual gas pressure and the extremely low deposition rates used due to the hardware limitations. The relatively high base pressure results in a continuous build-up of physisorbed gas molecules, on the substrate surface, which hinder coalescence of growing coating islands. This gave rise to a high concentration of nanometric voids inside the growing films. The density these coatings were calculated by measuring the difference in weight of the substrate before and after the deposition process and dividing this quantity by the coating thickness multiplied by the CSA of the substrate. These values are reported in table 2 and provide support the hypothesis that the coatings contain significant nanometric porosity which is invisible to the optical microscope and SEM, figure n.3.6. From this table, it can be seen, that the sputtered coatings have very low hardness. The only exception is the sputter deposition of W, which has a very high hardness, even if the coating density is only 0.8 of the theoretical value. This, is believed to be due, to the difference in mass between the residual gas molecules, [H_2O (18amu), O_2 (32amu), and nitrogen (28amu)] and that of W (184amu). As a result, W particles lose little kinetic energy during binary collisions with residual gas particles on the substrate surface. Chum Gao *et.al.* [26] used this phenomenon by intentionally increasing the chamber pressure to decrease ad-atom mobility and deposit films with nanometric grains containing nano-voids, thus enhance their magnetic properties.

IBSD Al_2O_3	IBSD Ti_xO_y	IBSD C	IBSD W	IBAD Al_2O_3	RIBAD TiN	RIBAD Ti_xO_y	IBSD C/IBAD Al_2O_3
2.97E-02	2.60E-02	1.80E-01	7.25E-04	8.00E-06	2.51E-12	9.20E-04	2.80E-07

Table 2. Wear resistance of various coatings, subjected to the pin-on-disc test, the units used to represent the volume of material removed by the pin are $\text{mm}^3(\text{Nm})^{-1}$

At room temperature, residual reactive gases occupy the reactive sites of the substrate surface and “act as a source of mechanical stresses to pin grain boundaries and vacancies”. In turn, this results in poorly adherent films, which are either amorphous or have very small grains G. Konczos *et. al.*[27]. At higher temperature the incorporated gases give rise to mechanical stresses in the coatings, and significantly modify both their electrical and optical properties. The presence of these adsorbed gases can also change the deposition mode from epitaxial to polycrystalline or amorphous, depending on the extent of contamination. The continuous formation of residual gas molecular film on the surface is responsible of atomic shadowing. This, eventually, leads to the formation of nano trenches in the surface, which when covered would give rise to the voids reported.

Despite the high residual gas pressure and the low deposition rate, the coating adhesion and wear resistance, reported by P. I. Ignatenko *et.al.* for IBSD TiN are significantly better than those of RIBAD TiN deposited by on the same substrates [28]. This appears to be in contrast with the results obtained by the author in whom the deposition of IBSD of TiN resulted in a loosely bound mixture of titanium oxides and nitride, with exceedingly poor mechanical properties. This difference originates mainly from the difference in operating parameters used. In fact, in the research at hand, the substrate temperature was not allowed to exceed

	Density gmm ⁻³	Coefficient of friction during wear test	Hardness GPa	Adhesion Nmm ⁻² * Max 35Nmm ⁻²
IBSD Al ₂ O ₃	2.92	0.86	0.44	18.2
IBSD Ti _x O _y	2.16	0.68	1.28	12.8
IBSD W	16.3	0.56	33.64	16.25 ²
IBSD C	1.9	0.095	0.11	2.3 ¹
IBSD C on IBAD Al ₂ O ₃	-	0.014	20.85	10.73 ⁶
IBAD TiN	5.4	0.21	16-26.8	35 ^{3,5}
IBAD Ti _x O _y	3.85	0.42	8.33	33.5 ⁵
IBAD Al ₂ O ₃	3.9	0.68	2.4 - 26.5	34.1 ^{4,5}

Table 3. Mechanical properties of coatings

1. Coating flakes off spontaneously after 5 days of exposure in atmosphere
2. Coating develops visible cracks and pores after 3 weeks of exposure in atmosphere
3. Coating develops blisters after 12- 36 months
4. Partial coating and resin failure
5. Coating delaminates but does not debond
6. Failure of resin-coating bond
7. Resin adhesive strength in tension is 35Nmm⁻²

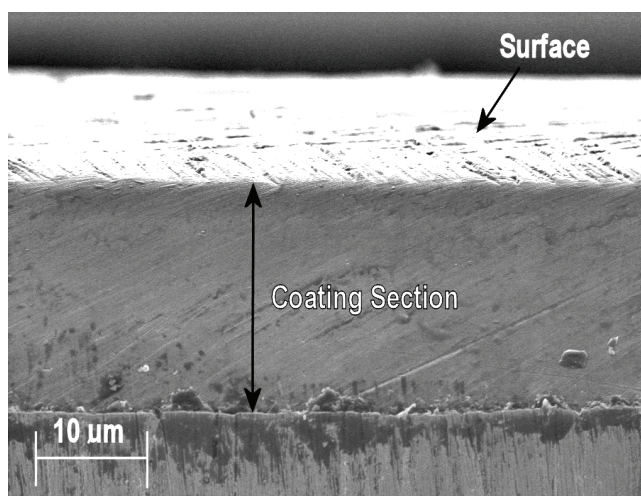


Fig. n.3.6. A sectioned IBSD Al₂O₃ coating, deposited by sputtering Al with O₂⁺ for 432hrs, showing a “thick” and uniform coating

80°C and no substrate bias was used, whilst P. I. Ignatenko *et.al.* applied a deposition temperature of 500°C and a substrate bias of -200V. This is believed to be responsible for the considerable improvement of, both, the coating hardness and adhesion to such an extent that it actually outperformed RIBAD TiN deposited on the same substrate. In fact published

results suggest that under appropriated deposition conditions and with a base pressure in the range of 1×10^{-10} mbar IBSD coatings are generally superior to their counterparts deposited using other PVD techniques.

Results published by I. Petrova *et.al.* show that low density coatings result when metal films are deposited with an impurity arrival rate much higher than that of the metal itself [29]. They also stated that, for alumina deposited under similar conditions, adequate mechanical properties cannot be achieved at deposition temperatures lower than 500°C in case of ion beam bombardment and 800°C when no ion beam irradiation is applied. The findings of this investigation concur with the findings of G. Konczos *et.al.*, whose conclusions are based on experimental data gathered from work carried out by a number of researchers, over several decades.

3.6 Effect of the surface condition on the low temperature PVD coatings for magnesium alloys

In the deposition of hard coatings on magnesium alloys, magnesium oxide present on the substrate is a weak link and is thought to be responsible for the poor coating adhesion. This oxide is unstable, due to a misfit between the lattices of the cubic oxide and that of the hexagonal metal, resulting in a Pilling-Bedworth factor less than one. In addition, when exposed to humid atmosphere, magnesium oxide reacts to form hydroxide, further compromising coating adhesion, R.S. Busk [30]. While investigating plasma surface treatment of magnesium alloys H. Hoche *et.al.* [31] has shown, that the presence of magnesium oxide, at the interface of a hard coating, is detrimental for the coating hardness and adhesion. They suggest that the weak bond of the MgO, with the parent metal inhibits, the formation of compressive stresses in hard coatings deposited on top of the MgO, resulting in lower hardness and adhesion. This was amply demonstrated in a separate publication by Hoche *et.al.* [32] who report the performance of three coating systems namely $9\mu\text{m CrN}$, $2.1\mu\text{m TiN}$ and $0.5\mu\text{m}$ anodised Mg + $3\mu\text{m Al}_2\text{O}_3$. In their new setup, they used an RF magnetron source to sputter the condensable material, while feeding the reactive gas. Also, by applying a high substrate bias voltage for 20 minutes, it was possible to remove the surface oxide from the magnesium substrates. Subsequent formation was prevented by gradually reducing the bias voltage and allowing the coating to grow without interrupting the sputtering process. The hardness of the TiN and Al_2O_3 coatings deposited with this method is 42.86GPa and 22.07GPa respectively. The former is surprisingly higher than the corresponding hardness values of 28 - 34GPa reported by Jorge Nuno and Marcolino Carvalho [33]. This difference was despite the fact that the substrate in this case was tool steel, with hardness ranging between 50-60 HV.

In a separate investigation the author has demonstrated that because of the marked difference between the atomic weight of magnesium and aluminium atoms and that of zinc, iron, manganese, and zirconium elements which are often present in the most common magnesium alloys, a phenomenon known as sputter amplification is likely to take place during the sputter cleaning of the surface [34]. This process results in the roughening of the surface and the consequent reduction of the coating performance.

Attempts to form stoichiometric MgO on magnesium at reduced pressures and low temperatures (0 - 200°C) in the past has failed, Kurth. M *et.al.* [35]. In their report they described the formation of a nanometric oxide film which is semi conductive, with a band gap of circa 2eV. In their article they also report that previous attempts to grow thicker MgO layers at elevated temperature, invariably, resulted in cracks in the coating, consequently

leading to poor adhesion and corrosion protection. In contrast, work conducted by F. Stippich *et.al.* has shown that magnesium oxide can be grown, under controlled conditions, to form a protective layer [36]. In their work, they explain that IBAD deposited MgO, using 5-15KeV Ar⁺ and an I/C of 0.2, can generate a range of useful crystal structures which can offer moderate corrosion protection on their own, but more importantly can be used to provide support for more protective surface layers.

The intrinsic softness of magnesium and its alloys also contributes to degrade the properties of hard coatings deposited on these materials. In order to minimise this effect, the coating thickness deposited on magnesium alloys has to be substantially greater than that used on harder substrate materials in order to provide adequate protection. The effect of coating thickness on the wear rate of IBAD Al₂O₃ coating deposited on AM50 substrates was investigated by the author. This investigation uncovered that as the coating thickness is increased, the scatter in wear data becomes less significant and the wear resistance is considerably improved. An interesting result obtained in this investigation was the fact that as the coating thickness was increased from 1µm to 2.5µm there was a corresponding deterioration in wear resistance, figure n.3.7. Increasing the thickness further resulted in the expected rapid improvement. In order to understand the change in the wear mechanism operating on these coatings and explain the initial anomaly, two series of wear tests were carried out. In the first instance, a series of pin-on-disc wear tests were conducted on coatings having thicknesses of 0.85µm, 3.8µm, 5.6µm, & 7µm. In these tests, the pin was allowed to wear through the whole thickness of the coating. In the second set of experiments, the time required for failure of the coating derived from the first set of experiments, was used to determine the duration for two thirds of the coating to be worn off. The results of these tests are given in figures n.3.8 and n.3.9 (pages 149-150).

From figure n.3.8, it can be seen that, for both 0.85µm and 3.8µm thick coatings, the sliding of the pin on the surface results in plastic deformation of the substrate material, leading to a wear process known as gouging. This results in a series of characteristic "V" shaped cracks on the surface of the 3.8µm thick coating pointing towards the sliding direction. Numerous tiny cracks are formed along the edge of the wear track. Interestingly, on the 0.85µm thick coating, no cracks are visible; despite of the extensive plastic deformation of the surface. Both the 5.6µm and the 7µm thick coatings display no sign of plastic deformation or cracking of the surface.

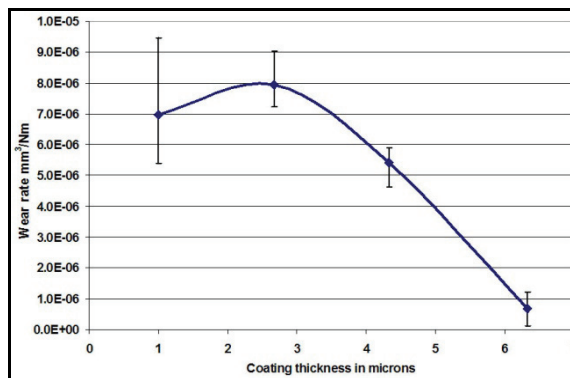


Fig. n.3.7. Effect of coating thickness on the wear rate of IBAD Al₂O₃ coatings deposited with an I/C ratio of 0.3 and subjected to the pin-on-disc test.

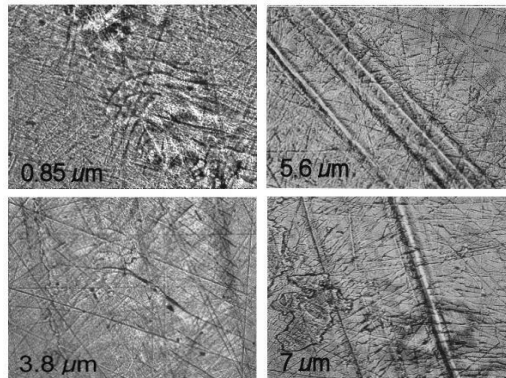


Fig. n.3.8. Optical micrographs of Al_2O_3 coatings with different thickness and an I/C ratio of 0.3, showing wear tracks produced by running the pin-on-disc test, for two thirds the time required for the pin to wear through the respective coating

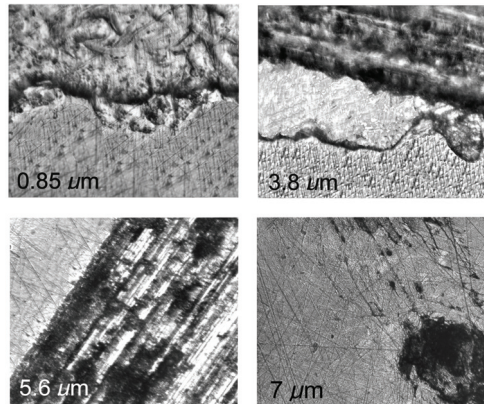


Fig. n.3.9. Optical micrographs of Al_2O_3 coatings deposited with an I/C of 0.3 and different coating thickness, showing wear tracks produced by running the pin-on-disc test until failure

Figure n.3.9 indicates that in the case of the $0.85\mu\text{m}$ thick coating, the cracked coating is still present on the surfaces even when the pin has penetrated substantially in the substrate. It is believed that the plastic behaviour exhibited in this micrograph, is caused by the high magnesium oxide content in the alumina coating, originating from the substrate. EDX measurements show that out of the $0.84\mu\text{m}$ thick layer a minimum of $0.4\mu\text{m}$ is actually interphase material having grading chemical composition, figure n.3.10.

The addition of 3-10% magnesium oxide to alumina, significantly, reduces the grain size of sintered alumina [37]. In his clinical trials, H. B. Skinner [38] found, that the reduction in alumina grain size, by alloying with magnesium oxide, resulted in increased wear resistance and toughness of the alumina-bearing surfaces used for hip joint replacement. However, the deformation of the thin coating observed in the present work could simply be due to the shallow thickness of the coating. Reports published by D.R. Clarke and W. Pompe [39] who

investigated the failure of the interface of thin hard coatings subjected to compressive stress, support this second hypothesis. In their findings, they stated that the critical radius for interface separation is inversely proportional to the coating thickness.

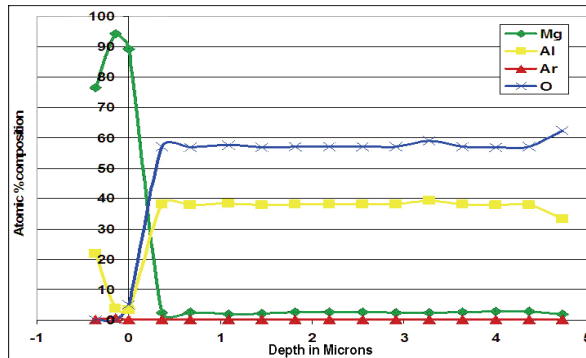


Fig. n.3.10. EDX measurement conducted on sectioned IBAD Al_2O_3 coating prepared with an I/C of 0.3, showing an interface thickness of $0.6\mu\text{m}$

The $3.8\mu\text{m}$ thick coating, on the other hand, is completely removed from the surface, revealing the microstructure of the AM50 substrate. In fact, figure n.3.9 provides evidence of coating delamination suggesting that at this coating thickness, the shear stress at the interface is too high to provide adequate performance. Increasing the coating thickness to $5.6\mu\text{m}$ reduces the shear stress at the interface sufficiently; to avoid delamination as can be seen in the same figure. Increasing the coating thickness further to $7\mu\text{m}$, results in a substantial improvement in the wear resistance. In effect, only some patches of coating from the inside of the wear track were removed by a debonding mechanism. It is thought that in this case both abrasive and fatigue wear takes place. Also, the Si_3N_4 sphere used as the counter facing wear component wears significantly in this case. This gradual increase in the contact area resulted in a reduction of the contact stresses acting on the coating. As the contact pressure is reduced, there is a marked reduction in abrasive wear, until the coating eventually fails by fatigue.

3.7 Corrosion resistance of AM50 substrates, coated with various thickness

The evaluation of the corrosion resistance of the coated magnesium samples was conducted using the acidified saline solution immersion test developed by General Motors, B.L. Taiwari and J. J. Bommarito [40]. In another publication a similar setup was designed to conduct potentiodynamic tests on the coated surface [34]. For these tests, the coated area of the specimen acts as the working electrode of the potentiostat. For this series of experiments four coating systems were selected. The RIBAD TiN and IBAD Al_2O_3 for their good wear resistance, and IBSD Ti_xO_y and Al_2O_3 for their good corrosion resistance. Three coating thickness of each were deposited, namely $1\mu\text{m}$, $3\mu\text{m}$, and $5\mu\text{m}$. Figure n.3.11 summarises the results of 48 hours immersion tests, using acidified 5%NaCl solution at PH6. It is immediately apparent, that, the corrosion resistance increases with coating thickness. $1\mu\text{m}$ and $3\mu\text{m}$ of RIBAD TiN and IBAD Alumina prove to provide inadequate protection, in fact, magnesium corrosion products are rapidly leached out of the surface and the coating is subsequently detached. Increasing the coating thickness to $5\mu\text{m}$ results in a substantial improvement, even if, the coatings still show some signs of superficial corrosion damage.

Figure n.3.12 is a plot of the weight loss ratio of coated samples, relative to that of the uncoated substrate material. From this chart, it can be concluded, that for all the various thickness investigated, TiN coatings have a negative influence on the corrosion resistance of the substrate. It can also be seen that at 1 μ m thickness, the corrosion damage on a TiN coated sample is 2.8 times that of the corresponding uncoated material. In comparison, 1 μ m IBSD Ti_xO_y and 1 μ m IBAD Al₂O₃ do not affect the corrosion process. Figure 4.49 shows small pinholes on the surface of a 3 μ m RIBAD TiN coating. These defects result in visible damage in the coating, even after just 30min of immersion.

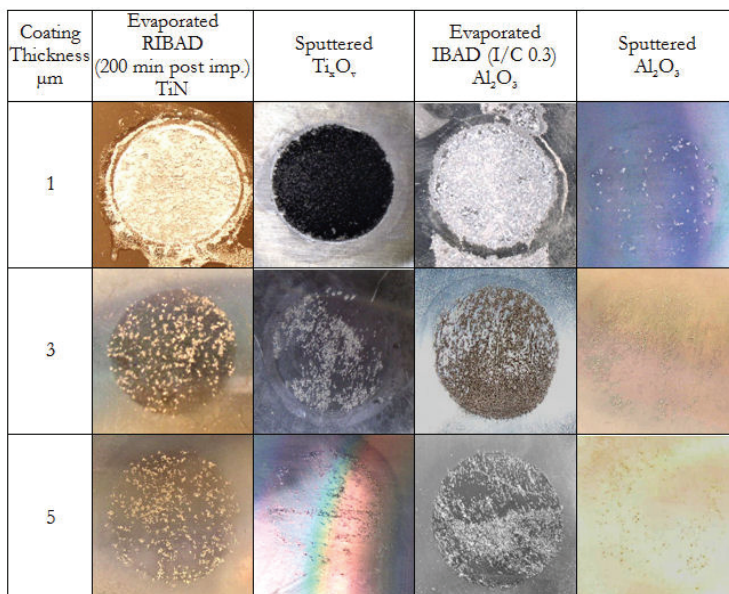


Fig. n.3.10. Showing extent of surface damage following immersion of the various coated substrate in acidified 5% NaCl solution at PH 6 and 20°C for 48 hours.

The corrosion protection of all coatings improves with coating thickness. This is in agreement with the results published by Hollstein *et.al.* [41] maintain that TiN coatings, with a thickness lower than 4 μ m are not suitable to protect Mg and its alloys from corrosion. Moreover, the results published by this group demonstrate, that single layered TiN coatings have very high porosity. The performance of 1 μ m IBSD Al₂O₃ is, surprisingly, better than the IBSD Ti_xO_y coating of the same thickness, and even, better than that of all other coatings tested, even those that are thicker. This enhanced protection is attributed to two important differences in the deposition parameters. The first, and probably the most important, is the fact that aluminium has a lower melting temperature than titanium, and thus sputtering aluminium at temperature, as low as 30°C, results in a T_s/T_m ratio of 0.33 [zone II of the structure zone model (SZM)], while that for titanium is only 0.19 (Zone I of the SZM). Besides, aluminium has a higher sputtering yield than titanium; which means, that, with the same ion beam current, the Al metal arrival rate attained during sputter deposition, is higher. The ratio of metal arrival rate to residual gas molecules, though still far from unity, is however, somewhat higher than that attained during the sputtering of Ti.

As mentioned above, operating in zone one of the structure zone model results in a low density coating, with a high porosity density, and hence, inferior corrosion resistance. The lower adhesion of Ti_xO_y coatings, when compared to the IBSD Al_2O_3 , together with the higher XRD signal yield of the latter, provide further support to this hypothesis.

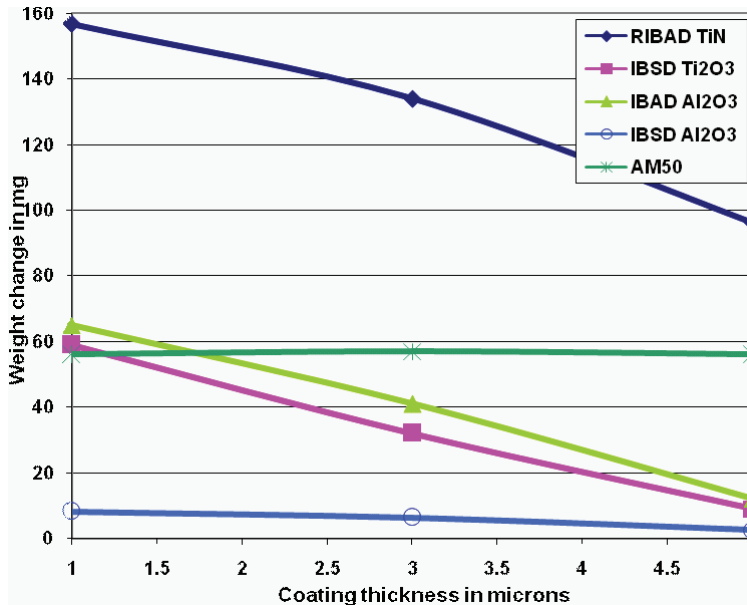


Fig. n.3.12. Weight change of AM50 substrates coated with various thickness and subjected to 48 hours immersion in acidified 5% NaCl solution, following the procedure described in section 3.2.2.4

In the case of IBAD Al_2O_3 coatings, the condensable flux was generated by the electron beam evaporation of aluminium oxide, which resulted in a flux of oxide molecules giving rise to a T_s/T_m ratio of 0.13. Nevertheless, in this technique, additional kinetic energy is supplied to the growing film by the high energy ion source. Therefore unlike the IBSD coatings, IBAD Al_2O_3 has a high density and hardness. The defects, in this case, originate from high stresses set up by residual gas trapped in the coating and which generate micro cracks and pores. Similar defects in the coating are shown in figure n.3.13. During, the evaporation of the alumina slug within the crucible, globules of alumina may gather charge and be expelled from the crucible, some of which deposit on the sample. Those that remain form inclusions, while those that fall off create pores on the surface, see figure n.3.13. This problem is more prominent at high evaporation rates.

From figure n.3.12, it can be concluded that 5 μ m IBAD Al_2O_3 coated magnesium substrates perform comparably to the IBSD coatings. However, from Figure n.3.10, it becomes evident that despite the weight loss is similar; the IBAD Al_2O_3 surface is damaged to a greater extent than that of the IBSD coatings. This is believed to be due to the large number of defects present, many of which are smaller than the thickness of the coating. Therefore, this standoff in performance, between the two coatings, is not likely to take place for longer exposure times. In such case, IBSD coatings are expected to yield better performance.

Al_2O_3 IBAD coated gravity cast AM50 substrates, perform relatively bad, when compared to their squeeze cast AS21 counterpart. The reason for this dissimilarity is thought to be due to the high porosity present in the former. While treating magnesium alloys, using various commercial surface engineering processes [3] discovered that the porosity in the base metal determines the porosity in the coatings. In fact, he attributes the inferior behaviour of coatings deposited on cast magnesium alloys to those on wrought counterparts, to the presence of pores on the surface.

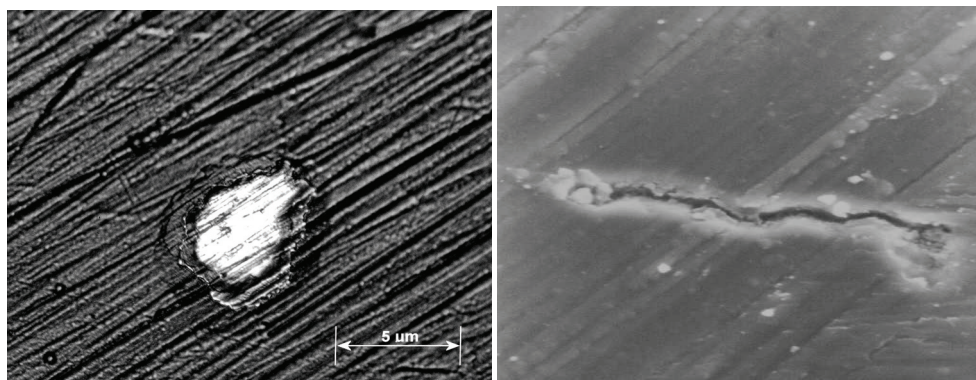


Fig. n.3.13. Left: Pore on IBAD Al_2O_3 coating deposited on AM50 substrate, Right: Crack present in the cross section of IBAD on an Al_2O_3 coating deposited with an I/C of 0.45.

In the case of the $1\mu\text{m}$ thick IBAD Al_2O_3 coated substrate the active corrosion mechanism is filiform corrosion. This corrosion mechanism operates on surfaces covered with damaged passive coatings. In this case corrosion starts from defects in the coating and propagates underneath the coating producing trenches in the surface. Hoche *et.al.* [31] reported similar corrosion mechanism operating both on $9\mu\text{m}$ CrN and $0.5\text{ MgO} + 1.5\mu\text{m}$ Al_2O_3 coated AZ91 magnesium alloys. While filiform corrosion took place in both cases, the damage experienced on the CrN coated substrate was much greater. This was ascribed to the conductivity of the CrN coating.

S. Korablov *et.al.* [38] explored into the performance of TiN, (Ti,Al)N and CrN PVD coated steel in various aqueous solutions. This investigation showed that nitride coatings can protect the substrate very effectively, in neutral and alkaline solutions. They are, however, rapidly damaged in acidic solution. According to S. Korablov *et.al.*, the nitride coatings are compromised by corrosion products, which initiate at coating defects and spread through the interface causing extensive damage to the coating. This is in net agreement with the findings reported here.

Figure n.3.14 illustrates a series of potentiodynamic tests, conducted on alumina coated substrates, in neutral 5% NaCl solution. In this chart, curve A shows the polarization behaviour of a $10\mu\text{m}$ IBAD coating on AS21 substrate, while curves B, C, and D show the polarization behaviour of $1\mu\text{m}$, $5\mu\text{m}$, and $15\mu\text{m}$ IBSD coatings deposited on AS21 substrates. At first sight, it is apparent that the free corrosion potential of the $10\mu\text{m}$ IBAD coating is higher than that of the $1\mu\text{m}$ thick IBSD coating. Also, the free corrosion potential of IBSD coatings decreases gradually with coating thickness. Still, perhaps, the most important difference in these curves is their lowering of the pitting potential, from 0.6V to below the

range covered by the potentiostat in use, namely (-2.5V). The vast difference in performance, maybe, can be better appreciated, by comparing the damage produced on the coated surface of the substrates during the polarization experiments.

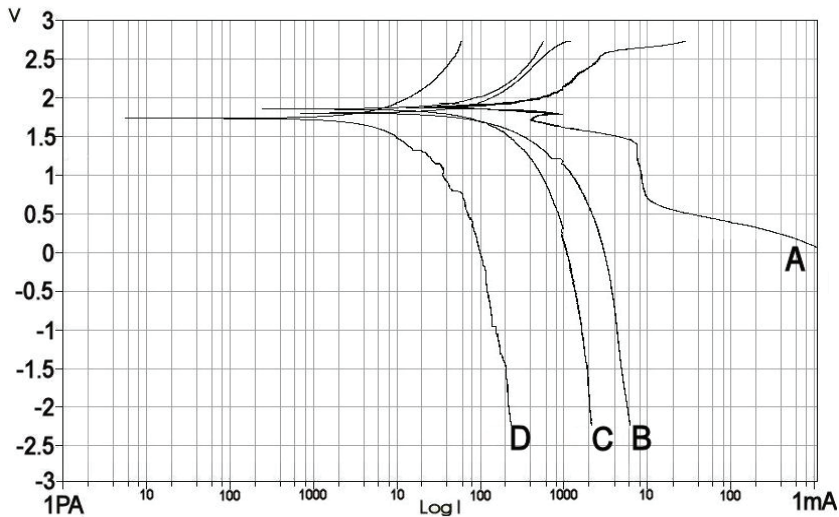


Fig. n.3.14. Potentiodynamic tests on Al_2O_3 coated AS21 magnesium alloy. Curve A illustrates the behaviour of the $10\mu\text{m}$ IBAD Al_2O_3 , while plots B, C and D illustrate the behaviour of 5, 10 and $15\mu\text{m}$ of IBSD Al_2O_3 .

From the polarization curve A, it can be seen, that as the sample surface is driven into the anodic region, the current through the defects in the coating increases. At some point, however, this current becomes saturated and further increase in voltage results in very little increase in current. This effect is known as concentration polarization. This corresponds to the dissolution of magnesium through tiny pores in the coating. As corrosion conditions are made more aggressive, the pores grow in diameter and eventually merge to form large pits. This corresponds to a sudden increase in current, which can be observed in curve A at 0.6 volts, and is known as the pitting potential.

From curves B, C, and D of figure n.3.14, it can be seen, that, IBSD alumina coatings do not experience pitting during potentiodynamic tests; through the whole range of polarization voltage used. This is because these coatings have a lower defect concentration, and thus, the pinholes on the surface are further apart than those in the coating represented by curve A. In the former case, therefore, pores cannot merge to form pits or at least, would take much longer to do so. This results in a high resistance to the flow of Mg^{2+} out of the surface, which is represented by the steep gradient in the polarization curves for the IBSD coatings.

Hikmet Altun and Sadri Sen^[98] have conducted extensive potentiodynamic testing of AlN sputter deposited coatings on a range of AZXX magnesium alloys. The coating thickness used for this set of experiment consisted of, $3\mu\text{m}$ of AlN together with, an Al interlayer of a few nm. The coating provided little protection, to all but one alloy of the series investigated, namely AZ91. For the AlN coated AZ91, the coating provided reasonable good protection with a reported pitting potential a little bit higher than 700mV. Hikmet Altun and Sadri Sen, attribute the limited protection provided by those coatings, to the deposition process related

defects, namely cracks and pores in the coatings. This is in accord with the findings in this research, and those reported by all other researchers mentioned above. The pitting potential for AlN coated AZ91 is reasonable close to that measured on IBAD Alumina coated AS21, produced in this study. The slightly better performance shown in figure n.3.14 (curve A) of the latter is attributable to the higher thickness.

The results obtained in the previously reported immersion tests contrary to those obtained in the potentiodynamic testing. This difference in performance was also observed by F. Stippich *et.al.* [36], while investigating the corrosion protection offered by various magnesium oxide coatings on magnesium alloy substrates. In their study, pure MgO coatings outperformed alloyed MgO and IBAD MgO coatings in potentiodynamic testing. However, they proved inferior during salt spray testing. Stippich *et.al.* concluded that for the purpose of electrochemical testing, greater protection is offered by coatings with amorphous structures, as these have lower porosity. Then again, the mechanical properties of the coatings are more influential in salt spray tests, than in potentiodynamic examination.

4. Conclusion

In the light of the above discussion, it is reasonable to believe that the low ad-atom mobility during sputter deposition resulted in highly amorphous IBSD oxide coatings; with good corrosion resistance but relatively poor mechanical properties, even for coating thickness below $3\mu\text{m}$. Conversely, IBAD coatings contain many defects, which lower their resistance to corrosive solutions. These coatings can, however, be substantially improved either by increasing the coating thickness, or by depositing additional coatings with minimal surface porosity. It can also be concluded that conductive coatings, such as, carbon in the form of graphite, titanium nitride and tungsten, can significantly accelerate corrosion by setting up galvanic corrosion. This either results in severe pitting, or filiform corrosion, which will eventually detach the coating completely from the surface.

It was shown that even using conventional hardware developed for the surface engineering of steels, it is possible to deposit coatings that exhibit wear and corrosion resistance onto magnesium alloys. In this study, a hybrid coating was produced by combining the good mechanical properties of IBAD Al_2O_3 , with the low surface porosity of IBSD C. This resulted in a coating with good overall performance and satisfied the objectives of this project. This work has also served to demonstrate that there is still ample room for improvement, both in the deposition system and ultimately in the protective coatings.

Results published by the various researchers working in this field amply demonstrate that there are two major obstacles for the deposition of dense protective coatings at low temperature. These are the shadowing of the incoming ad-atoms by the shape of the substrate or the texture of its surface and the incorporation of unwanted molecules from the residual gas. The effect of the latter can be easily mitigated by reducing the base and operating pressures, while the former problem is much more difficult to solve. This was traditionally dealt with by incorporating complex substrate manipulators which continually move the substrate surface during deposition in order to expose shadowed features. Unfortunately this approach is not very economical as it requires a large capital expenditure and significantly prolongs the process time. Another problem with these technologies is the inherent delicate nature of the complex equipment used which is prone to very expensive breakdowns.

A more practical approach involves the immersion of the component being treated in the plasma and the application of a pulsed high voltage during deposition, a process known as

Plasma Immersion Ion Implantation & Deposition (PIIID). This comparatively simple solution offers a number of advantages with respect to the more traditional IBAD / RIBAD techniques. The first and most important advantage is that fact that with this technology the energetic charged particles are attracted directly on to the substrate surface. This means that in this case, with very little exceptions the line of sight problem is nonexistent. In addition provided that the sample is properly cooled, the energy density that can be applied on the growing film with this technology is much higher. This means that the condensable flux intensity can be increased without compromising the coating properties resulting in much higher deposition rates. Another important advantage of this setup is the possibility to easily modify the surface of the substrate before deposition. If fact this setup is particularly suitable for the preparation of duplex and multilayer coatings.

Notwithstanding these important advantages it is unlikely that the PIIID technology will ever offer the same degree of process parameter control over the IBAD / RIBAD or the IBSD systems. These are likely to maintain their dominance in specific applications where accurate control of the coating crystal structure is required.

5. Reference

- [1] Kondrat'ev S. Yu. , Yaroslavskii G. Ya., & Chaikovskii B. S. (1986). Strength of Materials, Volume 18, number 10 / October, pages 1325 - 1329, Springer US.
- [2] Polmear J. (1995). *Light alloys Metallurgy of light metals, Third edition*, Hodder & Stoughton, ISBN: 0-340-63207-0, Huddersfield, WY, United Kingdom. pg. 196-20
- [3] Michael M. Avedesian & Huge Barker, (1999). *Magnesium and Magnesium Alloys, ASM specialty handbook published by the materials information society*, ISBN: 0-87170-657-1, United States. pg.194-210, 145, 157, & 159.
- [4] Gaines L., Cuenca R., Stodolsky F., & Wu S. (1996). Potential Automotive Uses of Wrought Magnesium Alloys, Automotive Technology Development, Detroit, Michigan.
- [5] Friedrich H. & Schumann S. (2002). Mineral Processing and Extractive Metallurgy: *IMM Transactions section C*, Volume 111, number 2, August, pages 65-71(7).
- [6] Morton P.H. (1992). *Surface engineering and heat treatment, past, present, and future*. Institute of Metals, ISBN: 0901716014, London. pg.12-51
- [7] W. Ensinger (1992). Ion beam assisted deposition with a duoplasmatron, *Review of Scientific Instruments* Volume 63, Issue 4, April, page 2393.
- [8] Bestetti M., Cavallotti P.L., Da Forno, & A.and Pozzi S. (2007). Anodic oxidation and powder coating for corrosion protection of AM60B magnesium alloys, *Transactions of the Institute of Metal Finishing*, Volume 85(6), pages 316- 319.
- [9] Bestetti M., Barlassina F., Da Forno A., & Cavallotti P.L. (2008). Effect of electrolyte composition on micro-arc anodization of AM60B magnesium alloy, *Metallurgical Science and Technology*, Vol. 26-1 - Ed. 2008, Torino, Italy.
- [10] Klingenberg M., Arps J., Wei R., Demaree J., & Hirvonen J. (2002). 'Practical Applications of Ion Beam and Plasma Processing for Improving Corrosion and Wear Protection', *Surface and Coatings Technology* Volumes 158-159, September, Pages 164-169.
- [11] Arnold H. Deutchman & Robert J. Partyka, (2002). Ion Beam Enhanced Deposited (IBED) Tribological Coatings for Non-Ferrous Alloys, *Proceedings from the 1st*

- International Surface Engineering Congress and the 13th IFHTSE Congress*, 7-10 October, Columbus Ohio, USA.
- [12] Tadatsugu Itoh, (1989). *Beam Modification of Materials 3. Ion Beam Assisted Growth*. Elsevier, ISBN: 0444872809, Amsterdam and New York. pg.170-179
- [13] Arnold H. Deutchman, & Robert J. Partyka, (2002). 'Comparison of the Properties of PVD and IBED Hardcoats (TiN and Cr₂N)', *Proceedings from the 1st International Surface Engineering Congress and the 13th IFHTSE Congress*, 7-10 October, Columbus Ohio, USA.
- [14] Shin-Hui Wang, Ching-Chun Chang, & J. S. Chen, (2004). Effects of substrate bias and nitrogen flow ratio on the resistivity, density, stoichiometry, and crystal structure of reactively sputtered ZrN_x thin films, *Journal of Vacuum Science and Technology A: Vacuum, Surfaces, and Films*, Volume 22, Issue 5, September, pages 2145-2151.
- [15] Emmerich R., Enders B., & Ensinger W. (1992). Ion beam assisted deposition of thin films and coatings: Part 1, *Surface Modification Technologies VI, Proceedings of the Sixth International Conference on Surface Modification Technologies*, Chicago USA, Novemb, ISBN: 0-87339-217-5.
- [16] André Anders, (2000). *Handbook of Plasma Immersed Ion Implantation and Deposition*. Published by wiley-interscience, New York, ISBN: 0-471-24698-0. pg.177-209
- [17] Mändl S., Brutscher J., Günzel R., and Höller W. (1996). Design Considerations for Plasma Immersion Ion Implantation Systems, *Nuclear instruments and methods in physics research B*, Volume 112, , pages 252-254. [27]
- [18] Emmerich R., Enders B., & Ensinger W. (1992). Ion beam assisted deposition of thin films and coatings: part 2, *Surface Modification Technologies VI, Proceedings of the Sixth International Conference on Surface Modification Technologies*, Chicago USA, Novemb, November 2-5, ISBN: 0-87339-217-5.
- [19] Enders B., Emmerich R., & Ensinger W. (2000). Ion beam assisted deposition under off-normal ion incidence: an experimental and analytical study of re-sputtering effects, *Surface and Coatings Technology* Volumes 128-129, 1 June, Pages 303-307.
- [20] Emmerich R., Enders B., & Ensinger W. (1992). Ion beam assisted deposition of thin films and coatings: part 3, *Surface Modification Technologies VI, Proceedings of the Sixth International Conference on Surface Modification Technologies*, Chicago USA, Novemb, ISBN: 0873392175.
- [21] Hopf C., Jacob W., & von Keudell A. (2005). Ion-induced Surface Activation, Chemical Sputtering, and Hydrogen Release during Plasma-assisted Hydrocarbon Film Growth, *Journal of Applied Physics*, volume 97, number 9, pages 094904.1-094904.6
- [22] Müller K.H., & Karl-Heinz. (1987) (Date of Current Version: 07 July 2009). Stress and microstructure of sputter-deposited thin films: molecular dynamics investigations, *Journal of Applied Physics*, Volume 62, issue 5, ISSN: 0021-8979. pages 1796-1799.
- [23] Valvoda B. (1996). Structure of TiN coatings, *Surface and coatings technology*, volume 80, no 1-2, pages 61 - 65.
- [24] Kiyotaka Wasa & Shigeru Hayakawa, (1992). *Handbook of Sputter Deposition Technology principles technology and applications*, Noyes publications, Berkshire. RG12 8DW. UK, ISBN: 0-8155-1280-5. pg.65-78

- [25] Hua M. , Ma H.Y. , Mok C.K. , & Li J. (2004). Tribological Behavior of Patterned PVD TiN Coatings on M2 Steel, *Journal of Tribology letters*, Volume 17, Number 3, pages 645-653.
- [26] Gao Chum, Malmhall Roger, & Chen Ga-Lane, (1997). Quantitative characterization of sputter-process-induced nano-voids and porous film state in magnetic thin films, *IEEE transactions on magnetics*, volume 33, no. 5, ISSN: 0018-9464, pages 3013-3015.
- [27] Konczos G., Bársony I. & Deák P. with the support of the Tempus Sjep 09614-95, (1998). *Introduction to materials science and technology*. A textbook of the technical university of Budapest. For the P.h.D. students in physics. Chapter 5
- [28] Ignatenko P. I., Klyakhina N. A., & Badekin M. Yu. (2005). Structure and properties of films grown on Si, Ta, Ti, Mo, W, and Ni substrates by reactive ion-beam sputtering, *Journal of Inorganic Materials*, Vol. 41, number 2, pp. 148-151. Translated from *Neorganicheskie Materialy*, Vol. 41, number 2, 2005, pp. 193-196.
- [29] Petrov I., Brana P.B., Hultman H., & Greene J.E. (2003). Microstructural evolution during film growth, *Journal of Vacuum Science and Technology A*, Volume 21, number 5, September-October, ISSN: 0734-2101 , Page(s): S117 - S128.
- [30] Busk R.S. (1987). Magnesium and its alloys, *International Magnesium Association 1987*, Hilton Head, South Carolina, pages S497-S499.
- [31] Hoche H., Scheerer H., Probst D., Broszeit E., & Berger C. (2003). Development of a plasma surface treatment for magnesium alloys to ensure sufficient wear and corrosion resistance, Proceedings of the Eight International Conference on Plasma Surface Engineering, *Surface and coating technology*, Volume 174-175, Pages 1018-1023.
- [32] Hoche H., Blawert C., Broszeit E., & Berger C. (2005). Galvanic corrosion properties of differently PVD-treated magnesium die cast alloy AZ91, proceedings from teh Asian-European International Conference on Plasma Surface Engineering 2003, *Surface and Coating Technology*, Volume 193, pages 223-229.
- [33] Nuno Jorge and Carvalho Marcolino, (2001). *Lower friction and wear resistant coatings. Microstructure and mechanical properties*. Groningen University Press, Netherlands, ISBN 90 367 1378 1.
- [34] Dong H. (2010). *Surface engineering of light alloys*, CRC press, woodheadpublishing uk, ISBN 1 84569 537 2. Pg. 307
- [35] Kurth M., Graat P. C. J., Carstanjen H. D., & Mittemeijer E. J. (2006). The initial oxidation of magnesium: an *in situ* study with XPS, HERDA and ellipsometry, *Surface and Interface Analysis*, Volume 38, Pages 931-940.
- [36] Stippich F., Vera E., Wolf G. K., Berg G., & Friedrich Chr. (1998). Enhanced corrosion protection of magnesium oxide coatings on magnesium deposited by ion beam-assisted evaporation, *Surface and Coatings Technology*, Volume 103-104, pages 29-35.
- [37] Vander G. F. Voort, (2006). *ASM Handbook, Volume 9. Metallography and Microstructures*. ISBN: 0-87170-706-3. pg.1061-1062
- [38] Korablov S., Basavalingu B. & Yoshimura M. (2005). Wet corrosion of nitride PVD films in supercritical solutions, *Corrosion Science*, Volume 47, Issue 6, pages 1384-1402.
- [39] Clarke D.R. & Pompe W. (1999). Critical radius for interface separation of a compressively stressed film from a rough surface, *Acta Materialia*, Volume 47, Number 6, pages 1749-1756(8).

- [40] Taiwari B.L. & Bommarito J. J. (2002). A novel technique to evaluate the corrosion behaviour of magnesium alloys, *General Motors R&D Center, Kaplan, HI editor, Magnesium Technology*, TMS, Warrendale, PA, pages 269-275.
- [41] Hollstein Frank, Wiedemann Renate, & Scholz Jana (2003). *Characteristics of PVD-coatings on AZ31hp magnesium alloys*, *Surface and Coating Technology*, Volume 162, pages 261-268.

Anodization of Magnesium Alloys Using Phosphate Solution

Koji Murakami¹, Makoto Hino¹ and Teruto Kanadani²

¹Industrial Technology Research Institute of Okayama Prefectural Government

²Okayama University of Science

^{1,2}Japan

1. Introduction

Magnesium alloys are increasingly utilized recently to improve fuel consumption of vehicles by reducing their weight. Suppression of oscillation, shielding of electromagnetic wave, rigidity and recyclability of the alloys are also advantages in electric and electronic products as well as in automotive applications (Cole, 2003). However, magnesium is one of the materials which bear stain most easily because of its quite low potential region where metallic magnesium can exist in wet environment (Pourbaix, 1974; Mears & Brown, 1945) (Fig. 1).

As protective coatings for magnesium alloys, conventional anodizations by Dow17 and HAE (Evangelides, 1955; Company, 1956; 1981; 1998; Ono & Masuko, 2003) treatments have successfully been utilized, but these methods require harmful chemical agents such

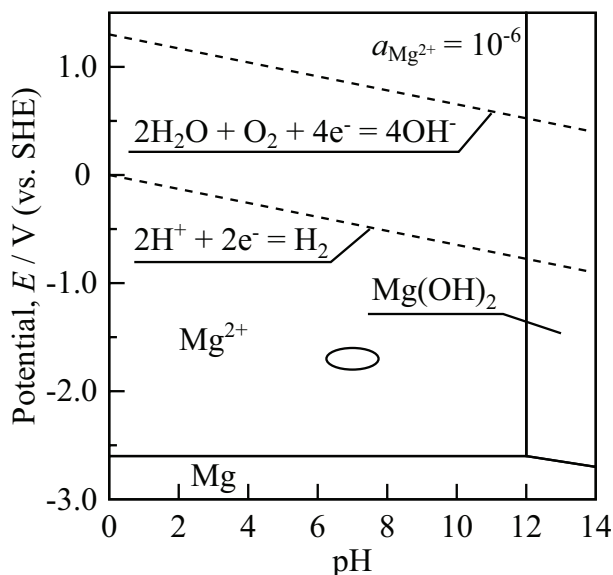


Fig. 1. Potential-pH diagram of magnesium-water system (Pourbaix, 1974; Mears & Brown, 1945) (circled area shows rest potential).

as chromium oxide (VI) and fluoride which have recently been restricted by the RoHS (Restriction of the use of certain Hazardous Substances in electrical and electronic equipment) directive and current trend for reducing environmental load. Another protection of magnesium alloys by anodization is performed using phosphate solution (Barton, 1998; Saijo et al., 2005; Murakami et al., 2007; Hino et al., 2007; Murakami et al., 2008; Saijo et al., 2008; Hino et al., 2008) whose electrolyte consists of phosphate and ammonium salt. Because of the simple electrolyte for the anodization, its environmental load is quite lighter compared with those of Dow17 and HAE.

The main purpose of this chapter is to clarify the microstructures and mechanisms of corrosion protection on the anodized surfaces by elucidating the differences in modes of protections. In section 2, formation of anodized layer through electrolysis in phosphate solution with electric discharge is discussed by microstructural observation. Mechanisms of corrosion protection on the anodized surfaces are clarified in section 3 by electrochemical measurements and microscopy.

2. Microstructure of anodized layer

2.1 Experimental

Die-cast plates of ASTM AZ91D (Mg-9.1Al-0.75Zn) magnesium alloy, rolled sheets of AZ31B (Mg-2.9Al-0.85Zn) magnesium alloy and cast high-purity magnesium (99.95 mass%) were used as substrates. Here, high-purity magnesium is designated as '3N-Mg' in the following sentences. Chemical compositions of the substrates are shown in Table 1. After the substrates were degreased and etched in a potassium hydroxide solution and a phosphate solution, respectively, they were anodized either in Dow17 (Company, 1956; 1981; 1998; Ono & Masuko, 2003) or in phosphate electrolyte (Barton, 1998; Saijo et al., 2005; Murakami et al., 2007; Hino et al., 2007; Murakami et al., 2008; Saijo et al., 2008; Hino et al., 2008). The electrolysis in phosphate solution was carried out by using a commercial solution (Anomag CR1 and CR2, Henkel Japan Co., Ltd.) according to its instruction. The counter electrodes were plates of stainless steel (JIS SUS316L or AISI 316L) which face both surfaces of the specimen, and the temperature of the electrolyte was 298 ± 5 K. The mode of electrolysis in the phosphate solution can be DC (direct current) or AC (alternating current) (Saijo et al., 2008), but only DC electrolysis is discussed in this chapter.

Figure 2 shows the appearance of the specimen during anodization. After initiation of electrolysis, the surface of the specimen was covered with an anodized layer whose color turned to white within a few seconds. The amount of gas generated on the surface increased with the growth of the anodized layer (Fig. 2(a)), and the surface was then covered with a visible local discharge or sparks when the bias reached 200 V (Fig. 2(b)). Thickness of anodized layer was changed by varying the bias at which an electrolysis was terminated.

The anodized specimens underwent electron probe microanalysis (EPMA) and transmission electron microscopy (TEM). X-ray diffraction patterns on the anodized surfaces were taken under Seemann-Bohlin geometry of the incident angle $\omega=1^\circ$ with parallel beam optics (wavelength $\lambda_{CuK\alpha}=0.1542$ nm). The specimens for cross-sectional observation and elemental

substrate	Al	Mn	Zn	Si	Cu	Ni	Fe	Mg
AZ91D	9.1	0.28	0.75	0.05	0.025	0.001	0.004	bal.
AZ31B	2.87	0.38	0.85	0.014	0.0004	0.0003	0.003	bal.
3N-Mg	0.003	0.002	0.003	0.004	<0.001	<0.001	0.002	>99.95

Table 1. Chemical compositions of substrates (in mass%).

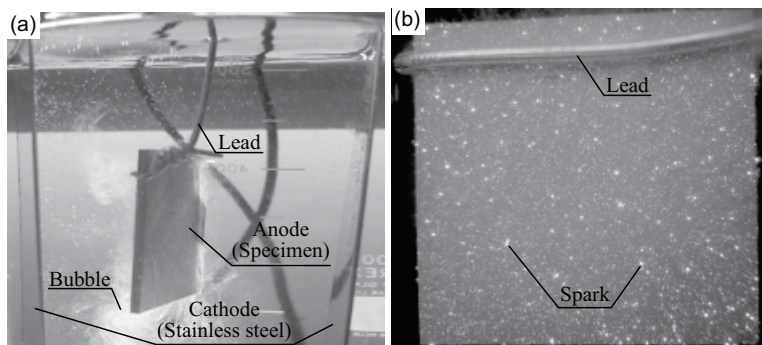


Fig. 2. Appearance of specimen during anodization ((a) immediately after initiation of electrolysis, (b) sparks on substrate).

analysis were prepared by using argon ion beam (acceleration voltage 5 kV). The surfaces were coated by epoxy resin for protection of the anodized layers before argon ion etching. Electron probe microanalysis (EPMA) with wavelength-dispersive X-ray spectrometer was used for elemental analysis. Hereafter, a specimen of AZ91D anodized in the phosphate solution, whose thickness of the anodized layer is 5 μm , is designated as 'AZ91D-phosphate-5 μm ' for simplicity.

2.2 Experimental results

Figure 3 shows the X-ray diffraction patterns taken from the anodized surfaces on AZ91D, AZ31B and 3N-Mg. The surface of AZ91D-Dow17 (Fig. 3(a)) shows chromium oxide (Cr_2O_3),

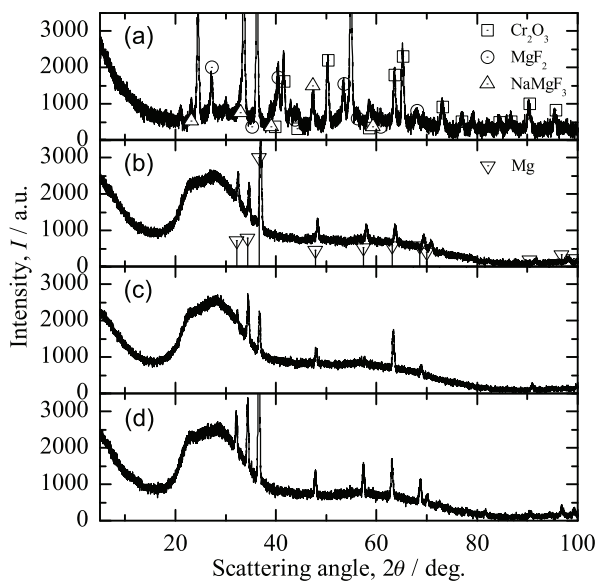


Fig. 3. X-ray diffraction patterns taken from the anodized surfaces ((a) AZ91D-Dow17, (b) AZ91D-phosphate-10 μm , (c) AZ31B-phosphate-10 μm , (d) 3N-Mg-phosphate-10 μm).

magnesium fluoride (MgF_2) and sodium magnesium fluoride (NaMgF_3) as crystalline substances. On the other hand, those in AZ91D/AZ31B/3N-Mg-phosphate- $10\mu\text{m}$ show broad scattering peaks at $20^\circ < 2\theta < 40^\circ$ (Fig. 3(b)-(d)), and the overlying peaks indicate the magnesium matrix of the substrates.

Figure 4 shows the cross-sectional microstructure of the anodized surfaces and concentrations of oxygen, magnesium, aluminum and phosphorus in the anodized layers on AZ91D/AZ31B/3N-Mg-phosphate- $10\mu\text{m}$ obtained by EPMA. Most of the pores in the anodized layer of AZ91D-Dow17 (Fig. 4(a)) were filled with epoxy resin used for the sample preparation, and many paths were formed linking the surface and the substrate. Figures 4(b)-(f) also show porous structures in the anodized layers. The atomic ratio of the elements in the anodized layers is shown in Fig. 4(g), where atomic percent of oxygen varies from 50 to 70 at.% and that of phosphorus from 10 to 20, depending on substrate.

Figure 5 shows the bright- and dark-field images of the fragment of the anodized layer of AZ91D-phosphate- $20\mu\text{m}$. Although there was no characteristic microstructure in the fragment at the beginning of the TEM observation, some areas were damaged by a few seconds' irradiation of electron beam to form bubbles or show swelling. The selected area diffraction pattern taken from the dotted rectangular area in Fig. 5(a) consisted of a strong halo ring, weak Debye rings and diffraction spots. The Debye rings and the diffraction spots matched those of spinel (MgAl_2O_4), and the dark-field image (Fig. 5(b)) taken using a diffraction spot of spinel including a part of the Debye rings showed particles of 10^1 - 10^2 nm in size. Debye rings of magnesium oxide (MgO) were also observed in other fragments, but the rings were diffuser than those of spinel.

2.3 Discussions

As Figs. 3, 4 and 5 show, the anodized layers obtained in phosphate electrolyte mainly consist of amorphous matrix and fine crystallites of spinel and magnesium oxide. Although the anodized layer obtained in Dow17 mainly shows crystalline substances, the layer might contain amorphous magnesium oxide which could not be clearly detected by XRD. Anodizing current at the electrolysis is due to continuing local discharges on the surface covered by insulator or anodized film. Substrate as well as anodized layer, melted by spark due to discharge during anodization, are considered to be solidified rapidly, forming amorphous-based layer which contain small crystallites of spinel, magnesium oxide and spherical or irregularly shaped pores. Anions in the electrolyte which are attracted at the anodized surface during electrolysis are mainly hydroxide ions and phosphates (PO_4^{3-}). Phosphorus detected by EPMA in the anodized layers (Fig. 4(g)) is picked up during solidification, and the spherical pores are thought to be filled by oxygen gas which has been generated by oxidation of hydrogen in hydroxide ions ($4\text{OH}^- \rightarrow 2\text{H}_2\text{O} + \text{O}_2 + 4\text{e}^-$). This mode of local discharge, which is accompanied by rapid solidification and formation of an anodized layer, is thought to reach a steady state in a period at a given bias, which determines the amount or the thickness of the anodized layer.

The formation of the anodized layer in the phosphate solution can qualitatively be understood by solidification of molten magnesium oxide which contains aluminum. Figure 6 shows the binary phase diagram of $\text{MgO-Al}_2\text{O}_3$ system (Osborn, 1953; Bansal & Heuer, 1974). According to the concentration of aluminum (Fig. 4(e)), the bulk composition is roughly at the broken line, and the anodized layers consist of magnesium oxide and spinel if crystallization thoroughly occurs during the solidification. That mode of solidification is considered to occur in another anodization (Liang et al., 2005), where magnesium oxide and spinel are

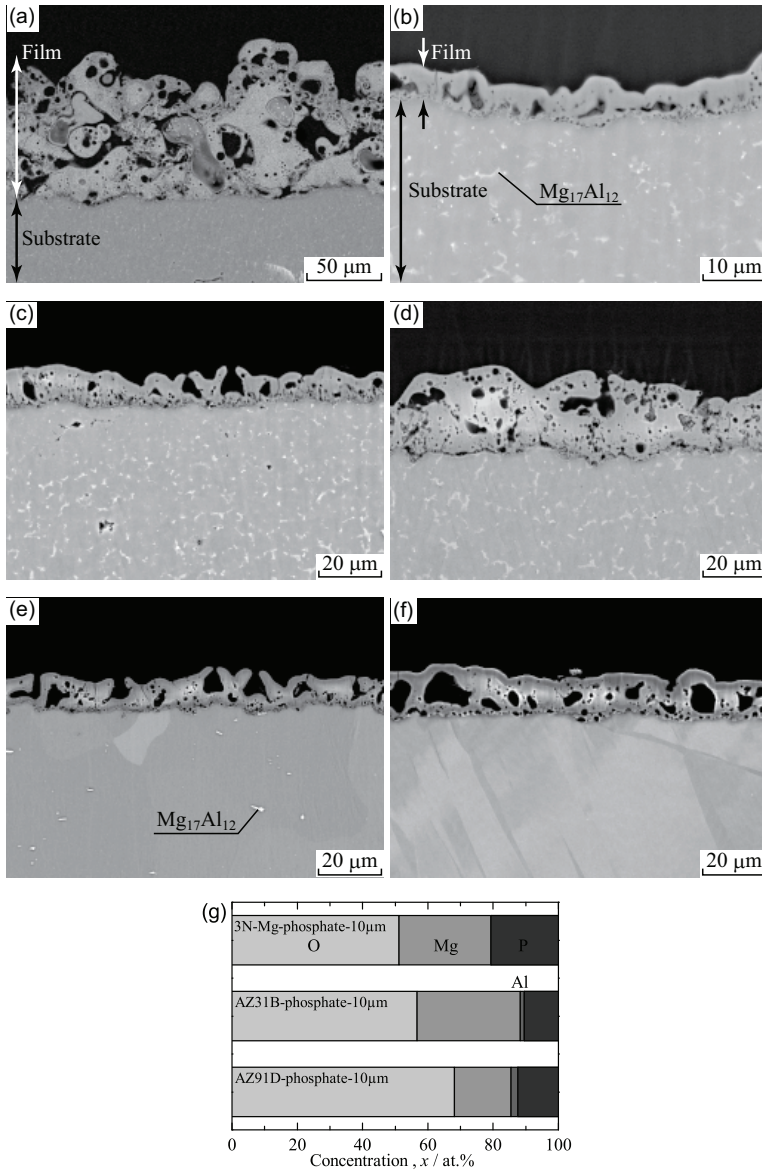


Fig. 4. Cross-sectional backscattered electron images and compositions of the anodized layers ((a) AZ91D-Dow17, (b) AZ91D-phosphate-5μm, (c) AZ91D-phosphate-10μm, (d) AZ91D-phosphate-20μm, (e) AZ31B-phosphate-10μm, (f) 3N-Mg-phosphate-10μm, (g) Compositions of the anodized layers).

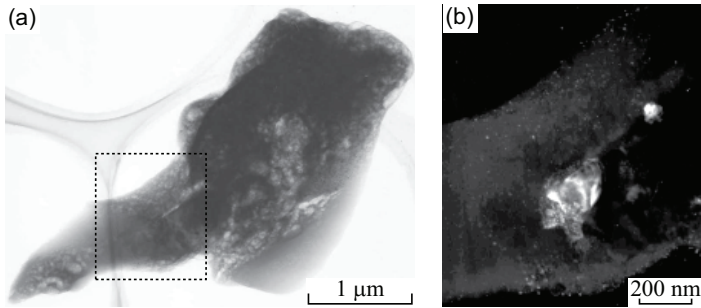


Fig. 5. Transmission electron micrographs of a fragment of anodized layer in AZ91D-phosphate-20 μm ((a) Bright-field image, (b) Magnified dark-field image of the dotted rectangular area in (a)).

detected by X-ray diffraction measurements. On the other hand, those substances are only confirmed by TEM observation in this case, and the main portion of the anodized layer is amorphous (Bonilla et al., 2002).

The difference might be due to the amount of phosphorus in the electrolyte, which modifies the liquidus lines of the system and brings supercooled liquid. During the solidification, magnesium oxide firstly precipitates in the liquid, then, some portion of the supercooled liquid decomposes into fine crystallites of magnesium oxide and spinel. However, most of the supercooled liquid is considered to solidify in amorphous state because of the large cooling rate in the electrolyte. Since $\text{Mg}_{17}\text{Al}_{12}$ phase in the substrate contains large amount of aluminum, aluminum concentration is locally higher than the dotted line in Fig. 6. In that case, spinel firstly precipitates from the liquid, and rather coarse crystallites in Fig. 5(b) are considered to have formed through this process.

By assuming that valences of oxygen, magnesium, aluminum and phosphorus are 2, 2, 3 and 5,

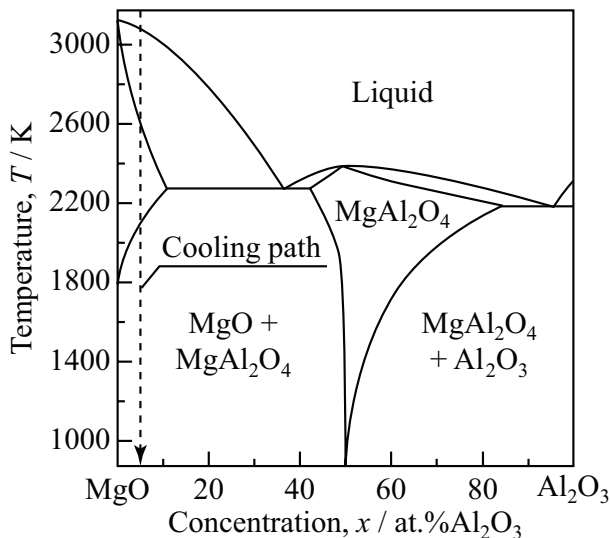


Fig. 6. Binary phase diagram of $\text{MgO}-\text{Al}_2\text{O}_3$ system (Osborn, 1953; Bansal & Heuer, 1974).

respectively, composition of the anodized layers in the case of AZ91D is roughly expressed as $(\text{MgO})_x(\text{MgAl}_2\text{O}_4)_{17-x}(\text{Al}_2\text{O}_3)_{x-16}(\text{P}_2\text{O}_5)_{6.5}$ from Fig. 4(g). The summed amount of oxygen in this chemical formula is 52.5 which is less than the measured value 68, and the gap is thought to be due to water molecules picked up in the anodized layer. Here, elements of oxygen, magnesium, aluminum and phosphorus do not necessarily form the above stoichiometric compounds which have long-range order to show sharp peaks for X-ray diffraction, but the elements in the amorphous anodized layer are assumed to be close to these compounds in terms of short-range order.

The same discussion shows $(\text{MgO})_x(\text{MgAl}_2\text{O}_4)_{32-x}(\text{Al}_2\text{O}_3)_{x-31.5}(\text{P}_2\text{O}_5)_5$ for AZ31B and $(\text{MgO})_{28}(\text{P}_2\text{O}_5)_{10.5}$ for 3N-Mg. In these cases, the summed amount of oxygen is 58.5 and 80.5, respectively, while the measured values are 57 and 51. The difference, in which oxygen is calculated to be excessive according to the above assumption, is considered to be due to an inappropriate assumption for the valences of magnesium or phosphorus. That is, chemical state for each element should be $\text{MgO}_{1-\delta}$ or $\text{PO}_{2.5-\epsilon}$.

3. Corrosion protection by anodized layer

3.1 Experimental

After anodization by the above procedures, the specimens underwent salt spray test (SST, JIS Z2371 or ASTM B-117) and electrochemical measurements for assessing corrosion protectivity of the anodized surfaces. Part of the anodized specimens had their surfaces trenched by ceramic knife, then the corrosion behavior of the exposed areas in the environment of SST was examined by optical and electron microscopies. Electrochemical properties of the anodized layers were evaluated by linear sweep voltammetry (LSV) or by monitoring corrosion current at constant potential (CP). The electrolyte was a solution of 5 mass% sodium chloride whose pH was 6.5, the counter electrode was a plate of titanium coated with platinum, the reference electrode was a standard calomel electrode (SCE) with a saturated solution of potassium chloride, and each working electrode had a square window of $25 \times 25 \text{ mm}^2$. The rate of potential sweep was 1 mV/s in the measurement of LSV, and the potential was -1.4 V vs. SCE in CP.

For qualitative assessment of the formation of magnesium phosphate layer on the substrate due to the changes of the anodized layer in wet environment, 3N-Mg was pickled by phosphoric acid, then, immersed in solutions of trisodium phosphate dodecahydrate ($\text{Na}_3\text{PO}_4 \cdot 12\text{H}_2\text{O}$) of pH 3, 7 or 11 for 30 s at 298 K. Here, the pH of each solution was set by adding phosphoric acid to the solution of trisodium phosphate dodecahydrate whose concentration was originally 100 kg/m^3 . Here, the concentration of phosphate is based on a conventional conversion treatment which utilizes manganese phosphate (Hawke & Albright, 1995).

3.2 Experimental results

3.2.1 Salt spray test

Figure 7 shows the anodized surfaces of AZ91D after SST of 0, 518 and 2160 ks. Although corrosion products were observed locally on the surface of AZ91D-Dow17 as indicated by the broken circles, the anodized layer itself was kept as it had been before SST even in the areas surrounding the corrosion products. On the other hand, the surface of AZ91D-phosphate-10 μm was free from visible corrosion products and had only slight discoloration on the entire surface. In the magnified optical images of the discolored surfaces,

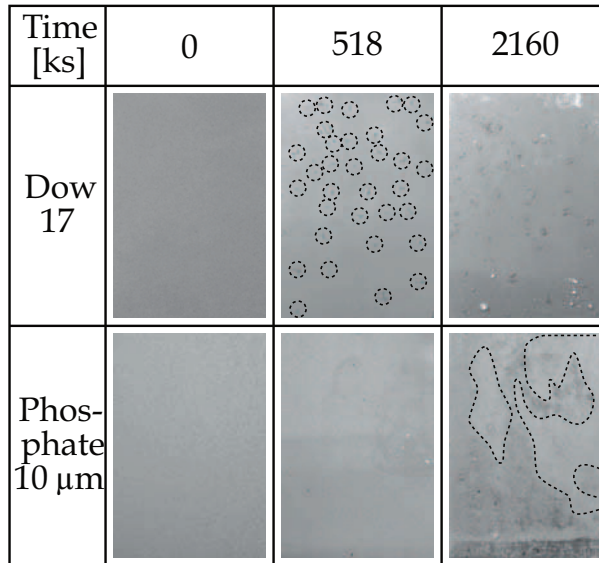


Fig. 7. Anodized surfaces of AZ91D after salt spray test (Circles in AZ91D-Dow17-518ks indicate corrosion products, and lighter areas enclosed by broken curves in AZ91D-phosphate-10μm-2160ks correspond to reduction in anodized layer).

those areas showed local disappearance of the anodized layers especially inside the broken curves, but no remarkable corrosion product was found on those areas.

Figure 8 shows the corrosion product on the as-cast surface after salt spray test for 86.4 ks. Corrosion products with layered structure (Fig. 8(a)) were found locally on the surface, and they were identified mainly as magnesium hydroxide by X-ray diffraction (Fig. 8(b)).

Figures 9, 10, 11, 12 and 13 show the trenched areas on the anodized surfaces after SST. Since the trenched areas were not protected by anodized layers and the substrates were exposed to the wet environment containing chloride ion, the area became a starting point of corrosion in the case of AZ91D-Dow17 as shown in Fig. 9. On the other hand, Fig. 10 shows no

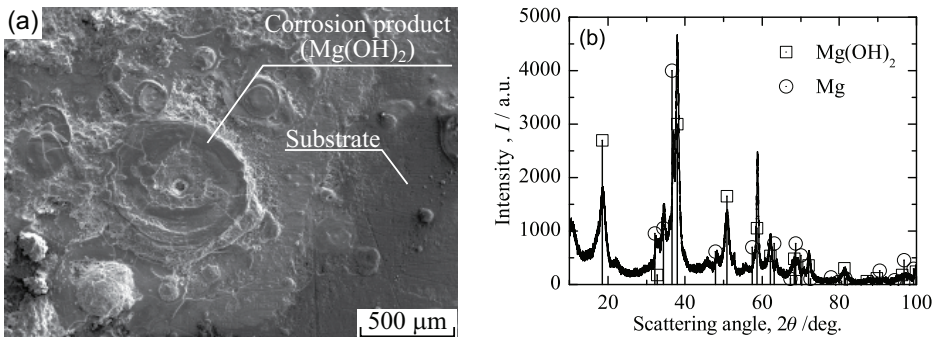


Fig. 8. Corrosion product on the as-cast AZ91D after salt spray test for 86.4 ks ((a) Secondary electron image, (b) X-ray diffraction pattern).

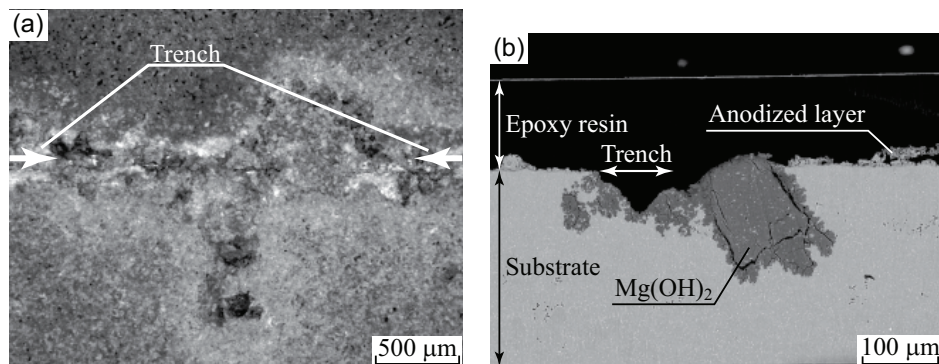


Fig. 9. Trenched surface of AZ91D-Dow17 after salt spray test for 1990 ks ((a) Optical image, (b) Cross-sectional backscattered electron image).

remarkable corrosion product (magnesium hydroxide) even in the trenched area, and cracked films were newly formed on the trenched surfaces during the test which consist of oxygen, magnesium and phosphorus (Figs. 11, 12 and 13). In the cases of AZ91D-phosphate-10 μm and AZ31B-phosphate-10 μm , aluminum was also contained in the regenerated film.

Figure 14 shows the anodized surfaces of AZ91D-phosphate-10 μm after SST for 346 ks and 1990 ks. The original anodized surface with porous morphology was kept locally after SST for 346 ks (Fig. 14(a)). Intensities of O- $K\alpha$ and P- $K\alpha$ characteristic X-rays are comparable on the original porous areas and many parts of the flat ones which lost the original morphology (Fig. 14(b),(d)). This indicates that anodized layer still remains on those areas despite the change in morphology, but most of the anodized layer was lost on the areas where the intensity of Mg- $K\alpha$ remarkably increases in Fig. 14(c). However, the morphology of the surface drastically changed after SST for 1990 ks, showing cracked areas (dark areas in Fig. 14(e)) and flat areas with less cracks (bright areas in Fig. 14(e)). Intensities of O- $K\alpha$ and P- $K\alpha$ characteristic X-rays are higher on the small fragments of $\sim 10\ \mu\text{m}$ in size which exist in the cracked areas of Fig. 14(e) than on the flat areas which seem to have lost the fragments.

3.2.2 Electrochemical properties

Figure 15 shows the polarization curves of the raw and the anodized (phosphate) surfaces obtained by LSV in 5 mass% sodium chloride solution. Anodization can successfully suppress the anodic current or corrosion rate for each substrate, and each corrosion potential is shifted

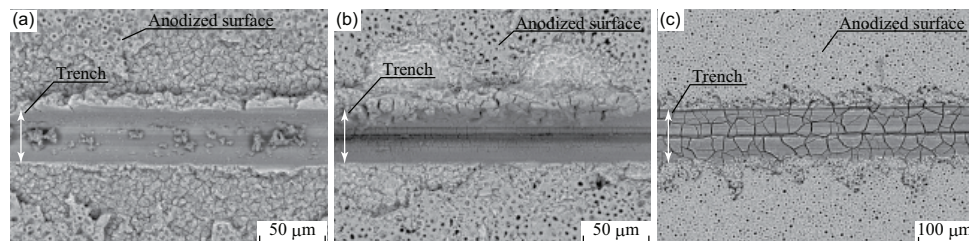


Fig. 10. Backscattered electron images of the trenched areas on the anodized surfaces after salt spray test for 605 ks ((a) AZ91D-phosphate-10 μm , (b) AZ31B-phosphate-10 μm , (c) 3N-Mg-phosphate-10 μm).

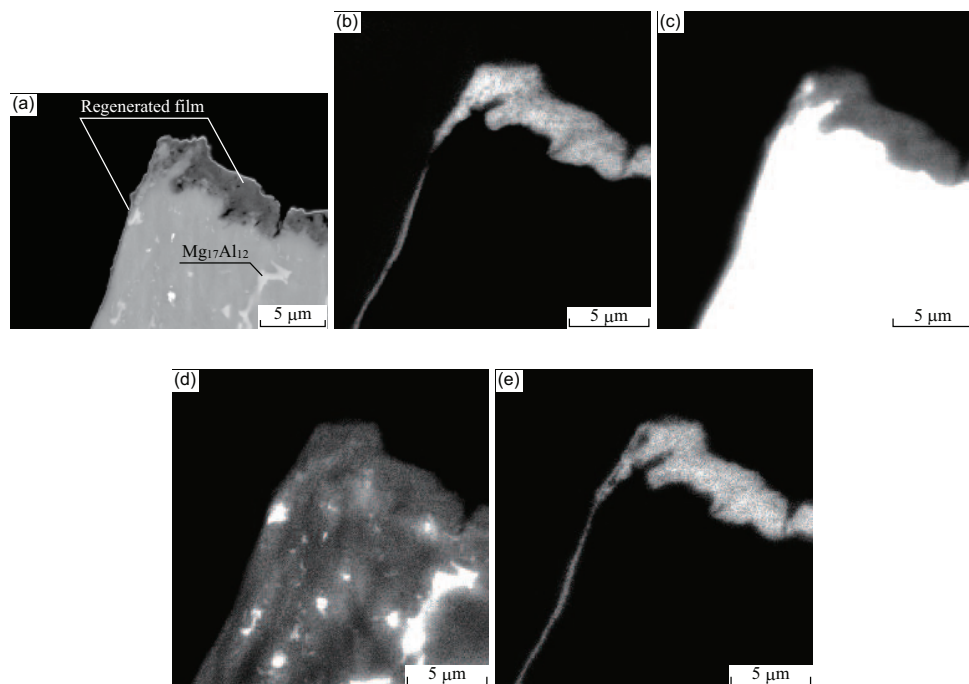


Fig. 11. Cross-sectional analyses of the trenched area on AZ91D-phosphate-10 μm after salt spray test for 605 ks ((a) Backscattered electron image, (b) Intensity map of O- $K\alpha$ characteristic X-ray, (c) Mg- $K\alpha$, (d) Al- $K\alpha$, (e) P- $K\alpha$).

to less noble side by 150-200 mV compared with that of the untreated substrate. The anodized surfaces showed local corrosion as the potential proceeded into the anodic side.

Figure 16 shows the temporal change in current density on AZ91D-Dow17 and AZ91D-phosphate-20 μm held at a constant potential of -1.4 V (vs. SCE) in 5 mass% sodium chloride solution. While the anodic current rapidly increased immediately after the beginning of the measurement in the case of AZ91D-Dow17, AZ91D-phosphate-20 μm showed a plateau where anodic current density was $\sim 10^{-2}$ A/m² before the substrate began to show local corrosion and hydrogen gas was correspondingly generated. After these electrochemical measurements, the cross section of AZ91D-Dow17 showed corrosion of the substrate above which an anodized layer still remained. On the other hand, corrosion of the substrate was observed only beneath the areas where the anodized layer disappeared in the case of AZ91D-phosphate-20 μm .

Figure 17 shows the surface morphology of 3N-Mg after immersion into the trisodium phosphate solutions. The treatment by the solution of pH = 11 (Fig. 17(d)) showed no visible reaction on the substrate which resulted in almost the same surface as that obtained by pickling (Fig. 17(a)), and the treatment by the solution of pH = 3 (Fig. 17(b)) resulted in intense dissolution of the substrate. On the other hand, the solution of pH = 7 brought about precipitation of salt and its resulting local coating on the substrate.

3.3 Discussions

Figures 7, 9, 10, 11, 12 and 13 show that the mechanism of corrosion protection is largely different between the case of Dow17 and that of anodization in phosphate electrolyte. Since paths exist in the porous anodized layer (Dow17) which link the substrate and the surface, corrosion begins at the points where the substrate contacts water which infiltrates from the surface within 500 ks after the initiation of SST. From the point that the anodized layer obtained in Dow17 was kept as it had been after the anodization even at the areas which surround the corrosion products (Fig. 7), its mode of corrosion protection is close to that by tin plating on iron, where red rust is brought immediately by defects or damages on the plated surface which expose iron substrate.

On the other hand, the discoloration of AZ91D-phosphate-10 μm in Fig. 7 does not correspond to formation of magnesium hydroxide (Fig. 8), but to disappearance of the original anodized layer (Fig. 14). The areas are thought to be anodic sites where the anodized layer dissolves into sodium chloride solution during salt spray test. The morphology of the anodized layers on AZ91D-phosphate-10 μm changed from porous one (Fig. 4) to cracked one (Fig. 14(e)-(h)) during SST. The cracked areas are similar to the newly formed surfaces (Fig. 10) in the trenched area, and their morphology is also similar to that obtained by conversion coating which utilizes phosphate solution (Hawke & Albright, 1995). This mode of corrosion well suppresses intense corrosion of magnesium alloys or formation of magnesium hydroxide.

Although the anodized layers obtained in phosphate electrolyte are electrochemically less noble than the substrate, Figs. 15 and 16 show its dissolving rate into water or corrosion rate is quite low (Cai et al., 2006). Increase in thickness of the anodized layer is thought to correspond to the enlargement in the range of sacrificial protection, which means elongated duration in practical use. That is, corrosion protectivity is maintained even on the areas where the original anodized layer is mechanically lost, as long as the remaining one nearby

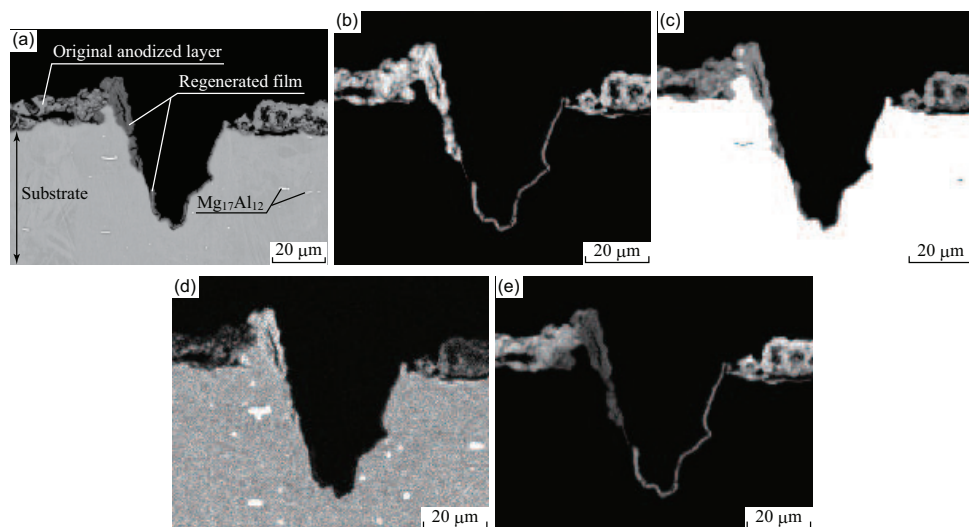


Fig. 12. Cross-sectional analyses of the trenched area on AZ31B-phosphate-10 μm after salt spray test for 605 ks ((a) Backscattered electron image, (b) Intensity map of O- $K\alpha$ characteristic X-ray, (c) Mg- $K\alpha$, (d) Al- $K\alpha$, (e) P- $K\alpha$).

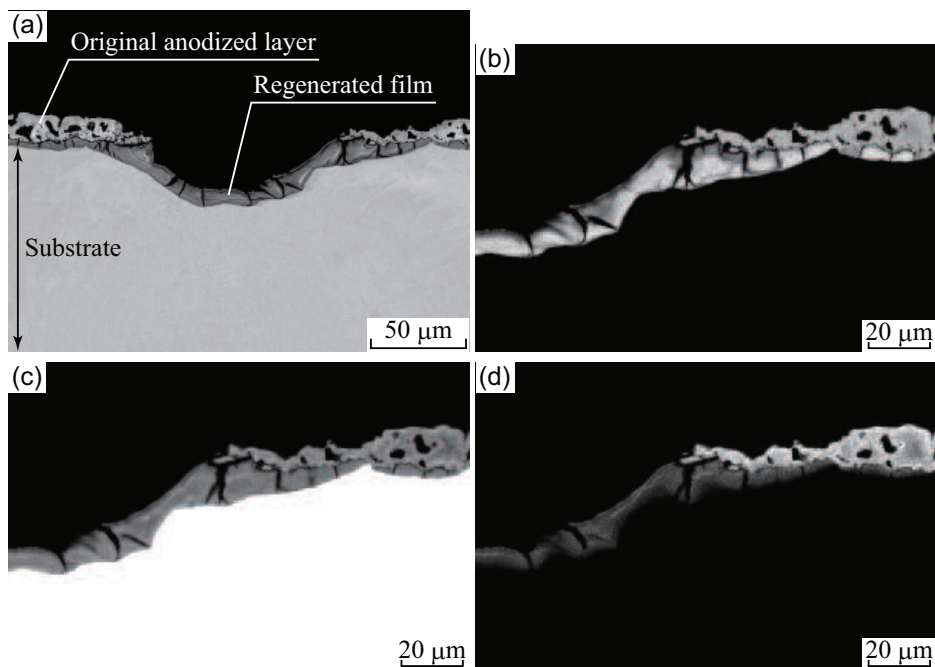


Fig. 13. Cross-sectional analyses of the trenched area on 3N-Mg-phosphate-10 μ m after salt spray test for 605 ks ((a) Backscattered electron image, (b) Intensity map of O-K α characteristic X-ray, (c) Mg-K α , (d) P-K α).

can provide the components required for the formation of another protective layer observed in Figs. 11, 12, 13 and 14(e)-(h). In addition to the sacrificial protection (thermodynamics) and the low dissolving rate (kinetics) of the anodized layer obtained in phosphate electrolyte, the wet environment containing dissolved components as phosphate, which have originally existed in the anodized layer, is considered to have an appropriate pH and work as a solution for conversion treatment to form another protective layer on the substrate. The amorphous structure of the anodized layer obtained in phosphate electrolyte might be one of the reasons for these electrochemical phenomena or excellent corrosion protectivity, and detailed analyses of conversion coatings should give additional information. The elements working in the sacrificial function and the changes in oxidation number, as well as the mechanism of the following formation of another protective layer, will hopefully be clarified in the future work. The regenerated films which consist of oxygen, magnesium, aluminum and phosphorus (Figs. 11, 12 and 13) are thought to be obtained by dissolution of the anodized layers and following formation of an insoluble or poorly soluble salt as magnesium phosphates ($\text{Mg}_3(\text{PO}_4)_2 \cdot 4\text{H}_2\text{O}$, $\text{Mg}_3(\text{PO}_4)_2 \cdot 8\text{H}_2\text{O}$) or magnesium hydrophosphates ($\text{MgHPO}_4 \cdot 3\text{H}_2\text{O}$, $\text{MgHPO}_4 \cdot 7\text{H}_2\text{O}$). When the formation rate of the above dense inert film surpasses that of magnesium hydroxide, corrosion which spoils the appearance of a product can be well suppressed. Although the films show some cracks in them, their adhesion to the substrates is better than that of magnesium hydroxide (Fig.9), and the front of each crack where the substrate is exposed can be covered successfully with the inert film mentioned above. Thus, the areas covered with the regenerated films are thought to avoid formation of magnesium

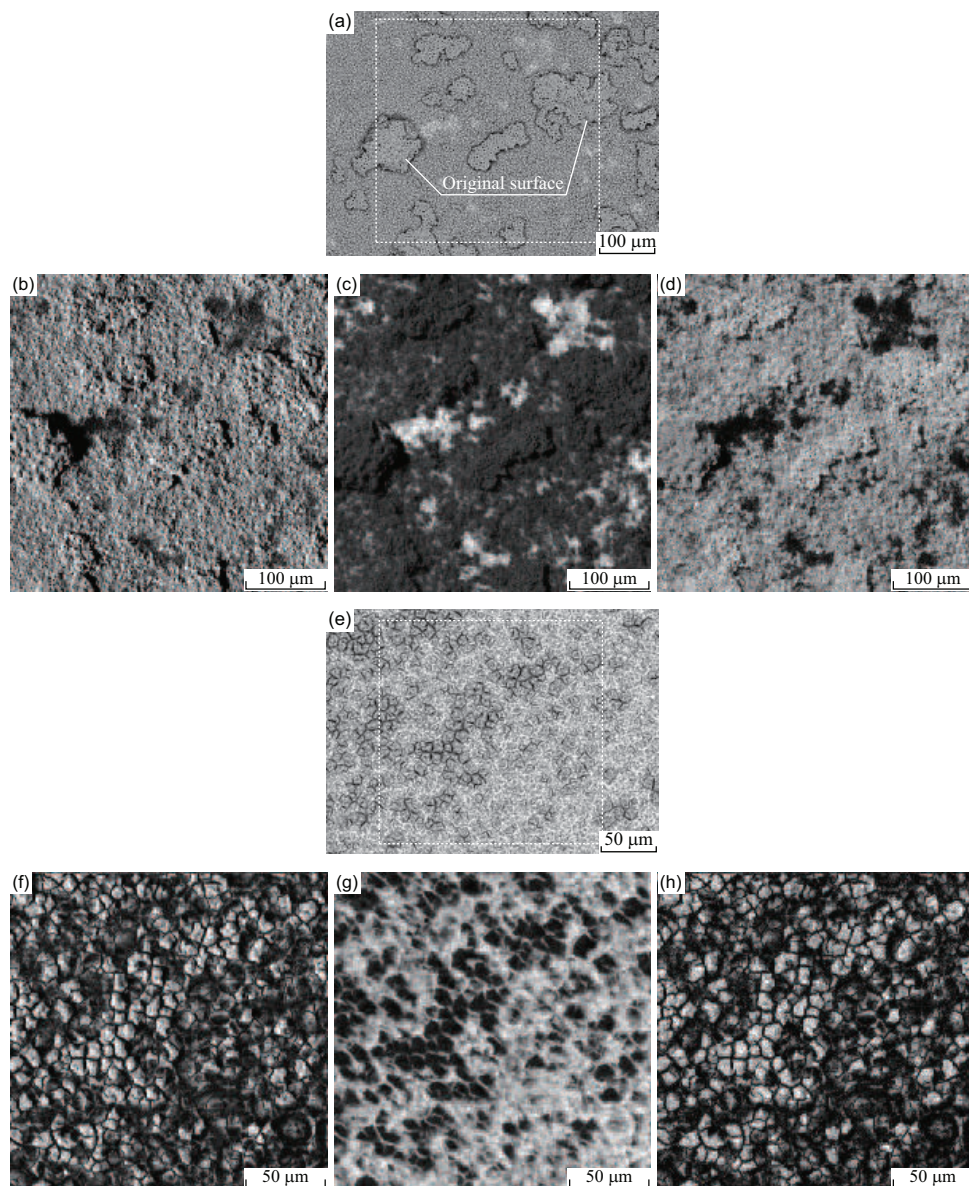


Fig. 14. Anodized surface of AZ91D-phosphate-10 μ m after salt spray test for (a)-(d) 346 ks and (e)-(h) 1990 ks ((a) Backscattered electron image, (b) Intensity map of O-K α characteristic X-ray in the dotted rectangular area of (a), (c) Mg-K α , (d) P-K α , (e) Backscattered electron image, (f) Intensity map of O-K α in the dotted rectangular area of (e), (g) Mg-K α , (h) P-K α).

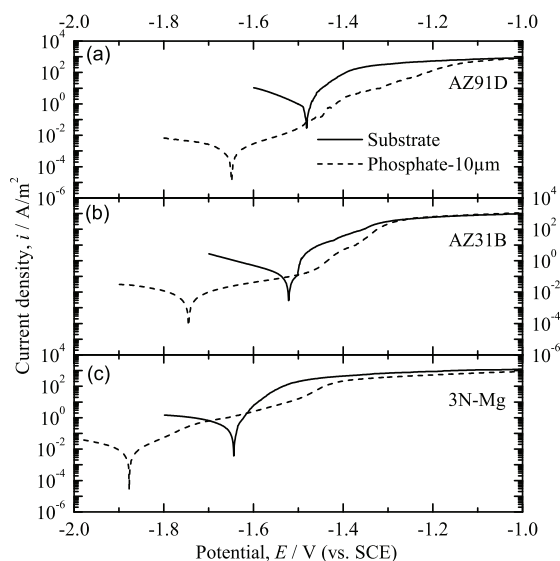


Fig. 15. Polarization curves of the raw and the anodized (phosphate) surfaces obtained by LSV in 5 mass% sodium chloride solution ((a) AZ91D, (b) AZ31B, (c) 3N-Mg, Sweep rate 1 mV/s).

hydroxide or visible corrosion as long as the original anodized layer exists on the surface and keeps dissolving slowly into the wet environment. Here, electrons generated by dissolution or oxidation of magnesium in the substrate are thought to be consumed by the reduction of hydrogen ion ($2\text{H}^+ + 2\text{e}^- \rightarrow \text{H}_2$) which occurs near the anode sites.

Since thickness of the regenerated film is the largest in the case of 3N-Mg and the second largest in the case of AZ31B, the formational rate of the film is thought to become larger for a substrate whose corrosion resistance is poorer. That is, the regenerated film is the

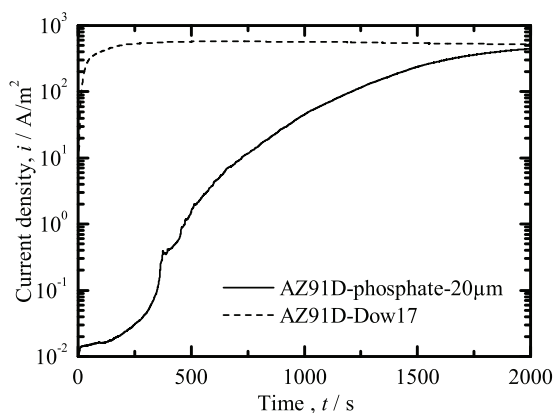


Fig. 16. Temporal change in current density on AZ91D-Dow17 and AZ91D-phosphate-20 μm held at a constant potential of -1.4 V (vs. SCE) in 5 mass% sodium chloride solution.

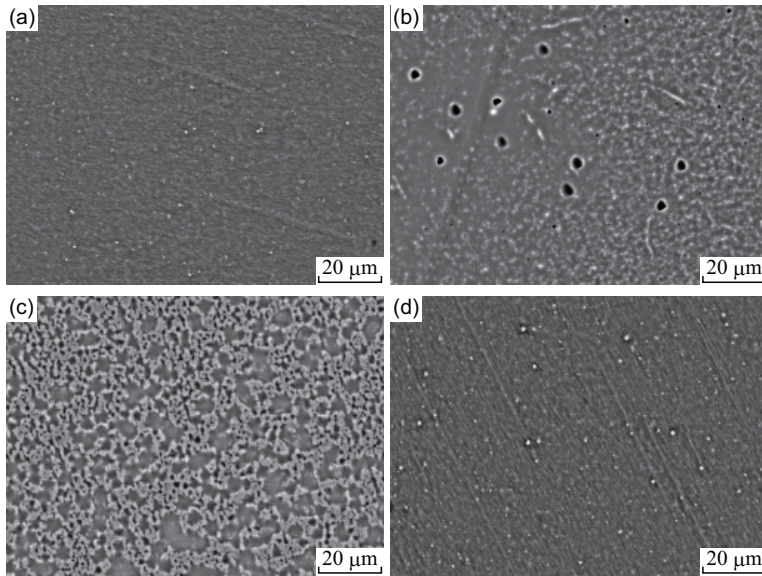


Fig. 17. Surface morphology of 3N-Mg after immersion into the trisodium phosphate solutions ((a) After pickling, (b) pH = 3, (c) pH = 7, (d) pH = 11).

result of reaction of substrate (magnesium) with dissolved chemical agents as phosphate ion (PO_4^{3-}), hydrogen phosphate ion (HPO_4^{2-}), dihydrogen phosphate ion (H_2PO_4^-), or aqueous phosphoric acid (H_3PO_4) at certain pH. From the point that a film is obtained at pH = 7 in the solution of trisodium phosphate (Fig. 17(c)) which can successfully cover the highly active surface of magnesium, the pH of the environment near the trench is supposedly ~ 7 where hydrogen phosphate ion (HPO_4^{2-}) and dihydrogen phosphate ion (H_2PO_4^-) predominate. This is explained by setting pH = 7 ($[\text{H}^+] = 10^{-7}$) for $K_{a1} = \frac{[\text{H}^+][\text{H}_2\text{PO}_4^-]}{[\text{H}_3\text{PO}_4]} = 7.5 \times 10^{-3}$, $K_{a2} = \frac{[\text{H}^+][\text{HPO}_4^{2-}]}{[\text{H}_2\text{PO}_4^-]} = 6.2 \times 10^{-8}$, $K_{a3} = \frac{[\text{H}^+][\text{PO}_4^{3-}]}{[\text{HPO}_4^{2-}]} = 2.1 \times 10^{-13}$. A schematic illustration of dissolution of the original anodized layer and regeneration of the protective film is shown in Fig. 18.

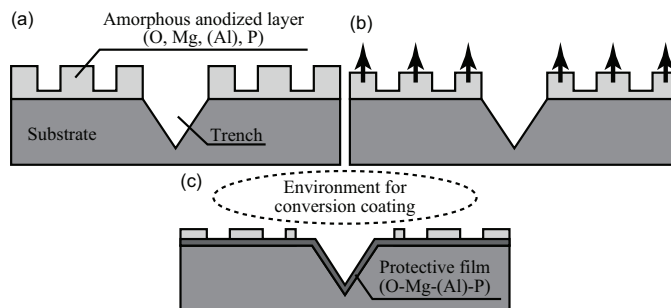


Fig. 18. Schematic illustration of the mechanism of corrosion protection during salt spray test ((a) before test, (b) dissolution of anodized layer, (c) formation of protective layer on the exposed areas of the substrate).

4. Summary

In this chapter, microstructure of anodized layer on magnesium alloys and high-purity magnesium obtained by electrolysis in phosphate solution and corrosion protection by the anodized layers were discussed. The main results can be summarized as follows.

1. The anodized layers obtained in phosphate electrolyte consist of amorphous matrix and fine crystallites of spinel and magnesium oxide.
2. The anodized layers show sacrificial function in wet environment, while that in Dow17 shows barrier protection by passive film.
3. Corrosion protection by anodized layers formed in the phosphate electrolyte is based on electrochemically less nobleness of the original anodized layers whose dissolving rate is quite low. That is, ideal sacrificial function is provided on the substrates in terms of thermodynamics and kinetics.
4. Formation of another protective film on the areas where the original anodized layer is lost prevents substrates from bearing remarkable corrosion product of magnesium hydroxide.

5. References

- (1981). Military Specifications and Standards (1981) MIL-M-45202C.
- (1998). American Society for Testing and Materials (1998) ASTM D 1732-67.
- Bansal, G. K. & Heuer, A. H. (1974). *Phil. Mag.* 24: 709–722.
- Barton, T. (1998). U.S. Pat. 5792335.
- Bonilla, F. A.; Berkani, A.; Liu, Y.; Skeldon, P.; Thompson, G. E.; Habazaki, H.; Shimizu, K.; John, C. & Stevens, K. (2002). *J. Electrochem. Soc.* 149: B4–B13.
- Cai, Q.; Wang, L.; Wei, B. & Liu, Q. (2006). *Surf. Coat. Tech.* 200: 3727–3733.
- Cole, G. S. (2003). *Mater. Sci. Forum* 419-422: 43–50.
- Company, T. D. C. (1956). GB Pat. 762195.
- Evangelides, H. (1955). U.S. Pat. 2723952.
- Hawke, D. & Albright, D. L. (1995). *Metal Fin.* 93: 34–38.
- Hino, M.; Murakami, K.; Hiramatsu, M.; Saijo, A. & Kanadani, T. (2007). *Mater. Sci. Forum* 539-543: 1691–1695.
- Hino, M.; Murakami, K.; Saijo, A. & Kanadani, T. (2008). *Mater. Trans.* 49: 924–930.
- Liang, J.; Guo, B.; Tian, J.; Liu, H.; Zhou, J.; Liu, W. & Xu, T. (2005). *Surf. Coat. Tech.* 199: 121–126.
- Mears, R. B. & Brown, C. D. (1945). *Corrosion – Nat. Assoc. of Corr. Eng.* 1: 113–118.
- Murakami, K.; Hino, M.; Hiramatsu, M.; Nakai, K.; Kobayashi, S.; Saijo, A. & Kanadani, T. (2007). *Mater. Trans.* 48: 3101–3108.
- Murakami, K.; Hino, M.; Hiramatsu, M.; Nakai, K.; Kobayashi, S.; Saijo, A. & Kanadani, T. (2008). *Mater. Trans.* 49: 1057–1064.
- Ono, S. & Masuko, N. (2003). *Mater. Sci. Forum* 419-422: 897–902.
- Osborn, E. F. (1953). *J. Am. Ceram. Soc.* 36: 147–151.
- Pourbaix, M. (1974). *Atlas of Electrochemical Equilibria in Aqueous Solutions*, National Association of Corrosion Engineers, Houston, Texas, USA.
- Saijo, A.; Hino, M.; Hiramatsu, M. & Kanadani, T. (2005). *Acta Metall. Sinica* 18: 411–415.
- Saijo, A.; Murakami, K.; Hino, M. & Kanadani, T. (2008). *Mater. Trans.* 49: 903–908.

Improvement in Corrosion Fatigue Resistance of Mg Alloy due to Plating

Sotomi Ishihara¹, Hisakimi Notoya² and Tomonori Namito¹

¹*Dept. Of Mechanical Engineering, University of Toyama*

²*Takamatsu Plating Co. Ltd.
Japan*

1. Introduction

Magnesium alloys are very attractive as structural materials, because they are extremely light, possessing excellent specific tensile strength, good stiffness, good cutting performance, and good vibrational absorption [1]. In addition, the recycling energy requirement of these alloys is only 4-5% of the energy required to obtain magnesium from the ore [1]. Due to their energy and weight saving characteristics, magnesium alloy are considered to be good candidates for material in auto parts, portable personal computers, and telephones.

However, magnesium alloys have not been extensively used until recently, because of their vulnerability to corrosion. When considering the use of magnesium alloys as structural materials, a thorough understanding of the corrosion-fatigue characteristics is necessary to reflect the results in machine design. Further, improvement in the corrosion fatigue performance of magnesium alloys is highly desirable to realize their potential as structural materials.

Surface treatments, such as coating or plating of the material surface have been examined for enhancement of the corrosion fatigue resistance of magnesium alloys, and in general they have not been successful.

In this paper, two types of plating treatments, i.e., electroless-Ni-plating [2] and electrolytic Ni-plating [3] were applied to the Mg alloy AZ31 to improve the corrosion fatigue resistance of the alloy. Corrosion fatigue lives and fatigue behavior of the specimens were investigated in detail and their mechanisms will be also discussed. Specific contents in this chapter are summarized as follows.

In section 2 [2], fatigue tests were performed on electroless nickel-plated magnesium alloy specimens in laboratory air and 3% sodium chloride solution. In laboratory air, the effect of surface treatments (plating, blasting and polishing) on the fatigue lives of specimens was found to be minimal. However, in 3% sodium chloride solution, the electroless Ni-plated specimens were found to have shorter fatigue lives than those of the polished and blasted specimens. In order to study the fatigue mechanisms, successive observations of the specimen surfaces were conducted during the fatigue process in both laboratory air and sodium chloride solution. Observations of the fracture surfaces were also conducted to clarify the fatigue mechanism.

In section 3 [3], the fatigue behavior of electrolytically nickel-plated Mg alloy both in laboratory air and in a corrosive environment (3% NaCl) were described. The fatigue

lifetimes, the crack initiation and the propagation behaviors of both plated and unplated specimens were studied in order to determine the effect of a nickel coating. In air, the nickel plating was detrimental because of the easy nucleation of fatigue cracks at depressions in the coating which resulted from the plating process. However, in 3% NaCl, the fatigue properties of plated specimens were markedly superior to those of unplated specimens due to their good resistance to corrosion. Further improvement in the fatigue lives of Ni-plated specimens is expected if the plating process can be modified to eliminate the formation of defects such as surface depressions.

2. Effect of electroless-Ni-Plating on corrosion fatigue behavior of Mg alloy[2]

Dr. Nan performed corrosion fatigue tests on AZ31B magnesium alloy [4], and clarified shorter fatigue lives than those in non-corrosive laboratory air, especially in the lower stress amplitude region. Electroless Ni plating is expected to be beneficial in improving the corrosion fatigue performance of magnesium alloys. However, studies on fatigue behavior of electroless Ni plated magnesium or other alloys have been limited. Punch-Cabrera et al. [5] studied the corrosion fatigue lives of electroless Ni deposited 7075-T6 aluminum alloy in 3% sodium chloride solution. They reported that the deposition increased the corrosion fatigue lives by 60–70% in the low cycle fatigue region of 10^4 – 10^5 cycles. Contreras et al. [6] reported a remarkable decrease in the fatigue lives of electroless Ni deposited AISI-1045 steel in laboratory air. Saeid et al. [7] investigated the fatigue behavior of electroless Ni deposited Ck45 steel in laboratory air. They also reported that the electroless Ni deposit decreased the fatigue life, because cracks were initiated early during the fatigue process at the interface between the deposit and substrate. Therefore, these results reported to date regarding the effectiveness of electroless Ni deposits on the fatigue lives of alloys are rather different.

In the present study, fatigue tests were conducted on electroless Ni plated AZ31 magnesium alloy specimens in laboratory air and 3% sodium chloride solution, in order to study the effect of electroless Ni plating on fatigue life. For comparison, specimens with different surface treatments, machine-polishing and glass bead-blasting, were also tested. The fatigue mechanisms of the electroless Ni-plated Mg alloy specimens in both laboratory air and 3% sodium chloride solution were studied in detail.

2.1 Specimens and experimental methods

2.1.1 Specimens

The material used in the present study was an extruded AZ31 magnesium alloy. Its chemical composition is listed in Table 1. The main chemical compositions of the material are 3 wt.% aluminum and 1 wt.% zinc. The yield strength, tensile strength, elongation and Young's modulus of the material were found to be 200 MPa, 275 MPa, 11.0% and 45 GPa, respectively. Specimens were machined into a round bar shape with a minimum diameter of 5.6 mm, as shown in Fig. 1.

Wt.(%)								
Al	Zn	Mn	Fe	Ni	Si	Pb	Ca	Mg
2.98	0.97	0.004	0.007	0.005	0.02	0.01	0.04	Bal.

Table 1. Chemical compositions of the material used

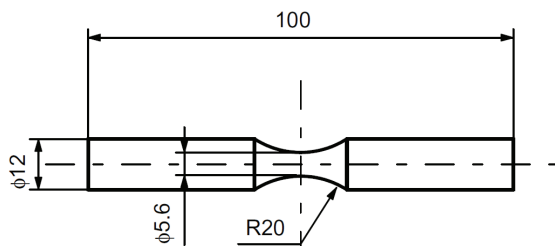


Fig. 1. Shape and dimensions of the specimen (mm).

Solution-pH	Plating time [min]	Plating temperature [K]	Plating bath	Plating thickness [μm]
6.0	60	344	Heat-resistant resin	24

Table 2. Conditions used for electroless Ni-plating

Blasting pressure[MPa]	Blasting distance[m]	Blasting material
0.39	0.1	Glass beads, 150 μm in diameter

Table 3. Conditions employed for glass bead-blasting in the present study

The as-machined specimens were blasted with glass beads, followed by electroless Ni plating prior to the fatigue tests. Tables 2 and 3 show the conditions for the electroless Ni plating and blasting treatments, respectively. Machine-polished specimens were also prepared by polishing the as-machined specimen with emery papers and diamond pastes. Fatigue tests of the glass bead-blasted and machine-polished specimens were conducted for comparison with the electroless Ni plated specimens.

2.1.2 Experimental methods

Fatigue tests were conducted using a cantilever type rotating bending fatigue machine. The tests were conducted at a frequency of 30 Hz, and at an R ratio of -1 . 30 Hz was chosen as a typical frequency, since no significant effect of frequency was observed on the corrosion fatigue behavior within the range of 1–60 Hz. Fatigue tests in laboratory air were conducted at room temperature with humidity of 63–73%.

Corrosion fatigue tests were performed by dripping 3% sodium chloride solution in ion exchanged water onto the specimen surface at a constant rate using a metering pump. The corrosive solution was maintained at a temperature of 298 K. The replica method was used for the successive observations of the specimen surfaces during the fatigue process.

Fatigue tests were interrupted at constant intervals for taking replicas. The collected replicas were examined using an optical microscope with a magnification of 400 times, in order to obtain information regarding crack size and shape during the fatigue process. A part of each specimen was observed directly with an optical microscope to study how cracks propagate and interact with the microstructure of the material. The specimen hardness was measured with a microhardness testing machine under experimental conditions of a 100 g load for 30 s of load time.

2.2 Experimental results

2.2.1 Characterization of the electroless Ni-plated film

Fig. 2(a) shows the cross section of an electroless Ni plated specimen. Good adhesion between the Ni plating film and the magnesium alloy (substrate) is observed, because no abrasion was observed along the interface between the plating and substrate, both before and after the fatigue tests. However, sedulous investigation of the interface revealed that local defects are present in the plating film, as shown in Fig. 2(b). The defect density within the plating film was 0.2 per mm. The average thickness of the plated Ni film was $24\ \mu\text{m}$. The hardness of the plating film was $HV_{100} = 487$, while that of the magnesium alloy (substrate) was $HV_{100} = 57$. The latter possesses only 1/8 hardness of the former, indicating a large difference in hardness. Electron probe micro-analysis (EPMA) determined that the chemical composition of the plating film was 92 wt.% Ni and 8 wt.% P.

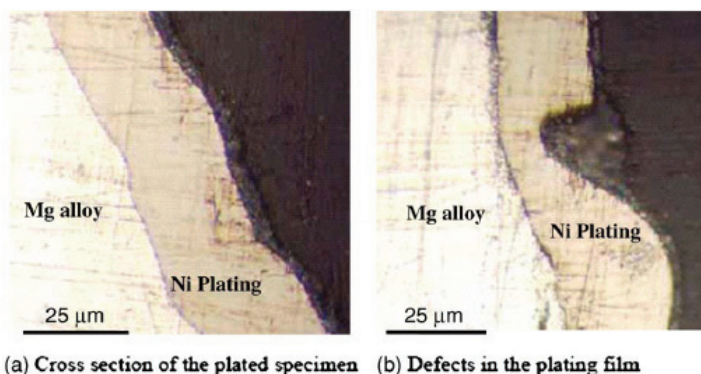


Fig. 2. Cross sections of the electroless Ni plated specimen. (a) Cross section of the plated specimen, (b) Defects in the plating film.

2.2.2 Effects of the surface treatments on the fatigue lives

Fig. 3 shows S-N data in laboratory air for the three types of surface treated specimens, polished, blasted, and electroless Ni plated specimens. The solid curve in the figure indicates the approximated S-N curve for the three types of specimens. The dashed line in the figure represents the S-N curve previously reported by the present authors [8] using similar AZ31 magnesium specimens with polished surfaces. The curve was added to make up for limited experimental data of the polished specimen. The dashed line agrees well with the present S-N curve (solid curve) of the specimens with three different surface treatments. Therefore, we can conclude that the S-N data measured in laboratory air are not affected by the surface treatments under the present experimental conditions.

The value of the fatigue limit ranged from 120 to 130 MPa, regardless of the different surface treatments.

Fig. 4 shows S-N curves for the three different type specimens, machine-polished, glass bead-blasted and electroless Ni plated specimens in 3% sodium chloride solution. The solid line in the figure indicates the S-N curve in laboratory air that is shown in Fig. 3.

The corrosion fatigue lives for the polished specimens are equal to those of the blasted specimens. The dashed line in the figure shows the S-N curve for the both polished and blasted specimens. On the other hand, the corrosion fatigue lives for the electroless Ni

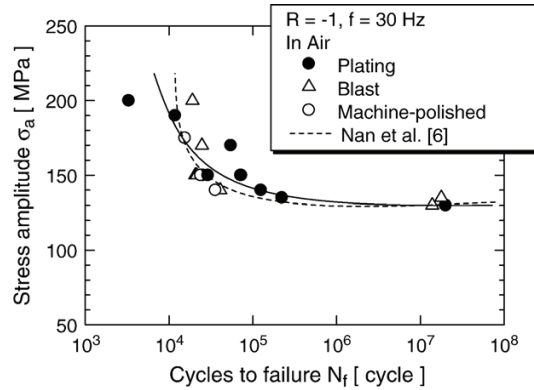


Fig. 3. S-N curves of the plated, polished and blasted specimens in laboratory air. Effect of the surface treatments on fatigue life was minimal in laboratory air.

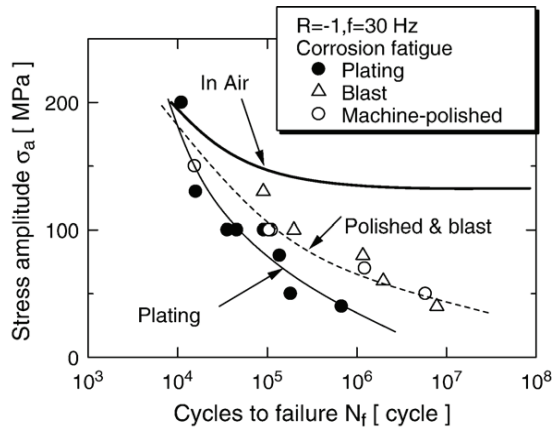


Fig. 4. S-N curves of the plated, polished and blasted specimens in 3% sodium chloride solution. The corrosion fatigue lives of the plated specimens were shorter than the blasted and polished specimens.

plated specimens were shorter than those of the polished and blasted specimens at constant stress amplitudes.

As expected with corrosion fatigue, the fatigue limit disappeared, and significant decreases in the corrosion fatigue lives were observed with the decrease in stress amplitude, regardless of the specimen surface treatment. This observation is common with that of previous studies of other materials, such as steel and aluminum alloy [9, 10].

2.2.3 Successive observations during fatigue process

Fig. 5 shows successive observations for the electroless Ni plated specimen tested in laboratory air at 150 MPa and failed at $N_f = 2.9 \times 10^4$. In these figures, crack initiation is indicated by a solid curve, as it is not so conspicuous due to the rough surface of the plated specimen. Surface irregularities are preminent in the electroless Ni plated specimen, as a

result of plating particles and surface roughening by the blasting. Fig. 5(b) at $N = 6160$ cycles, a crack $60 \mu\text{m}$ in length can be seen on the plated specimen surface. This crack propagated to $240 \mu\text{m}$ in length at $N = 12,320$ cycles, as shown in Fig. 5(c). In laboratory air, specimen surface damage such as depressions of the plated surface, which will be later explained in the section on corrosion fatigue, were not observed in these figures.

Fig. 6 shows the results of successive observations of the electroless Ni plated specimen in 3% sodium chloride solution, which was tested at 100 MPa and failed at $N_f = 4.6 \times 10^4$. In Fig. 6(b) at $N = 10560$ cycles, a $150 \mu\text{m}$ crack was observed to propagate on the plated specimen surface. This crack propagated to $345 \mu\text{m}$ in length at $N = 15,840$ cycles, as shown in Fig. 6(c). During the corrosion fatigue process, a depression of the plated specimen

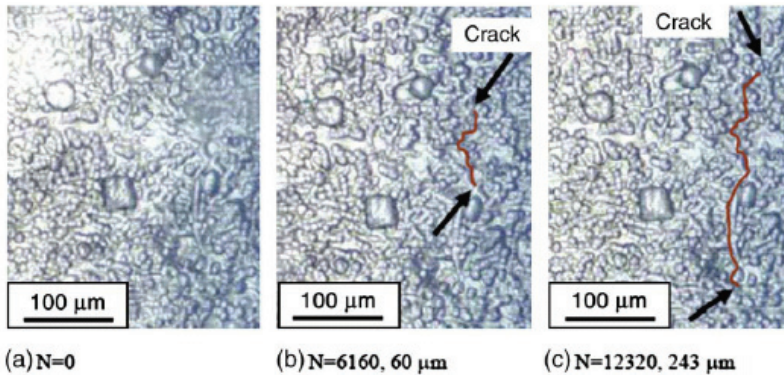


Fig. 5. Successive observations of the electroless Ni plated specimen during the fatigue process in laboratory air tested at stress amplitude 150 MPa ($N_f = 2.9 \times 10^4$). The crack initiated at the specimen surface, as indicated by the arrows.

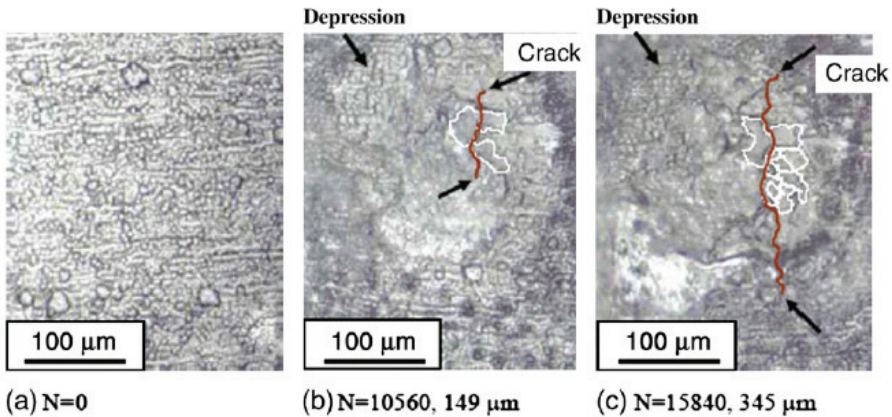


Fig. 6. Successive observations of the electroless Ni plated specimen during the fatigue process in 3% sodium chloride solution tested at stress amplitude 100 MPa ($N_f = 4.6 \times 10^4$). A depressed portion appeared on the specimen surface, and a crack initiated within the depressed area.

surface (ca. 270 μm diameter) was observed as indicated in the figures. The mechanism for the depression of the plated specimen surface is discussed later.

2.2.4 Crack propagation behavior

Fig. 7(a) shows the crack propagation curves in laboratory air at a stress amplitude of 150 MPa for both the electroless Ni plated and the polished specimens. There is little difference observed between the crack propagation curves of both specimens. Fig. 7(b) shows the crack propagation curves in sodium chloride solution at a stress amplitude of 100 MPa for both the electroless Ni plated and the polished specimens. A crack is initiated earlier in the electroless Ni plated specimen than in the polished specimen. This shortening in the crack initiation corresponds well with the experimental finding that the corrosion fatigue lives of the electroless Ni plated specimens became shorter than those of the polished specimens.

Figs. 8(a) and (b) show the relations between the crack propagation rate da/dN (m/cycle) and the stress intensity factor range ΔK ($\text{MPa m}^{1/2}$) in laboratory air and sodium chloride solution, respectively. ΔK was calculated as $1.04 \times 0.73 \sigma_a \sqrt{\pi a}$, where σ_a is the stress

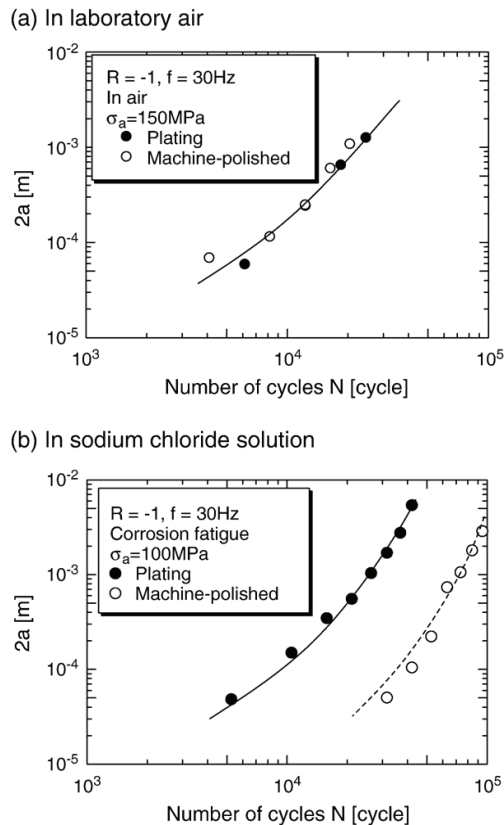


Fig. 7. Crack growth curves ($2a$ - N) in corrosive environments, where $2a$ is the crack length and N is the number of loading cycles. (a) In laboratory air. (b) In sodium chloride solution.

amplitude, a is a half crack length, 1.04 is the stress concentration factor for the notch introduced in the specimen. 0.73 is a modification factor for assuming a crack shape as a half circular one. As can be seen from these figures, no differences in the relations of da/dN - ΔK between the electroless Ni plated and the polished specimens are seen for either conditions of laboratory air or sodium chloride solution. The solid curves shown in these figures indicate the approximated curves of the da/dN - ΔK relation.

2.2.5 Fractography

Fig. 9 shows the fracture surface of an electroless Ni plated specimen failed at 2.22×10^5 cycles and a stress amplitude of 135 MPa in laboratory air. The semi-circular shaped fatigue crack, as indicated by the dotted line in the figure, which may have started from the specimen surface, can be seen on the fracture surface of the plated specimen. In the polished

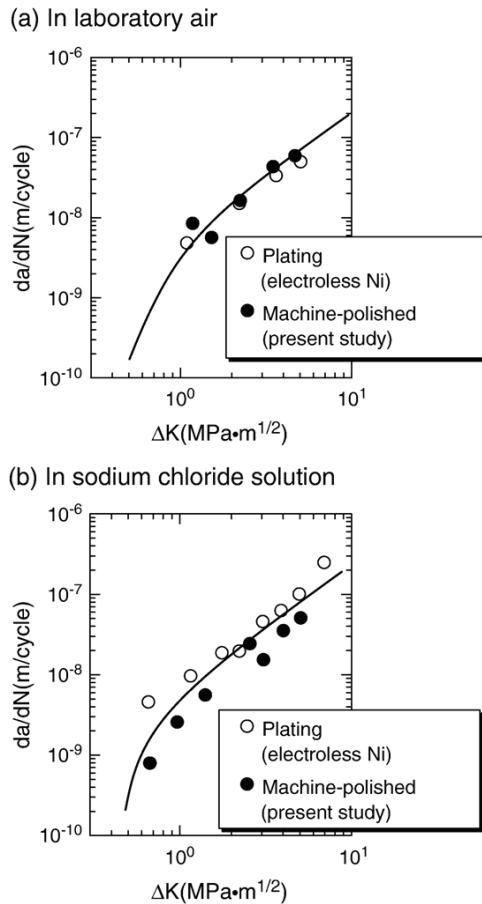


Fig. 8. Relationship between the crack propagation rate da/dN and the stress intensity factor range ΔK for the electroless Ni plated and polished specimens. (a) In laboratory air. (b) In 3% sodium chloride solution.

specimen, a similar semi-circular shaped fatigue crack initiated from the specimen surface was also observed on the fracture surface. Other plating damage, such as the depression or detachment of the plating film was not observed. This indicates that good cohesion was maintained during the fatigue process in laboratory air. The above observation corresponds well with the fact that plating depressions were not seen during the successive observations in laboratory air (Fig. 5).

Fig. 10 shows a fracture surface of the electroless Ni plated specimen that failed in sodium chloride solution at 9×10^4 cycles and a stress amplitude of 100 MPa. Unlike with laboratory air, a corrosion pit was initiated in sodium chloride solution at the interface between the plating film and the substrate, as indicated in the figure. The corrosion pit diameter was estimated as 300 μm . This estimated diameter is almost equivalent to the diameter of the plating depression shown in Fig. 6. The fatigue crack initiated from the bottom of the corrosion pit as indicated in the figure, and then caused the final failure of the specimen.

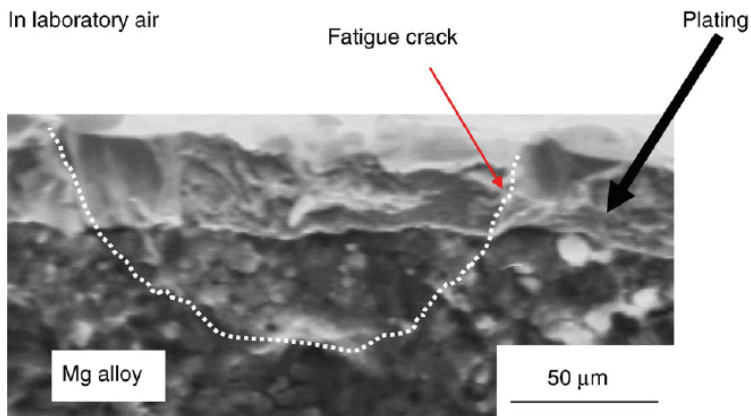


Fig. 9. Fracture surface of the electroless Ni plated specimen, failed at 2.23×10^5 cycles and stress amplitude of 135 MPa in laboratory air.

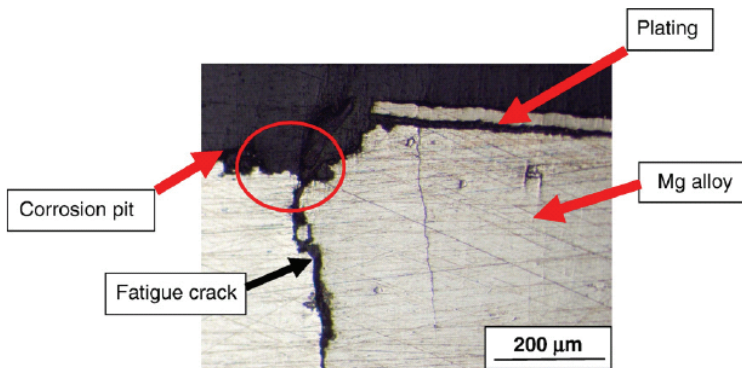


Fig. 10. Fracture surface of the electroless Ni plated specimen, failed at 9×10^4 cycles and stress amplitude of 100 MPa in sodium chloride solution.

2.3 Discussion

2.3.1 Comparison between the fatigue lives in laboratory air and those in sodium chloride solution

As shown in Fig. 4, the corrosion fatigue lives in sodium chloride solution were shortened compared with those in laboratory air. This shortening of the corrosion fatigue lives was observed regardless of the specimen treatment; polished, blasted or electroless Ni plated. However, the worst case was the electroless Ni plated specimens.

During the corrosion fatigue process, corrosion pits were initiated at the specimen surface (polished and blasted specimens) or the interface between the plating and the Mg alloy (electroless Ni plated specimen). A crack was initiated from the bottom of the corrosion pit that reached a critical depth for crack initiation, as shown in Fig. 10, then propagated and was followed by final failure of the specimen.

On the other hand, in laboratory air, cracks were initiated from the surface defects, for example, from nonmetallic inclusions or slip lines on the specimen surface of the polished and blasted specimens. This might also be true for the case of the electroless Ni plated specimen, because differences in the crack initiation and propagation behavior were not observed between the electroless Ni plated and the polished specimens, as shown in Fig. 7(a). The fatigue crack may initiate from the surface of the plating film.

With regard to crack propagation behavior, comparison of the $da/dN-\Delta K$ relation in laboratory air (Fig. 8(a)) and in 3% sodium chloride solution (Fig. 8(b)) revealed no differences in crack propagation.

Therefore, the corrosion fatigue lives of the three different specimens were shortened in sodium chloride solution compared to laboratory air, because the crack initiation processes were hastened due to the initiation and growth of corrosion pits.

2.3.2 Corrosion fatigue lives of the electroless Ni plated specimens

The corrosion fatigue lives of the electroless Ni plated specimens became shorter than those of the polished and blasted specimens.

In general, compressive residual stresses are introduced to the specimen surface by electroless Ni plating or blasting treatment [11-13]. Roughening of the specimen surface is also induced by the blasting treatment. Compressive residual stresses are known to improve the fatigue strength. On the other hand, surface roughening has a negative effect on the fatigue strength, because it hastens crack initiation.

As can be seen from Fig. 3, the S-N curves in laboratory air were not affected by the specimen surface treatments of electroless Ni plating, polishing or blasting. This indicates that the compressive residual stresses and surface roughening, which might be introduced into the specimens by plating and blasting, were not sufficiently large to affect the fatigue lives of both types of specimens.

Therefore, another mechanism, other than compressive residual stresses and surface roughening, is required to explain the lower corrosion fatigue strength of the electroless Ni plated specimens compared with those of the blasted and polished specimens.

Fig. 11 shows an SEM (scanning electron microscopy) photograph of the electroless Ni plated specimen surface. Small plural pores are seen to be initiated on the specimen surface as indicated by the arrows in the figure. Fig. 12 shows a cross section of the electroless Ni plated specimen in sodium chloride solution, which was tested and interrupted at half of the fatigue life. A corrosion pit initiates at the interface between the plating film and the substrate as indicated in the figure. During the corrosion fatigue process, it is considered

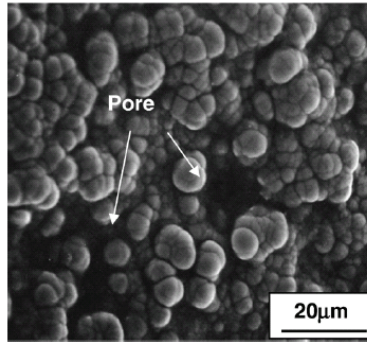


Fig. 11. SEM photograph indicating the specimen surface morphology of the electroless Ni plated specimen.

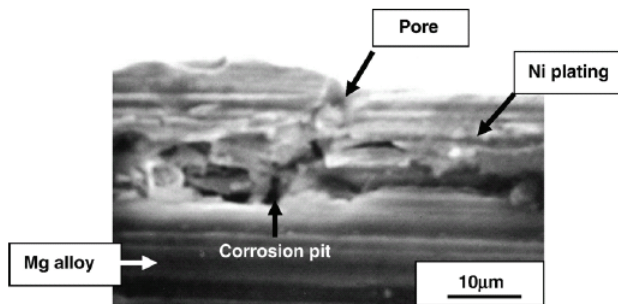


Fig. 12. Cross section of the electroless Ni plated specimen, which was tested and interrupted during fatigue in sodium chloride solution. The corrosion pit is found to be initiated at the interface between the plating and the matrix.

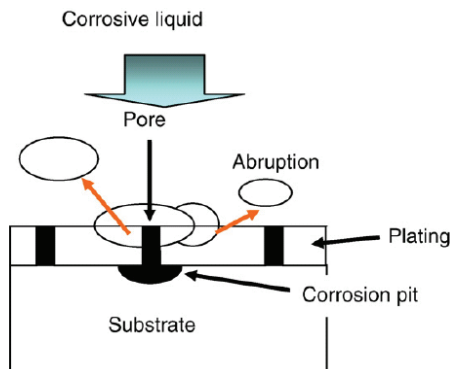


Fig. 13. Schematic illustration showing the mechanism for abrasion of the plating membrane in sodium chloride solution.

that the corrosive solution infiltrates to the interface through the small pores indicated in Fig. 12, and this leads to local corrosive reactions.

Fig. 13 shows a schematic illustration of the mechanism for the depression and abruption of the plating film during the corrosion fatigue process. Firstly, corrosive solution infiltrates to the interface through the small pores during the corrosion fatigue process. Then, the pH value decreases and leads to local corrosive reaction at the interface, followed by the initiation and growth of the corrosion pit. A crack

The results, as validated by Fig. 7(b), indicate that the corrosion fatigue lives of the initiates at the bottom of the corrosion pit and leads to the final failure of the specimen. The depression and abruption of the plating film might be induced at the location where the corrosion pit initiated and grew. With regard to the crack propagation behavior, no significant differences were observed, for the various surface treatments, in either laboratory air or sodium chloride solution, as shown in Fig. 8, electroless Ni plated specimens became shorter than those of the polished and blasted specimens primarily due to the acceleration of the crack initiation process in the electroless Ni plated specimens.

3. Corrosion fatigue resistance of an electrolytically-plated Mg alloy [3]

Surface treatments, such as coating or plating of the material surface have been examined for enhancement of the corrosion fatigue resistance of magnesium alloys, and in general they have not been successful. For example, Khan et al. [14, 15] found no effect on the fatigue properties of anodized AM60 Mg alloy tested in 55% humidity and 80% humidity environments. Eifert and Thomas [16] also investigated the effect of anodizing on the fatigue performance of WE43A-T6 Mg alloy in laboratory air and found that anodizing decreased the fatigue strength by 10% in the high cycle regime. Such results are not surprising since anodized coatings are not impervious to moisture. In addition, Ishihara et al. [2] found that an electroless-nickel plating had no beneficial effect on the corrosion fatigue behavior of AZ31 magnesium alloy.

There have been a few investigations involving the surface treatment of base materials other than magnesium which have been successful in improving resistance to corrosion fatigue. For example, Puchi-Cabrera et al. [5] found the fatigue life of 7075-T6 aluminum alloy plated with electroless-nickel and tested in a 3% NaCl solution to be 60–70% higher relative to the unplated condition. Asquith et al. [17] studied the aluminum alloy 2024 which had been subjected to both a coating developed by plasma electrolytic oxidation (PEO) and shot peening. The surface treated alloy was tested in laboratory air. They reported that the double surface treatment resulted in an improvement in fatigue life.

On the other hand, Contreras et al. [6] found the fatigue life of AISI-1045 carbon steel coated with an electroless-nickel plating and tested in an ambient atmosphere to be significantly reduced. A similar result was reported by Saeid et al. [7] for CK45 carbon steel plated with an electroless-Ni coating. In this case the reduction in fatigue life was attributed to early crack initiation at the interface between the matrix and the plating. Cirik and Genel [18] studied the effect of varying thickness of an anodic coating on 7075 aluminum alloy in laboratory air, and found that the anodic coating reduced the fatigue strength.

As reviewed above, a number of investigations of surface-coating methods for the improvement of fatigue strength have been conducted, and in particular case of magnesium alloys none of approaches cited above has been shown to be beneficial. In addition, the fatigue crack initiation and propagation behavior of surface treated specimens have not been examined in any detail.

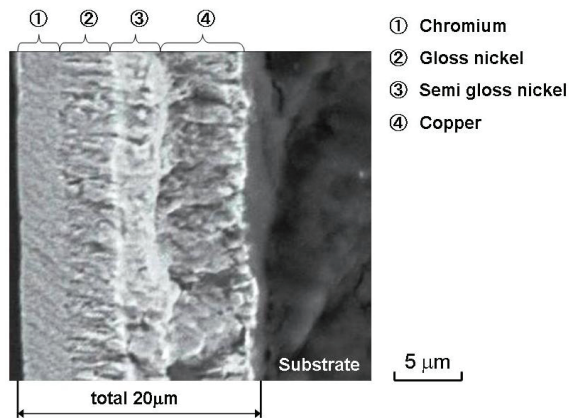
In the present investigation the influence of a protective barrier coating of nickel, which is electrochemically much more noble than magnesium, on the corrosion fatigue properties of a magnesium alloy, AZ31B, will be examined. In addition, the fatigue crack initiation and crack growth processes will be studied using a replica technique.

3.1 Specimens and experimental procedures

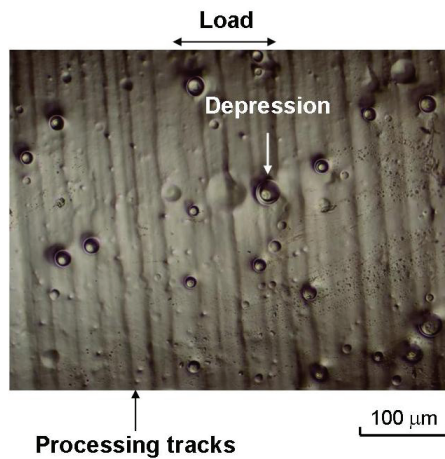
3.1.1 Specimens

a. Materials

The chemical composition and mechanical properties of the commercially-available extruded AZ31B magnesium alloy used in the present study are listed in Table 1 and Table 2, respectively. The main chemical components of the alloy are Al (3 wt.%) and Zn (1 wt.%). The balance is Mg together with trace amounts of other elements.



(a) Cross section of the plated film.



(b) Plated specimen surface.

Fig. 14. Optical micrographs of the plated film.

b. Unplated specimens

Round bar rotating bending fatigue specimens with a minimum diameter of 5.6 mm were machined from the as-received round bar ($\phi 15$ mm). Prior to testing the as-machined specimen surfaces of the gauge section of specimens were polished with 400–2000 emery-papers and then with diamond paste with grit size of 1 μm to obtain a mirror-like finish (roughness: 0.07 μm). The stress amplitude applied to the specimen was calculated by multiplying the nominal stress by a stress concentration factor of 1.02.

c. Plated specimens

The plated specimens were prepared by cleaning the as-machined specimens in alkali solution, followed by the application of a 20 μm - thick multilayer-electrolytic coating. The plating was conducted at conditions, pH: 4–5, temperature: 318–328 K, and current density: 3–5 A/dm². The detailed plating procedures were as follows:

1. *Bath compositions*: nickel sulfate, nickel chloride, and acidum boricum.
2. *Plating times*: total 30 min including degreasing.
3. *Additive*: the brightening agent (gloss agent) was added to improve the plating quality.

Fig. 14a shows a cross section through the multi-layered coating which consists of an inner 7–8 μm layer of copper, two 4–5 μm intermediate layers of nickel (semi-gloss and gloss nickel) and an outer 3 μm layer of chromium. The outer chromium layer on the specimen surface was applied for the purpose of improving the surface finish and for providing additional corrosion protection. The gloss and semi-gloss nickel layers are applied to improve a surface finish, and to get a good adhesiveness to the substrate, respectively. The inner copper layer on the substrate was applied for the purpose of improving adhesiveness of the film to the substrate.

Fig. 14b shows the specimen surface of a plated film. Many circular depressions (a real density: 28 mm²) with diameters from 10 to 100 μm are present on the plated surface. These depressions are assumed to have been generated by hydrogen gas evolution during the plating process; however, the detailed mechanism of depression formation is unknown at present. In addition to depressions, small bumps (protuberances) were also formed, Fig. 14A.

3.1.2 Experimental procedures

Rotating bending fatigue tests were conducted in the frequency range of 10–30 Hz in laboratory air at room temperature and with a relative humidity of 68%. Fatigue tests of unplated specimens were carried out in air and in 3% NaCl solution. Fatigue tests on plated specimens were carried out in these two environments plus additional tests in purified water. Prior studies [19] have shown that a dripping process of the NaCl solution onto the specimen surface was more detrimental to corrosion fatigue properties than was a total immersion process, due to the greater supply of oxygen which in turn increases the rate of the cathodic reduction. This dripping process was used in the present investigation. The solution was dripped onto the specimen surface during cyclic loading at a constant rate of 3.67 g/min.

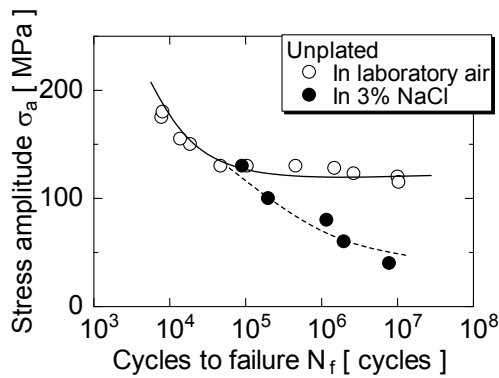
The replica method was used for the successive (continuous) observations of the specimen surface during the fatigue processes of the unplated and plated specimens. Fatigue tests were interrupted periodically to obtain replicas of the specimen surfaces at a constant interval of cycles, ΔN . The interval was usually 5–7% of the total fatigue life N_f . Thus, a total of 15–20 replicas were collected for one fatigue test. The replicas enable measurement of the crack length during the fatigue crack growth process. It is considered that the replication did not affect the corrosion fatigue behavior or mechanism, since the corrosion fatigue lives were not changed so much with or without employing the replica.

An optical microscope (Olympus-BX51 M) was used to examine the replicas. When a fatigue crack was clearly identified on one of the later replicas, the earlier replicas were re-examined to determine the earliest fraction of life at which a fatigue crack could be identified. Micrographs of the cracks were obtained using a camera system (Olympus-DP12). A crack propagation curve was constructed by plotting the crack lengths $2a$, measured as a function of the number of cycles N . In addition, the fracture surfaces were observed using a scanning electron microscope (SEM; Hitachi High-Technologies, TM-1000).

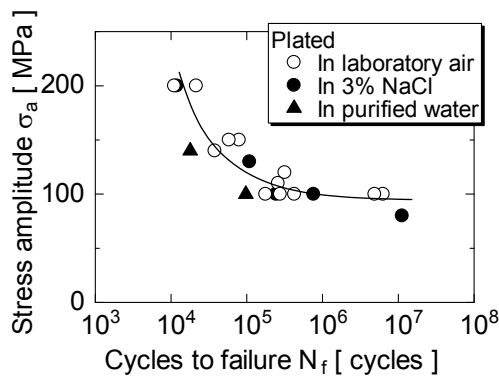
3.2 Experimental results

3.2.1 Effect of electrolytic coating on the fatigue life in laboratory air and in corrosive environments

Fig. 15(a) shows stress-cycle ($S-N$) curves of the unplated specimens in laboratory air and in a corrosive environment (3% NaCl solution). The solid and broken lines in the figure have been approximately fitted to the experimental results. As can be seen from the figure, the corrosion fatigue lives of unplated specimens are significantly decreased in 3% NaCl,



(a) Unplated specimens.



(b) Plated specimens.

Fig. 15. Effect of environment on the $S-N$ curves for both (a) unplated specimens and (b) plated specimens.

especially in the low stress amplitude region. In air, fatigue cracks initiated at surface inclusions; in 3% NaCl, fatigue cracks initiated at corrosion pits which were responsible for the large decrease in fatigue strength relative to air [20]. Fig. 15(b) shows $S-N$ curves of the electrolytically-plated specimens in laboratory air and in the purified water and the in the 3.5% NaCl environments. It is noted that for the plated specimens no significant effect of environment was found, a demonstration of the protective behavior of the coating. However, in comparison with Fig. 15(a), the fatigue strength of the plated specimens in air is less than of the unplated specimens.

3.2.2 Successive observations during the fatigue processes

Fig. 16A shows the results of successive observations of the plated specimen surface during the fatigue process in laboratory air at a stress amplitude of 140 MPa as obtained by the replica technique. The fatigue life, N_f , at this stress amplitude was 38,700 cycles. Fig. 16A-a shows that the specimen surface prior to fatigue loading ($N = 0$) contained a semi-spherical depression which was 54 μm in diameter and 15 μm in depth. After cyclic stress loading at $N = 6000$ cycles (15% of life), a crack had already initiated from at the bottom of the depression, as indicated by the arrow in Fig. 16A-b. At 10,000 cycles, the crack had propagated to a length of 250 μm (Fig. 16A-c). The fracture surface of this specimen in the area of crack initiation is shown in Fig. 17b, and some debonding between the outer chromium and the nickel layer can be seen.

Fig. 16B shows the results of successive observations of the plated specimen surface during the corrosion fatigue process in purified water at a stress amplitude of 140 MPa. In this case the fatigue life was $N_f = 17,911$ cycles. An elliptically-shaped bump was present on the specimen surface, and is indicated by the dashed curves in the figure. This bump is believed to have been created during the plating process. As revealed by subsequent examination, an

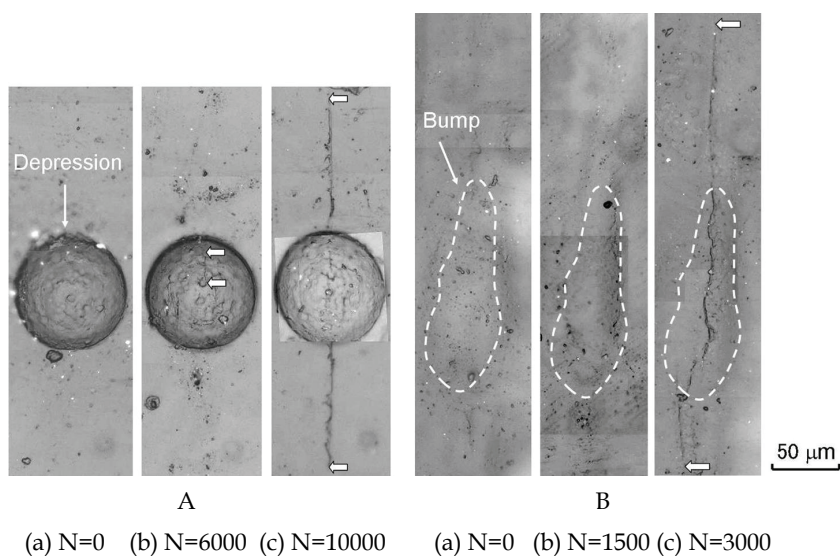


Fig. 16. Successive observations of the plated surface during the fatigue process in [A] laboratory air and [B] in purified water, at a stress amplitude of 140 MPa.

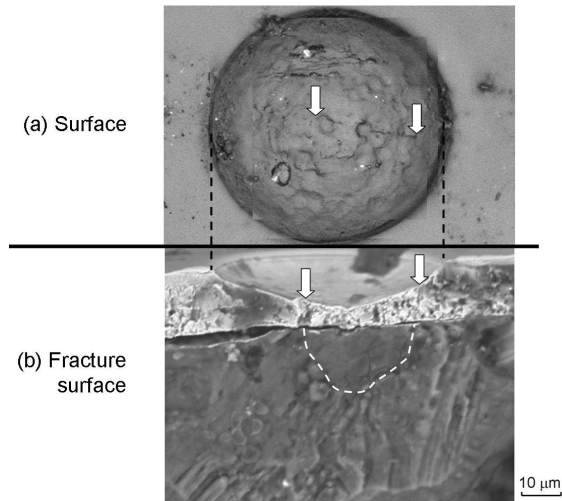
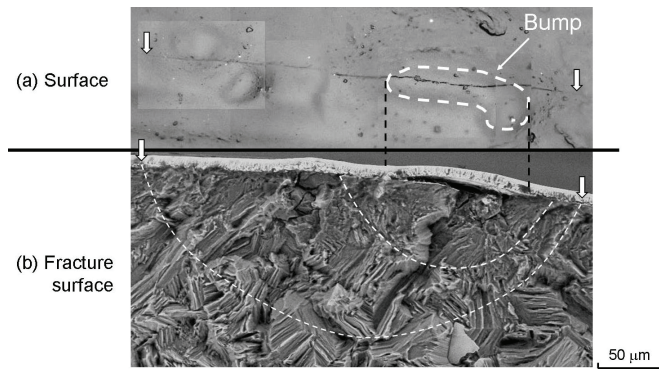
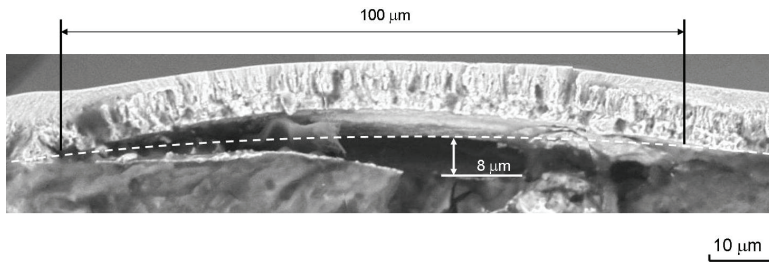


Fig. 17. Fracture surface of the plated specimen (in laboratory air, $\sigma_a = 140$ MPa, $N_f = 38,700$ cycles).



[A] In laboratory air, $\sigma_a = 100$ MPa, $N_f = 177,049$ cycles. Arrows indicate crack tips.



[B] Magnification of the bump shown in Fig. 18[A].

Fig. 18. Fracture surface of the plated specimen (in laboratory air, $\sigma_a = 100$ MPa, $N_f = 177,049$ cycles).

irregularly-shaped depression was found below this bump, at the interface between the copper and the substrate. At 1500 cycles, no crack was observed at the surface at the bump, Fig. 16B-b. However, at 3000 cycles, a crack of a length of 300 μm appeared suddenly on the specimen surface at the location of the bump, Fig. 16B-c.

In all of the fatigue tests of plated specimens, fatigue cracks were found to initiate either at a depression (SN-type) or at a bump (IN-type), regardless of the environment.

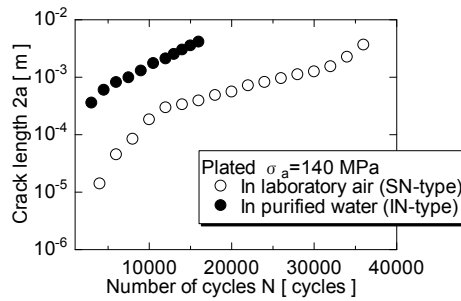
Fig. 17a shows a crack initiated at a depression at 16% of life. Fig. 17b shows the subsequent fracture surface at this location.

Fig. 18 shows combined micrographs of the surface and fracture surface of the plated specimen which had been tested in laboratory air. The specimen had been cyclically loaded at a stress amplitude of 100 MPa until failure at 177,049 cycles.

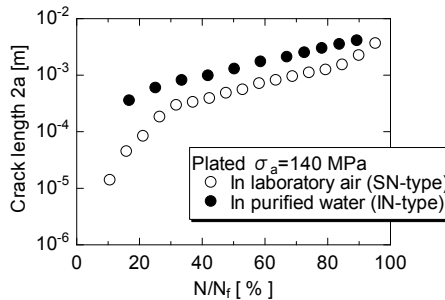
A crack initiated from the bottom of the depression located along the interface between the copper layer and the substrate, and then propagated along the surface and into the specimen. The depression is located just beneath a bump. Fig. 18B shows a magnified micrograph of Fig. 18a indicating the appearance and size of the depression (100 μm long and 8 μm deep). The stress concentration due to the geometry may have promoted crack initiation at the bottom of the depression.

3.2.3 Crack propagation behavior

Fig. 19a and b shows the relations between crack length ($2a$) vs. the number of stress cycles (N) and $2a$ vs. fatigue life ratio (N/N_f), respectively, where N_f is the total fatigue life. The



(a) $2a$ vs. N .



(b) $2a$ vs. N/N_f .

Fig. 19. Crack propagation behavior for plated specimens at a stress amplitude of 140 MPa. Crack length ($2a$) as a function of (a) the number of stress cycles (N), and (b) the fatigue life ratio (N/N_f).

fatigue processes of plated specimens were measured in laboratory air and in purified water at a constant stress amplitude of 140 MPa. When several cracks initiated during the fatigue process, the crack length for the main crack which led to final failure of the specimen was plotted.

For the plated specimen, the crack (SN-type) was initiated early at 10% of the fatigue life during the fatigue process, which indicates that the total fatigue life of the plated specimen is almost equal to the crack propagation life. However, for the IN-type plated specimen, a crack with a length of 200 μm suddenly appeared on the specimen surface at N/N_f equal to 20%. The crack in the IN-type specimen is also expected to initiate early during the fatigue process, as for the SN-type specimen, because the crack propagation curves and fatigue lives of both specimens are almost the same.

Three-dimensional finite element analysis was conducted using commercial software, Ansys, to study stress distribution around the depression. The analysis revealed that stress concentration factor for the present depression was 2.1, and the distance over which the dominant stress falls off to nil stress concentration was about 90 μm from the center of the depression. The value of the stress concentration factor was also estimated as, $k = 2.13$ [21] by considering the notch shape and sizes appearing in Fig. 17. These results suggest that in the SN-type specimen, the rate of crack propagation accelerated in the region of $2a < 180 \mu\text{m}$, due to the effect of stress concentration at the semi-spherical notch (SN-type), while in the region $2a > 180 \mu\text{m}$, no acceleration in the rate of crack propagation occurred, because the location of the crack tip deviated from the area influenced by the stress concentration. In addition to the above notch effect, effect of crack geometry (a depression) on crack closure and local chemistry is also considered to be important factors influencing the above crack propagation behavior. Further study is needed to clarify these issues.

Fig. 20 shows log-log plot of the rate of crack propagation da/dN (m/cycle) and the stress intensity factor range ΔK ($\text{MPa m}^{1/2}$) for the plated specimens in laboratory air and purified water. Eq. (1) was used to calculate ΔK , where the value of 0.73 was introduced with the assumption that the crack shape is a semi-circular [22]. In Fig. 20, the stress concentration at the notch, as discussed in Fig. 19, was not taken into a consideration in the calculation of ΔK , since an exact solution for stress intensity factor (SIF) of the crack emanating from the depression is not available at present. The relationships of da/dN vs. ΔK in laboratory air and in purified water are almost the same, in other words, the environmental effects have no influence on the relationship at the rate of the crack propagation, above 10^{-9} m/cycle. Environmental effect is expected to exist at the region of the lower rate of the crack propagation. Nan et al. [20] investigated the rate of crack growth of the extruded AZ31 Mg alloy in laboratory air and 3% sodium chloride solution. They reported that in the rate of the crack growth, above 10^{-9} m/cycle, there is no acceleration due to the corrosive environment. A similar result was also reported by Khan et al. [14, 15] in the study of Mg alloy. They studied the rate of crack propagation under the low (55%) and the high (80%) humidity in laboratory air. At the rate of crack growth above 10^{-9} m/cycle, effect of the atmosphere humidity on the rate of crack propagation was not observed.

$$\Delta K = 0.73\sigma_a\sqrt{\pi a} \quad (1)$$

The relationship between da/dN and ΔK is expressed by Eq. (2):

$$da/dN = 6.5 \times 10^{-9} (\Delta K - 0.45)^2 \quad (2)$$

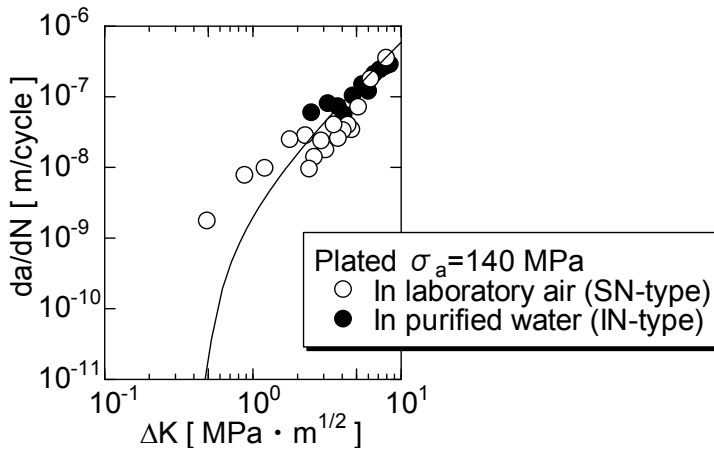


Fig. 20. Relationship between the crack propagation rate da/dN , and the stress intensity factor range ΔK , for the Ni-plated specimen.

3.3 Discussion

3.3.1 Fatigue mechanism of the Ni-plated specimen

Experimental observations revealed that two types of crack initiation mechanism occur in the plated specimens, as schematically illustrated in Figs. 21a (SN-type) and b (IN-type). In both cases, under repeated loading, a crack initiates at the bottom of the depression, where stress concentration occurs. The crack then propagates in the direction of the substrate, which leads to the final failure of the specimen.

These semi-spherical depressions and cavities were observed to be present prior to fatigue loading, and therefore they are assumed to be introduced into the specimen by hydrogen gas evolution during the plating process. For investigating effect of hydrogen gas on the fatigue life of the material, the following experiment was conducted. After plating, the

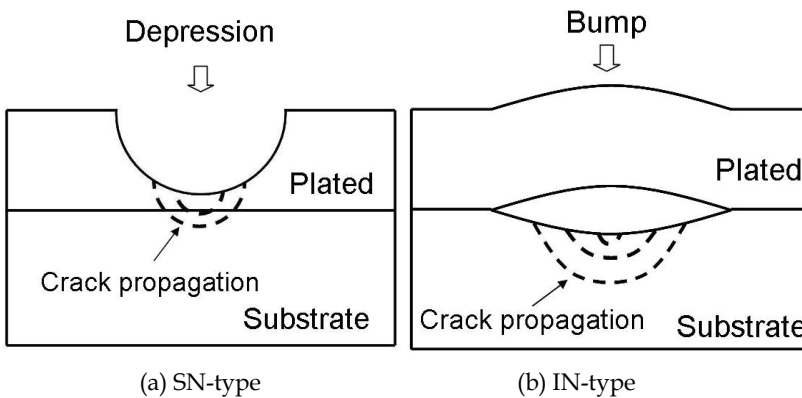


Fig. 21. Schematic illustration of the fatigue mechanism for the Ni-plated specimens: (a) SN-type and (b) IN-type.

specimens were heated in a furnace at 523 K for 2 h, to eject atomic hydrogen stored inside of the specimen. Then the fatigue life of the heated specimen was compared with the one for the unheated specimen. The comparison showed no effect of the heating. So, it is considered that the effect of the atomic hydrogen on the fatigue life is not pronounced enough to affect the fatigue life.

The fatigue mechanisms of the plated specimens are expected to be the same, regardless of the environment, because the fatigue life in laboratory air and in 3% NaCl solution (or in purified water) are in good agreement with each other, as shown in Fig. 15b. The fatigue limit for the plated specimen is slightly decreased compared with that for the unplated specimen in laboratory air, Fig. 15. This is because depressions or cavities act as crack initiators during the fatigue process. The fatigue life of the Ni-plated specimen will be improved by the elimination of surface or interface depressions.

3.3.2 Corrosion fatigue resistance of the electrolytically-plated magnesium alloy

In the case of the electroless plated specimen reported by Ishihara et al. [2], small holes were introduced in the plating-film during the plating process. In the corrosive environment, corrosive liquid reached the substrate through these small holes, and generated the corrosion pit at the interface between the plating-film and the substrate. Early crack initiation and shorter fatigue life were induced by the corrosion pit formation. However, in the present Ni-based electrolytic plated specimen, the plating-film is thought to prevent direct contact between Mg substrate and corrosive liquid during the corrosion fatigue process, due to dense and sound plating-film, Fig. 14. A measurement of polarization curve revealed that corrosion current density for the present Ni-based electrolytic plated specimen was 0.18 A/m^2 , which is lower than 0.73 A/m^2 for the electroless plated specimen. The result indicates that the corrosion resistance of the former is superior to the latter. This is the main reason why the fatigue lives of the Ni-based electrolytically-plated specimen were not affected by the corrosive environment, as shown in Fig. 15b.

4. Conclusions

Fatigue tests were performed in laboratory air and in corrosive environments using Mg alloy AZ31 specimens with two types of plating, i.e. electroless Ni-plating and electrically Ni-plating. The following conclusions were obtained:

[A] Electroless Ni-Plating:

Fatigue tests were conducted in laboratory air and 3% sodium chloride solution using three types of surface treated specimens, machine-polished, glass bead-blasted and electroless Ni plated Mg alloy specimens. The following conclusions were reached.

1. In sodium chloride solution, fatigue lives were significantly lowered compared with those in laboratory air, regardless of the three types of specimen treatment.
2. In laboratory air, the S-N curves were not affected by the specimen surface treatments. On the other hand, the corrosion fatigue lives for the electroless Ni plated specimens became shorter than those for the polished and blasted specimens at constant stress amplitudes. The corrosion fatigue lives for the polished specimens were almost the same as those for the blasted specimens.

3. No significant differences in crack propagation behavior due to the different surface treatments were observed in either laboratory air or sodium chloride solution. The rates of crack propagation were almost the same for measurements in both laboratory air and sodium chloride solution.
4. Corrosive solution infiltrated to the interface through the small pores within the plating film during the corrosion fatigue process. This led to local corrosive reactions at the interface, and corrosion pits were initiated. Cracks were initiated at the bottom of the corrosion pits and propagated, leading to the final failure of the specimen. The corrosion fatigue lives of the electroless Ni plated specimens became shorter than those of the polished and blasted specimens, primarily because of the acceleration of the crack initiation process in the electroless Ni plated specimens.

[B] Electrolytically Ni-Plating:

1. The corrosion fatigue lives of the Ni-plated specimens were almost the same as those measured in laboratory air, which indicated a beneficial effect of electrolytic Ni-plating to protect Mg alloys from damage due to corrosion fatigue.
2. Two types of crack initiation sites were found in the Ni-plated specimens, regardless of the test environment. Cracks were initiated from depressions on the specimen surface (SN-type), or from depressions located along the interface between the substrate and plate, i.e., between magnesium alloy and copper (IN-type).
3. The SN-type crack was initiated early during the fatigue process in the Ni-plated specimen, at 10% of the fatigue life. For the IN-type Ni-plated specimen, a crack with a length of 200 μm suddenly appeared on the specimen surface at N/N_f equal to 20%.
4. The fatigue life of the Ni-plated specimen will be improved by the elimination of surface or interface depressions which are introduced during the plating process.

5. Acknowledgements

These studies were performed under a grant from JSPS (NO. 20560069). The authors express their thanks to JSPS. In addition, they thank Takamatsu Plating Co. Ltd., for providing financial support during the course of the present study.

6. References

- [1] Y. Kojima, Handbook advanced magnesium technology, Kallos Publishing Co. Ltd., Tokyo (2000).
- [2] S. Ishihara, H. Notoya, A. Okada, Z. Y. Nan and T. Goshima, Effect of electroless-Ni-plating on corrosion fatigue behaviour of magnesium alloy, *Surface coating technology*, Vol.202, pp.2085-2092, 2008.
- [3] S. Ishihara, T. Namito, H. Notoya, A. Okada, and T. Goshima, Corrosion fatigue resistance of magnesium alloy with electrolytic Ni-plating, *International Journal of Fatigue*, Vol.32, pp. 1299-1305, 2010.
- [4] Z. Y. Nan, PhD thesis, University of Toyama, 2005.

- [5] E.S. Puchi-Cabrera, C. Villalobos-Gutiérrez, I. Irausquim, J. La Barbera-Sosa and G. Mesmacque, Fatigue behavior of a 7075-T6 aluminum alloy coated with an electroless Ni-P deposit, *Int J Fatigue* 28 (12) (2006), pp. 1854–1866.
- [6] G. Contreras, C. Fajardo, J.A. Berríos, A. Pertuz, J. Chitty and H. Hintermann *et al.*, Fatigue properties of an AISI 1045 steel coated with an electroless Ni-P deposit, *Thin Solid Films* 355–356 (1999), pp. 480–486.
- [7] T. Saeid, S. Yazdani and N. Parvini-Ahmadi, Fatigue properties of a Ck45 steel coated with a post-heat treated Ni-Cu-P electroless deposit, *Surf Coat Technol* 200 (20–21) (2006), pp. 5789–5793.
- [8] Z.Y. Nan, S. Ishihara, T. Goshima and R. Nakanishi, Scanning probe microscope observations of fatigue process in magnesium alloy AZ31 near the fatigue limit, *Scr Mater* 50 (4) (2004), pp. 429–434.
- [9] S. Ishihara, S. Saka, Z.Y. Nan, T. Goshima and S. Sunada, Prediction of corrosion fatigue lives of aluminum alloy on the basis of corrosion pit growth law, *Fatigue Fract Eng Mater Struct* 29 (2006), pp. 472–480.
- [10] S. Ishihara, S. Saka, Z.Y. Nan, T. Goshima, H. Shibata and B.L. Ding, Study on the pit growth during corrosion fatigue of aluminum alloy, *Int. J. Mod. Phys. B* 20 (25,26 & 27) (2006), p. 3975.
- [11] J.A. Diaz, M. Passarrelli, J.A. Berríos and E.S. Puchi-Cabrera, Fatigue behavior of a 4340 steel coated with an electroless Ni-P deposit, *Surf. Coat. Technol.* 149 (2002), p. 45.
- [12] Rajan Ambat and W. Zhou, Electroless nickel-plating on AZ91D magnesium alloy: effect of substrate microstructure and plating parameters, *Surf. Coat. Technol.* 179 (2004), p. 124.
- [13] J.Y. Song and Jin Yu, Residual stress measurements in electroless plated Ni-P films, *Thin Solid Films* 415 (2002), p. 167.
- [14] S. Alam Khan, Y. Miyashita, Y. Mutoh and T. Koike, Effect of anodized layer thickness on fatigue behavior of magnesium alloy, *Mater Sci Eng A* 474 (2008), pp. 261–269.
- [15] S. Alam Khan, Y. Miyashita, Y. Mutoh and T. Koike, Fatigue behavior of anodized AM60 magnesium alloy under humid environment, *Mater Sci Eng A* 498 (2008), pp. 377–383.
- [16] A.J. Eifert and J.P. Thomas, Influence of anodization on the fatigue life of WE43A-T6 magnesium, *Scripta Mater* 40 (8) (1999), pp. 929–935.
- [17] D.T. Asquith, A.L. Yerokhin, J.R. Yates and A. Matthews, Effect of combined shot-peening and PEO treatment on fatigue life of 2024 Al alloy, *Thin Solid Films* 515 (2006), pp. 1187–1191.
- [18] E. Cirik and K. Genel, Effect of anodic oxidation on fatigue performance of 7075-T6 alloy, *Surf Coat Technol* 202 (2008), pp. 5190–5201.
- [19] S. Ishihara, Z.Y. Nan, A.J. McEvily, T. Goshima and S. Sunada, On the initiation and growth behavior of corrosion pits during corrosion fatigue process of industrial pure aluminum, *Int J Fatigue* 30 (2008), pp. 659–1668.
- [20] Z. Y. Nan, S. Ishihara and T. Goshima, Corrosion fatigue behavior of extruded magnesium alloy AZ31 in sodium chloride solution, *International Journal of Fatigue*, Vol. 30, No. 7, pp.1181–1188, 2008.

- [21] M. Nishida, Stress concentration, Morikita Publishing Co., Ltd., Tokyo (1967) p. 526-529.
- [22] A.J. McEvily, A method for the analysis of the growth of short fatigue cracks. In: J. Pohluda, Editor, *Materials structure and micromechanics of fracture*, Trans Tech Publications, Switzerland (2005) p. 3-10.

High Functionalization of Magnesium Alloy Surface by Superhydrophobic Treatment

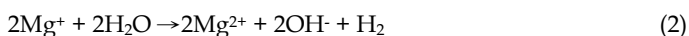
Takahiro Ishizaki¹, SunHyung Lee² and Katsuya Teshima²

¹*National Institute of Advanced Industrial Science and Technology (AIST), Nagoya 463-8560*

²*Department of Environmental Science and Technology, Faculty of Engineering, Shinshu University, Nagano 380-8553 Japan*

1. Introduction

Magnesium and its alloys have excellent physical and mechanical properties such as low density, good electromagnetic shielding, and high strength/weight ratio (Gray & Luan, 2002; Yong et al., 2008). Thus, they are expected to be applied to various industries such as the aerospace, automobile, and railway industries (Mordike & Ebert, 2001; Phani et al., 2006; Ha & Kim, 2006). Their poor corrosion resistance, however, hinders their use on a larger scale. The corrosion of magnesium and magnesium alloys occurs via the following reaction (Baril et al., 2007; Song et al., 1997):



According to equations (1), (2), (3) and (4), the contact of magnesium alloy with water triggers the corrosion reaction. Thus, it is important to prevent the contact of magnesium alloy with water to suppress the progress of corrosion. In order to realize this, various methods such as chemical conversion, electroplating, and anodic oxidization have been developed (Barchiche et al., 2007; Lian et al., 2006; Liu & Gao, 2006; Montemor & Ferreira, (2007). The films prepared by these surface treatments always contain pores, pine-holes, cracks etc. The porosity and defect density are critically important to the quality of a film. In addition, the film thickness and film density are important factors from the viewpoint of anticorrosion performance. However, the advantage offered by the lightweight properties of magnesium alloy might be lost if the thickness and density of the applied coating are increased. Thus, it is crucial to develop a coating technology to improve anticorrosion performance, while maintaining the advantage offered by the lightweight properties of magnesium alloys. A corrosion resistant hydrophobic film formed on AZ91D Mg alloy through a simple dipping process has recently been reported (Song, 2010). This hydrophobic

film improved the corrosion resistance of magnesium alloy AZ91. Thus, a superhydrophobic coating would be also a promising technology for improving anticorrosion performance because it would inhibit the contact of a surface with water and environmental humidity. A superhydrophobic surface would be of great importance to many industrial applications and could present a solution to the long-standing problems of environmental contamination and corrosion of metals and metal alloys (Liu et al., 2009; Roach et al., 2008; Xu et al., 2008).

The superhydrophobic phenomenon can be commonly observed in many plants in nature such as lotus leaf and it is known as the Lotus effect (Barthlott & Neinhuis, 1997). The superhydrophobic surfaces on many plants are created by a cooperation of binary structures at nano- and micrometers scales and coverage of wax-like materials on them. The special micro-nano-binary structures increase the surface roughness and minimize the contact area between the leaf and liquid, which can endow the leaf with self-cleaning superhydrophobicity. The development of various fabrication techniques for superhydrophobic surface by mimicking the surface of the lotus leaves has been a hot subject. The artificial superhydrophobic surfaces have been fabricated mostly by controlling the surface roughness and topography, followed by surface modification using organic monolayers with hydrophobic functional groups (Guo et al., 2005; Qian & Shen, 2005). The controls of the surface roughness and topography have been accomplished through various techniques such as anodic oxidation (Thieme et al., 2001), electrodeposition and chemical etching (Shi et al., 2005; Shirtcliffe et al., 2005; Zhang et al., 2004), plasma etching (Lejeune et al., 2006), laser treating (Khorasani et al., 2005), chemical vapour deposition (Huang et al., 2005), sol-gel processing (Shirtcliffe et al., 2003), electrospinning (Acatay et al., 2004; Singh et al., 2005), and so on.

Recently, superhydrophobic treatments have been applied to various engineering material surfaces such as steel, copper, zinc, and aluminum, to improve their corrosion performances (He et al., 2009; Qian & Shen, 2005; Qu et al., 2007; Thieme & Worch, 2006; Wang et al., 2006). Liu et al. demonstrated the preparation of a superhydrophobic surface on copper by chemical etching and surface modification with n-tetradecanoic acid and investigated the corrosion resistant performance in seawater by electrochemical measurements (Liu et al., 2007). They concluded that the superhydrophobic surface considerably reduced the corrosion rate of copper due to its special morphology. He et al. fabricated a superhydrophobic surface on anodized aluminum by modifying myristic acid and estimated the corrosion resistant performance by electrochemical impedance spectroscopy (He et al., 2009). The superhydrophobic surface greatly improved the corrosion resistance of aluminum. In this way, a superhydrophobic surface has been shown to be effective for improving the corrosion resistance of engineering materials. However, it was widely assumed that the advantages of a superhydrophobic surface would disappear if it was completely immersed in a solution; thus, there was little attention paid to the application of superhydrophobic surfaces equipped with anticorrosion performances to metal surfaces. As a consequence, there are few reports on the application of a superhydrophobic surface to magnesium alloys. Jiang et al. reported the fabrication of a bioinspired superhydrophobic surface on Mg-Li alloy (Liu et al., 2008). The superhydrophobic surface was fabricated by chemical etching and surface modification with a CF₃-terminated self-assembled monolayer (fluoroalkyl silane self-assembled monolayer: FAS-SAM). They estimated the corrosion resistant performance by investigating the relationship between the time of exposure to air

and the change in static water contact angles on the superhydrophobic surface of the Mg-Li alloy. The surface showed stably superhydrophobic properties for over three months. However, the surface was not exposed to a corrosive environment such as diluted NaCl aqueous solution, so it is difficult to conclude that the superhydrophobic property provides high corrosion resistance to the magnesium alloy.

In this chapter, we introduce some experimental results on the fabrication and corrosion resistant performance of superhydrophobic surface formed on magnesium alloy. At first, we present an example of the formation of nanosheets on magnesium alloy surface. The crystalline nanosheets were successfully formed on magnesium alloy AZ31 by a facile surfactant-free hydrothermal treatment using aqueous solution. The nanosheets formed surface had hierarchical structures at micro- and nanometer scales so they could be used as a template of superhydrophobic surface. Next, we show superhydrophobic surface on magnesium alloy fabricated by microwave plasma-enhanced chemical vapor deposition (MPECVD) process. Here, the anticorrosion resistance and the chemical stability of the superhydrophobic film were described based on the results of electrochemical impedance spectroscopy (EIS) and water contact angle measurements. Finally, we describe a facile, simple, and time-saving method to create superhydrophobic surface on magnesium alloy by a simple immersion process at room temperature. The superhydrophobic surface was fabricated through the following two steps. First, crystalline CeO_2 film was vertically formed on the magnesium alloy by immersion in cerium nitrate aqueous solution within 20 min. Next, the film were covered with fluoroalkylsilane molecules (FAS) within 30 min by immersing in toluene solution containing FAS and tetrakis(trimethylsiloxy)titanium (TTST). The FAS coated CeO_2 film showed a static contact angle of more than 150° , that is, superhydrophobic property. The chemical stability of the superhydrophobic surface on magnesium alloy AZ31 would be also discussed.

2. Formation of nanosheets on magnesium alloy surface

In this section, we report a facile surfactant-free synthesis of vertically self-aligned $\text{Mg}_{1-x}\text{Al}_x(\text{OH})_2(\text{NO}_3)_x \cdot n\text{H}_2\text{O}$, $\text{Mg}_{1-x}\text{Al}_x(\text{OH})_2(\text{NO}_3)_x \cdot n\text{H}_2\text{O}$ and $\text{Mg}(\text{OH})_2$, and $\text{Mg}(\text{OH})_2$ nanosheets on a magnesium alloy substrate (AZ31); these nanosheets were fabricated on magnesium alloy AZ31 as a hierarchical structure at micro- and nanometer scales by a simple hydrothermal synthesis using aqueous solutions. The hierarchical structures could be used as a template of superhydrophobic surface.

Aqueous ammonium solution containing NH_4NO_3 and NaOH was used for the fabrication of $\text{Mg}(\text{OH})_2$ nanosheets. This ammonium solution was obtained by dissolving 0.1 M NH_4NO_3 and then adding 1 ml of 0.1 M NaOH. The dissolution process was carried out at room temperature by stirring the solution mixture for a few minutes. All chemicals were of reagent grade and used without any pretreatment. Magnesium alloy AZ31 (composition: 2.98% Al, 0.88% Zn, 0.38% Mn, 0.0135% Si, 0.001% Cu, 0.002% Ni, 0.0027% Fe, and the rest is Mg) with a thickness of 1.5 mm was used as the substrate. The substrates were ultrasonically cleaned in ethanol for 10 min. After the cleaning, the substrates were dried with inert Ar gas. The cleaned magnesium alloy substrates were introduced in a Teflon-lined autoclave with a 50 ml capacity. The autoclave was filled with the aqueous ammonium solution mixture to fill 40% of its capacity. The autoclave was maintained at temperatures of 120–180 °C for 1–24 h and subsequently left to cool to room temperature. After the samples were subjected to the treatments, the substrate was ultrasonically cleaned in ethanol for 10 min and dried with Ar gas.

Figures 1(a), 1(b), 1(c), and 1(d) show FE-SEM images of the sample surfaces after hydrothermal treatment at 150 °C for 1, 3, 6, and 12 h, respectively. All the samples exhibit nanosheets that are aligned at fairly inclined angles with respect to the surface. When the treatment time was less than 3 h, the nanosheets were locally formed on the surfaces. In contrast, after treatment for over 12 h, the nanosheets were observed to be vertically aligned over the entire substrate surface and appeared to be partly in the form of multi-layers (Figures 1(c) and (d)). Figures 1(e)–(h) show the enlarged versions of the FE-SEM images shown in Figures 1(a)–(d), respectively. The vertically aligned nanosheets became dense as the treatment time increased. The nanosheets exhibit an edge length in the range of approximately 50–750 nm and a thickness of 20–50 nm. It was difficult to determine the height of the fabricated nanosheets because of the flake-like morphology of the crystallites; moreover, several individual crystals were found to have a length of approximately 1 μm .

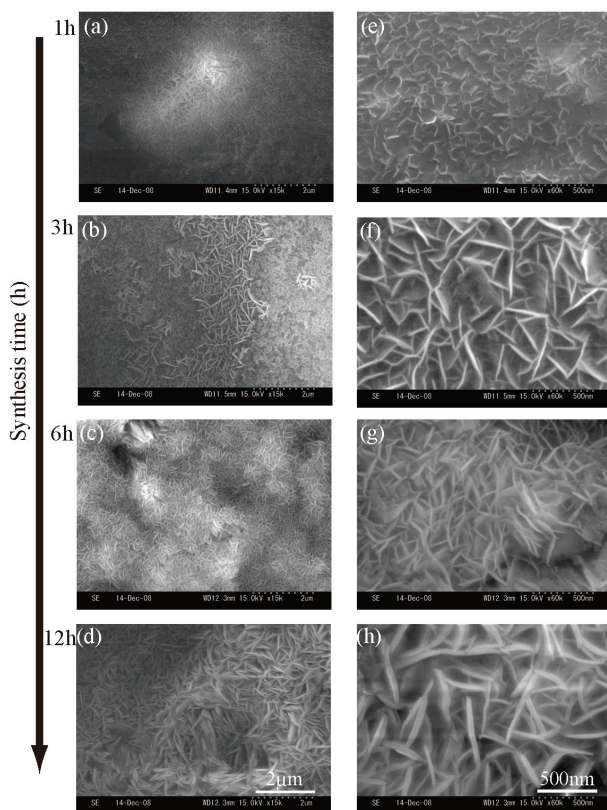


Fig. 1. FE-SEM images of sample surfaces after hydrothermal treatment at 150 °C for (a) 1 h, (b) 3 h, (c) 6 h, and (d) 12 h. (e), (f), (g), and (h) are the enlarged FE-SEM images of (a), (b), (c), and (d), respectively. [Reproduced by permission of The Royal Society of Chemistry, CrystEngComm., 2009, 11, 2338.]

Figures 2(a), 2(b), and 2(c) show FE-SEM images of the samples surfaces hydrothermally treated for 6 h at 120, 150, and 180 °C, respectively. These images show that the sheets are

predominantly perpendicular to the substrate. At the treatment temperature of 120 °C, we clearly observe a rosette-like structure formed by the curved nanosheets. The nanosheets with sizes of 0.5–1 μm are densely formed in the rosette-like structure. The rosette-like structures somewhat appear to be laid on a carpet of vertically aligned nanosheets. An increase in the treatment temperature to 150 °C was found to result in the formation of compact and continuous nanosheets due to an increase in nucleation and growth rates. When the treatment temperature reaches 180 °C, dense hexagonal nanosheets were observed. The edges of these hexagonal formations are clearly observed. This indicates that the crystalline quality of these nanosheets is very high. The size and thickness of the nanosheets obtained at 180 °C are larger than those of the nanosheets treated at 150 °C.

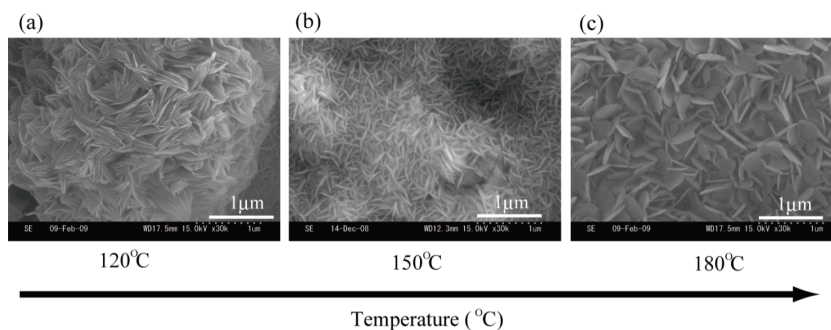


Fig. 2. FE-SEM images of sample surfaces after hydrothermal treatment for 6 h at (a) 120 °C, (b) 150 °C, and (c) 180 °C. [Reproduced by permission of The Royal Society of Chemistry, CrystEngComm., 2009, 11, 2338.]

Figure 3 shows the XRD patterns of the obtained samples after their hydrothermal treatment at 150 °C for 3–24 h. In the case of all samples, some peaks attributable to the hydroxalite (HT)-like structure were clearly observed, which were assigned to $Mg_{1-x}Al_x(OH)_2(NO_3)_x \cdot nH_2O$ intercalated with nitrate anions (Xu & Zeng, 2001). The diffraction peaks are indexed according to the 3R symmetry (Cavani et al., 1991; Kuma et al., 1989; Rives & Ulbarri, 1999). The intensity of the diffraction peak corresponding to the [003] plane is almost the same, irrespective of the treatment time. This indicates that the crystal growth of the $Mg_{1-x}Al_x(OH)_2(NO_3)_x \cdot nH_2O$ in the [003] plane occurs within 3 h of initiating the hydrothermal treatment at 150 °C. The XRD pattern of the vertically aligned nanosheets on the AZ31 substrate is distinctly different from that of the randomly oriented HT microcrystalline powder due to the observation of several rational orders of (00 l) reflections (Yates & West, 1983). Such an arrangement of the hexagonal nanosheets with the c -axis parallel to and the ab -face perpendicular to the geometrically untreated substrate has not been observed in HT films thus far. Chen et al. have reported that the hexagonal nanosheets with c -axis parallel to the porous anodic alumina/aluminium (POA) substrate, which was fabricated by anodizing an aluminium metal sheet, were formed on the POA substrate (Chen et al., 2006). This might be due to the change in the surface energy with changing surface roughness because of the porous nature of the substrate surface. In addition to the peaks attributable to $Mg_{1-x}Al_x(OH)_2(NO_3)_x \cdot nH_2O$, a few peaks attributable to hexagonal $Mg(OH)_2$ are also clearly observed. A diffraction peak of [101] reflection, which has the highest intensity according to the JCPDS file number 44-1482, become stronger with

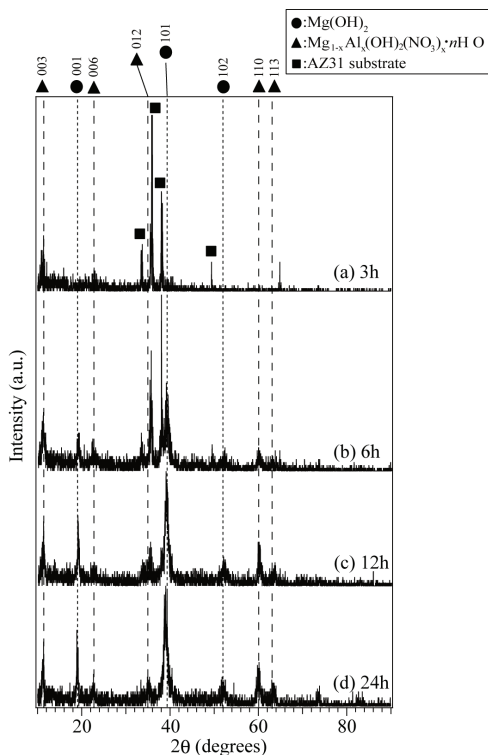


Fig. 3. XRD patterns of sample surfaces after hydrothermal treatment at 150 °C for (a) 3 h, (b) 6 h, (c) 12 h, and (d) 24 h. [Reproduced by permission of The Royal Society of Chemistry, CrystEngComm., 20019, 11, 2338.]

increasing treatment time; this observation implies the formation of hexagonal $\text{Mg}(\text{OH})_2$. It should be noted that the intensity of the diffraction peak of [001] plane increased with increasing treatment time. According to JCPDS file number 44-1482, the intensity ratio of I_{001}/I_{101} is 0.53. However, the intensity ratio of I_{001}/I_{101} for the fabricated $\text{Mg}(\text{OH})_2$ nanosheets increased from 0.44 to 0.63 with treatment time. This indicates that the $\text{Mg}(\text{OH})_2$ crystallite dimensions are preferentially restricted along the crystallographic c -axis. This result is in good agreement with the SEM observations. Figures 4(a), 4(b), and 4(c) show the XRD patterns of the samples after hydrothermal treatment for 6 h at 120, 150, and 180 °C, respectively. At the treatment temperature of 120 °C, two peaks originating from the HT-like structure and assignable to $\text{Mg}_{1-x}\text{Al}_x(\text{OH})_2(\text{NO}_3)_x \cdot n\text{H}_2\text{O}$ are clearly observed. The two peaks at $2\theta = 10.4^\circ$ and 20.8° are assigned to the [003] and [006] reflections of $\text{Mg}_{1-x}\text{Al}_x(\text{OH})_2(\text{NO}_3)_x \cdot n\text{H}_2\text{O}$, respectively. This means that the treated surfaces were well crystallized with a preferential hexagonal orientation along the [003] plane, which is a characteristic feature of the spontaneous texture axis of $\text{Mg}_{1-x}\text{Al}_x(\text{OH})_2(\text{NO}_3)_x \cdot n\text{H}_2\text{O}$. Crystalline $\text{Mg}(\text{OH})_2$ phases were not formed at the treatment temperature of 120 °C. This indicates that the rosette-like structure formed by the curved nanosheets and the vertically aligned nanosheets beneath the rosette-like structure are crystalline $\text{Mg}_{1-x}\text{Al}_x(\text{OH})_2(\text{NO}_3)_x \cdot n\text{H}_2\text{O}$. The XRD pattern in Figure 4(b) shows some peaks that are

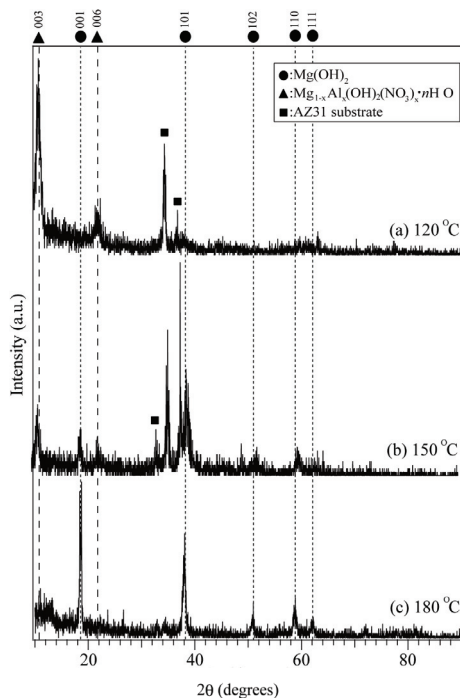


Fig. 4. XRD patterns of sample surfaces after hydrothermal treated for 6 h at (a) 120 °C, (b) 150 °C, and (c) 180 °C. [Reproduced by permission of The Royal Society of Chemistry, CrystEngComm., 2009, 11, 2338.]

attributable to crystalline hexagonal $\text{Mg}_{1-x}\text{Al}_x(\text{OH})_2(\text{NO}_3)_x \cdot n\text{H}_2\text{O}$ and $\text{Mg}(\text{OH})_2$. An increase in the treatment temperature led to the formation of crystalline $\text{Mg}(\text{OH})_2$. The XRD pattern of the sample surface treated at 180 °C shows only some peaks assignable to $\text{Mg}(\text{OH})_2$. The degree of orientation was roughly estimated from the ratio of the peak intensities arising from [001] and [101] planes, i.e., I_{001}/I_{101} , which is 0.53 for the powder diffraction standard of $\text{Mg}(\text{OH})_2$. The degree of orientation was estimated to be 1.49 for the sample treated at 180 °C, indicating the high degree of crystallographic orientation in this sample. This result is in agreement with the SEM observations. At this temperature, the crystallites exhibited a clear plate-like shape with the edges preferentially directed out of the AZ31 substrate. This indicates that the strong preference of crystallographic orientation observed can be regarded as an increase in the growth rate of the crystallites due to an increase in the treatment temperature.

Figure 5 shows the FT-IR spectra of the powder samples hydrothermally treated at 150 °C in the region of 400–4000 cm^{-1} . The most predominant spectral feature is the intense sharp peak observed at 3696.9 cm^{-1} . It has been known that pure $\text{Mg}(\text{OH})_2$ exhibits a single band at 3698 cm^{-1} , owing to the high basicity of its O-H groups (Bensi, 1959; Xu & Zeng, 2000). Another sharp peak at around 1384.6 cm^{-1} is attributable to the ν_3 vibrational mode of NO_3^- in the interlayer with D_{3h} symmetry (Yates & West, 1983). A weak shoulder band at around 830 cm^{-1} appears due to the ν_2 vibrational mode of the same anion (Chisem & Jones, 1994; Qian & Zeng, 1997; Xu & Zeng, 1999). A weak broad band in the region of 1630–1650 cm^{-1} is

attributed to the hydroxyl-deformation mode of water (Kloprogge et al., 2005). The lattice vibrations of metal-oxygen bonds (M-O) are also observed at around 550 cm^{-1} (Kannan et al., 1995; Labajos et al., 1992). It is possible that some of these bands overlap with the broad band due to the d-mode of O-H or that the vibrations occur in the wavenumber region below the measured range. The XPS spectra of the sample treated at $150\text{ }^\circ\text{C}$ revealed that the Mg 1s peak arising from the formed nanosheets can be separated into two peaks. The two peaks centred at 1302.7 and 1303.8 eV are assigned to $\text{Mg}(\text{OH})_2$ and metal Mg, respectively (Haycock et al., 1978; Yates & West, 1983). Trace amount of aluminium with a concentration of less than 5 at% was detected in the nanosheets at the vicinity of the surface. This supports the fact that the nanosheets comprised of $\text{Mg}_{1-x}\text{Al}_x(\text{OH})_2(\text{NO}_3)_x \cdot n\text{H}_2\text{O}$ and $\text{Mg}(\text{OH})_2$.

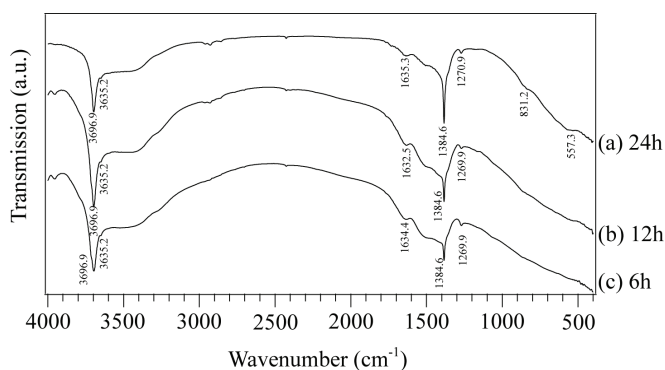


Fig. 5. FT-IR spectra of sample surfaces after hydrothermal treatment at $150\text{ }^\circ\text{C}$ for (a) 6 h, (b) 12 h, and (c) 24 h. [Reproduced by permission of The Royal Society of Chemistry, CrystEngComm., 2009, 11, 2338.]

Figure 6 shows the representative TEM images of the powder sample for the nanosheets formed on the magnesium alloy substrate that was hydrothermally treated at $150\text{ }^\circ\text{C}$ for 24 h. Two main morphologies are observed: the vertically and horizontally aligned nanosheets and the nanoneedles. In Figures 6(b) and 6(c), several vertically aligned nanosheets with a thickness of 10–30 nm and nanoneedles with diameters of ca. 3–10 nm can be observed. The selected area electron diffraction (SAED) patterns exhibit rings corresponding to the [001], [101], and [102] planes of $\text{Mg}(\text{OH})_2$. These patterns are consistent with the XRD patterns. In the higher magnification TEM image shown in Figures 6(b) and 6(c), the horizontally aligned nanosheets were also observed; these nanosheets were thin with large areas. Figure 6(d) shows the high-resolution TEM (HRTEM) image of the nanosheet. Three types of lattice fringes (L_a , L_b , and L_c) originating from the single domain are clearly observed. All the lattice-fringe spacings are found to be equal to those of the 101 plane of hexagonal $\text{Mg}(\text{OH})_2$. The prominence of the lattice fringe of d_{101} among the observed nanocrystallites suggests that the aggregative growth of the nanosheets is concentrated in the [101] direction. In addition, two types of Moire fringes (R_1 and R_2) are clearly observed in the HRTEM image. The Moire fringes are attributed to the rotation of the lattice planes having equal lattice spacing. According to previous studies, the nanoneedles could be the vertically aligned nanosheets or the nanosheets that are rolled up (Chen & Gao, 2004; Chen & Gao, 2005). The nanosheets would aggregate vertically by driving forces arising from the local stress and the decrease in the surface-free energy of the nanosheets. It is believed that the thin nanosheets

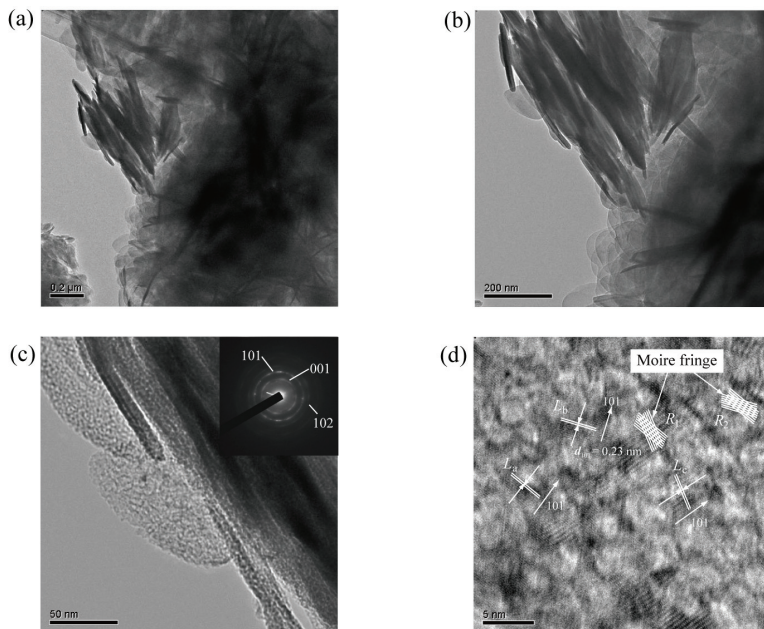


Fig. 6. (a) TEM image of powder sample of nanosheets hydrothermally treated at 150 °C for 24 h; (b) enlarged TEM image of (a); and (c) enlarged TEM image of (b). The inset shows the ED pattern of the nanosheet; (d) shows the HRTEM image of the nanosheet. [Reproduced by permission of The Royal Society of Chemistry, CrystEngComm., 2009, 11, 2338.]

specific surface energy, Liete et al. suggested that the surface energy of the 001 facet of hexagonal SiO_2 , which is comparable to the hexagonal $\text{Mg}(\text{OH})_2$, is higher than that of the other facets (Leite et al., 2003). In our system, the ammonium ion may preferentially get adsorbed on the 001 surface of hexagonal $\text{Mg}(\text{OH})_2$ to lower the high potential energy of the system. This might hinder the growth of nanocrystals in the [001] direction.

The growth behaviours of the nanosheets, comprising of crystalline $\text{Mg}_{1-x}\text{Al}_x(\text{OH})_2(\text{NO}_3)_x \cdot n\text{H}_2\text{O}$, $\text{Mg}_{1-x}\text{Al}_x(\text{OH})_2(\text{NO}_3)_x \cdot n\text{H}_2\text{O}$ and $\text{Mg}(\text{OH})_2$, and $\text{Mg}(\text{OH})_2$, depend on the experimental conditions; the single most important factor influencing the growth behaviour was found to be the treatment temperature. At 120 °C, the rosette-like structure formed by the curved nanosheets of crystalline $\text{Mg}_{1-x}\text{Al}_x(\text{OH})_2(\text{NO}_3)_x \cdot n\text{H}_2\text{O}$ was observed. It is worth noting that some previously reported LDH intercalated compounds showed a curved plate-like or sheet morphology (Ogawa & Asai, 2000; Xu & Braterman, 2003); these morphologies are formed by the cooperative organization of the intercalated anions and the cationic metal hydroxide layers. In our study, the unique morphology observed is considered to be induced by the interaction extrusion stress between nanocrystals. On increasing the treatment temperature to 150 °C, the shapes of the nanosheets are changed. The sample contains two types of crystalline structures, $\text{Mg}_{1-x}\text{Al}_x(\text{OH})_2(\text{NO}_3)_x \cdot n\text{H}_2\text{O}$ and $\text{Mg}(\text{OH})_2$; thus, no traces of curved nanosheets are observed in the sample treated at 150 °C. This might be due to the fact that on formation of $\text{Mg}(\text{OH})_2$, the interaction extrusion stress between the nanocrystals was relaxed. As a result, the interaction extrusion stress during the cooperative organization of the intercalated anions and the cationic metal hydroxide layers

could produce the curved structures. As shown in Figure 2(c), further increase in treatment temperature to 180 °C yielded larger crystals with sharp edges. The crystal structure in the crystallites corresponded to $\text{Mg}(\text{OH})_2$. At this temperature, the crystallites exhibited a distinct plate-like shape with the edges preferentially directed out of the AZ31 substrate. It is likely that this layer grows via a dissolution-precipitation mechanism. Nordlien et al. have supposed that amorphous platelets of $\text{Mg}(\text{OH})_2$ were initially formed by the precipitation of Mg^{2+} or other soluble magnesium species (Nordlien et al., 1997). These nanosheets appeared to be formed by the mechanical rupture of the outer layer of the amorphous $\text{Mg}(\text{OH})_2$ film rather than the precipitation of soluble magnesium hydroxide; this is because the nanosheets were locally formed on the surface, as shown in Figure 1(a). The film rupture can be attributed to the internal stress generated in the formed amorphous $\text{Mg}(\text{OH})_2$ film (Schultze & Lohrengel, 2000). With an increase in treatment time, the crystalline $\text{Mg}(\text{OH})_2$ nanosheets could be formed by the precipitation of magnesium hydroxide and the subsequent formation of the amorphous $\text{Mg}(\text{OH})_2$ film.

Crystalline nanosheets were successfully formed on magnesium alloy AZ31 by carrying out a facile surfactant-free hydrothermal treatment. The crystal structures and shapes of the nanosheets changed with the treatment temperature. We found that on treatment at 120 °C, rosette-like structure made from curved nanosheets of crystalline $\text{Mg}_{1-x}\text{Al}_x(\text{OH})_2(\text{NO}_3)_x \cdot n\text{H}_2\text{O}$ was formed. An increase in treatment temperature to 150 °C led to the formation of plate-like nanosheets of crystalline $\text{Mg}_{1-x}\text{Al}_x(\text{OH})_2(\text{NO}_3)_x \cdot n\text{H}_2\text{O}$ and $\text{Mg}(\text{OH})_2$. Further increase in temperature to 180 °C yielded larger crystals with sharp edges. The crystallites were crystalline $\text{Mg}(\text{OH})_2$ with a distinct hexagonal shape with the edges preferentially directed out of the magnesium alloy. In this study, the substrates themselves were used as the source of magnesium and aluminium to form the nanosheets. This facile and inexpensive approach as a uniform large-scale treatment for the fabrication of nanosheets can be an interesting tool for a variety of applications.

3. Superhydrophobic surface on magnesium alloy fabricated by microwave plasma-enhanced chemical vapor deposition (MPECVD) and its corrosion resistance

In this section, we report fabrication and corrosion resistant performance of the superhydrophobic film deposited on magnesium alloy AZ31 by electrochemical measurements. The superhydrophobic film was deposited on magnesium alloy AZ31 by microwave plasma-enhanced chemical vapor deposition (MPECVD). In addition, the chemical stabilities of a superhydrophobic surface on magnesium alloy AZ31 in aqueous solutions of various pHs were also demonstrated.

Magnesium alloy AZ31 (composition: 2.98% Al, 0.88% Zn, 0.38% Mn, 0.0135% Si, 0.001% Cu, 0.002% Ni, 0.0027% Fe, and the rest is Mg) with a size of 10 X 10 X 1.5 mm was used as the substrate. The substrates were ultrasonically cleaned in absolute ethanol for 10 min. Each cleaned substrate was placed on the substrate stage in the MPECVD system. The MPECVD system consisted of a Vycor glass discharge tube attached with a microwave cavity and a deposition chamber made of stainless steel. Superhydrophobic films were then deposited on the substrates using the MPECVD system (Ishizaki et al., 2007; Wu et al., 2002). The chamber of the MPECVD system was evacuated to 5.0 Pa prior to the deposition. A 2.45-GHz generator supplied microwave power of 250 W, and the raw materials were a gas mixture of trimethylmethoxysilane (TMMOS; $(\text{CH}_3)_3\text{SiOCH}_3$) and Ar. Ar gas was required for

maintaining the microwave discharge. The partial pressures of TMMOS and Ar were kept constant at 35 and 60 Pa, respectively. The deposition time was changed from 10 to 30 min. The substrate temperature remained below 333 K during the deposition.

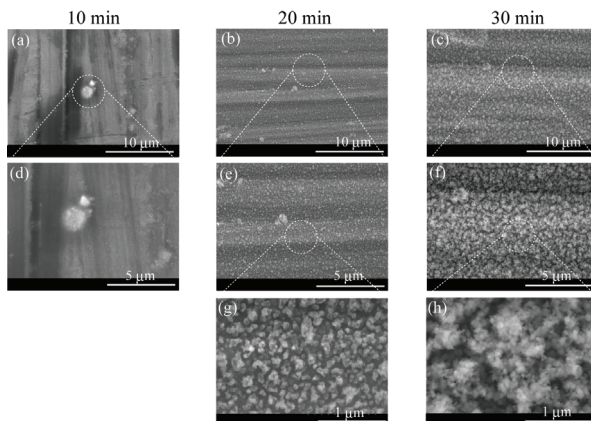


Fig. 1. FE-SEM images of a film on magnesium alloy AZ31 surfaces deposited for (a) 10, (b) 20, and (c) 30 min by the MPECVD process; (d) enlarged FE-SEM image of (a); (e) enlarged FE-SEM image of (b); (f) enlarged FE-SEM image of (c); (g) enlarged FE-SEM image of (e); and (h) enlarged FE-SEM image of (f).topography is important for fabricating a superhydrophobic surface. [Electrochimica Acta., 10.1016/j.electacta.2010.06.064. Copyright ©ELSEVIER (2010)]

Figure 1(a), (b), and (c) shows FE-SEM images of the film on magnesium alloy AZ31 surfaces deposited for 10, 20, and 30 min, respectively, by MPECVD. Figure 1 (d), (e), and (f) shows enlarged images of fig. 1 (a), (b), and (c), respectively. The film coverage increases with an increase in preparation time. When the deposition time was less than 10 min, the surface coverage of the film was low and the film surface was smooth compared to those deposited for 20 and 30 min. When the preparation time was prolonged to more than 20 min, the surfaces were covered with the films. The film coverage became higher with an increase in the preparation time. Figure 1 (g) and (h) shows enlarged images of fig. 1 (e) and (f), respectively. In the high magnification FE-SEM images (fig. 1 (g) and 1 (h)), aggregated particles were clearly observed. The particles were composed of nanoparticles with sizes of 20–150 nm. Most of these particles would be prepared in a clustering process in the gas phase and condensed on the substrate. The clusters deposited on the magnesium alloy surface, leading to an irregular surface topography composed of granular particles and minute pores with a few hundred nanometers in diameter.

Figure 2 (a), (b), and (c) shows topographic images of the film surface deposited for 10, 20, and 30 min, respectively. As clearly seen in fig. 2, the root mean square roughness of the film-deposited surface increased from 13.7 to 153.5 nm with an increase in preparation time. These results agree with the results of the FE-SEM images. The increase in the surface roughness would form a porous structure in the film. The porous structures in the film would permit an enhancement of the surface air fraction in the pores and reduce the actual area of rough surface in contact with the water. Thus, such topography provides high water repellency to the surface if the surface were covered with hydrophobic functional groups.

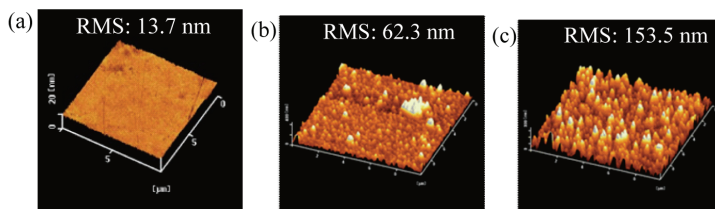


Fig. 2. Topographic images of the film surface deposited for (a) 10, (b) 20, and (c) 30 min. RMS means root mean square roughness of each surface. [Electrochimica Acta., 2010, 55, 7094. Copyright @ELSEVIER (2010)]

Information on the chemical bonding states, chemical composition, and surface functional groups of the film deposited for 30 min were investigated with FT-IR and XPS. XPS measurements revealed that the film surface consisted of Si, O, and C atoms with atomic concentrations of 24.5, 32.9, and 42.6 at%, respectively. The FT-IR analyses provided information that all the films mainly consisted of SiO_x and $-\text{CH}_3$; thus indicating that the surfaces were covered with hydrophobic $-\text{CH}_3$ groups. The XPS and FT-IR results agree well with our previous results (Ishizaki et al., 2007; Wu et al., 2004). Next, we estimated the surface wettability of the film deposited by water contact angles measurements.

Figure 3 shows the relationship between water contact angles onto the film surface deposited on magnesium alloy AZ31 and the deposition time. The water contact angles increased with an increase in preparation time. The surface of the film deposited for 10 min had a water contact angle of c.a. 105° and was shown to be hydrophobic. In contrast, when the preparation time was over 20 min, the water contact angles of the surfaces were more than 150° , resulting in the superhydrophobic surface. This result indicates that the increase in the static water contact angles has a close relationship with the increase in the surface roughness of the deposited film. In addition, the film coverage also increased with an increase in deposition time. Due to these effects, the wettability of the film coated surface increased greatly, resulting in the superhydrophobic surface.

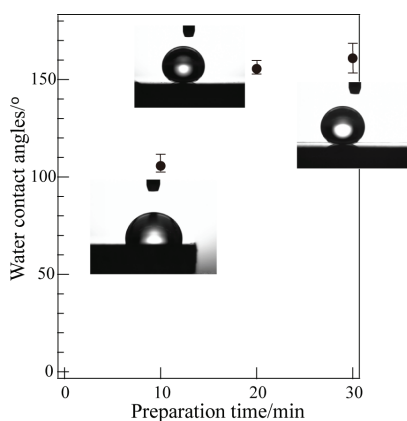


Fig. 3. Relationship between water contact angles on the film surface deposited on magnesium alloy AZ31 and the deposition time. [Electrochimica Acta., 2010, 55, 7094. Copyright @ELSEVIER (2010)]

All electrochemical measurements were performed in 5.0 wt% NaCl aqueous solution, pH 6.2, at room temperature, using a computer-controlled potentiostat under open circuit conditions. The superhydrophobic film coated magnesium alloy AZ31 and a platinum plate were used as the working and counter electrodes, respectively. A saturated calomel electrode (SCE) was used as the reference electrode. The reference electrode was set in the close vicinity of the circular window. The superhydrophobic film coated AZ31 substrate was immersed in the NaCl solution for 30 min, allowing the system to be stabilized, and potentiodynamic polarization curves were subsequently measured with respect to the OCP at a scanning rate of 0.5 mV/s from -400 to +800 mV. EIS measurements were conducted in the frequency ranges between 0.1 Hz and 100 kHz, with a sinusoidal signal perturbation of 10 mV and five points per decade. All the samples were immersed for 30 min before all the impedance measurements. The experimental EIS spectra were interpreted based on equivalent electrical analogues using the program Zplot2.0 to obtain the fitting parameters.

Figure 4 shows the potentiodynamic polarization curves of the superhydrophobic film coated and bare AZ31. The deposition time of the superhydrophobic film was 30 min. As compared to the corrosion current density (j_{corr}) of the bare AZ31 substrate (9.25×10^{-5} A/cm²), that of the coated AZ31 substrate (7.41×10^{-8} A/cm²) decreased by more than three orders of magnitude. The corrosion potential (E_{corr}) of the AZ31 was ca. -1507 mV. Hydrogen evolution dominates at more negative potentials than E_{corr} , resulting in an increase in the cathodic currents. On the other hand, E_{corr} of the coated AZ31 substrate is ca. -1487 mV and is slightly more positive than that of the bare AZ31. A substantial change in E_{corr} was not detected by the superhydrophobic film. It was reported that silica or zirconia film did not shifted clearly E_{corr} to positive direction (Tamar & Mandler, 2008). Our superhydrophobic film consisted of silica and -CH₃ groups. Thus, the E_{corr} would hardly change compared to the bare AZ31. However, the coating of superhydrophobic film decreased significantly both the anodic and cathodic current density. This indicates that the AZ31 substrate coated with the superhydrophobic film has a higher anticorrosion performance than the bare AZ31. The corrosion resistances of the film deposited on magnesium alloy AZ31 and bare AZ31 were estimated by electrochemical impedance spectroscopy. The Nyquist plots obtained from superhydrophobic films (deposition time: 20

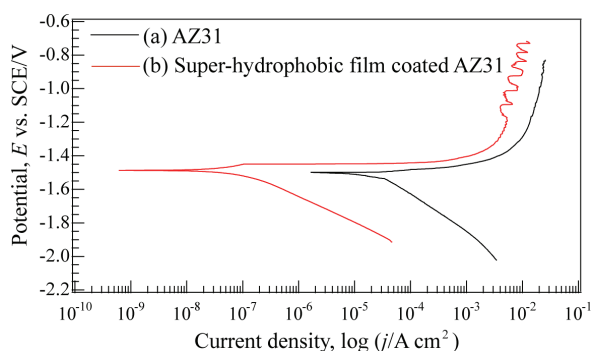


Fig. 4. Potentiodynamic curves of (a) untreated and (b) super-hydrophobic film coated magnesium alloy AZ31. The deposition time of the super-hydrophobic film was 30 min. The scanning rate was 0.5 mV / s. [Electrochimica Acta., 2010, 55, 7094. Copyright @ELSEVIER (2010)]

and 30 min), hydrophobic film (deposition time: 10 min), and bare AZ31 after immersion in 5wt% NaCl solution are presented in fig. 5. The inset of fig. 5 shows the enlarged Nyquist plot. All three surfaces behave quite differently, so we applied different equivalent circuits to fit the Nyquist plots. Three types of equivalent circuits are shown in fig.6.

As shown in fig. 5, the capacitive loops are not perfect semicircles. This phenomenon is known as the dispersing effect (Wu et al., 1999). When the dispersing effect is observed in impedance behavior, the double-layer does not behave as an ideal capacitor. In this case, a constant phase element (CPE) is often used as a substitute for the capacitor in the equivalent circuit to fit the impedance behavior of the electrical double layer more accurately. The CPE is a special element whose value is a function of the angular frequency ω and whose phase is independent of the frequency. Its admittance (Y) and impedance (Z) are described as follows:

$$Y_{CPE} = Y_0(i\omega)^n \quad (5)$$

$$Z_{CPE} = 1 / Y_0(i\omega)^{-n} \quad (6)$$

where Y_0 is the magnitude of the CPE, ω is the angular frequency, and n is the exponential term of the CPE.

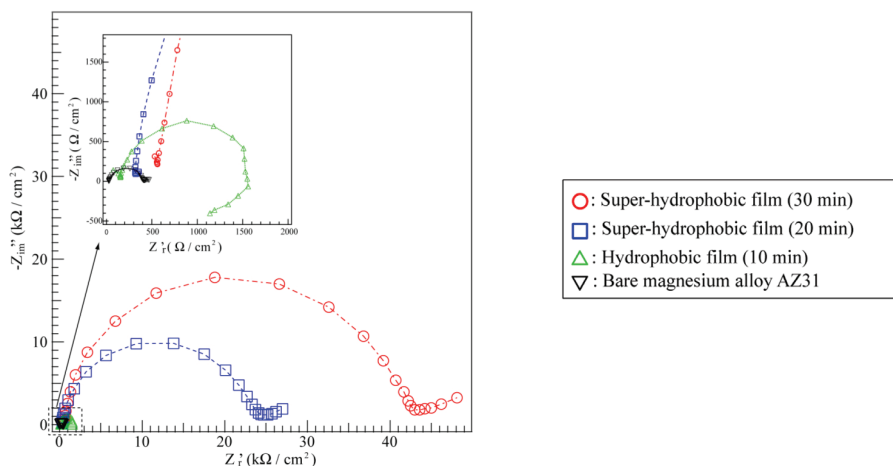


Fig. 5. Nyquist plots obtained from super-hydrophobic films (deposition time: 20 and 30 min), hydrophobic film (deposition time: 10 min), and bare AZ31 after immersion in 5wt% NaCl solution. The inset shows enlarged Nyquist plots. [Electrochimica Acta., 2010, 55, 7094. Copyright @ELSEVIER (2010)]

Figure 6 (a) shows the equivalent circuit model representing the electrochemical behavior of the bare AZ31 surface, which shows one time constant. In this circuit, R_{ct} means the charge transfer resistance, CPE_{dl} is the constant phase element of the electrical double layer, and R_s is the solution resistance. Figure 6 (b) shows the equivalent circuit model representing the electrochemical behavior of the film surface deposited for 10 min. This surface does not show a superhydrophobic property but a hydrophobic property, as shown in fig. 4. R_c is film resistance. The capacitive loop at high frequency can be interpreted as the electrical double layer capacitance CPE_{dl} in parallel with a charge transfer resistance R_{ct} . An inductance behavior can be seen at the low frequency region. L and R_L are often used to

explain the inductive loop at low frequency, which originates from adsorbed/desorbed intermediates or other species on the electrode surface (Liu et al., 2007). In the case of the electrode protected with the superhydrophobic film, the equivalent circuit model should consider two time constants in the corresponding impedance spectrum, as shown in fig. 6 (c), since the film has a rough surface with many minute pores. C_c would normally be assigned to the capacitance of a surface film, which is based on various factors such as film with the interface reaction between the film and substrate. The parallel combination of R_c which is based on various factors such as film thickness and defect structure. The $R_{ct} || C_{dl}$ elements in Fig. 6 (c) represent the impedance and C_c shows impedance with the interface reaction between the electrolytic solution and the film. R_{air} and C_{air} are typically associated with the resistance and capacitance of air within a minute pore, respectively. The $R_{air} || C_{air}$ elements were arranged in parallel to above-mentioned these two elements with considering that the many minute pores would be filled with air. By applying this equivalence circuit model in Fig.6 (c) to the Nyquist plots for superhydrophobic film deposited for 20 and 30 min, we obtained better fitting results.

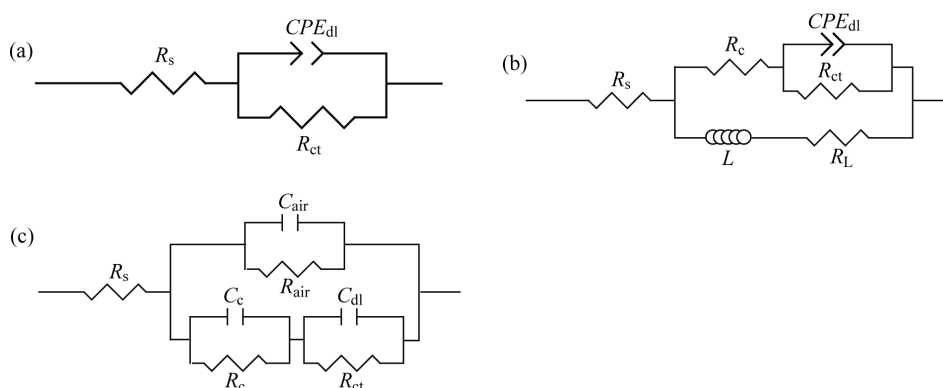


Fig. 6. Equivalent circuits of the studied system (a) bare AZ31 surface, (b) hydrophobic surface (deposition time: 10 min), and (c) super-hydrophobic surface (deposition time: 20 and 30 min). [Electrochimica Acta., 2010, 55, 7094. Copyright @ELSEVIER (2010)]

As clearly seen in fig. 5, R_{ct} values of the samples estimated in the 5 wt% NaCl solution rapidly increased with an increase in the hydrophobicity. This indicates that the hydrophobicity plays an important role in improving the anticorrosion performance of the magnesium alloy. With an increase of the deposition duration the corrosion current density (j_{corr}) decreases, whereas the resistance R_{ct} increases. The double layer capacitances decrease with an increase in the hydrophobicity. The inhibition efficiency (IE%) can be calculated from the charge transfer resistance as follows (Ma et al., 2002):

$$IE = (R_t - R_{t0}) / R_t \times 100 \quad (7)$$

where R_t is the charge transfer resistance of the film-deposited AZ31 and R_{t0} is the resistance of the bare AZ31. The IE of the film deposited for 10, 20, and 30 min were estimated to be 71.4, 98.3, and 99.1%, respectively. The IE considerably increased with an increase in the hydrophobicity of the film surface. This indicates that our superhydrophobic film effectively suppressed the progress of the corrosion reaction. Figure 7 presents the evolution of the

impedance spectra of the superhydrophobic film coated AZ31 after different times of immersion in 5 wt% NaCl solution. As clearly seen in fig. 7, the capacitive loops at high and medium frequencies and tail at low frequencies are observed. The capacitive loops can be attributed to the charge transfer of the corrosion process and the tail might be associated with a diffusion process across the corrosion layer (Feliu et al., 1990). The capacitive loops decreased gradually with an increase in the immersion time. This indicates that the anticorrosion performance of the superhydrophobic film is lowered gradually with immersion time. The lowering of the anticorrosion performance might be due to the localized corrosion. Once local corrosion begins at the film surface, the hydroxide ions are produced in the NaCl solution. As a result, the pH in the vicinity of superhydrophobic film increases locally. Due to the local pH change, the superhydrophobic film might dissolve locally because SiOx components in our superhydrophobic film could be dissolved as HSiO_3^- ion species in the solution at pH ranging from 10 to 12 (Pourbaix, 1974). Thus, the diameter of the capacitive loops that is closely related to the corrosion rate could decrease. However, the charge transfer of the superhydrophobic film coated AZ31 after immersion in 5 wt% NaCl solution for 24 h is much greater than that of uncoated AZ31. This indicates that the superhydrophobic film can improve the anticorrosion of magnesium alloy in the NaCl solution.

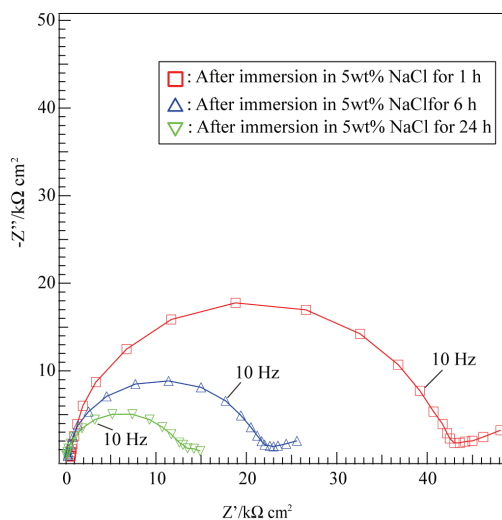


Fig. 7. Evolution of Nyquist plots of the super-hydrophobic film coated magnesium alloy AZ31 after immersion in 5 wt% NaCl aqueous solution for (a) 1 h, (b) 6 h, and (c) 24 h. [Electrochimica Acta., 2010, 55, 7094. Copyright @ELSEVIER (2010)]

From a theoretical point of view, to inhibit corrosion, it would be very effective to minimize the wetted area on a solid surface immersed in the NaCl aqueous solution. A superhydrophobic surface would be a means to achieve this since the superhydrophobic surface has many roughness structures that could trap air at the solid-liquid interface. Minimizing the wetted area on a solid surface might be achieved if an air layer formed on the superhydrophobic surface could be stabilized within the roughness grooves. Quéré et al. demonstrated that the air entrapment state would be metastable for the following conditions (Bico et al., 2002):

$$\cos\theta \leq (f_1 - 1) / (\gamma - f_1) \quad (8)$$

where f_1 is the fraction of the solid/liquid interface below the drop in contact with the solid, γ is the roughness ratio of the surface, and θ is the contact angle. According to equation (8), if θ is higher than 90° , the air would be trapped below the liquid (within the surface). After EIS measurement, the water contact angle of superhydrophobic surface was still c.a. 141° . This proves that the air layer was stabilized within the roughness grooves in the process of the whole experiment. Our superhydrophobic treatment could reduce considerably the probability of adsorption of aggressive ion species (Cl^-) to the superhydrophobic film deposited magnesium alloy AZ31, and the AZ31 surface was thus protected. Moreover, our superhydrophobic film has great roughness structures, as shown in figs. 1 and 2. Such roughness structures had many minute spaces and thus can easily trap air within the minute spaces between the roughness structures, preventing the most part of the Cl^- ions from reaching the bare AZ31 surface.

We successfully deposited a superhydrophobic film on magnesium alloy AZ31 through the MPECVD process. The film surface showed a water contact angle of more than 150° , that is, superhydrophobicity. The anticorrosion resistance of the deposited film was estimated by potentiodynamic and EIS measurement.

4. Rapid formation of superhydrophobic surface on magnesium alloy coated with cerium oxide film and its chemical stability

In this section, we report a simple immersion process at room temperature for the fabrication of superhydrophobic surface on magnesium alloy. The chemical stabilities of the superhydrophobic surfaces on magnesium alloy were also examined from view points of durability and corrosion resistance.

Magnesium alloy AZ31 (composition: 2.98% Al, 0.88% Zn, 0.38% Mn, 0.0135% Si, 0.001% Cu, 0.002% Ni, 0.0027% Fe, and the rest is Mg) with a thickness of 1.5 mm was used as the substrate. The substrates were ultrasonically cleaned in absolute ethanol for 10 min. After the cleaning, the substrates were dried with inert Ar gas. The cleaned magnesium alloy substrates were immersed in an acidic solution containing 0.05 M cerium nitrate ($\text{Ce}(\text{NO}_3)_2$) with pH experimentally measured to be c.a. 4.5 at room temperature. The solution was agitated with magnetic stirrer at a rotation of 100 rpm during the immersion. The immersion time was changed from 0.5 to 20 min. After immersion, the samples were thoroughly washed in absolute ethanol. Finally, the washed samples were immersed in 40 ml of toluene solution containing 400 μl of FAS ($\text{CF}_3(\text{CF}_2)_7\text{CH}_2\text{CH}_2\text{Si}(\text{OCH}_3)_3$) and 40 μl of tetrakis(trimethylsiloxy)titanium ($(\text{CH}_3)_3\text{SiO})_4\text{Ti}$) (TTST) for 30 min. The TTST molecules were used as catalysis to promote hydrolysis and/or polymerization of FAS molecules.

Figure 1 shows FE-SEM images of the sample surfaces after immersion in cerium nitrate aqueous solution for (a) 0.5, (b) 1, (c) 3 (d) 5, (e) 10, and (f) 20 min. After 0.5 min of immersion, the surface of the magnesium alloy was covered with a coating film with island-like particles. However, the coverage was not complete. After 1 min of immersion, the substrate surface was covered with almost complete coating on which some microcracks were formed (Fig. 1(b)). When the immersion time was prolonged to more than 3 min, the coating became thick enough to cover the substrate. On the other hand, cracks with larger crack-width were also formed (Fig. 1(c)). These cracks divided whole coating into pieces separated by relatively large cracks. Several relatively small microcracks were observed

within each piece, as can be seen in Fig. 1 (d)-(f). These cracks in the coating film could be formed after withdrawing the sample from the solution due to the shrinkage in volume. This shrinkage occurred by the evaporation of the water molecules containing in the coating film, allowing cracks to form. Figure 1 (g), (h), and (i) shows the enlarged versions of the FE-SEM images shown in Fig. 1(b), (d), and (f), respectively. All the samples exhibit nanosheets that are aligned at fairly inclined angles with respect to the surface. When the treatment time was less than 1 min, the nanosheets were locally formed on the surfaces. In contrast, after treatment for over 3 min, the nanosheets were observed to be vertically aligned over the entire substrate surface. The vertically aligned nanosheets became dense as the treatment time increased. The nanosheets exhibit an edge length in the range of approximately 200–1000 nm and a thickness of 20–50 nm. The aggregation of the nanosheets could lead to an irregular surface topography with nanoscale pores composed of valleys and hills. Such surface texture is suitable for fabricating a superhydrophobic surface. An increase in the immersion time to 20 min was found to result in the formation of compact and continuous nanosheets due to an increase in nucleation and growth periods. Figure 2 shows XRD pattern of the obtained sample after immersion in cerium nitrate aqueous solution for 20 min. Some broad and sharp peaks were clearly observed. The sharp peaks were attributed to magnesium alloy substrate, while the broad peaks were assigned to cerium oxide with cubic system, which are indexed based on the JCPDS data (Card No. 43-1002). The five broad peaks at approximately $2\theta = 28.5, 33.1, 47.5, 56.3$ and 76.7° were assigned to the 111, 200, 220, 311, and 331 diffraction peaks of cerium oxide with the cubic phase. These broad peaks also confirm the existence of nanosized grains in the major overlay. This agrees well with results of FE-SEM observation.

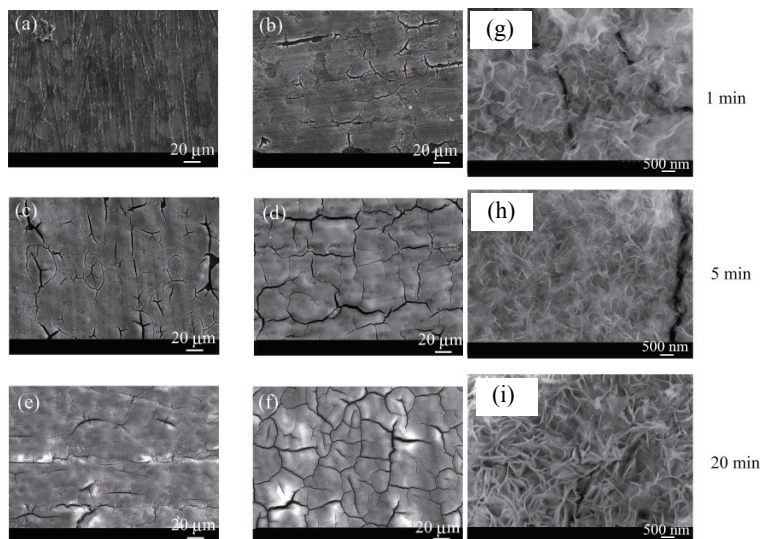


Fig. 1. FE-SEM images of the sample surfaces after immersing in cerium nitrate aqueous solutions at room temperature for (a) 0.5, (b) 1, (c) 3, (d) 5, (e) 10, and (f) 20 min. (g) Enlarged versions (b). (h) Enlarged versions in (d). (i) Enlarged versions in (f). [Reprinted with permission, Langmuir, 26, 9749, 2010. Copyright @American Chemical Society (2010)]

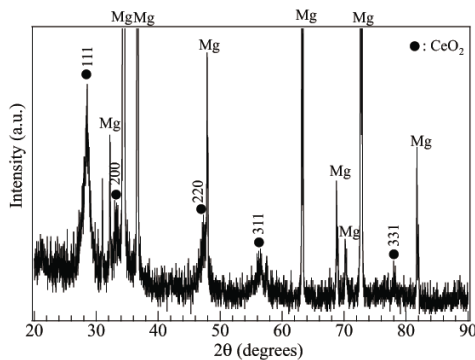


Fig. 2. XRD pattern of the obtained sample after immersion in cerium nitrate aqueous solution for 20 min. [Reprinted with permission, Langmuir, 26, 9749, 2010. Copyright @American Chemical Society (2010)]

Figure 3 (a) shows a cross sectional TEM image of the sample after immersion in cerium nitrate aqueous solution for 20 min. It is known that the magnesium alloy AZ31 surface had an oxide layer with a thickness of c.a. 50 nm (Liu & Fang, 2005). The existence of the oxide layer supports that the magnesium alloy is active when exposed to atmosphere. Our film fabricated had a thickness of c.a. 2 μm and exhibited a three layered structure with a slightly porous layer (marked as 1 in Fig. 3 (a)) as an under layer intimately in contact with the magnesium alloy substrate and a compact layer (marked as 2 in Fig. 3 (a)) as an intermediate layer, and a fibrous layer (marked as 3 in Fig. 3 (a)) as the major top layer. The composition of the each layer was measured by EDAX analyses. The slightly porous layer showed that the atomic concentration of Mg, O, Al, and Zn was 81.14, 14.03, 3.72, and 1.11 at%, respectively, suggesting that this layer was primarily a mixture of magnesium and

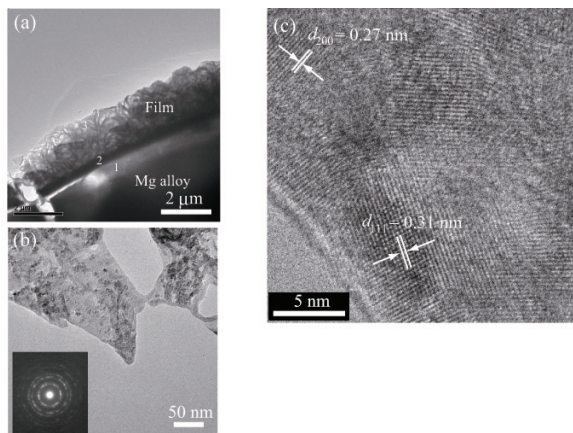


Fig. 3. (a) Cross-sectional TEM image of the sample after immersion in cerium nitrate aqueous solution for 20 min. (b) TEM image of the tip of the fibrous layer. The inset shows the SAED pattern. (c) High-resolution TEM image of the CeO_2 nanosheet. [Reprinted with permission, Langmuir, 26, 9749, 2010. Copyright @American Chemical Society (2010)]

aluminum hydroxides and oxides. On the other hand, except for magnesium, zinc and oxide, cerium was detected in both the compact and fibrous layer. Both layers could be mixtures of cerium and magnesium hydroxides and oxides. It should be noted that the fibrous layer greatly contributed to the greater coating thickness, although this layer was formed discontinuously. The discontinuity of the fibrous layer correlated well with the results of the SEM observation. Figure 3 (b) shows the high magnified TEM image of the tip of the fibrous layer. The high magnified TEM image revealed that the nanosheet comprised of many minute nanosized crystallinity. The selected area electron diffraction (SAED) patterns exhibit some rings corresponding to the [111], [200], [220], [311] and [331] planes of CeO_2 .

These patterns are consistent with the XRD patterns. The discrete spots on the rings suggest that the crystals were of good crystallinity. Figure 3 (c) shows high-resolution TEM image of the nanosheet. Lattice fringes with interplanar spacings, $d_{111} = 0.31$ and $d_{200} = 0.27$ nm can be clearly observed and are consistent with the cubic phase.

The control of the microstructures was achieved by varying the immersion time. To fabricate superhydrophobic surface, FAS coating was performed on the CeO_2 nanosheets by immersing it in the toluene solution containing FAS and TTST molecules for 30 min. The wetting properties were evaluated by water contact angle measurements of the samples surfaces fabricated by immersion in cerium nitrate aqueous solution for 20 min and the samples obtained after FAS coating. Figure 4 (a) shows a shape of water droplet on the as-prepared surface composed of CeO_2 nanosheets. When a water droplet was dropped on the as-prepared surface, it spreaded onto the sample surface very quickly, indicating the superior super-hydrophilic property of the sample surface. This is in line with the very low contact angle, $3 \pm 2^\circ$, of the as-prepared sample surface composed of CeO_2 nanosheets. Such a small contact angle is attributed to the presence of $-\text{OH}$ groups on the surface of the CeO_2 nanosheets, leading to superhydrophilicity. However, the sample surface became superhydrophobic after simply immersing the sample in toluene solution containing FAS and TTST for 30 min. Figure 4 (b) shows a water droplet behavior on the CeO_2 nanosheets surface after FAS coating. The static water contact angle of these modified sample surface was found to be $155 \pm 2^\circ$, clearly revealing that the surface changed from superhydrophilicity to superhydrophobicity. Figure 4 (c) shows a digital photograph image of a shape of water droplets on the superhydrophobic surface. The digital photograph image of water droplets with uniform size on the surface of the FAS modified CeO_2 nanosheets gives a direct demonstration of superhydrophobicity of the treated surface. From these results, we

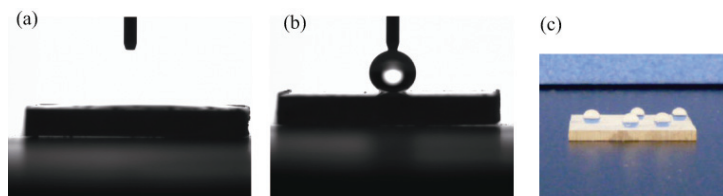


Fig. 4. (a) Shape of water droplet on the as-prepared surface composed of CeO_2 nanosheets. (b) Water droplet behavior on the CeO_2 nanosheets surface after FAS coating. (c) Digital photograph image of a shape of water droplets on the super-hydrophobic surface. [Reprinted with permission, Langmuir. 26, 9749, 2010. Copyright @American Chemical Society (2010)]

concluded that the FAS coating by catalyst-assisted immersion process was successfully achieved and the process of FAS coating was completed within 30 min. Moreover, the effects of the microstructures based on CeO_2 nanosheets on wetting properties were investigated by dynamic contact angle measurements. Figure 5 shows the relationship between advancing and receding water contact angles and immersion time in cerium nitrate aqueous solutions. All the samples for dynamic contact angle measurements were separately prepared as follows. First, they were immersed in the cerium nitrate aqueous solution for set time. Next, the CeO_2 coated samples were modified with FAS molecules. As clearly seen in Fig. 5, the advancing and receding contact angles gradually increased with an increase in the immersion time. The water contact angles hysteresis (the difference between the advancing and receding water contact angles) also become small with an increase in the immersion time. It is known that the surface wettability is controlled by the chemical composition and surface roughness of solids (Liu & Fang, 2005). The water contact angle of a smooth surface can reach to c.a. 120° , but on the micropatterned surface or hierarchical structures, the water contact angles can reach to maximum value of c.a. 178° (Hosono et al., 2005). This suggests that the fabrication of the hierarchical structures is a crucial factor for the fabrication of superhydrophobic surface (Zhu et al., 2006). Our surface fabricated by the CeO_2 film has hierarchical structures. The rough surface can trap a large fraction of air within the micro- and nanotextured surfaces created between the nanosheets. The trapped air can greatly increase the air-liquid interface, which prevents the water droplets from penetrating into the grooves of the surfaces. Our surface fabricated showed the advancing water contact angle of more than 150° and the contact angle hysteresis of less than 10° . These results support that the water droplets do not penetrate into the grooves. Thus, the micro- and nanostructures based on the CeO_2 nanosheets not only enhance the surface hydrophobicity but also reduce the contact angle hysteresis by decreasing the contact area between solid and liquid at their interface and the continuity of the three-phase contact line at the solid-liquid interface.

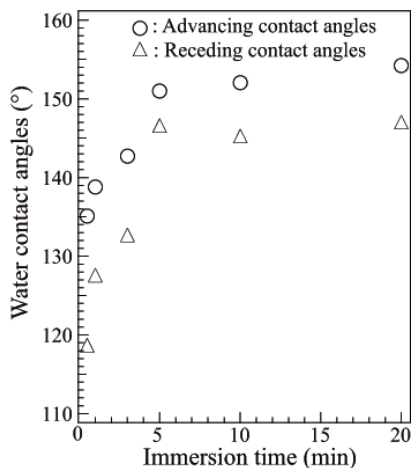


Fig. 5. Advancing and receding water contact angles of the sample surfaces after FAS coating as a function of immersion time in cerium nitrate aqueous solutions. [Reprinted with permission, Langmuir, 26, 9749, 2010. Copyright ©American Chemical Society (2010)]

To apply the superhydrophobic surface to industrial fields, it is very important to reveal the chemical stability of the superhydrophobic film in the aqueous solution. Chemical stability of superhydrophobic surface on magnesium alloy AZ31 was estimated by measuring static water contact angles of the superhydrophobic surfaces after immersing in aqueous solutions at various pHs for constant times. Figure 6 shows changes in static contact angles of the sample surface fabricated by immersion in cerium nitrate aqueous solution for 20 min and FAS coating for 30 min as a function of immersion time in aqueous solutions at pH = 4.0, 7.0, and 10.0, that is, acidic, neutral, and alkaline solutions. All the plots in fig. 6 show the averaged values of water contact angles measured at different five points. The error bars for each plot mean maximum and minimum water contact angles, which were measured at different plot points on same sample. For all the solutions, the static water contact angles of the superhydrophobic surfaces gradually decreased with time evolution. This indicates that the density of the hydrophobic functional groups on the surface could be reduced by immersing the samples in each pH solution. The static water contact angles decreased to be in the ranges of c.a. 140 ± 2 to $150 \pm 2^\circ$ within 60 min after immersion in each pH's solution. However, the static water contact angles after the immersion for 60 to 360 min hardly changed. The averaged static water contact angles of the superhydrophobic surfaces after the immersion in the solutions at pH = 4, 7, and 10 for 24 h were estimated to be $139.7 \pm 2^\circ$, $140.0 \pm 2^\circ$, and $145.7 \pm 2^\circ$, respectively.

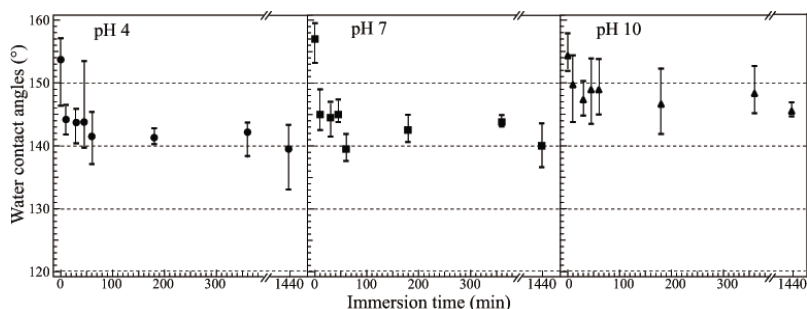


Fig. 6. Changes in static contact angles of the sample surfaces as a function of immersion time in aqueous solutions at pH = 4.0, 7.0, and 10.0. The super-hydrophobic surfaces were fabricated by immersion in cerium nitrate aqueous solution for 20 min and FAS coating for 30 min. All the plots show the averaged values of water contact angles measured at different five points on same samples. The error bars for each plot mean maximum and minimum water contact angles. [Reprinted with permission, Langmuir, 26, 9749, 2010. Copyright @American Chemical Society (2010)]

Figure 7 shows potentiodynamic curves of (a) bare magnesium alloy and (b) superhydrophobic surface on magnesium alloy. The corrosion potential, E_{corr} , of the superhydrophobic surface was more positive than that of bare magnesium alloy. The shift of the E_{corr} in the positive direction could be linked to an improvement of the protective properties of the superhydrophobic film formed on the AZ31 magnesium alloy. The corrosion current density, j_{corr} , of the superhydrophobic film coated AZ31 (8.11×10^{-7} A/cm²) decreased by more than one order of magnitude as compared to that of the uncoated one (6.71×10^{-6} A/cm²). These results indicate that the superhydrophobic film has good corrosion resistance.

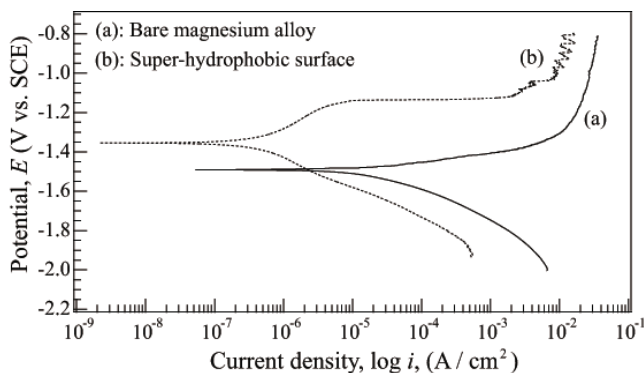


Fig. 7. Potentiodynamic curves of (a) bare magnesium alloy and (b) super-hydrophobic surface on magnesium alloy. The scanning rate was 0.5 mV/s. [Reprinted with permission, Langmuir, 26, 9749, 2010. Copyright @American Chemical Society (2010)]

We have developed a facile, simple, and time-saving method to create superhydrophobic surface on magnesium alloy by a simple immersion process. The FAS modified CeO_2 nanosheets surface showed a static contact angle of more than 150° , resulting in the formation of superhydrophobic surface. The contact angles hysteresis decreased with an increase in the immersion time in the cerium nitrate aqueous solution. The shortest processing time for the fabrication of the superhydrophobic surface was within 40 min. Chemical stability of the superhydrophobic surface on magnesium alloy AZ31 was investigated. In addition, the chemical stability of the superhydrophobic surface in the solutions at pH ranging from 1 to 14 was also examined. Moreover, the corrosion resistance of the superhydrophobic surface on the magnesium alloy was investigated using electrochemical measurements.

5. Conclusion and outlook

In this chapter, we showed experimental studies on the formation of hierarchical structures composed of crystalline nanosheets and two types of superhydrophobic surfaces by surface treatment. The hierarchical structures formed on magnesium alloy could be used as a template of superhydrophobic surface. All electrochemical measurements revealed that the superhydrophobic treatments by MPECVD process greatly improved the corrosion resistance of magnesium alloy. Water contact angle measurements showed that the superhydrophobic film had highly chemical stability to acidic and neutral aqueous solution. Finally, we reported a facile, simple, and time-saving method to create superhydrophobic surface on magnesium alloy by a simple immersion process at room temperature. The superhydrophobic surface showed highly chemical stability to the solution at pH ranging from 1 to 14. The electrochemical potentiodynamic measurements revealed that the superhydrophobic film have good corrosion resistance. These results suggest that superhydrophobic treatments would be a promising mean for improving greatly the corrosion resistance of magnesium and its alloys.

Magnesium and its alloys are one of the most promising materials for reducing vehicle weight, lowering fuel consumption and reducing CO_2 emission. An extremely low corrosion resistant property of the magnesium alloys, however, restricts larger scale use toward the

various applications. At present, though a great deal of work of academic and commercial interest on surface treatments of magnesium alloys has been carried out, still more remains to be done in order to improve considerably their corrosion resistances. In the future, we believe work on the development of surface treatments to improve considerably their corrosion resistances will continue to expand rapidly.

6. References

- Acatay, K.; Simsek, E.; Ow-Yang, C. & Menciloglu, Y. Z. (2004). Tunable, superhydrophobically stable polymeric surfaces by electrospinning. *Angewandte Chemie International Edition*, 43, 39, 5210-5213, 1521-3773.
- Barchiche, C. -E.; Rocca, E.; Juers, C.; Hazan, J. & Steinmetz, J. (2007). Corrosion resistance of plasma-anodized AZ91D magnesium alloy by electrochemical methods. *Electrochimica Acta*, 53, 2, 417-425, 0013-4686.
- Baril, G.; Galicia, G.; Deslouis, C.; Pebere, N.; Tribollet, B. & Vivier, V. (2007). An impedance investigation of the mechanism of pure magnesium corrosion in sodium sulfate solutions. *Journal of The Electrochemical Society*, 154, 2, C108-C113, 0013-4651.
- Barthlott, W. & Neinhuis, C. (1997). Purity of the sacred lotus, or escape from contamination in biological surfaces. *Planta*, 202, 1, 1-8, 0032-0935.
- Benesi, H. A. (1959). Infrared spectrum of $Mg(OH)_2$. *Journal of Chemical Physics*, 30, 3, 852, 0021-9606.
- Bico, J.; Thiele, U. & Quéré, D. (2002). Wetting of textured surfaces. *Colloids and Surfaces A: Physicochemical and Engineering Aspects*, 206, 1-3, 41-46, 0927-7757.
- Callies, M. & Quere, D. (2005). On water repellency. *Soft Matter*, 1, 1, 55-61, 1744-683X.
- Cavani, F.; Trifiro, F. & Vaccari, A. (1991). Hydrotalcite-type anionic clays: Preparation, properties and applications. *Catalysis Today*, 11, 2, 173-301, 0920-5861.
- Chen, D. & Gao, L. (2004). Novel morphologies of nickel sulfides: nanotubes and nanoneedles derived from rolled nanosheets in a w/o microemulsion. *Journal of Crystal Growth*, 262, 1-4, 554-560, 0022-0248.
- Chen, D. & Gao, L. (2005). A new and facile route to ultrafine nanowires, superthin flakes and uniform nanodisks of nickel hydroxide. *Chemical Physics Letters*, 405, 1-3, 159-164, 0009-2614.
- Chen, H.; Zhang, F.; Fu, S. & Duan, X. (2006). In situ microstructure control of oriented layered double hydroxide monolayer films with curved hexagonal crystals as superhydrophobic materials. *Advanced Materials*, 18, 23, 3089-3093, 0935-9648.
- Chisem, I. C. & Jones, W. (1994). Ion-exchange properties of lithium aluminium layered double hydroxides. *Journal of Materials Chemistry*, 4, 11, 1737-1744, 0959-9428.
- Feliu, S.; Galvan, J. C. & Morcillo, M. (1990). The charge transfer reaction in Nyquist diagrams of painted steel. *Corrosion Science*, 30, 10, 989-998, 0010-938X.
- Gray, J. E. & Luan, B. (2002). Protective coatings on magnesium and its alloys - a critical review. *Journal of Alloys and Compounds*, 336, 1-2, 88-113, 0925-8388.
- Guo, Z.; Zhou, F.; Hao, J. & Liu, W. (2005). Stable biomimetic super-hydrophobic engineering materials. *Journal of the American Chemical Society*, 127, 45, 15670-15671, 0002-7863.
- Haycock, D. E.; Kasrai, M.; Nicholls, C. J. & Urch, D. S. (1978). The electronic structure of magnesium hydroxide (brucite) using X-ray emission, X-ray photoelectron, and

- auger spectroscopy. *Journal of the Chemical Society, Dalton Transactions*, 1978, 11, 1791-1796, 1472-7773.
- He, T.; Wang, Y.; Zhang, Y.; Iv, Q.; Xu, T. & Liu, T. (2009). Super-hydrophobic surface treatment as corrosion protection for aluminum in seawater. *Corrosion Science*, 51, 8, 1757-1761.
- Hosono, E.; Fujihara, S.; Honma, I. & Zhou, H. (2005). Superhydrophobic perpendicular nanopin film by the bottom-up process. *Journal of the American Chemical Society*, 2005, 127, 39, 13458-13459, 0002-7863.
- Huang, L.; Lau, S. P.; Yang, H. Y.; Leong, E. S. P.; Yu, S. F. & Prawer, S. (2005). Stable superhydrophobic surface via carbon nanotubes coated with a ZnO thin film. *The Journal of Physical Chemistry B*, 109, 16, 7746-7748, 1520-6106.
- Ishizaki, T.; Saito, N.; Inoue, Y.; Bekke, M. & Takai, O. (2007). Fabrication and characterization of ultra-water-repellent alumina-silica composite films. *Journal of Physics D: Applied Physics*, 40, 1, 192-197, 0022-3727.
- Ishizaki, T.; Cho, S.P.; Saito, N. (2009). Morphological control of vertically self-aligned nanosheets formed on magnesium alloy by surfactant-free hydrothermal synthesis. *CrystEngComm*, 11, 2338-2343, 1466-8033.
- Ishizaki, T.; Saito, N. (2010). Rapid formation of a superhydrophobic surface on a magnesium alloy coated with a cerium oxide film by a simple immersion process at room temperature and its chemical stability. *Langmuir*, 26, 9749-9755, 0743-7463.
- Ishizaki, T.; Saito, N.; Saito, N.; Takai O. (2010). Corrosion resistance and chemical stability of super-hydrophobic film deposited on magnesium alloy AZ31 by microwave plasma-enhanced chemical vapor deposition. *Electrochimica Acta*, 2010, 55, 7094.
- Kannan, S.; Velu, S.; Ramkumar, V. & Swamy, C. S. (1995). Synthesis and physicochemical properties of cobalt aluminium hydrotalcites. *Journal of Materials Science*, 30, 6, 1462-1468, 0022-2461.
- Khorasani, M.; Mirzadeh, H. & Kermani, Z. (2005). Wettability of porous polydimethylsiloxane surface: morphology study. *Applied Surface Science*, 242, 3-4, 339-345, 0169-4332.
- Kloprogge, J. T.; Hickey, L. & Frost, R. L. (2005). The effect of varying synthesis conditions on zinc chromium hydrotalcite: a spectroscopic study. *Materials Chemistry and Physics*, 89, 1, 99-109, 0254-0584.
- Kuma, K.; Paplawsky, W.; Gedulin, B. & Arrhenius, G. (1989). Mixed-valence hydroxides as bioorganic host minerals. *Origins of Life and Evolution of Biospheres*, 19, 5, 573-602, 0169-6149.
- Labajos, F. M.; Rives, V. & Ulibarri, M. A. (1992). Effect of hydrothermal and thermal treatments on the physicochemical properties of Mg-Al hydrotalcite-like materials. *Journal of Materials Science*, 27, 6, 1546-1552, 0022-2461.
- Leite, E. R.; Giraldi, T. R.; Pontes, F. M.; Longo, E.; Beltrán, E. A. & Andrés, J. (2003). Crystal growth in colloidal tin oxide nanocrystals induced by coalescence at room temperature. *Applied Physics Letters*, 83, 8, 1566-1568, 0003-6951.
- Lejeune, M.; Lacroix, L.M.; Bretagnol, F.; Valsesia, A.; Colpo, P. & Rossi, F. (2006). Plasma-based processes for surface wettability modification. *Langmuir*, 22, 7, 3057-3061, 0743-7463.

- Lian, J. S.; Li, G. Y.; Niu, L. Y.; Gu, C. D.; Jiang, Z. H. & Jiang, Q. (2006). Electroless Ni-P deposition plus zinc phosphate coating on AZ91D magnesium alloy. *Surface and Coatings Technology*, 200, 20-21, 5956-5962, 0257-8972.
- Liu, C. S. & Fang, S. K. (2005). Formation of cerium conversion coatings on AZ31 magnesium alloys. *Journal of The Electrochemical Society*, 152, 2, B54-B59, 0013-4651.
- Liu, H.; Szunerits, S.; Xu, W. & Boukherroub, R. (2009). Preparation of superhydrophobic coatings on zinc as effective corrosion barriers. *ACS Applied Materials & Interfaces*, 1, 6, 1150-1153, 1944-8244.
- Liu, K.; Zhang, M.; Zhai, J.; Wang, J. & Jiang, L. (2008). Bioinspired construction of Mg-Li alloys with surface with stable superhydrophobicity and improved corrosion resistance. *Applied Physics Letters*, 92, 18, 183103, 0003-6951.
- Liu, T.; Chen, S.; Cheng, S.; Tian, J.; Chang, X. & Yin, Y. (2007). Corrosion behavior of superhydrophobic surface on copper in seawater. *Electrochimica Acta*, 52, 28, 8003-8007, 0013-4686.
- Liu, Z. & Gao, W. (2006). Electroless nickel plating on AZ91 Mg alloy substrate. *Surface and Coatings Technology*, 200, 16-17, 5087-5093, 0257-8972.
- Ma, H.; Chen, S.; Niu, L.; Zhao, S.; Li, S. & Li, D. (2002). Inhibition of copper corrosion by several Schiff bases in aerated halide solutions. *Journal of Applied Electrochemistry*, 32, 1, 65-72, 0021-891X.
- Montemor, M. F. & Ferreira, M. G. S. (2007). Electrochemical study of modified bis-[triethoxysilylpropyl] tetrasulfide silane films applied on the AZ31 Mg alloy. *Electrochimica Acta*, 52, 27, 7486-7495, 0013-4686.
- Mordike, B. L. & Ebert, T. (2001). Magnesium: Properties - applications - potential Materials. *Science and Engineering A*, 302, 1, 37-45, 0921-5093.
- Nordlien, J. H.; Ono, S.; Masuko, N. & Nisancioglu, K. (1997). A TEM investigation of naturally formed oxide films on pure magnesium. *Corrosion Science*, 39, 8, 1397-1414, 1757-1761.
- Ogawa, M. & Asai, S. (2000). Hydrothermal synthesis of layered double hydroxide-deoxycholate intercalation compounds. *Chemistry of Materials*, 12, 11, 3253-3255, 0897-4756.
- Phani, A. R.; Gammel, F. J. & Hack, T. (2006). Structural, mechanical and corrosion resistance properties of Al₂O₃-CeO₂ nanocomposites in silica matrix on Mg alloys by a sol-gel dip coating technique. *Surface and Coatings Technology*, 201, 6, 3299-3306, 0257-8972.
- Pourbaix, M. (1974). *Atlas of Electrochemical Equilibria in Aqueous Solutions*, p. 458, National Association of Corrosion Engineers, 65-11670, Huston, Texas, USA.
- Qian, B. & Shen, Z. (2005). Fabrication of superhydrophobic surfaces by dislocation-selective chemical etching on aluminum, copper, and zinc substrates. *Langmuir*, 21, 20, 9007-9009, 0743-7463.
- Qian, M. & Zeng, H. C. (1997). Synthesis and characterization of Mg-Co catalytic oxide materials for low-temperature N₂O decomposition. *Journal of Materials Chemistry*, 7, 3, 493-499, 0959-9428.
- Qu, M.; Zhang, B.; Song, S.; Chen, L.; Zhang, J. & Cao, X. (2007). Fabrication of superhydrophobic surfaces on engineering materials by a solution-immersion process. *Advanced Functional Materials*, 17, 4, 593-596, 1616-301X.

- Rives, V. & Ulibarri, M. A. (1999). Layered double hydroxides (LDH) intercalated with metal coordination compounds and oxometalates. *Coordination Chemistry Reviews*, 181, 1, 61-120, 0010-8545.
- Roach, P.; Shirtcliffe, N. J. & Newton, M. I. (2008). Progress in superhydrophobic surface development. *Soft Matter*, 4, 2, 224-240, 1744-683X.
- Schultze, J. W. & Lohrengel, M. M. (2000). Stability, reactivity and breakdown of passive films. Problems of recent and future research. *Electrochimica Acta*, 45, 15-16, 2499-2513, 0013-4686.
- Shi, F.; Wang, Z. & Zhang, X. (2005). Combining a layer-by-layer assembling technique with electrochemical deposition of gold aggregates to mimic the legs of water striders. *Advanced Materials*, 17, 8, 1005-1009, 0935-9648.
- Shirtcliffe, N. J.; McHale, G.; Newton, M. I. & Perry, C. C. (2003). Intrinsically superhydrophobic organosilica sol-gel foams. *Langmuir*, 19, 14, 5626-5631, 0743-7463.
- Shirtcliffe, N. J.; McHale, G.; Newton, M. I. & Perry, C. C. (2005). Wetting and wetting transitions on copper-based super-hydrophobic surfaces. *Langmuir*, 21, 3, 937-943, 0743-7463.
- Singh, A.; Steely, L. & Allcock, H. R. (2005). Poly[bis(2,2,2-trifluoroethoxy)phosphazene] Superhydrophobic Nanofibers. *Langmuir*, 21, 25, 11604-11607, 0743-7463.
- Song, G.; Atrens, A.; Stjohn, D.; Nairn, J. & Li, Y. (1997). The electrochemical corrosion of pure magnesium in 1 N NaCl. *Corrosion Science*, 39, 5, 855-875, 1757-1761.
- Song, G. -L. (2010). "Electroless" deposition of a pre-film of electrophoresis coating and its corrosion resistance on a Mg alloy. *Electrochimica Acta*, 55, 7, 2258-2268, 0013-4686.
- Tamar, Y. & Mandler, D. (2008). Corrosion inhibition of magnesium by combined zirconia silica sol-gel films. *Electrochimica Acta*, 53, 16, 5118-5127, 0013-4686.
- Thieme, M.; Frenzel, R.; Schmidt, S.; Simon, F.; Hennig, A.; Worch, H.; Lunkwitz, K. & Scharnweber, D. (2001). Generation of ultrahydrophobic properties of aluminium - A first step to self-cleaning transparently coated metal surfaces. *Advanced Engineering Materials*, 3, 9, 691-695, 1438-1656.
- Thieme, M. & Worch, H. (2006). Ultrahydrophobic aluminium surfaces: properties and EIS measurements of different oxidic and thin-film coated states. *Journal of Solid State Electrochemistry*, 10, 9, 737-745, 1432-8488.
- Wang, S.; Feng, L. & Jiang, L. (2006). One-step solution-immersion process for the fabrication of stable bionic superhydrophobic surfaces. *Advanced Materials*, 18, 6, 767-770, 0935-9648.
- Ha, W. & Kim, Y. -J. (2006). Effects of cover gases on melt protection of Mg alloys. *Journal of Alloys and Compounds*, 422, 1-2, 208-213, 0925-8388.
- Wu, X.; Ma, H.; Chen, S.; Xu, Z. & Sui, A. (1999). General equivalent circuits for faradaic electrode processes under electrochemical reaction control. *Journal of The Electrochemical Society*, 146, 5, 1847-1853, 0013-4651.
- Wu, Y.; Sugimura, H.; Inoue, Y. & Takai, O. (2002). Thin films with nanotextures for transparent and ultra water-repellent coatings produced from trimethylmethoxysilane by microwave plasma CVD. *Chemical Vapor Deposition*, 8, 2, 47-50, 0948-1907.

- Wu, Y.; Bekke, M.; Inoue, Y.; Sugimura, H.; Kitaguchi, H.; Liu, C. & Takai, O. (2004). Mechanical durability of ultra-water-repellent thin film by microwave plasma-enhanced CVD. *Thin Solid Films*, 457, 1, 122-127, 0040-6090.
- Xu, W.; Liu, H.; Lu, S.; Xi, J. & Wang, Y. (2008). Fabrication of superhydrophobic surfaces with hierarchical structure through a solution-immersion process on copper and galvanized iron substrates. *Langmuir*, 24, 19, 10895-10900, 0743-7463.
- Xu, Z. P. & Zeng, H. C. (1999). Interconversion of brucite-like and hydrotalcite-like phases in cobalt hydroxide compounds. *Chemistry of Materials*, 11, 1, 67-74, 0897-4756.
- Xu, Z. P. & Zeng, H. C. (2000). In-situ generation of maximum trivalent cobalt in synthesis of hydrotalcite-like compounds $Mg_xCo^{II}_{1-x-y}Co^{III}_y(OH)_2(NO_3)_y \cdot nH_2O$. *Chemistry of Materials*, 12, 9, 2597-2603, 0897-4756.
- Xu, Z. P. & Zeng, H. C. (2001). Abrupt structural transformation in hydrotalcite-like compounds $Mg_{1-x}Al_x(OH)_2(NO_3)_x \cdot nH_2O$ as a continuous function of nitrate anions. *The Journal of Physical Chemistry B*, 105, 9, 1743-1749, 1520-6106.
- Xu, Z. P. & Braterman, P. S. (2003). High affinity of dodecylbenzene sulfonate for layered double hydroxide and resulting morphological changes. *Journal of Materials Chemistry*, 13, 2, 268-273, 0959-9428.
- Yates, K. & West, R. H. (1983). Monochromatized Ag L α X-rays as a source for higher energy XPS. *Surface and Interface Analysis*, 5, 4, 133-138, 0142-2421.
- Yong, Z.; Zhu, J.; Qiu, C. & Liu, Y. (2008). Molybdate/phosphate composite conversion coating on magnesium alloy surface for corrosion protection. *Applied Surface Science*, 255, 5, 1672-1680, 0169-4332.
- Zhang, X.; Shi, F.; Yu, X.; Liu, H.; Fu, Y.; Wang, Z.; Jiang, L. & Li, X. (2004). Polyelectrolyte multilayer as matrix for electrochemical deposition of gold clusters: toward superhydrophobic surface. *Journal of the American Chemical Society*, 126, 10, 3064-3065, 0002-7863.
- Zhu, W. Q.; Feng, X. J.; Feng, L. & Jiang, L. (2006). UV-manipulated wettability between superhydrophobicity and superhydrophilicity on a transparent and conductive SnO₂ nanorod film. *Chemical Communications*, 2006, 26, 2753-2755, 1359-7345.

Application of Positron Annihilation Spectroscopy to Studies of Subsurface Zones Induced by Wear in Magnesium and its Alloy AZ31

Jerzy Dryzek¹ and Ewa Dryzek²

¹*Institute of Physics, Opole University, ul. Oleska 48, 45-052 Opole*

²*Institute of Nuclear Physics PAN, ul. Radzikowskiego 152, 31-347 Kraków
Poland*

1. Introduction

Interaction of sliding bodies is an important aspect of numerous applications and subject of many studies (Solecki, 1989). Generally, when two surfaces are loaded together the true contact area is much smaller than the apparent one. The true contact is only at high points or asperities of the surfaces where the interactions in the atomic scale take place. Relative movement between the surfaces leads to friction and wear processes. The rate of wear is controlled by the load, the relative velocity and the behaviour of the material near asperities. The region of asperities can be plastically deformed and the stress is transported to the deeper laying region that becomes elastically deformed (Fig. 1).

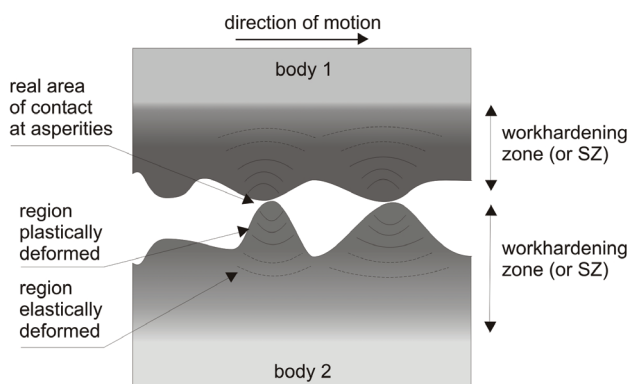


Fig. 1. Schematic diagram of the contact of two metal surfaces. The SZ is denoted as a dark grey area.

A composition and physical properties of the subsurface zones are substantially modified in comparison to those of the bulk (Wert, 1989), (Rice et al., 1989). The outermost zone contains original specimen material but also chemical species from the counterface and from the

environment, e.g. adsorbed polar particles, water, gases and oxides. Usually, it appears homogeneous and has very fine structure. Its boundaries may be confirmed by elemental analysis. In case of metals this zone is from 10 nm to 20 nm thick. Underneath, there lays the zone consisting entirely of the original specimen material but it is heavily plastically deformed. The zone acquired new structure and properties due to the repetitive tribocontact, e.g., it may become usually harder than the original material. Usually, there are the reorientation and disintegration of crystallites in it. The next zone represents the original specimen material in an undisturbed state. This zone experiences elastic deformation. However, its structure and properties are identical to those prior to the tribotest. It is accepted to call the region below the worn surface the subsurface zone (SZ), which was induced by the friction process. It seems that this zone reflects all the processes which occur at the worn surface and can be a key to the understanding of the wear process. The SZ can be studied by different methods. The residual stress depth distribution or the microhardness profiles are the common engineering methods. For detail studies the electron microscopy techniques or XRD techniques are applied. The positron annihilation spectroscopy is also used for studies of the SZ. It offers a possibility of detecting and distinguishing between open-structure crystal defects such as dislocations, vacancies, and voids in metals. All they are induced by any deformation of the material.

2. Brief review of positron techniques

The positron is an antiparticle of the electron; their interaction may cause the transformation of their mass into the electromagnetic radiation called annihilation rays. The main process (99.8% probability) is emission of two photons. Their detection is the base of the positron annihilation spectroscopy. The sources of positrons are mainly isotopes emitting positrons via β^+ decay, ^{22}Na and ^{68}Ge \ ^{68}Ga are commonly used in the solid state studies. Positrons emitted in β^+ decay have a continuous energy spectrum what means that its energy can be in a range limited by a maximum energy characteristic for the isotope. Positrons from the radioactive source cannot be implanted into a solid at a strictly defined depth. Typical implantation ranges characterized by linear-absorption coefficient are of the order of a few tenths of millimeter and depend on the density of the solid and the atomic number (Dryzek, Singleton, 2006). (The reciprocal of the so called linear-absorption coefficient for magnesium is equal to 144 μm for positrons emitted from ^{22}Na , and this quantity can be treated as the implantation range.) Hence, the positron as a probe penetrates certain, relatively large volume in the atomic scale. It should be noted that the positron beam technique allowing to implant positrons of low energy into a defined depth at the range of micrometers are in use (Krause-Rehberg & Leipner, 1999).

As a charged particle, a positron injected into a solid interacts inelastically and elastically with other charged objects, i.e., electrons and nuclei, and loses rapidly its kinetic energy until it becomes thermalized. Being in a thermodynamic equilibrium with the host, the positron is scattered by phonons and walks randomly. The random walk lasts much longer than the thermalization process, i.e. between 100 ps and 500 ps. It is sufficient for a positron to penetrate the volume occupied by ca. 10^7 atoms, mainly interstitial regions in the host lattice, before it annihilates with the emission of two almost collinear photons in opposite directions with of energy about 511 keV, Fig. 2. The positive charge of the positron causes that it annihilates mainly with the valence or conduction electron. The probability of the annihilation with the core electrons is much lower.

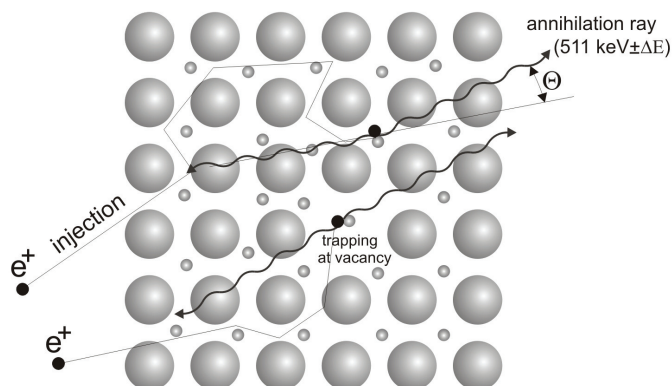


Fig. 2. The positron paths in a metal crystal lattice. Positron moves across interstitial regions between the ions or atoms (big grey spheres) and finally finds an electron (small grey spheres). In some cases it can be trapped at a vacancy or other open volume defect of crystalline lattice. ($\Delta E = p_z c / 2$, $\Theta = p_{x,y} / (m_0 c)$, where $p_{x,y,z}$ are the components of the electron momentum, m_0 is the electron rest mass and c is the speed of light.)

The positron during its diffusion can be trapped in regions of lower than average electron density like vacancies, vacancy agglomerates, dislocations, microvoids or small pores if they exist. They are defects of the crystalline lattice. The localization in such regions is due to the repulsion between the positron and the positive atomic cores. It is easy to distinguish where the annihilation takes place. Electrons in the interstitial regions have higher momentum than those in the vacancy-type defects, thus the total momentum of the emitted photons tags these annihilation places. Due to the thermalization the momentum of the positron can be neglected but the electron momentum cannot. The measurement of the deviation from the co-linearity of the two photons, the angle θ in Fig.2, is the simplest way to deduce the total momentum of the annihilating pair, it means the electron. Another method is the measurement of the Doppler broadening of the annihilation line which is also sensitive to the momentum of the annihilating electron. The vacancy-type defect, which traps positrons, contains fewer electrons than the interstitial regions; it causes the significant change in the annihilation rate. In other words, the annihilation in the lower-electron density region induces the increases of the positron lifetime. Indeed, the positron lifetime, i.e. the time interval between the "birth" of a positron and its annihilation, is larger for positrons localized in defects than in the interstitial. As it was stated above the time of implantation is much smaller than the time of random walk. The theoretical calculations supported by numerous of experimental results show additionally that the average lifetime of positrons localized in small vacancy clusters is very sensitive to their size. Hence, the identification of the kind of the trap: single vacancy or a multiple vacancy is possible. In magnesium, the mean bulk lifetime of positrons is equal to 225 ps, while the lifetime of positrons trapped at vacancies in this metal is 253 ps. For the measurement of the positron lifetime, the isotope ^{22}Na is usually used as a positron source. After emission of the positron, the gamma photon of energy 1275 keV is emitted from the excited state of the ^{22}Ne . This photon tags the "birth" of the positron and the emission of the annihilation ray tags its "death". The time between both events is simple to measure using a typical spectrometer and

it is equal to the positron lifetime in the implanted sample. The positron lifetime spectroscopy is a powerful tool for studies of condensed matter at atomic level (Brandt & Dupasquier, 1983).

3. Studies of the SZ by positron techniques

There are several advantages of this technique in comparison with the transmission electron microscopy. The positron as a probe can be implanted from external source into a sample which does not need any special treatment. The measurements are non-destructive using samples as they are. Only a pair of relatively flat samples treated in the same way is required to sandwich a positron source. The examples of the use of this technique for studies of vacancies, dislocations, fatigue damage, hydrogen trapping, and SZ do not exhaust the list of possible applications (Dupasquier & Mills, 2004). The disadvantage is the fact that positrons are mobile particles and scan relatively large volume of the sample before annihilation. For that reason positron annihilation can be used for studies of the whole SZ.

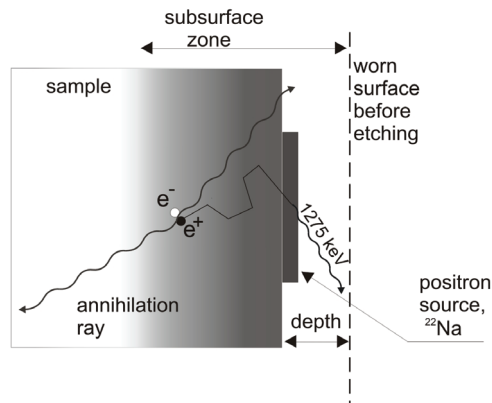


Fig. 3. A positron path in the sample. The positron is emitted from the ^{22}Na isotope which is located on the surface. The depth marked in the figure, represents the thickness of the layer etched from the worn surface. (In the typical experiment the identical sample is located also on the right side of the positron source. It is not shown in the figure for simplicity.)

It is known that after dry sliding of a ductile sample against a harder counterpart the plastically deformed layers occur below the surface. According to some models and a transmission electron microscopic studies that layers contain mainly dislocations and dislocation cells (Hirth & Rigney, 1976). Motion of dislocations induced by plastic deformation accompanying sliding contact generates large amount of point defects. Thus, dislocations can be associated with the point defects, like vacancies or interstitial atoms (Hull, 1975). Vacancies, due to their mobility at room temperature or temperature induced by sliding treatments, can join together and form vacancy clusters. The dislocation network can be studied directly by TEM. In general, detection of vacancies and small vacancy clusters using this method is more challenging task. Similarly, the microhardness profile measured in the SZ gives information on work hardening connected to a large extent with increase of dislocation density. As was mentioned above positrons are very sensitive and unique probes for point defects such as vacancies and vacancy clusters, and also dislocations. (It should be mentioned that interstitial atoms are not detected by positron techniques.) Additionally, detection of the depth profile of

the defect concentration and hence the detection of the SZ induced by the surface treatment may be performed. A great amount of point defects like vacancies associated with dislocations (in aluminum) (Dryzek & Dryzek, 2004) or vacancy clusters (in copper) (Dryzek & Polak, 1999) was found below the worn surface using this method. Their concentration decreased with depth and reached the bulk value at a depth of hundreds of micrometers. The limited implantation range of positrons from ^{22}Na gives the opportunity to determine the total range of the crystal lattice changes induced by friction and wear. In order to do it, the technique based on the sequenced etching of the layers from the worn surface and measurements for instance the positron lifetime was proposed, Fig. 3 (Dryzek et al., 1997). It allows us to scan the depth of the sample from the worn surface. That technique is very efficient, because due to the great sensitivity of the positrons to the open volume defects it allows us to detect the total range of the SZ even the regions where only elastic deformation took place. The relatively simple experimental procedures and high sensitivity exceed the electron microscopy techniques, XRD and another engineering technique, i.e., microhardness measurements.

As it was mentioned already the thermalized positrons penetrate the large volume of the sample. Additionally, the implantation profile of energetic positrons exhibits the exponential decay with the maximal value at the surface (Dryzek & Singleton, 2006). In case of magnesium the depth of implantation range of the positrons emitted from the ^{22}Na isotope is about 144 μm , it means that about 63% of the positrons are located in the layer of such a thickness. From that reason it is difficult to define the exact current depth where the positrons are implanted. In our measurement procedures we trace the dependencies of the positron lifetime as the function of the etched layer thickness, called "depth", Fig. 3.

4. Studies of the SZ in pure magnesium

The success of the positron annihilation techniques in studies of the SZ in pure copper and aluminium encourages us to extend their application for studies of the SZ generated during friction in pure magnesium and its selected alloy. It is commonly accepted that the microstructural parameters, the crystal structure, degree of chemical order, the grain boundaries, stacking faults and the precipitations influence the plastic deformation and fractures.

4.1 The SZ detected by conventional positron technique

Magnesium has a close-packed hexagonal crystalline structure, low strength and high damping due to the easy motion of dislocations at room temperature. As a hexagonal metal with $c/a > 1.633$ magnesium has only three independent slip systems which may occur on either non close packed planes or in non close-packed direction. The main deformation mode is a basal slip, i.e. a slip on the (0001) plane with a $(11\bar{2}0)$ Burgers vector. Because this vector lies in the basal plane, no plastic strain parallel to the c-axis is present. However, such a strain can be produced by twinning; the easiest and most common is $\{10\bar{1}2\}$ (Tenckhoff, 1968). Also, a prismatic slip $\{10\bar{1}0\}(11\bar{2}0)$ and a pyramidal slip $\{10\bar{1}1\}(11\bar{2}0)$ were observed, but their critical resolved shear stress at room temperature was one hundred-times greater than that for basal plane (Kelley & Hosford, 1968). This can be not sufficient to accommodate an arbitrary change in the shape as it is in the case of copper or aluminium which possess at least 12 independent slip systems.

Polycrystalline magnesium samples of purity 99.9 % were annealed at a temperature of 400 °C during 3 hr in the flow of N₂ gas. This ensures that initially the samples contain only residual defects which do not affect the positron characteristics. The measurement of the positron lifetime spectra for such virgin samples revealed only one lifetime component equal to 226±1 ps. As it was reported, this value corresponds to the bulk value for magnesium.

The surface of such a sample was sliding in a tribotester against a rotated disc made from the martensitic steel (steel SW18 hardness about 670 HV0.1) of diameter 50 mm with a certain load. The treatment was performed in air, no oxidation was observed. The velocity of the disc relative to the surface of the sample was equal to 5 cm/s. During this test we obtained the value of the friction coefficient equal to 0.24 and the specific wear rate, defined as worn volume per unit sliding distance per unit load, equal to $(8.0\pm 0.8)\times 10^{-13}$ m³/N m.

The measurements of the positron lifetime spectra in the sequenced procedure reveal only one lifetime component. This was a surprise, because usually in deformed metals or alloys, due to the existence of several kinds of defects, two or three components are observed. The values of the positron lifetime ranged from about 248 ps to the bulk value equal to 226 ps. The former value is slightly lower than the value of the lifetime for the positron trapped in the single vacancy in magnesium host, i.e. 253 ps (Schaefer, 1987). Thus the detected values did not originate from this defect. We can argue that this is due to dislocations decorated by vacancies, or jogs. Such defects located near a dislocation are deformed due to a stress field, and the positron lifetime becomes lower than that in the single vacancy. It can be concluded by analogy to other metals, i.e., aluminium (Häkkinen et al., 1989), nickel and iron (Onitsuka et al., 2001) and zinc (Campillo et al., 2000) because no theoretical data reported yet. The net dislocation line is a weak trap for positrons, but it is accompanied by jogs, vacancies or interstitial atoms produced during its motion caused by plastic deformation. The positrons annihilating in all of those defects and in the bulk contribute to the lifetime spectrum but due to the finite time resolution of the spectrometer one can resolve only the average value. Thus, the positron lifetime obtained from the deconvolution procedure may be treated as the mean lifetime.

Fig. 4 presents the dependency of the measured positron lifetime depth profile for four values of the applied load during the sliding treatment of the magnesium samples. The samples were exposed to the friction treatment at the distance of 9 m in all cases. A common feature of the dependencies is a gradual decrease of the positron lifetime with depth down to the bulk value at a certain depth. It tags the total range of the SZ, which depends on the applied load. For the lower value of the load, 25 N, it is about 150 µm, and for the highest, 150 N, it is 440 µm (see Table 1). As in our former studies concerning the SZ in pure aluminium the experimental dependencies can be well described by a simple exponential decay function (Dryzek & Dryzek 2004),

$$\tau(z) = \tau_0 + a \exp(-z / d_0), \quad (1)$$

where z is the depth or the thickness of the material etched away τ_0 , a and d_0 are the fitted parameters. The solid line in Fig.4 presents the best fit of relation (1) to the experimental points obtained for the highest applied load of 150 N. The fitted parameters obtained for all samples are gathered in Table 1. The parameter d_0 characterizes the SZ. It is worth noticing that its value increases when the load increases (Table 1).

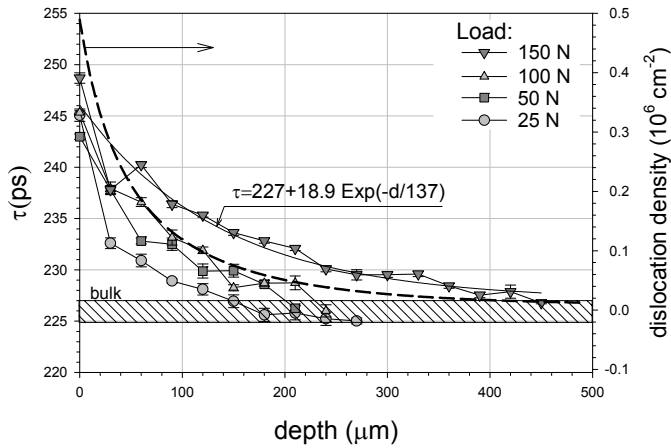


Fig. 4. Depth profile of the positron lifetime measured for pure magnesium samples after sliding against a rotated martensitic steel disc during 3 min (sliding distance 9 m) with different applied loads. The solid line presents the best fit of relation (1) to the experimental points obtained for the load of 150 N. The dashed line corresponds to the estimated dislocation density depth profile (load 150 N) obtained from relation (2) taking into account relation (1). The shaded region represents the bulk positron lifetime in pure magnesium (Dryzek et al., 2005).

Surface Treatment		τ_0 (ps)	a (ps)	d_0 (μm)	Total range of the SZ (μm)
Load (N)	Sliding distance (m)				
25	9	225.9±0.6	18.5±1.3	40±6	150±30
50	9	226.2±1.5	16.6±1.5	82±20	200±30
100	9	225.3±1.7	19.4±1.7	98±23	240±30
150	9	227.0±1.8	19.0±1.4	137±28	440±30
25	45	230.1±1.0	18.4±1.3	50.8±9.0	>270 ±30

Table 1. Values of the parameters from relation (1) fitted to the experimental points presented in Figs 4 and 5 obtained for well annealed magnesium samples after dry sliding against martensitic steel; the sliding conditions are stated in the first column.

If we treat the measured positron lifetime as the mean positron lifetime and assume that dislocations are the traps localizing positrons, dislocation density can be estimated. According to the trapping model, the mean positron lifetime is related to the dislocation density, ρ_d , as follows:

$$\bar{\tau} = \tau_{bulk} \frac{1 + \tau_{sat} \nu \rho_d / b}{1 + \tau_{bulk} \nu \rho_d / b}, \tag{2}$$

where $\tau_{bulk}=226$ ps and τ_{sat} is the lifetime for a dislocation saturated sample; in our case we assume it is equal to 248 ps. Further, b is the Burgers vector and ν is the trapping efficiency;

in the case of a dislocation in magnesium it is equal to $3.23 \times 10^{-6} \text{ s}^{-1} \text{ cm}^3$ (Mehta et al., 2004). Putting relation (1) into relation (2) as the mean positron lifetime, we can estimate the dislocation density profile. In Fig. 4 the dashed line follows such a profile for a sample exposed to sliding with a load of 150 N. It indicates a strong gradient of the dislocation concentration in the SZ. This gradient slightly decreases with the increase of the sliding distance but the value of the positron lifetime at the worn surface does not change, as it is visible in Fig. 5. In this figure the positron lifetime profiles obtained for two samples exposed to the sliding treatment with the same load of 100 N but for different sliding distances are depicted.

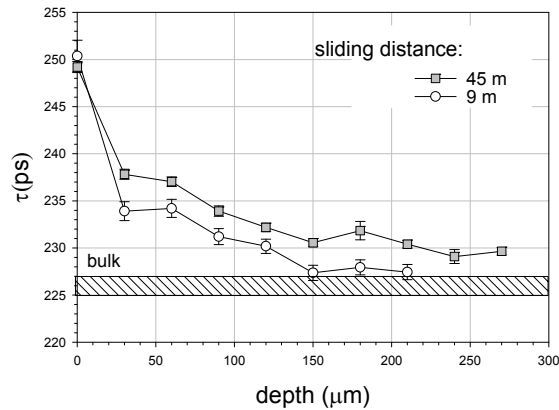


Fig. 5. Depth profile of the positron lifetime measured for the pure magnesium samples exposed to the dry sliding against a martensitic steel disc with a load of 25 N at the sliding distances 9 m and 45 m, respectively. The shaded region represents the bulk positron lifetime in pure magnesium (Dryzek et al., 2005)

4.2 Microhardness profile in the SZ

The microhardness profiles measured using the commercially available Micro-Combi-Tester (CSEM) for the samples after sliding with different loads exhibit different shapes. In this measurement the Vickers indenter with the maximum load of 20 mN was applied. The velocity of the load increase was equal to 40 mN/min. The profile is depicted in the Fig. 6 for two selected samples. It is interesting to notice that the microhardness initially increases with the depth from the worn surface and at a certain depth reaches the maximum and then decays to the bulk value. The total depth of the microhardness profile is about 120 μm, which is lower than that detected by the positron technique (see Table 1). We have also observed a similar fact for the aluminium alloys (Dryzek & Dryzek, 2006). The discrepancy between the microhardness profile and positron lifetime profile can be explained by the fact that only positron technique is sensitive to point defects created in a great amount during plastic deformation while the microhardness is not.

4.3 The SZ in pure magnesium detected by slow positron beam

The conventional techniques where positrons are emitted from the radioactive source, i.e. ^{22}Na are not suitable to detect the region close to the worn surface. The convenient tool for this purpose is the positron beam technique where monoenergetic positrons forming a beam

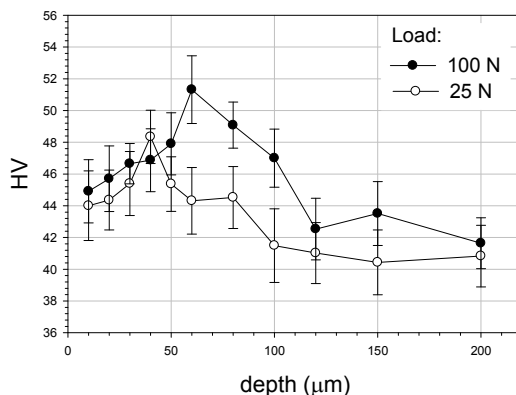


Fig. 6. Depth profiles of the microhardness measured for pure magnesium samples after dry sliding against a rotated martensitic steel disc during 3 min (sliding distance 9 m) with different applied loads (Dryzek et al., 2005)

are implanted in the sample at a desired depth. In our experiment the positron energy was ranged from 0.1 keV to 25 keV. This allows us to scan a magnesium sample to the depth up to 4 μm from the top surface, which previously was exposed to dry sliding. In this case the so called S-parameter was measured as the function of positron energy instead of positron lifetime. The so-called S-parameter defined as the ratio of the area under the fixed center part of the annihilation line to the area under the whole annihilation line is a suitable line shape parameter that characterizes the annihilation line broadening. If the annihilation with electrons having lower momentum increases, the value of the S-parameter also increases. This takes place when positrons annihilate from the localized state, e.g. trapped in vacancies or vacancy clusters where the electron density is lower in comparison to the interstitial region. Similarly to the positron lifetime, the value of the S-parameter can tag the change in the vacancy or vacancy cluster concentration.

Fig. 7 presents the obtained dependence for the well annealed reference sample and samples whose surfaces were exposed to dry sliding. The value of the S-parameter on the surface is significantly lower than in bulk at the depth of 4 μm . This indicates that on the surface there is present a layer different from the bulk, i.e. the magnesium oxide layer. The change in the slope of the dependencies at the depth of c.a. 100 nm indicates that this is the thickness of the magnesium oxide layer. Using the VEPFIT (Veen et al., 1990) program, we were able to describe the experimental data for the well annealed sample assuming existence of two regions, the first at the surface and second inside. The thickness of the outer layer evaluated from the fit was equal to 107 ± 1 nm and the positron diffusion length was equal to 70 ± 1 nm. This value in the interior equals to 780 ± 150 nm which seems to be extremely large in comparison to other materials. The latter would correspond to the positron diffusion in the polycrystalline bulk magnesium. For the sample whose surface was exposed to sliding with the highest load of 100 N the outer layer thickness increased to 150 ± 10 nm. This is connected with the fact that during sliding the mixed layer containing the magnesium oxide is created on the surface. Its thickness increases with increase of the applied load. The increase of the sliding time does not affect the thickness of the mixed layer as it can be seen in Fig. 8. The etching of the samples in the in a 5% water solution of acetic acid reduced the thickness of the oxide layer but did not remove it.

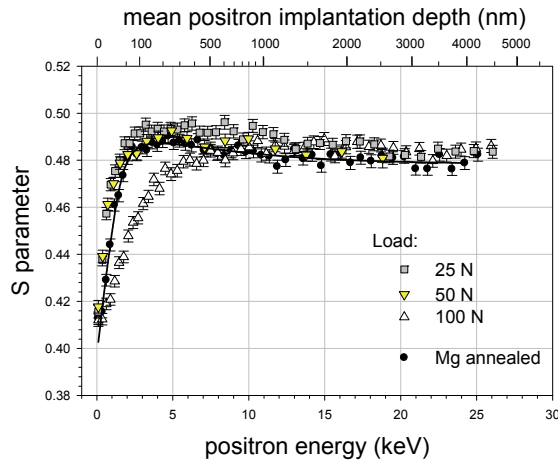


Fig. 7. The S-parameter vs. positron beam energy for the reference sample and samples after dry sliding with different loads for the sliding distance of 9 m. The solid line represents the theoretical dependence obtained using VEPFIT program for the well annealed magnesium sample (Dryzek et al., 2007).

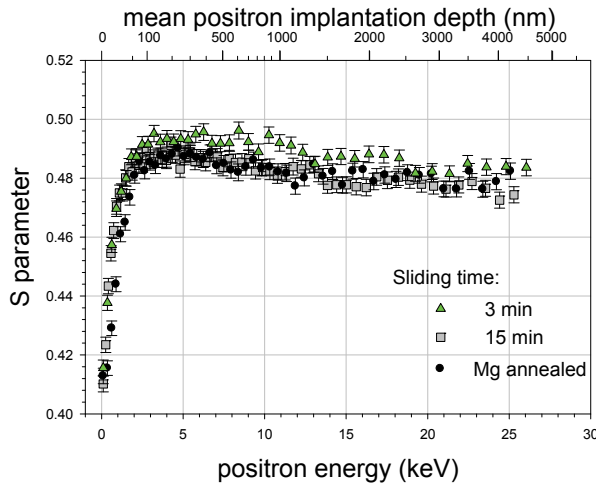


Fig. 8. The S-parameter vs. positron beam energy for reference sample and samples after dry sliding for different sliding times corresponding to sliding distances 9 m and 45 m for the load of 25 N (Dryzek et al., 2007).

Concluding, it can be stated that on and under the worn surface in pure magnesium after dry sliding mainly dislocations with accompanying defects, like vacancies and jogs, are created. Their concentration decays exponentially with increase of depth. The total range of the SZ is more than one hundred micrometers and depends on the applied load and sliding distance. Thus the type of the crystal structure and lack of the well developed slip systems

has minor effect on the total range of the SZ in magnesium. The mixed layer containing the magnesium oxide created on the worn surface has the thickness of about 150 nm.

5. The SZ in magnesium alloy AZ31

In technical applications the pure magnesium is not in use then we performed similar studies for magnesium-based alloy Mg₉₆Al₃Zn₁ (Goodfellow), temper as drawn, analogous to the commercial AZ31 alloy. The Mg-Al-Zn alloy system is well known. The addition of Al, Zn or both these elements results in increase in the strength and decrease in the ductility of the magnesium alloy. Al and Zn both act as solid solution strengtheners. Both alloying elements form precipitates with Mg in alloy matrix, e.g. Mg₁₇Al₁₂ discontinuous intermetallic phase (Bowles et al., 2007). However, XRD measurements did not reveal the existence of such a phase in our sample.

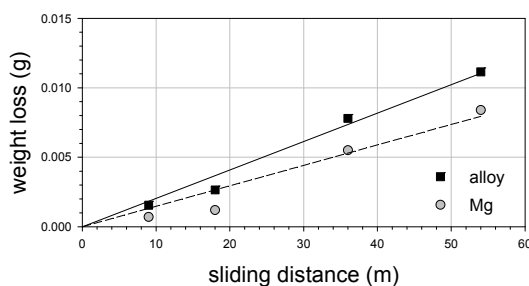


Fig. 9. Weight loss of the magnesium alloy and pure magnesium pins as functions of sliding distance against the rotated steel disk at the velocity of 5 cm/s and the applied load of 100 N (Dryzek & Dryzek 2007).

We compared the specific wear rates calculated from the weight loss measured for different sliding distances for the alloy and pure magnesium (99.9% purity) in Fig. 9. The specific wear rate for the alloy is equal to $(1.11 \pm 0.10) \times 10^{-12} \text{ m}^3/\text{Nm}$ and is about 40% higher than for pure magnesium. The measured values of the friction coefficient of the alloy and magnesium against the steel disc, equal to 0.20 and 0.24, respectively, are comparable.

The measurement of the positron lifetime spectrum for the virgin, reference sample of the alloy reveals only one lifetime component equal to 226 ± 1 ps. This value is the same as the value of positron lifetime in bulk in pure magnesium and will be treated as the bulk lifetime in the alloy. After dry sliding, similarly to pure magnesium in all measured lifetime spectra only one lifetime component was resolved. Its value ranged from the bulk value, equal to 226 ± 1 ps, to about 240 ps. Nevertheless, on closer inspection a second, long-lived component equal c.a. 1450 ps was found but its intensity was close to 1 %.

The sequenced measurement of the positron lifetime spectrum after etching away a certain thickness of the alloy samples after sliding at the same distance of 36 m with different loads applied: 50 N, 100 N and 150 N reveals well defined depth profiles. In Fig. 10, the value of the main lifetime component and the intensity of the long-lived component are depicted as functions of depth. The striking feature of the results obtained is the short range of the SZ, which is additionally hardly affected by the applied load. The total range is about 100 μm and it is much lower than in pure magnesium. (For comparison the depth profile of the positron lifetime measured for pure magnesium after sliding in similar conditions is

presented in this figure as well.) As above the equation (1) describes well the decay of the positron lifetime as the function of depth.

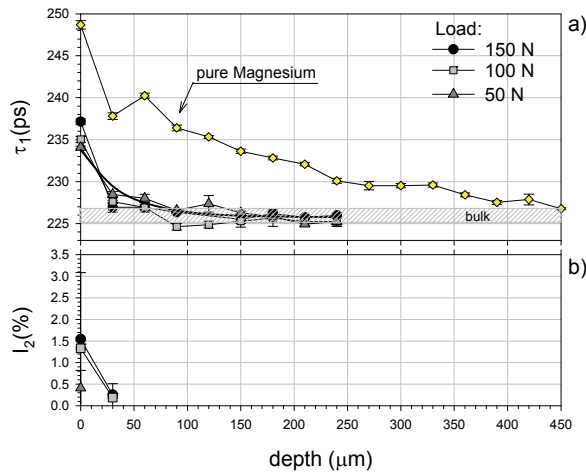


Fig. 10. The main positron lifetime a) and the intensity of the long-lived component b) as functions of depth or etched layer thickness measured for the alloy samples after sliding at the same distance of 36 m with different loads applied: 50 N, 100 N and 150 N. For comparison, the value of the main positron lifetime component for the pure magnesium sample which was exposed to sliding with the normal load of 150 N at a sliding distance of 9 m is also presented a). The solid line represents the best fit of equation (1) to the experimental points measured for the alloy sample exposed to sliding with the normal load of 100 N. The reference bulk positron lifetime in the alloy is also indicated (hatched area) (Dryzek & Dryzek 2007).

It is interesting that in opposition to the results for pure magnesium the d_0 parameter decreases with the increase of the applied load – for the load of 50 N it is equal to 38.0 ± 1 μm for the load of 100 N it is equal to 23.0 ± 4 μm and for 150 N it is equal to 12.6 ± 3 μm. The solid line in Fig. 10 a represents an example of the best fit of the equation (1) to the experimental points. The intensity of the long-lived component, Fig. 10 b, decays quickly and at the depth of about 30 μm disappears.

In Fig. 11 a, we depicted the profiles of the main lifetime component for the alloy samples after sliding with the same load of 100 N for three different sliding distances. The exponential decay of the τ_1 value with depth is clearly visible and the total depth of the SZ is about 50 μm. The d_0 parameter in all cases is about 15 ± 2 μm and does not depend on sliding distance within the accuracy of the measurement. In Fig. 11 b, the decay of the intensity of the long-lived component is clearly visible and at the depth of about 30 μm it also disappears.

The Vickers microhardness profile was measured for two selected samples whose surfaces were exposed to sliding. The obtained results are depicted in Fig. 12. The microhardness value decreases quickly with depth and the dependency can be described by an exponential decay function, similar to that given by equation (1). The best fit is presented as the solid line in Fig. 12. The value of the parameter d_0 was equal to 26.2 ± 7 μm for the sample exposed

to sliding with the applied load of 100 N and the sliding distance of 54 m and 16.2±2 μm for another sample with the applied load of 50 N and the sliding distance of 18 m. These values correspond well with those obtained from the positron lifetime measurement (Fig. 10a, 11a) and they confirm the short range of the SZ created in the alloy.

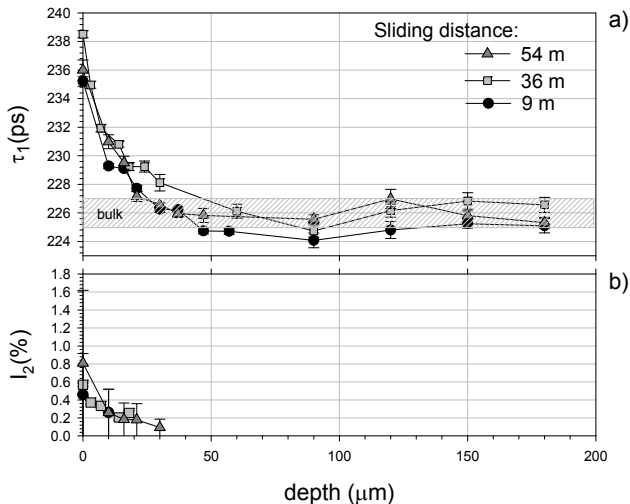


Fig. 11. The main positron lifetime a) and the intensity of the long-lived component b) as functions of depth or etched layer thickness measured for the alloy sample after sliding at different distances with the normal load of 100 N. The reference bulk positron lifetime in the alloy is also indicated (hatched area) (Dryzek & Dryzek 2007).

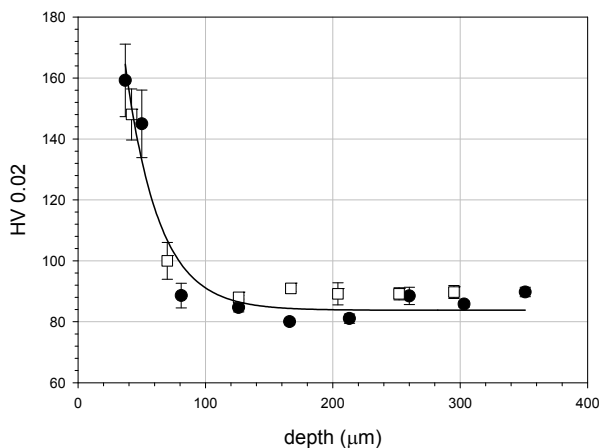


Fig. 12. The Vickers microhardness profile for the alloy samples after sliding at the distance of 18 m with the normal load of 50 N (open square) and at the distance of 54 m with normal load of 100 N (filled circles). The solid line (a) is the best fit of the exponential function $HV=89.4+779exp(-d[\mu m]/16.2)$ to the open square points (Dryzek & Dryzek 2007).

The short range of the SZ in the alloy in comparison to the pure magnesium indicates the great role of alloying in the process of its creation. Adding other atoms into this structure we can effectively obstruct the slip system, thus a depth expansion of deformation induced on the worn surface is hindered. A similar phenomenon was observed in aluminium alloys for which the range of the SZ was shortened in comparison to pure aluminium (Dryzek & Dryzek, 2004). This supports the role of dislocations in forming of the SZ which originated on or just below the worn surface and can move into the interior of the damaged sample. Adding atoms, precipitates or other structural elements which inhibit movement of dislocations in the alloy host influences also the depth expansion of the SZ. As we have found, the total range of the SZ reflects the range of the plastic deformation. It is worth noticing that the range of the SZ correlates inversely with the wear rate. Above we marked that for the alloy the wear rate is higher than for pure magnesium. Similar correlations were observed also for aluminium alloys. During sliding energy dissipates causing creation of structural defects, vacancies, dislocations and others. The short range of the SZ implies that this energy is deposited in a narrow region near the surface. Thus one could expect more defects there than would be in a wider range. If structural defects are responsible for wear thus more defects should imply higher wear rate. Our experimental observations are focused rather on the microscopic origin of the wear induced by crystalline defects. Nevertheless, their distribution and total depth of plastic deformation underneath the worn surface is the macroscopic parameter, which is omitted in other wear models.

The detection of the lifetime component equal to c.a. 1450 ± 100 ps in the measured spectra is a surprise. Such a weak long-lived component between 1000 and 5000 ps was reported in nanocrystalline metals like iron, nickel and was attributed to the formation of ortho-positronium at the surface of voids. Positronium is the positron-electron bound state similar to hydrogen and can be created for instance in molecular solids, where the empty volume allows to create it. The minimal radius of such a volume which is suitable for creation of such a bound state is about 0.19 nm. We believe that voids of radius bigger than this can be located in the SZ at the depth less than 30 μm . More detail calculation allows us to estimate their radius 0.23 ± 0.01 nm. It is quite possible that the voids can be produced on special dislocation arrangements created during plastic deformation at large strains. They could nucleate cracks. It is not excluded that presence of oxide in the surface layer favors formation of positronium.

Concluding the result obtained for alloy AZ31 we can state that the total range of the SZ detected is about 100 μm and it is much lower than that detected for the pure magnesium which was between 150 μm and 440 μm . This can affect the wear process on the surface. The specific wear rate for this alloy has a higher value than for pure magnesium. Thus the alloying of magnesium has the significant role for the SZ constitution.

6. References

- Bowles, A.L.; Bakke P.; Westegen H. (2007). A New Look at the Al-Mg-Zn Family – Focus on Tailoring Properties Through Compositional Control, *Magnesium, Proceedings of 7th Conference on Magnesium Alloys and Their Applications*, pp. 93-99, ISBN 978-3-527-31764-6, Dresden, VILEY-VCH, Weinheim

- Brandt W., Dupasquier A. (eds.) (1983). *Positron Solid-State Physics*, Proceedings of the International School of Physics "Enrico Fermi", North-Holland Publishing Company, ISBN 0-444-86521-7, Amsterdam, New York, Oxford
- Campillo J.M., Plazaola F., de Diego N., (2000). Positron Lifetime Calculations for Defects in Zn. *Journal of Physics: Condensed Matter*, Vol. 12, No. 46, 9715-9723, ISSN 0953-8984
- Dryzek J., Dryzek E., Stegemann T., Cleff B., (1997). Positron Annihilation Studies of Subsurface Zones in Copper. *Tribology Letters*, Vol. 3, No. 3, 269-275, ISSN 1023-8883
- Dryzek J; Polak A. (1999). Subsurface Zone Studied by Positron Lifetime Measurements. *Tribology Letters*, Vol. 7, No. 1, July 1999, 57-60, ISSN 1023-8883
- Dryzek J., Dryzek E., (2004). Subsurface Zone in Aluminium Studied by Positron Lifetime Spectroscopy. *Tribology Letters*, Vol. 17, No. 2, 147-153, ISSN 1023-8883
- Dryzek J., Dryzek E., Suzuki T., Yu R. (2005) Subsurface Zone in Pure Magnesium Studied by Positron Lifetime Spectroscopy. *Tribology Letters*, Vol. 20, No. 1, 91- 97, ISSN 1023-8883
- Dryzek J., Singleton. D. (2006). Implantation Profile and Linear Absorption Coefficients for Positrons Injected in Solids from Radioactive Sources ^{22}Na and $^{68}\text{Ge}/^{68}\text{Ga}$. *Nuclear Instruments and Methods in Physics Research Section B*, Vol. 252, No. 2, 197-204, ISSN 0168-583X
- Dryzek J.; Dryzek E., (2006). The Detection of Subsurface Zones in Aluminium Based Alloys 2017A and 6101A Using a Positron Annihilation Technique Lifetime Spectroscopy. *Tribology International*, Vol. 39, No. 7, 669-677, ISSN 0301-679X
- Dryzek J.; Dryzek E., (2007). The Subsurface Zone in Magnesium Alloy Studied by the Positron Annihilation Techniques, *Tribology International*, Vol. 40, No. 9, 1360-1368, ISSN 0301-679X
- Dryzek J.; Schut H.; Dryzek E., (2007). Subsurface Zones in Magnesium Detected by Variable Energy Positron Beam. *Physica Status Solidi (c)* Vol. 4, No. 10, 3522-3525, ISSN 1610-1642
- Dupasquier A.; Mills A. P. jr. (eds.) (1993). *Positron Spectroscopy of Solids*, Proceedings of the International School of Physics "Enrico Fermi", IOS Press, ISBN 90-5199-203-3, Amsterdam, Oxford, Tokyo, Washington DC
- Hirth J.P.; Rigney D.A. (1976). Crystal Plasticity and the Delamination Theory of Wear, *Wear*, Vol. 39, No. 1, 133-141, ISSN 0043-1648
- Hull D. (1975). *Introduction to Dislocation*, Pergamon Press, ISBN 0-08-018129-5 Oxford
- Häkkinen H.; Mäkinen S.; Manninen M. (1989). Positron States in Dislocations: Shallow and Deep Traps. *Europhysics Letters*, Vol. 9, No. 8, 809-814, ISSN 0295-5075
- Kelley E.W.; Hosford W.F. (1968). Plain Strain Compression of Magnesium and Magnesium Alloy Crystals. *Transactions of the Metallurgical Society of AIME*, Vol. 242, No. 1, 5-13, ISSN 0543-5722
- Krause-Rehberg R.; Leipner H.S. (1999). *Positron Annihilation in Semiconductors*, Springer-Verlag, ISBN 3-540-64370-0, Berlin, Heidelberg, New York
- Mehta D.S.; Masood S.H.; Song W.Q. (2004). Investigation of Wear Properties of Magnesium and Aluminium Alloys for Automotive Application. *Journal of Materials Processing Technology*, vol. 155-156, 30 November 2004, 1526-1531, ISSN 0924-0136

- Onitsuka T.; Ohmura M.; Takenaka M.; Kuramoto E. (2001). Positron Lifetime Calculation for Interstitial Clusters in Fe and Ni. *Materials Science Forum*, Vol. 363-365, 163-166, ISSN 0255-5476
- Rice S.L.; Nowotny H.; Wayne S.F. (1989). A Survey of the Development of Subsurface Zones in the Wear of Materials. *Key Engineering Materials*. Vol. 33, 77-100, ISSN1013-9826
- Schaefer H.-E. (1987), Investigation of Thermal Equilibrium Vacancies in Metals by Positron Annihilation. *Physica Status Solidi (a)*. Vol. 102, No. 1, , 47-65, ISSN 0031-8965
- Solecki R. (editor) (1989). The Role of Subsurface Zones in the Wear of Materials. *Key. Eng. Mater.* Vol. 33, ISSN:1013-9826.
- Tenckhoff E. (1988), *Deformation Mechanisms, Texture and Anisotropy in Zirconium and Zircaloy*, Special Technical Publication STP 966 ASTM, ISBN 0-8031-0958, Philadelphia
- Wert J.J. (1989). Role of Microstructure in Subsurface Damage Induced by Sliding Contact. *Key Engineering Materials*, Vol. 33, 101-134, ISSN1013-9826.
- Van Veen, A. Schut H., de Vries J., Hakvoort R.A. and Ijpma M.R. (1991). Analysis of Positron Profiling Data by Means of "Vepfit". *Positron Beam for Solids and Surfaces*, AIP Conf. Proc., Vol. 218, No. 1, eds. P.J. Schultz, G.R. Massoumi and P.J. Simpson, 171-198, ISSN: 0094-243X

DLC Coating on Magnesium Alloy Sheet by Low-Temperature Plasma for Better Formability

Yu IRIYAMA and Shoichiro YOSHIHARA
University of Yamanashi
Japan

1. Introduction

Magnesium (Mg) alloy has been attracting great attention as a promising light-metal material which has various potential applications because of its various unique and great properties. They are, for example, a smaller density, about two-thirds of Al, the greatest specific strength among all the metals, superior machining property, shielding of electromagnetic wave, and vibration absorbability. Taking advantage of them, Mg is expected to be used as structural components for automobile, lap-top computer, cell phone, and you name it, and it could replace aluminum in many areas. In general, the weight of any products with Mg body would be reduced which enables us to handle the products easier. More specifically, for example, Mg body could increase the gas mileage of automobile and protect computers and cell phones from unexpected vibration or electromagnetic waves.

In spite of the numerous advantages, however, Mg materials have not been used widely up to now. It is because there is a drawback to the workability in Mg. In the metal forming process, in general, press forming is popular, which increases the productivity and decreases the manufacturing cost and environmental load. However, since seizing of Mg in press forming is easily happened, forming of Mg is often processed by forging and die-casting. The formability of Mg alloys is especially poor at room temperature because of their hexagonal close-packed structure. Hence, there are few slip planes in the case of a pyramid surface or cylinder surface at room temperature. Furthermore, these slip planes are easily activated at elevated temperatures. Therefore, the deep-drawing process of Mg alloy sheets is generally conducted at high temperatures (approximately 200 °C). During the deep-drawing process, even at an elevated temperature, it is necessary to use a lubricant, such as molybdenum disulfide (MoS₂) based grease, which can maintain the performance. However, such lubricants have disadvantages such as a high cost, difficulty in degreasing and poor workability. Moreover, the large amount of lubricant waste raises has an adverse effect on the environment. Therefore, new techniques of lubrication that have less impact on the environment are immediately required.

In recent years, various studies on dry press forming, which does not involve the use of any lubricants during plastic processing, have been performed (Kataoka, 2006).

Dry press forming is also attractive as a forming technique with zero emissions. However, it is difficult to apply this method to the forming of metal sheets.

The feasibility of deep-drawing has been studied using ceramic dies (Kataoka et al., 2004). Ceramic dies have been successfully applied to the deep drawing of mild steel and pure copper sheets but not to the deep-drawing of titanium sheets. In the deep-drawing of metal alloy sheets, a pretreatment, in which an adhesive tribological coating is formed, is effective for improving workability when using alumina and zirconia dies. Adapting the design of the ceramic die to each material is indispensable for realizing dry forming. However, the workability of ceramic tools is poor for complicated shapes, which is limited to simple shapes. Thus, the use of electroconductive ceramic tools has been proposed (Tamaoki et al., 2006). Electroconductive ceramic tools can be formed by electrical discharge machining methods. Using an electroconductive ceramic as a plastic-forming tool, high drawability was confirmed and the dry deep-drawing of what was successfully performed up to 10,000 times.

We have also tried to increase formability of Mg alloy sheet, and obtained some good results by local heating-cooling technique (Yoshihara et al., 2003) and the control of blank holder force (Yoshihara et al., 2005) in deep-drawing process.

Diamond-like carbon (DLC) thin film could be a promising alternative to the wet lubricant. DLC is a general term of amorphous carbon or hydrocarbon, expressed as a-C or a-C:H, which is stable in chemically and physically and has a low friction coefficient. DLC is usually prepared by plasma CVD using hydrocarbon monomer gases such as methane. This dry process has been reevaluated as an environmentally friendly system in recent years since it exhausts little hazardous and toxic compounds and it does not require drying process, which can save energy and time. Similarly, DLC coating is not a new technique, but it has been regaining more expectation recently and many applications have been proposed. DLC coating on Mg is one of them, of which research have been reported on not only lubrication but also corrosion protection (Yamauchi et al., 2005; Konca et al., 2006; Yamauchi et al., 2007; Choi et al., 2007a; Choi et al., 2007b; Wu et al., 2010; Dai et al., 2010).

The use of a die coated with DLC for deep-drawing has been proposed owing to the excellent tribological properties of DLC (Kataoka et al., 2005). The use of a DLC coating has been found to eliminate the need for any lubricants to prevent the adhesion of aluminum to the die material. Also, the DLC coating prolongs the die lifetime to up to 10,000 deep-drawing operations.

Similarly, the use of a die coated with a chemical vapor deposition (CVD) diamond film has also been proposed, because the film has superior tribological properties to a DLC film (Tamaoki et al., 2007). It was confirmed that CVD-diamond-coated dies could perform for 100,000 deep-drawing operations on a stainless-steel sheet (SUS304) without the use of lubricants.

On the other hand, a thin hard film coating such as a DLC coated can also be used to improve the lifetime and dimensional accuracy of tools (D'Errico et al., 1998). For instance, thin PVD layers can be coated on a mold to increase the lifetime of tools (Reisal et al., 2003; Tillmann et al., 2009).

The surface of tools is easily damaged upon coming into contact with hard materials and by repeated scratching. For the prolongation of the tool lifetime, thin layers deposited by PVD have been employed. It was confirmed that the tool lifetime was increased when the friction between the tool and hard materials was reduced by the PVD layer. Many studies of coating technique for tools in press forming have been practiced.

In our research, we coated DLC film on Mg alloy sheet using low-temperature plasma in order to reduce the surface friction, which enables the Mg alloy sheet to be press-formable without lubricant. We mainly introduce and present our original experimental results on

this subject. And in the last section, we added some data of DLC coated Al alloy sheet. The formability of Al is superior to Mg, but it still requires lubricant even at an elevated temperature.

2. Nomenclature

BHF	: Blank holder force
CVD	: Chemical vapor deposition
D	: Blank diameter
D_d	: Die diameter
D_p	: Punch diameter
DLC	: Diamond-like carbon
DR= (D/D_p)	: Drawing ratio
LDR= (D_{max}/D_p)	: Limiting drawing ratio
R_p	: Punch shoulder radius
R_d	: Die shoulder radius
RF	: Radio frequency
R_a	: Average of surface roughness
R_z	: Maximum height of surface roughness
RD	: Rolling direction
TD	: Transverse direction
TEOS	: Tetraethoxysilane

3. Experimental procedure and evaluation methods

3.1 Materials

Used Mg alloy sheet was 0.5-mm thick AZ31B-O, which was purchased from Osaka Fuji Corp. The composition of AZ31B-O is listed in Table 1. As shown in this table, the Mg alloy contains about 3% of Al, 1% of Zn, and small amounts of Mn and Si. The Mg alloy sheet was cut into suitable sizes for each testing and characterizing method, and cleaned ultrasonically in distilled ethanol before use.

Al	3.5	Ca	<0.01
Zn	0.9	Ni	<0.001
Mn	0.64	Fe	0.002
Si	0.01	Mg	balance
Cu	<0.01		

Table 1. Composition (%) of Mg alloy sheet, AZ31B-O

As gases for plasma CVD of DLC, methane and hydrogen were used. As for plasma deposition of silicon layer, tetraethoxysilane ($\text{Si}(\text{OC}_2\text{H}_5)_4$) was used.

As lubricants for deep drawing, MoS_2 and GM100 (Nihon Kohsakyu Co., $\nu = 38.38 \text{ mm}^2/\text{s}$ at $40 \text{ }^\circ\text{C}$) were used.

3.2 DLC coating

DLC coating and silicon-layer coating were carried out with a plasma polymerization apparatus (Samco International, PD-S10) shown in Figure 1. Most of the cases, silicon layer was coated first on Mg alloy sheet, then DLC was coated continuously without breaking the vacuum. A capacitively coupled radio-frequency (13.56 MHz) plasma was created between a pair of stainless-steel electrodes (160-mm d., 60-mm gap). Mg alloy sheet samples were placed underneath the top electrode, to which the power was supplied. The electrode was not heated intentionally. The flow rate of TEOS was controlled with a needle valve while methane and hydrogen were introduced into the reactor through a mass flow controller (Tylan FC-770A). The pressure of the system was monitored with an absolute pressure gauge (MKS Baratron 122AA). During the plasma coating, deposition rate and total thickness were monitored with a deposition monitor (Leybold Inficon, XTM/2) that had a quartz oscillator sensor coated with gold, which was placed beside the bottom and ground electrode.

The deposition was conducted at the plasma power of 150 W and various flow rates and durations. The standard plasma condition for TEOS coating was 150 W, 3 sccm, 3 min, and that for DLC coating was 150 W, 10 min, 25 sccm of the mixture of CH₄ and H₂.

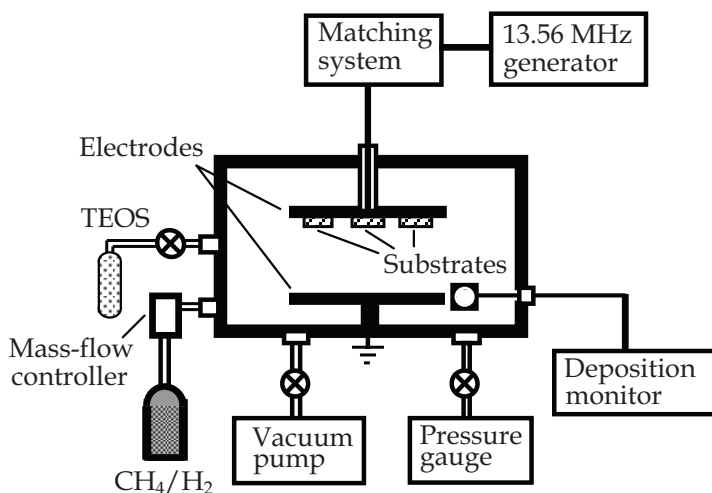


Fig. 1. Low-temperature plasma reactor used for DLC and silicon layer coatings (Iriyama et al., 2008)

3.3 Surface analysis

In addition to the thickness measurement with a deposition monitor placed beside the bottom electrode, we measured the thickness directly on the sample with a surface profile measuring system (ULVAC, Dektak3 ST).

Surface chemical composition of DLC coated Mg alloy sheets were analyzed with X-ray photoelectron spectroscopy (XPS, JEOL, JPS-9200).

In compensation for the data of XPS, glow discharge spectroscopy (GDS, Rigaku GDA750) was used for the analysis of surface concentration of hydrogen.

Surfaces of DLC coated Mg alloy sheets were observed with scanning electron microscope (SEM, Elionix, EXM-3500).

The surface roughness was measured in the direction of the TD cross section. The sliding speed was 0.1 mm/s, the sliding distance was 3-5 mm and surface roughness was measured at regular intervals of 0.002 mm. The reference length was 0.8 mm.

3.4 Adhesion test

For the evaluation of the adhesivity of the DLC coatings on Mg alloy sheet, cross-cut test was carried out. In the test, the surface layer of DLC coated Mg alloy sheet was cut straight with 1-mm interval for X- and Y-axes to make one-hundred 1-mm squares in a 10-mm square. An adhesive tape (Nichiban, Serotepu) was placed on it with a good contact. Then the tape was pulled back toward 180° angle. The adhesivity was evaluated from the number of unpeeled squares out of 100.

3.5 Friction test

Friction tests were carried out using a ball-on-disc type friction-testing machine (tribometer). Figure 2 shows a schematic illustration of the friction testing machine and Table 2 shows the conditions of the friction tests. The 0.5 N of vertical load was applied to Mg alloy sheet (30-mm d.) on the turntable. The friction coefficient was measured while the turntable was rotated at a circumferential velocity of 10 mm/s.

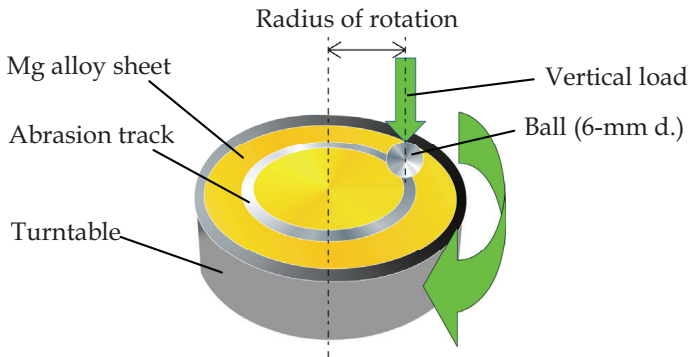


Fig. 2. Schematic illustration of friction test machine (Tsuji et al., 2009)

Vertical load (N)	0.5
Circumferential velocity (mm/s)	10
Rotation frequency (rpm)	30
Radius of rotation (mm)	10
Ball material	SUJ2

Table 2. Experimental condition of friction test (Tsuji et al., 2009)

3.6 Circular-cup deep-drawing test

Figure 3 is a schematic illustration of the deep-drawing apparatus and Table 3 shows typical conditions in the deep-drawing test. The compact press-forming machine with the capability of providing a punch thrust force of 5 kN was used in this experiment. This machine can generate an arbitrary blank-holding force and punch speed.

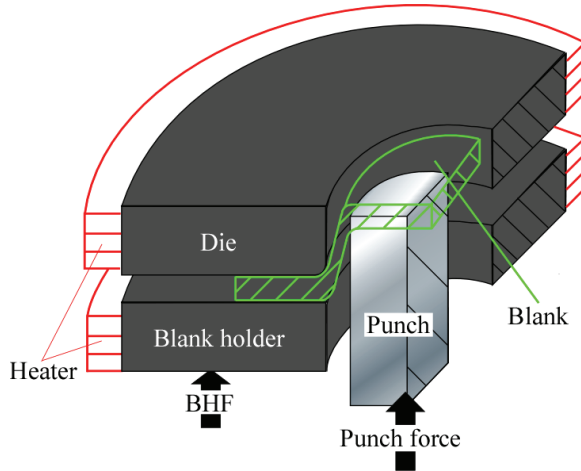


Fig. 3. Schematic illustration of deep-drawing equipment (Tsuji et al., 2009)

Punch speed (mm/s)		0.5
BHF (N)		50, 100, 150, 200, 250, 300
Temperature (°C)		200
Drawing ratio ($DR=D/D_p$)		2.0, 2.1, 2.2, 2.3
Punch	Diameter: D_p (mm)	9.5
	Shoulder radius: R_p (mm)	1.5
Die	Diameter: D_d (mm)	11.1
	Shoulder radius: R_d (mm)	1.0

Table 3. Experimental conditions in deep drawing test (Tsuji et al., 2009)

The effect of the DLC coating on the LDR of the Mg alloy sheet was also investigated, and DLC coated blanks were compared with blanks coated with the other lubricants in terms of the maximum punch load and the drawn-cup height. Moreover, it was determined whether the DLC coated blanks were suitable for plastic processing.

4. DLC coating and its fundamental properties

4.1 DLC coating

DLC is a general term of amorphous carbon or hydrocarbon, and there is no strict definition in chemical structure. Therefore, many kinds of hydrocarbon are used as starting material and many kinds of DLC have been prepared. In this research, we used a mixture of CH_4 and H_2 as a monomer gas for DLC coating. Figure 4 is a photograph of the original Mg alloy sheet and DLC coated Mg alloy sheet. DLC coating exhibited gold color.

Figure 5 shows deposition rate of DLC measured with the deposition monitor beside the bottom electrode, as shown in Figure 1, when the concentration of CH_4 in the gas mixture varied in total flow rate of 25 sccm. The deposition rate monotonously increased with CH_4 concentration, which is naturally expected because methane supplies main chain of DLC.



Fig. 4. Photograph of the original Mg alloy sheet (left) and DLC coated Mg alloy sheet (right)

However, the deposition rate is dependent on position in a reactor. In our research, from our previous study on the position of Mg alloy sheet for DLC coating in the reactor, underneath of the top powered electrode was found to be better than the bottom ground electrode in view of deposition efficiency and coating properties. Therefore, we placed the Mg samples underneath of the top electrode.

Since the thickness monitor is not placed near the top electrode, we measured the coating thickness directly with the surface profile system. Figure 6 shows the relationship between

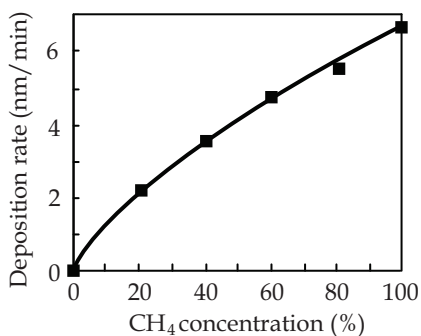


Fig. 5. Deposition rate of DLC coating as a function of CH₄ concentration in CH₄/H₂ mixture. Plasma power, 150 W; total flow rate, 25 sccm. (Iriyama et al., 2008)

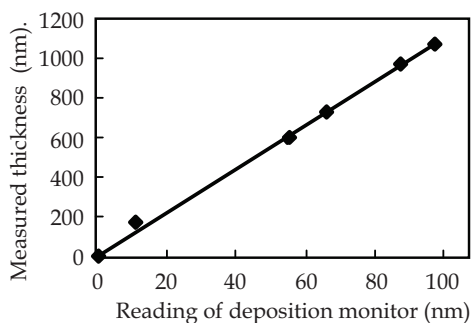


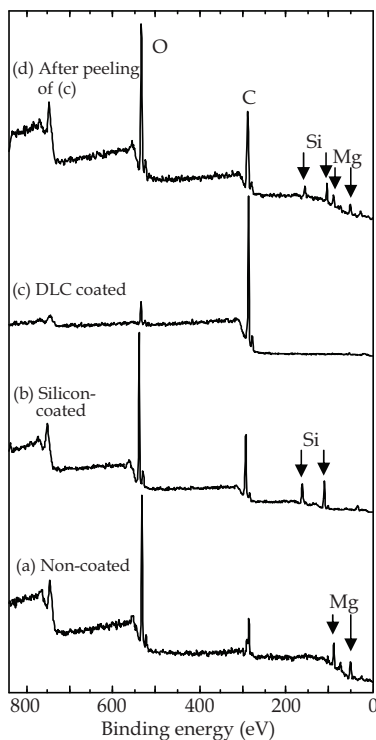
Fig. 6. Relationship of coating thicknesses between deposition-monitor readings and measured values in a surface profile system (Iriyama et al., 2008)

thicknesses measured with the deposition monitor and the surface profile measuring system. This relation is a simple proportion with the slope of 11. Therefore, we regard the actual thickness as the product of the readings of the deposition monitor multiplied by 11.

4.2 Chemical surface analysis and adhesion of DLC

In general, the adhesion between organic and inorganic materials is poor. Since DLC is categorized into an organic material, the adhesion between DLC and metal (Mg) is naturally expected to be poor. Therefore, usually, Si containing intermediate layer is inserted between them. Also in our preliminary study, most of the DLC coatings we prepared in various conditions directly on Mg alloy sheet were found to fail the peeling test. In our research, therefore, we used TEOS plasma coating for the intermediate layer. TEOS was used as a monomer and deposited on Mg alloy sheet directly before DLC coating, which is expected to improve the adhesivity.

In order to examine the chemical structure and chemical composition of the TEOS- and DLC coated Mg alloy surfaces, we analyzed them with XPS. Figure 7 shows XPS wide spectra of the surfaces of Mg alloy sheet: (a) non-coated, (b) silicon-layer coated, (c) silicon-layer and DLC coated, (d) after peeling test of (c), in which the DLC coating was intentionally removed.



(a) Non-coated; (b) silicon-layer coated; (c) silicon layer and DLC coated; (d) after surface peeling of (c). Silicon layer: 150 W, 3 min. DLC: CH₄ 60%, 150 W, 10 min.

Fig. 7. XPS wide spectra of Mg alloy sheet surfaces. (Iriyama et al., 2008)

There are naturally Mg 2s and 2p peaks at 50-100 eV on the original Mg alloy sheet. After silicon-layer coating, Mg peaks disappeared and Si 2s and 2p peaks appeared instead at 110-160 eV. After successive DLC coating, C1s peak (280-290 eV) with great intensity was found while Si signals were disappeared. Then, when the DLC coating was peeled off, C1s peak was drastically reduced and Si and Mg peaks were recovered. Since the intensity of Si and Mg signals in Fig.7d are not very strong, it is difficult to identify which interface or layer is responsible for the failure, Mg/silicon or silicon/DLC.

One of the reasons we expect the adhesivity improvement is a formation of Si-C covalent bond (Capote et al., 2008). Figure 8 shows Si2p XPS spectra of (a) TEOS coated and (b) TEOS and DLC coated Mg alloy sheet surfaces. In this particular sample for XPS, DLC was coated for only 5 nm in order for the interface to be analyzed. In TEOS coated surface (a), only Si-O peak was found, while in DLC coated surface on TEOS coating (b), Si-C peak was newly found, which is effective in the adhesivity.

Most of the cases, the adhesion is improved by the Si containing intermediate layer. But based on all the XPS results presented above, if the coating is to be peeled off, we suppose the locus of failure is the cohesive failure of silicon layer. Since silicon layer has a brittle nature, the coating conditions should be carefully selected.

In XPS analysis, deconvolution of narrow spectra could provide precise chemical structure of surfaces. Even for a hydrocarbon peak, the deconvolution enables us to distinguish sp^3 and sp^2 carbons, in which the peaks for sp^3 and sp^2 are located at around 285.2 and 284.3 eV, respectively (Mizokawa et al., 1987; J. Diaz et al., 1996). Figure 9 is an example of

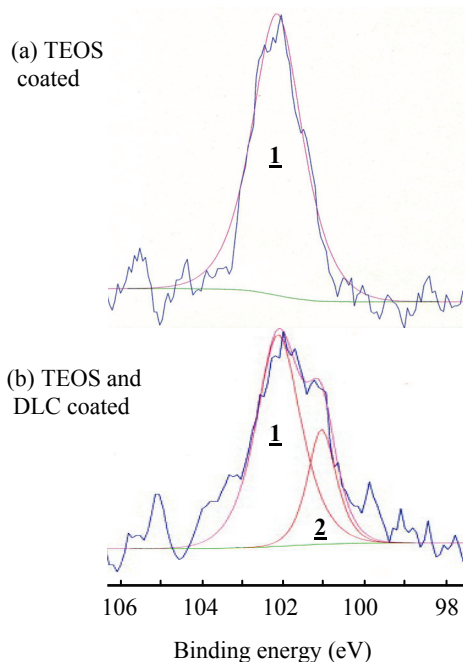


Fig. 8. Si2p XPS spectra of (a) TEOS coated and (b) TEOS and DLC coated Mg alloy sheet surfaces. **1**, Si-O bond; **2**, Si-C bond. (b) DLC: CH_4 60%, ca. 5-nm thick. (Iriyama et al., 2009)

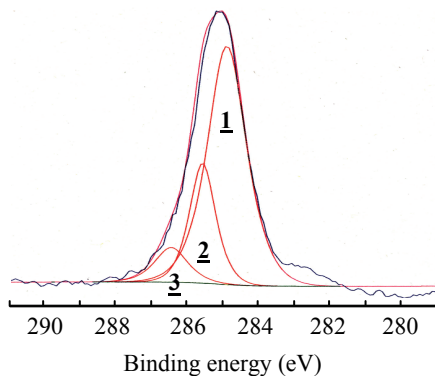


Fig. 9. C1s XPS spectrum of TEOS and DLC coated Mg alloy sheet surface. 1, sp^2 ; 2, sp^3 ; 3, C-O. DLC, CH_4 60%. (Iriyama et al., 2009)

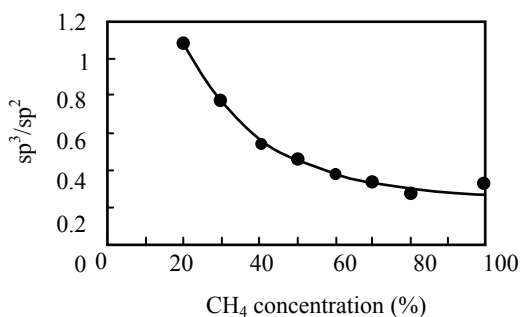


Fig. 10. Ratio of sp^3/sp^2 on the surface of DLC coated Mg alloy sheet estimated by deconvoluted C1s XPS spectra as a function of CH_4 concentration in DLC coating. (Iriyama et al., 2009)

deconvoluted C1s XPS spectrum of DLC coating. 1 and 2 in the figure represent sp^2 and sp^3 , respectively. The relationship between sp^3/sp^2 and CH_4 concentration in DLC coating is shown in Figure 10. As is expected, sp^3 decreases as the CH_4 concentration increases.

When we deal with organic materials, we are always reminded of the defect of XPS: hydrogen cannot be detected. Along with XPS, ATR-FTIR is often used for the analysis of surface chemical structure, but glow discharge spectrometry (GDS) may be the easiest technique to compensate XPS analysis. In GDS measurement, by subjecting a sample to plasma, relative contents of all the elements including H that constitute the surface of the sample are obtained by the analysis of emission in plasma. Figure 11 shows the relationship between H content and CH_4 concentration in DLC coating. The results can be naturally explained that the relative content of H found in the DLC coating was inversely proportional to CH_4 concentration in plasma gas.

Most of the cases, the silicon layer improved the adhesion of DLC on Mg alloy sheet. We measured the adhesivity of TEOS and DLC coatings deposited at various conditions on Mg alloy sheets by cross-cut test. Figure 12 shows the results of the cross-cut test for the samples coated with various TEOS flow rates (1 to 4.5 sccm) and various CH_4 concentrations (10% to 80%) in the total flow rate of 25 sccm with H_2 . The greater number of unpeeled square

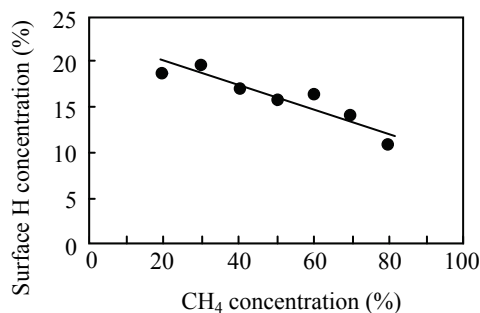


Fig. 11. Surface H concentration on DLC coated Mg alloy sheet measured by GDS as a function of CH₄ concentration in DLC coating. (Iriyama et al., 2009)

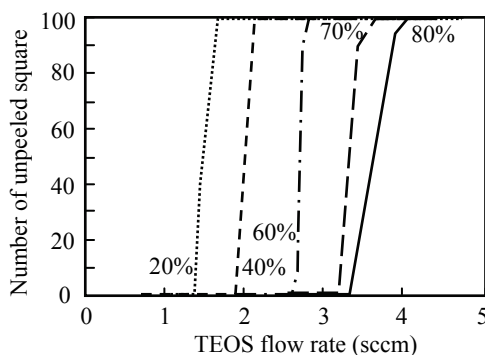


Fig. 12. The number of unpeeled squares in the adhesion test of TEOS- and DLC coated Mg alloy sheet. Percentages in the figure denote CH₄ concentration in DLC coating. (Iriyama et al., 2009)

shows greater adhesivity. As far as the deposition rate is concerned, which is dependent on the monomer concentration, higher TEOS flow rate and higher fraction of CH₄ shows greater values. Therefore, since the other plasma parameters are fixed, the thicknesses of the layers for the tested samples were varied.

From this figure, for any given CH₄ concentration, the higher TEOS flow rates show better adhesivity. Regarding the CH₄ concentration, it is interesting that the lower concentration showed better adhesivity although the coating layer is thinner. Probably, at a low deposition rate, DLC coating with good interaction with silicon layer was obtained.

Through the cross-cut test, the relatively high adhesion was found to be obtained under following conditions: TEOS, 150 W, 3-5 sccm, 1-3 min; CH₄/H₂, 150 W, 25 sccm (CH₄ 60-80%), 10 min. The thicknesses of silicon layer and DLC coating prepared under those conditions were estimated to be 50-200 and 400-600 nm, respectively.

4.3 Surface morphology and surface roughness of DLC coated Mg alloy sheet

The surface morphology of DLC coated Mg alloy sheets was observed with SEM. Figure 13 shows SEM photographs of the surfaces of Mg alloy sheet coated by different manner. When

DLC was coated directly on Mg (Fig.13b), oriented long flakes are found, which are obviously ready to come out. When only TEOS was coated on Mg (Fig.13c), on the other hand, a regular dense waving pattern was found, which looked tight and rigid and seems to have good adhesion and might be favorable in lowering the surface friction coefficient. This pattern was found on the most of TEOS coated Mg alloy sheets but not on the direct DLC coating on Mg regardless of the CH_4 concentration. The adhesivity could be judged by the close look of those photographs. Then, when DLC was coated after TEOS coating (Fig.13d), the appearance did not change from TEOS coating (Fig.13c), keeping the waving pattern, and the adhesivity seems to be good. When DLC was coated thicker (30 min) after TEOS coating (Fig.13e), a high internal stress caused peeling, but it is interesting to refer that the waving pattern of TEOS coating has been inherited.

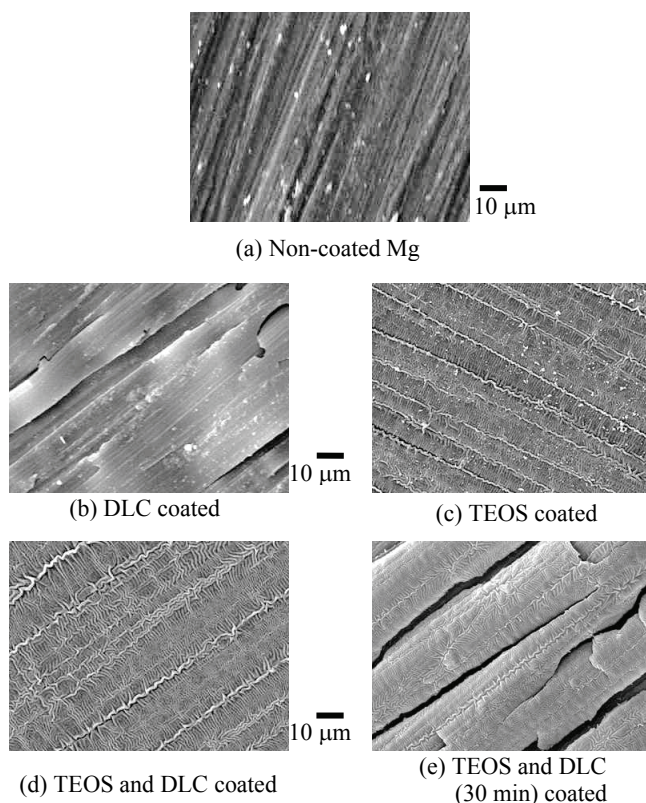


Fig. 13. SEM photographs of (a) non-coated, (b) TEOS coated, (c) DLC coated, and (d, e) Si and DLC coated Mg alloy sheet surfaces. (d, e) DLC, CH_4 60%; (e) DLC, 30 min. (Iriyama et al., 2009)

Figure 14 shows the surface roughness curves of the non-coated and DLC coated Mg alloy sheets. As shown in the figure, R_z and R_a for non-coated Mg alloy sheet were 1.65 and 0.24 μm , respectively, while those of DLC coated Mg alloy sheet were 1.78 and 0.21 μm , respectively. Those values were comparable, and it is confirmed that the surface roughness remains almost unchanged by DLC coating.

4.4 Surface friction of DLC coated Mg alloy sheet

Figure 15 shows approximate friction coefficient-sliding distance curves of various Mg alloy sheets. They are, three DLC coated (different plasma condition) and two lubricant-coated (MoS_2 and GM100) Mg alloy sheets along with non-coated one. The average friction coefficient for each specimen calculated based on this figure is shown in Table 4. It is possible to reduce the surface friction coefficient of DLC to less than 0.1 if you want to, but our objective was to obtain the friction coefficient comparable to MoS_2 .

The friction coefficient of DLC coated Mg alloy sheet was reduced significantly from 0.42 to 0.16-0.18, which is the same level to MoS_2 lubricated one. For a DLC coating in general, the friction coefficient of 0.16-0.17 is not very low, but it is low enough for the present application, and other factors may be contributed to the formability of the Mg alloy sheet.

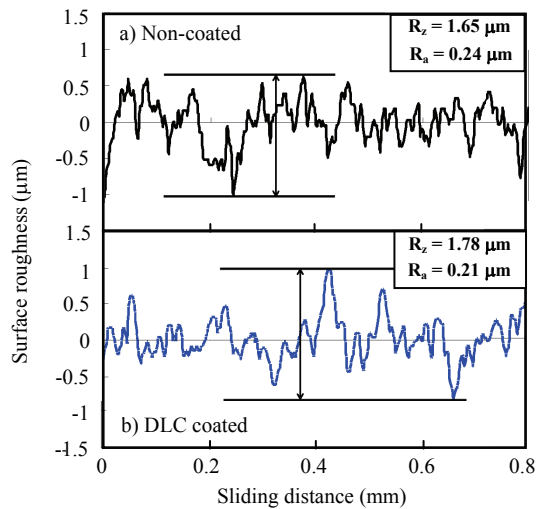


Fig. 14. Surface roughness curves of (a) non-coated and (b) DLC coated Mg alloy sheets (Tsuji et al., 2009)

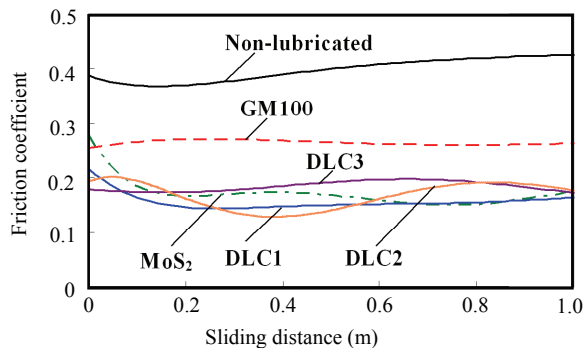


Fig. 15. Friction coefficient of DLC- and lubricant-coated Mg alloy sheets (Tsuji et al., 2009)

Type of lubricant	Friction coefficient
DLC1	0.16
DLC2	0.17
DLC3	0.18
MoS ₂	0.17
GM100	0.26
Non-lubricated	0.42

Table 4. Friction coefficient of DLC- and lubricant-coated Mg alloy sheets (Tsuji et al., 2009)

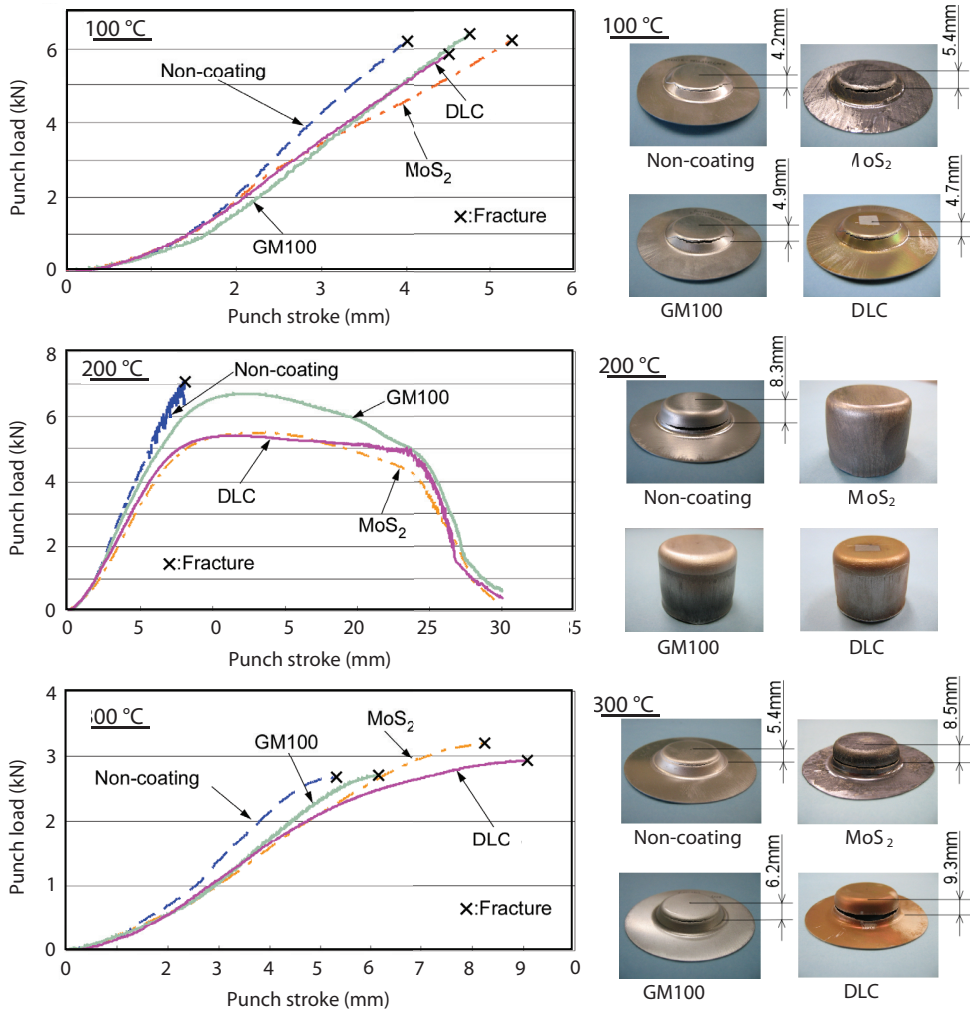


Fig. 16. Punch load-punch stroke curves for DLC- and lubricant-coated Mg alloy sheets at various temperatures, and photographs of the drawn cups. (Tsuji et al., 2008)

4.5 Circular-cup deep-drawing test

The ultimate objective of this research “better formability” comes to press forming and deep drawing. For the circular-cup deep-drawing test, we used DLC coatings with small friction coefficient because there is a clear correlation between friction coefficient and formability. Figure 16 depicts punch load-punch stroke curves and the photographs of the drawn cup at 100, 200 and 300 °C for DLC and other lubricant-coated Mg alloy sheets. Table 5 shows the maximum punch load and punch stroke at the maximum punch load point under various conditions and temperatures.

At 100 °C, the height of the drawn cup of DLC coating was the same as the height of the drawn cup of MoS₂ and GM100. These results were superior to those obtained in the case of non-coating at the maximum punch load and punch stroke. At this temperature, little effect of lubrication including DLC coating observed: difference of deep drawability among the lubricated Mg alloy sheets was not ascertained.

At 200 °C, in case of DLC coating, MoS₂, and GM100, samples survived the complete deep-drawing process without fracture. Moreover, the maximum punch load of the DLC coating and MoS₂ was 5.39 and 5.47 kN, respectively: 5.39 kN for DLC coated Mg alloy sheet was the lowest in any other conditions. Non-coated one immediately fractured. DLC coated Mg alloy sheet had good deep drawability comparable to that for MoS₂ lubricated one.

At 300 °C, in case of DLC coating the punch stroke was the longest of any other conditions. It was observed that the DLC coating reduces the punch load and affects deep drawability. It was confirmed that the DLC coating has a distinct lubrication capability which is as good as the lubricant for the plastic processing of a Mg alloy sheet. Furthermore, it was made clear that DLC coating improves the deep drawability of Mg alloy sheet.

Conditions of lubricant	Max. punch load (kN)			Punch stroke (mm) (Max. punch load point)		
	100 °C	200 °C	300 °C	100 °C	200 °C	300 °C
DLC coating	5.84	5.39	2.94	4.53	11.44	9.08
MoS ₂	6.21	5.47	3.20	5.27	13.10	8.35
GM100	6.39	6.72	2.70	4.78	12.16	6.71
Non coating	6.21	7.14	2.67	4.03	8.12	5.32

Table 5. Maximum punch load and punch stroke (Tsuda et al., 2008)

Figure 17 is the success-fail diagram of circular-cup deep-drawing for DLC coated and GM100 lubricated Mg alloy sheets. In this figure, circle mark “O” indicates successful of deep-drawing, “X” the fracture at the punch shoulder, and triangle mark the fracture at the wall.

The LDRs for the deep-drawing of DLC coated and GM100 lubricated Mg alloy sheets were predicted from the intersection of the two thick lines in the figure. For the determination of the LDR, deep-drawing tests were carried out under conditions similar to those at the intersection. As results, Mg alloy sheet was possible to deform up to LDR= 2.23 for DLC coated and LDR= 2.20 for GM100 lubricated.

Figure 18 shows the distribution of the wall thickness from the bottom to the edge of the drawn-cup with a DLC coated in the directions of RD- and TD-cross-sections. The wall thickness was the same as the initial thickness at the bottom of the drawn-cup. The reduction of the wall thickness and tensile elongation at the punch shoulder were confirmed in both directions and the thickness increased at the side wall. On the other hand, the reduction in thickness of the punch shoulder and the deformation in the RD-cross-section direction were inhibited in comparison with that in the TD-cross-section direction. The reason was the effect of the anisotropy (r value) of the Mg alloy sheet. For the evaluation of the lubricating performance of the DLC coating, three wall thickness distribution points at the punch shoulder, at the side wall part, and at the brim of the cup were compared with those for GM100 lubricated Mg alloy sheets. The reduction of the wall thickness for DLC coated was less than that for GM100 lubricated. As a result, it was confirmed that the DLC coating has good lubricating performance compared with GM100.

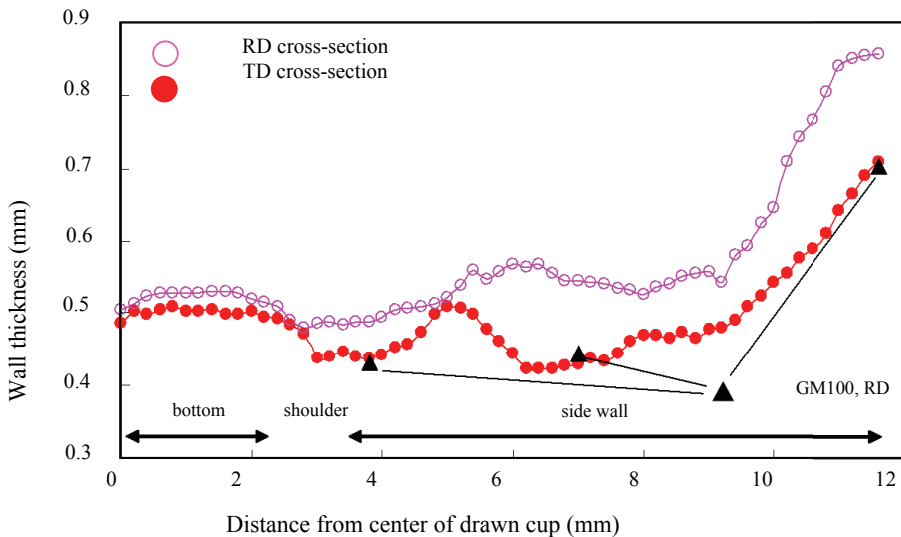


Fig. 18. Wall thickness distribution of drawn cup of DLC coated Mg alloy sheet. BHF, 150 N; temperature, 200 °C; DR, 2.1. (Tsuiji et al., 2009)

5. DLC Coating on aluminum alloy sheet

As a comparison to Mg alloy sheet, DLC was coated on aluminium (Al) alloy sheet, another versatile light metal. Also in the press forming of Al alloys, lubricating oil is used to prevent the adhesion of Al alloys to the forming tools. Therefore, new lubricating techniques, preferably dry system, are an urgent necessity.

Al alloy sheet used in this experiment was A5052-O (0.5-mm thick). Disk of the Al alloy sheet (18.05-mm d.) was used for both friction test and deep drawing.

DLC was coated in the same manner as that on Mg alloy sheet. Also, the conventional lubricant GM100 was used for a comparison.

Figure 19 shows the results of peeling test, which depicts the adhesivity of DLC on Al alloy sheet. If you compare this figure with Fig.12, which corresponds to Mg alloy sheet, you will see that Al has less dependency on TEOS flow rate: Al alloy sheet can achieve good adhesivity at wide plasma deposition condition.

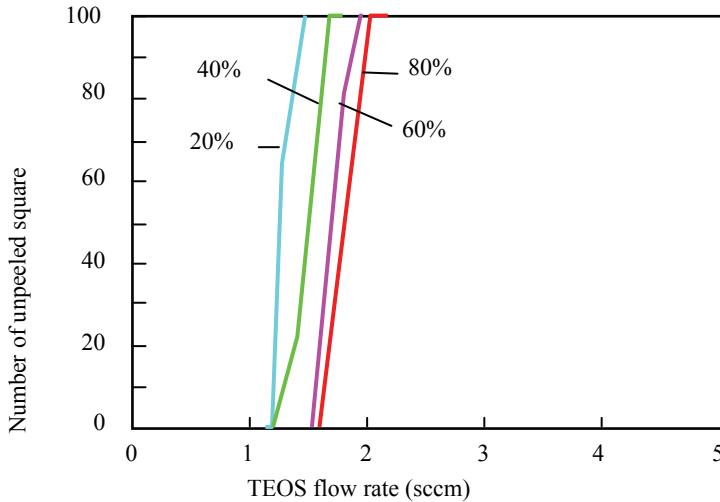


Fig. 19. The number of unpeeled squares in the adhesion test of TEOS- and DLC-coated Al alloy sheet. Percentages in the figure denote CH₄ concentration in DLC coating.

Figure 20 shows approximate friction coefficient-sliding distance curves at (a) room temperature and (b) 200 °C.

At room temperature, the average friction coefficient of non-coated Al alloy sheet was 0.60, which was reduced to 0.43 by GM100 lubrication. Further, much lower values, 0.16-0.2, were marked by DLC coated ones, which exhibited good lubricating performance.

At 200 °C, extremely low friction coefficient, 0.03, was obtained by two of three DLC coated ones, while that of GM100 lubricated one was reduced somewhat. On the contrary, that of non-coated one was increased, because the adhesivity of the aluminum alloy increased with temperature. From these results, DLC coating is expected to have a good property for deep drawing, too.

Figure 21 shows the punch load curves in deep drawing of (a) DLC coated and (b) GM100 lubricated Al alloy sheets at 200 °C. The deep-drawing apparatus used for Al alloy sheet was a compact press-forming machine, which is different from the one used for Mg alloy sheet. The deep-drawing test was conducted at a punch thrust force of 5 kN and three punch speeds, 0.05, 0.5, and 5.0mm/s, for the investigation of the effect of the strain ratio on deep-drawability.

From this figure, it was found that the maximum punch load of DLC coated Al alloy sheet was about 40% less than that of GM100 lubricated one at each punch speed. The deep-drawing of DLC coated Al alloy sheet was also completed at room temperature, but the maximum punch load exceeded 2 kN for all punch speeds.

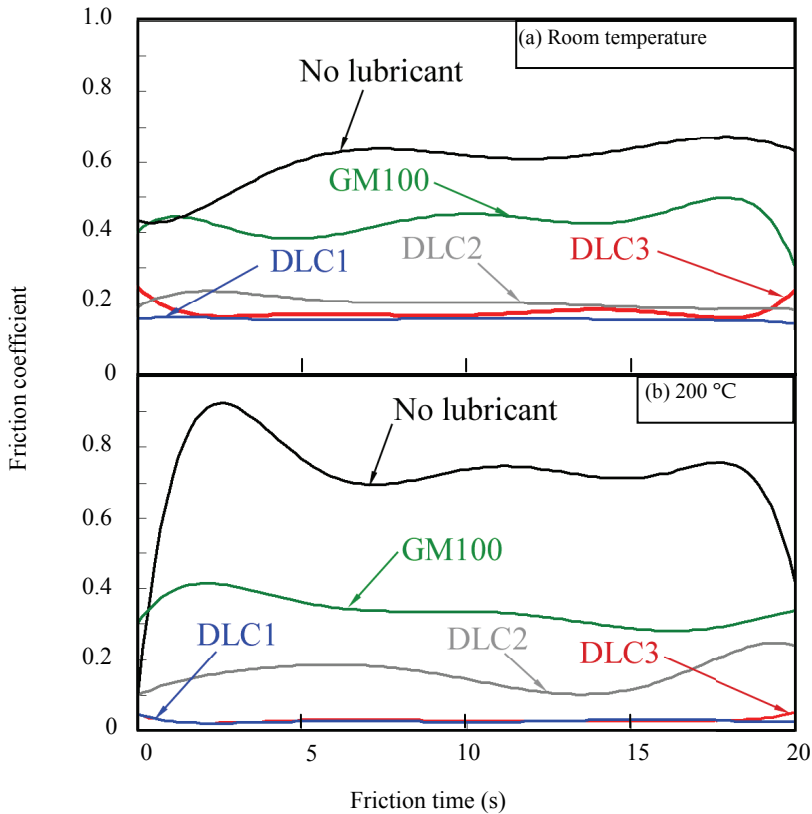


Fig. 20. Friction coefficient-friction time curves of DLC coated and GM100 lubricated Al alloy sheets at (a) room temperature and (b) 200 °C (Horiuchi et al., 2010)

As for the relationship between the punch load and the maximum punch speed, there is a regular correlation as shown in Fig. 21: the punch load increased with the punch speed. On the contrary, in the deep-drawing of DLC coated Al alloy sheet at room temperature, an inverse correlation was found: the punch load decreased with increasing punch speed. These phenomena can be explained by the strain rate sensitivity (m value) of A5052. The m value is positive at 200 °C, but it is negative at room temperature. From these results, the maximum punch load is affected by the dependence of the punch speed on temperature.

6. Conclusion

DLC coating on Mg alloy sheet had a good adhesion by the support of the intermediate silicon layer, which have not increased or induced exfoliation. DLC coating on Mg alloy sheet, which had a high lubricating capability, reduced the surface friction coefficient to the same level for MoS₂ lubricant. The deep-drawing of DLC coated Mg alloy sheet was successful at 200 °C. It was confirmed that the LDR of DLC coated Mg alloy sheet was 2.23,

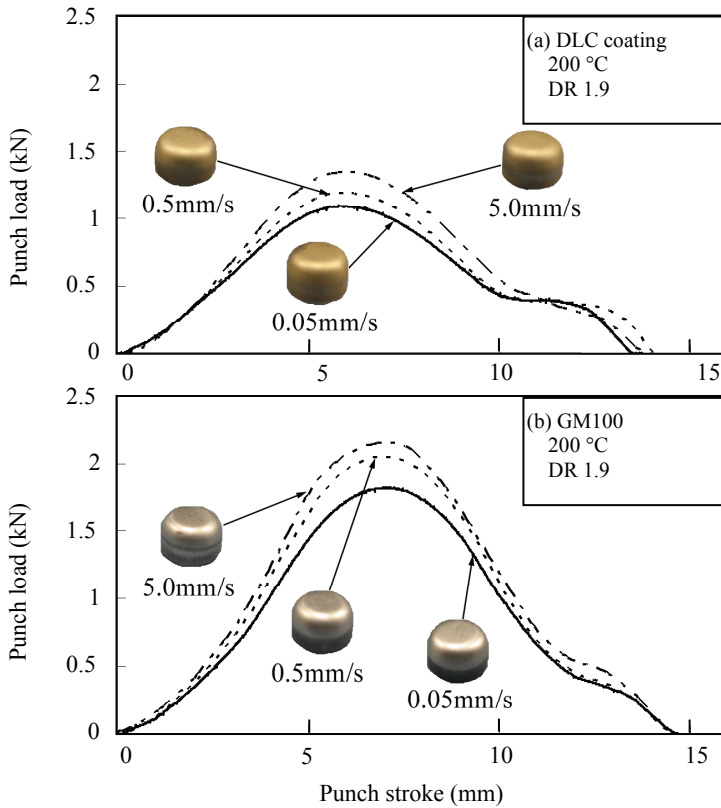


Fig. 21. Punch load-punch stroke curves for (a) DLC coated and GM100 lubricated Al alloy sheets at varied punch speeds. (Horiuchi et al., 2010)

while those of MoS₂ and GM100 lubricated Mg alloy sheet were 2.30 and 2.20, respectively. The punch load of DLC coated Mg alloy sheet was lower than those of MoS₂ and GM100 lubricated ones. It is concluded that the use of the DLC coating improved the formability of Mg alloy sheet compared with the use of other lubricants. Similar results were also found on the DLC coated Al alloy sheet. The formability will be further improved by the optimization of DLC coating conditions.

This technique, coating on forming material rather than die, is useful for complex-shaped press forming. It is necessary for DLC coating to have a good adhesivity for better formability, but one of the ultimate goals is self-removal after press forming.

7. References

Capote, G.; Bonetti, L. F.; Santos, L. V.; Trava-Airoldi, V. J. & Corat, E. J. (2008). Adherent amorphous hydrogenated carbon films on metals deposited by plasma enhanced chemical vapor deposition. *Thin Solid Films*, 516(12), 4011-4017.

- Choi, J.; Nakao, S.; Kim, J.; Ikeyama, M. & Kato, T. (2007a). Corrosion protection of DLC coatings on magnesium alloy. *Diamond Relat. Mater.*, 16(4-7), 1361-1364.
- Choi, J.; Kim, J.; Nakao, S.; Ikeyama, M. & Kato, T. (2007b). Friction properties of protective DLC films on magnesium alloy in aqueous NaCl solution. *Nucl. Instrum. Methods Phys. Res., Sect. B*, 257(1-2), 718-721.
- D'Errico, G. E.; Calzavarini, R. & Vicenzi, B. (1998). Influence of PVD coatings on cermet tool life in continuous and interrupted turning. *J. Mater. Proc. Technol.*, 78, 53-58.
- Diaz, J.; Paolicelli, G.; Ferrer, S. & Comin, F. (1996). Separation of the sp³ and sp² components in the C1s photoemission spectra of amorphous carbon films. *Phys. Rev.*, B54(11), 8064-8069.
- Dai, W.; Wu, G. & Wang, A., (2010). Preparation, characterization and properties of Cr-incorporated DLC films on magnesium alloy, *Diamond Rel. Mater.*, 19(10), 1307-1315
- Horiuchi, T.; Yoshihara, S. & Iriyama, Y. (2010). Deep drawability of DLC-coated A5052 Aluminum alloy sheet. *Proceedings of 4th International Conference on Tribology in Manufacturing Processes - ICTMP 2010*, pp.691-700, Nice, France, June 2010.
- Iriyama, Y.; Sakurai, S.; Yoshihara, S. & Tsuda, S. (2008). "Reduction of friction coefficient of magnesium alloy sheet by DLC coating with low-temperature plasma. *J. Photopolym. Sci. Technol.*, 21(2), 245-250.
- Iriyama, Y.; Nakano, Y.; Yoshihara, S. & Tsuji, Y. (2009). DLC coating on magnesium alloy sheet by low-temperature plasma" *J. Photopolym. Sci. Technol.*, 22(4), 485-490.
- Kataoka, S.; Murakawa, M.; Aizawa, T. & Ike, H. (2004). Tribology of dry deep-drawing of various metal sheets ceramics tools. *Surf. Coat. Technol.*, 177-178, 582-590.
- Kataoka, S.; Motoi, A.; Tamaoki, K.; Murakawa, M.; Noguchi, H. & Kihara, J. (2005). Improvement in DLC thin film adhesion and its application to dry deep drawing. *J. Jpn. Soc. Technol. Plast.*, 46(532), 412-416 (in Japanese).
- Kataoka, S. (2006). Tools for dry press working, *J. Jpn. Soc. Technol. Plast.*, 47(546), 569-573 (in Japanese).
- Konca, E.; Cheng, Y.-T. & Alpas, A. T. (2006). Sliding wear of non-hydrogenated diamond-like carbon coatings against magnesium. *Surf. Coat. Technol.*, 201(7), 4352-4356.
- Mizokawa, Y.; Miyasato, T.; Nakamura, S.; Geib, M. & Wilmsen, C. W. (1987). The C KLL first-derivative x-ray photoelectron spectroscopy spectra as a fingerprint of the carbon state and the characterization of diamondlike carbon films. *J. Vac. Sci. Technol.*, A5(5), 2809-2813.
- Reisal, G.; Wielage, B.; Steinhäuser, S. & Hartwig, H. (2003). DLC for tools protection in warm massive forming. *Diamond Rel. Mater.*, 12, 1024-1029.
- Tamaoki, K.; Kataoka, S. & Minamoto, K. (2006). Dry cylindrical cup drawing using electroconductive ceramic tools. *J. Jpn. Soc. Technol. Plast.*, 48, 930-934 (in Japanese).
- Tamaoki, K.; Kataoka, S.; Kanda, K. & Takano, S. (2007). Applying CVD diamond film to alloy tool steels. *Proceedings of the 2007 Japanese Spring Conference for the Technology of Plasticity*, p.177 (in Japanese).
- Tillmann, W.; Vogli, E.; Gathen, M. & Momeni, S. (2009). Development of wear resistant pressing moulds for the production of diamond composites. *J. Mater. Proc. Technol.*, 209, 4268-4273.
- Tsuda, S.; Yoshihara, S.; Tsuda, S.; Iriyama, Y. & Sakurai, S. (2008). Effect of DLC coating on deep drawability of AZ31 magnesium alloy sheet. *Proceedings of the 25th*

- International Manufacturing Conference, IMC 25*, pp.23-30, Dublin Institute of Technology, Ireland, Sep. 2008.
- Tsuji, Y.; Yoshihara, S.; Tsuda, S.; Iriyama, Y. & Nakano, Y. (2009). Effect of DLC coating on limiting drawing ratio of AZ31 magnesium alloy sheet. *Proceedings of the ASME 2009, International Mechanical Engineering Congress & Exposition, IMECE2009-10947*, pp.1-6, Lake Buena Vista, Florida, USA, Nov. 2009.
- Yamauchi, N.; Demizu, K.; Ueda, N.; Cuong, N. K.; Sone, T. & Hirose, Y. (2005). Friction and wear of DLC films on magnesium alloy. *Surf. Coat. Technol.*, 193(1-3), 277-282.
- Yamauchi, N.; Ueda, N.; Okamoto, A.; Sone, T.; Tsujikawa, M. & Oki, S. (2007). DLC coating on Mg-Li alloy. *Surf. Coat. Technol.*, 201(9-11), 4913-4918.
- Yoshihara, S.; Yamamoto, H.; Manabe, K. & Nishimura, H. (2003). Formability Enhancement in magnesium alloy deep drawing by local heating and cooling technique. *J. Mater. Proc. Technol.*, 143-144, 612-615.
- Yoshihara, S.; Manabe, K. & Nishimura, H. (2005). Effect of blank holder force control in deep-drawing process of magnesium alloy sheet. *J. Mater. Proc. Technol.*, 170, 579-585.
- Wu, G.; Sun, L.; Dai, W.; Song, L. & Wang, A. (2010). Influence of interlayers on corrosion resistance of diamond-like carbon coating on magnesium alloy, *Surf. Coat. Technol.*, 204(14), 2193-2196.

Instrumental Chemical Analysis of Magnesium and Magnesium Alloys

Michihisa Uemoto

*Tokyo Metropolitan Industrial Technology Research Institute, Jonan Branch
Japan*

1. Introduction

Magnesium is the lightest of all the commonly used metals. It is one of the most abundant elements in the earth's surface, amounting to a mass fraction of *c.a.* 2.5 %. It has been prepared for industry as metal and alloy ingots; the latter are most often made with aluminum. Various magnesium-based alloys have been developed and mainly applied to transport facilities and mobile electric devices because they have the best strength-to-weight ratio of any of the commonly used structural alloys. Practically, they are used for housing of laptop computers, mobile phones, and digital cameras, moreover, materials for acoustic diaphragm, units of vehicles, nursing-care equipments, anode for sacrificial protection, *etc.* Some special alloys with rare earth metals, which show high strength properties at elevated temperatures (Rokhlin, 2003), have been recently applied to aircraft and space machinery, automobile and railcar products. Accordingly, the chemical composition of magnesium and its alloys have already been standardized from major to trace quantities. International Organization for Standardization (ISO 8287, 2000; ISO 16220, 2005), American Society for Testing and Materials (ASTM B92/B92M-07, 2007; ASTM B93/B93M-07, 2007), and Japan Industrial Standard (JIS H2150, 2006; JIS H2221, 2006; JIS H2222, 2006) provide the standards of metal ingots, wrought alloys, and casting alloys separately, where vast kinds of designation, chemical constituents with permissible ranges, and chemical impurity with maximal allowable limits are denoted therein. Moreover, the wrought alloys with extruded or forged shapes to make sheets, bars, pipes, tubes, wires, *etc.* have been specialized in ISO (ISO 3116, 2007), ASTM (ASTM B107/B107-07, 2007), and JIS as several particular standards. Table 1 shows the chemical composition of unalloyed magnesium with different purities denoted in ISO 8287.

However, standardization of analytical methods to determine metal elements therein is quite insufficient. In 2006, ISO confirmed five old standards for minor analyses with gravimetry and titrimetry, and eleven ones for trace analyses with photometry and atomic absorption spectrometry, all of which were established in the 1970s and 1981. On the contrary, in 2008 ASTM withdrew the standard test methods for chemical analysis in view of a lack of information on reliability therein (ASTM E35-88, 2002), where a chill cast specimen can only be affordable to be analyzed with the ASTM test method using spark source atomic emission spectrometry (ASTM B95435-07, 2007). JIS denotes most plentiful standard methods that feature classical wet techniques and instrumental analyses corresponding with concentrations in the materials and accuracy needed, but they are standardized mostly in 1990's with flame atomic absorption spectrometry for trace analyses. Consequently in all cases, there existed no methods for the determination of trace amounts

of metals with inductively coupled plasma atomic emission spectrometry (ICP-AES), which is nowadays one of the most conventional *de facto* standard instrumental methods for the trace analysis of metal elements. Table 2 shows a list of the analytical methods made up from ISO and JIS standards. In this Table, some new standards of JIS by the author and his members using ICP-AES are also shown in the last four lines, details of which are described below.

Material designation		Chemical composition % mass fraction													
In accordance with ISO 2092	In accordance with EN 12421	min. or max.	Al	Mn	Si	Fe	Cu	Ni	Pb	Sn	Na	Ca	Zn	Others (each)	Mg ^a
ISO Mg 99.5	EN-MB 10010	min. or max.	-	-	-	-	-	-	-	-	-	-	-	-	99.5
		max.	0.1	0.1	0.1	0.1	0.1	0.01	-	-	0.01	0.01	-	0.05	-
ISO Mg 99.80A	EN-MB 10020	min. or max.	-	-	-	-	-	-	-	-	-	-	-	-	99.80
		max.	0.05	0.05	0.05	0.05	0.02	0.001	0.01	0.01	0.003	0.003	0.05	0.05	-
ISO Mg 99.80B	EN-MB 10021	min. or max.	-	-	-	-	-	-	-	-	-	-	-	-	99.80
		max.	0.05	0.05	0.05	0.05	0.02	0.002	0.01	0.01	-	-	0.05	0.05	-
ISO Mg 99.95A	EN-MB 10030	min. or max.	-	-	-	-	-	-	-	-	-	-	-	-	99.95
		max.	0.01	0.006	0.006	0.003	0.005	0.001	0.005	0.005	0.003	0.003	0.005	0.005	-
ISO Mg 99.95B	EN-MB 10031	min. or max.	-	-	-	-	-	-	-	-	-	-	-	-	99.95
		max.	0.01	0.01	0.01	0.005	0.005	0.001	0.005	0.005	-	-	0.01	0.005	-

^a By difference

Table 1. Chemical composition of unalloyed magnesium denoted in ISO 8287

This chapter outlines instrumental methods of the analysis and especially focuses on ICP-AES. The methods of trace analyses in magnesium and its alloys by ICP-AES are described with results of interlaboratory testing of the analyses, which have been put into practice prior to standardization by the author. The concept of the testing protocol, which must be acceptable for practical technicians with various environments and skills, will be emphasized in the chapter. The protocols evaluated in the testing have been provided as recently established JIS standards, which are the first standardized analytical methods on magnesium and its alloys by ICP-AES.

2. Instrumental methods of analysis

2.1 Outline of the instruments for material analysis

In material analysis, verification and evaluation of chemical components and impure elements mostly designated in standards are indispensable. Hence elemental quantification is first needed with high reliability, which allows atomic spectroscopy to rank first for this kind of analysis.

Atomic spectroscopy has undoubtedly become a major tool on trace analysis of metals in materials, where inductively coupled plasma atomic emission spectrometry (ICP-AES) and atomic absorption spectrometry (AAS) have been widely used as archetypal methods around laboratories. They observe atomic spectra on measurement, which are generated in ultraviolet and visible region due to radiative transitions of outer orbital electrons between the ground state and excited state of an atom. The spectra are elementally specific and their signal intensities relate to the concentrations of the elements, thus allowing selective qualification and quantification. Samples must be dissolved with acids to prepare as solutions prior to determination. When the sample solutions are introduced into the instruments, they are made to aerosols with nebulizers, subsequently desolvated and dissociated to atoms with heat sources such as plasmas and flames. In general, obtainable spectra in the atomic spectroscopy can be classified into three categories: (a) spontaneous

emission from a higher excited state to a lower state; (b) absorption of radiation corresponding with a transition from a lower state to a higher state; and (c) induced resonant emission for the transition from a higher state to a lower state just after the absorption of external distinctive radiation. ICP-AES utilizes the spectra of type (a), because high temperature of 5000-6000 K generated in argon ICP makes almost all the atoms in a higher excited state. On the other hand, AAS does the ones of type (b) because kinds of flames generated with acetylene premixed with air or nitrous oxide and electrical furnaces, which are typically suitable as excitation sources for AAS, can reach relatively low temperature in the region of 2000-3000 K only to make them in a lower state. The last category of type (c) is applied to atomic fluorescence spectrometry, which is neither less popular in practical laboratories nor commercially available than ICP-AES and AAS.

element	ISO			JIS		
	method	number:year	dynamic range (%)	method	number:year	dynamic range (%)
Al	gravimetry	791:1973	1.5-12.0	gravimetry	H1332:1999	1.5-12.0
	colorimetry	3255:1974	0.01-0.20	titrimetry	H1332:1999	2.0-11.0
				colorimetry	H1332:1999	0.01-0.20
				flame AAS	H1332:1999	0.0005-0.05, 0.001-0.05
Zn	titrimetry	1783:1973	0.10-8.0	titrimetry	H1333:1999	0.1-7.0, 0.4-7.0
	flame AAS	4194:1981	0.1-6	flame AAS	H1333:1999	0.0002-8.0, 0.1-6.0
Mn	colorimetry	809:1973	0.01-0.8	colorimetry	H1334:1999	0.02-1.0, 0.01-0.8, 0.0002-0.1
	colorimetry	810:1973	<0.01	flame AAS	H1334:1999	0.0005-0.5
	colorimetry	2353:1973	0.02-0.2 *			
Si	colorimetry	1975:1973	0.01-0.6	colorimetry	H1335:1998	0.02-0.50, 0.001-0.05, 0.01-0.6
Cu	colorimetry	794:1976	0.002-0.4	colorimetry	H1336:1999	0.0005-0.5, 0.002-0.4, 0.0003-0.03
				flame AAS	H1336:1999	0.005-0.4
Ni	colorimetry	4058:1977	0.0005-0.05	flame AAS	H1337:1999	0.0002-0.04
Fe	colorimetry	792:1973	0.002-0.05	colorimetry	H1338:1999	0.002-0.05, 0.0005-0.05
				flame AAS		0.001-0.08
Zr(soluble)	colorimetry	1178:1976	0.1-1.0	colorimetry	H1340:1998	0.05-1.0
Zr(insoluble)	colorimetry	2354:1976	0.02-0.3	colorimetry	H1340:1998	0.02-0.3
Th	gravimetry	5196-1:1980	0.2-5.0	-	-	
	titrimetry	5196-2:1980	0.2-5.0			
Rare Earths	gravimetry	2355:1972	0.2-10	gravimetry	H1345:1998	0.2-10.0
Ca	-	-	-	flame AAS	H1341:1990	0.01-0.1
Sn	-	-	-	ICP-AES	H1342:2008	0.0005-0.01
Pb	-	-	-	ICP-AES	H1343:2008	0.0005-0.01
Cd	-	-	-	ICP-AES	H1344:2010	0.00005-0.001
Be	-	-	-	ICP-AES	H1339:2010	0.00005-0.001, 0.00005-0.002
				flame AAS	H1339:2010	>0.001

* the method for alloys containing Zr, rare earths, Th, & Ag

Table 2. List of standardized analytical methods for magnesium and magnesium alloys in ISO and JIS

Transitions of electrons take place not only between the outer shells but also from the outer to an inner as a result of external excitation. When X-ray or one of the related beams such as accelerated electron and heavy charged particle (proton or α -particle in usual) is irradiated to an atom, an electron in the inner may be ejected to have a vacancy, producing an excited ion. An electron from the outer shell almost immediately fills it, emitting elementally specific X-ray corresponding to a difference of the two energy levels. This refers to as one of X-ray spectroscopy. Instrumentation with electrically operated X-ray tubes is most conventional and sophisticated as X-ray fluorescence spectrometry(XRF). It needs no dissolution as pretreatment step and allows direct measurements on materials.

Atoms generated in the ICP are easy to lose electrons to become positively charged ions owing to its high temperature, which are feasible to be detected with mass analyzers. Actually major part of elements in the plasma is not atomic but ionic, where the emissions from the transitions in the atoms and ions are both utilized in ICP-AES. Consequently inductively coupled plasma mass spectrometry (ICP-MS) has been developed, combining the ICP and mass analyzers for ultra trace analysis of metals.

Further explanation on the outline should be directed to recently published books on atomic and X-ray spectroscopy including ICP-MS. (Broekaert, 2005; Welz & Borges, 2009) Another book on ICP-AES and ICP-MS is also convenient for Japanese users. (Uemoto, 2008)

2.2 Inductively Coupled Plasma Atomic Emission Spectrometry (ICP-AES)

Atomic emission spectrometry (AES) is the oldest atomic spectrometric technique capable of multi-elemental detection. Chemical flames and plasmas generated on arc, spark, and glow discharges have been used as excitation sources. However, appearance of high frequency plasma has transformed this technique into the cutting-edge one, which is capable of determining trace metals selectively below ppm levels over larger dynamic ranges than any other spectrometric technique. This method is often called as inductively coupled plasma optical emission spectrometry (ICP-OES). The plasma, an ionized gas of argon at very high temperature (5000-6000K), is generated at high frequency (usually 27 or 40 MHz) under argon gas flow in three concentric quartz tubes known as a plasma torch. The torch is encircled at the top by an induction coil connected to a generator, where the magnetic field induced in the gas stream forms the plasma. Its concentric toroidal structure allows sample solution as an aerosol into the center of the plasma, thus enabling its efficient desolvation, vaporization, atomization, excitation, and ionization. These characteristics of the argon ICP applicable to a wide variety of elements lead to sensitive multi-elemental determination relatively independent of matrix elements. Figure 1 shows a schematic view of the inductively coupled plasma.

ICP-AES consists of simple units as shown in Figure 2. The electromagnetic energy necessary to sustain the plasma is transferred from the high frequency generator unit to the emission unit that consists of the torch and the induction coil. Sample aerosols are carried with argon gas into the plasma, where the emission lights from the plasma are introduced into the spectrometer unit and intensities of monochromated lines are measured in the detector unit, a whole of which is fully regulated by the controller unit.

Device technology in ICP-AES has further been designed and now the instruments have some selectable specifications in relation to the adaptability and performance of the system. The principal innovations to be mentioned are described as follows; Although the ICP can be originally viewed radially (side-on), an alignment for axial (end-on) viewing with horizontally generated plasma has been devised in order to gain sensitivity due to longer path length than the radial viewing. In the former, the plasma is positioned at a 90 deg angle

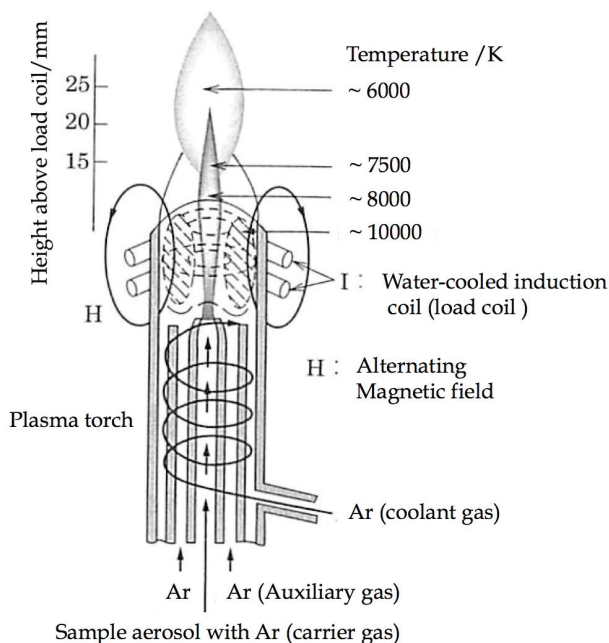


Fig. 1. Schematic view of the inductively coupled plasma

with the detector, while in the latter, the ICP and detector are positioned in the same optical axis. The latter certainly brings higher sensitivity but interferences due to coexisting elements are known to be severe; the spectrometer could be originally divided into two categories; monochromator and polychromator. The former is used to build up sequential scanning system, while the latter is for simultaneous detection system with one detector by one element, both of which utilize the first-order light dispersion. Another spectrometer with so-called 'echelle' grating and a prism to spread all the dispersed lights with high orders on a plane has been developed. It seems preferable to set up this spectrometer with the axial viewing system because emission lights dispersed by wavelength with the echelle spectrometer is darker than those with other spectrometers. Detectors to convert lights to electrical currents have greatly been developed. Photomultiplier tube (PMT), consists of a photocathode and a dynode, had been an unique device for receiving photons, efficient amplification of electrons, and generating electrical currents on measurement. Solid-state detectors, all of which are categorized under the term charge transfer device (CTD), are modern types of detectors having state-of-the-art technology. As the PMT is restricted to assess the signal at only one point, it costs not a few time to scan over spectral vicinity around an analyte line. Recent CTDs have several tens of squared micrometers in size, so are feasible to be spread over the area of a focal plane to obtain a two-dimensional picture of the spectra at once. They are called as array detectors and the smallest pictorial unit of a solid-state detector is called pixel. The CTDs are subcategorized in proportion to its characteristics; photodiode array (PDA), charge injection device (CID), charge coupled device (CCD), and segmented charge coupled device (SCCD), where the PDA were only installed in research instruments before development of the other ones. Their selection and usage is up to the vendors of ICP-AES in accordance with their developments.

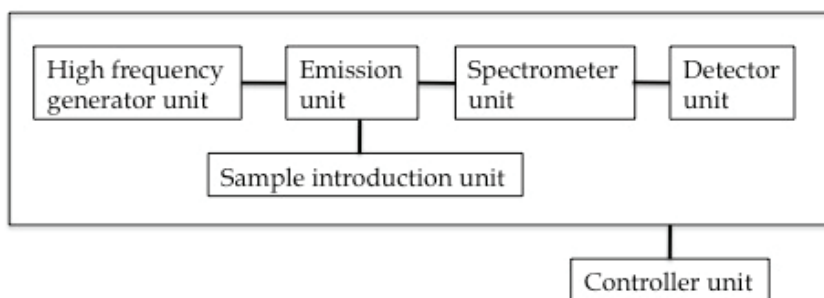


Fig. 2. Components of ICP-AES

In material analysis, a type of the radial viewing is recommended because effects of matrix elements with the radial viewing (magnesium and other minor elements in this case) are lighter than those with the axial one. Another reason can be claimed that damage of the outer tube in the torch during measurement is more severe when plasma turns on horizontally, which is the normal position of the axial viewing geometry.

A practical guide that links with theory and applications has been available to all levels of users (Nölte, 2003).

2.3 Atomic Absorption Spectrometry (AAS)

Another conventional method for determination of trace metals in materials is surely atomic absorption spectrometry. Chemical flames made from acetylene premixed with air or nitrous oxide is typically used for atomization. Electrical furnaces are also used, but all of them have maximum temperatures of c.a. 3000 K as the thermal sources, which cannot allow sufficient atomization for all elements. In addition, matrix interferences are more severe compared to ICP-AES due to relatively low temperatures. Sample solutions are usually aspirated and introduced as aerosols into a laminar flame, through which the specific light beam of an element passes to be absorbed by the atoms. Different from atomic emission, External radiation source is needed for atomic absorption. A hollow-cathode lamp (HCL) is widely used for an intense line source of individual element, which is a glass container with a hollow cylinder as cathode and a ring as anode filled in an inert gas under low pressure. The metal atoms sputtered with the inert gas are excited by collisions with electrons and emit the characteristic atomic emission lines. The bandwidth of the line from HCL is narrow enough that a spectrometer with higher resolution is not required than that of ICP-AES. Another invention in AAS is the modulation system of signal amplification. In all cases, voltage is applied to HCL in an alternating or a pulsing mode, thus emitting intermittent radiation. A detected absorption signal is magnified with a lock-in (phase-sensitive) amplifier that detect signal based on modulation at the same frequency as that of the line source. Consequently AAS can be equipped in relatively low costs and allows easier operation than other techniques on atomic spectrometry. A disadvantage of the AAS is of course on the requirement of setting of single elemental HCL one by one, although continuum source AAS with high resolution optics has recently been appeared on the market. Another disadvantage is the non-linearity of calibration curves due to self-absorption when absorbance becomes higher than 0.5 to 1, where a dynamic range more than one order of magnitude should not be expected.

AAS has a few more techniques on atomization and background correction; they should be referred to a tutorial and technical textbook for further understanding of the characteristics and practices of the AAS. (Vandecasteele & Block, 1993).

2.4 Inductively Coupled Plasma Mass Spectrometry (ICP-MS)

ICP-MS is definitely one of the prior tools for ultra trace analysis of metals in materials although sensitive types of modern ICP-AES can afford to measure the metals to a level of ng cm^{-3} (ppb) or so. For example, unalloyed magnesium with high purities must contain less than 0.001 % of lead and 0.00005 % of cadmium as denoted in the ASTM standard, hence measurements to a level of ppb or below in sample solutions are necessarily required for proper evaluation. ICP-MS will surely play a more important role on ultra trace analysis. Several types of mass spectrometers to combine ICP, which are not only quadrupole spectrometer but also magnetic sector, time of flight, ion trap ones *etc.*, have been developed. Among ICP-MS equipments those with quadrupole mass analyzer are most popular and often called ICP-QMS. One drawback of ICP-MS in material analysis is that it is not an optical analysis but a particle one, *i.e.* matrix elements introduced to the instrument are stored and accumulated on the mass analyzers and detectors different from the cases of ICP-AES. In ICP-AES, contamination of the matrix elements is restricted to the sample introduction unit that is demountable and easy to clean out. Consequently in ICP-MS, the background levels of matrix elements that appear in a historical record of measurements surely increase gradually due to contamination, which must be unavoidable especially in material analysis. At last, ratios of the concentration of an analyte to the tolerable concentrations of matrix elements to be loaded in the instruments are critical for measurements, not absolute concentration of the analyte. ICP-MS is remarkably more sensitive in the measurements but tolerable maximal concentration is also lower than ICP-AES. Modern technology may reveal that currently equipped ICP-AES should have priority even in the ultra trace analysis of materials.

A comprehensive handbook specialized on ICP-MS should be noticed. (Nelms, 2005)

2.5 Spark source Atomic (optical) Emission Spectrometry

Arc and spark excitation techniques are very common and have been used especially in metallurgical laboratories even now. Direct current arc, which consists of a continuous discharge between a pair of metal or graphite electrodes, is beneficial for sensitive qualification in spite of relatively poor precision. Sparks, intermittent electrical discharges of a few microseconds under high electrical potentials, are used for quantification in spite of poor sensitivity because of relatively high precision. Spark source AES requires no dissolution of a sample and only applies to conductive materials, therefore it especially suits metallic samples with flat surfaces, and is utilized for daily routine analysis in industrial laboratories.

One of the great disadvantages of spark source AES is the need of reference materials that must be exactly matched as possible in concentrations of both matrixes and analytes with the samples, which is a consequence that the method has strong matrix effects and no chemical preparation can be employed. As a matter of fact, this method is significantly effective in evaluation laboratories dealing with metallic materials connected with productive lines on condition that they can afford to have working reference materials verified with the other

techniques such as ICP-AES. Of course certified reference materials commercially available are valid, but vast kinds of them must be lined up before measurement.

2.6 X-ray Fluorescence spectrometry (XRF)

Identical to the atomic spectroscopy, X-ray spectroscopy is based on the measurements of emission, absorption, and fluorescence of electromagnetic radiation as well as its scattering and diffraction. Fluorescent spectrum of elements, accompanied by an electron transition from an outer shell to an inner one of the electron orbital, is specific on wavelength, *i.e.* energy of its own. It can be detected with two types of the instrument that has a wavelength-dispersive spectrometer and an energy-dispersive one. The latter allows relatively simple design without driving units. Moreover portable and handheld instruments of this type have recently been commercially available for *in situ* analysis. XRF has a big merit that allows direct measurements by contacting the device onto materials without dissolution processes. However if quantification is needed, XRF is highly dependent on the matrixes just like the spark source AES. Furthermore it depends on the flatness, roughness and coating conditions of a sample, thus reference materials that is exactly close to the sample in concentrations of matrixes, analytes, and surface conditions are required for determination. Fundamental parameter approaches for analysis of bulk and multilayer samples without standards have been investigated, where theoretical calculation of signal intensities originated from constituent elements seems to be successful to no small extent. Although the analytical results cannot be comparable in accuracy with atomic spectrometric techniques followed by dissolution, rough determination of metallic constituents in materials and identification of alloys are considered to be available using the fundamental parameter method.

3 Analytical procedures with ICP-AES

3.1 Concept of the testing and protocol

The analytical method to be proposed as a standard seems to be acceptable for practical technicians with various environments and skills because a committee for drafting standard methods must consists of the interested manufacturers and users of the material, and also independent staffs as advisers; namely, the standard method should be held in common between manufacturers, distributors, users, consumers, and researchers. In this study, prerequisites for the methods were concluded as follows: the methods involving experienced handling, such as separation and concentration procedure should be avoided as much as possible; commercial ICP-AES instruments are almost suitable for measurements in this method; reagents and glassware are commercially available and easily obtainable among laboratories; the methods satisfy routine analysis requirements. Therefore procedures involving simple dissolution with acids and volumetric preparation, sample nebulization, and matrix matched assay standards for calibration were developed as a protocol for the tests. On the other hand, details on pretreatment operations were left to the various styles of the participants.

3.2 Interlaboratory testing

The participants concerning the testing were technical staff members belonging to chemical laboratories of the organizations in Japan, organizations that make up one of the committees

of the Japan Magnesium Association. Another participant assisted in testing by spark source atomic emission spectrometry.

Two certified reference materials (CRM) and four real samples of magnesium and magnesium alloys were used. Two CRMs, a magnesium (No.C61XMgP20A) and a magnesium alloy (No.C65XMG50) supplied as chippings, were purchased from MBH Analytical Ltd. (Barnet, England), where the latter contains *c.a.* 8 % of aluminum, 0.4 % of zinc and 0.4 % of manganese in mass fraction. One of the real alloys named 'AZ91D' in the ASTM standard contains *c.a.* 9 % of aluminum, 0.7 % of zinc, and 0.3 % of manganese. Another one, 'AM60B', contains 6 % of aluminum and 0.4 % of manganese. All of the real samples were prepared by one of the participants, where the ingots were bored with drills and the drilled pieces were separately packed and sealed under an airtight condition using argon gas, which had *ca.* 20 g in mass per bag to be sent to the participants as test samples. The participants were requested to determine tin and lead in these samples by a following protocol of the analyses. In a second test they were requested to determine cadmium and beryllium by a similar protocol. The calibration procedure with matrix matching must be made using high-pure magnesium oxide with 99.99% (Kanto Chemicals, Tokyo), aluminum, and zinc. The analytical results must be reported as an average of the individually duplicate or triplicate runs.

The interlaboratory testing for determination of tin and lead had three series, the first of which is to check the validity of a protocol using the CRM and following determination of a real magnesium sample. The second series was to optimize matrix concentration of the sample solutions, which is indispensable to achieve for sample nebulization. Three matrix concentrations of 1, 2, and 4 % were prepared and measured separately. The last one was used to analyze real magnesium alloys with a matrix matching procedure under the optimized concentration.

All reagents used were of analytical grade or further highly purified grade, which were commercially available, and used without special designation.

Participants in eight organizations totally used nine ICP-AES equipments with eight different types in the testing, as shown in Table 3. Several different characteristics listed in the Table were useful in this study, considering that the standard methods to be constructed must be suitable for various types of equipments.

Model	Vendor	Viewing position	Nebulizer	Spray chamber	Spectrometer	Detector
(ICP-AES)						
PS-1000UV	LeemanLabs.	Radial	Hildebrand Grid	Scott	Echelle+Prism	PMT
SPS-1700HVR	Seiko	Radial	Concentric	Scott	Monochrometer	PMT
SPS1500VR	Seiko	Radial	Concentric	Scott	Monochrometer	PMT
SPS3000	Seiko	Radial	Concentric	Cyclonic	Monochrometer	PMT
SPS4000	Seiko	Radial	Concentric	Scott	Monochrometer	PMT
SPS7800	Seiko	Radial	Concentric	Scott	Monochrometer	PMT
Vista-MPX	Varian	Axial	Concentric	Cyclonic	Echelle+Prism	CCD
Vista-Pro	Varian	Axial	Concentric	Cyclonic	Echelle+Prism	CCD
(Spark Source AES)						
PDA-5500 II	Shimadzu	-	-	-	Polychromator	PMT

Table 3. Instruments of ICP-AES and Spark AES used in the interlaboratory testing

3.3 Protocol for the testing

A protocol for the dissolution of a sample as preparation was documented as follows:

1. One gram of a sample was weighed to a digit of 0.1mg and transferred to a borosilicate beaker of an appropriate size (200~300 cm³).
2. Concentric nitric and hydrochloric acids of high purity were diluted twice with water, respectively, to make their stock solutions, *i.e.* 6.0 mol dm⁻³ of hydrochloric acid and 6.8 mol dm⁻³ of nitric acid.
3. Water as well as the twice-diluted nitric and hydrochloric acid solutions were poured into a beaker, which was subsequently covered with a watch glass, and the sample was dissolved through conventional heating after a vigorous reaction with the evolution of nitrogen dioxide gas. The dissolution process was gentle on heating so as to suppress the volatilization of acids.
4. The sample was prepared to a solution to 50 cm³ with a volumetric flask, which contained a matrix concentration of 2 %.
5. The prepared solutions were made to finally have 0.4 mol dm⁻³ of nitric acid and 0.1 mol dm⁻³ of hydrochloric acid. The volumes and orders of the acids to be added are up to the participants.
6. To weigh 2 g of a sample and to prepare a solution to 100 cm³ was also acceptable as an alternative operation.
7. A sample had to be pretreated in duplicate or triplicate runs.

In the second series, the above-mentioned protocol was modified so as to prepare sample solutions of 4%, *i.e.* 2 g (4 g) of a sample was weighed to dissolve and prepare a solution of 50 cm³ (100 cm³), thereby allowing subsequent dilution to those of 2 and 1 %.

A protocol for the preparation of standard solutions was documented as follows:

1. Magnesium oxide (99.99 % or higher in purity) was dissolved with a nitric acid solution, to prepare a 4 % solution of magnesium(II) in 0.4 mol dm⁻³ of nitric acid and 0.1 mol dm⁻³ of hydrochloric acid.
2. Aluminum (99.99 % or higher in purity) was dissolved with the nitric and hydrochloric acid solutions by five to one in volume, to prepare 0.36 % solution of aluminum(III) in 0.5 mol dm⁻³ of nitric acid.
3. Zinc (99.99 % or higher in purity) was dissolved with the nitric acid solutions, to prepare a 0.1 % solution of zinc(II) in 0.5 mol dm⁻³ of nitric acid.
4. A series of standard assay solutions of tin and lead having concentrations of 0, 0.5, and 1.0 µg cm⁻³ for metal samples and 0, 1.0, and 2.0 µg cm⁻³ for alloy ones were prepared, by diluting commercially available 1 mg cm⁻³ standard solutions of the metals or their solutions of the same concentrations prepared by dissolving high pure metals. Another series of cadmium and beryllium of 0, 0.5, and 1.0 µg cm⁻³ were prepared separately for the second test. The concentrations of matrix components had to be identical with the samples, by diluting the stock solutions of the elements as stated: Mg 2 % (unalloyed metal), Mg 1.8 %-Al 0.18 %- Zn 0.02 % (AZ91D alloy), Mg 1.88 %-Al 0.12 % (AZ60B alloy). The calibration ranges could vary appropriately according to the contents of the samples.

A Protocol for a measurement with ICP-AES was documented as follows:

The sample solutions were nebulized to be introduced directly into the plasma. Atomic emission spectra, free from spectral interferences, should be visually identified at two affordable wavelengths, where the background wavelengths are pointed out at both ends of each peak. After introducing the assay standard solutions to make a calibration line, the

sample solutions are aspirated. If repeated measurements (usually in triplicate) showed a descending tendency, the sample and standard solutions had to be prepared with an internal standard element, such as cobalt(II), thus suppressing the influence of any clogging at the orifice of a nebulizer.

4. Results of the interlaboratory testing

4.1 Results of tin and lead in the testing

Table 4 gives results of interlaboratory testing in the first series, analytical values of tin and lead of the CRM, magnesium. Each laboratory reported average values of independent duplicate or triplicate runs with adequate repeatability. The data by different analysts, dates, or equipment in the same laboratory were regarded as independent data sources. Fairly good accuracy, *i.e.* trueness and precision, was achieved by comparing the average values with the certified values of the CRM and the standard deviations with their uncertainties, respectively. Moreover, comparable data with spark source atomic emission spectrometry using an identical CRM supplied as a disk could be obtained to show that the concentration of tin and lead were 71 and 59 $\mu\text{g g}^{-1}$, respectively, which confirmed the accuracy of the data and the validity of the protocol.

Data No.	C _{Sn}	C _{Pb}
1	70	55
2	74	57
3	68	56
4	70	52
5	81	59
6	72	57
Average	73	56
SD	4.6	2.4
RSD, %	6.4	4.2
<i>n</i>	6	6
95% confidence interval	4.9	2.5
Certified values	73	61
Uncertainty ^a	6	7

Unit: $\mu\text{g g}^{-1}$

a. Noted in the certificate as the 95% confidence interval derived from the analysis results

Table 4. Tin and lead concentrations in the certified reference material of magnesium as the interlaboratory testing

Table 5 gives the effect of the matrix concentrations and the type of nebulizers, as well as the results in the second series of testing. The decreased number of available data is due to not only troublesome operations, but also the fact that the nebulizers for high salt concentrations were already installed into the ICP-AES instruments in the laboratories of the participants.

Data No.	$C_{Pb} / \mu\text{g g}^{-1}$					
	Standard nebulizer			High salts nebulizer		
	$C_{Mg}, \%$			$C_{Mg}, \%$		
	1	2	4	1	2	4
1	4.0	4.7	4.7	6.0	6.3	6.0
2	6.0	6.7	7.3	5.3	7.3	6.7
3	—	—	—	6.0	5.1	4.0
4	—	—	—	5.8	5.7	5.7
Average	5.0	5.7	6.0	5.8	6.1	5.6
SD	1.4	1.4	1.9	0.3	1.0	1.1
RSD, %	28	25	31	5	16	20
<i>n</i>	2	2	2	4	4	4

Table 5. Effect of matrix concentrations and type of nebulizers on lead concentrations in the real sample of magnesium

The data of No.1 and No.2 could be compared in detail, as shown in Table 6. In the former, concentric nebulizers of standard ('TR-30-A2') and high salts ('TR-30-C2') made by Meinhard Glass Products (Colorado, USA) and SPS4000 were used for measurements. In the latter, those of standard ('Conical') and high salts ('SeaSpray') made by Glass Expansion (West Melbourne, Australia) and Vista-Pro were used. In both Tables, the data seem to be independent of the matrix concentrations, but their precision obtained using nebulizers for high salt concentrations was better than those using standard ones. It is noteworthy to mention that there occurred a certain type of damage onto the outer tube and clogging of the inner tube in a plasma torch due to the introduction of solutions of 4 % for hours, especially into a horizontally aligned torch for axial viewing. Solutions of 1 % may have had insufficient emission peaks on insensitive instruments. Hence, the preparation of a sample solution to a matrix concentration of 2 % and measurements using nebulizers for high salt concentrations were considered to be preferable. Besides, another type of nebulizers for high salt concentrations, named Hildebrand grid nebulizer (Teledyne Leeman Labs., New Hampshire, USA) is also available.

Table 7 gives the results of interlaboratory testing in the first and third series on the real samples of magnesium and magnesium alloys, which were also average values of independent duplicate or triplicate runs with severally adequate repeatability. In the third series, a concentric nebulizer for high salt concentrations, 'SeaSpray' nebulizer was distributed to each participant in advance for acquiring better precision. Slight atomic emission peaks could only be observed for measurements of tin in all the real samples, which led to determinations with poor precision. But the results were adequate as JIS standards because the corresponding material standards describe upper limits of $50 \mu\text{g g}^{-1}$ for tin. The concentrations of lead in the samples were fairly good on reproducibility, as shown in the table. Although some more information on reliability may well be reported as measurement uncertainty, validity of the protocol using the CRM and dispersive characteristics expressed as standard deviations were separately taken into account for discussion. The reasons are as follows: many practical problems about measurement uncertainty encountered by accredited testing laboratories have been claimed; (Visser, 2004) the participants in industry were reluctant to make use of the available measurement uncertainties owing to their unfamiliarity. Also, the reproducibility of the analytical data

used in this study is one of the major factors that contribute to the total measurement uncertainty, considering that the analytical data coincided well with their certified values.

Matrix concentration, %	Run	$C_{Pb} / \mu\text{g g}^{-1}$	
		Type of nebulizer	
		Standard ('TR-30-A2')	High salts ('TR-30-C2')
1	1st	5	5
	2nd	4	6
	3rd	3	7
	Average	4.0	6.0
	SD	1.0	1.0
	RSD, %	25	17
2	1st	5	6
	2nd	4	7
	3rd	5	6
	Average	4.7	6.3
	SD	0.6	0.6
	RSD, %	12	9
4	1st	5	6
	2nd	4	6
	3rd	5	6
	Average	4.7	6.0
	SD	0.6	0.0
	RSD, %	12	0

a. Meinhard nebulizers of standard ("TR-30-A2") and high salt concentrations ("TR-30-C2") and ICP-AES (SPS-4000) were used (data No.1 in Table 5)

Matrix concentration, %	Run	$C_{Pb} / \mu\text{g g}^{-1}$	
		Type of nebulizer	
		Standard ('Conikal')	High salts('SeaSpray')
1	1st	6	6
	2nd	7	5
	3rd	5	5
	Average	6.0	5.3
	SD	1.0	0.6
	RSD, %	17	11
2	1st	6	8
	2nd	8	8
	3rd	6	6
	Average	6.7	7.3
	SD	1.2	1.2
	RSD, %	17	16
4	1st	6	7
	2nd	8	7
	3rd	8	6
	Average	7.3	6.7
	SD	1.2	0.6
	RSD, %	16	9

b. Glass Expansion nebulizers of standard ("Conikal") and high salt concentrations ("SeaSpray") and ICP-AES (Vista-Pro) were used (data No.2 in Table 5)

Table 6. Effect of matrix concentrations and type of nebulizers on lead concentrations in the real sample of magnesium

Data No.	Unalloyed Mg		'AZ91D' alloy ^a		'AM60B' alloy ^b	
	Sn	Pb	Sn	Pb	Sn	Pb
1	2	7.5	4	44	0	9
2	—	—	5	39	-1 ^c	10
3	0.5	6.5	1	44	0	11
4	1	5	<1	53	<1	11
5	<1	2 ^c	<1	53	<1	12
6	3.1	9.7	1.4	41	2.5	10
7	—	—	2	40	1	8
8	—	—	2	41	1	9
9	1	6	2	41	1	9
10	1	6	—	—	—	—
Average	1.6	6.8	2.5	44	0.9	9.9
SD	1.0	1.6	1.5	5.4	0.9	1.3
RSD, %	59	24	59	12	100	13
<i>n</i>	6	6	7	9	6	9

Unit: $\mu\text{g g}^{-1}$.

a. Al, 9%; Zn, 0.7%; Mn, 0.3%

b. Al, 6%; Mn, 0.4%

c. Statistically omitted.

Table 7. Tin and lead concentrations in the real samples of magnesium and magnesium alloys as the interlaboratory testing

Data No.	C _{Cd}	C _{Be}
1	36	13
2	36	13
3	36	15
4	35	12
5	36	12
6	37	12
Average	36	13
SD	0.6	1.2
RSD, %	1.8	9.1
<i>n</i>	6	6
95% confidence interval	0.7	1.2
Certified values	35	13
Uncertainty ^a	3	1

Unit: $\mu\text{g g}^{-1}$.

a. Noted in the certificate as the 95% confidence interval derived from the analysis results.

Table 8. Cadmium and beryllium concentrations in the certified reference material of magnesium alloy as the interlaboratory testing

The influences of some characteristics of ICP-AES listed in Table 3 concerning the analytical data were investigated by sorting these data, which revealed no significant tendency. The average values of lead in the magnesium and magnesium alloys were almost independent of the type of chambers, viewing positions, and type of detectors studied. This may be natural, but is an important fact to be confirmed for constructing standards, especially on trace determination in coexisting matrices.

4.2 Results of cadmium and beryllium in another testing

Table 8 gives the results of another separate interlaboratory testing, determination of cadmium and beryllium of the CRM, magnesium alloy. The remarks of the values in the table were almost the same as those in Table 4. Fairly good accuracy was also achieved in the case of the magnesium alloy. Cadmium and beryllium are more sensitive than tin and

Data No.	Unalloyed Mg-1		Unalloyed Mg-2		'AZ91D' alloy ^a		'AM60B' alloy ^b	
	Cd	Be	Cd	Be	Cd	Be	Cd	Be
1	0	0	0	0	0.4	8	0	11
2	0.1	0	0	0	0.5	8	0	11
3	0	0	0	0	0.6	8	0	11
4	0.1	0	0.1	0	0.6	6	0.1	4.6
5	<1	<1	<1	<1	0.6	12	<1	9
6	-0.06 ^c	-0.12 ^c	0.16	-0.05 ^c	0.6	13	4	8.5
7	0.01	0.02	0	0	0.6	11	0.06	8.6
8	<2	<0.2	<2	<0.2	<2	11	<2	8.8
9	<6	<0.1	<6	<0.1	<6	11	<6	8.6
Average	0.0	0.0	0.0	0.0	0.6	10	0.7	9.1
SD	0.1	0.0	0.1	0.0	0.1	2.3	1.6	2.1
RSD, %	-	-	-	-	14	24	234	23
<i>n</i>	5	5	6	5	7	9	6	9

Unit: $\mu\text{g g}^{-1}$.

a. Al, 9%; Zn, 0.7%; Mn, 0.3%

b. Al, 6%; Mn, 0.4%

c. Statistically omitted.

Table 9. Cadmium and beryllium concentrations in the real samples of magnesium and magnesium alloys as the interlaboratory testing

lead, therefore easier to determine with ICP-AES. Table 9 gives the results on the real samples of magnesium and magnesium alloys, where concentrations of cadmium were too low to show significant values. In most cases, beryllium is added to magnesium alloy ingots for die castings to enhance their incombustibility; hence it could be naturally determined to *ca.* 10 $\mu\text{g g}^{-1}$. Beryllium is denoted in JIS H 2222 and allowed to use as an additive element to mass fraction of 0.0005-0.0015 %, but is very toxic as well as cadmium. It should be monitored not to exceed the permissive levels in the material.

5. Standardization of the analytical methods

The protocols evaluated in the testing were acceptable for not only the participants but also whom it might concern in Japan. They were fleshed out, formatted and submitted to an analytical committee of the magnesium industry, Japan Magnesium Association, as the original drafts for JIS standards. After an interview by Japan Industrial Standards Committee (JISC), they have been revised and provided as JIS standards. The three of them (JIS H1342, 2008; JIS H1343, 2008; JIS H1344, 2010) are newly established standards with ICP-AES, while the remainder (JIS H1339, 2010) is an updated one with ICP-AES, in addition to the flame AAS already denoted in an earlier version.

In ISO, there has been a recent action for standardization of the analytical method in the material. A standard named 'determination of lead and cadmium' is now under the level of Draft International Standard (ISO/DIS 11707, 2010), where a technical committee /subcommittee named TC79/SC5, the title of which is 'magnesium and alloys of cast and wrought magnesium', deals with this standard. The author commits himself to this standard with the achievement of the ICP-AES techniques as mentioned in this study. He has also proposed to standardize new methods for determination of another hazardous trace metals in magnesium and magnesium alloys as a future work in ISO.

6. Conclusion

This study was designed in order to obtain an analytical basis for the concerned new standard methods with ICP-AES. In order to put excellent evaluation of the materials into practice, we must continuously know much about the analytical instruments and their characteristics. Magnesium alloys will further be developed in a wider variety as special lightweight materials; moreover a forecoming 'sound material-cycle society' will require another evaluation for used materials. Material development and its analysis as evaluation should be forwarded in a body. Furthermore, international standardization must be accompanied with its advance in order to obtain better performance in production and distribution of the material.

7. References

ASTM B 92/B 92M-07 (2007). Standard Specification for Unalloyed Magnesium Ingot and Stick for Remelting, ASTM International, Pennsylvania.

- ASTM B 93/B 93M-07 (2007). Standard Specification for Magnesium Alloys in Ingot Form for Sand Castings, Permanent Mold Castings and Die Castings, ASTM International, Pennsylvania.
- ASTM B 107/B 107M-07 (2007). Standard Specification for Magnesium-Alloy Extruded Bars, Rods, Profiles, Tubes, and Wire, ASTM International, Pennsylvania.
- ASTM E35-88 (2002). Standard Test Methods for Chemical Analysis of Magnesium and Magnesium Alloys, (Withdrawn 2008), ASTM International, Pennsylvania.
- ASTM B954-07 (2007). Standard Test Method for Analysis of Magnesium and Magnesium Alloys by Atomic Emission Spectrometry", ASTM International, Pennsylvania.
- Broekaert, J.A. (2005). Analytical Atomic Spectrometry with Flames and Plasmas, Second, Completely Revised and Extended Edition, Wiley-VCH, ISBN 3-527-31282-X, Weinheim
- ISO 3116 (2007). Magnesium and magnesium alloys - Wrought magnesium alloys, International Organization for Standardization, Geneva.
- ISO 8287 (2000). Magnesium and magnesium alloys - Unalloyed magnesium -Chemical composition, International Organization for Standardization, Geneva.
- ISO 16220 (2005). Magnesium and magnesium alloys - Magnesium alloy ingots and casting, International Organization for Standardization, Geneva.
- ISO/DIS 11707 (2010). Magnesium and magnesium alloys - Determination of lead and cadmium, International Organization for Standardization, Geneva.
- JIS H 2150 (2006). Magnesium Ingots, Japan Industrial Standards Committee, Tokyo.
- JIS H 2221 (2006). Magnesium Alloy Ingots for Castings, Japan Industrial Standards Committee, Tokyo
- JIS H 2222 (2006). Magnesium Alloy Ingots for Die Castings, Japan Industrial Standards Committee, Tokyo
- JIS H 1342 (2008). Methods for Determination of Tin in Magnesium and Magnesium Alloys, Japan Industrial Standards Committee, Tokyo.
- JIS H 1343 (2008). Methods for Determination of Lead in Magnesium and Magnesium Alloys, Japan Industrial Standards Committee, Tokyo.
- JIS H 1339 (2010). Methods for Determination of Beryllium in Magnesium and Magnesium Alloys, Japan Industrial Standards Committee, Tokyo.
- JIS H 1344 (2010). Methods for Determination of Cadmium in Magnesium and Magnesium Alloys, Japan Industrial Standards Committee, Tokyo.
- Nelms, S.M. ed. (2005). ICP Mass Spectrometry Handbook, Blackwell Publishing, ISBN 978-1-4051-0916-5, Oxford.
- Nölte, J. (2003). ICP Emission Spectrometry A practical Guide, Wiley-VCH, ISBN 3-527-30672-2, Weinheim
- Rokhlin, L.L. (2003). Magnesium Alloys Containing Rare Earth Metals, Taylor & Francis, ISBN 0-415-28414-7, London
- Uemoto, M.; Nagaoka, M. & Fujinuma, H. (2009). Interlaboratory Testing for Determination of Trace Amounts of Tin and Lead in Magnesium and Magnesium Alloys by Inductively Coupled Plasma Atomic Emission Spectrometry, Analytical Sciences, Vol.25, No.5, 717-721, ISSN 0910-6340

- Uemoto, M. ed (2008). Principles and practices of ICP emission and ICP mass spectrometry, Ohmsha, ISBN 978-4-274-20539-2, Tokyo (in Japanese).
- Vandecasteele, C. & Block, C.B. (1993). Modern Methods for Trace Element Determination, John Wiley & Sons, ISBN 0-471-94039-9, Chichester
- Visser, R (2004). Measurement uncertainty: practical problems encountered by accredited testing laboratories, *Accred. Qual. Assur.*, Vol.9, No.11-12, 717-723, ISSN 0949-1775.
- Welz, B. & Borges, D.L.G.(2009). Atomic Spectrometry and Elemental Analysis, In: *Encyclopedia of Applied Spectroscopy*, Andrews, D.L. (Ed.), 421-476, Wiley-VCH, ISBN 978-3-527-40773-6, Weinheim